Feasibility Study of a Heat-powered Liquid Piston Stirling Cooler

Samuel Blair Langdon-Arms

PhD

2017

Feasibility Study of a Heat-powered Liquid Piston Stirling Cooler

Samuel Langdon-Arms

Design and Creative Technologies

Department of Mechanical Engineering

2017

A thesis submitted to

Auckland University of Technology

in fulfilment of the requirements for the degree of

Doctor of Philosophy

Abstract

This thesis presents a feasibility study of the proposed liquid piston Stirling cooler or LPSC, which is a 4-cylinder double-acting alpha-type Stirling machine capable of utilising a heat input to produce a cooling effect. The novel aspects of the work include: (a) the first known experimental results of the two heater-LPSC configuration, and the associated performance predictions from a validated third order computer model; (b) development of two independent methods for obtaining the system's operational frequency; (c) evidence and quantification of the Rayleigh-Taylor instability in reciprocating liquid pistons, and the mitigation of this instability via the use of piston floats; and finally (d) the development of design constraints and recommendations specific to the LPSC.

The LPSC is a tri-thermal, thermo-mechanical, free-piston system based on the Siemens-Stirling configuration first proposed in the late 1970s. A test-rig was constructed and used as part of an experimental investigation into understanding the complex multi-degree of freedom system and identifying its feasibility for heat-powered cooling applications. In its current, un-optimised state, it has proven to be functional over a wide range of mean gas pressures (1 bar–6 bar) and relatively low heat source temperatures (80°C–150°C). A third order model of the LPSC was constructed in the computer modelling software, Sage. The model encompasses the complex system dynamics and heat transfer characteristics and is validated against experimental results. The model was used to predict a more optimised piston geometry which led to the first tangible cooling effect in subsequent experiments, in the range of 5°C below ambient.

Evidence of a liquid piston acceleration limit, likely resulting from the Rayleigh-Taylor (RT) instability phenomenon, is consistently observed during the experiments. The use of submerged polyethylene piston floats is found to increase surface stability and enable

maximum accelerations of 25 ms^{-2} to 30 ms^{-2}. The two heater configuration, with two adjacent heated spaces connected in series with two adjacent absorber spaces, is shown to be the optimal configuration for cooling performance, with relative phase angles close to 90° and a conversion ratio of heater gas pressure amplitude to absorber gas pressure amplitude of 1.02 to 1. When considering test-rig performance at 150°C heater temperature and a maximum charge pressure of 6 bar, the Sage model predicts a thermal COP of 0.53 for the current set-up (19.3 mm diameter, 94 cm long liquid water pistons). This rises to 0.59 with the installation of 23 mm diameter, 3 m long liquid pistons. When the working gas in the model is replaced with hydrogen, the performance of the LPSC increases significantly: the COP increases by 2.7%, to 0.6, the cooling capacity increases by 59.1%, the cold-side temperature in the primary absorber is decreased from 13.1°C to 7°C, and the second law efficiency increases from 5.3% to 9.9%.

A number of design considerations for the LPSC are explored. The existence of a potential piston acceleration limit imposed by the RT instability imposes a constraint on the minimum piston length. A crude capacity evaluation is also conducted, which indicates that a LPSC capable of generating a cooling effect of approximately 5 kW is feasible using 15 L liquid water pistons. Based on the research findings, it is deduced that such an LPSC system is feasible both technically and commercially, although to what extent in either regard is still unknown.

Table of Contents

Attestation of Authorship

I hereby declare that this submission is my own work and that, to the best of my knowledge and belief, it contains no material previously published or written by another person (except where explicitly defined in the acknowledgements), nor material which to a substantial extent has been submitted for the award of any other degree or diploma of a university or other institution of higher learning.

Signed:

Samuel Langdon-Arms

List of Figures

List of Tables

List of Abbreviations

0HEAT	LPSC configuration with zero heaters
2HEAT	LPSC configuration with two heaters
3HEAT	LPSC configuration with three heaters
4HEAT	LPSC configuration with four heaters
BDC	Bottom Dead Centre
CFCs	Chlorofluorocarbons
CFD	Computational Fluid Dynamics
CHP	Combined Heat and Power
COP	Coefficient of Performance
DAQ	Data Acquisition
EOM	Equation of Motion
FPSE	Free-Piston Stirling Engine
GS	Gas Space
HCFCs	Hydrochlorofluorocarbons
HX	Heat Exchanger
ID	Inner Diameter
IEA	International Energy Agency
IECEC	International Energy Conversion Engineering Conference
ISEC	International Stirling Engine Conference
LH	Left Hand
LPSC	Liquid Piston Stirling Cooler
MDOF	Multiple Degrees of Freedom
OD	Outer Diameter
ODE	Ordinary Differential Equation
OECD	Organisation for Economic Co-operation and Development
ORC	Organic Rankine Cycle
PID	Proportional-Integral-Derivative
PV	Photovoltaic

PV-T	Photovoltaic-Thermal
PVC	Polyvinyl Chloride
REHC	Renewable Energy Heating and Cooling
RH	Right Hand
RT	Rayleigh-Taylor
SACE	Solar Air Conditioning in Europe
SHC	Solar Heating and Cooling
SSR	Solid State Relay
TDC	Top Dead Centre
TES	Thermal Energy Storage
VC	Vapour Compression

Acknowledgements

Firstly, I would like to thank my two main supervisors. To Dr Martin Neumaier, who hosted/tolerated me during my (extended) stay in Germany, you were an absolute pleasure to work with and I will miss our mid-afternoon coffee-infused discussions almost as much as I will the German beer. To Dr Michael Gschwendtner, during the course of this project your council and support, both academically and personally, has been absolutely immense, and far in excess of what is mandatory (from a job requirement standpoint). I can't imagine having guidance from a better mentor or friend, and I am extremely grateful your extensive list of virtues included patience.

I would like to acknowledge the financial support of AUT university for facilitating this research opportunity, Fachhochschule Rosenheim for hosting me during my time in Germany, and the Todd Foundation, who supported this research since it began in 2013. A Special mention should also be made for TS-dot Engineering Limited for initiating this project.

I would also like to express my gratitude to my friends and family who have stubbornly supported me from the outset. Specifically: my mother Michelle Arms; my father Blair Langdon; my sister Kate Langdon-Arms; and lastly, my fiancé Nicolette Bobsien, for her tireless love, encouragement and friendship during this journey.

For Nelva Arms and Kay Langdon

Intellectual Property Rights

The work described in this thesis is a continuation of a joint project between Samuel Langdon-Arms, the New Zealand sponsor company TS-dot Engineering Limited, and the University of Applied Sciences Rosenheim in Germany.

Confidential Material

This thesis contains confidential and commercially sensitive material. It is under restricted access until 1 December 2019.

Nomenclature

A	Liquid piston surface area
A_S	Solar collector surface area
A_x	Flow area in x-direction
C	Damping constant
C_p	Capacitance of a parallel-plate capacitor
COP	Coefficient of performance
d_p	Separation distance between plates
e	Mass-specific total gas energy
$\dot{E}_{vis}$	Rate of viscous energy loss
$\dot{E}_{kin}$	Rate of kinetic energy loss
f	Frequency
F	Experience factor
g	Gravitational constant
I_p	Solar irradiance
k	Spring constant
k_p	Liquid piston spring constant
K	Kinetic flow loss coefficient
L	Liquid piston length
m	Liquid piston mass
n	Unit outward normal vector of surface, s
p	Pressure
p_0	Charge pressure
P	Power
q	Axial heat flux
q	Heat-flux vector
Q_w	Empirical film heat transfer per unit length
Q_A	Heat rejected to ambient
Q_C	Heat rejected to ambient

Q_E	Heat absorber as the cooling effect
Q_G	Heat supplied by solar thermal collector
Q_S	Heat energy deposited to the solar collector
R	Gas constant
R_F	Viscous flow resistance term
R_t	Liquid piston U-tube radius
s	Surface of volume, v
t	Time
T_C	Cold-side temperature
T_H	Hot-side temperature
T_L	Low temperature
T_M	Medium temperature
T_{max}	Maximum temperature
T_{min}	Minimum temperature
v	Control volume
V_0	Mean gas volume
V_S	Swept volume
V_{lp}	Liquid piston volume
$\mathbf{V}$	Newtonian-frame flow velocity vector
$\boldsymbol{V_r}$	Boundary-relative flow velocity vector
W	Work
x	Displacement
X	Displacement amplitude
α_{Max}	Maximum acceleration limit
γ	Ratio of specific heats
ε	Mass-specific internal energy
ε_r	Dielectric material constant
ε_0	Electric constant
η	Thermal efficiency

ρ	Density
$\boldsymbol{\sigma}$	Stress tensor
φ	Phase angle
ω	Angular frequency

1 Introduction

1.1 Energy from the Sun

It is almost trivial to observe—but nonetheless very true—that all life on Earth is dependent on the sun's incoming radiation (along with a small amount of geothermal energy). Indeed, from an evolutionary perspective, it is unlikely that complex life would have been possible without the sun providing a near-constant source of energy into Earth's 'closed' thermodynamic system.

Humankind's dependence on the sun has changed dramatically throughout our history as a species. Prior to the Neolithic Revolution (approximately 12,000 years ago) humans relied on the sun only for light and warmth (Bocquet-Appel, 2011). It was not until the development and adoption of agriculture that humans began to actively control and wield the sun's power. Cultivated crops and domesticated animals allowed large centralised populations to exist, which eventually led to non-farming specialists who drove rapid technological advancement.

Humans began to replace themselves as prime movers in energy-intensive processes, firstly with animals, and then with mechanical systems such as waterwheels and windmills. Although stored solar energy in the form of biomass had long been used for heating and basic manufacturing, it was discovered that even greater benefits were offered by stored solar energy in the form of fossil fuels—the high energy density and relative abundance allowed large amounts of energy to be rapidly procured, easily transported, and efficiently released when desired.

Over the last hundred years humankind has consumed fossil fuels at a rate never before seen or even contemplated; the sheer quantity of atmospheric emissions has begun to transform the Earth's climate and ecosystems. Along with the limited availability of

fossil fuel resources, this fact has led to a conscientious push for the development of new sustainable technologies capable of reducing our consumption and dependence on fossil fuels. Advancements made in the understanding of the physical world (including mathematics, thermodynamics, material science, and electromagnetism) mean that we can convert the sun's solar energy directly into a number of usable forms for a large range of end-use objectives—including transportation, power generation, and water treatment, as well as process heating, cooling, and air-conditioning.

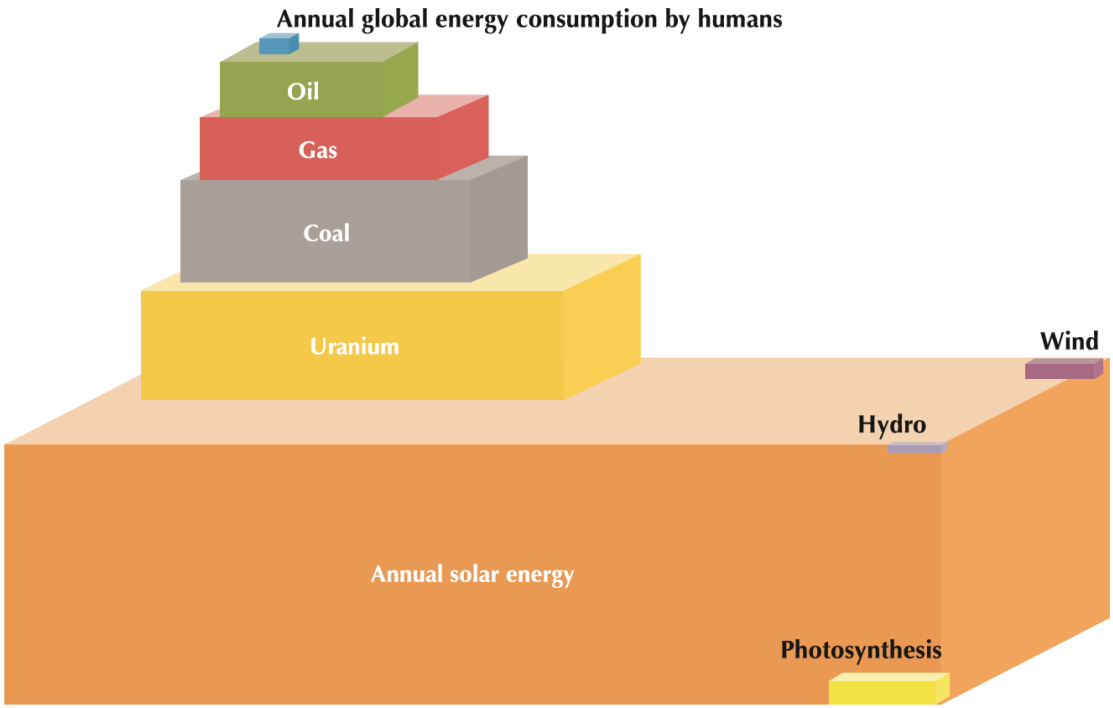

Figure 1.1 – Total energy resources.
© OECD/IEA 2011 "Solar Energy Perspectives" IEA Publishing. Licence: www.iea.org/t&c.

It is now possible to quantify the available potential of the solar resource that would be required to replace fossil fuels. The solar radiation which reaches Earth's biosphere (after subtracting about 30% of the incoming radiation which is reflected away) totals approximately 3.8 YJ per annum (Smil, 2010). This figure is four orders of magnitude greater than the world's total final energy consumption reported by the International Energy Agency (IEA) for 2010, of 8677 million tonnes of oil equivalent or 363 EJ (IEA, 2012). This means that one hour's worth of incident solar radiation is more than the total

energy that human civilisation currently uses in a year. Figure 1.1 shows the relative scales of energy sources available. The main omission is geothermal energy, which has a very high theoretical potential, but is likely to be much harder to exploit than solar energy.

1.2 Solar Heating and Cooling Rationale

Research into Solar Heating and Cooling (SHC) has attracted a great deal of interest over the last few decades. SHC utilises the distributed nature of the solar resource to provide tailored direct heating and cooling services where needed. In 1977 the International Energy Agency established the SHC Programme as one of its first initiatives. The IEA is an autonomous body which was founded in 1974, within the framework of the Organisation for Economic Co-operation and Development (OECD), to implement an international energy programme. New Zealand is one of 29 member countries of the IEA (IEA, 2016).

One of the agency's main aims is to improve the world's energy supply and demand structure by developing alternative energy sources, and increasing the efficiency of energy use. In 2007 the IEA released a publication entitled 'Renewables for Heating and Cooling – Untapped Potential'. This publication reviewed the technologies, market conditions and relative costs for heat and cold production using biomass, geothermal and solar-assisted systems (IEA, 2007). Within this report, Renewable Energy Heating and Cooling (REHC) was described as the "sleeping giant" of renewable energy potential from a global perspective. The report stated that: "In recent years, and in many regions, policies developed to encourage the wider deployment of renewable electricity generation, transport bio-fuels and energy efficiency have over-shadowed policies aimed at REHC technology deployment." (p. 15).

In 2012 the IEA released another report entitled "Technology Roadmap – Solar Heating and Cooling" (IEA, 2012). In this document the IEA identifies the present day rationale

for SHC, including increased resilience against the volatility of oil, gas and electricity prices, reduced transmission costs, and the creation of regional and local jobs. According to this report, "… by 2050, solar energy could annually produce 16.5 EJ of solar heating, more than 16% of total final energy use for low temperature heat, and 1.5 EJ solar cooling, nearly 17% of total energy use for cooling. For solar heating and cooling to play its full role in the coming energy revolution, concerted action is required by scientists, industry, governments, financing institutions and the public." (p. 1).

1.3 Solar Cooling Background

In many ways solar energy is more suited to cooling applications than it is to heating. Solar cooling technologies benefit from the strong correlation between the intensity of the solar resource and the energy demand for cooling, especially for air-conditioning applications. Figure 1.2 compares the annual heating and cooling demand profiles with the solar collector supply potential in Central Europe.

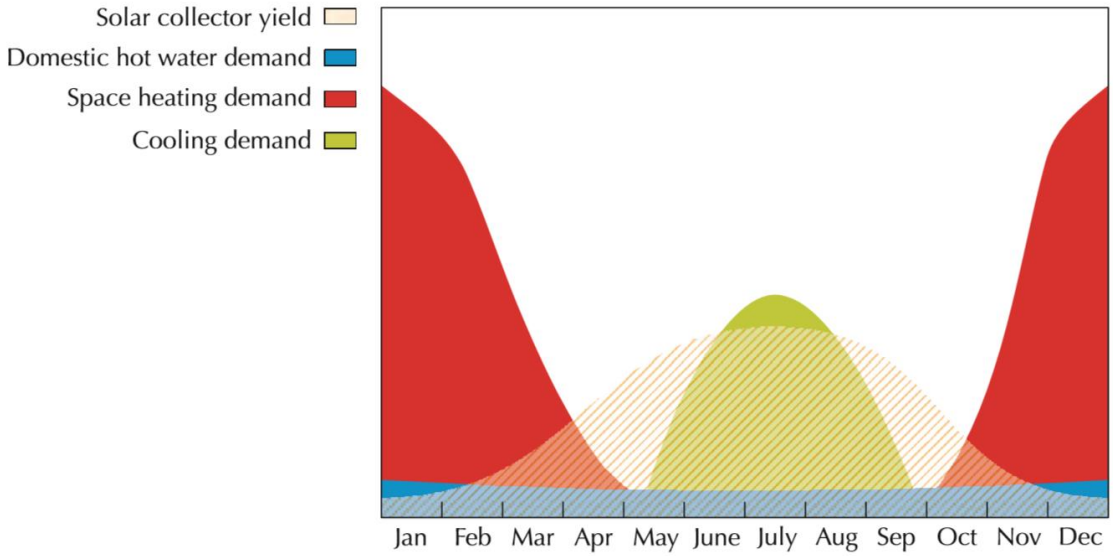

Figure 1.2 – Heating and cooling demand profiles compared with solar collector supply for Central Europe. © OECD/IEA 2011 "Solar Energy Perspectives" IEA Publishing. Licence: www.iea.org/t&c.

The International Institute for Refrigeration (IIR) estimated that 15% of total electricity production is used for refrigeration and air-conditioning—with these processes

accounting for 45% of the total energy demand in domestic and commercial buildings. Cooling demand is rapidly increasing in many parts of the world, particularly in moderate climates. The potential for solar air-conditioning systems in Europe was highlighted by Balaras et al. (2007). The authors referred to the rapid growth of the air-conditioning industry as a leading cause in the dramatic increase in electricity demand. This is creating peak loads for electric utilities during hot summer days, which frequently leads to 'brown out' conditions when the grid is barely capable of meeting demand. The spread of solar cooling technologies would contribute to the reduction of this peak loading scenario and the unnecessary use of fossil and nuclear energy currently being relied upon.

Solar cooling technology can be traced back to the 1878 Universal Exposition in Paris, when Augustin Mouchot and his assistant, Abel Pifre, showcased their 'sun Engine' and produced the first block of ice using concentrated solar energy[1] (Perlin, 1999). But, even so, solar cooling technology is still in its relative infancy compared to solar heating technology. Solar heating technology first saw large-scale deployment with solar water heaters in countries such as Japan, Australia, and Israel during the 1960s (IEA, 2011). Since then, new technologies for other applications have been developed and adopted for a range of other uses. Solar refrigeration, on the other hand, received great interest during the 1970s oil crisis. While this interest continued into the 1980s, improvements in the competing vapour compression technology as well as higher generation efficiencies in electrical power plants have hindered its commercial viability (Lamp & Ziegler, 1998).

In 2010 the global solar thermal collector capacity equalled 195.8 GW (thermal), corresponding to 279.7 million square metres of collector surface area. By the end of 2011 this figure was estimated to have grown by 25% to 245 GW (Weiss and Mauthner, 2012,

[1] The method used was an early form of absorption cooling, with the concentrated solar heat engine producing steam, which provided the heat input to drive an absorption cycle based on an ammonia solution.

as cited in IEA, 2012). At this same point in time, it was estimated that only 750 solar cooling technology systems had been installed worldwide (Mugnier and Jakob 2012, as cited in IEA, 2012), accounting for a tiny fraction of total installed solar collector capacity (< 0.1%).

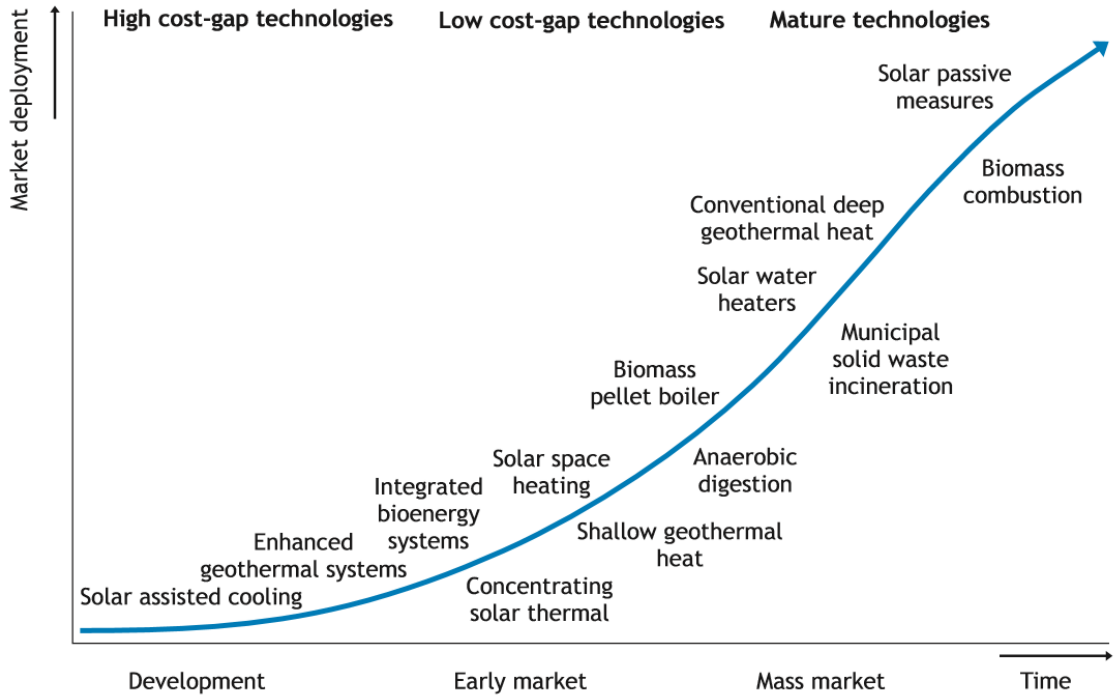

Figure 1.3 – Renewable Heating and Cooling Technology Development.
© OECD/IEA 2007 "Renewables for Heating and Cooling" IEA Publishing. Licence: www.iea.org/t&c.

Figure 1.3 depicts the current market deployment positions of renewable heating and cooling technologies. Solar-assisted cooling technologies are designated as being in the development stage. This stage is characterised by a much higher cost than conventional refrigeration technology. While the economics of large systems have been more favourable (due to economies of scale and equipment limitations in smaller capacities), the installation of small (<20 kW) solar cooling "kit" systems did increase considerably leading up until the economic crisis in 2008. At this point, new installations almost completely stopped (IEA, 2012): "Significant market growth is expected once the costs are further reduced as a result of continued research, development & demonstration investment." (IEA, 2007).

1.4 Research Objectives

This research project conducts a feasibility study into an integrated heat-powered Stirling refrigerator that employs liquid pistons. This machine is termed the liquid piston Stirling cooler (LPSC) and the underlying principle of the proposed concept is to use heat as the primary form of energy input so as to directly produce cold temperatures—as opposed to the sequence of generating electricity first, and then using the electricity to drive a traditional refrigeration system. The primary end-use target is for solar cooling applications; however, the machine can also be powered by waste heat or other low-temperature heat sources.

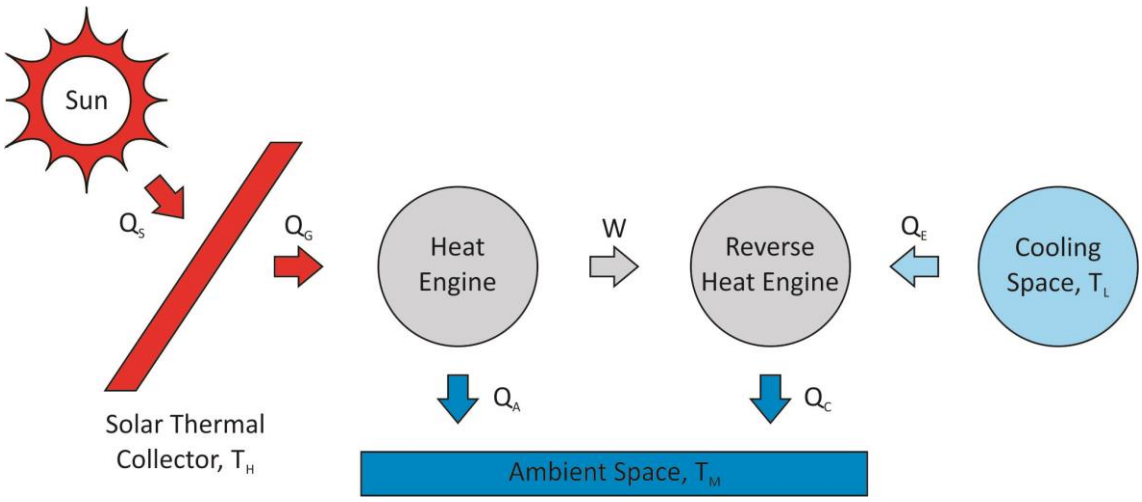

Figure 1.4 – Traditional thermo-mechanical cooling procedure using separate Stirling machines

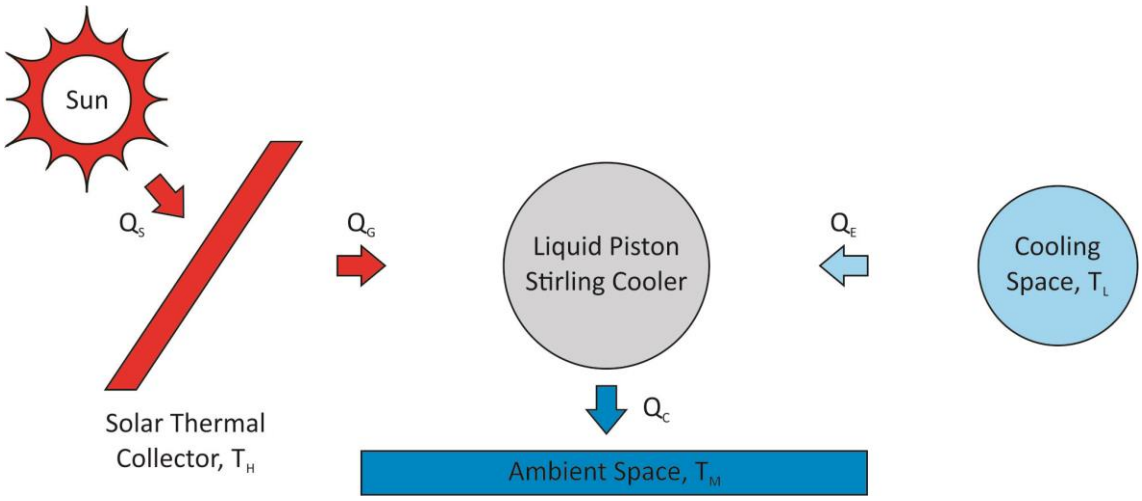

Figure 1.5 – Proposed thermo-mechanical cooling procedure using a single Stirling machine

Figure 1.4 shows how a traditional thermo-mechanical Stirling system would function, and Figure 1.5 shows how the proposed system simplifies the process. The proposed system aims to combine the forward and reverse heat engine units into a single sealed system that transforms the work internally. The focus is on the development of an environmentally-friendly refrigeration unit that will not only operate in an efficient and reliable way, but which can also be manufactured in a cost-effective way. The long term objective of the proposed research project is to develop a solar-powered refrigerator in the lower capacity range of up to 5 kW of cooling power. A schematic of the proposed system is shown in Figure 1.6. The system comprises four liquid piston Stirling engines, or 'Fluidynes' (West, 1971), connected in series.

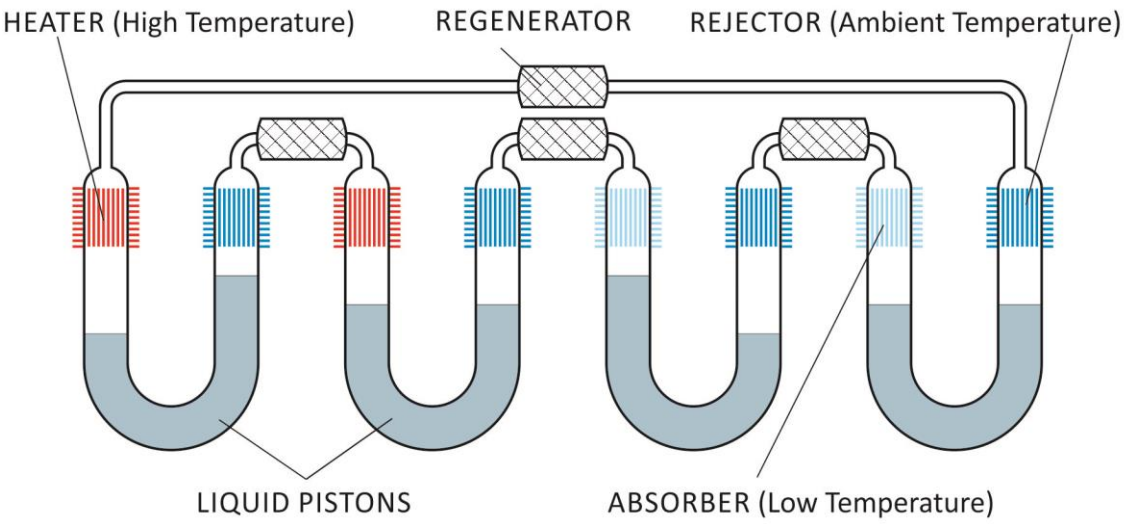

Figure 1.6 – Liquid piston Stirling cooler (LPSC) concept

This concept is very similar to the double-acting Siemens-Stirling configuration explained in the later Section 2.2.5 and depicted in Figure 2.7. A major difference is that liquid free-pistons are employed—in comparison to solid pistons that are connected to an external work coupling mechanism. The use of liquid pistons makes piston seals and lubrication redundant, which reduces cost and makes the system almost maintenance-free. The system can also be hermetically sealed as no work transfer takes place across the system boundary. However, the use of liquid pistons does add another degree of

difficulty to the analysis of the system, as the interaction between liquid columns and adjacent gas spaces of varying gas pressures has not been extensively researched in this context.

The other main difference is that two of the hot heat exchangers have been converted into absorbers. Gas expansion occurs in both types of components and heat still flows into the system through the absorbers—but the difference is that gas expansion in the heaters is induced by the high temperature heat input, which results in work being done on the liquid pistons; whereas in the absorber, the gas is forced to expand due to the relative motion of adjacent pistons as they move away from each other. In this forced expansion, the gas cools and absorbs heat through the absorber heat exchanger fins and walls, thus creating the cooling effect. Essentially, the work produced as a result of the heat input from the hot heat exchangers is used to force heat absorption by the working gas in the absorbers, resulting a reduction in temperature below ambient conditions.

In totality, the system behaves as a set of heat engines coupled with a set of reversed heat engines—all combined into a single, hermetically-sealed system with the work being transferred internally. The heat energy flowing into the system through the heaters and absorbers is then rejected at ambient temperature through the rejectors (when the gas undergoes compression). The rejectors are kept close to ambient temperature via a water coolant system, which is explained in more detail in Chapter 4. The arrangement of heated spaces (or engines) to absorber spaces (reverse engines) can be manipulated so as to structure the system into a number of different operating configurations—each individually assessed in order to identify the most promising configuration. The concept was first proposed by the father of Fluidyne machines, C. D. West, and tested in the late 1970s and early 1980s by a few research groups with limited success. Gerstmann and Friedman patented a four U-tube machine which was designed to use low-quality solar

heat to produce heat or coolth (Gerstmann & Friedman, 1979), while a similar idea was presented at the 1982 International Energy Conversion Engineering Conference (IECEC), except that the liquid pistons were replaced with solid pistons and bellow seals (Cook-Yarborough, 1982). There was a debate amongst experts as to whether or not this type of machine would function at all (Martini, 1983). W.R. Martini from Martini Engineering reported that neither group had been able to successfully achieve a functioning test-rig and decided to conduct some experiments to test the concept himself. He conducted experiments using lamp oil as the fluid for the liquid pistons and tested air, helium and hydrogen as working gases[1]. Heater temperatures in the range of 170°C–200°C were tested with an undefined charge pressure, assumed to be atmospheric. Using air as the working gas, the system would only operate with all four expansion spaces being heated, while with helium and hydrogen, the system achieved self-sustained operation using three heated spaces. The fourth space, an absorber, was measured as achieving temperatures 6°C below ambient. No attempt at explaining how the machine functioned in detail was attempted, and there was no mention made of achieving results with only two of the four heaters operating. Since this time, there has not been much interest in this machine as a potential heat-powered cooling system. It would appear that the inability to produce successful tests with any two heater configurations has dissuaded continued research efforts.

1.5 Methodology

In the words of C. D. West: "The best way to learn something about Fluidyne engines is to build one and operate it" (West, 1983, p. 53). As with Martini's proof of concept, this is the approach taken in this research project. Preliminary experiments based on this concept were carried out in 2011 at the University of Applied Sciences in Rosenheim (FH

[1] For the details of the experiments the reader is directed to the aforementioned paper (Martini, 1983).

Rosenheim) in collaboration with the New Zealand company TS-dot Engineering Limited. The results were promising, with the achievement of a self-starting 4-cylinder system. Although the amplitude of oscillation of the pistons was minimal, pressure readings showed that, as hoped, the system achieved steady-state motion with adjacent pistons having a phase difference of 90°. These preliminary experiments incorporated concentric tubes for housing the liquid pistons, whereas all subsequent experiments employed U-tube shaped housings. The U-tube shaped housings conferred several advantages, allowing for the manipulation of the diameter of the liquid pistons and other parameters, as well as reducing the complexity of the physical modelling of the liquid piston motion. The preliminary findings of the initial experiments were then expanded upon and used to develop an experimentally validated, numerical model of a heat-powered liquid-piston Stirling Cooler in order to understand how to tune and optimise the system.

The numerical modelling was initially based on a combination of two software tools: the commercial Stirling simulation software Sage, and the standard programming language MATLAB. The MATLAB model was intended to be used, along with some simplifying assumptions, to model the physical mechanics of the liquid pistons and gas spaces in order to determine an approximate frequency of the system. Next, using this frequency, a Sage model would be employed to assess the performance characteristics of the system[1]. The need for the MATLAB model was to satisfy Sage's requirement for the frequency as an input, which was unknown and variable for an unconstrained system like the one proposed. During the course of the research, this step was circumvented by utilising a symmetrical property of the system, which will be discussed in further detail in Section 4.2.9. The end result was that the MATLAB model was no longer a prerequisite for the

[1] In other words, the MATLAB model would take care of the dynamics of the machine, while Sage would deal with the thermodynamics.

Sage model, allowing the Sage model to be used in isolation as an independent tool for comparison with the experiments.

Alongside the development of the computer models, the experimental test-rig was designed, modified and commissioned. The test-rig was used to generate behavioural data for a range of operating conditions and configurations which could then be compared with a Sage model. Once the system was more fully understood and the models experimentally validated, they could be used to identify design and configuration improvements that would enhance cooling performance.

The intention was to develop an understanding of the dynamics, fluid-mechanics and thermodynamics associated with the interaction of oscillating free pistons and adjacent gas spaces in this 4-cylinder arrangement—and thus to evaluate the potential performance of such a machine in a "real-world" context. If found to have the performance potential to warrant further research, this would begin to lay the foundations for a new generation of environmentally-friendly integrated solar-powered refrigerators or air-conditioners.

1.6 Novel Aspects of the Work

The novel contributions to knowledge of this research project include the following:

1. The first comprehensive experimental analysis of the LPSC in three primary configurations, including attempts to explain reasons behind the behaviour differences between each.
2. The deduction of the operational frequency of the system both analytically and computationally using an specialised optimisation procedure.
3. Production of a validated third order computer model capable of predicting system behaviours for all tested configurations.

4. Identification of the optimal configuration for heat-powered cooling applications and quantification of the potential cooling capability for a real system when evaluated with optimised piston dimensions.
5. Evidence of the implications of the Rayleigh-Taylor instability and the resulting acceleration limit in liquid piston machines with inherently high natural frequencies.
6. An experimental assessment of submerged liquid piston floats and their ability to increase the RT acceleration limit at the cost of increased system friction.
7. The deduction of design considerations specific to the LPSC system with four double-acting alpha-type Stirling subsystems connected in series.

2 Literature

2.1 Solar Cooling Technologies

There are two types of solar cooling approaches: passive and active. Passive solar cooling is an essential consideration during any building design process, and can produce significant energy savings. In some cases, passive solar design can reduce heating and cooling demand in new buildings by as much as half, and the additional investment costs are largely compensated for by the consequent reduction in capacity of the heating and cooling systems they allow for (IEA, 2009). Examples may include seasonal sun protection, thermal masses, ventilation, solar chimneys, solar walls, shading and the evaporation of water. For the purposes of this thesis only active solar cooling technologies are considered and discussed.

The technology options for active solar cooling can generally be divided into two groups: those that rely on electric power generated by Photovoltaic (PV) cells; and those that use the heat obtained by solar collectors to drive their cooling systems. Both types of collection technology have their own advantages and disadvantages. Photovoltaic collectors have relatively low efficiencies (~10%), but this can often be compensated for by the high Coefficients of Performance (COP) of their associated cooling technologies. Solar-thermal collectors typically have much higher efficiencies (20%–60%), but their associated technologies have lower COP values. Furthermore, the efficiencies of solar collectors vary significantly depending on their type, and the temperature difference between the collectors and their surroundings (Goswami, Kreith, & Kreider, 1999).

It will be shown later that the performance of the cooling technology itself significantly affects the size (and therefore cost) of the solar collection system, and neither of the two collection options is excluded by its present or forecast future cost/performance alone. It

should also be noted that hybrid PV-thermal (PV-T) systems are being developed, which are capable of delivering both electricity and heat, in order to increase the total gains of any single system. PV-T collectors are seen as a promising technology which can potentially provide the most efficient way to use solar energy and avoid 'roof competition'. Such systems have been under development for some time but are not yet market-ready (IEA, 2012).

Comparison criteria need to be identified in order to assess potential active solar cooling systems. From the thermodynamic point of view, the cooling effect generated per unit of incident solar radiation is of greatest interest. This is called the solar-to-cooling or overall thermal efficiency, and will be the basis of comparison before considering cost. A brief overview of each of the main solar cooling technologies is presented in the following sections. For clarity, hybrid cooling systems, where two or more cooling technologies are combined, are not assessed because they do not provide further insight into the relative performance of competing technologies.

2.1.1 Solar Electric

Solar electric cooling systems use the electricity generated by PV cells to power a cooling cycle of some description. The solar electric option is currently led by vapour compression (VC) technology. Vapour compression systems are commonly found in household refrigerators. They are well understood and have had years of development, optimisation and mass manufacture. The only difference between conventional VC systems and solar electric cooling is that the electricity required by the compressor is supplied by a PV system and not the grid. A schematic of a typical VC system is shown in Figure 2.1.

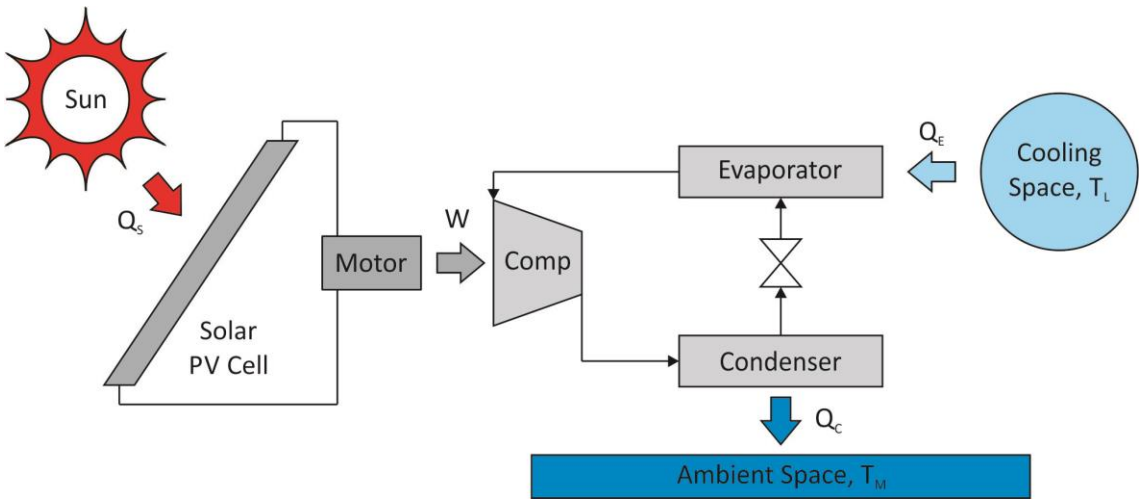

Figure 2.1 – Solar electric cooling with vapour compression system.

The conversion efficiency of a PV panel is defined as the electrical output, W (kW), divided by the product of the solar irradiance perpendicular to the panel surface, I_P (kW/m^2), and the panel surface area, A_S (m^2):

$$\eta_{PV} = \frac{W}{Q_S} = \frac{W}{I_P \times A_S}$$

The cooling efficiency of the VC cycle, also known as the Coefficient of Performance (COP), is given as the cooling effect, Q_E (kW), divided by the power consumption, W:

$$COP = \frac{Q_E}{W}$$

The overall solar-to-cooling efficiency is expressed as:

$$\eta_{SC-Electric} = \frac{Q_E}{Q_S} = \eta_{PV} \times COP$$

As a consequence of the relatively large efforts devoted to improving VC technology for use in conventional refrigeration systems, its performance is very high compared with other electric-powered cooling systems. It should be noted that COP values are very dependent on both the cooling temperature being sought and the available heat rejection

temperature. Currently refrigeration systems with COP values in the range of 3–6 are commercially available across typical operating temperature ranges, resulting in total solar-to-cooling COPs in the range of 0.3–0.6. Traditional VC systems have employed non-natural refrigerants such as Chlorofluorocarbons (CFCs) or Hydrochlorofluorocarbons (HCFCs) which contribute to ozone depletion and/or global warming. The alternatives to the vapour compression cycle include reversed Stirling engines, thermoelectric systems, magnetic cooling systems and thermo-acoustic cooling systems. As reported by Kim and Infante Ferreira (2008), these systems are currently unable to compete with vapour compression technology based on performance and cost.

2.1.2 Solar Thermal

Solar thermal systems use the heat provided by solar collectors to power a 'heat engine' or a 'thermal compressor', and a wide range of competing technologies are currently available. The efficiency of solar collectors decreases with increased operating temperatures as a consequence of higher ambient heat losses. Conversely, the potential efficiency of the heat engine or thermal compressor increases with higher source temperature. Solar thermal systems must be designed and optimised with these competing trends in mind, and different collector technologies will perform better over different temperature ranges.

2.1.2.1 Thermo-mechanical Cooling

Thermo-mechanical cooling systems use the heat generated by solar collectors to drive a heat engine, thus producing mechanical work which is used in a reversed heat engine to deliver a cooling effect. A schematic of such a system is shown in Figure 2.2.

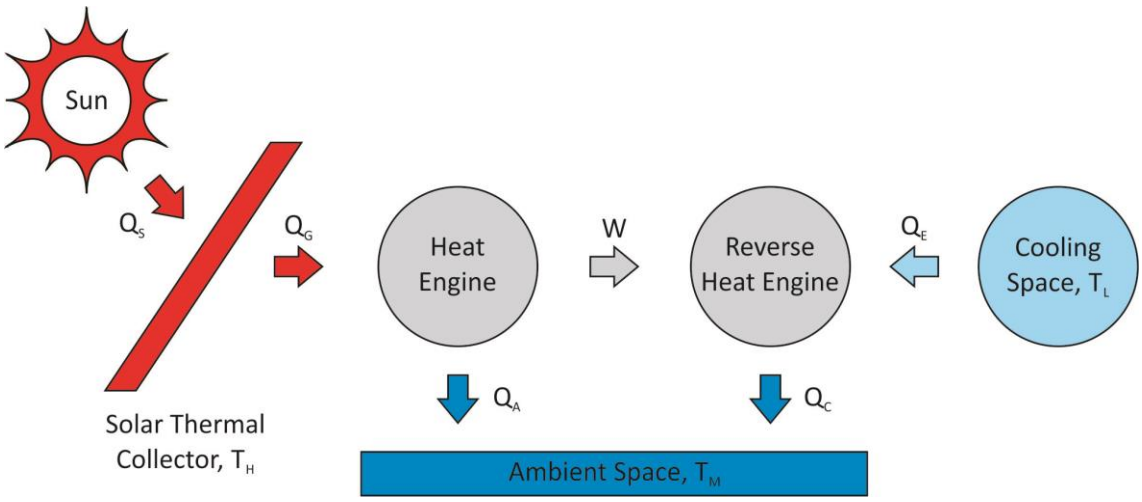

Figure 2.2 – Thermo-mechanical Cooling System.

The ratio of heat supplied by the solar collector, Q_G (kW), to the perpendicular solar radiation striking the collector surface, Q_S (kW), is called the thermal efficiency of the solar collector, $\eta_{Collector}$:

$$\eta_{Collector} = \frac{Q_G}{Q_S}$$

Optical and thermal losses ensure that the value of $\eta_{Collector}$ is always less than 1. The subsequent equation gives the thermal efficiency of a heat engine (also known as the first law efficiency), which is defined as the work output, W, produced per unit of heat input, in this case Q_G. The remaining balance of heat, Q_A, is rejected to ambient:

$$\eta_{Engine} = \frac{W}{Q_G}$$

The cooling efficiency (or COP) of the reversed heat engine is the same as that represented for the VC cycle, that being the cooling effect, Q_E, divided by the work consumption, W. The thermal energy rejected by the reversed heat engine, Q_C, is the sum of W and Q_E. The thermal cooling efficiency of the thermo-mechanical system is therefore the product of these two values, the COP of the reversed heat engine and the heat engine efficiency:

$$\eta_{TC-Thermo-mech} = \eta_{Engine} \times COP = \frac{Q_E}{Q_S}$$

The overall solar-to-cooling efficiency is then the product of the collector efficiency and the thermal cooling efficiency:

$$\eta_{SC-Thermo-mech} = \eta_{Collector} \times \eta_{TC-Thermo-mech}$$

The theoretical limit of heat engine efficiency is defined by the efficiencies of ideal Carnot cycles operating between the same temperature ranges. The Carnot efficiencies can be expressed as functions of the heat sink and source temperatures. These are shown below for heat engines and reversed heat engines respectively:

$$\eta_{t,Carnot} = \frac{T_H - T_M}{T_H}$$

$$COP_{Carnot} = \frac{T_L}{T_M - T_L}$$

When multiplied together these two Carnot efficiencies provide the upper limit for the thermal cooling efficiency, or COP, of a heat-driven cooling machine, $\eta_{TC\text{-}Carnot}$, for a tri-thermal system such as the one depicted in Figure 2.2:

$$\eta_{TC-Carnot} = \frac{T_L(T_H - T_M)}{T_H(T_M - T_L)} \tag{2.1}$$

Since the efficiencies of thermal heat engines vary depending on the source and sink temperatures, it is beneficial to compare the performance of real machines to the ideal efficiency of a Carnot machine operating between the same temperatures. This comparison is known as the second law efficiency, and provides a measure of how close a real machine (with unavoidable frictional and heat losses) is to performing as an ideal machine (with no parasitic losses). It is important to consider and maximise a system's

efficiency, because the overall efficiency of the system effectively determines the required collector surface area for a particular cooling capacity. The cost of the solar collectors is usually the most significant single contributor to the overall system cost, and therefore the economic viability of any potential solar cooling technology is highly dependent on the overall solar-to-cooling efficiency. In the case of solar a thermal cooling system, this means high second law efficiencies are desirable. There are two main contenders for the heat engine component of the thermo-mechanical cooling system: The Organic Rankine Cycle (ORC), and the Stirling engine.

Organic Rankine Cycle

The Organic Rankine Cycle (ORC) is similar to a VC cycle running in reverse. An organic working fluid is evaporated at high pressure and expanded through a turbine to produce work, which is then converted into electricity. In the case of a cooling system, the electric power generated would be used to power a VC cooling machine. The performance of the Rankine cycle is noted to benefit from economies of scale. Many large-scale nuclear and fossil-fuelled power plants employ the Rankine cycle to generate power via steam turbines. At lower temperatures (<300°C) organic working fluids are preferred, as—amongst other reasons—they do not condense during the expansion phase, thus mitigating turbine blade erosion. A review of the various low-grade heat power generation applications for the ORC was conducted in 2011 (Tchanche, Lambrinos, Frangoudakis, & Papadakis, 2011). The authors noted that turbines at low capacity (less than 1MW) are unsuitable for the ORC due to high manufacturing costs and low efficiencies. When discussing other potential expander technologies, they observed that many have been investigated since the 1990s, but none have emerged with the performance required to compete in the lower capacity market. Nguyen, Doherty and Riffat (2001) built and tested a prototype of a low temperature ORC system which operated with evaporation and

condensation temperatures of 81°C and 38°C respectively. The system used n-pentane as the working fluid and a radial flow turbine. The electric output generated was 1.44 kW with a thermal efficiency of 4.3%. This corresponds to a second law efficiency of 35%. The total cost of the system was estimated at £21,560, with the turbine-generator unit contributing 37% of this cost.

Stirling Engine

In theory, the Stirling cycle has the potential to match ideal Carnot efficiencies; in practice most second law efficiencies are between 20%–70% (Walker, Reader, Fauvel, & Bingham, 1994). Stirling systems are more suitable for lower capacity implementation: their efficiencies are highest when their surface area to volume ratio is high; they are often self-starting; and typically, do not require auxiliary power. There are a number of other advantages which promote the use of Stirling technology, including reliable operation with little to no maintenance, minimal noise, and inert working gases which are environmentally friendly. One interesting concept, which is the basis of this research project, is to integrate the heat engine and reversed heat engine components into a single machine where the mechanical work is transferred internally by the working gas. Stirling technology will be discussed in more detail later in Section 2.2.

Alternative Thermo-mechanical Options

Ejector refrigeration technology is also a candidate and has been used for train and domestic air-conditioning. Although construction of these systems is relatively simple, competitive COP levels are unlikely to be reached due to the unavoidable energy losses associated with the high velocity function of the ejectors. Consequently, their use is limited to niche applications where low-cost waste heat is available (Hong, Alhussan, Zhang, & Garris Jr, 2004). Another interesting possibility is the Vuilleumier machine,

which is a tri-thermal thermo-mechanical system capable of using a heat input for heating and cooling applications. On the surface, they appear similar to Stirling engines, although they have some major differences. They do not use compression pistons, only displacers (which require an external energy input), and the expansion and compression of the gas is driven by a change in temperature (thermal compressor) rather than a change in pressure, as in mechanical compressors. If this were a comparison of heat-powered heat-pumps, then a more thorough explanation would be warranted; however, the technology currently has a very limited presence in solar cooling applications and as such is rarely mentioned in technological reviews of the field. Nonetheless, research into the Vuilleumier machine is on-going in the field of heat-pump applications (Carlsen, 1994). A comparison between Vuilleumier and Stirling heat-pumps is provided by Wurm, Kinast, Roose, & Staats (1991).

2.1.2.2 Sorption Technologies

The dominant technologies in solar cooling today are sorption technologies. Sorption cooling relies upon a physical and chemical phenomenon where one substance is attracted to—and attaches to—another, resulting in a change in phase. Absorption refers to the process where one substance, usually a liquid or gas, is absorbed by another in a different state, i.e. solid or liquid. Adsorption, on the other hand, refers to the adherence of one substance onto the surface of another, usually a solid.

Absorption cooling dates back to the early 1800s following experimental observations made by Nairne in 1777 (Stephan, 1983). The technology continued to evolve until absorption systems were being used in large numbers in France, England and Germany for industrial applications. However, from 1880 they began to be displaced by electrically-driven VC technologies. Following the high energy prices caused by the First World War, absorption chillers saw a resurgence from 1920–1940, when most of the

fundamental theory was laid. VC technology completely dominated from the 1950s onward, until the oil crisis in the 1973 initiated a surge of research into alternative technologies. Adsorption cooling did not emerge until the 1970s as a result of the ground-breaking work of Tchernev (1980). Tchernev noticed that the zeolite mineral adsorbs a large quantity of water vapour when chilled, and with subsequent heating, the zeolite desorbs the water vapour.

In sorption cooling, the substance which acts as the refrigerant is called the sorbate and exhibits a lower boiling point than the other of the two substances, the sorbent. The technology can be employed in closed or open cycles. Closed sorption cycles share many similarities with thermo-mechanical systems; they operate tri-thermally and are limited and evaluated by similar thermodynamic equations. The major difference is that instead of a harnessing a mechanical device for energy transfer, the sorption phenomenon acts as a 'thermal compressor'. Open sorption cycles are quite different in that they treat air directly—they are often called desiccant cooling systems because they use a sorbent, or desiccant, to draw moisture from humid air. A typical closed sorption cooling system schematic is shown in Figure 2.3.

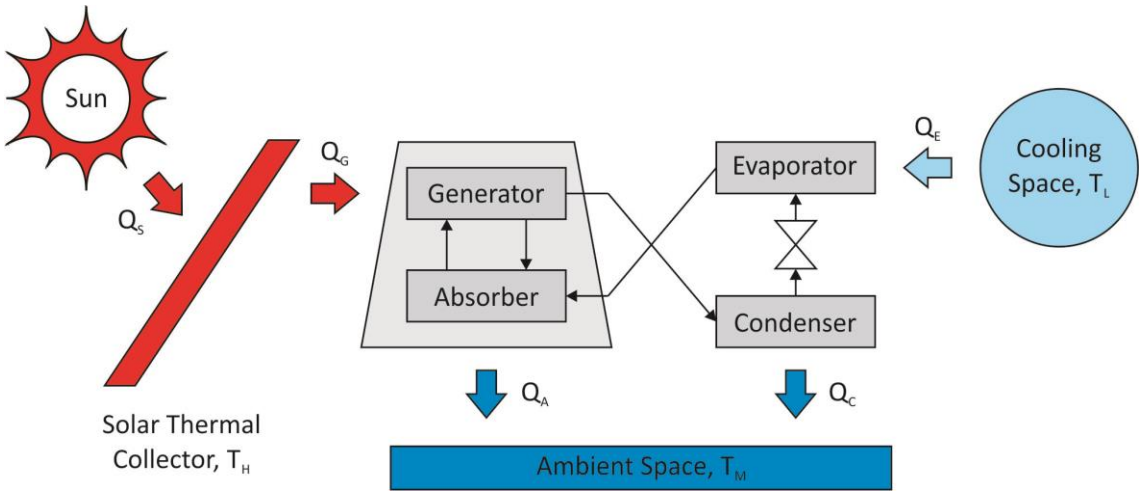

Figure 2.3 – Closed Sorption Cooling System.

In the absorber the liquid sorbent absorbs sorbate vapour from the evaporator and thus releases the heat of condensation, Q_A, to ambient. This sorbent/sorbate mixture is then heated in the generator with the heat supplied, Q_G. The sorbate vapour produced travels to the condenser, while the regenerated sorbent returns to the absorber to repeat the absorption process. The sorbate vapour—now at elevated pressure—releases the heat of condensation, Q_C, in the condenser, and is then evaporated at reduced pressure to take up the cooling load, Q_E. In the case of an adsorption system, the solid sorbent is much harder to transport between absorber and generator states. For this reason, multiple adsorption beds are typically used, which alternate between the two states to provide continuous cooling.

It is important to note that since the system does not generate electricity, electrical power needs to be provided for the circulation pump. This electrical requirement is usually neglected but it was reported that the success or failure of a sorption cooling system depends largely on the magnitude of the parasitic losses. Albers, Kühn, Petersen and Ziegler (2011) reported that parasitic losses are usually undesirably large, with magnitudes of 10%–50% of cooling loads. The thermal cooling efficiency of a sorption cooling cycle is defined as the cooling effect generated, Q_E (kW), divided by the heat energy provided by the solar collectors, Q_G (kW):

$$\eta_{TC-Sorption} = COP_{Sorption} = \frac{Q_E}{Q_G}$$

This quantity is usually referred to as the COP of the sorption system. Multiplying this quantity by the collector efficiency yields the overall solar-to-cooling efficiency for a sorption system:

$$\eta_{SC-Sorption} = \eta_{Collector} \times \eta_{TC-Sorption}$$

The thermal cooling efficiency of a sorption cooling cycle can be compared to the ideal Carnot efficiency for a tri-thermal system—in the same manner as for thermo-mechanical systems—in order to measure how closely they perform to an ideal cycle. A number of different sorption technologies with sorbent/sorbate pairs have been developed for different capacities and temperatures in recent decades. A review of these was included by Albers et al. (2011). Table 2.1 gives a market overview of thermally-driven sorption cooling systems available in Europe.

Table 2.1 – Overview of sorption cooling options

Process	Closed cycles		Open cycles	
	Solid	Liquid	Solid	Liquid
Working pairs of sorbent/refrigerant	Water/Silica gel Water/Zeolite Activated Carbon/Ammonia	Water/Lithium bromide Ammonia/Water	Water/Silica gel Water/Zeolite	Water/Lithium chloride
Technology	Adsorption	Absorption	Adsorption	Absorption
Cooling capacity	8 kW–500 kW	10 kW–5000 kW	20 kW–350 kW	10 kW–350 kW

Absorption cycles are the most common sorption approach adopted for solar cooling. Balaras et al. (2007) evaluated 54 solar cooling systems from the European Union project, Solar Air Conditioning in Europe (SACE). Of these, approximately 70% of the surveyed systems were based on the absorption cooling cycle, 10% adsorption and 10% were desiccant. The remaining 10% were comprised of other solar cooling technologies, or the technology was not specified. Roughly 40% of the projects were identified as being in the research phase, 40% in the development phase and 20% in the production phase. All of the systems in the production phase were based on absorption cooling. The performances of some of the systems are shown in Figure 2.4.

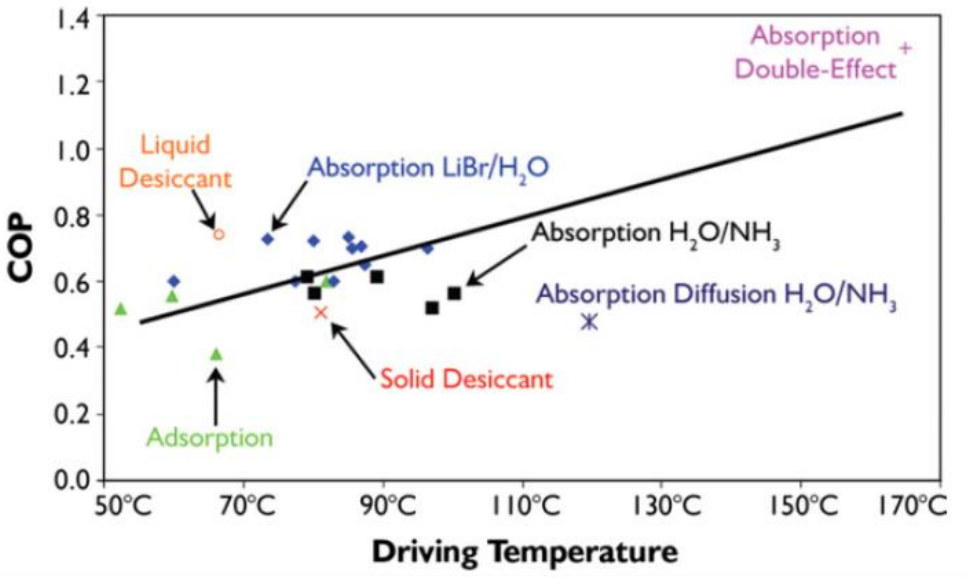

Figure 2.4 – COP of Sorption systems reviewed in SACE project.
From "Solar air conditioning in Europe – An overview" by Balaras et al., 2007. Renewable and Sustainable Energy Reviews, 11, p. 299–314. 2007 by Elsevier Ltd. Reprinted with permission from Elsevier.

The comparison does not include the auxiliary power requirements for pumps or fans. Purely based on the COP values, it would seem that adsorption technology underperforms that of absorption. However, since the adsorption systems were operating with a lower driving temperature, their second law efficiencies were actually higher (38% on average) than the average value of the other technologies (31%). Cost is not addressed in this comparison (economic viability of technologies is discussed in the next section when considering the current and future prospects of solar cooling).

2.1.3 Summary of Solar Cooling Technology Prospects

There have been a number of solar cooling technology reviews completed over the last two decades. Some focussed purely on sorption systems (Albers et al., 2011; Anyanwu, 2003, 2004; Balaras et al., 2007; Choudhury, Saha, Chatterjee, & Sarkar, 2013; Fan, Luo, & Souyri, 2007; Henning, 2007; Nkwetta & Sandercock, 2016; Zhai, Qu, Li, & Wang, 2011). A few other reviews included thermo-mechanical and PV-based technologies as well (Kim & Infante Ferreira, 2008; Otanicar, Taylor, & Phelan, 2012). Almost all of these reviews recommend sorption technology as the current leading technology in terms

of cost versus performance. The drawback with using solar electric systems is the associated use of PV panels—the poor efficiency and high cost tends to inflate total system cost to a level above that of solar thermal sorption-based systems (which employ cheaper solar thermal collectors). Thermo-mechanical systems fall short in that their solar collector costs plus heat engine costs are usually higher than a PV panel capable of delivering the same electrical output (Kim & Infante Ferreira, 2008).

In today's market, sorption technologies are more competitive than solar thermal and solar electric systems. This competitiveness is more pronounced when considering medium to large scale installations, where the cost of complicated systems with a higher degree of componentry is justified. When analysing small installations (<20 kW), it is unclear which technology is the most suitable and which will be the most suitable in the future. T. Otanicar et al. (2012) highlighted this point after reviewing over 20 solar cooling technology reviews compiled during the last 3 decades. Their interest was in small system cooling capacity systems and they stated "relatively few studies have undertaken a technical and, perhaps more importantly, an economic comparison between solar thermal and solar PV cooling systems… the results to date are mixed, motivating our interest to conduct further analysis" (p. 1288). They predict that in 2030 solar electric cooling systems will be more cost-effective than solar thermal systems based on the high COPs of VC technology and targeted PV cost reductions. They did concede, however, that if the refrigeration technology costs were to decrease and their performance was to increase (particularly if their COPs rose above 1) then solar thermal cooling could be competitive.

The cost of solar collectors in a solar thermal cooling system is much lower as a percentage of the overall cost than for solar electric systems, although the refrigeration technology often contributes a larger fraction of the cost. As mentioned before, the solar-

to-cooling system efficiency effectively fixes the surface area of the solar conversion system (whether PV or thermal collector) depending on the cooling capacity required and the solar resource available. Combined with the fact that the solar conversion apparatus is usually the single largest contributor to capital cost (Kim & Infante Ferreira, 2008) it is evident that a high efficiency (and in the case of thermal systems this implies a high second law efficiency) will generally lead to a cheaper system.

Irrespective of the current competitiveness between potential solar cooling technologies, it is evident that they are restricted to niche applications, where the adoption of more economical and conventional systems (such as VC systems powered by mains electricity) is restricted by situational constraints. In order to bridge this price gap, the IEA and many industry experts have concluded that advancements in both solar collector/PV technology and heat-driven cooling system performance are required. "The task is also urgent if we are to make sure that investment decisions taken now do not saddle us with sub-optimal technologies in the long term." (IEA, 2012, p. 1).

2.2 Stirling Engine Technology

Stirling machines are based on a reciprocating mechanism that operates on the compression and expansion principles of a gaseous working fluid. They can act as a heat engine or as a heat pump/refrigerator (reversed heat engines). A heat engine receives heat from a high-temperature heat source, converts a portion of this into work, and rejects the rest to a lower-temperature heat sink. A heat pump is capable of 'lifting' heat from a low-temperature source to a sink at elevated temperature with an external work input. Arguably a Stirling machine's most important component is the 'thermal regenerator', a heat exchanger that is capable of internally recycling a large portion of the heat energy flow from one cycle to the next. It is this novel component which enables the ideal Stirling

cycle to match the maximum theoretical efficiency possible for a heat engine, the Carnot efficiency.

2.2.1 History

The history of Stirling technology is documented in 'The Stirling Alternative' by Walker et al. (1994). The Stirling engine was invented by Dr Robert Stirling in 1815, a minister and inventor from Galston, Scotland. He and his brother James worked on regenerative power systems together for a number of years. At the time, there was a lot of interest in what were then termed 'air engines' or 'hot-air engines', and during the 19th century these systems became the preferred substitute for steam engines. They were able to compete economically, and were considerably safer to operate since they did not require a steam boiler. Power generation, water pumping and driving machinery were the main uses for air engines. The machines were quite bulky and the usual output was in the order of a few horsepower. The largest engine ever built produced 224 kW at 9 rpm—designed and constructed by John Ericsson in 1850 and installed in a 2200 tonne-ship called the USS ERICSSON, it operated with four massive 4.5 m diameter pistons running at a stroke of 1.8 m.

With the development of the internal combustion engine and commencement of commercial petroleum drilling towards the end of the 19th century, air engines fell out of favour, and production was effectively non-existent by the First World War. In the 1930s the Philips Electric Company (Netherlands) began research into Stirling engines, with the initial interest of developing a replacement power source for valve radios—this work would eventually lead to a worldwide resurgence of Stirling technology interest and research. Within 5 years the research team was able to develop a 1 kW Stirling engine exhibiting efficiency, speed and power density figures an order of magnitude superior to any previous air engine. The market opportunity for the intended application of the engine

fell through, but Philips Electric Company saw the value in the technology that had been developed, and began working on higher capacity systems. Alternative working fluids were introduced (hydrogen and helium) to allow higher speeds and operating densities and the 'air engine' term was disused. This work led to licensing agreements with General Motors (1958–1970) and subsequently the Ford Motor Company (until 1980), but the projects were unexpectedly terminated to the surprise of those involved.

In the late 1960s, Philips established another licensee, United Stirling from Sweden. The initial focus of United Stirling was on developing a quiet, low-polluting bus engine. Although the engines developed had excellent performance, it was concluded that they would not compete on price and work shifted to the development of several 25 kW–75 kW models for applications in marine propulsion, solar power and non-nuclear submarine battery charging. A recurring theme propagated, where promising results and progress lost out to political shifting and a volatile financial environment. United Stirling eventually downsized, but they had success with their submarine battery charging projects, where they were able to lengthen the underwater endurance by a factor of 5–8 for the 1200 tonne Nacken class of submarine. During the 1980s, a classified project was funded by the German Ministry of Defence, with a licensing arrangement eventually announced between two Philips licensees (including Kockums, a partner of United Stirling) in 1990 for the production of a 600 kW engine as a propulsion system. The break-up of the Soviet Union in December 1991 resulted in the project's suspension. Kockums has since produced Stirling Air Independent Propulsion (AIP) systems for submarines of the Swedish navy (Harboe-Hansen, 1995) and Japan (Scott, 2005).

Although the majority of Stirling research and development is owed to Philips (and their licensees), there have been other significant contributors. In 1964 William Beale (an Ohio University professor) invented the free-piston Stirling engine. He determined that the

kinematic linkage coupling the crankshaft, displacer, and piston was unnecessary. He went on to form the company Sunpower Incorporated, which according to their website have delivered fully engineered prototype and pre-production systems for aerospace, military and domestic use since 1974 (Sunpower Inc., n.d.). Other fields of Stirling engine research have included that of an artificial heart (in 1964). This led to the formation of the Stirling Technology Company in 1984, who presently offer a 3.5 kW generating Stirling engine called the ST-5 for domestic use (Stirling Technology, n.d.).

A number of other initiatives were started elsewhere in many different countries with research in Japan particularly abundant (Walker et al., 1994). In 1981 the first international conference devoted entirely to Stirling engines was held in London and organised by the Institution of Mechanical Engineers. The event attracted considerable interest and was attended by over 200 people. It became known as the first International Stirling Engine Conference (ISEC), and it has continued as a biennial fixture to the present day. The 17th and most recent ISEC was held in Newcastle, UK, in August 2016. A noteworthy Stirling-based endeavour which realised commercialisation followed the research efforts of Dr Don Clucas and Professor John Raine at the University of Canterbury in New Zealand. A company called Whisper Tech Ltd. was formed in 1995 and pioneered a domestic combined heat and power (CHP) system capable of producing 1 kW_e and 10 kW of heat. Running off natural gas, WhisperGen systems are now installed in hundreds of European homes (WhisperGen Ltd., n.d.). An extensive review of Stirling developments into the 21st century was conducted by Kongtragool and Wongwises (2003).

2.2.2 Stirling for Cooling

The potential of the Stirling cycle for refrigeration has been known for just about as long as power generation applications. The earliest reference dates back to 1834 when John

Herschel identified this possibility in a letter to the British Periodical, The Athenaeum. However, it was not until the research by Philips that the foundational theory was laid for commercialisation. Philips determined that the best market opportunity was in the development of refrigerators that could be used in cryogenics, i.e. capable of achieving extremely low temperatures (<110 K). A research team was established in 1948, and the results were impressive. Their first machine, with a cooling capacity of 1 kW at 80 K, went to market in 1956 and was virtually unchallenged. Since that time the 'Stirling cryocooler' market has evolved to the point where cooling systems in applications as diverse as electronic components and spacecraft are being developed. Walker et al. (1994) discuss the apparent potential for Stirling refrigerators to be used for near ambient temperature cooling such as those required in domestic and commercial settings or for air-conditioning. They remarked that at that point in time, very few companies were developing such systems and that the market appeared to be wide open.

Presently, Stirling-based cooling systems feature in the cryocooler, air liquefaction, and heat pump commercial markets (Thombare & Verma, 2008). These systems typically require a work input in order to function (this is usually via an electric motor). In the case where thermal energy is to be used as the only external input, useful work would first need to be produced with a Stirling system operating as a heat engine. This work could then be used to power a reversed Stirling heat engine in order to generate a cooling effect. A general form of this thermo-mechanical cooling approach was shown in earlier in Figure 2.2. When considering the use of conventional Stirling machines that operate with mechanical work coupling mechanisms, it is important to note that two separate Stirling machines are required to operate in unison.

2.2.3 The Ideal Stirling Cycle

The ideal Stirling cycle is comprised of four thermodynamic processes acting upon a working fluid. The four processes are depicted on Figure 2.5.

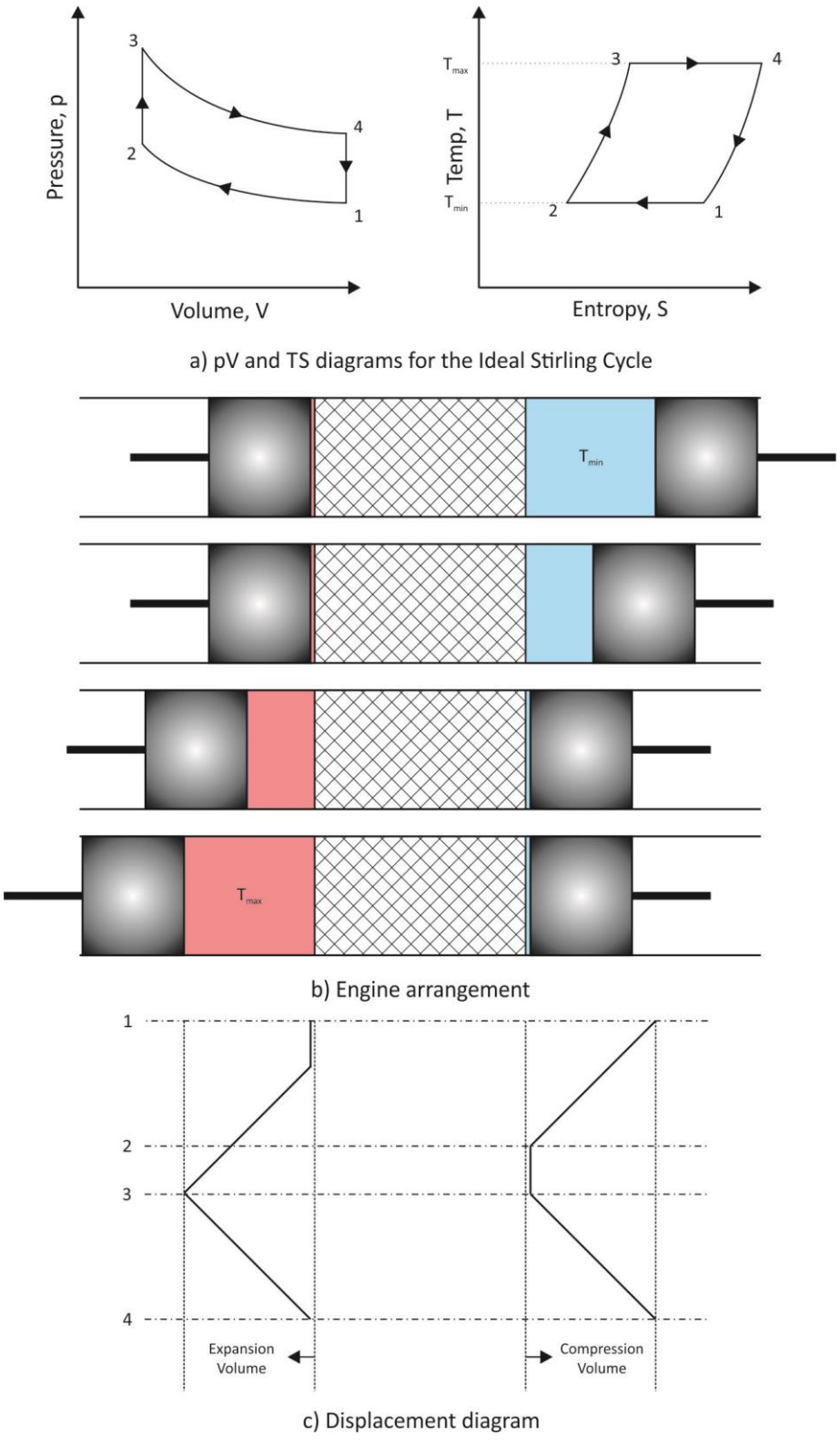

Figure 2.5 – The ideal Stirling Cycle.

Figure 2.5 (a) shows the pressure-volume (p-V) and temperature-entropy (T-S) graphs for an ideal gas, and Figure 2.5 (b) depicts a two-piston, one-cylinder arrangement to aid in the visualisation of each process. The displacement profiles of each piston can be seen in Figure 2.5 (c). The two pistons are separated by a thermal regenerator. The space to the left of the regenerator is called the expansion space and is maintained at a high temperature, T_{max}. The compression space to the right of the regenerator is maintained at a low temperature, T_{min}. The four processes which make up the ideal Stirling engine cycle are:

Process 1–2 *Reversible isothermal heat rejection* – The working fluid is compressed in the compression space, and heat is transferred at constant temperature through the surrounding cylinder wall.

Process 2–3 *Reversible isochoric heat transfer out of storage (externally adiabatic)* – both pistons move simultaneously towards the hot end. The working fluid, initially at T_{min}, flows through the regenerator matrix and absorbs heat until it emerges in the expansion space at T_{max}.

Process 3–4 *Reversible isothermal heat addition* – As the compression piston comes to a halt at the regenerator entrance, the expansion piston continues to move away, and the working fluid is expanded at constant temperature. Heat is transferred from the cylinder walls into the working fluid as the pressure falls.

Process 4–1 *Reversible isochoric heat transfer into storage (externally adiabatic)* – Both pistons move simultaneously towards the cold end, and the regenerator matrix absorbs heat from the working fluid as it returns to the compression space to repeat the process.

A number of assumptions are made for this ideal analysis:

1. There are no frictional or leakage losses within the system.
2. All processes are thermodynamically reversible, with infinite rates of heat transfer between working fluid and cylinder walls.
3. The regenerator is perfect, i.e. it induces no pressure loss and has an infinite surface area and heat capacity.
4. All of the working fluid is in either the compression or expansion space during the compression and expansion processes.
5. The pistons are able to be moved in a discontinuous manner

In the set-up described above, the Stirling cycle would be operating as a power-generating system, with positive net work done on the pistons. In essence this is a consequence of higher pressure during the expansion process as compared with the compression stage. If the system were to be reversed so that expansion took place at the cold end, the machine would resemble a refrigerator and would require an external work input to continue operating. It is a very mechanically elegant trait that real Stirling machines are able to seamlessly ‘flip’ between these two operating modes with relative ease (as Philips frequently did in demonstration of their units in order to impress visitors) (Hargreaves, 1991).

2.2.4 Practical Limitations

As noted earlier, the ideal Stirling cycle has the same first law efficiency as the ideal Carnot cycle. In reality, however, there are a number of practical limitations which reduce the achievable efficiency of real Stirling machines. The assumptions made in the ideal analysis above are not justifiable for any practical implementation. West (1986) conducted a thorough analysis of these shortcomings. The main detracting influences affecting practical Stirling engines are as follows:

1. **Adiabatic losses** – In the compression and expansion processes the heat transfer is assumed to occur isothermally. For a real system there is limited time available for the heat transfer to take place, and heat transfer coefficients between working fluid and cylinder walls are limited by the physical properties of the gas and cylinder material. As the speed of a cycle increases, less time is available for heat transfer to occur. At the extreme, a cycle operating fast enough would result in no heat transfer occurring at all. Hence, the compression and expansion processes tend from isothermal to adiabatic as speed increases for a particular machine. The cycle efficiency is always reduced by adiabatic behaviour, even though power output may increase. As reported by West (1986) adiabatic losses are more important for low temperature machines such as those operating with waste heat or from flat plate solar collectors.

2. **Hysteresis losses** – This effect is related to the semi-adiabatic behaviour of the working fluid as described above. Essentially it results from the real temperature fluctuations of the working fluid during the expansion and compression processes. Heat is transferred back and forth between the working fluid and the cylinder wall, but heat is rejected by the working fluid at a higher temperature than heat is received from the cylinder wall. This manifests as a direct reduction in the work output of the system. It is interesting to note that this loss is zero for both the isothermal (therefore no temperature fluctuation) and adiabatic (no heat transfer occurs) cases. There is a point in between where the hysteresis losses are at a maximum, which—according to West—lies in the range of most practical machines. The combination of hysteresis and adiabatic losses can reduce optimum second law efficiency by up to 10%.

3. **Pressure losses** – The working fluid inevitably experiences frictional resistance as it is moved around during the cycle. The bulk of this resistance is seen in the regenerator matrix and the resulting pressure loss contributes to a reduced work output. Empirical fluid friction data can be used to estimate the pressure loss and correlations have been developed for different regenerator designs and matrix materials.

4. **Leakage losses** – A reduction in performance occurs when the working fluid leaks past the pistons or into the gap between pistons and cylinder (called appendix gap losses).

The magnitude of the losses mentioned above depends on the system configuration, system optimisation, operating temperatures, the capacity of the system, operating speed, the type of working fluid, materials used, etc. The end result is that the second law efficiency of any real Stirling engine will always be significantly less than the ideal cycle. West reported that the second law efficiency for real Stirling engines has been seen to be in the range of 5%–80% Carnot efficiency, with 5% corresponding to the first hot air engines used in the early 1800s, and 80% for modern high performance Stirling engines.

2.2.5 Stirling System Configurations

There are two broad categories of Stirling machines: single-acting and double-acting. For single-acting machines the working fluid only acts upon one end of the power piston(s); whereas for double-acting machines both ends of the power piston(s) are acted upon during a single cycle. There are three types of single acting machines; these are shown in Figure 2.6.

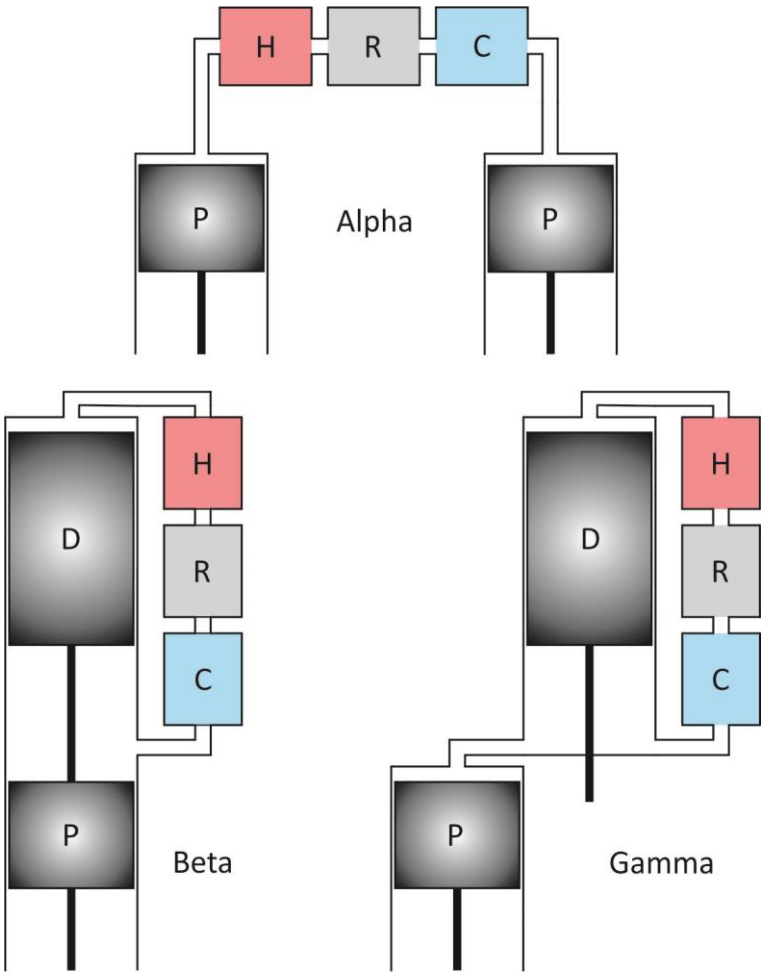

Figure 2.6 – Single acting Stirling machine configurations.

The alpha-configuration is very similar to the set-up that was used to explain the ideal Stirling cycle. It incorporates two pistons, whereas the beta- and gamma-configurations employ a 'power piston' and a 'displacer'. The displacer carries out the role of transferring the working fluid back and forth between the hot and cold heat exchangers; the power piston transfers work to (and from) the working fluid. A power piston will have a large pressure but small temperature difference across it, whereas a displacer will have a large temperature but small pressure difference. In the beta configuration the power piston and displacer are housed within the same cylinder; in the gamma configuration they are located in different cylinders.

Double-acting configurations are essentially a number of single-acting systems that have been integrated into a single machine. This may be done for increased capacity

applications, or where the cost of additional componentry required for multiple single-acting systems is not justified. An example of a double-acting machine of the Siemens-Stirling type is shown in Figure 2.7. This configuration is the basis of the WhisperGen CHP unit mentioned earlier.

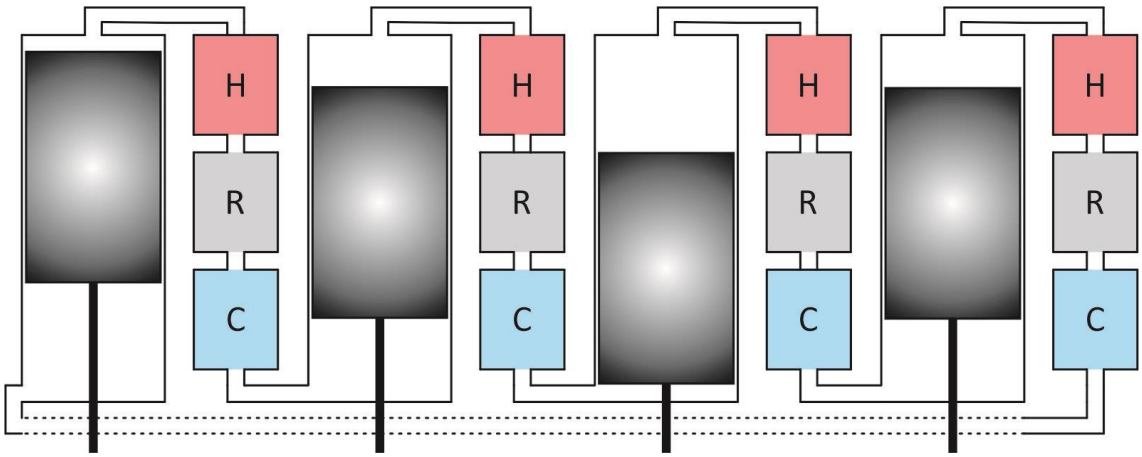

Figure 2.7 – Four-cylinder double-acting Siemens-Stirling configuration.

There have been many other configurations investigated; however, no single configuration has prevailed as the most suitable for all applications. In general, single-acting gamma and beta machines are considered more suitable for small systems (<20 kW). This is largely due to less complicated sealing requirements in comparison with two-piston machines. For larger capacity systems the double-acting Siemens-Stirling type is usually employed.

2.2.5.1 Work Output Coupling Systems

As is the case with conventional internal combustion engines, a problem is presented by the typical desire for power output in the form of rotary motion, which is mismatched with the reciprocating nature of Stirling-based machines. Many creative mechanisms have been invented to couple the pistons and displacers of Stirling engines to the drive shaft. A review by Thombare and Verma (2008) discussed the various options available based on the application and configuration including the slider crank, rhombic drive,

swash plate, Ross rocker, Ringbom and free-piston forms. The incorporation of a work-coupling system substantially increases the complexity of the machine's construction and introduces additional losses and extra design considerations. This has the effect of increasing the system's cost, maintenance requirements, and noise output as well as reducing overall efficiency. The presence of piston side-loads and in particular—the need for sealing components, have caused performance and maintenance problems for a number of Stirling engine ventures in the past.

2.2.6 Free-Piston Stirling Engines

As previously mentioned, William Beale invented the free-piston Stirling engine (FPSE) in 1964, making it a relatively modern variation of the Stirling machine. Free-piston Stirling engines have no kinematic mechanism coupling the reciprocating elements: either to each other, or to a common rotating shaft. Instead, the elements move entirely in response to the gas and/or other spring forces acting upon them. In a kinematic machine the coupling results in only a single degree of freedom for the overall system, whereas in the case of the FPSE (since the power pistons and displacers are free to move independently) the machine behaves as a multiple degrees of freedom (MDOF) system. As a consequence, the dynamics and thermodynamics of the FPSE machine are intimately linked, and their influences on each other are a critically important design consideration. The free-piston Stirling engine is a dynamic system that operates at a relatively constant resonant frequency. Figure 2.8 shows the Sunpower M100, a relatively simple FPSE design (Urieli & Berchowitz, 1984).

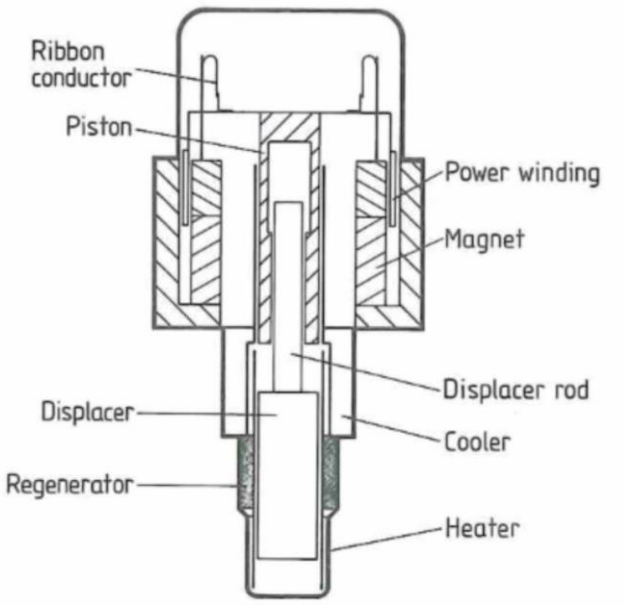

Figure 2.8 – Sunpower M100 FPSE

The relationship between dynamics and thermodynamics in a FPSE machine means that they are typically self-starting. As the expansion space is heated, the system develops into an unstable equilibrium, with a build-up of potential energy. Any slight agitation will cause the machine to oscillate and vibrate as the balance between energy input and energy dissipation commences. The ability for FPSE to self-start is one of the main advantages they have over their kinematic counterparts, and can provide unique benefits in the type of applications for which they are suited.

Another advantage of the absence of a linkage mechanism is that there are no side-loads exerted by the reciprocating components on the cylinder walls. As previously shown in Section 2.2.5, side-loads result from the resolution of the axial forces within linking mechanisms into the transverse plane. Without side-loads, the cylinder is free from uneven wear, and the requirements placed on lubrication and sealing are relaxed to the point where the working fluid itself can be used as the lubricant. The absence of linkage mechanisms also means that in some cases the FPSE can be hermetically sealed during production, i.e. by eliminating the requirement for a physical link into the working space (in order to extract or impart motion) it is possible to develop a much simpler and cheaper

machine that does not require dynamic seals. The main drawback of the FPSE is that the absence of a kinematic work coupling mechanism means that there is no longer the direct capacity for a work output via a rotating shaft. Many machines employ rotating shafts in order to deliver their required input power, and in this context the FPSE would then be at a considerable disadvantage. There are however many applications which do have a direct need for reciprocating motion, including pumps, compressors and others.

2.2.7 Liquid Piston Stirling Machines

Invented by Colin D. West in 1969, the liquid piston Stirling machine is a special type of the free-piston Stirling configuration, where the pistons are not physically connected to a work-coupling device. West published the first major textbook dedicated to liquid piston Stirling engines in 1983, in which he provided a review of the state-of-the-art of liquid piston Stirling engines, as well as discussing the history of the liquid piston concept dating back to 1698 (West, 1983). Also known as a 'Fluidyne', a liquid piston Stirling engine employs liquid columns of water in place of conventional solid pistons. The pistons can be accommodated in a 'U-tube' arrangement, as shown in Figure 2.9, or they can be housed in concentric tubes.

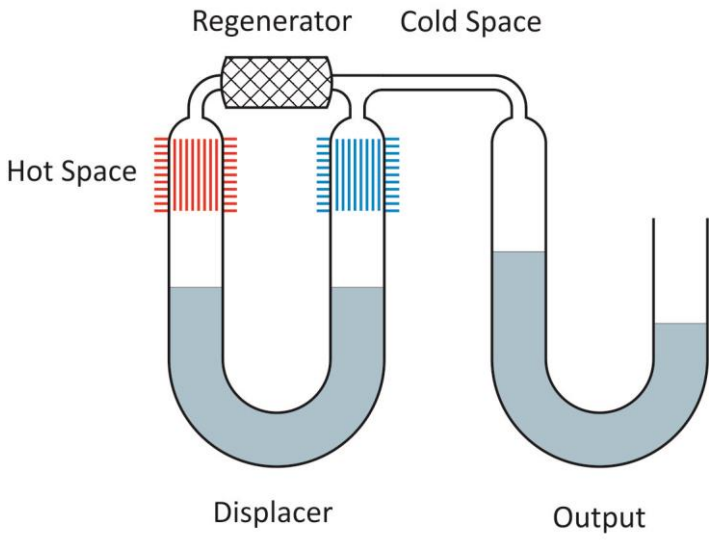

Figure 2.9 – Basic 'Fluidyne' operation.

The use of liquid pistons allows a number of significant design advantages over solid piston-based Stirling machines. They provide a low-cost, easily accessible and environmentally-friendly alternative. There is no need for tight manufacturing tolerances or mechanical seals (a recurring design issue for Stirling engines), and they allow for a simple housing and cylinder design. Fluidyne machines are also typically self-starting and require little to no maintenance. The price paid for these advantages are the increased fluid friction losses as the pistons oscillate, and the liquid phase change occurring in the gas space. This has led to Fluidyne machines having relatively low efficiencies.

Since West's work was first publicised in 1974, the design of Fluidyne machines has been significantly refined, and they have seen limited commercial success powering water pumping systems, and have also been proposed for low-capacity heat-driven power generation (Orda & Mahkamov, 2004; Slavin, Bakos, & Finnikov, 2009; Stevens, 2010; Van de Ven, 2009). In the late 1980s research was conducted on the physical basis of the excitation relationship between the tuning line (output piston) and the displacer piston, and how this varied with system pressure (Fauvel, Reader, & Walker, 1989; Fauvel & West, 1990). In 1994 Fauvel and Yu designed a Fluidyne as a low-cost irrigation pump using existing steel barrels (Yu & Fauvel, 1994b). Their design exhibited large liquid flow losses but they experimentally verified improvements to reduce these. In the same year they presented an investigation into regenerator design for Fluidynes (Yu & Fauvel, 1994a).

In 2003 Özdemir and Özgüç presented a mathematical model for analysing a Fluidyne engine (Özdemir & Özgüç, 2003). The model attempted to incorporate the phase change occurring at the liquid piston surfaces by adopting control volume analysis at the interfacial regions (with the help of a number of simplifying assumptions). They noted that although their model was quite simple, it agreed well with their experimental data.

Orda and Mahkamov (2004) published performance data of three different Fluidyne prototypes they had constructed for use as water pumps (two of these systems were driven by solar collectors).

In 2009, Slavin et al. analysed a novel 'Fluidyne' machine theoretically capable of producing 97 kW with a 37% thermal efficiency and a second law efficiency of 52%. It is stated that "Heat-resistant floats on the surface of water pistons ensure heat insulation between working gas and water and prevent intensive evaporation of water." (Slavin et al., 2009, p. 1163), but no further details of the floats are provided. A particularly interesting aspect of this engine design is the offset heat exchangers which incorporate small fans, pumping the working fluid repeatedly through the heat exchangers multiple times each cycle. Coupled with the low frequency of operation this allows for the expansion and compression stages to closer resemble isothermal processes by reducing the dead volume. Van de Ven (2009) explores the rationale behind liquid piston Stirling engines and identified many research challenges facing the technology. These include: modelling the liquid pistons' behaviour; modelling system dynamics; optimizing for maximum power output and power density; assessing the stability of the liquid/gas interface; material selection for the liquid; material selection for the engine components; and energy storage for operating engines in reversed mode as heat pumps.

Frictional losses are well understood for developed laminar and turbulent pipe flows; this is not, however, the case for oscillating flows where the boundary layer is constantly redeveloping (or not fully developing at all). These losses were experimentally investigated in 2010, where simple experiments involving liquid pistons of a variety of tubing sizes and configurations were carried out (Stevens, 2010). Using log decrement analysis, some evidence was shown of a linear correlation between liquid volume and an equivalent damping coefficient, although this did not take into account the fact that the

damping coefficient may be dependent on piston amplitude itself. The following year Stevens and Mason set up a Fluidyne test bed powered by concentrating sunlight using a Fresnel lens (Mason & Stevens, 2011).

A comprehensive review of Stirling cycle engines for recovering low and moderate heat was recently published (Wang, Sanders, Dubey, Choo, & Duan, 2016). The review included a section specifically assessing liquid piston Stirling machine research projects, the majority of which were associated with water pumping applications. Compared with other types of Stirling machines, the Fluidynes assessed in the review achieved very low efficiencies (0.1%–5%). It is evident from the work carried out so far that the two major factors which reduce the thermal efficiency of Fluidyne systems (in comparison to conventional Stirling systems) are:

1. Phase change occurring on liquid piston surfaces exposed to the gas space.
2. Fluid friction between the liquid piston and cylinder walls during oscillation.

If the potential of the Fluidyne machine is ever going to be harnessed, it seems that having a clear understanding of the influence of these processes, and indeed ways of mitigating their negative effects, is required.

The primary objective for the LPSC system considered in this research project is the development of an understanding of its behaviour in various configurations, and which configuration leads to the best cooling performance. Once this is completed, the relative significance of the effects of phase change and fluid friction in the pistons can be considered and investigated further.

2.3 Theoretical Background Analysis

2.3.1 Introduction

The analysis of real Stirling engines is very complicated. Within a real engine there exists a three-dimensional field of complex fluid-mechanics and heat transfer processes which not only vary spatially, but also vary with time in a cyclic manner. Obtaining a mathematical representation of these processes with the aim of predicting machine performance is not simple. Even in the modern era, developing Stirling models which are accurate to within 15%–20% is considered impressive.

This complexity arises from the very nature of the Stirling engine; the movement of the piston(s) and displacer (if applicable) induces reciprocating gas flows, and thus transient heat transfer interactions. In the case of kinematic engines, the movements of these components is at least governed by the physical linkages of the work coupling mechanisms. This is not the case for FPSEs. The motion of the piston(s) is dictated by the same fluid flow and heat transfer processes that they induce through their oscillation. The resulting feedback system produces a strong co-dependence between the dynamics and the thermodynamics of a FPSE, and is of critical importance when it comes to the design process. Historically, the disciplines of vibrational dynamics and thermodynamics/fluid-mechanics have been separate fields of expertise within mechanical engineering as a whole. This has been to the detriment of the level of interest in (and development of) FPSEs since their invention 50 years ago. This chapter aims to introduce the reader to the preliminary analysis tools and techniques used in FPSE design, and to highlight the escalating levels of their complexity.

2.3.2 FPSEs as Vibrating Systems

Throughout the design process it is helpful to consider FPSEs as a vibrating system of mass and spring elements. Pistons and displacers are represented by mass elements, which

are interconnected via spring elements (the spring elements approximate the behaviour of the gas spaces). Dampers can be added to model frictional losses. Figure 2.10 shows a basic spring and mass system for clarification purposes.

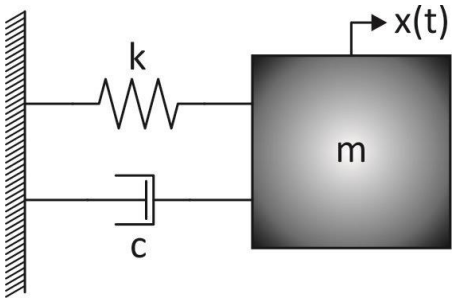

Figure 2.10 – Simple spring-mass-damper system

The equation(s) of motion of the mass element(s) can be deduced by applying Newton's second law, which yields a set of solvable linear Ordinary Differential Equations (ODEs) of the form:

$$m\ddot{x} + c\dot{x} + kx = 0 \tag{2.1}$$

The oscillatory displacement profiles of the mass elements are assumed to follow that of simple harmonic motion, with solutions of the form:

$$x(t) = X\cos(\omega t + \varphi) \tag{2.2}$$

Where X is the amplitude of oscillation, ω is the angular frequency of oscillation, and φ is the mass element's phase angle. For MDOF systems, the equations of motion become more complex, and can be difficult to solve analytically. Depending on the level of detailed analysis required, this basic model of the FPSE can be developed and modified to better approximate the real system in a number of ways. As the ODEs produced become more complicated, they can be solved through the use of computers and numerical integration methods. By analysing the engine in this manner, it is possible to obtain some important characteristics of the FPSE based on its configuration and overall dimensions.

2.3.2.1 Gas Springs

Assuming ideal gas behaviour and considering small changes in gas volume, the gas spaces can be modelled with the following simply-derived spring constant approximations for both the adiabatic and isothermal cases:

$$k_g = \frac{\partial F}{\partial x} = A\frac{\partial p}{\partial x} = \frac{nA^2 p_0\left(\frac{V_0}{V_0 - Ax}\right)^n}{V_0 - Ax} \approx \frac{nA^2 p_0}{V_0}$$

$$k_{g,Adiabatic} = \frac{\gamma A^2 p_0}{V_0} \tag{2.3}$$

$$k_{g,Isothermal} = \frac{A^2 p_0}{V_0} \tag{2.4}$$

Where x is displacement, n is the polytropic index, γ is the ratio of specific heats (C_P/C_V) of the gas, A is the U-tube cross-sectional area, p_0 is the mean (charge) gas pressure and V_0 is the mean gas space volume.

2.3.2.2 Liquid Pistons

In the case of liquid pistons in the form of U-tubes, it is important to note the addition of the restoring force of gravity which can play an important role in the dynamics of the system. This force depends linearly on the displacement of the piston, and as such can be incorporated as an extra spring element. This is discussed in further detail in Chapter 4. The resulting spring constant is:

$$k_p = 2A\rho g \tag{2.5}$$

2.3.2.3 Vector Plot Representations

Vector representation is a convenient method of interpreting piston and displacer motions. Elements exhibiting a simple harmonic response can be analysed by deconstructing their

displacement, velocity and acceleration functions. Earlier, the general solution for the displacement of a mass element within a linear vibrating system was:

$$x(t) = X\cos(\omega t + \varphi)$$

By differentiating with respect to time, the following equations for velocity and acceleration are obtained as:

$$\dot{x}(t) = -\omega X\sin(\omega t + \varphi) \tag{2.6}$$

$$\ddot{x}(t) = -\omega^2 X\cos(\omega t + \varphi) \tag{2.7}$$

These functions can be plotted as rotating vectors with lengths equal to the coefficient terms, X, ωX and $\omega^2 X$, which represent the amplitudes of displacement, velocity and acceleration respectively. The angle $(\omega t + \varphi)$ is measured anticlockwise from the positive x-axis. As time, t, increases, the vectors rotate anti-clockwise about the origin, with each revolution encapsulating the pistons' progression through one cycle of physical oscillation. Figure 2.11 shows the vector plot for the generic case described above.

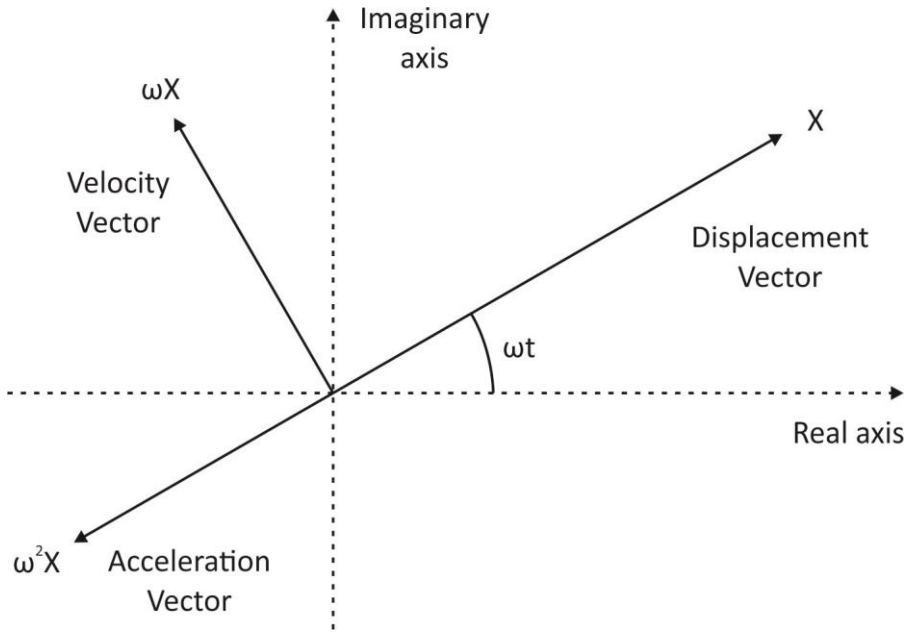

Figure 2.11 – Vector representation of the generic solutions for piston or displacer motion.

Projecting the vectors onto the x-axis for any particular time yields their instantaneous value, while the amplitudes provide maximum values, and the phase angles between vectors can provide interesting insights into system dynamics. For example, in the above case the acceleration vector leads the velocity vector by 90º, which also leads displacement by 90º. This notation will be used extensively in the results and discussion section of this thesis.

2.3.3 Power Estimation

At the beginning of any engine design process, it is important to attain rough estimates for the power and efficiency of a machine based on general dimensions and operating conditions. The ideal Stirling cycle pictured earlier in Figure 2.5 yields the following formula for the cyclic work:

$$W = \oint pdV = mR(T_H - T_C)\ln\left(\frac{V_1}{V_2}\right)$$

where m is the gas mass, R is the gas constant, T_H is the heat source temperature, T_C is the heat sink temperature, and V_1 and V_2 are the gas volumes at states 1 and 2 respectively. Knowing the machine's operating frequency, f, would therefore yield the power output as:

$$P = fW$$

Unfortunately, for the reasons previously mentioned in Section 2.2.4, the real Stirling cycle is unable to match this level of performance. Work was conducted by Martini (1978) in identifying an 'experience factor', F, which could be used to scale this power estimate and account for the various real world losses. His work was taken further by William Beale, who observed that the real power output of a number of machines was also proportional to mean pressure, p_0, and swept volume, V_S. Walker (1979), West (1981),

and Senft (1982) then further expanded on Beale's relationship to include temperature dependence. The result was:

$$P = FfV_S p_0 \frac{T_H - T_C}{T_H + T_C} \tag{2.8}$$

It should be noted that, in general, specific Stirling engine configurations share similar *F* values, so designing unique or significantly different engines may require the identification of more suitable *F* values. The average value of *F* is 0.25, but can be as high as 0.35.

2.3.4 Frequency Estimation

In kinematic engines the frequency can be the most difficult parameter to estimate accurately prior to the design process. The frequency depends on many factors that are as yet undetermined, for example, the external loading profile. In the case of the FPSE, however, since the frequency is essentially held constant by the overarching dynamics of the system, it is possible to attain a good estimate for most configurations relatively simply. The machine is approximated as a series of springs and masses, as previously described in Section 2.3.2, and the natural frequency of the system obtained by evaluating the system's natural undamped response. An example of this is shown below for the simple spring and mass system mentioned earlier. From Equation 2.7, the piston's acceleration is:

$$\ddot{x}(t) = -\omega^2 X \cos(\omega t + \varphi)$$

Substituting the above into the undamped equation of motion gives:

$$-m\omega^2 X \cos(\omega t + \varphi) + kX \cos(\omega t + \varphi) = 0$$

which simplifies to:

$$\omega = \sqrt{\frac{k}{m}} \text{ or } f = \frac{1}{2\pi}\sqrt{\frac{k}{m}}$$

Although this gives a good estimate for the operational frequency, in reality the true frequency will vary depending on any loading, damping and the true nature of gas expansion. Also, information about the piston amplitude is currently unknown and requires more sophisticated analysis techniques to identify. These points are further discussed in the following sections.

2.3.5 First Order Analysis

Stirling engine analysis methods are categorized into three tiers: first order, second order and third order. The categorisation of these tiers is based on the level of complexity employed in the analysis technique. First order analysis, being the simplest, utilises a large number of assumptions intended to idealise the system. Numerous first order analysis schemes have been proposed throughout the literature, however, they all utilise a number of key assumptions first employed by Gustav Schmidt at the German Polytechnic Institute of Prague in 1871 (Schmidt, 1871).

2.3.5.1 Schmidt Analysis

The Schmidt analysis considers the following simplifying assumptions:

1. The working fluid behaves as an ideal gas
2. The working fluid mass remains constant
3. The instantaneous gas pressure is uniform throughout each gas space
4. The gas space is comprised of isothermal sections
5. The mass elements (pistons and displacers) motion is sinusoidal or reflects simple harmonic motion.

It is important to consider the validity of these assumptions. Assumptions 1 and 2 are reasonable, especially in the case of FPSEs where the extent of sealing required can be non-existent. Assumption 3 neglects fluid-friction-induced pressure drops across the working space. These losses are usually more pronounced in high speed engines, so in the case of lower frequency liquid piston engines the assumption is more acceptable.

The fourth assumption is where the most significant deviations from real systems occurs. This step involves dividing the gas space into regions of constant temperature—for example, a typical approach is to have three separate regions for the expansion, compression and regenerator spaces—which essentially neglects any transient heat transfer phenomenon occurring within these spaces, and assumes isothermal gas behaviour throughout. This assumption also implies instantaneous temperature change for mass flows to (and from) adjacent zones. Although this assumption considerably decreases the potential accuracy of this analysis method, an important analytical advantage is attained in its place. The pressure profile of the gas space is linearized with respect to piston (and displacer) displacement, as the only factors affecting instantaneous workspace pressure are the relative positions of associated mass elements. The workspace pressure is given by the following equation:

$$P = mR\left(\frac{V_E}{T_E} + \frac{V_R}{T_R} + \frac{V_C}{T_C}\right)^{-1} \tag{2.9}$$

where the subscripts *E*, *R* and *C*, refer to the expansion, regenerator and compression spaces respectively. In the above case, the only variable quantities are the volumes in the compression and expansion space, which depend on the mass element displacement variables. Coupled with assumption 5, it is possible to integrate over a complete cycle and obtain a closed-form expression for the cyclic work estimate. Assumption 5 is

generally valid, the majority of kinematic and FPSE configurations produce mass element displacement profiles closely resembling sinusoidal motion with constant phase angles.

Since its development, Schmidt analysis has been significantly refined, and applied to all types of Stirling engine configurations and applications—thus providing a simple way to access the potential performance of a machine based on engine dimensions and operating parameters. In the case of a complicated FPSE with multiple degrees of freedom, obtaining closed-form solutions is not possible; although the development of computers has aided in the efficacy of numerically integrated solutions, which has led to a resurgence of interest in Stirling engine analysis.

2.3.6 Second Order Analysis

Second order analysis methods arise from reconsidering some of the Schmidt assumptions, and adopting more complicated modelling techniques to improve or eliminate the various shortcomings. As previously discussed, assumptions 1, 2 and 5 are the most well-founded when considering FPSEs, and so therefore assumptions 3 and 4 are usually those targeted for improvement. The literature on second order analysis schemes is very extensive, and will not be discussed in great detail here, although some important second order concepts will be highlighted. For further information, the reader is directed to arguably one of the most comprehensive contributions of second order analysis methods, Martini's Stirling Engine Design Manual (1978).

Considering assumption 4, Schmidt analysis typically assumes that gas temperatures are equal to the associated surface metal temperatures in the heater and cooler isothermal sections. Martini introduced a modification to this approach in which realistic estimates of the gas temperatures in these regions are obtained through an iterative process and are used instead. A brief overview of the procedure is now described. Having used first order analysis to obtain an estimate of the basic power output, the required basic heat input is

obtained by dividing by the Carnot efficiency. Estimates of various losses such as gas conduction, radiation, shuttle losses, regenerator losses, flow losses and others are then added to this basic heat input to yield the net heat input, which is the total heat supply required per cycle. The heat transfer coefficient for the high temperature heat exchanger is then calculated, and used to equate the gas-to-metal temperature difference required to achieve the aforementioned net heat input. A similar approach is taken for the cooler side. The newly identified gas temperatures can then be used in the Schmidt analysis to obtain a more realistic basic power output, and the process repeated until the gas temperatures converge. In the modern era, iterative calculations like that described above are trivial and essentially instantaneous when carried out by computers. The majority of time is spent on establishing the algorithms necessary. For this reason, it can be desirable to consider third order analysis schemes, as they can demand a similar amount of setting up, but produce more accurate results.

2.3.7 Third Order Analysis

Third order analysis is the most intricate approach to the simulation of Stirling systems, and aims to remove the need for many of the simplifying assumptions employed for first and second order analysis. This is done by attempting to evaluate the entire spectrum of thermo-fluid interactions experienced by the working gas throughout the operation of the machine, as well as the energy flows existing through and into the machine components. Computational modelling has become popular in number of mechanical engineering fields, and most undergraduate programs offer specialised courses on computational fluid mechanics and computational solid mechanics. Third order analysis essentially employs aspects of these fundamental modelling techniques, while also incorporating the specifics associated with Stirling engine processes. As with second order analysis schemes, the literature on third order methods is very extensive and is not critically important in the

context of this thesis. A brief summary of the general approach is outlined here, with further detail of the specific modelling software and approach used in this project presented in Section 4.2.

The procedure begins by discretising the gas space volume into a number of individual cells. The fundamental conservation equations of mass, energy and momentum are constructed for each cell, and continuity conditions established between adjacent cells to create a network of interconnected equations for fluid properties. By applying certain boundary conditions based on the real-life machine configurations and empirical correlations when necessary, the vast system of equations can be solved numerically over a predefined time interval. The resolution of the matrix of cells can be increased along with the time increment until the solution becomes independent of both, resulting in numerically assessable profiles for the gas pressure(s) and mass element motion(s). From these functions, the machine performance indicators can be evaluated and operating parameters adjusted for the purposes of design improvements or general understanding. In recent decades a number of specialised software entities have been developed for conducting the complex analysis described above, some specifically for Stirling engines (Dyson, Wilson, & Tew, 2004).

3 Heat-powered Liquid Piston Stirling Cooler Test-rig

3.1 Preliminary Design

The initial LPSC test-rig was designed and commissioned at FH Rosenheim, Germany. Figure 3.1 shows the test-rig assembly when the experimental investigation began in late 2013.

Figure 3.1 – First liquid piston Stirling cooler (LPSC) set-up with U-tubes.

The image shows each of the four gas spaces, embodied by the ‘H’ shaped housings, resting above the wooden support structure, two in the foreground and two in the background. Each of these is connected in series to the adjacent housing sections via a steel U-tube, which completes the desired geometry of the system, as portrayed in Figure 3.2. Also shown are the designations of each of the four gas spaces (GS1–GS4) and pistons (Pistons A–D), which are frequently referred to throughout the rest of this thesis.

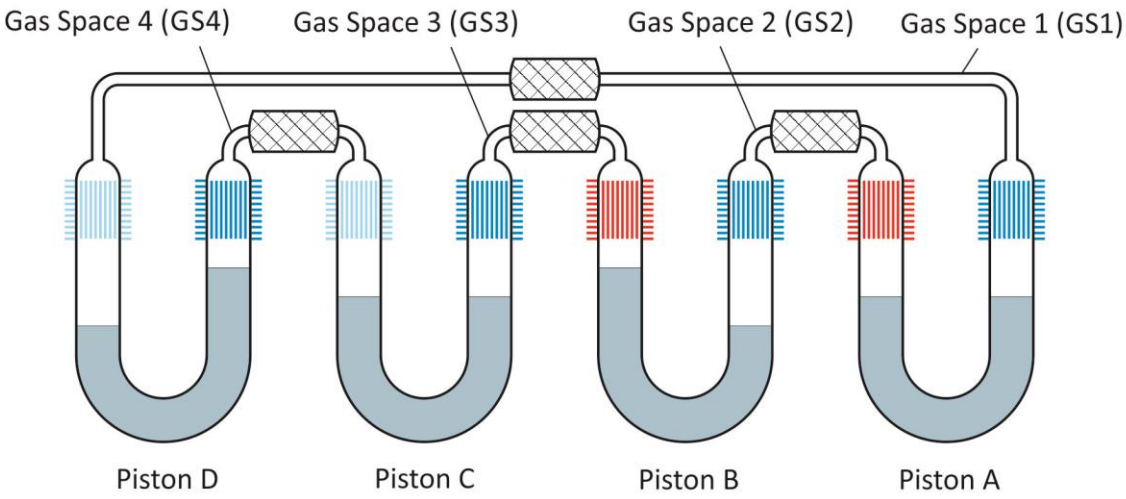

Figure 3.2 – Liquid piston Stirling cooler Schematic.

It was anticipated that the machine’s performance would be sensitive to small changes in certain system parameters, such as the diameter or volume of liquid pistons, the clearance between the liquid piston surface and the entrance to the heat exchangers, the mean pressure (or charge pressure) in the gas spaces or the number of absorbers versus heaters. For this reason, the design of the test-rig allowed changes in the geometry of the system so that its performance across a range of operating conditions could be analysed. For example, the liquid piston U-tubes can be exchanged with others of different diameters.

Figure 3.3 shows an indicative schematic of a quarter section of the overall system and identifies where the measurement equipment takes readings for data collection. The arrangement is the same for each of the four subsystems. Since the primary interest is in the behaviour of the liquid piston Stirling system, the heat input does not come from a

solar source but instead is supplied by electric heating cartridges used in conjunction with a heat exchanger. This enables more efficient, simplified experimentation with a constant and reliable heat source. An integrated solar collector system will potentially be considered for future research.

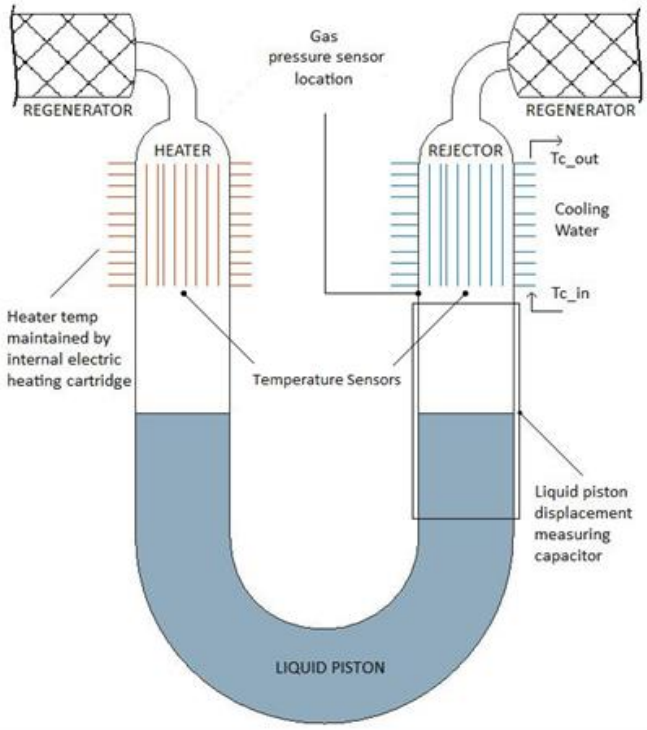

Figure 3.3 – Subsystem composition. The LPSC machine is comprised of four of these units connected in series.

In terms of data collection, eight thermocouples are installed in the gas spaces directly under each heat exchanger. These provide real-time temperatures of the gas in each of the compression and expansion spaces. Four pressure transducers are installed on the cold side of each gas space below the temperature sensor ports. All of these measurement devices are used in conjunction with LabVIEW to monitor, organise and collect the data for analysis. The engineering design software SolidWorks was employed to design the heat exchanger, regenerator and housing components.

3.1.1 Heat Exchangers

All eight heat exchangers used in the LPSC machine are identical in design and were manufactured in Rosenheim, Germany. Figures 3.4 and 3.5 show the annular finned design employed in the system.

Figure 3.4 – Brass heat exchanger showing side view of the annular fins and protrusion for heating cartridge access (RHS).

Figure 3.5 – Brass heat exchanger end showing a view of the annular fins (note that the large channel is for temperature probe installation access).

These components were designed prior to the commencement of this investigation, and as such, will not be discussed in great detail. Brass was the chosen material, because of its favourable heat transfer properties and malleability for the intricate component geometry. Each heat exchanger incorporates an internal bored section which is exposed to atmosphere and not connected to the hermetically sealed gas space. In the case of the four 'hot' heat exchangers, this bore is fitted with a cylindrical electric heating cartridge, which provides the heat input to the system. Each heater can be individually isolated, and when one of the heaters is not activated that space then becomes a potential absorber, i.e. as a result of the relative motions of adjacent liquid pistons, the working gas is forced to expand, drawing heat from the surrounding housing, and lowering its temperature. The four 'cold' heat exchangers have an internal cold water fitting, and during operation this provides a steady flow of cooling water into (and out of) the cavity, in order to transport the rejected heat. Each of the four fittings is connected in series with a PVC tube and fed by a single water supply.

3.1.2 Housing and Regenerator

The housing components are constructed out of stainless steel. They encapsulate the gas space around the heat exchangers, and provide the structural support for the regenerator matrix occupying the space between the hot and cold sides. There are eight individual housing components—one for each heat exchanger. They are connected via vacuum seals and clamped together to form a hermetically sealed space. Figure 3.6 shows an individual housing component, and Figure 3.7 shows a version preassembled with a heat exchanger.

Figure 3.6 – Stainless Steel housing component.

Figure 3.7 – Stainless Steel housing component assembled with brass heat exchanger and vacuum clamp.

The space between the top surface of the heat exchanger fins on the hot side and the top surface of the heat exchanger fins on the cold side is filled with regenerator material. In order to permit swift assembly and disassembly the material used was steel shot: small steel spheres approximately 1 mm in diameter. Each half of the 'H' housing is filled separately before covering the open surface with a thin steel mesh to contain the steel shot, then clamping both faces of the regenerator together. Figure 3.8 shows the steel shot regenerator material.

Figure 3.8 – Steel shot material used in the regenerators (with an average diameter of 1 mm).

3.1.3 Liquid Pistons

Standard steel tubing was selected as the material for the piston tubes. This material was selected over other potential options primarily to allow for the potential variation in piston tube dimension. Each U-tube is divided into two parts. The largest of these two parts comprises 75% of the whole U-tube, and attaches to the underside of the hot heat

exchanger housing via an expansion flange—which also incorporates the pressure and temperature sensor ports shown in Figure 3.9.

Figure 3.9 – Liquid piston housing U-tubes with expansion flange fittings.

The same vacuum seal and clamp attachments (common to the whole set-up) are used to fix the flange to the heat exchanger housings. To complete the U-tube assembly, a smaller section of straight tube extends from the underside of the cold heat exchanger with the same expansion flange, and both U-tube openings are connected via a clear PVC tube section. This provides viewing access to the liquid piston surface, which is crucial in assessing system operation and troubleshooting. When installed, the PVC tube is heated in hot water and slid over the ends of both tube sections before being fixed in place via ring clamps. The initial steel tube size utilised was 15 mm outer diameter, with 1 mm wall thickness, whereas the PVC had an average internal diameter of 12.3 mm. Liquid water is measured out and added to each of the U-tubes, resulting in functional U-shaped liquid pistons.

3.1.4 PID Controller

The power supplied to the heating cartridges is regulated by a PID controller, in conjunction with a Solid State Relay (SSR) that is linked to a thermocouple in contact

with the interior surface of one of the heat exchanger's fins. The circuit diagram for this configuration is shown below in Figure 3.10.

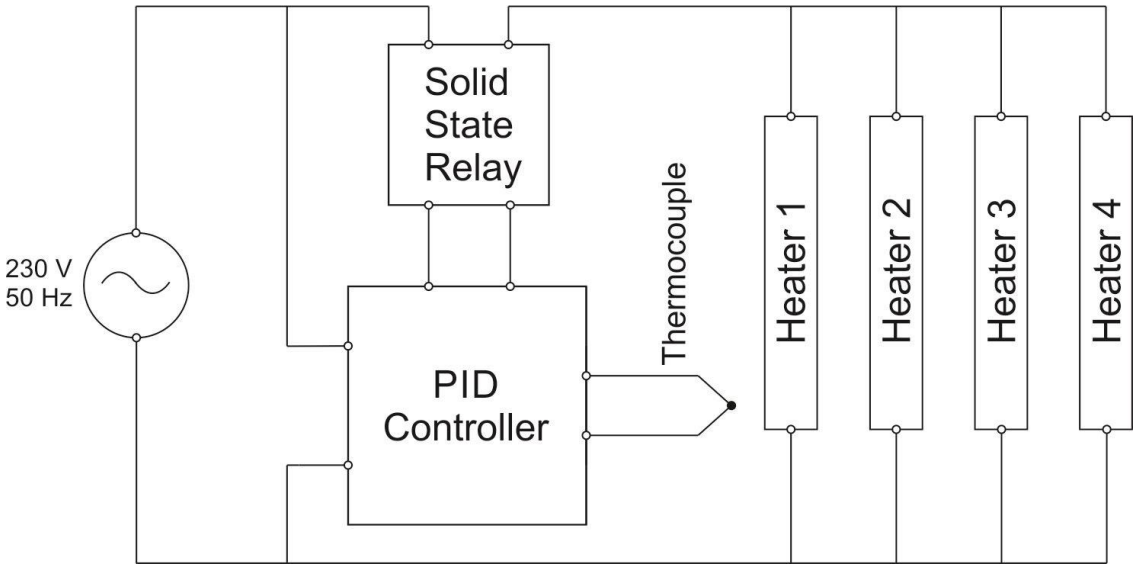

Figure 3.10 – Controller Circuit for regulating the power supply to the heaters.

This arrangement allows for the heat source temperature to be set and remain constant over the course of each experiment. It should be noted that out of the four potential heaters only one heat exchanger fin temperature is monitored and controlled. The other heater(s) are connected in parallel so that they are all supplied with the same amount of power, and thus heat input (assuming similar thermal resistances, etc.). Figure 3.11 shows the PID controller installation, including an isolation box containing all of the associated circuitry and the SSR. The user interface displays the set-point temperature (green) and the current temperature (red).

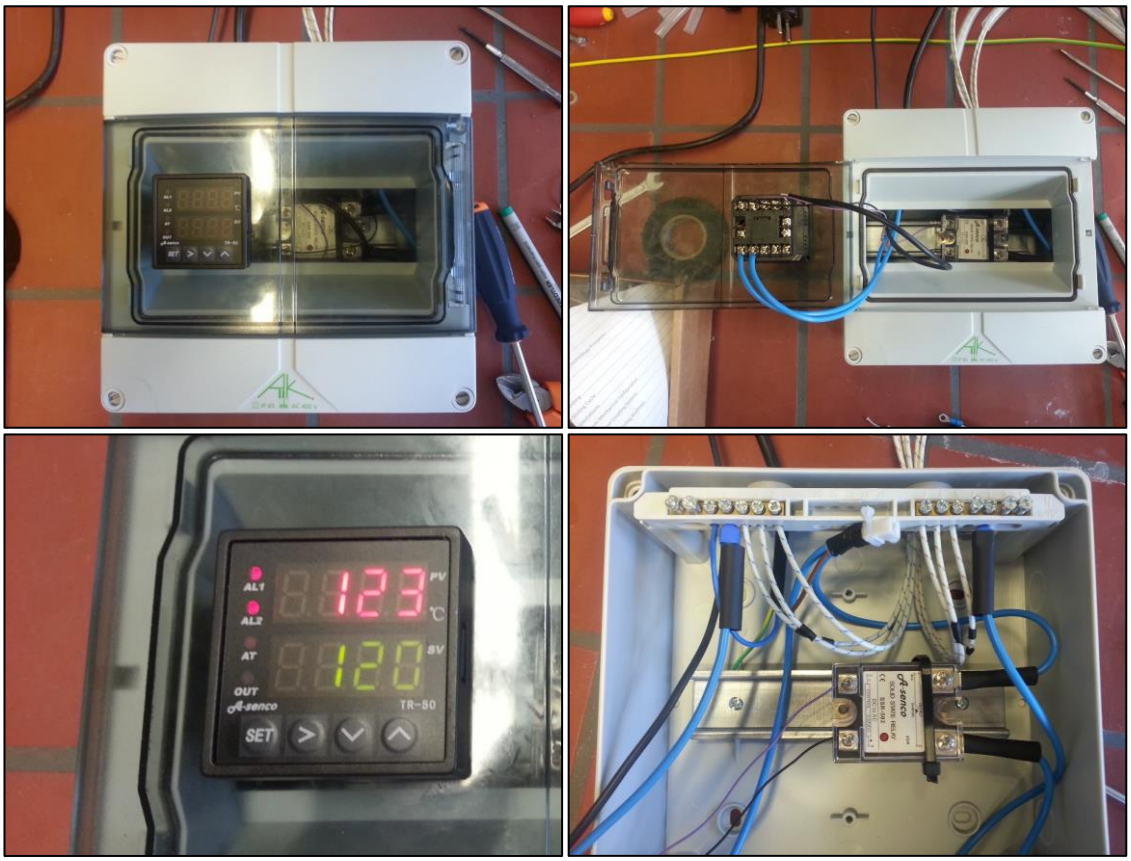

Figure 3.11 – PID controller and SSR housing images.

3.1.5 Temperature and Pressure Sensors

Aside from the temperature sensor that was used to measure the fin surface temperature of the primary hot heat exchanger, eight additional temperature sensors were employed for data collection. All eight sensors were installed through ¼-inch compression fittings in the walls of the liquid piston expansion flanges (situated just below the gas entry points into the hot and cold heat exchangers). This was identified clearly in Figure 3.3 in Section 3.1 and also shown in Figure 3.12. The purpose of these temperature sensors was to collect gas temperature data on both the hot and cold sides of the gas space. The types of thermocouples used were J-type sheathed thermocouples. The sizes used were either the 1.5 mm × 150 mm or the 1.5 mm × 100 mm variety, as these were readily available within the laboratory. The thermocouples where calibrated using single point calibration at the boiling point of water.

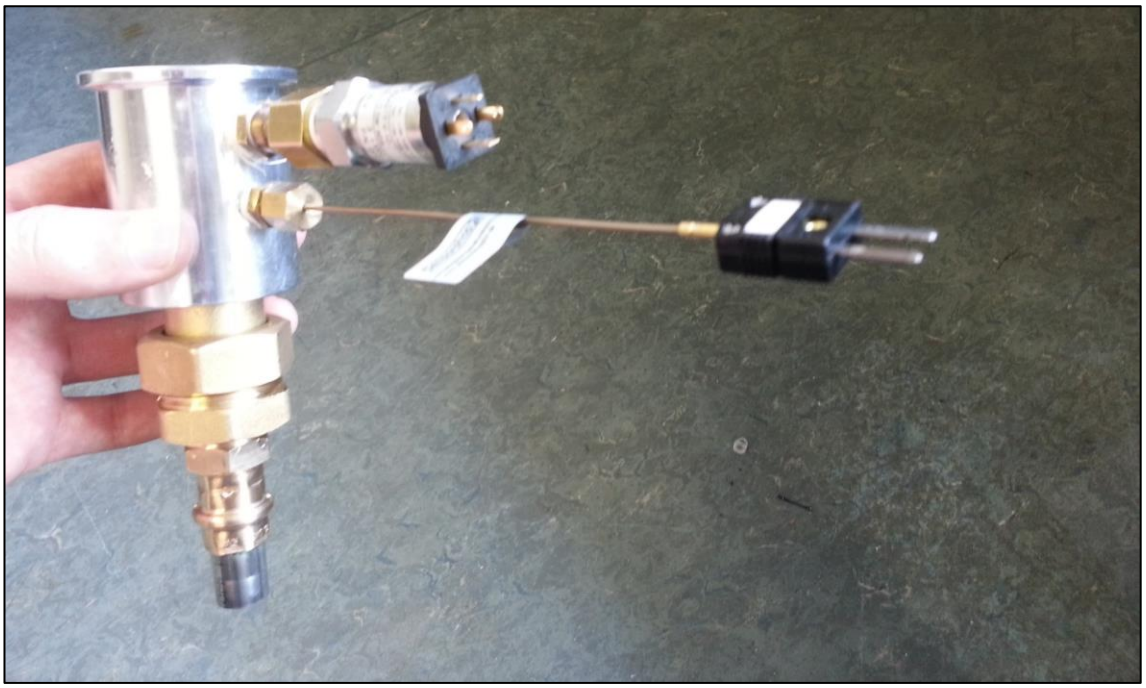

Figure 3.12 – Pressure transducer and temperature sensor ports. Also visible is the gland fitting used to connect to the top of the piston U-tubes.

Each gas space was also fitted with a single pressure transducer in the same vicinity of the thermocouples, but only on the cold heat exchanger side. The pressure transducers were Omega PAA21Y-V-10 and PAA21Y-V-16. Two of each type were used: the first has an operating range of up to 10 bar; the second up to 16 bar. Each provides a 0-10 V output signal, which was connected via a PCI card to the LabVIEW data collection software. The pressure transducers came pre-calibrated, but two of the four possessed small offset errors which remained consistent over the experimental pressure range. The pressure sensor installed in GS3 exhibited an offset of +0.006 bar, while the GS4 sensor had an offset of -0.012 bar. These errors were accounted for in the LabVIEW data acquisition (DAQ) file. Figure 3.12 shows one of the pressure transducers installed in the U-tube expansion flange.

All eight temperature sensors were connected back to a National Instruments USB-6211 bus-powered data acquisition module that was configured within LabVIEW. The pressure transducers were powered by a benchtop power supply unit, and the signal outputs connected to a PCI DAQ bus through a CB-68LP terminal board, along with the

displacement sensors discussed in the next section. The same LabVIEW file was used to configure the sensor outputs for data acquisition.

3.1.6 Piston Displacement Sensors

A capacitive sensor was used to measure the displacement of the liquid pistons. The capacitance of a parallel-plate capacitor is given in the following equation:

$$C_p = \varepsilon_r \varepsilon_0 \frac{A_p}{d_p} \tag{3.1}$$

where ε_r is the dielectric constant of the material between the plates, ε_0 is the electric constant, A_p is the plate area and d_p is the separation distance between the plates.

The capacitor enshrouds the displacement range of one surface of a liquid piston. Since water is a far better dielectric than air (or helium/hydrogen), the capacitance of the capacitor changes significantly as the piston surface moves up and down. Based on the above equation, this change should be close to linear and can be used to measure liquid piston displacement during operation. This approach was chosen to combat the potential irregularities in the liquid surface during oscillation since the measured capacitance would primarily depend on the volume of water encased within the measurement space.

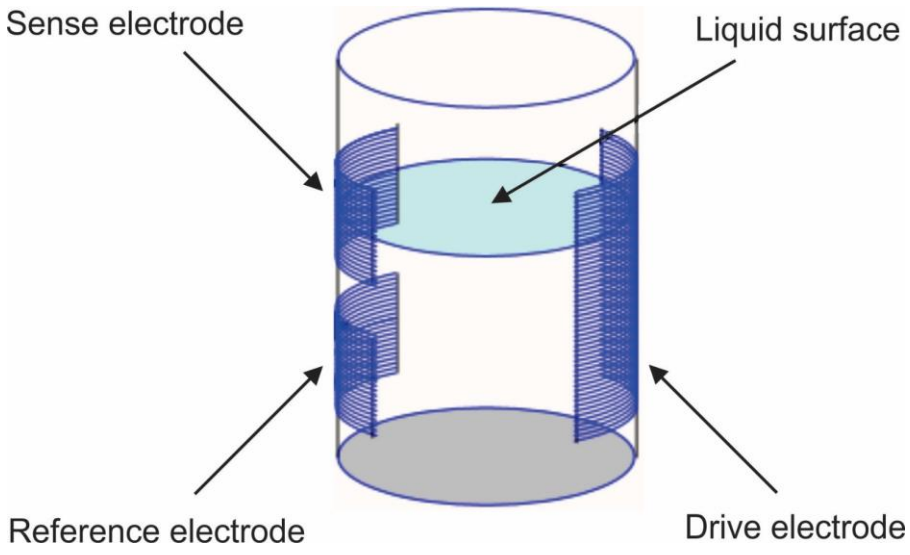

Figure 3.13 – Capacitive sensor setup for measuring piston displacement.

In the original set-up two capacitors were used for each piston in the manner shown in Figure 3.13. One would be installed across a lower section of the U-tube where the liquid surface never crossed in order to act as a reference capacitance. The second capacitor would be installed so that its centre was bisected by the resting position of the liquid piston surface. During operation, as the surface moved up and down, the changing volume of liquid contained within the capacitor would vary its capacitance. Figure 3.14, shows the initial set-up of the capacitive sensors.

Figure 3.14 – First generation capacitive sensors used for measuring liquid piston displacements.

The sensors were constructed from copper film which could be cut and shaped to fit the shape of the piston tubes being used. The electrodes were then connected in pairs via a Wheatstone bridge which compared the variable capacitance to the reference capacitance—and led back to a common circuit board which included amplification, filtering and rectification procedures, before providing 0–10 V output signals for the PCI board and DAQ system. A circuit diagram of this system can be found in Appendix I. This technique was employed in the initial experiments and was found to have a very high sensitivity, and a capability to tolerate high oscillation frequencies. The capacitive sensors went through many iterations and ended up causing substantial delays in the experimental process. Their commissioning, calibration and performance is discussed further in Sections 3.2.3 and 6.1.

3.2 Commissioning and Modifications

Before experimentation began, it was unknown whether the system would be capable of self-starting, or indeed starting at all. It was also unclear over what range of operating conditions the liquid piston surfaces would remain stable, as this would depend on the frequency and amplitude of any oscillation. Fortunately, the system did prove to be self-starting when preliminary testing began. A period of practical problem-solving followed the initial testing, which involved making alterations to the test-rig in order to improve its functionality, usability and controllability. These alterations are summarised below.

3.2.1 Piston Floats

One of the major adaptations was the inclusion of piston floats. At the beginning of the project it was unclear as to whether some form of piston float would be required. In the ideal scenario, piston surface instability would be mitigated through indirect means, i.e. via geometric design and the prevailing operating conditions such as frequency, charge pressure and piston dimensions. Unfortunately, in order to determine whether such

operating conditions existed, the system first needed to be well understood and optimised. Preliminary results revealed that the liquid pistons became unstable (and their surfaces would disintegrate) at charge pressures above 2 bar. With the scope of the investigation including pressures up to 6 bar, some form of surface stability measure was required. It was decided that piston floats would be therefore incorporated into the test-rig—in order to limit the disintegration of the liquid piston surfaces as piston amplitude and frequency increased with charge pressure beyond stable limits.

Very little research has been conducted in the field of liquid piston float design and any mention of them is vague and unspecific. Therefore, the floats incorporated were of an original design. As previously mentioned, however, optimisation of float design would likely prove redundant as the piston geometry is varied throughout the experimental investigation. For this reason, the development of the optimised piston floats was identified as being of secondary importance to the main objective of evaluating performance trends.

A number of potential float options were considered and tested. Submerged floats were selected over above-surface floats for simplicity reasons. The two main factors of float design are geometry and material. The material must be water and heat resistant and have a density lower than that of water, while the geometry must be simple to produce. It was theorized that the most suitable material would have a density relatively close to that of water, so that during operation the float would retain its vertical position relative to the liquid surface as it moved up and down—as opposed to oscillating above and below the surface due to buoyancy and inertial effects. The different materials tested included wood, polystyrene, and polyethylene.

Following a number of trial experiments—using various float prototypes—polyethylene cylindrical floats were eventually selected as they outperformed the other options, and

could be easily machined to varying dimensions in the workshop. The density of the polyethylene used was also the closest to that of water—being one of the only plastics with a relative density of less than one.

Initially, 10 mm × 20 mm cylindrical polyethylene floats were installed. But at the higher end of the temperature and pressure ranges to be investigated, a significant amount of piston water was still able to by-pass the floats, and interfere with the temperature sensors above. It became apparent that an optimal float diameter would exist, where the clearance created would be sufficiently small to reduce piston leakage, whilst remaining large enough not to increase the annular fluid friction too much. Eventually piston floats of diameter 11.5 mm (PVC tube side) and 12 mm (steel tube side) and 20 mm in length were settled upon. An example of the floats used can be seen in Figure 3.15.

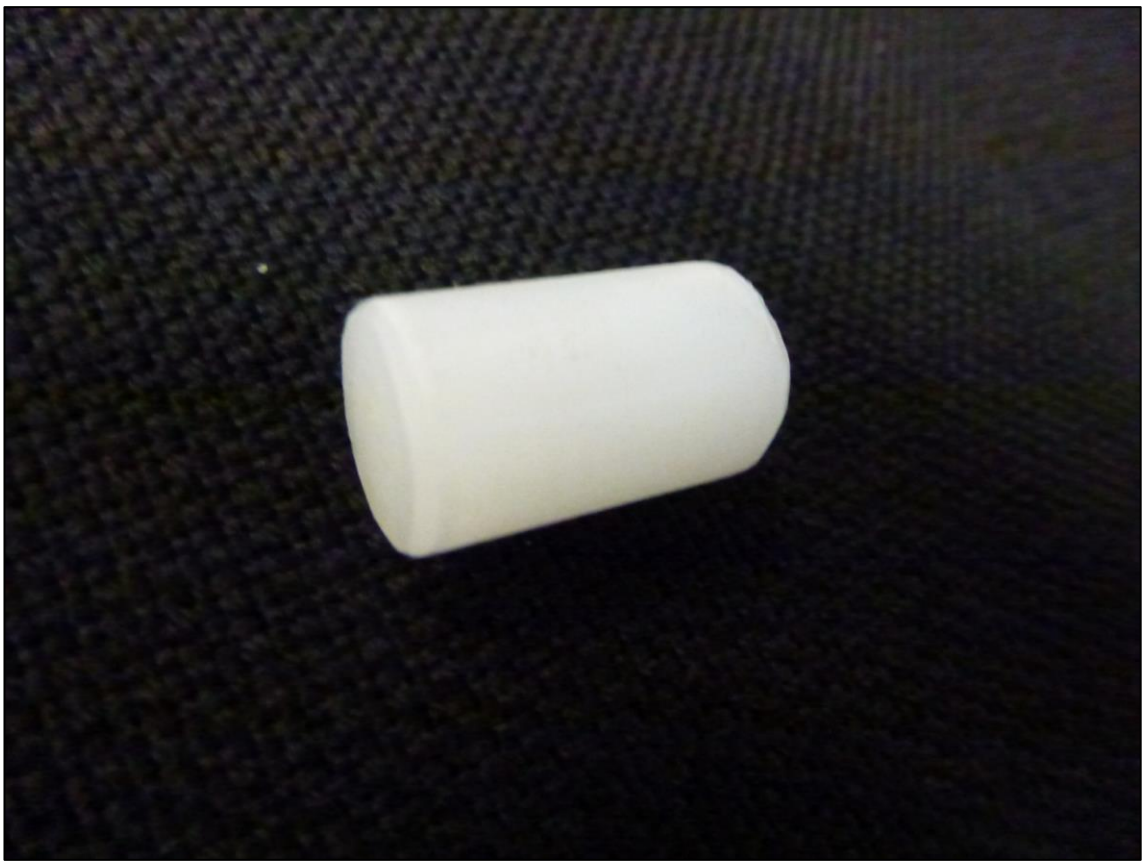

Figure 3.15 – Cylindrical polyethylene liquid piston float for improved surface stability.

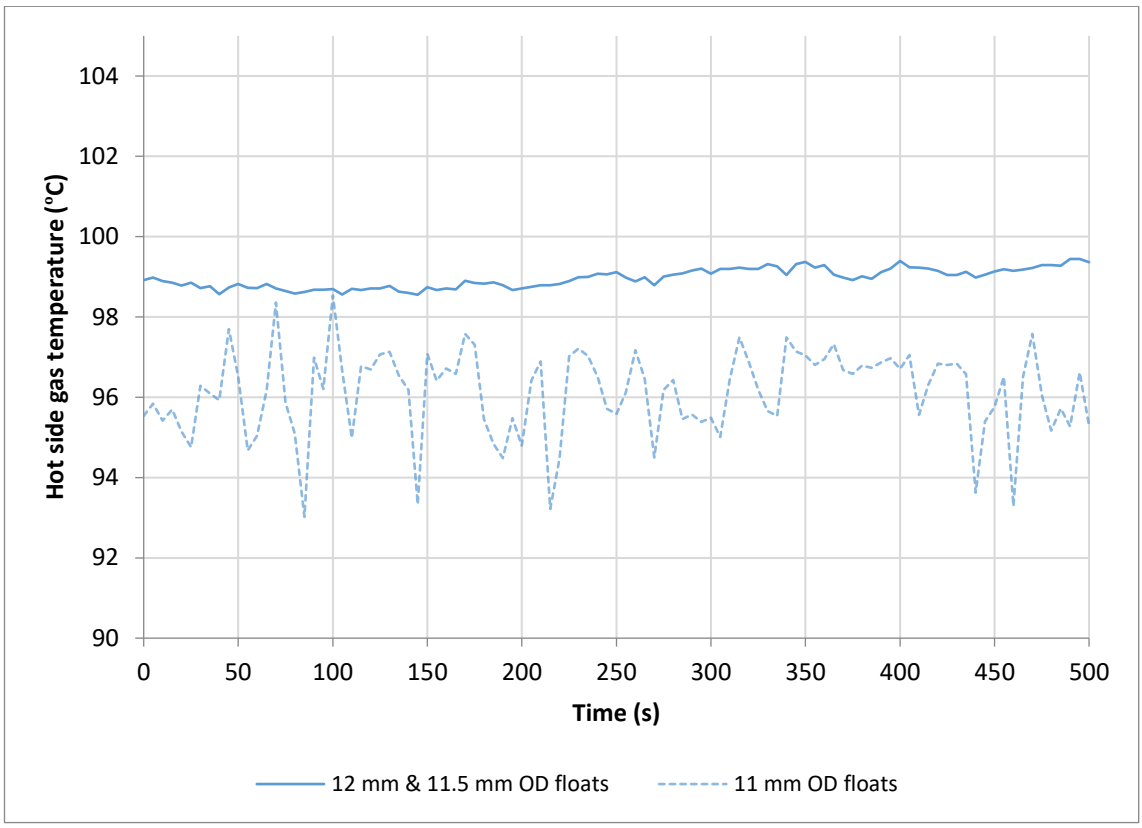

Figure 3.16 – Gas temperature stability comparison for different float diameters. Experiments were conducted with the 3HEAT configuration with 150 °C heaters and 4 bar charge pressure.

Figure 3.16 shows how the change from 11 mm floats on both sides of the U-tubes (to 11.5 mm and 12 mm floats) improved piston stability. The irregular readings from the 11 mm experiment are presumed to result from water droplets bypassing the piston floats and interfering with the thermocouple installed above. By increasing float diameter, the clearance gap was reduced, increasing the effects of surface tension and limiting the possibility for water droplets to escape. The 11.5 mm and 12 mm floats resulted in more stable temperature readings and the stability improvements were also visually apparent when observed through the PVC tube section. The larger floats did hinder the self-starting ability of the system, particularly at lower charge pressures. This meant that 'jump starts' were required more frequently[1]. Conversely, operation was now stable for higher pressures and temperatures, which was of greater importance.

[1] Jump starting the system involved manually exciting a small piston amplitude by pulsating the piston housing at close to the expected frequency.

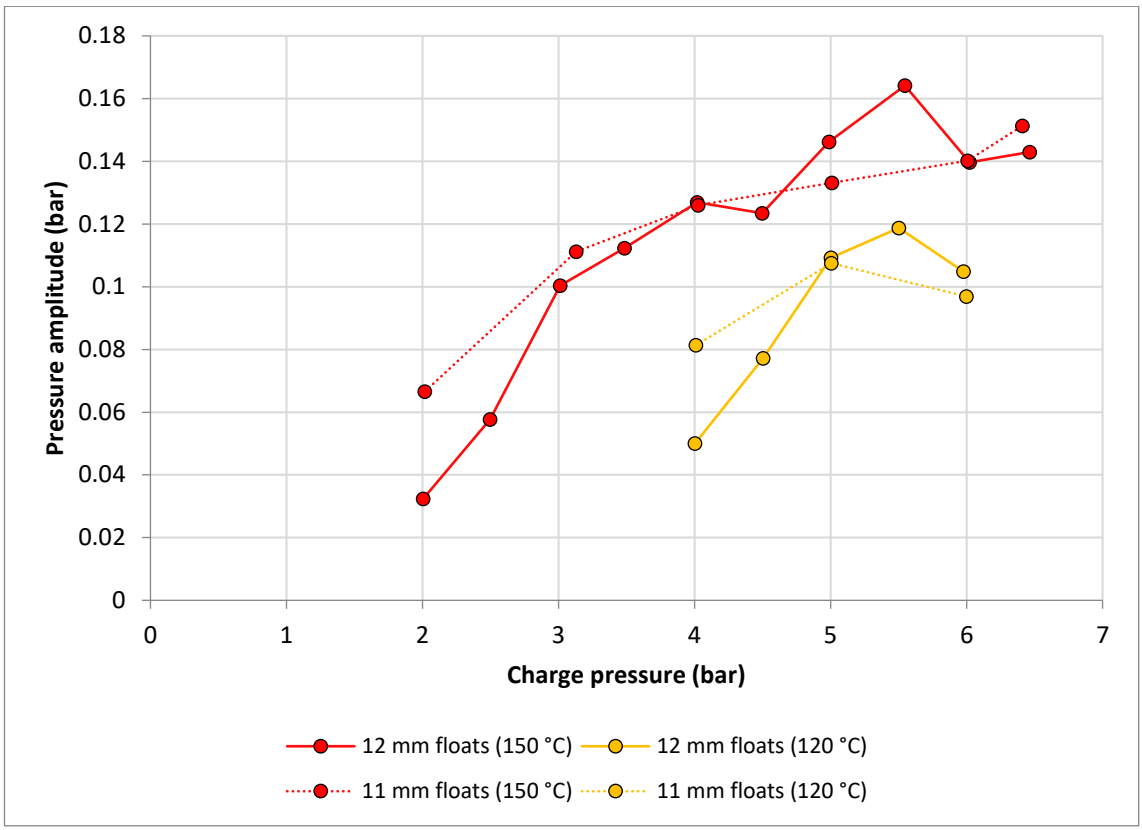

Figure 3.17 – The impact of piston float diameter on the development of pressure amplitudes within the gas spaces.

Figure 3.17 shows how the pressure amplitude was affected by the change in piston float diameter. At lower charge pressures, the larger floats have more of an impact on stifling operation; however, as mean pressure or temperature increases, this effect is less evident. In this case the additional benefits on piston and temperature stability become more relevant. For this reason, the subsequent experimental investigation continued with the 11.5 mm (PVC side) and 12 mm (steel side) floats installed within the 15 mm piston tubes. A more substantive investigation into float design could be of value to the future of this system (or any similar liquid piston machines) and is discussed in Chapter 8.

3.2.2 Pressure Manifold

A pressure manifold was installed as an interface between the main compressed air line and the feed lines of the individual gas spaces. During the commissioning phase it became apparent that each of the four gas spaces required independent control and isolation valves

in order to manage charging/discharging as well as for isolating each space during operation and locating pressure leakages. A schematic of the manifold is shown in Figure 3.18.

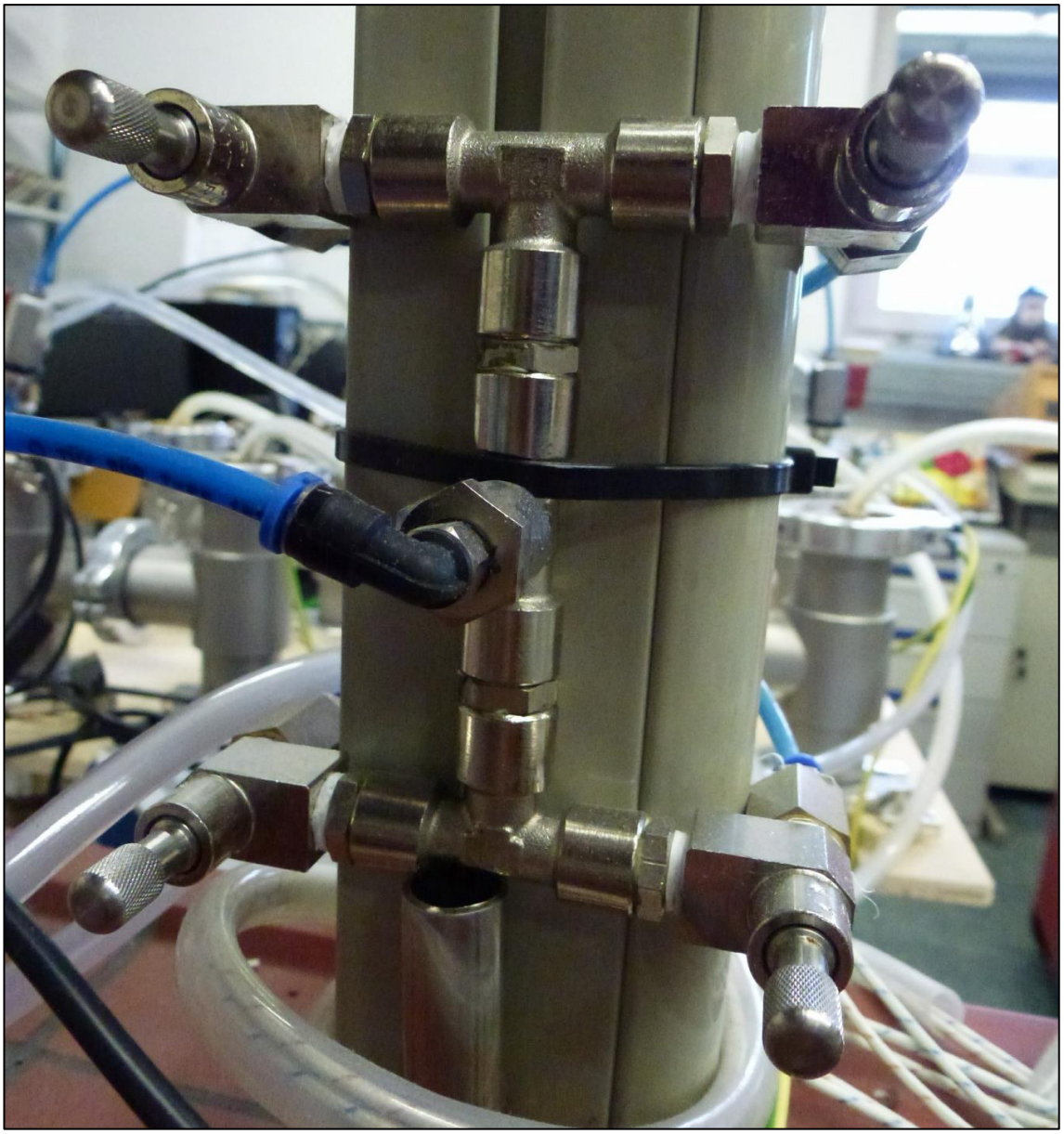

Figure 3.18 – Pressure manifold with individual control valves for each subsystem.

3.2.3 Displacement Sensors

The displacement sensors proved to be the most time-consuming and troublesome of all aspects of the experimental investigation. Numerous iterations of the sensors were tested and modified following the establishment of the basic principles of operation (using the set-up outlined in Section 3.1.6). The largest obstacles faced in commissioning the

displacement sensors to a satisfactory level were those of signal noise and calibration. It was discovered that the output signal from the displacement sensors was very sensitive to any handling of the sensor wires—and also their proximity to any other sensor wires. An extensive trial and error procedure was initiated in order to solve this problem. Some examples of the attempted fixes included moving the reference capacitor sensors from the test-rig to an entirely separate duplicate set of U-tubes situated nearby, as well as reconfiguring the circuity of the sensor system multiple times in order to eliminate potential ground loop interference. Eventually, the noise issue was mitigated by installing shielded cable wires of exactly equal length for the sense and drive electrodes—and disconnecting the reference sensors entirely, and replacing them with a miniature breadboard equipped with an array of small ceramic capacitors. Since the reference capacitance does not change during normal operation, it can be provided by a separate input source. Figure 3.19 shows the breadboard and capacitive sensor circuit set-up prior to its installation on the test-rig stand.

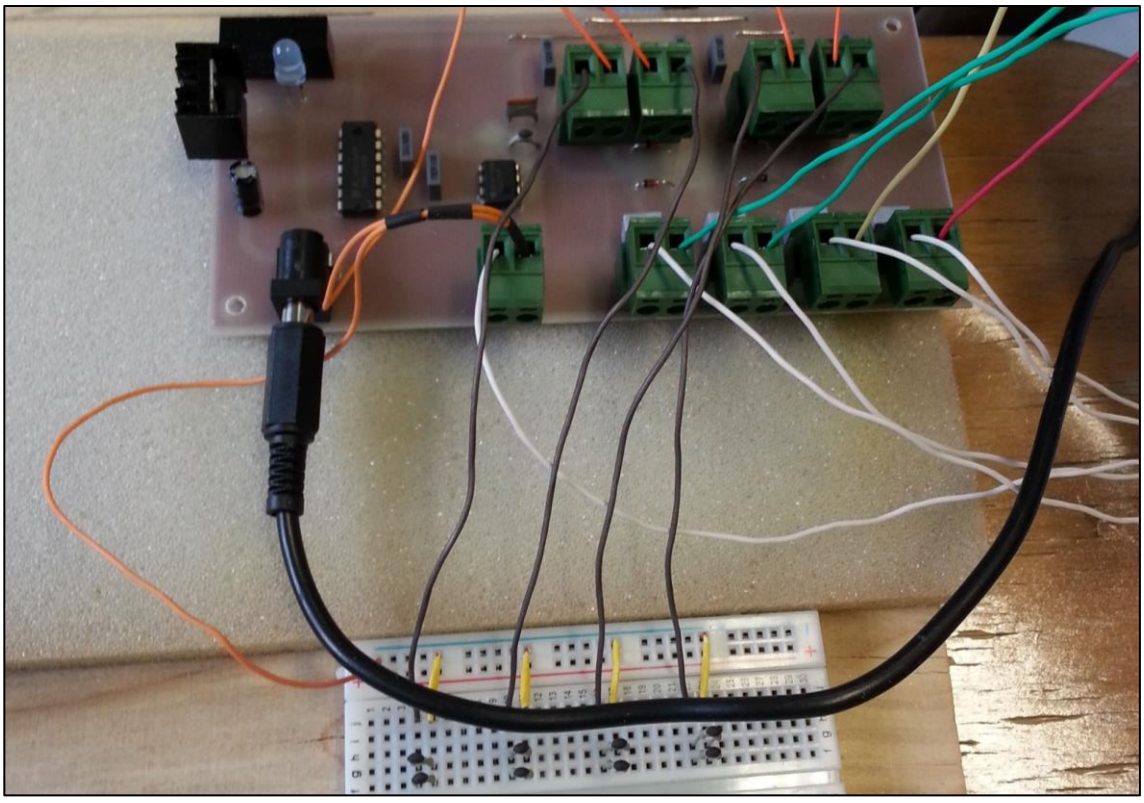

Figure 3.19 – Capacitive sensor circuit with reference capacitors.

In this form, each reference capacitor is represented by two 30 µF capacitors in parallel, creating a total capacitance of 60 µF. This arrangement was found to produce the highest signal resolution for the 15 mm piston tubes through the LabVIEW interface. It should be noted that the reference capacitance required is specific to each piston diameter and U-tube material in use. By removing the reference capacitor from the sensor installation on the piston tube, the measurement stroke range is effectively doubled since the sense electrode can be increased in length to match that of the drive electrode. A beneficial consequence of this modification is that the range of piston masses available for testing for each set of U-tubes is increased. Following the successful elimination of signal noise, the displacement sensors could now be calibrated. Figure 3.20 shows the typical displacement sensor output data over a period of one second.

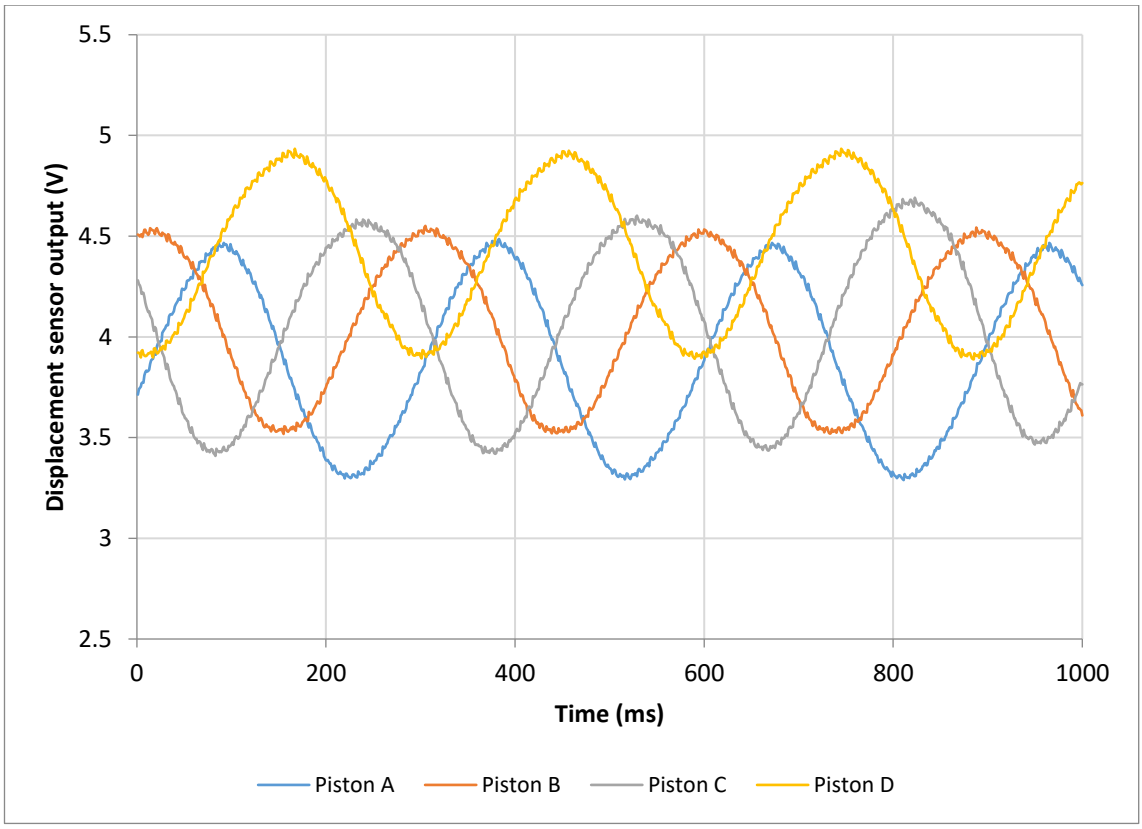

Figure 3.20 – Piston displacement profiles over one second interval during a typical experiment. This experiment was at 3 bar and 105°C with 100 ml liquid pistons.

From this information, the piston phase angles and amplitudes can be determined. It should be noted that the difference in vertical offsets of the data is due to the differences

in physical sensors and their positioning on the U-tubes themselves. The phase angles are calculated by using the least mean squares method to approximate the displacement profiles as sine functions, as shown in Figure 3.21.

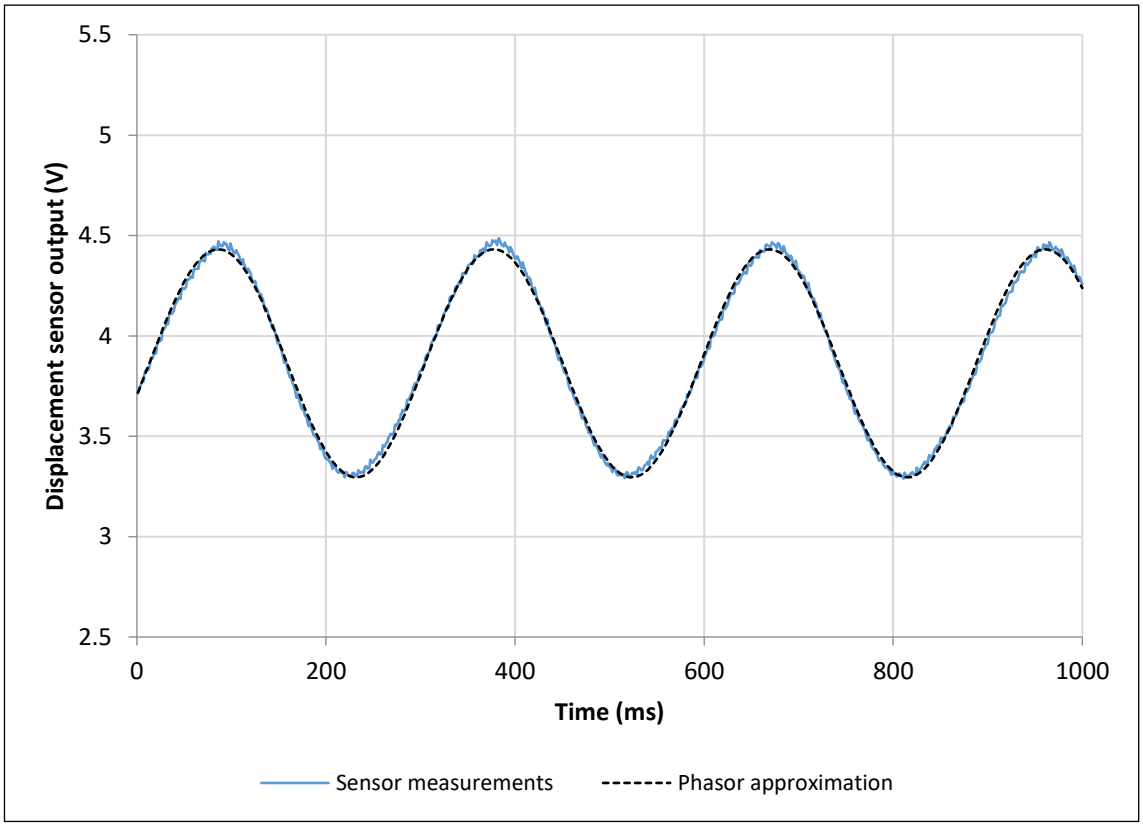

Figure 3.21 – Example of phasor representation and optimisation for Piston A displacement profile using least mean squares approximation.

The phasor approximation of the piston displacement profile thus developed shows good agreement with the actual displacement profile measured by the capacitive sensors—indicating that the assumption of simple harmonic motion is valid. The final requirement was to calibrate the sensor voltage output with actual piston amplitude. Due to the slight geometric and spatial differences, each of the four sensors needed to be calibrated separately. In order to calibrate the sensors, 8-times slow motion video of the piston motion was recorded at increasing levels of piston amplitude and frequency. Each piston U-tube was fitted with an external scale covering the PVC tube section where the piston surface oscillates, as shown in Figure 3.22.

Figure 3.22 – Scales for calibrating displacement sensors with slow motion video recordings.

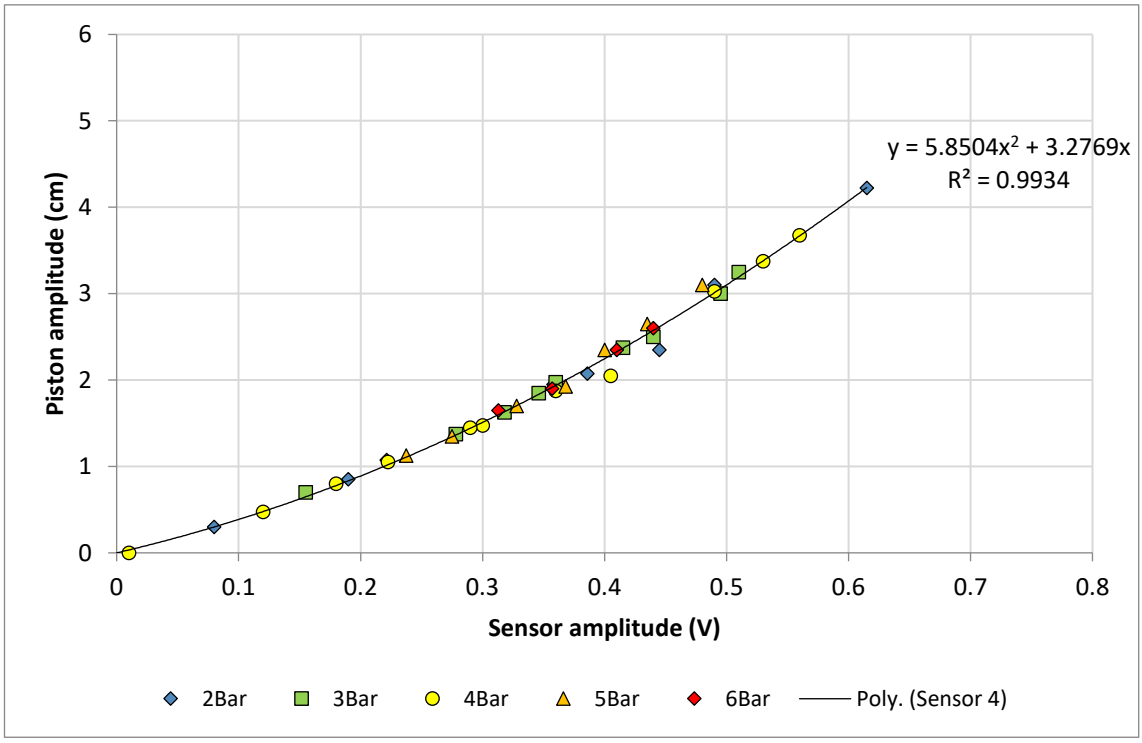

Figure 3.23 – Displacement sensor 4 calibration curve comparing sample experiment readings with slow motion video displacements.

The piston amplitudes obtained from the slow motion videos were compared with the output signals from the capacitive sensors. Each sensor behaved similarly during

calibration with slight differences in the calibration coefficients. Figure 3.23 shows the relationship between piston amplitude and sensor output for one of the four sensors. In each of the four cases, the correlation between observed piston amplitude and sensor output appeared to closely resemble the quadratic form. When the idea of using capacitive displacement sensors was first discussed, it was theorized that this relationship would be linear. The capacitance of the section of the U-tube enclosed between the copper plates does increase linearly with an increase in water level as long as the piston surface is not in motion. This can be seen in Equation 3.1 from section 3.1.6 where capacitance is proportional to the dielectric constant. Since the dielectric constant of water is far greater than air, the aggregate dielectric constant is proportional to the volume of liquid water within the sensor. The problem is that this equation is only valid for materials with symmetric material thickness through all vertical cross sections. As the liquid piston oscillates, a thin layer of water develops on the inner surface of the U-tube. This has the effect of increasing the average overall capacitance measured by the sensor.

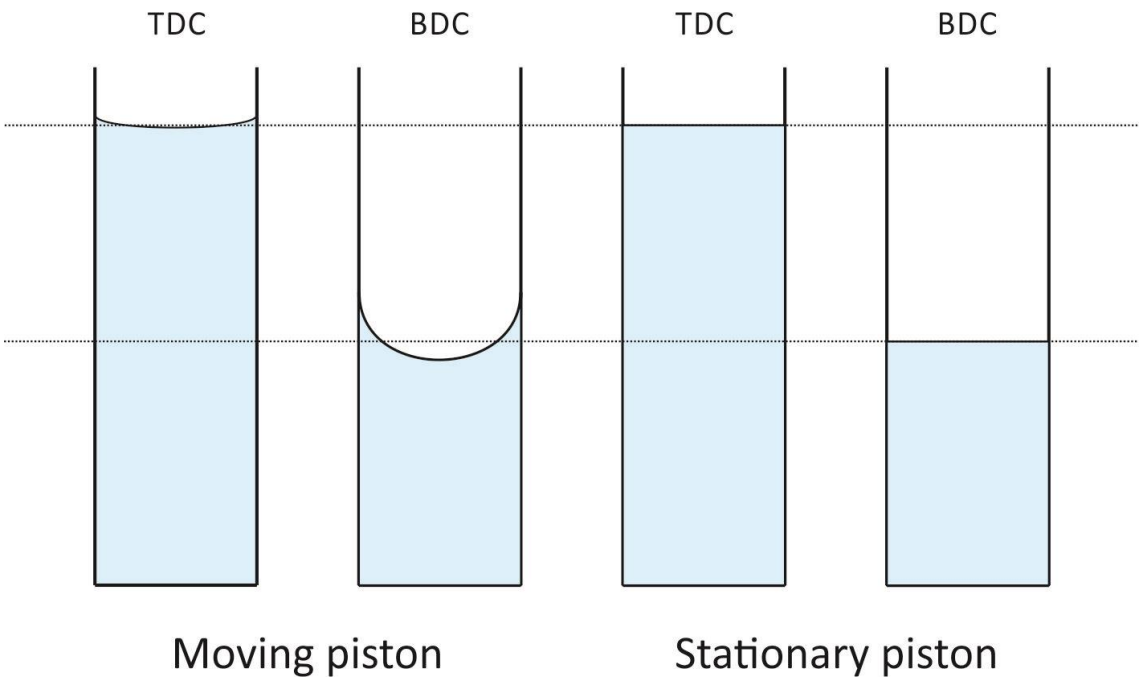

Figure 3.24 – Comparison of surface profiles between moving and stationary liquid pistons.

It is easiest to understand how this happens by considering the two capacitive limits measured by the sensor, these are shown in Figure 3.24. At top dead centre (TDC) the piston surface is roughly flat and the maximum capacitance is measured. At bottom dead centre (BDC) however, a layer of water film remains on a section of the U-tube above the piston surface. The capacitance measured at this position is higher than that which would be measured if the piston was given time to settle and acquire a flat surface, i.e. as per the stationary piston on the right hand side. Since the measured capacitance is higher at BDC, but roughly the same at TDC, the total range measured by the sensors is less than a corresponding set of flat surfaces (despite the same change in volume). This phenomenon becomes more pronounced as piston amplitude and frequency increase, thickening and spreading out the water layer. As a result, the capacitive sensors underestimate piston amplitude by larger and larger degrees as the actual amplitude increases, resulting in the quadratic relationship pictured earlier.

Fortunately, the correlation appears to be predictable, and does not appear to depend significantly on system charge pressure (although a slight dependence was observed). Quadratic trend lines were fitted to the calibration data. The quadratic trend lines fitted to the calibration data were used in all subsequent testing involving the 15 mm U-tubes, and are shown in table 3.1.

Table 3.1 – Displacement Sensor Calibration Coefficients. Fitted for $y = Ax^2 + Bx$, where y is piston amplitude (cm) and x is the sensor output (V).

Sensor	Calibration coefficients	
	A	B
A	5.501	3.140
B	6.337	3.040
C	5.381	3.057
D	5.850	3.277

3.2.4 Minor Alterations

Many minor improvements were also implemented throughout the commissioning and experimentation phase. The previously used PVC hose sections were increased in length by a factor of three to encompass the majority of one side of the U-tube. This allowed the displacement sensors to cover a greater potential amplitude range, and also enabled a larger range of liquid piston volumes/masses to be investigated. The clear PVC hose was replaced by fibre-reinforced PVC hose capable of withstanding up to 10 bar at 60ºC. The previous un-reinforced hose's structural integrity became compromised due to heat conduction from the hot side of the U-tube after prolonged use. Gland fittings (¾-inch) were installed at the top of each U-tube connection to facilitate piston access. This allowed each piston to be removed in isolation, without needing to take apart the housing components. It also allowed for the potential of easily installing piston U-tubes of different diameters, without altering the housing connections.

3.2.5 Experimental Accuracy

The main sources of error in the experimentation process come from the pressure, temperature, and displacement sensors. The pressure transducers have a stated total error range of ± 1%, however as described in Section 3.1.5, all four were calibrated together and resulting pressure tests showed agreement to 4 significant figures over the entire testing range. Although this does not necessarily guarantee true accuracy, it does indicate that the measured pressure amplitudes are very accurate and consistent across the four subsystems. Similarly, the stated error range of the thermocouples was ± 0.75%, however these were also recalibrated in the lab using a single point calibration test at the boiling point of water. In the case of the capacitive displacement sensors, the calibration method (outlined in Section 3.2.3) showed that a calibration curve could be fitted to the experimental data with a high R^2 value. The experimental error involved in their use was

conservatively estimated to be ± 10%, although for reasons discussed further in Section 6.1, the use of the capacitive sensors for piston displacement information was not continued for the second iteration of the experimental investigation. Instead an optical method was used, with an estimated error of ± 2.5 mm.

During the commissioning and early experimentation processes, it was identified that the system's behaviour was very transient in nature. Aside from the modal behaviour discussed in Chapter 5, the pressure amplitudes, piston displacements, and other measured variables showed gradual cyclic variation, even well after sufficient time had been allowed for the system to reach steady-state operation. This cyclic variation is not unexpected for a complex system such as the LPSC, where each of the four subsystems has direct, uncontrolled influence over its neighbouring subsystems. In order to collect data points for the experimental analysis, a time period of steady-state behaviour was identified for each experiment (of at least 5 minutes in length), and the parameters of interest were averaged over this period (see Section 5.1). In the majority of experiments, the cyclic variations contributed more significantly to the experimental uncertainty of the data than the accuracy of the data collection instrumentation itself. For this reason, and considering the current stage of the research project, the inclusion of a thorough error analysis in this thesis was decided against. With future test-rig and model refinement, the inclusion of error analysis will be re-evaluated.

3.2.6 Commissioned Test-rig Setup

After completing all of the necessary test-rig upgrades and commissioning procedures, the test-rig was ready for the primary data collection phase. Figure 3.25 shows the final state of the test-rig.

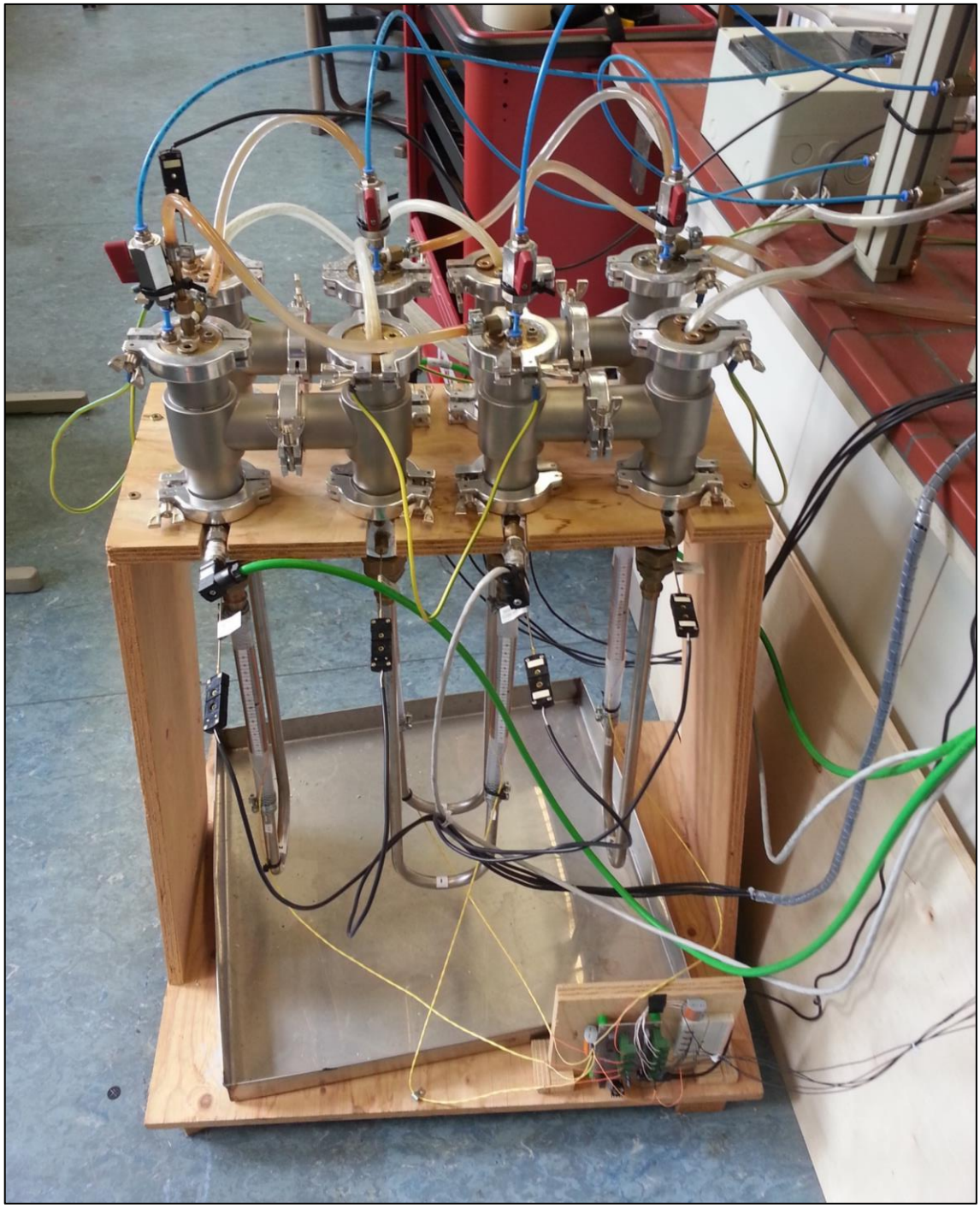

Figure 3.25 – Fully commissioned 15 mm OD piston tube test-rig.

3.3 Operating Configurations

The performance of the LPSC system can be evaluated in four different configurations. Operation with either 4, 3, 2 or 1 of the installed heaters can be selected, resulting in either 0, 1, 2 or 3 potential absorption spaces respectively. It was decided that the first three of

these would be investigated. These operating configurations will be referred to frequently throughout this document and as such are given the following abbreviations:

4HEAT – 4 Heaters, 0 Absorbers

3HEAT – 3 Heaters, 1 Absorber

2HEAT – 2 Heaters, 2 Absorbers

It should be noted that the reason the one-heater configuration is not considered is because it is unlikely that only one heater would be able to sustain operation of the other three subsystems—especially in light of the relatively low heat source temperatures being investigated within the scope of this research project. The results and discussions in later sections of this document will rely on this terminology, and schematics and descriptions clarifying the three configurations are shown below for reference. As identified in the literature review, and stated in Section 1.4, only the 3HEAT configuration has been successfully tested by other research groups.

3.3.1 4HEAT Configuration

Figure 3.26 shows the '4HEAT' configuration. The 4HEAT configuration occurs when all four heaters are turned on during operation. In this state, the system essentially becomes four forward heat engines in series—with the work produced only needing to overcome system friction in order to sustain operation. As a result, the 4HEAT configuration requires the lowest heater temperatures in order to achieve stable operation. Although obviously lacking any potential for cooling, this configuration is very useful for the purposes of computer model validation, and checking for inconsistencies in the behaviour of the four subsystems.

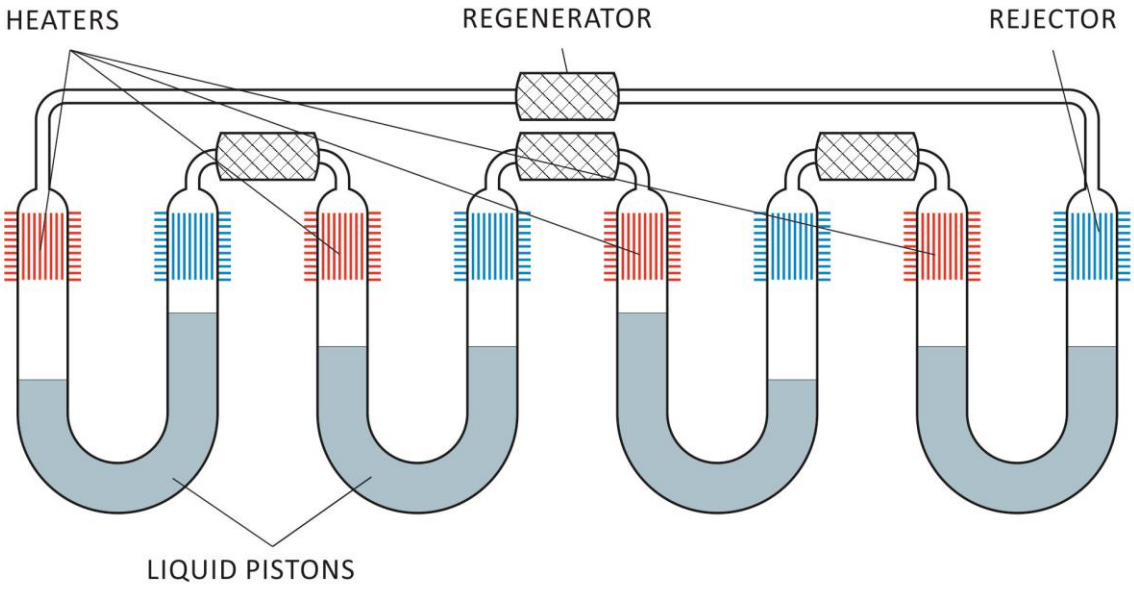

Figure 3.26 – 4HEAT configuration (4 Heaters, 0 Absorbers).

3.3.2 3HEAT Configuration

The second configuration to be tested was termed '3HEAT' and is where all but one heater is powered. The remaining unpowered hot heat exchanger space then becomes the only absorber, and experiences any cooling that the system is able to produce. The 3HEAT configuration is shown in Figure 3.27.

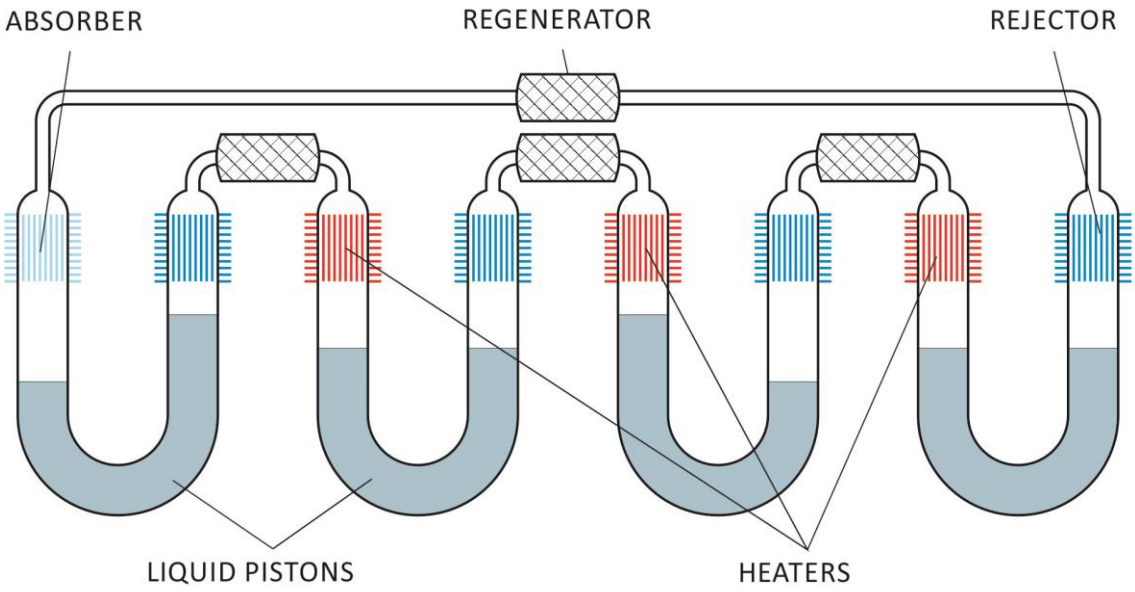

Figure 3.27 – 3HEAT configuration (3 Heaters, 1 Absorber).

3.3.3 2HEAT Configuration

The final configuration, '2HEAT' is the same as that displayed earlier in Figure 1.6, with two adjacent heaters being powered, and the two remaining unpowered heaters behaving as absorbers. It should be noted that with two powered heaters there is a choice: (a) alternate in series between heater/absorber, or (b) couple the two heaters next to each other. Both configurations are shown below in Figures 3.28 and 3.29.

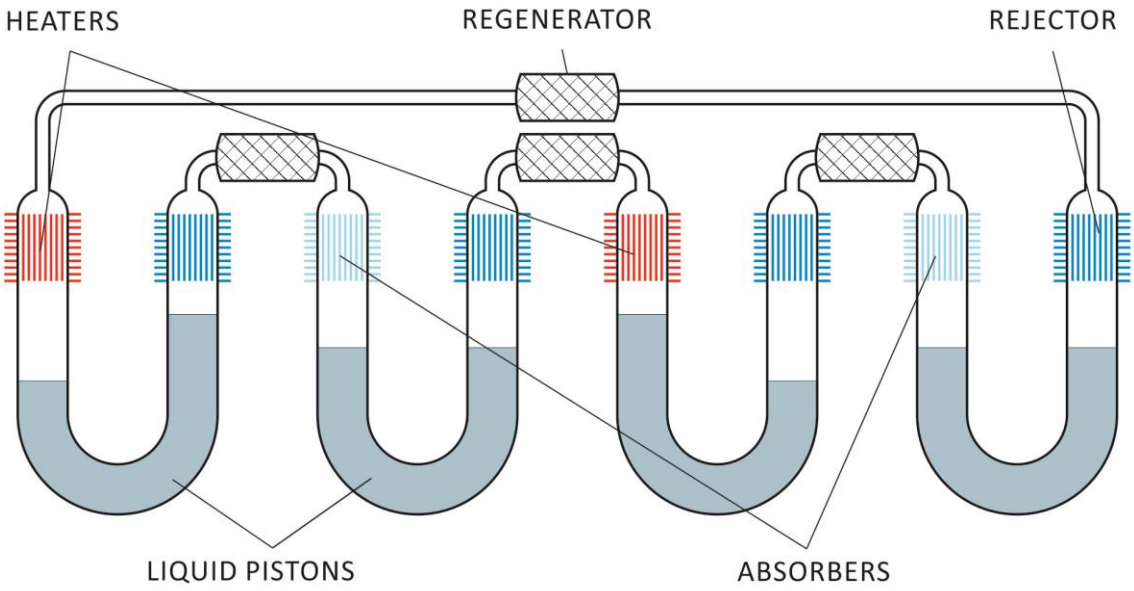

Figure 3.28 – 2HEAT configuration (a) with alternating heaters and absorbers (2 Heaters, 2 Absorbers).

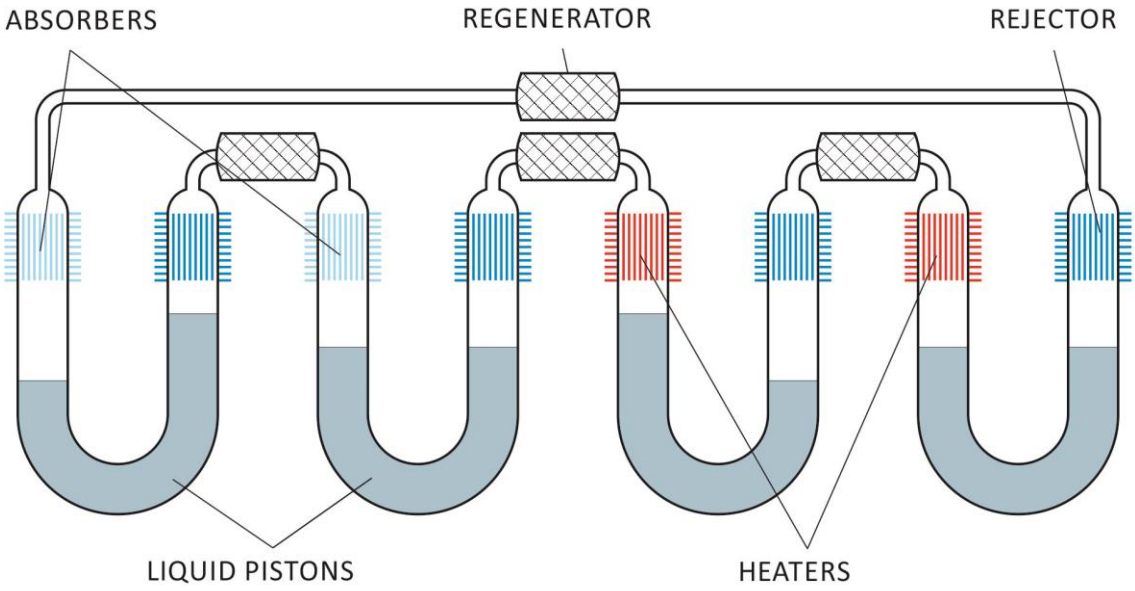

Figure 3.29 – 2HEAT configuration (b) with adjacent heaters (2 Heaters, 2 Absorbers).

Somewhat paradoxically, only arrangement (b) was operable, an explanation for why this was the case is suggested in Section 8.1.2. Unless otherwise specified, the term 2HEAT will be used when referring to the adjacent configuration.

3.4 Experimental Parameters

The key design parameters chosen for variation in this investigation were heater temperature, piston mass, and mean operating pressure. Initially only one piston diameter was tested. The aim of the first investigation was to validate the computer models and to identify piston dimensions for the next stage, which would hopefully improve system performance. Table 3.2 shows the range of independent variables which were employed for the first set of experiments.

Table 3.2 – Set of parameters for first experimental investigation.

Piston tube outer diameter (mm)	Configuration	Liquid piston volume (ml)	Heater surface temperature (°C)	Gas charge pressure (bar)
15	4HEAT	100	95, 100, 105	1-6
15	4HEAT	115	95, 100, 105	1-6
15	3HEAT	100	130, 140, 150	1-6
15	3HEAT	115	130, 140, 150	1-6
15	2HEAT	115	190	1-6

Two different piston masses were investigated, without any other changes to the system geometry, i.e. when adding piston mass (liquid water), the resulting working gas volume necessarily reduced so that the total internal volume of the system remained constant. For each operating configuration, experiments were carried out by varying the charge pressure by 0.5 bar increments, starting from atmospheric pressure (1 bar) up to the maximum pressure attainable with the local compressed air line (6 bar). The heater temperatures at which operation would begin were initially unknown, and as such were arrived upon by trial and error. The lowest corresponded to the situation where just enough heat was supplied for self-sustaining operation at the lower charge pressures; the

highest corresponded to higher charge pressures where the pistons become borderline unstable. A third temperature directly in between these two limits was added to help with experimental consistency. Encouragingly, the temperature ranges identified are similar to that which can be supplied by various forms of solar collectors (IEA, 2011). The 2HEAT experiments were only conducted at a temperature of 190°C. Notably missing from the table are the 2HEAT experiments with 100 ml pistons. For this configuration and piston mass, operation was unable to be achieved within the allowable maximum heater temperature of 200°C.

3.5 Experimental Procedure

A sequential list summarising the individual experimental procedure is outlined below.

1. *A visual check over of the test-rig is conducted*—the PVC hose ring clamps and the cooling water supply hoses are checked for water leaks. The compressed air regulation valve is set at 0-gauge pressure, and the gas spaces decompressed from the previous experiment. The isolation valve for each subsystem is opened, and a check is made that the visible liquid piston surfaces are level with each other. The piston floats are checked for air bubbles or any level of unusual submergence. The grounding cables connecting all four housing compartments are checked to ensure a common ground. The number of connected heaters is checked against the desired configuration (4HEAT, 3HEAT or 2HEAT) and the hot heat exchangers are noted for safety reasons. The DAQ computer is booted and LabVIEW initialised. The neutral outputs from the pressure, temperature and displacement sensors are checked.

2. *The cooling water supply is turned on*—this is done first to give time for the temperature on the rejection side to stabilise.

3. *The gas spaces are pressurised*—the main isolation valve on the manifold is opened and—if this is the first experiment of the day—a pressure test is conducted at 6 bar; otherwise the pressure is gradually increased to the required level. Close attention is paid to the surfaces of the liquid pistons, as any sudden motion may indicate a leak. The main isolation valve is closed.

4. *The heaters are powered*—the heater control unit is plugged in and the heater temperature set on the PID interface. The gas temperatures are monitored through LabVIEW until they reach the range known to sustain operation. This can take up to 5 minutes.

5. *The system's temperatures are normalised*—the four isolation valves are closed, and the system coaxed into motion via manual jump start if necessary. This initial operation moves gas through the heat exchangers and regenerator, and allows for the temperature profiles of the gas and housing to regulate to a level close to steady state. At this time, quite often the piston neutral positions will become offset as more of the gas in the hot spaces expands. (Note: if the piston oscillation becomes too unstable the isolation valves can be swiftly opened to stop the system.)

6. *The gas spaces are equalised*—following the system warm up, the isolation valves are reopened to allow the pistons to return to their neutral positions, and each subsystem to reset to equal gas volumes.

7. *The data acquisition is conducted*—the isolation valves are closed again and the data collection initiated. The main data file collects averaged data every 5 seconds, while supplementary 1-second pressure and displacement profile recordings can be taken at any time. The experiment is typically conducted for 30 minutes, with two or three profiles taken at intermittent times throughout. During the course of the experiment, the piston

tubes and sensor outputs are monitored for any unusual behaviour. Data acquisition is terminated when the experiment is complete.

8. *The experiment is concluded*—following the successful acquisition of experimental data, the isolation valves are opened, and piston oscillation ceases. Experiments are continued by proceeding from step 3, and investigating the range of charge pressures required, before changing the heater set temperature and repeating the process.

4 System Modelling

4.1 Analytical Modelling

4.1.1 Natural Frequency

In the context of system analysis via Sage modelling software, the most important characteristic parameter needed for the LPSC machine is its operational frequency. After experimenting with the test-rig during the commissioning phase, it was noticed that the system frequency was very consistent and predictable, regardless of the configuration being tested or what heater temperature was used. This is plausible given that the LPSC system comprises a series of mass elements (pistons) and springs (gas spaces and piston gravity) connected end on end in a loop. As identified in Section 2.3, once excited, such a system's natural vibrational behaviour has little dependence on factors other than geometry, mass and spring constant values. Unlike a machine exhibiting a work coupling mechanism, the frequency of the operation cannot be manipulated manually, and instead will settle at the natural frequency of the prevailing conditions and geometry.

As previously shown in Section 2.3.4, it is a simple task to derive the natural frequency of a single U-tube column open to the atmosphere at both ends. The same approach is now used to find an approximate analytical solution for the natural frequency of the LPSC system. Since all four pistons are connected to each other via gas spaces, the LPSC must be considered a MDOF system. Figure 4.1 gives a spring and mass representation of the LPSC.

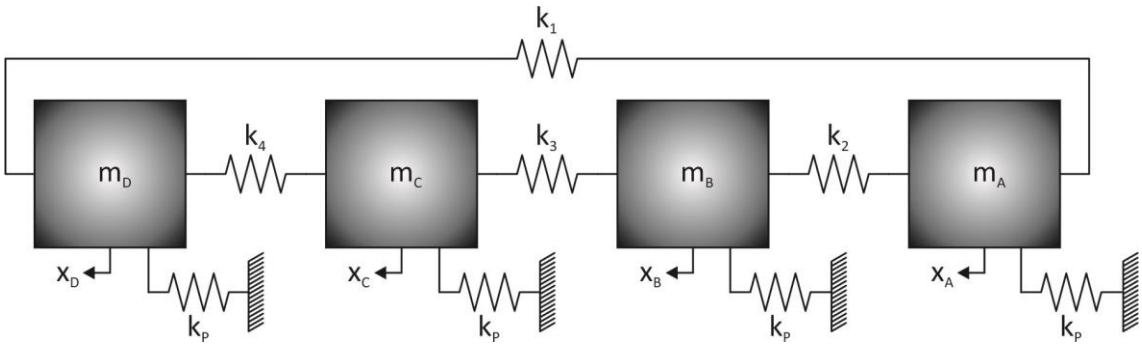

Figure 4.1 – Spring and mass representation of the LPSC.

In Figure 4.1 the restoring force of gravity is applied to the pistons via the springs denoted by the subscript *p*, while the gas springs are denoted by their corresponding gas space number. Applying Newton's second law, the equations of motion for each of the four pistons are deduced as follows:

$$m\ddot{x}_A + (k_1 + k_2 + k_P)x_A - k_2 x_B - k_1 x_D = 0 \tag{4.1}$$

$$m\ddot{x}_B + (k_2 + k_3 + k_P)x_B - k_3 x_C - k_2 x_A = 0 \tag{4.2}$$

$$m\ddot{x}_C + (k_3 + k_4 + k_P)x_C - k_4 x_D - k_3 x_B = 0 \tag{4.3}$$

$$m\ddot{x}_D + (k_4 + k_1 + k_P)x_D - k_1 x_A - k_4 x_C = 0 \tag{4.4}$$

Written in matrix form, the equations become:

$$\begin{bmatrix} m & 0 & 0 & 0 \\ 0 & m & 0 & 0 \\ 0 & 0 & m & 0 \\ 0 & 0 & 0 & m \end{bmatrix} \begin{bmatrix} \ddot{x}_A \\ \ddot{x}_B \\ \ddot{x}_C \\ \ddot{x}_D \end{bmatrix} + \begin{bmatrix} k_1 + k_2 + k_P & -k_2 & 0 & -k_1 \\ -k_2 & k_2 + k_3 + k_P & -k_3 & 0 \\ 0 & -k_3 & k_3 + k_4 + k_P & -k_4 \\ -k_1 & 0 & -k_4 & k_4 + k_1 + k_P \end{bmatrix} \begin{bmatrix} x_A \\ x_B \\ x_C \\ x_D \end{bmatrix} = 0$$

or

$$M\ddot{\boldsymbol{x}} + K\boldsymbol{x} = 0$$

Where *M* is termed the mass matrix and *K* the spring constant matrix. Remembering that a simple harmonic response can be assumed for each piston, it is possible to write:

$$\ddot{\boldsymbol{x}} = -\omega^2 \boldsymbol{x}$$

Therefore, the matrix equation can be simplified as:

$$(K - \omega^2 M)\boldsymbol{x} = 0 \tag{4.5}$$

Thus, the determinant of the matrix (K-$\omega^2 M$) must be zero. If each of the spring constants is assumed to be equal in both gas and piston cases, the resulting equation simplifies to the following for the natural frequency of the unforced, undamped LPSC system:

$$\omega_n = \sqrt{\frac{2k_g + k_P}{m}} \tag{4.6}$$

or, in terms of system parameters:

$$\omega_n = \sqrt{\frac{\frac{2nA^2 p_0}{V_0} + 2A\rho g}{m}} \tag{4.7}$$

$$f_n = \frac{1}{2\pi}\sqrt{\frac{\frac{2nA^2 p_0}{V_0} + 2A\rho g}{m}} \tag{4.8}$$

4.1.2 Schmidt Analysis of Frequency

The natural frequency deduced in the previous section neglects the impact of the heaters that, by heating the gas in certain sections of the gas space, force the system into motion. Of particular interest in the case of FPSEs, when considering Schmidt analysis, is that the forcing function for a heated engine can be expressed through its dependence on the mass element displacement terms in the equations of motion describing the system. This allows

a method for investigating frequency dependence on both operating configuration and heater temperature, which is useful in ensuing discussions in Chapters 6, 7 and 8. The following is a simplified Schmidt analysis, similar to that presented by Urieli & Berchowitz (1984), conducted for the sole purpose of investigating heater temperature influence on operating frequency.

Taking the equations of motion obtained for the LPSC machine's spring and mass equivalent system in the previous section (Equations 4.1–4.4), then by replacing gas springs with pressure forces, the following set of equations for the undamped piston motions is obtained:

$$m\ddot{x}_A + k_P x_A + A(p_2 - p_1) = 0 \tag{4.9}$$

$$m\ddot{x}_B + k_P x_B + A(p_3 - p_2) = 0 \tag{4.10}$$

$$m\ddot{x}_C + k_P x_C + A(p_4 - p_3) = 0 \tag{4.11}$$

$$m\ddot{x}_D + k_P x_D + A(p_1 - p_4) = 0 \tag{4.12}$$

where the pressures are denoted by the p terms and A is the piston cross-sectional area. Assuming the pressures oscillate around a mean value of pressure given by p_0, a linear approximation would have the form:

$$p = p_0(1 + ax_A + bx_B + cx_C + dx_D) \tag{4.13}$$

It is an expression of this form which is required for the pressures in Equations 4.9–4.12. From the assumptions for Schmidt analysis earlier described in Chapter 2, with isothermal gas space sections and uniform gas space pressure, Equation 2.9 gives:

$$p = mR\left(\frac{V_E}{T_E} + \frac{V_R}{T_R} + \frac{V_C}{T_C}\right)^{-1}$$

Extending this equation to include separate regions for the expansion/compression spaces and the heat exchangers, the pressure becomes:

$$p = MR\left[\frac{V_E}{T_H} + \frac{V_{HX}}{T_H} + \frac{V_R \ln(T_H / T_C)}{T_H - T_C} + \frac{V_{HX}}{T_C} + \frac{V_C}{T_C}\right]^{-1} \tag{4.14}$$

where M is the gas mass, R is the gas constant and V is volume, with subscripts E, HX, R, C, H and K representing the expansion, heat exchanger, regenerator and compression spaces respectively. T_H and T_C are the hot and cold side temperatures. Note that the temperature assumed in the regenerator is determined from the well-known mean effective temperature equation for a regenerator, which assumes a linear temperature profile. Also note that the only variable terms in this expression are the expansion and compression space volumes. Considering the first gas space, and substituting in with the following displacement dependent expressions for compression and expansion space volumes:

$$V_{E1} = A(E_1 - x_D)$$

$$V_{C1} = A(C_1 + x_A)$$

where E_1 and C_1 are the characteristic lengths of the neutral expansion and compression spaces respectively. Each gas pressure can be written as a function of displacements in the form:

$$p_1 = MR\left[\frac{A(E_1 - x_D)}{T_H} + \frac{V_{HX}}{T_H} + \frac{V_R \ln(T_H / T_C)}{T_H - T_C} + \frac{V_{HX}}{T_C} + \frac{A(C_1 + x_A)}{T_C}\right]^{-1}$$

which simplifies to:

$$p_1 = MR\left[S + \frac{Ax_A}{T_C} - \frac{Ax_D}{T_H} \right]^{-1}$$

where:

$$S = \left(\frac{AE_1}{T_H} + \frac{V_{HX}}{T_H} + \frac{V_R \ln(T_H / T_C)}{T_H - T_C} + \frac{V_{HX}}{T_C} + \frac{AC_1}{T_C} \right) \tag{4.15}$$

Factoring out the *S* variable gives:

$$p_1 = \frac{MR}{S}\left[1 + \frac{Ax_A}{T_C S} - \frac{Ax_D}{T_H S} \right]^{-1}$$

Noting that the *MR/S* term is equivalent to the charge pressure of the system (and therefore also the mean operating pressure) yields:

$$p_1 = p_0\left[1 + \frac{Ax_A}{T_C S} - \frac{Ax_D}{T_H S} \right]^{-1} \tag{4.16}$$

The final step in obtaining linear approximations for the gas pressures is to use binomial expansion, and neglect second order terms to invert the fraction in Equation 4.16. When performed for each gas space in the 4HEAT configuration, this yields:

$$p_1 = p_0\left(1 - \frac{Ax_A}{T_C S} + \frac{Ax_D}{T_H S} \right) \tag{4.17}$$

$$p_2 = p_0\left(1 - \frac{Ax_B}{T_C S} + \frac{Ax_A}{T_H S} \right) \tag{4.18}$$

$$p_3 = p_0\left(1 - \frac{Ax_C}{T_C S} + \frac{Ax_B}{T_H S} \right) \tag{4.19}$$

$$p_4 = p_0\left(1 - \frac{Ax_D}{T_C S} + \frac{Ax_C}{T_H S}\right) \tag{4.20}$$

These expressions now are in the form of the desired general linearized pressure equation described earlier, Equation 4.13. Substituting into the EOMs (4.9–4.12) and simplifying into matrix form gives:

$$\begin{bmatrix} m & 0 & 0 & 0 \\ 0 & m & 0 & 0 \\ 0 & 0 & m & 0 \\ 0 & 0 & 0 & m \end{bmatrix}\begin{bmatrix} \ddot{x}_A \\ \ddot{x}_B \\ \ddot{x}_C \\ \ddot{x}_D \end{bmatrix} + \frac{A^2 p_0}{S}\begin{bmatrix} \frac{k_P S}{A^2 p_0} + \frac{1}{T_H} + \frac{1}{T_C} & -\frac{1}{T_C} & 0 & -\frac{1}{T_H} \\ -\frac{1}{T_H} & \frac{k_P S}{A^2 p_0} + \frac{1}{T_H} + \frac{1}{T_C} & -\frac{1}{T_C} & 0 \\ 0 & -\frac{1}{T_H} & \frac{k_P S}{A^2 p_0} + \frac{1}{T_H} + \frac{1}{T_C} & -\frac{1}{T_C} \\ -\frac{1}{T_C} & 0 & -\frac{1}{T_H} & \frac{k_P S}{A^2 p_0} + \frac{1}{T_H} + \frac{1}{T_C} \end{bmatrix}\begin{bmatrix} x_A \\ x_B \\ x_C \\ x_D \end{bmatrix} = 0$$

Assuming similar piston spring constants, rearranging into the form of Equation 4.5 and solving for the zero determinant of the matrix (K-$\omega^2 M$), results in the following quartic equation (if ω^2 is considered the variable):

$$\left(\frac{A^2 p_0}{T_H S} + \frac{A^2 p_0}{T_C S} + k_P - m\omega^2\right)^4 + \left(-\frac{A^2 p_0}{T_H S}\right)^4 + \left(-\frac{A^2 p_0}{T_C S}\right)^4 - 2\left(-\frac{A^2 p_0}{T_H S}\right)^2\left(-\frac{A^2 p_0}{T_C S}\right)^2 = 0$$

Assuming the terms on the right cancel each other out, or at least are insignificant compared to the leftmost term (for low temperature systems this is justifiable as T_H and T_C are relatively close), the equation for the forced frequency becomes:

$$\omega_f = \sqrt{\frac{\frac{A^2 p_0}{S}\left(\frac{1}{T_H} + \frac{1}{T_C}\right) + k_P}{m}} \tag{4.21}$$

or

$$f_f = \frac{1}{2\pi}\sqrt{\frac{\frac{A^2 p_0}{S}\left(\frac{1}{T_H} + \frac{1}{T_C}\right) + k_P}{m}} \tag{4.22}$$

4.1.3 Frequency Dependence on Heater Temperature

Equation 4.22 shows that for a particular machine, geometry and operating pressure, the forced frequency is dependent only on the heat source and sink temperatures, T_H and T_C. A natural inclination is to wonder how sensitive the forced frequency is to changes in these temperatures. For this, the ratio of forced frequency (Equation 4.22) to natural frequency (Equation 4.8) can be analysed:

$$f_{ratio} = \frac{f_f}{f_n} = \frac{\omega_f}{\omega_n} = \frac{\sqrt{\dfrac{\dfrac{A^2 p_0}{S}\left(\dfrac{1}{T_H}+\dfrac{1}{T_C}\right)+2A\rho g}{m}}}{\sqrt{\dfrac{\dfrac{2nA^2 p_0}{V_0}+2A\rho g}{m}}}$$

which simplifies to:

$$f_{ratio}^2 = \frac{\dfrac{A^2 p_0}{S}\left(\dfrac{1}{T_H}+\dfrac{1}{T_C}\right)+2A\rho g}{\dfrac{2nA^2 p_0}{V_0}+2A\rho g}$$

Noting that the influence of the right hand terms in the above ratio can only contribute to a value closer to unity, they can be neglected for a conservative frequency ratio estimate:

$$f_{ratio}^2 = \frac{\dfrac{A^2 p_0}{S}\left(\dfrac{1}{T_H}+\dfrac{1}{T_C}\right)}{\dfrac{2nA^2 p_0}{V_0}}$$

$$f_{ratio}^2 = \frac{V_0}{2nS}\left(\frac{1}{T_H}+\frac{1}{T_C}\right)$$

Recalling that $p_0=MR/S$ and letting $V_0=MRT_0/p_0$ (where T_0 represents the equivalent average temperature of the unforced system i.e. T_C). The preceding equation simplifies to:

$$f_{ratio}^2 = \frac{M_n T_0}{2nM_f}\left(\frac{1}{T_H}+\frac{1}{T_C}\right)$$

where M_n and M_f are the gas space masses in the natural and forced response cases. From the ideal gas law, the mass ratio can be replaced with a temperature ratio, since charge pressure p_0, gas space volume V_0 and the gas constant R, are the same in both scenarios:

$$f_{ratio}^2 = \frac{T_f T_0}{2nT_n}\left(\frac{1}{T_H}+\frac{1}{T_C}\right) \tag{4.23}$$

As previously identified, the equivalent average temperature T_0 in the unforced case is the same as T_n. The polytropic index can be assumed to be 1 since isothermal behaviour is assumed in Schmidt analysis. Finally, neglecting the nonlinear temperature distribution through the heat exchangers, it is reasonable to approximate the average gas temperature in the forced case, T_f, as halfway between the sink and source temperatures, T_H and T_C. Substituting these conditions into Equation 4.23 and simplifying gives:

$$f_{ratio} = \sqrt{\frac{1}{2}+\frac{1}{4}\left(\frac{T_C}{T_H}+\frac{T_H}{T_C}\right)} \tag{4.24}$$

Considering that the sink temperature is in general close to ambient temperature, then using a value of T_C = 300 K, Equation 4.24 can be rewritten as a function only dependent on the heater temperature:

$$f_{ratio} = \frac{1}{2}\sqrt{2+\frac{T_H^2+90000}{300T_H}} \tag{4.25}$$

To gauge the sensitivity of this approximate frequency ratio to heater temperature change, the percentage difference between the forced and natural frequencies can be graphed for a range of heater temperatures.

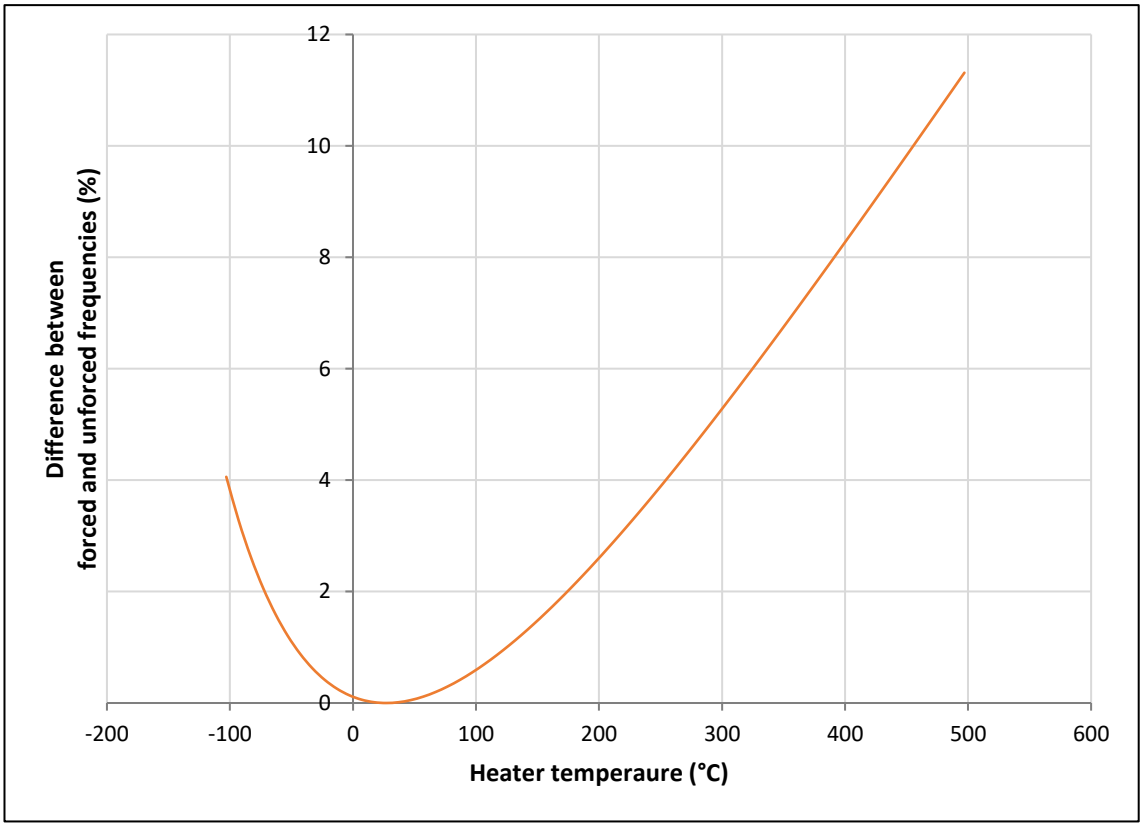

Figure 4.2 – Graph showing how little the heater temperature affects the operational frequency of the LPSC system.

Figure 4.2 shows a plot of this function over the temperature range of -100°C to 500°C. From the graph it can be inferred that the heater temperature has little impact on the operational frequency of the overall system. With heater temperatures of 450ºC, the change in operating frequency is less than 10%. In the investigation undertaken in this thesis, the heater temperatures being considered are in the order of 150ºC, which corresponds to a maximum difference in operating frequency of less than 2%.

It is important to remember that the frequency analysis summarised in Figure 4.2 is an approximation based on a number of simplifying assumptions and is not intended for precise quantification. A frequency comparison with the experimental results is

conducted in Section 6.2. Also worth mentioning is that the approximation for the frequency ratio given in Equation 4.25 considers the difference between the natural response or '0HEAT' configuration and the forced response of the 4HEAT configuration—thus the expected frequency differences are even less in the 2HEAT and 3HEAT configurations.

4.2 Sage Modelling

4.2.1 Description of Sage Modelling Software

With the advent of computers, the complex behaviour of oscillating thermodynamic systems has become open to investigation with unprecedented precision. Notorious for its deviation from ideal behaviour, the Stirling cycle has been one such target of dedicated computer simulation efforts. Developed by David Gedeon, Sage simulation software is specifically designed for modelling oscillating systems, such as Stirling engines and coolers, pulse-tube cryocoolers and other types of cryocoolers (Gedeon, 2010). Much more limited in terms of scope, user-friendliness and commercial development compared with software packages such as MATLAB, Sage makes up for this with its accuracy and fast solving speeds and has become one of the most reliable modelling tools for oscillating thermodynamic systems in higher education institutions and industry. Sage treats the working gas as one-dimensional and solves the governing equations implicitly in space and time. The grid includes all time values since a periodic solution is assumed. Hence, Sage is incapable of modelling transient cyclic processes, such as start-up behaviour.

Unlike traditional modelling approaches where a model is made up of a set of user-defined parameters and equations, Sage models are built component by component, allowing the geometry of the model to evolve with relative ease. Components representing different sections of the modelled system are added one by one and interconnected to build a complete system model. Each individual component is divided

into a user-defined number of cells, across which the three conservation equations of mass, momentum and energy are solved at each time increment. This is explained in more detail in Section 4.2.1.1. Components can be linked to each other through user-created boundary conditions, embodying their physical relationships with their surroundings. For example, fluid mass flow between a heat exchanger and a regenerator, or a force connection between a piston and adjacent gas space. Sage also encapsulates gas flow effects and heat transfer between and through components to determine realistic performance characteristics. In its ability to model heat transfer processes and fluid friction of oscillating flow, even through porous media such as the regenerator matrix, Sage can be regarded as a very powerful third order modelling tool.

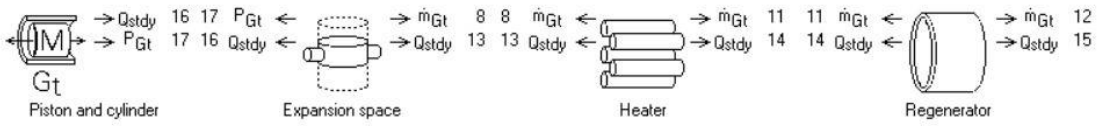

Figure 4.3 – Example showing the graphical interface of Sage. Mass and heat flow connections are embodied by arrow symbols indicating the axial direction of the connector.

Figure 4.3 shows part of a basic model subsystem in Sage. Model components are organized logically in a hierarchical tree structure, and sub-levels of each component are accessible in order to allow for parameter manipulation and the connection of different model components. These are shown in more detail for the LPSC model, later in this chapter. Each component of the system is subdivided into a user-defined number of spatial increments and analysed in a one-dimensional form. While Sage primarily models the thermodynamic behaviour of the working gas, it also takes into account the interaction of the gas with the adjacent walls, as well as heat transfer by conduction in the canister walls in both axial and radial directions. In this respect, Sage is somewhere between a one-dimensional and two-dimensional modelling tool.

Sage operates in a frequency domain and solves all fundamental conservation equations for each cell until it converges to a solution. Further features of this software package are a mapping tool, which allows a parameter study over a user-defined number of variables in a user-defined number of increments, and an optimisation tool. The components available range from different types of heat exchangers to pistons, cylinders, canisters, dashpots, springs and more. They are selected from an appropriate menu and connected via characteristic variables. For instance, various gas volumes are connected via a mass flow variable; a piston face is connected to the adjacent gas space via a pressure variable.

In the context of the LPSC, an apparent disadvantage of Sage is its requirement for cycle frequency and piston amplitudes as input parameters. These must therefore initially be obtained from the MATLAB model and then used as inputs in Sage to evaluate the system performance[1]. The resulting outputs from Sage include pressure and temperature profiles of each working space, as well as piston and gas pressure amplitudes and phase angles. The following descriptions about gas domain theory and the solution method are summarised from Sage's user manual, which should be consulted for further information.

4.2.1.1 Gas Domain Theory

The equations used by Sage are somewhat non-standard in the computational fluid-dynamics literature because they are designed specifically for one-dimensional internal flows with space-variable and time-variable flow area. Most CFD textbooks use a more general approach. Instead of merely stating the equations, an overview of their derivation is provided. Starting with the general Navier-Stokes equations in integral form, as found in Peyret and Taylor (1983), body forces shall be neglected and the prevailing convention of a fixed control volume is relaxed. Instead it is assumed that the control volume has

[1] As previously alluded to, this intermediate step was circumvented via a procedure which is explained in more detail in Section 4.2.9.

fixed inlet and exit boundaries, but the side boundaries can move. This results in a time-variable flow area. The side boundaries are impermeable so that flow enters and leaves only through the inlet and exit boundaries. A rubber tube with space-variable and time-variable cross-section is a useful thought picture, with the principal flow axis being the tube axis. In this control volume the integral gas dynamic equations are:

Continuity: $\frac{d}{dt}\int_v \rho dv + \int_s \rho \boldsymbol{n} \cdot \boldsymbol{V}_r ds = 0$

Momentum: $\frac{d}{dt}\int_v \rho \boldsymbol{V} dv + \int_s [(\boldsymbol{n} \cdot \boldsymbol{V}_r)\rho \boldsymbol{V} - \boldsymbol{n}\boldsymbol{\sigma}] ds = 0$

Energy: $\frac{d}{dt}\int_v \rho e dv + \int_s \boldsymbol{n} \cdot (\rho e \boldsymbol{V}_r - \boldsymbol{\sigma}\boldsymbol{V} - \boldsymbol{q}) ds = 0$

Where, $e = \varepsilon + u^2/2$ (mass-specific total gas energy), $\boldsymbol{n}$ = unit outward normal of s, $\boldsymbol{q}$ = heat flux vector, s = surface of υ, t = time, υ = control volume, $\boldsymbol{V}$ = Newtonian-frame flow velocity vector, $\boldsymbol{V}_r$ = boundary-relative flow velocity vector, ε = mass-specific internal gas energy, ρ = gas density and $\boldsymbol{\sigma}$ = stress tensor.

The continuity equation states that the time rate of change of mass in the control volume equals the rate at which mass leaves through its surface boundaries. The momentum equation is a statement of Newton's second law of motion: the time rate of change of control-volume momentum, less the momentum leaving through its surface boundaries, equals the net force acting on all surfaces. The energy equation states that the time rate of change of control-volume internal energy plus kinetic energy—minus that leaving through its surface boundaries—is equal to the net heat flux through its boundaries, plus the mechanical work done on its boundaries.

The equations are then converted into one-dimensional differential equations in conservative form: where dv in the time integrals is replaced with $A_x dx$, and where A_x is flow area and x is the principal flow direction. Taking the limit $\Delta x \rightarrow dx$ then dividing

through by *dx* and making some simplifications, the three equations take the following form. Note that for the surface integrals in each case the inlet and outlet boundaries are considered separately from the side boundaries. The stress tensor is empiricised as thermodynamic pressure, *p*, and as a viscous flow resistance term, R_F, which can be thought of as the force per unit length per unit flow area due to surface shear stress. The empirical film heat transfer per unit length, Q_w, is introduced to represent the integral for the negative z boundary in the energy equation, and *q* represents the axial heat flux.

The gas dynamic equations are therefore:

Continuity: $$\frac{\partial \rho A_x}{\partial t} + \frac{\partial \rho u A_x}{\partial x} = 0,$$

Momentum: $$\frac{\partial \rho u A_x}{\partial t} + \frac{\partial u \rho u A_x}{\partial x} + \frac{\partial p}{\partial x} A_x - R_F A_x = 0, \text{ and}$$

Gas energy: $$\frac{\partial \rho e A_x}{\partial t} + p \frac{\partial A_x}{\partial t} + \frac{\partial}{\partial x}(u \rho e A_x + u p A_x + q) - Q_w = 0$$

The purpose of these equations is to determine three implicit solution variables, which are chosen to be ρ, $\rho u A_x$ and ρe. The reason for making this choice is that all are roughly continuous across area discontinuities and, except for the factor A_x in the second, are standard in the field. Empirical terms R_F, Q_w and *q* are explained in further detail in the user manual.

The gas dynamic equations are tied together with an equation of state that serves to evaluate the dependent variables, pressure, *p*, and temperature, *T*, as functions of independent variables ρ, $\rho u A_x$ and ρe ($p(\rho,T)$ and $T(\rho,\rho u A_x,\rho e)$). The gas-property objects defined in the Stirling root model section of the user manual provide these functions.

4.2.1.2 Solution Method

The gas dynamic equations are discretized over a grid of points uniformly spaced throughout the domain and over the cycle period. On this grid, the three solution variables (highlighted earlier) are solved implicitly or interpolated explicitly according to the logic of a staggered-grid formulation. The underlying idea is to solve $\rho u A_x$ at alternate nodes from ρe and ρ to avoid solution instability and produce global conservation of mass, momentum and energy. Solution staggering is only carried out in the spatial direction. The concept of control volumes can be used to aid with the interpretation of the staggered-grid scheme. The boundaries of these control volumes can be imagined as lying on alternating nodes. At these boundaries, $\rho u A_x$ is solved, while ρ and ρe are solved at the midpoints. By using first-order central differencing in the continuity and energy equations, the global conservation of energy and mass automatically holds for the solved variables ρ and ρe. In other words, quantities leaving one control volume enter the adjacent one. The reason higher order differentiation is not used is that it would destroy this global conservation property, or complicate it greatly.

When the model is ready so be solved, a large system of nonlinear equations and their associated implicit variables will exist based on the model hierarchy. A nonlinear solver is employed and solves a sequence of linear approximations to the nonlinear equations. The coefficients of the linearized equations result from numerical partial derivatives of the evaluation functions taken with respect to the model's implicit variables. The result is a sparse matrix, solved with a special sparse-matrix solver. The solution becomes a search direction along which to seek the nonlinear solution. This process repeats until the nonlinear model equations are all satisfied within some given tolerance.

For a more in depth explanation of the inner workings of the Sage software, the reader is directed to the Sage user manual. The manual contains more than 400 pages of

information about every aspect of Sage, including but not limited to: variable types; turbulence models; optimisation algorithms; entropy generation; and, flow friction and heat transfer correlations.

4.2.2 Sage Model Overview

Initially a MATLAB model was constructed to estimate the operating frequency of the system. Ultimately, a method was developed which negated the need for the MATLAB model, thus allowing the Sage model to be used independently. The Sage model for the LPSC was created by dividing the machine into four subsystems, each comprised of ten main components representing different physical sections of the test-rig. Figure 4.4 shows how each of the model components relates to the LPSC test-rig. The tenth and last of the main components (not shown in the figure) is the liquid piston itself.

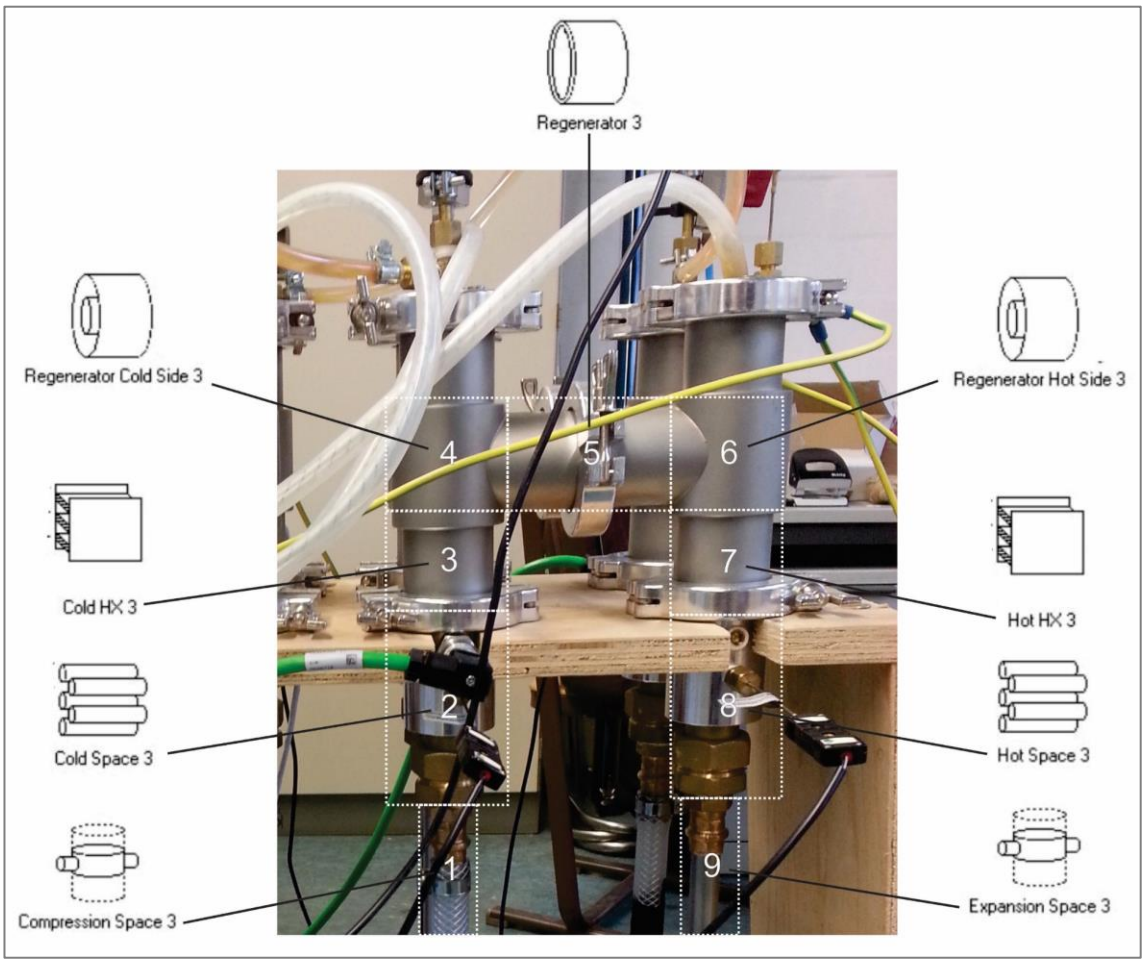

Figure 4.4 – Sage model component visualisation infographic with test-rig parts.

Figure 4.5 shows the corresponding graphical interface within Sage. Along with the main model components there are also some supplementary ones, such as the pressure source, which provides the gas charge pressure setting, the sink and source heat reservoir components, and the liquid piston accessories.

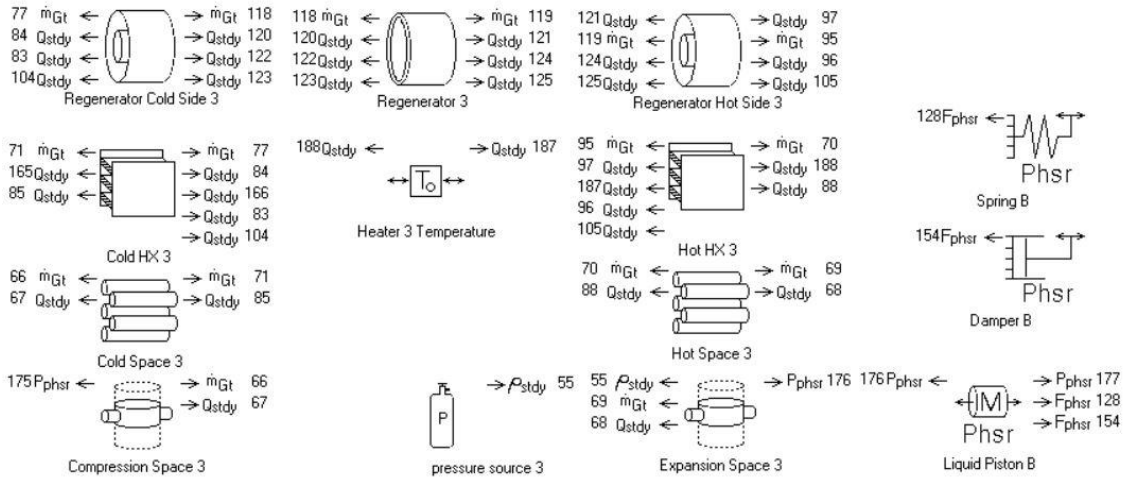

Figure 4.5 – Sage model of a liquid piston Stirling cooler subsystem.

Depicted in Figure 4.5 is only one of the four subsystems, with the complete model comprising all four connected in series. The components are arranged in the approximate shape of the actual housing and are connected in series using heat and mass flow linkages within Sage to construct the continuous loop of the enclosed space (these can be seen as the numbered arrows in the preceding figure). All of the components have internal geometric variables and material properties that were altered to resemble the desired physical system as closely as possible. The model necessarily incorporates simplifying assumptions relating to the heat transfer within the heat exchangers, and approximations for the viscous frictional effects in the liquid pistons as discussed later. The assumptions include a perfectly sealed system; no heat transfer losses to the surroundings; constant heat source and sink temperatures; and no evaporation of liquid from the surfaces of the pistons. The last assumption is almost certainly not valid and the limitations of this assumption are discussed later in Section 8.2.4. A brief explanation of the details of each of the main components is now outlined.

4.2.3 Compression and Expansion Spaces

The compression and expansion spaces, denoted by numbers 1 and 9 in Figure 4.4 represent the variable gas volumes that exist above the liquid piston surface within the U-tubes. The boundary of this space is the threaded connection with the gland fitting, and it thus encompasses the entire permissible piston stroke range. Figure 4.6 shows the hierarchical structure of the compression space model-component in the third subsystem.

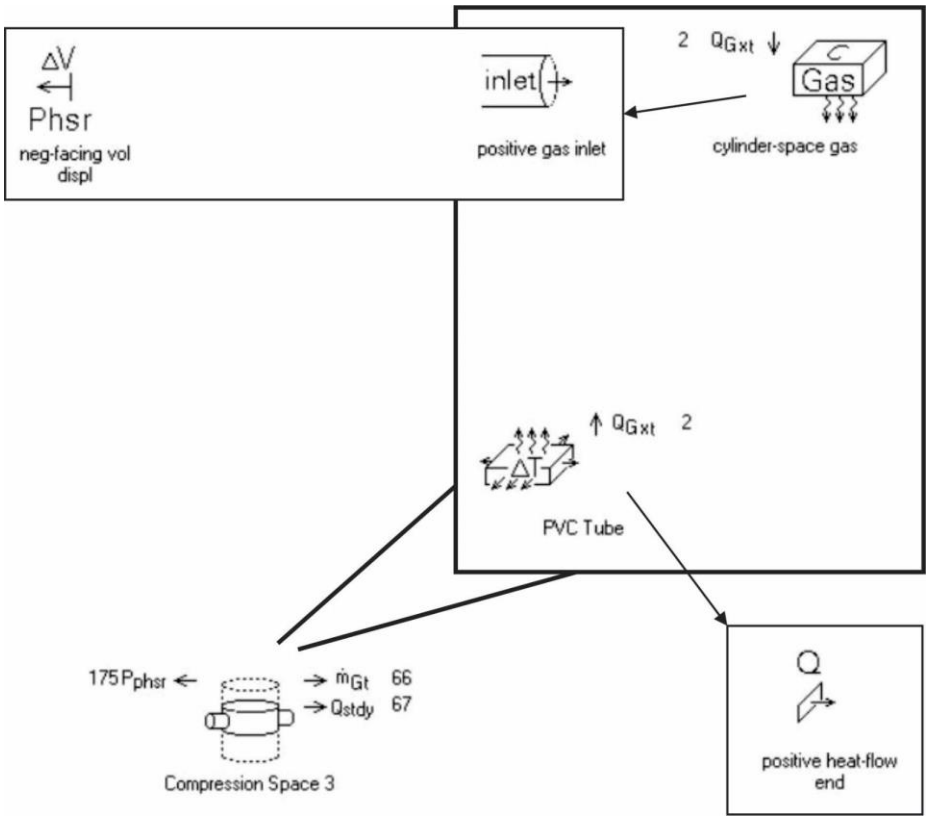

Figure 4.6 – Structure of the compression space model-component within Sage.

Two child components are required: the duct gas and a conductive surface element resembling the U-tube. These are some of the most basic Sage model components—only a small number of connections are required, including a pressure link to the adjacent piston, mass flow and heat conduction links to the space above, and the aforementioned charge pressure linkage (in the expansion space only). The majority of the geometric and material properties are defined at the root-component level by changing the input

parameters of the individual components. Table 4.1 summarises the parameters used in the compression and expansion spaces.

Table 4.1 – Compression and expansion space model-component input parameters

Description	Value	Component level
Number of spatial cells	2	Root
Mean-flow length (m)	$8x10^{-2}$	Root
Initial temperature (K)	300	Root
Wetted surface area (m^2)	$7.5x10^{-3}$	Root
Baseline volume (m^3)	$2.382x10^{-5}$	Root (recast)
Tube wall thickness (m) (PVC = 3.5 mm, Steel = 1 mm)	$3.5x10^{-3}$	Child
Tube material (PVC or Steel)	Steel (SS304)	Child

Mean-flow length is a parameter that corresponds to the swept distance of the piston. Sage uses the mean flow length to calculate the cross-sectional area of the generic cylinder element when regarding the cylinder as a passage. The length may vary by an order of magnitude without producing much effect on the simulation outputs (Gedeon, 2010), since nothing in the variable-volume gas domain model depends on length or flow area. The Sage manual advises using a rough value of length scaled to the modelled machine. In this case the average stroke expected, approximately 80 mm, in the compression and expansion spaces is selected. On the hot side, the material selected is stainless steel; on the cold side, polyester is selected (PVC is not a material option within Sage).

The most important parameters specified for these components are that of baseline volume and wetted surface area. Baseline volume is the component volume when all volume-displacement attachments are zero. It is critical because it directly effects the pressure ratio of the machine. Relative accuracy within a few per cent is recommended in the Sage manual. The value is derived from the dimensions of the U-tube and the measured distances to the hot and cold spaces above the pistons. It is also recast to the root component level so that all eight spaces can be manipulated with a single user defined

variable. The wetted surface area is the time-mean inner surface area of the tube, and not excessively critical since it has only a secondary effect on the cycle pressure through the heat transfer between the gas and wall. A value within 50% is recommended. The accuracy of this value is even less important in the case of low temperature machines. An area of 7500 mm^2 is calculated from the U-tube inner diameter and the straight-line distance separating the piston from the entrance to the cold and hot spaces.

4.2.4 Cold and Hot Spaces

Components 2 and 8 from Figure 4.4 are termed the cold and hot spaces respectively. These components serve to model the relatively complex geometry of the housing between the gland fitting and the entrance to the heat exchangers. This space includes a number of changes in cross-sectional area as well as the pressure and temperature sensor ports. Since the volume of these components remains constant, they are approximated as a single cylindrical tube, whose cross-section is a weighted average of the actual test-rig geometry in this section. The tube length is then established from the actual volume. Figure 4.7 depicts the hierarchical structure of these components.

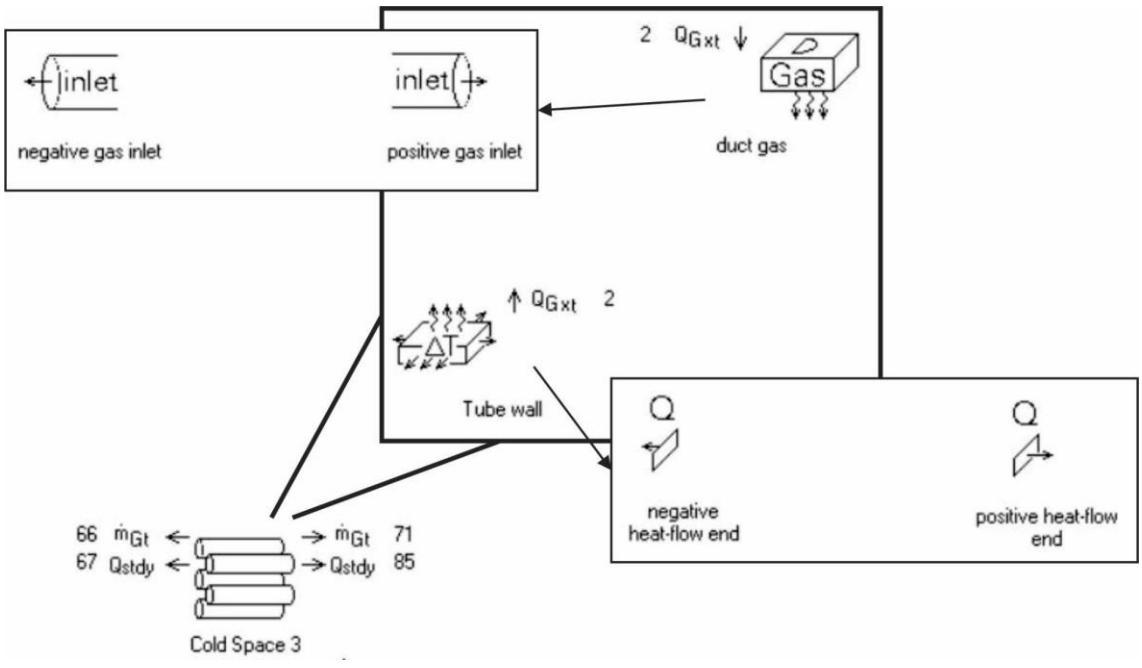

Figure 4.7 – Structure of the hot and cold space component within Sage.

As in the case of the compression and expansion spaces, only two child components are needed: the duct gas and a conductive surface element. Five continuity connections are required for these components: mass flows through the inlet and exits, conductive heat flows to the two neighbouring components, and a heat flow from the gas to the interior surface of the tube. Table 4.2 summarises the parameters used in the compression and expansion spaces. The material selected is brass, as the gland fitting takes up the majority of the total length.

Table 4.2 – Hot and cold space model-component input parameters.

Description	Value	Component level
Number of spatial cells	3	Root
Duct-length (m)	$1.42x10^{-1}$	Root
Mean wall roughness/Dhydraulic (non-dimensional)	$1x10^{-3}$	Root
Wall thickness (m)	$2.5x10^{-3}$	Root
Initial temperature (K)	300	Root
Tube inner diameter (m)	$1.941x10^{-2}$	Root
Number of tubes	1	Root
Material	brass	Child

4.2.5 Heat Exchangers

The heat exchanger model components, 3 and 7 from Figure 4.4, encompass the cylindrical housing section that contains the heat exchangers. Based on information within the Sage manual the appropriate arrangement and type of child components were incorporated to resemble an annular finned heat exchanger. Figure 4.8 shows their typical hierarchical structure, including heat and mass flow interconnections.

The heat exchangers are some of the more complicated model components. The second level of the hierarchy shows the four child components of the heat exchanger: duct gas, inner heat exchanger wall, heat exchanger fins and outer heat exchanger wall. The duct gas is connected via a heat flow path to the heat exchanger fins, which also share a heat flow path with the inner heat exchanger wall. Within the heat exchanger components of

the Sage model, heat transfer from the gas can only occur with one contact surface. The heat transfer from the gas to the outer wall was neglected in this section of the model, although the outer wall retains conductive heat transfer connections to the adjacent components. The remaining connections were exported to the root-component level as they required connections to the adjacent model components, hence all of the connecting arrows surrounding the root component, Cold HX 3, in the lower left of the Figure 4.8.

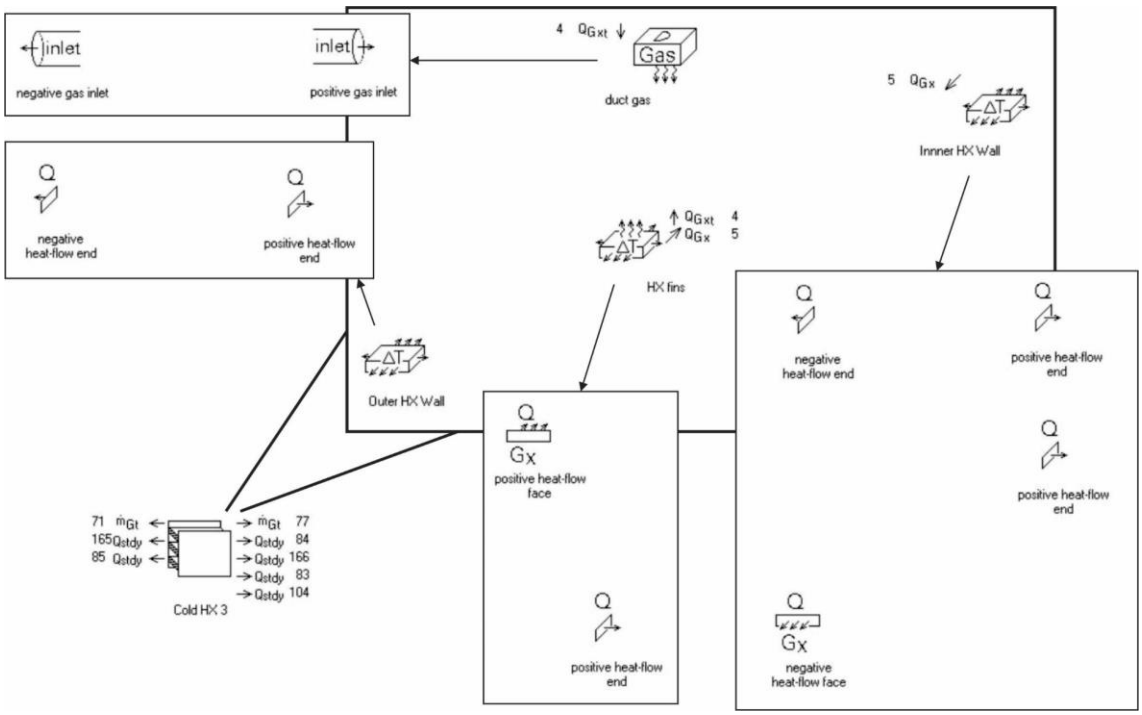

Figure 4.8 – Structure of the heat exchanger model-component within Sage.

By hovering over each connection it is possible to identify the child component to which it relates. The two mass flows, denoted by the m_{Gt} arrows, pertain to the duct gas flows through both inlet and exit boundaries of the neighbouring regenerator and cold space components. The inner walls of the hot heat exchangers are connected to heat sources that remain at constant temperature—for example, as 'Heater 3 Temperature' in Figure 4.5. Similarly, the cold heat exchangers are connected to a common heat sink, which is pre-set to the desired ambient temperature. The remaining heat flow connections include conduction paths through housing boundaries, and also from the top surfaces of the fins

into the regenerator matrix. Since all heat exchangers are identical, they all have the component inputs shown in Table 4.3.

Table 4.3 – Heat exchanger model-component input parameters.

Description	Value	Component level
Number of spatial cells	3	Root
Duct length (m)	$6x10^{-2}$	Root
Mean wall roughness (non-dimensional)	$1x10^{-3}$	Root
Initial temperature (K)	300	Root
Channel width (m)	$5x10^{-4}$	Root
Channel height (m)	$5x10^{-3}$	Root
Number of channels	90	Root
Fin thickness (m)	$7x10^{-4}$	Root
Fin conduction length (m)	$4.5x10^{-3}$	Child
Fin material	brass	Child
Inner HX wall circumference (m)	$9.425x10^{-2}$	Child
Inner HX wall thickness (m)	$8.75x10^{-3}$	Child
Inner HX wall material	brass	Child
Outer HX wall circumference (m)	$1.335x10^{-1}$	Child
Outer HX wall thickness (m)	$2.5x10^{-3}$	Child
Outer HX wall material	Aluminium	Child

The Sage user guide provides an appropriate method for relating an annular finned heat exchanger to the depicted rectangular-finned model component. The input values used in the heat exchanger components are self-explanatory, and are determined from the geometry of the components themselves. The reader is directed to the manual for further information about this procedure.

4.2.6 Regenerators

Three separate components are used to model the regenerators (identified in Figure 4.4 as numbers 4, 5 and 6). These components were used in order to account for the unusual and changing geometry of the regenerator spaces. The side sections have a cylindrical brass tube passing down and through their centres so as to provide access to the internal heat exchanger for the heating cartridges or cooling water. As a result, these spaces resemble a concentric tube configuration, whereas the central regenerator space is purely cylindrical and entirely filled with regenerator material. Also, the spaces are not

connected end on end, which complicates the model requirements. Figure 4.9 shows a graphical representation of the hierarchical structure of the centre regenerator component.

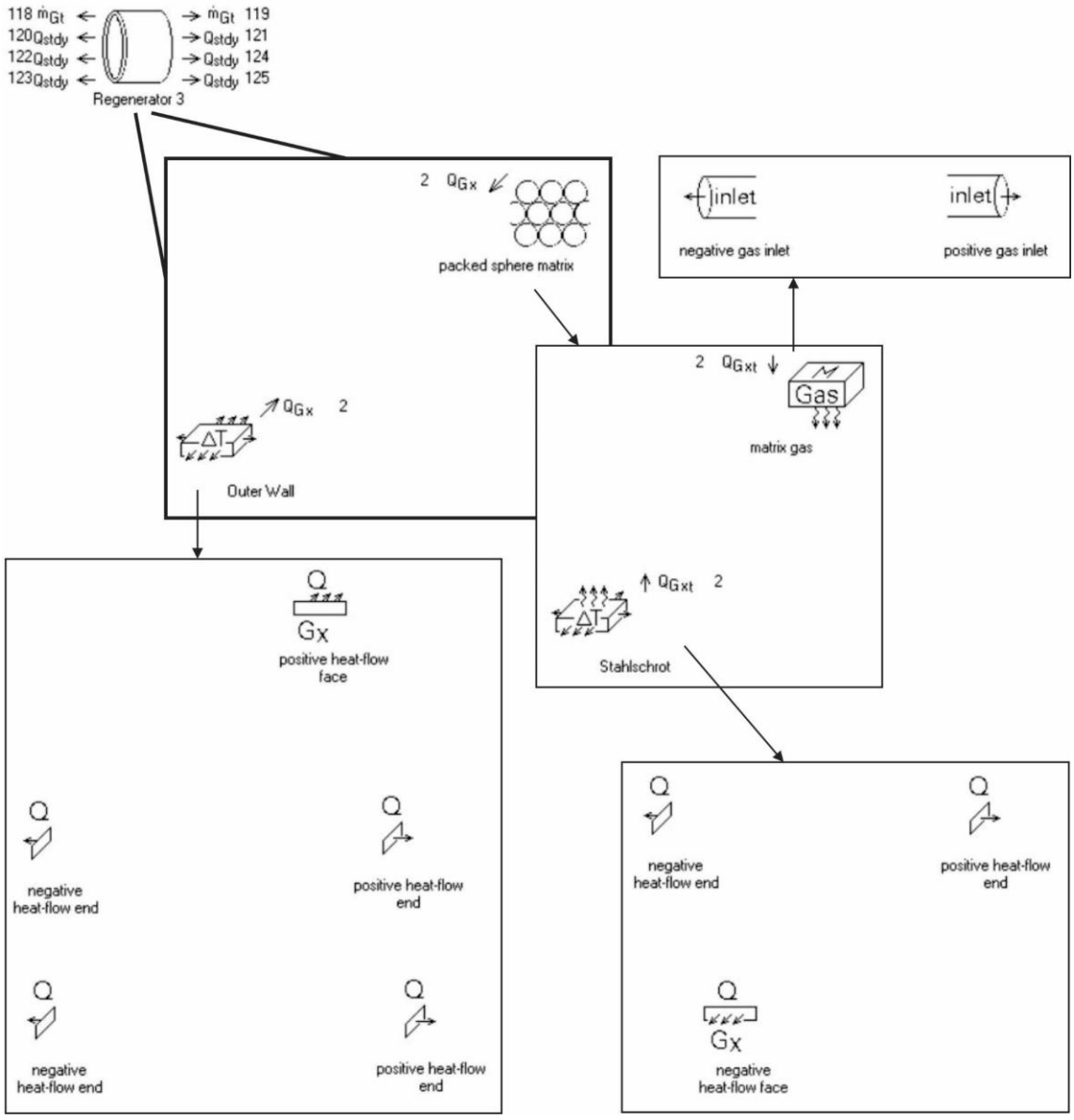

Figure 4.9 – Structure of the central regenerator model-component within Sage.

The centre regenerator component is modelled as a tubular canister with two child components: the packed sphere matrix and the outer wall. The matrix child component contains two further child components of its own: the duct gas and the steel shot material. Further information on why regenerators are modelled this way can be found in the Sage manual. The duct gas exhibits the familiar mass flow connections with the regenerator sides, and also shares a heat flow connection with the steel shot material, which can

conduct heat to the surface of the outer wall. Conductive heat flow paths exist for the outer wall's contact with the side regenerator components. Table 4.4 summarises the parameters used in the central regenerator component. The porosity of the regenerator material was estimated to be 0.39, based on loosely poured sphere packing void fractions.

Table 4.4 – Input parameter values for the central regenerator model-components.

Description	Value	Component level
Number of spatial cells	3	Root
Canister length (m)	$8x10^{-2}$	Root
Canister inner diameter (m)	$4x10^{-2}$	Root
Canister material	Alum6063	Root
Initial temperature (K)	300	Root
Canister wall thickness (m)	$2.5x10^{-3}$	Root
Matrix porosity	0.39	Child
Matrix sphere diameter (m)	$1x10^{-3}$	Child
Matrix material	Steel	Child

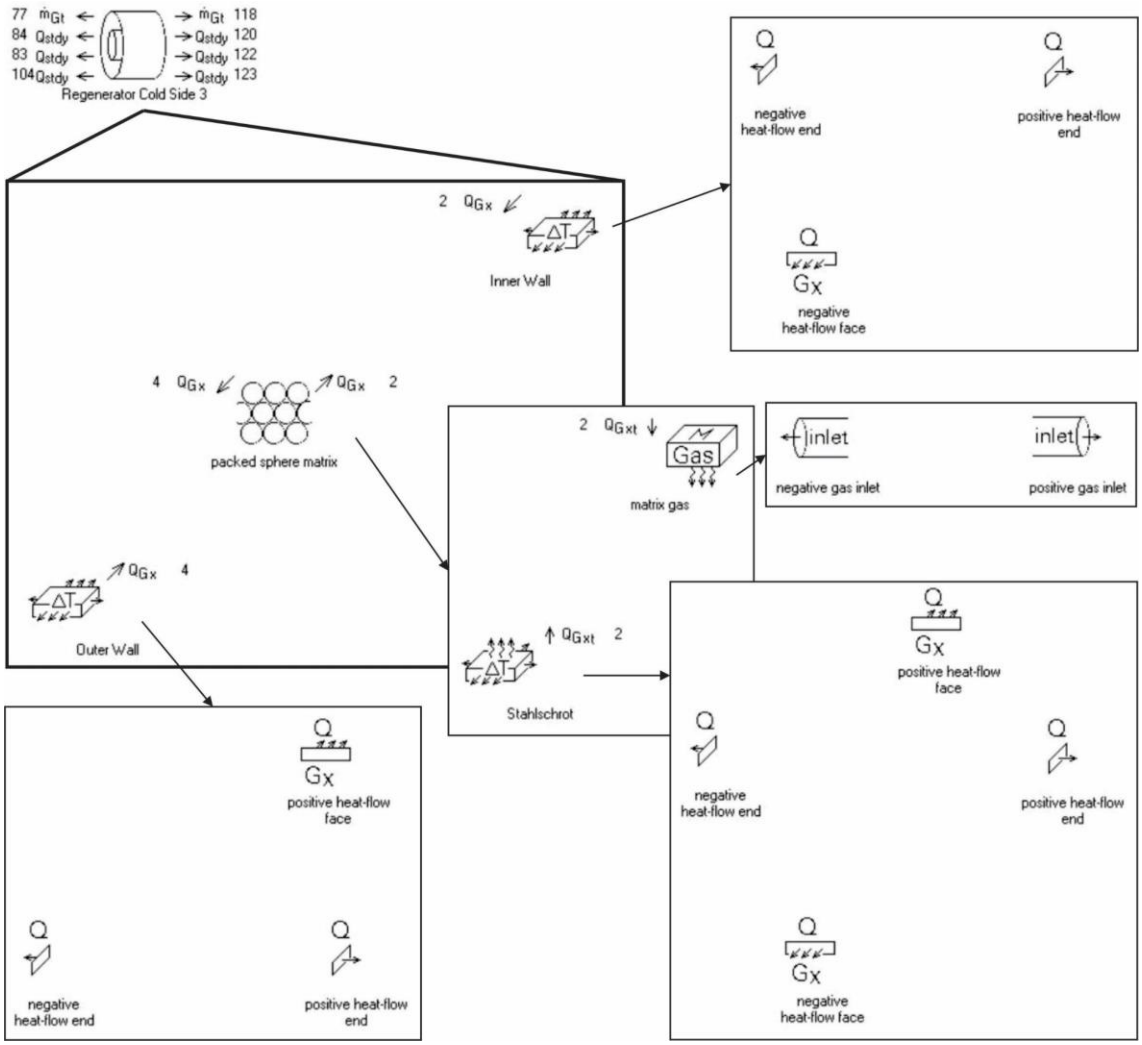

Figure 4.10 – Structure of the side regenerator model-component within Sage.

Figure 4.10 shows the structure of the side regenerator components. The side sections are modelled as annular canisters, with three child components: the inner and outer walls, both of which are conductive surface elements, and the packed sphere matrix material. As with the centre regenerator component, the matrix child component includes the duct gas and steel shot material. Heat flow paths exist between both walls and the matrix material. All three of these child components share conductive heat flow connections with the adjacent components, although it should be noted that since no inner wall exists in the centre regenerator, the flow paths are made to its outer wall instead. As with most gas space components, two mass flow connections exist for the inlet and outlets. Table 4.5 displays the input parameters used for the side regenerator model components.

Table 4.5 – Input parameters for regenerator side model-components.

Description	Value	Component level
Number of spatial cells	3	Root
Canister length (m)	$4x10^{-2}$	Root
Canister inner wall inner diameter (m)	$1.3x10^{-2}$	Root
Canister material	brass	Root
Initial temperature (K)	300	Root
Canister outer wall outer diameter (m)	$6.5x10^{-2}$	Root
Canister inner wall thickness (m)	$2.5x10^{-3}$	Root
Canister outer wall thickness (m)	$1.25x10^{-2}$	Root
Matrix porosity	0.39	Child
Matrix sphere diameter (m)	$1x10^{-3}$	Child
Matrix material	Steel	Child
Matrix radial thickness (m)	$5.5x10^{-3}$	Child

The Sage model deviates from the actual geometry in that it does not account for the elbow bends in the regenerator spaces, but this is considered to have negligible relevance given the early stage of research and development of this project. As the physical system is optimised with greater precision, so too can the computer models be improved and modified to better replicate its performance.

4.2.7 Liquid Pistons

On the right side of Figure 4.5 are the three components used to model the liquid piston: spring D, Liquid Piston D, and damper D. The piston itself is modelled as a solid free-piston, and is connected to the expansion and compression components of the adjacent gas spaces. In reality, the liquid piston's behaviour will deviate from that of a solid free-piston, and for this reason a spring and damper are also added to the model and connected to the piston. The spring is used to represent the restoring force imposed by gravity on the U-shaped piston as it oscillates back and forth, while the damper is used to account for fluid friction and kinetic losses (also commonly known as minor pipe flow losses) associated with the flow of the liquid during motion. The spring constant is simply derived from a force balance conducted on the liquid piston as a free body as identified in Section 2.3.2.2:

$$k_p = 2A\rho g$$

The damping coefficient of the viscous damper, C_{Damper}, is calculated by determining equivalent damping coefficients for the viscous and kinetic losses, C_{Vis} and C_{Kin}, in the fluid and summing them together. The average rate of viscous and kinetic energy loss for liquid pistons was estimated by West as:

$$\dot{E}_{Vis} = \frac{\pi\sqrt{\pi\rho f\mu}Lf^2V_S^2}{R_t^3}$$

and:

$$\dot{E}_{Kin} = 0.42\sum K\frac{\pi\rho f^3V_S^3}{2R_t^4}$$

where ΣK represents the sum of the kinetic flow loss coefficients and V_S, being the swept volume, is equal to:

$$V_S = 2\pi R_t^2 X$$

As identified in Section 2.2.7, the theory and experimentation for oscillatory flow problems is lacking, therefore the above equations are derived from well-known steady flow formulas. The limitations of assessing oscillatory flow losses with standard steady flow formulas is discussed further in Section 8.2.3.

In order to obtain the equivalent damping values, one can compare the average rate of energy lost through both viscous and kinetic mechanisms to that of a viscous damper, shown below. The average rate of energy loss for a damper is equal to the work done by the damping force per cycle multiplied by the frequency of oscillation:

$$\dot{E}_{damper} = W_{cycle} f$$

$$\dot{E}_{damper} = \pi \omega C_{damper} X^2 f$$

$$\dot{E}_{damper} = 2C_{damper} \pi^2 X^2 f^2$$

Equating the viscous losses to damping losses and rearranging the following expression for the equivalent viscous damping coefficient can be obtained as:

$$C_{Vis} = 2\pi^{1.5} L R_t \sqrt{\rho \mu f}$$

Similarly, an expression for the equivalent kinetic damping can be derived as:

$$C_{Kin} = 0.84 \sum K \pi^2 \rho f R_t^2 X$$

Now these effects are able to be incorporated into the model. The total damping coefficient used in the model is then:

$$C_{Damper} = C_{Vis} + C_{Kin}$$

C_{Damper} is recast as a user variable within Sage, which allows for it to be written as a function—and, as a result, it can vary with corresponding changes to its dependent variables during the solving process (piston radius, frequency, amplitude, etc.). While the majority of variables influencing the damping coefficient are the same for each piston, the kinetic component is influenced by piston amplitude. For this reason, each piston damper is designated its own damping coefficient variable.

The *K* values associated with the minor pipe losses in the U-shaped liquid piston are estimated to total 0.5, which includes two smooth 90° bends (0.15–0.25 each) and one small expansion/contraction (of negligible value) at the interface between the PVC and steel tube. The model sensitivity to this parameter is evaluated in Section 5.2.1. The effect of the floats is also expected to increase the cyclic power losses, but there is no research to indicate by how much, and hence is not currently included in the model. With the geometric and physical traits of the 'real-life' test-rig approximated, the model is almost complete. The final noteworthy characteristic of the model is that although three of the four pistons are modelled as free-pistons, the fourth is modelled as a constrained piston. This was found to be a necessity as the software would not converge on a solution with four free-pistons. The justification for constraining this piston is that its amplitude is found by optimising for a negligible net-work output, meaning the piston is essentially free, with its phase being pre-set to anchor the solver. This is explained in more detail in Section 4.2.9.

The diameter value used in the Sage model with 15 mm OD steel tubes is set to 12.65 mm. Although the manufacturer's specification for the PVC tube indicated that its internal diameter was 13.5 mm, a volumetric test concluded that the average internal diameter was actually 12.3 mm. On the steel side the internal diameter was measured to be accurate at 13 mm. Within the model only a single average diameter is used on both sides of the U-

tube to simplify the analysis. Therefore, the cross-sectional area assumed to take part in the force balance is provided by the average of these two diameters, 12.65 mm. It could be argued that the float diameters also need to be considered in this situation, since (due to the fluid boundary layers) their surface may be more representative of the area through which pressure and force are transmitted from the gas to the liquid. At this stage, speculating on the most accurate approximation for the effective cross-sectional area of the liquid pistons is unwarranted. It is a topic that could be revisited as the design is refined, and the model uncertainties reduced in other areas. Table 4.6 summarises the input parameters associated with the piston components.

Table 4.6 – Piston input parameters used in the Sage model for 100 ml pistons.

Description	Value	Component level
Spring constant (N/m)	variable	Root
Damping coefficient (Ns/m)	variable	Root
Piston mass (kg)	$1x10^{-1}$	Root (recast)
Piston face area (m^2)	$1.257x10^{-4}$	Child (recast)

4.2.8 Sage Model Input Requirements

Table 4.7 – General input parameters for LPSC Sage model.

Input Name	Description	Value
NTnode	Number of time nodes	9
Lnorm	Length scale (m)	$2.5x10^{-2}$
Freqnorm	Frequency scale (Hz)	4
Pnorm	Pressure scale (Pa)	$4x10^{5}$
Tnorm	Temperature scale (K)	300
Qnorm	Heat-flow scale (W)	100
Freq	Operational frequency (Hz)	-
Gas	Working gas	Ideal air
Xamp	Constrained piston amplitude (m)	-
Pmean	Charge pressure (Pa)	-
Theaters	Heater temperature (K)	-
Tcooling	Rejection temperature (K)	297
Rho	Liquid density (kg/m^3)	1000
Mew	Liquid viscosity (Ns/m^2)	$1x10^{-3}$
Ksum	Sum of minor pipe loss coefficients	$5x10^{-1}$
Pmass	Piston mass (kg)	$1x10^{-1}$
Vvariable	Expansion and compression space volumes (m^3)	$2.382x10^{-5}$
Dpiston	Piston diameter (m)	$1.265x10^{-2}$

Sage requires a number of general inputs for the Stirling machine before a simulation can be solved. The inputs window can be accessed separately and also includes the variables recast from model components, allowing for the manipulation of multiple system parameters from one location. For the LPSC model constructed for this project, these variables are listed in Table 4.7.

NTnode is the number of time nodes in the computational grids of all underlying model components containing grids. The influence of this value is discussed in the grid independence section, 4.2.11. The parameters, *Lnorm*, *Freqnorm*, *Pnorm*, *Tnorm* and *Qnorm* represent the normalisation constants for different system variables and influence the convergence of the solver. The most important of these is *Lnorm*, which is set to the approximate cube root of the largest stroke volume amplitude in the model. Advice for selecting appropriate values can be found in the Sage manual.

Of the remaining parameters, many have been recast to system level from model components (such as the piston mass); others include user created variables, such as *Ksum* and *mew* (for determining the piston damping constant). The four unspecified values in the table include the operation frequency, charge pressure, constrained piston amplitude and heater temperature. The charge pressure and heater temperatures are free to be varied depending on the operating range(s) of interest. For a conventional Stirling engine the frequency and piston amplitude would be known and available as inputs, however (as previously discussed), for the LPSC machine these are unknowns. This is, of course, precisely why modelling the LPSC is extremely complicated.

4.2.9 Frequency Deduction

It was initially intended that a computer model constructed in MATLAB would be used to predict the system frequency. The aim was primarily to obtain predictive results for the oscillation frequency, which could then be used as inputs for the more sophisticated Sage

model in order to analyse trends in the system's performance. Unfortunately, however, the Sage model was found to be extremely sensitive to the frequency input, and would generate vastly different results for small changes in the frequency input. A large amount of time was spent working with the Sage model, and it was thought that Sage's dependence on frequency as an input could not be circumvented. Despite this, after experimenting with many different model modifications, eventually a method was created which used Sage itself to provide the operating frequency for the 4HEAT configuration. This was a major breakthrough which allowed the model to be used independently for all LPSC simulations. The method is outlined below.

The process was developed by recognising the symmetric traits associated with the 4HEAT configuration. In the 4HEAT case where all four heaters are powered and supplied the same amount of energy, the resulting steady state amplitude of the liquid pistons must theoretically be equal as all four subsystems are identical and symmetrical. Furthermore, the relative phase angles between the pistons should also be 90º. Using these properties, and knowing the approximate range of permissible amplitude values, it was found that the in-built optimisation function[1] in Sage could converge on the frequency—if the objective function was carefully selected, and the starting estimates were already in close vicinity to the solution. An iterative process was employed, whereby either frequency or piston amplitude was selected as a floating variable, and the system optimised for either the smallest differences in piston amplitudes (objective function 1):

$$Obj_1 = |X_A - X_B| + |X_A - X_C| + |X_A - X_D|$$

[1] Within Sage, the optimiser's goal is to drive the pseudo-Lagrangian step-change to a small negative value. The pseudo-Lagrangian step-change is a measure of the relative change over the current step of the objective function. The value generally starts out large and negative and grows smaller as the optimisation converges to the minimum. The reader is directed to the user manual for more information about the optimisation process employed by Sage.

or minimal net-work output by the constrained piston (objective function 2):

$$Obj_2 = \left|W_{net,A}\right|$$

Initially the natural frequency provided by Equation 4.8 for the spring-mass system in Section 4.1 was used to provide the optimiser's frequency estimate. After recognising patterns in the frequency solutions, this was later modified to be the natural frequency determined using a polytropic index of 1.2 in the same equation. This was an essential step as the solver would converge on false solutions with near-zero piston amplitudes if the starting point was outside a certain local turning point. The process would continue with the piston amplitude being set and the frequency found, and then the frequency would be set, and the model optimised to find a more accurate piston amplitude. Eventually, the piston amplitudes would all be equal to within 0.1%, and the piston phase angles would be within the range 90° ± 0.5º. Both objective functions would converge to the same solutions—although objective function 1 was much more stable and generally converged more quickly (so it was used in the 4HEAT case[1]). Via this method both the piston amplitudes and frequency of operation for the 4HEAT configuration for any charge pressure and heater temperature set points could be determined.

Since the operating frequencies have shown very little dependence on heater temperature, they are almost identical when comparing 4HEAT, 3HEAT, and 2HEAT configurations with the same charge pressure. Therefore, the frequency obtained via this method can be used in the 3HEAT and 2HEAT simulations, despite the fact that the piston amplitude symmetry no longer applies.

[1] Another method involving optimising for 90º phase angles was also attempted, but the optimisation problem seemed to be ill-conditioned and the solver was unable to converge.

As a test for this, it is possible to assess the Sage model's frequency dependence on heater temperature, similar to the analysis in Section 4.1.2. Using the frequency deduction procedure described above, the operational frequency was obtained for the 15 mm 4HEAT system using two heater temperatures at the limits of the functional range. The highest charge pressure of 6 bar was used to produce the largest differences. The values obtained were 5.050 Hz and 5.076 Hz for 100°C and 150°C heater temperatures, respectively, which have a difference of 0.026 Hz or 0.51 % relative to the value at 100°C. The estimates obtained from Equation 4.25 for the percentage differences between unforced and forced frequencies are 0.59% and 1.48% at 100°C and 150°C respectively—a difference between the two of 0.89%. These values of 0.51% from Sage and 0.89% from the analytical approximation are very small and similar in magnitude, and therefore contribute to the validity of using the 4HEAT Sage model frequencies for 3HEAT and 2HEAT Sage simulations.

4.2.10 Solving 3HEAT and 2HEAT models

For reasons already discussed in relation to model convergence, one of the pistons must be modelled as a constrained piston. Within the model this component provides a number of referenceable outputs. Those of primary interest are the forcing function and net-work output. For the 3HEAT and 2HEAT simulations the second objective function is used to find the amplitude of Piston A. A user variable is created in Sage and recast to equal the net work of the piston. The piston amplitude is then optimized for a minimal absolute value in this variable. This corresponds to the case where the piston is behaving as a free piston, with no external influence, exactly as the other three pistons in the model automatically behave. An example of this optimisation process can be seen in Figure 4.11.

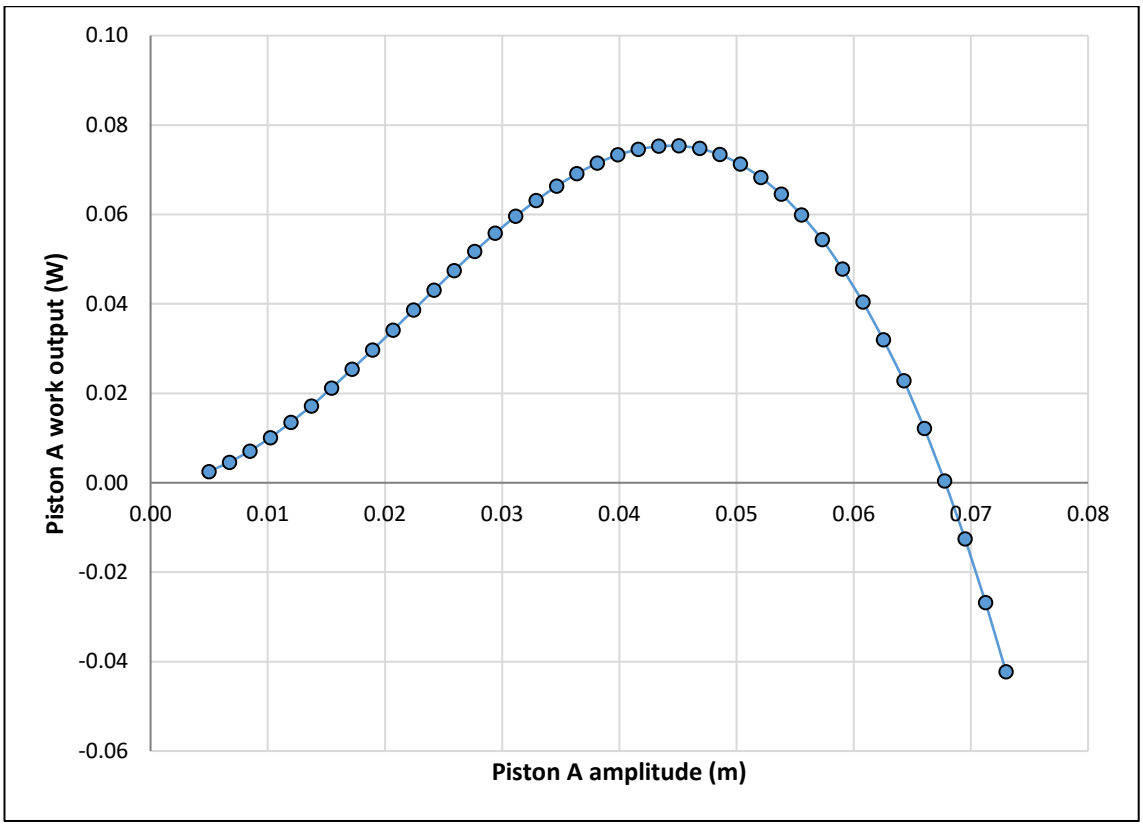

Figure 4.11 – Piston A work output mapped against piston displacement. Simulation was conducted for 3HEAT configuration at 4 bar and 150°C heaters with 100 ml pistons.

The work output from the constrained piston, Piston A, crosses the x-axis at approximately 0.0675 m, corresponding to an amplitude of 6.75 cm. This represents the amplitude at which the piston behaves as a free piston, requiring negligible external influence (aside from the spring and damper attached in the model). For displacements lower than this 6.75 cm, the piston provides a work output, as if it were connected to a coupling mechanism or linear generator. For values above 6.75 cm, the piston requires a net work input, as if it were a driven component. The amplitudes of the other three pistons automatically adjust, as they are inherently unconstrained, and always have a zero net work output. The figure above also explains why a number of convergence issues are associated with objective function 2. When optimising for minimal absolute piston work, the solver can converge towards zero amplitude if the initial value is to the left of the turning point at 0.045 m. For comparison, Figure 4.12 shows objective function 1 when mapped against piston displacement for a 4HEAT simulation.

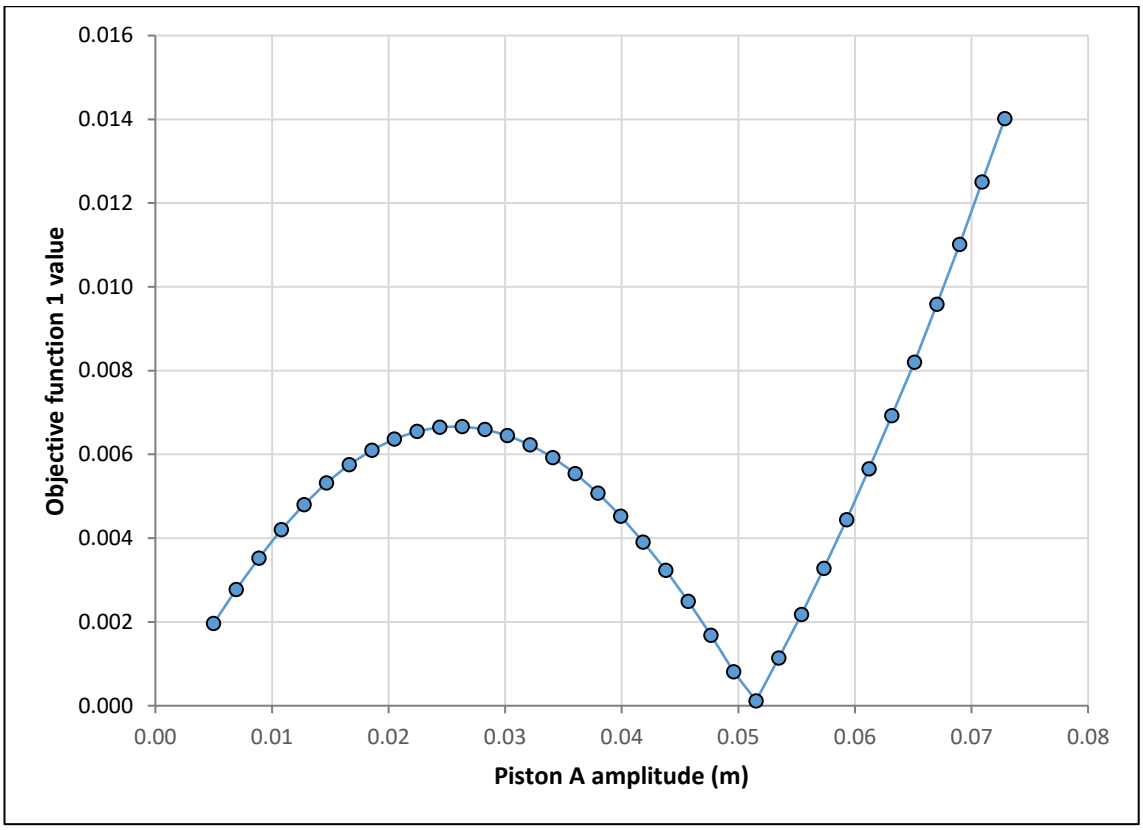

Figure 4.12 – Objective function 1 mapped against Piston A amplitude. Simulation was conducted for 4HEAT configuration at 4 bar and 100°C heaters with 100 ml pistons.

Convergence issues are sometimes encountered with objective function 1; but they are much more infrequent. This may be related to the shape of the two objective functions. Objective function 1, in Figure 4.12, appears to transition past the slope towards zero amplitude earlier than the net work of Piston A (objective function 2), in Figure 4.11.

4.2.11 Grid Independent Solutions

The sensitivity of Sage to a number of model-specific parameters was investigated in order to ensure simulation solutions were independent. These parameters were those not related to the physical test-rig dimensions or other properties, but model variables within Sage components. The relevant parameters are defined below.

NTnode—Number of time nodes in the computational grids of all underlying model components containing grids. This is an important parameter because it can significantly affect the solution time, accuracy and memory requirements. It can be likened to a mesh

size for the harmonic variables in the time domain. This value determines the number of harmonic terms output in the Fourier series solutions of system variables such as gas pressure and temperature. Changing this variable recreates all time grids in the model and initializes solution values by interpolating between solved values of the previous grid. The Sage manual advises using an odd value for this parameter. Table 4.8 shows how the model solution accuracy was affected by the *NTnode* parameter. A value of 9 was employed for the *NTnode* parameter since the increases in precision beyond this value were negligible.

Table 4.8 – Sage model sensitivity to NTnode parameter. (Example 3HEAT simulations at 4 bar with 150°C heaters and 100 ml pistons)

***NTnode* parameter**	**Piston A amplitude solution (cm)**	**Change (%)**
3	7.598	-
5	6.830	10.11
7	6.852	0.32
9	6.783	1.01
11	6.768	0.22
13	6.771	0.04
15	6.774	0.04

Ncells—The *Ncells* parameter is the number of spatial cells that a single component is divided into for the solution and is specific to each component. It is similar to the number of elements in a finite element model. The *Ncells* parameter was checked for each model component containing the working gas. Table 4.9 shows how the *Ncells* parameter affected the piston amplitude solution quantities when changed in a number of different components. The simulations were with the 4HEAT configuration and used parameters of 4 bar charge pressure and 100°C heater temperatures. As a result of the investigation only one *Ncells* parameter was changed from the default value and that was in the compression and expansion spaces, where the value was increased from 1 to 2.

Table 4.9 – Sage model sensitivity to Ncells parameter. (Example simulations at 4 bar with 100°C heaters and 100 ml pistons).

Component	*Ncells*	Piston amplitude solution (cm)	Change (%)
Expansion/ Compression Spaces (1 & 9)	1 (Default)	5.126	-
	2	5.194	1.33
	3	5.198	0.07
	4	5.202	0.08
	5	5.206	0.08
Heat exchangers (3&7)	1	5.493	-
	2	5.202	5.30
	3 (Default)	5.198	0.08
	4	5.208	0.19
	5	5.214	0.12
Central Regenerator (5)	1	6.502	-
	2	5.201	20.01
	3 (Default)	5.194	0.13
	4	5.186	0.15
	5	5.191	0.10

4.2.12 Complete Model Diagram

For reference, the entire Sage model, viewed at the component level, is shown on the following page as Figure 4.13.

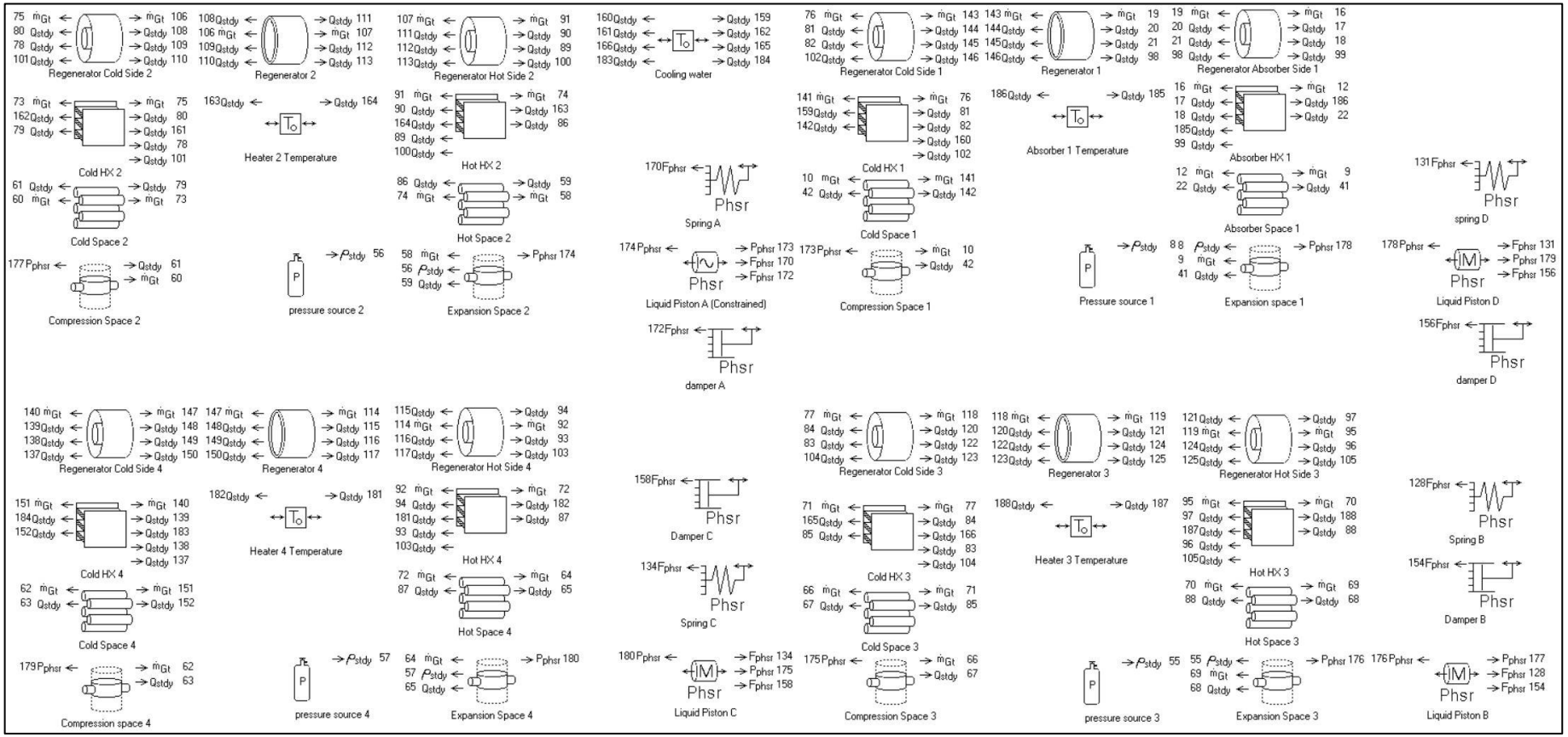

Figure 4.13 – Complete Sage model diagram

5 Results for 15 mm OD Piston Tubes

5.1 Experimental Results

The parameters included for the experimental investigation were summarised in Table 3.2 (in Section 3.4), and are reproduced here in Table 5.1.

Table 5.1 – Set of parameters for first experimental investigation (reproduced from Section 3.4).

Piston tube outer diameter (mm)	Configuration	Liquid piston volume (ml)	Heater surface temperature (°C)	Gas charge pressure (bar)
15	4HEAT	100	95, 100, 105	1-6
15	4HEAT	115	95, 100, 105	1-6
15	3HEAT	100	130, 140, 150	1-6
15	3HEAT	115	130, 140, 150	1-6
15	2HEAT	115	190	1-6

Examples of experimental results that were typical for each configuration tested are presented, in this section, and then the results for each parameter set from the table above are summarised (along with any interesting observations made during the experimental process). The results for the 4HEAT configuration are shown first—followed by 3HEAT and 2HEAT. The reader is encouraged to note that due to the early stage in the development of the LPSC machine, the emphasis is more on behavioural, trends and less on specific numerical evaluation.

5.1.1 4HEAT Configuration

As previously mentioned in Section 3.3.1, although the 4HEAT configuration has no cooling potential, its symmetry makes it very useful as a benchmark comparison for the modelling techniques (it was also very useful when testing out different modifications during the commissioning of the system). Understanding the 4HEAT system allows for a better understanding of the differences seen in the 3HEAT and 2HEAT configurations. The results presented here aim to familiarise the reader with the behaviour of the 4HEAT

configuration and how its performance is influenced by changes in the key design parameters in the table above.

Example results of a representative 4HEAT experiment are presented in Figures 5.1 and 5.2, and show the pressure amplitudes and heater temperature trends for a typical 4HEAT experiment lasting about 30 minutes. Figures 5.3 and 5.4 show the pressure and displacement profiles during a one second snapshot taken during the experiment. The experiment considered in this example case used heaters set at 105°C, 115 ml liquid pistons, and a gas charge pressure of 4.75 bar. The snapshot was taken at time, t = 1665 seconds (27 minutes and 45 seconds into the experiment).

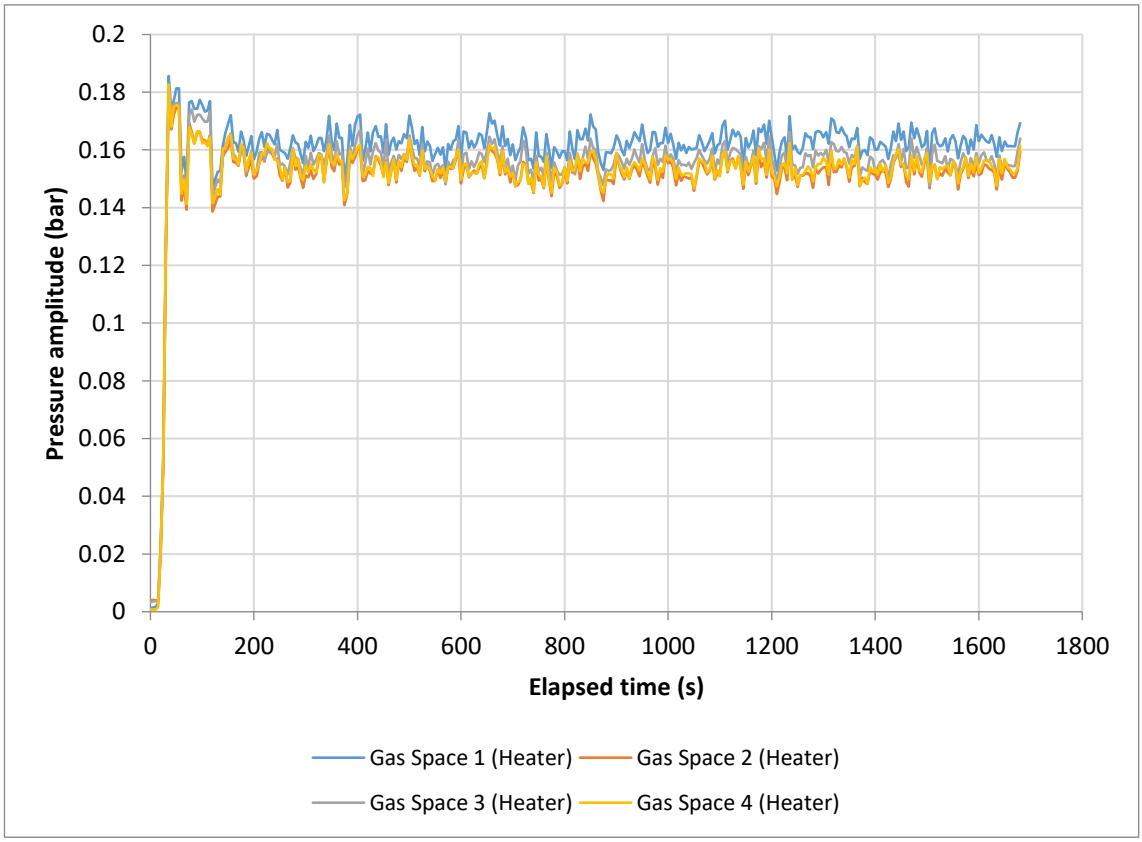

Figure 5.1 – Gas pressure amplitude variations during a typical 4HEAT experiment. The experiment was at 4.75 bar with 105°C set heater temperature and 115 ml liquid pistons.

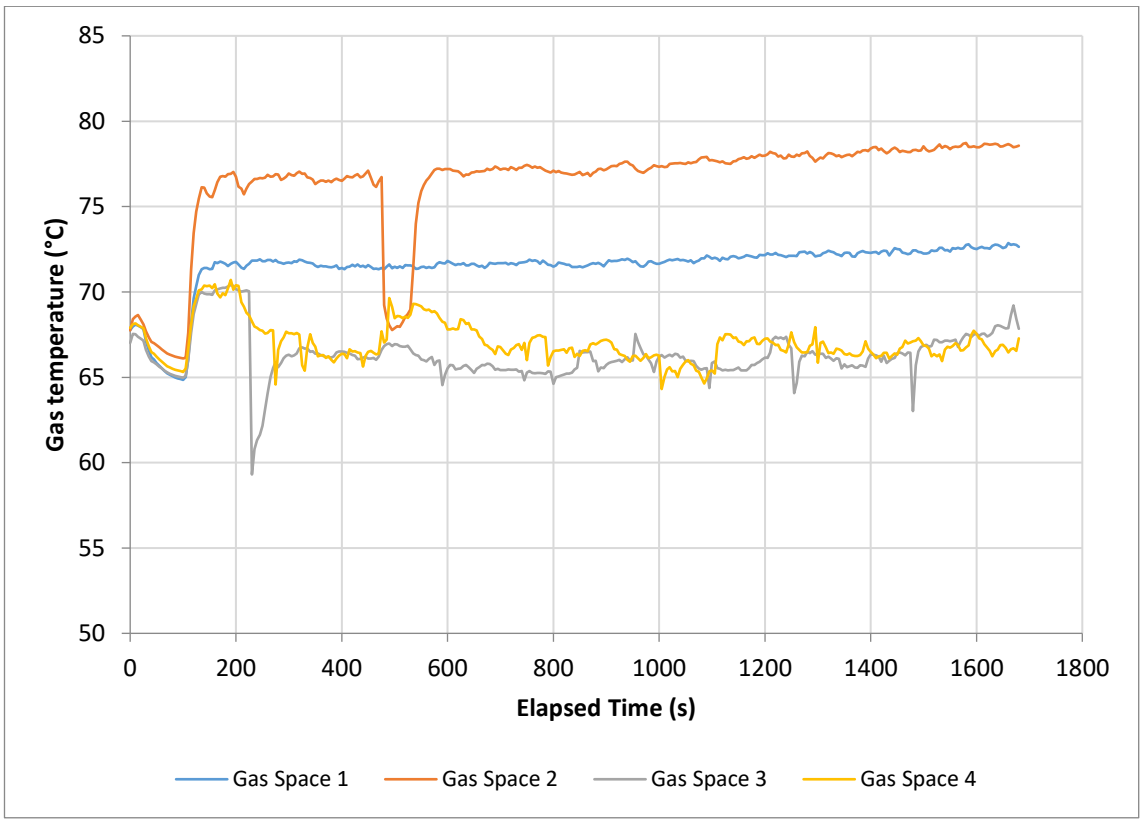

Figure 5.2 – Heater gas temperature variations during a typical 4HEAT experiment. The experiment was at 4.75 bar with 105°C set heater temperature and 115 ml liquid pistons.

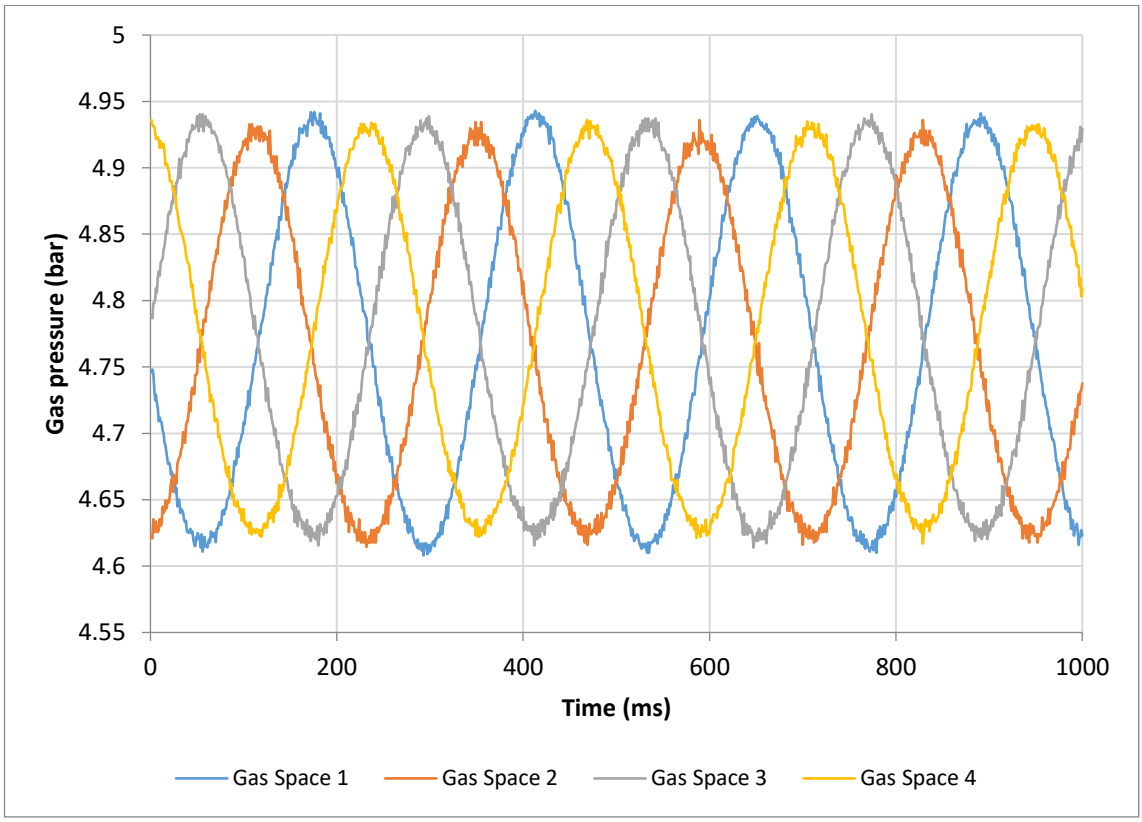

Figure 5.3 – Gas pressure profiles over one second interval during a typical 4HEAT experiment. The experiment was at 4.75 bar and 105°C with 115 ml liquid pistons. Snapshot time was 1665 seconds (27 minutes 45 seconds) into the experiment.

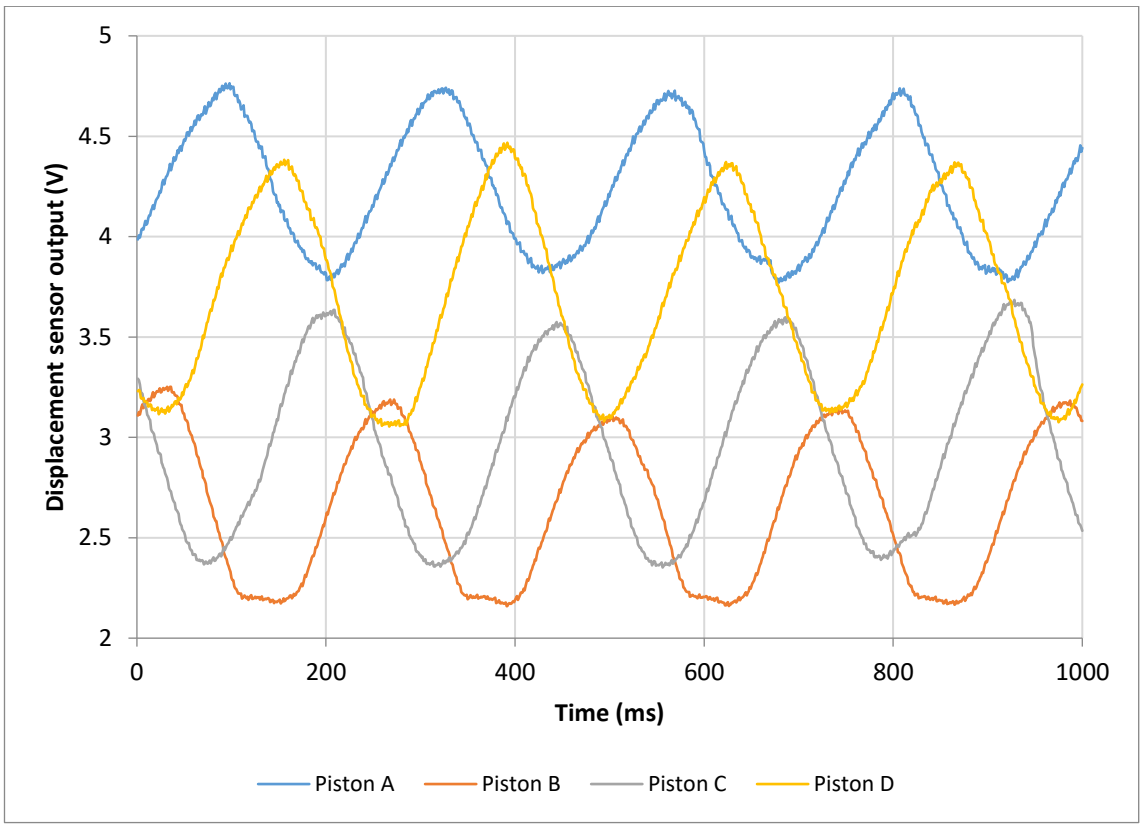

Figure 5.4 – Piston displacement profiles over one second interval during a typical 4HEAT experiment. The experiment was at 4.75 bar and 105°C with 115 ml liquid pistons. Snapshot was 1665 seconds (27 minutes 45 seconds) into the experiment.

The pressure amplitudes seen in Figure 5.1 are approximately equal for each of the four gas spaces and oscillate around 0.16 bar throughout the duration of the experiment. This is expected for the 4HEAT configuration as each sub-system would be identical were it not for small geometric and physical property differences associated with the real test-rig. The pressure amplitudes were always roughly equal to each other in the 4HEAT experiments. The average pressure ratio in the example experiment equates to 1.07, which is in the expected realm for a low temperature Stirling machine (Kolin, 1991). The hot side gas temperatures are seen in Figure 5.2 and span the range 66°C–79°C. The differences seen here are more unexpected, with each heater being supplied the same power via the PID heater controller. The cause of this is currently unknown, but possible explanations include differing thermal resistances in the heat exchanger to heating cartridge interface. The gas pressure profiles depicted in Figure 5.3 exhibit the expected

sinusoidal forms and look to have approximate relative phase angles of 90º, which is another expected characteristic of the symmetric 4HEAT configuration.

The displacement profiles in Figure 5.4 appear less uniform and consistent when compared with the pressure profiles. It is important to note that with liquid pistons the surface is prone to behave irregularly depending on frequency and amplitude. Considering the relatively high frequency (~4 Hz) and pressure in this case, the sensor outputs are acceptably accurate. The stability of the liquid pistons is a major topic throughout the results, and is investigated and discussed in further detail in Section 5.1.5 and thereafter. Although harder to infer, the phase angles of the pistons also appear to be approximately 90º, which was a consistent outcome of 4HEAT experiments. The displacement profiles show the output from the sensors in volts. These displacement profiles were fitted with sinusoidal functions by way of a least mean squares optimisation in Microsoft Excel as described earlier in Section 3.2.3. The calibration coefficients were then implemented to obtain the amplitudes and phase angles of each piston. This process was repeated for each piston, gas space pressure, and net pressure acting on the pistons, which allowed their behaviours to be interpreted as phasors.

With phasor representations obtained for the pistons and gas space pressures it is possible to conduct vector analysis and to quantify the volumetric changes for each gas space—and therefore investigate the performance of the machine. Table 5.2 shows the summary of the phasor expressions for the example experiment. The gas space and piston designations were made in Figure 3.2 (from Chapter 3). The phase angles are referenced to the Gas Space 1 pressure phasor. Visualising the values in the following table can be difficult, so it is often beneficial to construct the following graphics. Figure 5.5 shows the pressure and displacement phasors described in Table 5.2.

Table 5.2 – Phasor representations of gas pressure and piston displacement amplitudes for example 4HEAT experiment. The experiment was at 4.75 bar with 105°C with 115 ml liquid pistons. Snapshot was at 1665 seconds (27 minutes 45 seconds into experiment).

Phasor	Amplitude (bar or cm)	Phase angle (°)
Pressure 1 (P1)	0.161	0
Pressure 2 (P2)	0.151	94.0
Pressure 3 (P3)	0.155	179.7
Pressure 4 (P4)	0.152	272.0
Displacement A (XA)	3.49	138.1
Displacement B (XB)	3.16	232.4
Displacement C (XC)	3.37	321.7
Displacement D (XD)	3.32	43.8

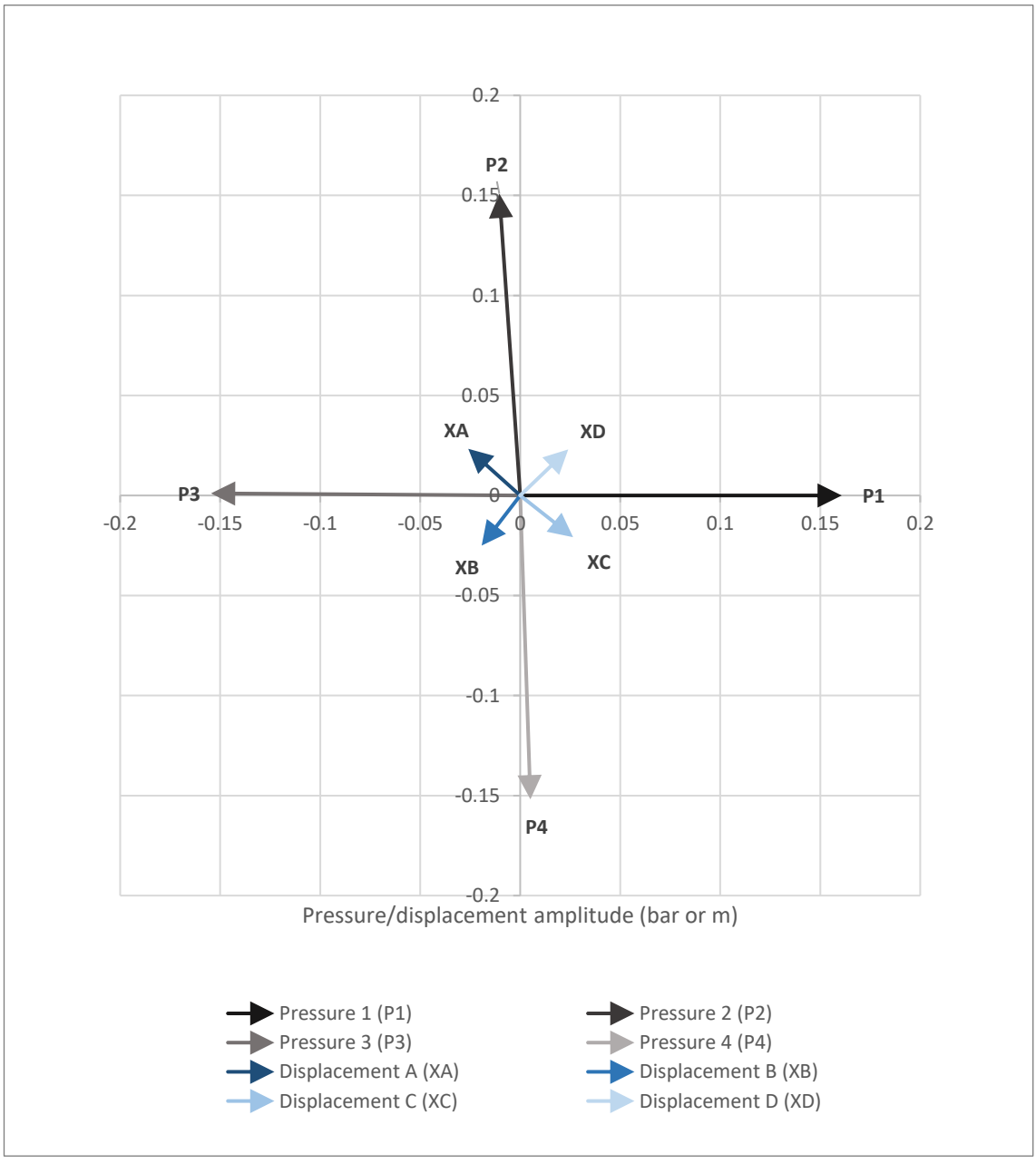

Figure 5.5 – Phasor plot of example 4HEAT experiment pressure and displacement profiles. Note the symmetry of the 4HEAT configuration results.

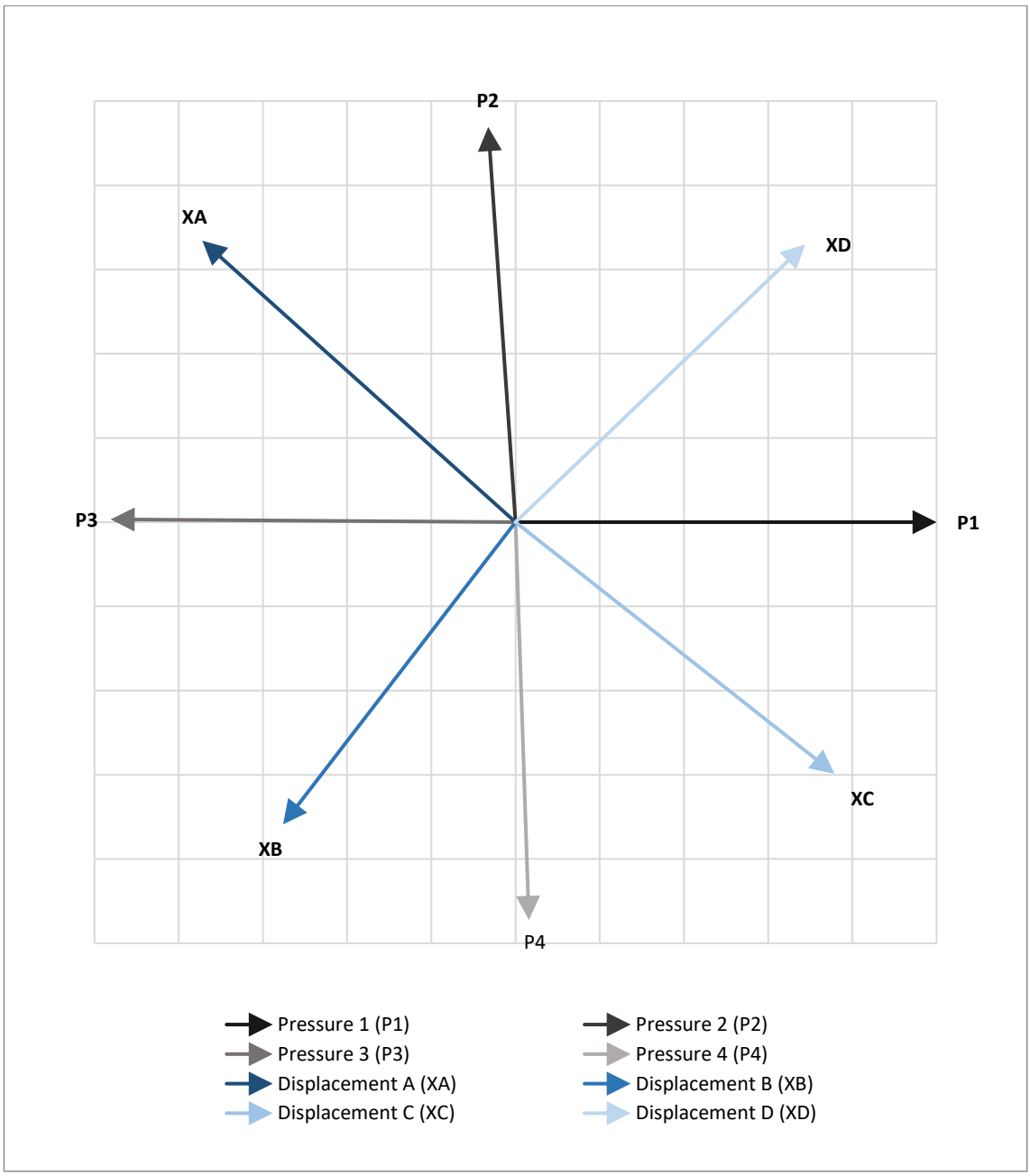

Figure 5.6 – Phasor plot of example 4HEAT experiment pressure and displacement profiles. The phasor magnitudes have been scaled for more clarity.

The phasor magnitudes can be scaled by dividing by the magnitudes of P1 and XA to produce the scaled phasor plot of Figure 5.6. In this form the phasor and their interrelationships are easier to interpret. As expected for the 4HEAT configuration, the phasor plot is quite symmetrical, with close to 90º angles separating the pressures and displacements from each other, as well as roughly 45º differences between piston displacements and pressures. The exact phase angles are shown in Figure 5.7.

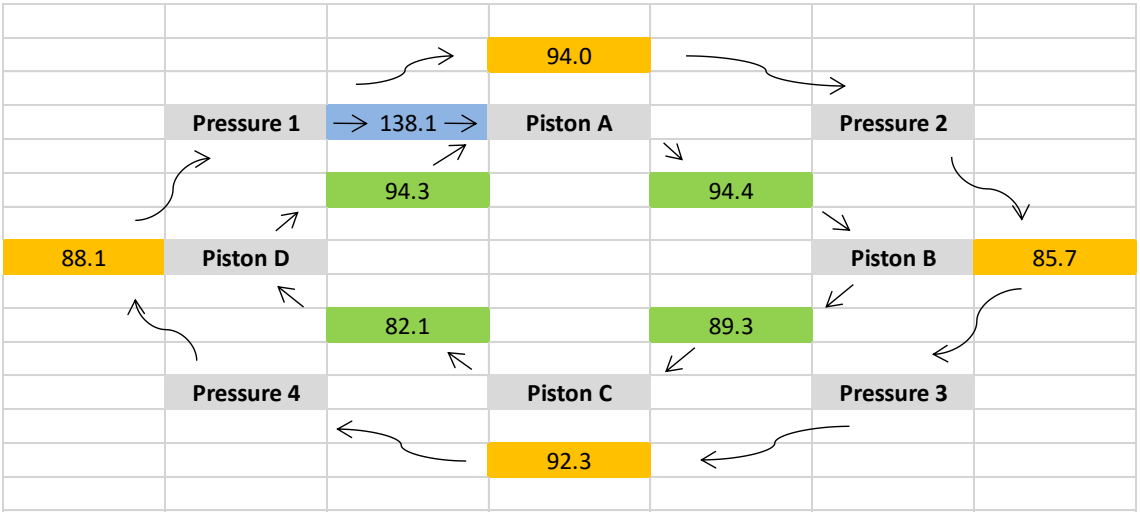

Figure 5.7 – Pressure and displacement phase angles for 4HEAT example experiment.

Comparing Figures 5.6 and 5.7 it is possible to review the associated phase angle values between different pressure and displacement phasors. The values in yellow boxes relay the phase angle difference between adjacent pressure phasors. Those in green relate to the piston phases and the single value in the blue box compares Piston A to Pressure 1. With this combination, any relative phase angle can be deduced. For example, subtracting the relative phase angle between pistons A & D (94.3°) from the angle between Pressure 1 and Piston A (138.1°), yields the phase difference between Pressure 1 and Piston D (43.8°). All remaining interrelationships of interest can be assessed using this method.

5.1.1.1 100 ml Piston Results

The results presented here summarise the experiments conducted with 100 ml piston volumes, using the 4HEAT configuration at three heater temperatures of 95°C, 100°C and 105°C, and across the charge pressure range of 2 bar–6 bar. Figures 5.8–5.15 show some of the key variables dependence on charge pressure and heater temperature—namely pressure amplitudes, piston displacements, phase angles and gas space temperature differentials.

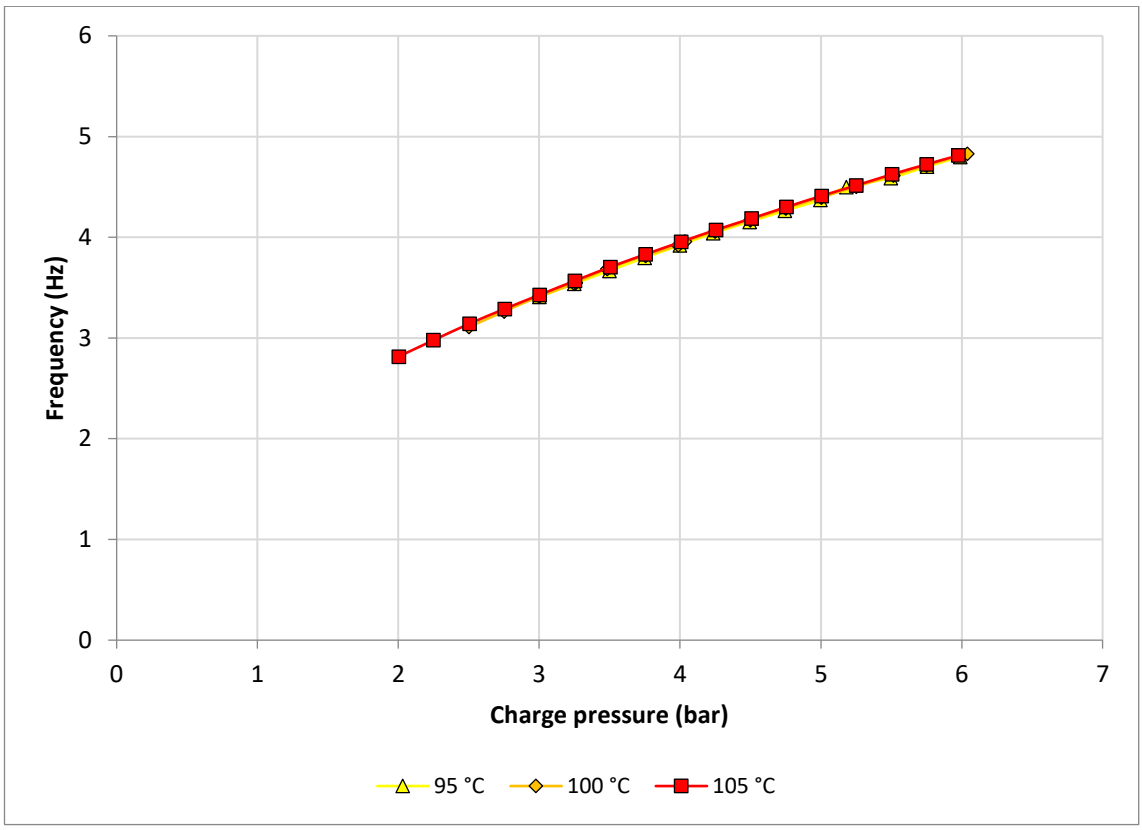

Figure 5.8 – Frequency variation with mean operating pressure for all 4HEAT configuration experiments using 100 ml liquid pistons

Figure 5.8 shows how the frequency of operation of the system changes with increasing gas pressure and for different heater temperatures. Experiments below 2 bar charge pressure did not achieve stable operation. As expected from the analytical approximation for frequency derived in Section 4.1, the shape of the above trend implies that frequency has a dependence on the square root of charge pressure (this will become more obvious when a direct comparison is made in Section 6.2). The changes in heater temperature in this case do not influence the operational frequency, which is an expected outcome based on the analysis conducted in Section 4.1.3. Figure 5.9 displays the pressure amplitude variations measured against increasing charge pressure for the 105°C heater temperature. As previously identified in the example experiment, the pressure amplitudes of each of the gas spaces are very similar, and they maintain this similarity across the entire charge pressure range investigated. The pressure amplitudes increase with charge pressure and appear to be converging towards a potential maximum value.

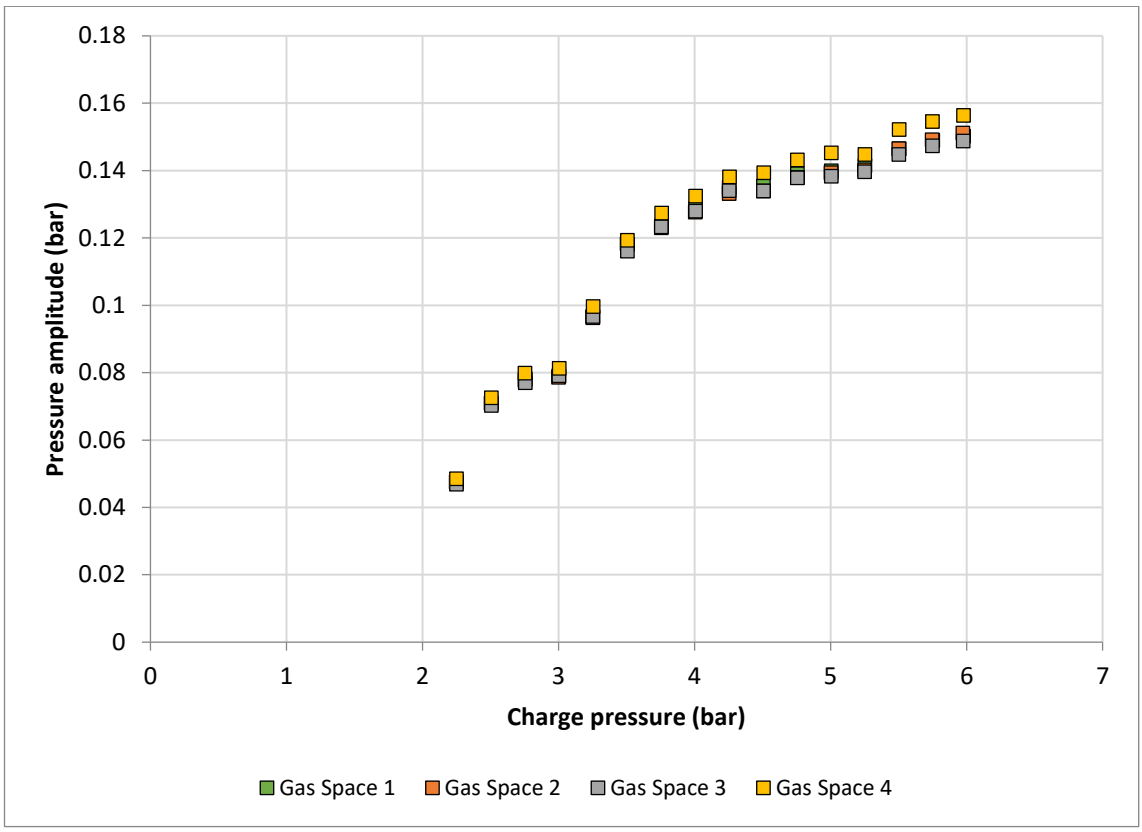

Figure 5.9 – Pressure amplitude variations of all gas spaces with increasing charge pressure for 4HEAT experiments conducted with 105°C heater temperatures and 100 ml pistons.

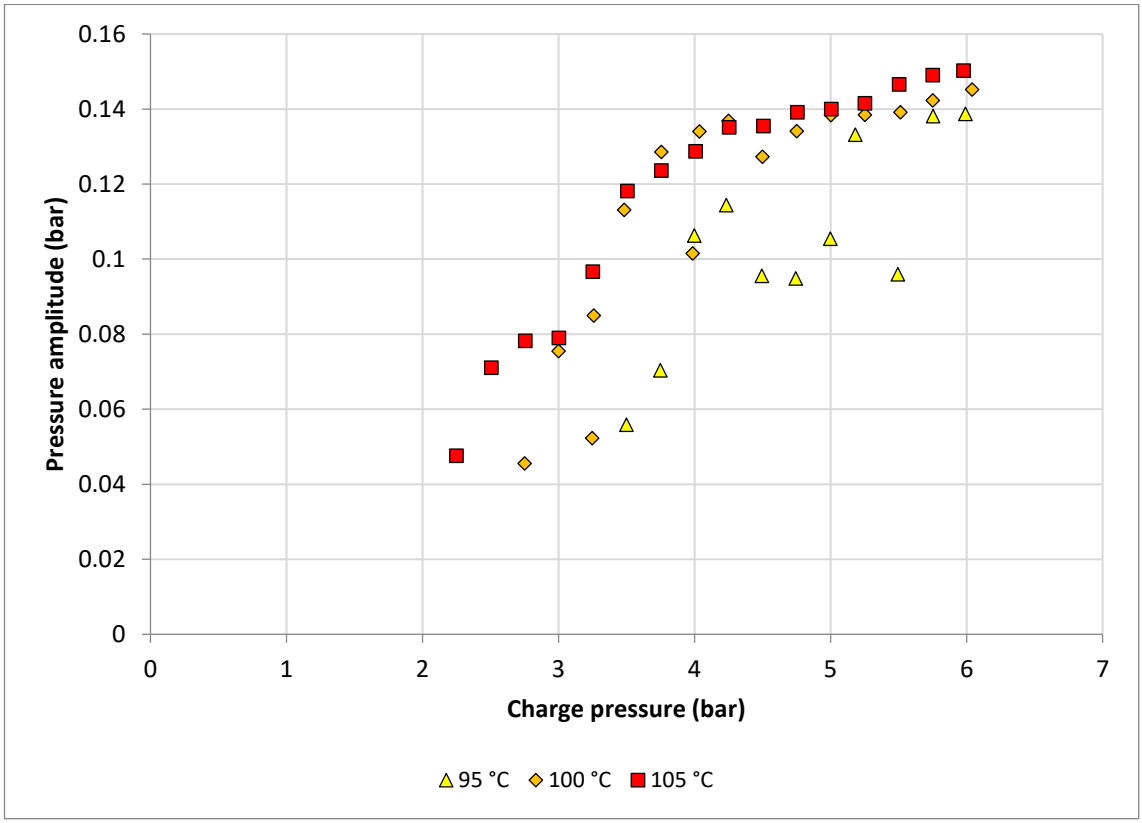

Figure 5.10 – Pressure amplitude variation of Gas Space 1 with changing charge pressure for all 4HEAT experiments using 100 ml liquid pistons.

Similar to Figure 5.9, Figure 5.10 displays the pressure amplitude variations with charge pressure, but for all three heater temperatures investigated. Due to the symmetry within the 4HEAT configuration, only Gas Space 1 measurements are graphed. The general influence of higher heater temperatures producing larger pressure amplitudes is evident. More interesting is the apparent separation of the data points into a number of ridges. This indicates the possibility of different stable regions of operation, which are subsequently referred to as modes. All of the 105°C results occupy the highest energy modes, with perhaps one existing between 2 bar–3 bar and another from 3 bar–6 bar. The 100°C data points occupy both the higher energy and lower energy modes, which seem to converge at approximately 4.5 bar. The 95°C series include some data points in-line with the lower energy mode seen in the 100°C results, as well as what appear to be either outliers or a lower energy mode between 4.5 bar and 5.5 bar. The phenomenon of these different operational modes was something consistently observed in the 15 mm U-tube experiments and is discussed in more detail in section 8.2.5.

Figure 5.11 shows the difference in gas temperatures between the compression and expansion spaces. Although relatively close in magnitude, a consistent trend is evident in the data—with the temperature difference in GS2 being the largest, GS1 and GS3 occupying similar middle values, and GS4 having the lowest difference. The compression space temperatures were all very similar for each sub-system as they were regulated by the cooling water, which was near ambient. The variance in these gas space temperature differentials is therefore attributed to different expansion space temperatures, which implies potentially different heater surface temperatures. As discussed in Section 3.1.4, the experimental set-up regulates the fin temperature of one heater (GS2), and each heater is supplied the same quantity of power. Therefore, there are two potential causes of these differences: either they are due to the variations in the thermal resistances within each hot heat exchanger sub-assembly; or, alternatively, due to other imperfections in the

geometric/thermal symmetry of the sub-systems, which causes the system to reach a stable operating point that does not reflect the precisely symmetrical behaviour of the theoretical 4HEAT system. In practice, achieving a perfectly symmetrical system is difficult, and unnecessary for a preliminary research endeavour akin to this one.

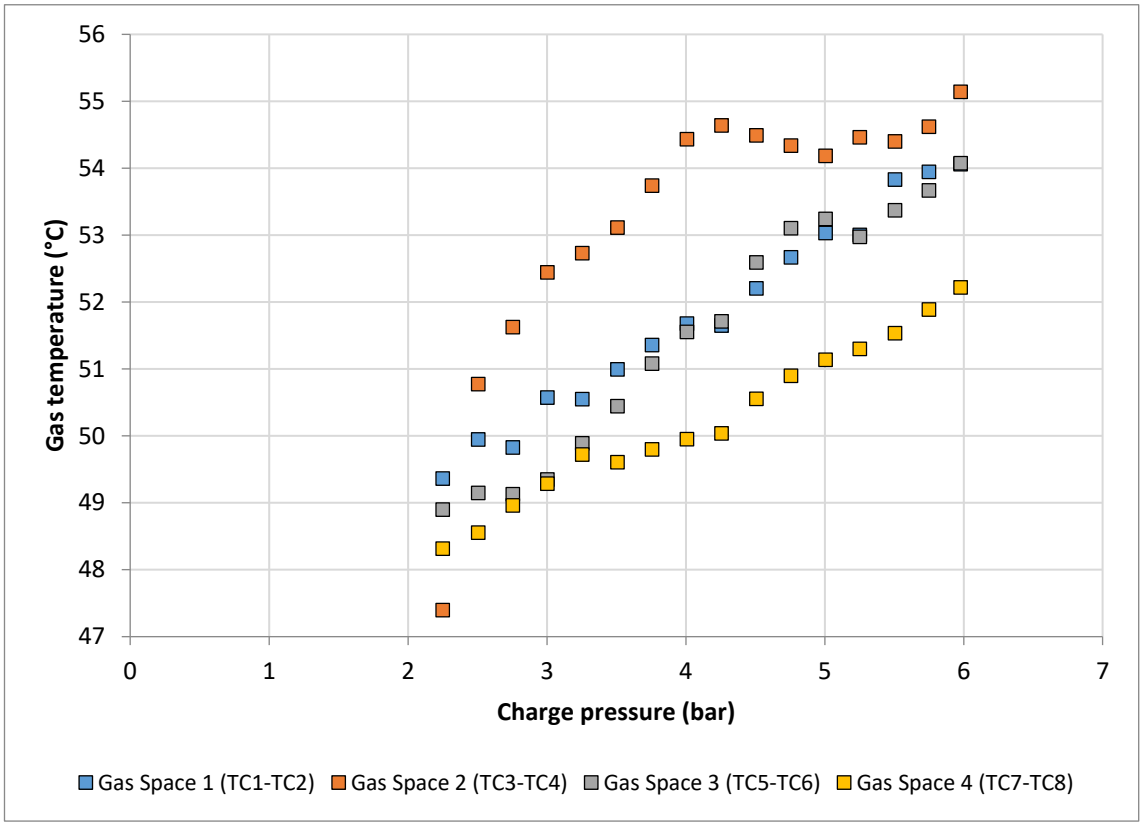

Figure 5.11 – Gas space temperature differentials and their variation with charge pressure for the 4HEAT experiments with 105°C heater temperatures.

The largest variance seen in Figure 5.11 is approximately 5ºC and occurs at 4.25 bar, between GS2 and GS4—however, this magnitude of inconsistency is still considered to be acceptable for the purposes of this project. Section 8.2.2 reviews the design of the experimental set-up and discusses recommendations for future experimental work. Interestingly, the local peak in gas space temperature difference (seen above at 4.25 bar) closely corresponds to the maximum piston amplitudes across the range of charge pressures tested. These are shown in Figure 5.12. The average piston amplitudes for each of the three heater temperatures are then shown in Figure 5.13.

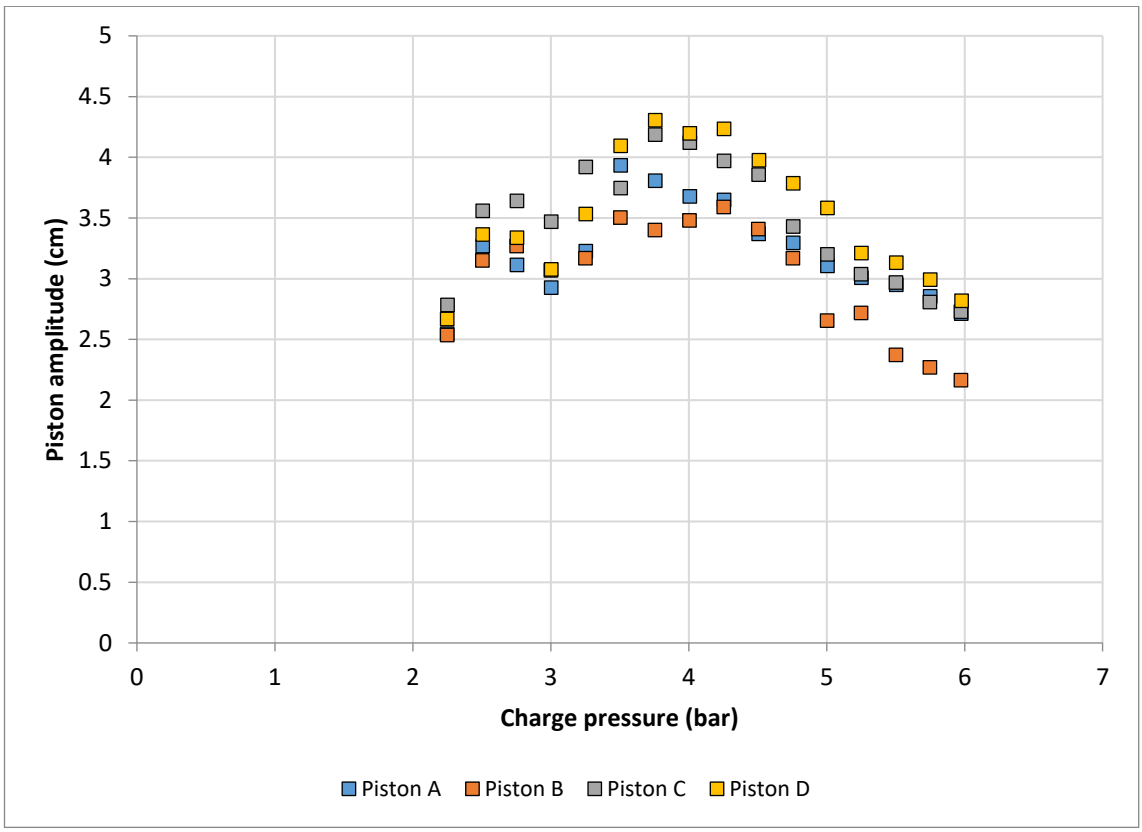

Figure 5.12 – Piston amplitude variation with charge pressure for the 105°C, 4HEAT configuration experiments using 100 ml liquid pistons.

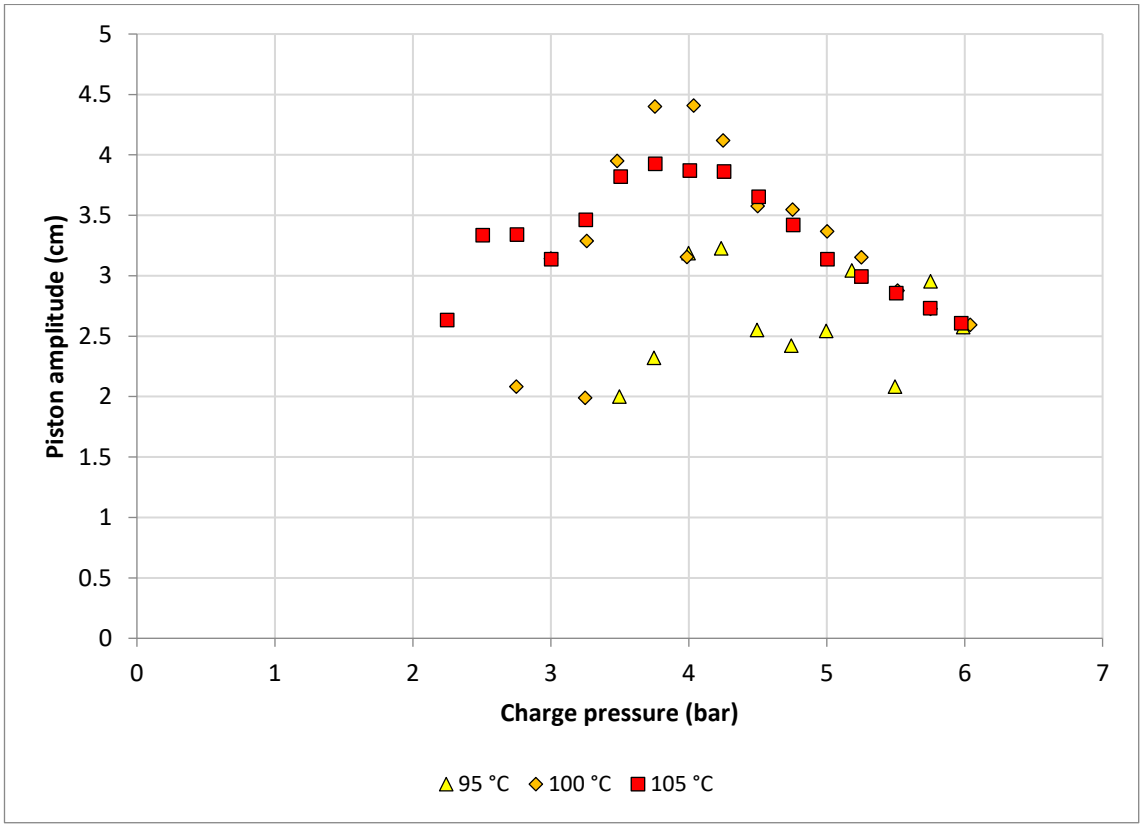

Figure 5.13 – Average piston amplitude variation with mean operating pressure for all 4HEAT configuration experiments using 100 ml liquid pistons.

The piston amplitudes increase with mean pressure from 2 bar–4 bar, before reaching their maximum at approximately 4 bar, and begin to decline as the charge pressure is increased from 4 bar–6 bar. An interesting characteristic of the behaviour of the system was that the ease with which the system started loosely followed the distribution of piston amplitude. At charge pressures close to 4 bar, the system was easy to start, requiring minimal manual excitation before the piston motion would self-amplify. The system became more and more difficult to start as the charge pressure moved away from 4 bar, requiring more vigorous manual excitation before reaching self-sustaining motion.

The average piston amplitudes in Figure 5.13 show that the other heater temperatures behave similarly, with the exception of the lowest temperature of 95ºC. The 100ºC results are very similar to the 105ºC results except for the experiments below 3 bar. The 100ºC experiments were not able to achieve stable operation below this point. A clear peak is seen at approximately 4 bar. It is worth noting that the same modal behaviour identified in the pressure amplitude plot of Figure 5.11 is evident in these results as well. Excluding some of the lower energy 95ºC results, the amplitudes for the different heater temperatures appear to converge along some form of an upper limit for charge pressures of 4.5 bar and higher. The shape of this limit resembles an inverse proportionality, where the product of pressure and piston amplitude is equal to some constant. This is investigated further and discussed in section 5.1.5.

The final graphs presented for the 4HEAT configuration in this general results section concern the pressure and piston displacement phase angles. Figure 5.14 shows how the phase angles of the pressure amplitude phasors vary with charge pressure. For clarity, the only experiments plotted are those at 105ºC heater temperature.

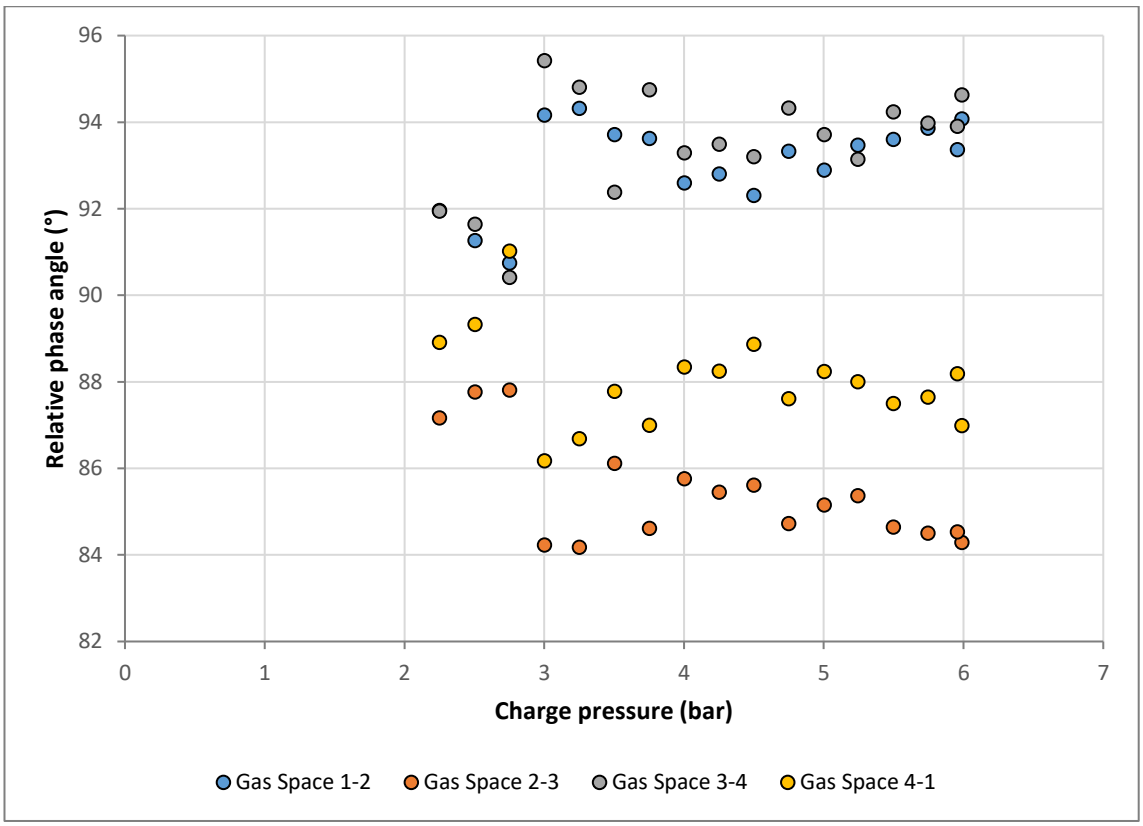

Figure 5.14 – Pressure phasor relative phase angles' variation with gas charge pressure for the 105ºC 4HEAT experiments with 100 ml liquid pistons.

The most striking feature of Figure 5.14 is the clear distinction between experiments below 3 bar charge pressure and experiments with 3 bar (and higher) charge pressure. The modal behaviour suspected earlier in the 105ºC experiments is confirmed by the differences in these phasor plots. The reasons why the different operational modes would have different phase angle relationships is not as obvious, however, and is discussed in later sections. Beyond 3 bar, the relative phase angles between the gas pressure amplitude phasors appears relatively consistent. Figure 5.15 shows the relative phase angles of the pistons across the charge pressure range. The phase angles oscillate around the expected value of 90°, but diverge further away from this value as charge pressure is increased, particularly in the range 5 bar–6 bar. Interestingly, this is also the range at which jump-starting the system becomes increasingly difficult, and the pistons' behaviour appears more unstable.

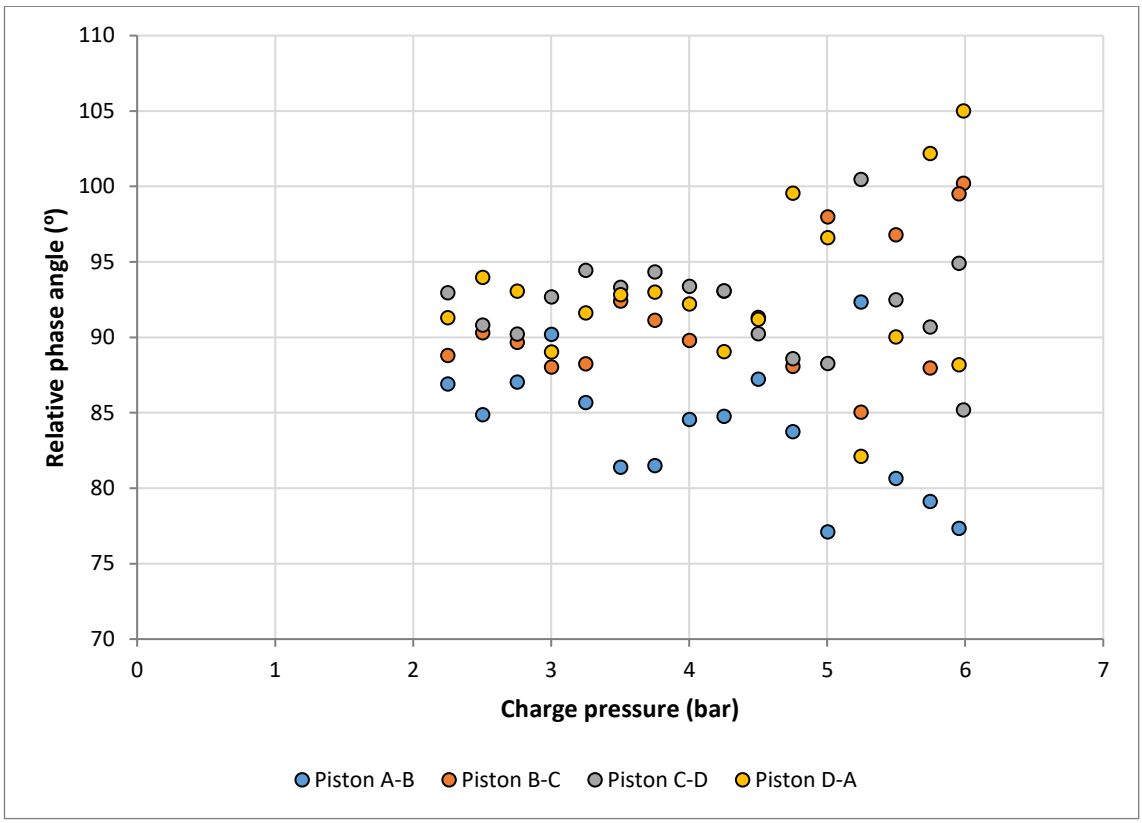

Figure 5.15 – Relative phase angles' variation with gas charge pressure for the piston displacement phasors in the 105°C 4HEAT experiments conducted with 100 ml liquid pistons.

5.1.1.2 115 ml Piston Results

The general trends and results for the 115 ml pistons were similar to that of the 100 ml pistons in the majority of cases, and thus they are not presented to the same extent in this section. Only instances where the results were significantly dissimilar or interesting are discussed. Figure 5.16 shows the pressure amplitude variation with charge pressure for the 105ºC experiments. As expected for the 4HEAT configuration, the pressure amplitudes are again roughly equivalent for each individual experiment. Also, just as in the case of the 100 ml pistons, there appears to be more than one stable mode of operation—with two upward trends in the data between 2 bar–4.5 bar that converge into a single slightly downward trend as charge pressure is increased above 4.5 bar. Figure 5.17 then shows the temperature differentials of each gas space for the same charge pressure range.

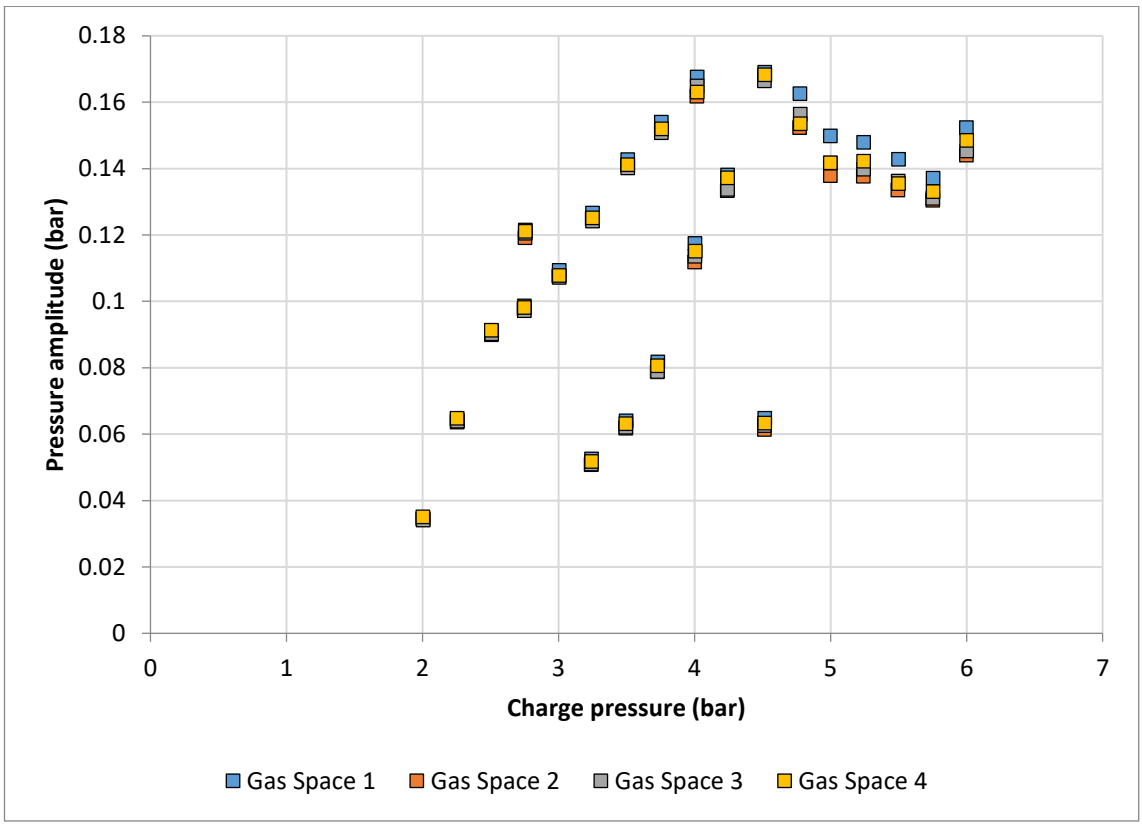

Figure 5.16 – Pressure amplitude variation with charge pressure for the 105°C 4HEAT experiments using 115 ml liquid pistons.

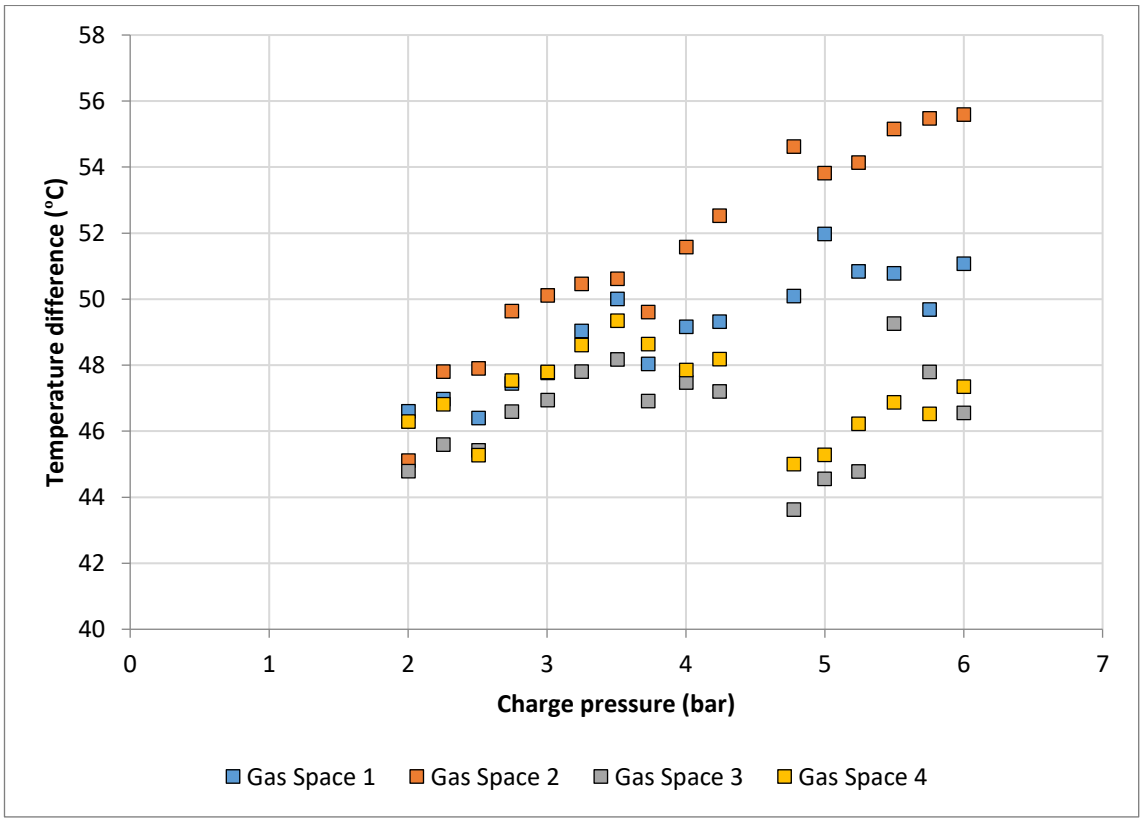

Figure 5.17 – Temperature differentials between the expansion and compression spaces for each gas space and their variation with charge pressure for the 105°C 4HEAT experiments with 115 ml liquid pistons.

The data points plotted in Figure 5.17 only include values from the highest energy operating states (i.e. the highest pressure amplitudes for each charge pressure). Although in the majority of cases the highest temperature difference is established in GS2 (as was the case with the 100 ml pistons) the trends are not as well defined as those seen in Figure 5.11, and the disparity between the highest and lowest differences is larger—reaching almost 10ºC at the higher charge pressure experiments. The relative phase angles of the pressure amplitude phasors are graphed in Figure 5.18 for the same set of experiments.

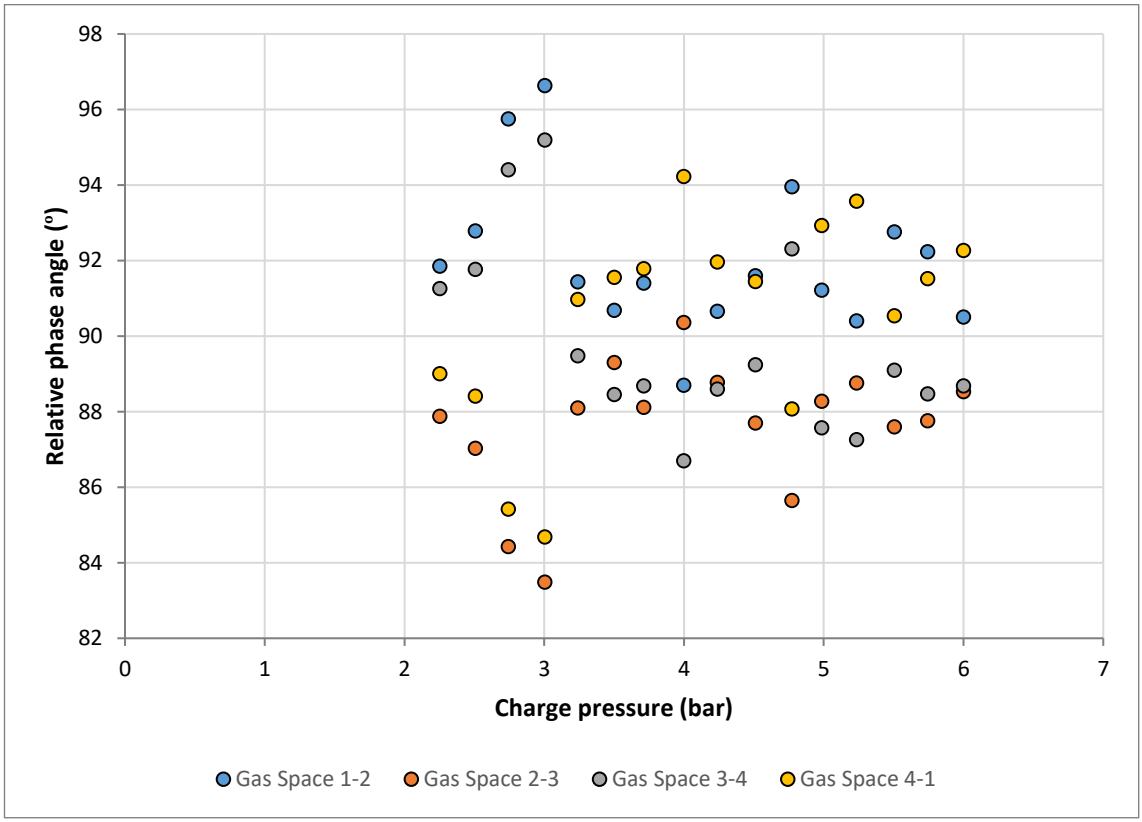

Figure 5.18 – Pressure phasor phase angles' variation with gas charge pressure for the 105ºC 4HEAT experiments with 115 ml liquid pistons.

Arguably the most interesting graph is the relative phase angle plot in Figure 5.18, which shows almost the complete opposite of that seen in Figure 5.14 for the 100 ml pistons. The phase angles diverge from 2 bar–3 bar before establishing different relationships closer to 90º for the charge pressure from 3 bar–6 bar. The cause of this 'flipping' between operating modes is discussed in Section 8.2.5.

5.1.1.3 4HEAT summary

The important findings and observations from the 4HEAT section are summarised and outlined here for clarity: (a) The phasor analysis shows that the symmetrical behaviour expected is evident which is verified by the pressure amplitude magnitude and phase angle similarities; (b) The experimental frequency trend has a dependence on the square root of pressure as predicted by the analytical solution obtained for the natural frequency of the LPSC system; (c) Increased heater temperature generally leads to higher pressure amplitudes, but the results imply that a number of stable modes of operation are present and can be occupied by different heater temperatures. Some of the phase angle data analysis shows a clear distinction between these modes; (d) The pressure amplitudes tend to increase with charge pressure until reaching an as yet unexplained threshold where experiments with different heater temperatures converge.

5.1.2 3HEAT Configuration

The 3HEAT configuration is one of the two configurations which has the potential to produce a cooling effect. With three subsystems producing work and one subsystem consuming work, the 3HEAT configuration has the desirable characteristic of containing only one absorption space—but it is not known how the dynamics of the three adjacent power-producing subsystems will impact the dynamics of the machine. The results presented here aim to illustrate the behaviour of the 3HEAT configuration, and how its performance is influenced by changes in the key design parameters in Table 5.2. As in the 4HEAT case, example results of a representative 3HEAT experiment are presented first. Figures 5.19 and 5.20 show the pressure amplitudes and heater temperature trends for a typical 3HEAT experiment.

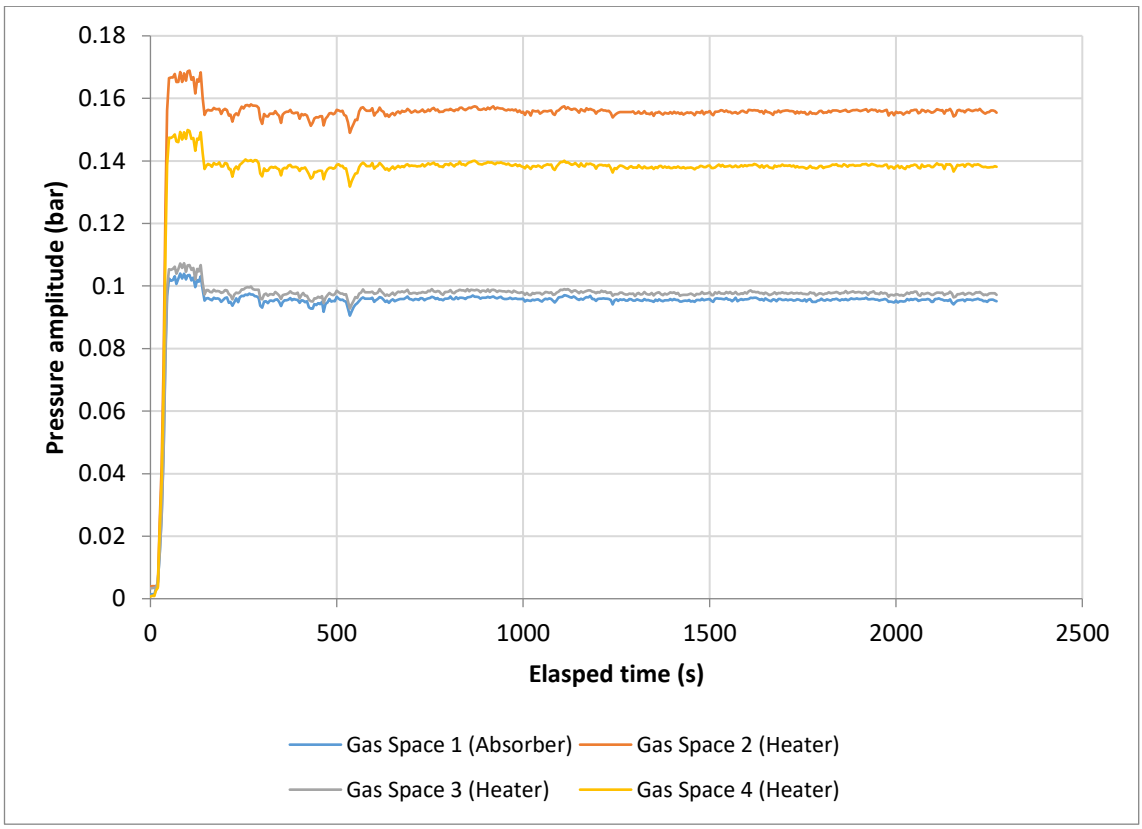

Figure 5.19 – Gas pressure amplitude variations during a typical 3HEAT experiment. The experiment was at 4 bar with 150°C set heater temperature and 100 ml liquid pistons.

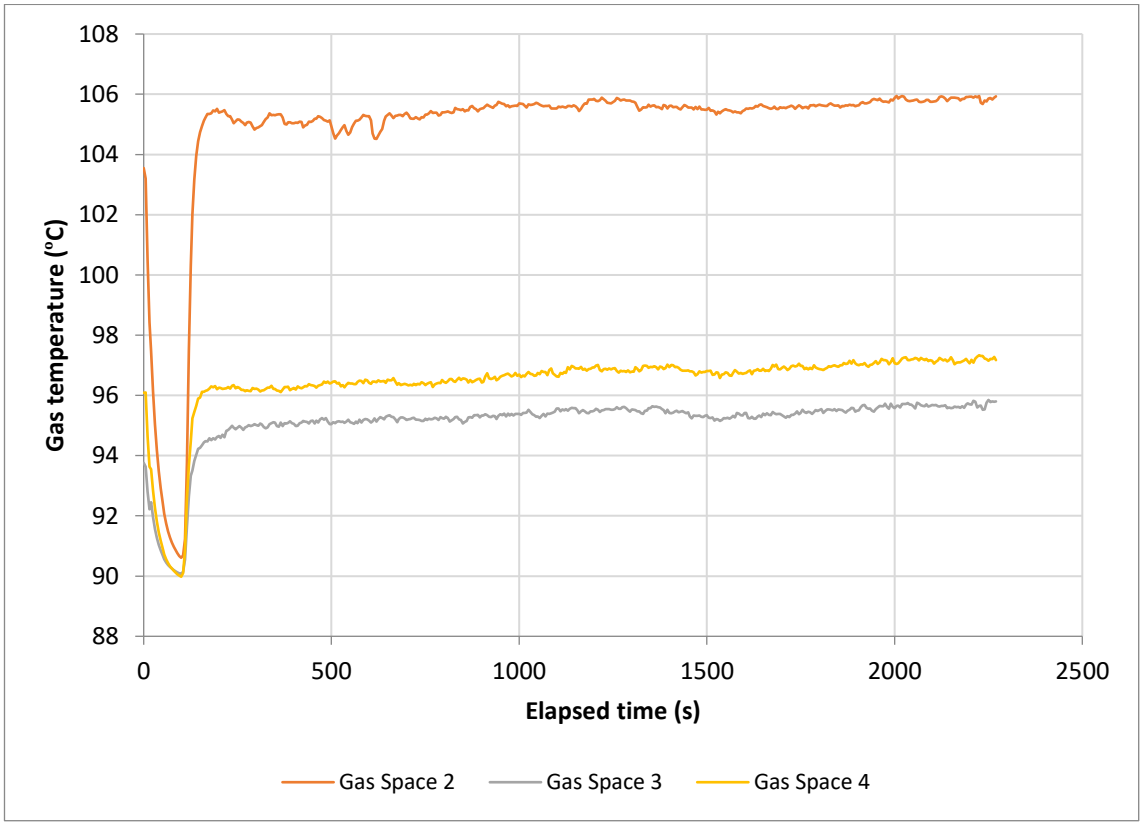

Figure 5.20 – Heater gas temperature variations during a typical 4HEAT experiment. The experiment was at 4 bar with 150°C set heater temperature and 100 ml liquid pistons.

The experiment considered in this example case used heaters set at 150ºC, 100 ml liquid pistons and a gas charge pressure of 4 bar. Unlike the 4HEAT configuration, the pressure amplitudes in Figure 5.20 vary significantly in magnitude. The pressure amplitudes developed in GS1 and GS3 are close to equal at approximately 0.1 bar. These two spaces are opposite each other in the series of four subsystems, with GS1 containing the absorber and GS3 a heater. With substantially higher pressure amplitudes of 0.155 and 0.140 bar, respectively, GS2 and GS4 contain the second and third heater, and are also opposite each other. These ratios in magnitude between the developed pressure amplitudes in each of the four gas spaces was something that occurred consistently during the majority of 3HEAT experiments and is later quantified. To some extent, the heater gas temperatures shown in Figure 5.20 reflect the differences in pressure amplitudes; the highest temperatures align with the highest pressure amplitudes, although the differences between GS2 and GS4 are much more pronounced in the temperature case. GS3 registers the lowest heater gas temperature of approximately 95°C, compared with GS2 (the highest), with approximately 105°C. These temperatures are higher than in the 4HEAT experiments, primarily because of the higher heater temperatures needed to account for the unpowered fourth subsystem, GS1.

Figures 5.21 and 5.22 show the pressure and displacement profiles during a one second snapshot taken during the experiment. The snapshot was taken at time, t = 1210 seconds (20 minutes and 10 seconds into the experiment). The pressure profiles graph shows a number of interesting characteristics. Firstly, all four pressure profiles appear to be roughly 90° out of phase with each other. The two lowest pressure amplitude profiles seen in spaces GS1 and GS3 appear very similar in maximum and minimum values, and are 180° out of phase; while the two larger pressure amplitudes, GS2 and GS4, are slightly different in terms of magnitude.

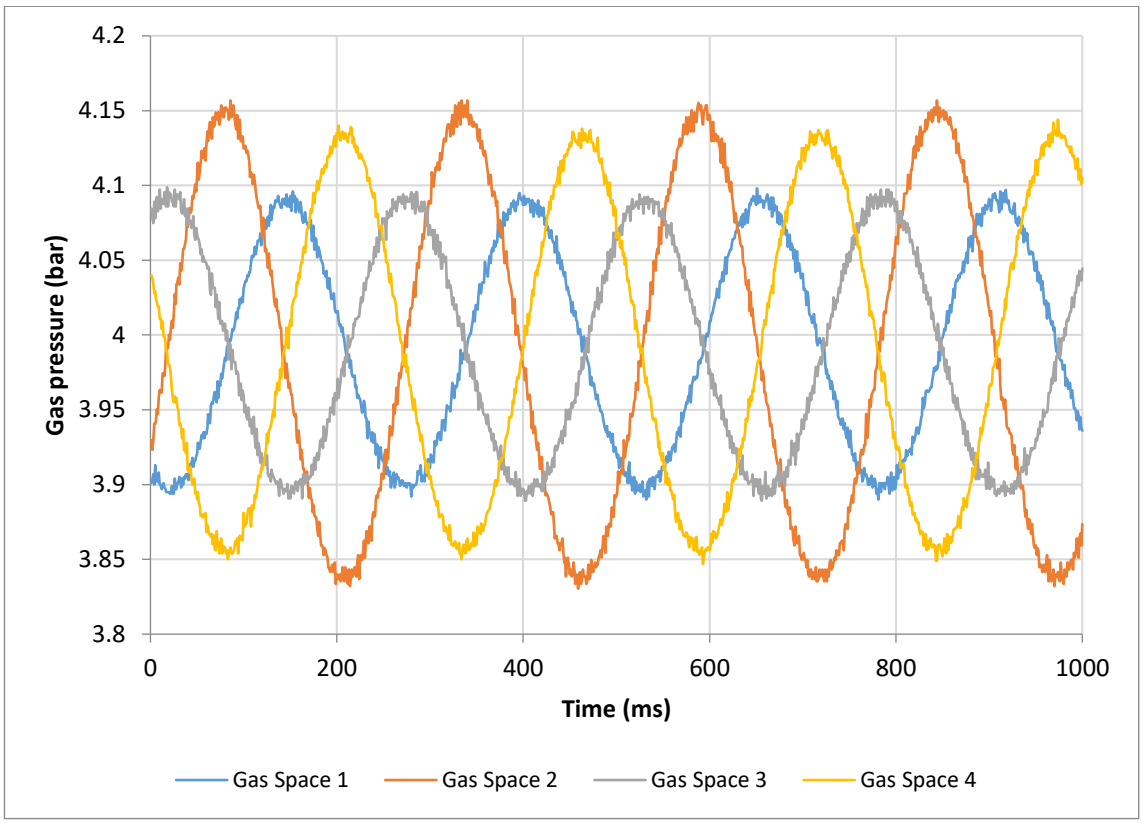

Figure 5.21 – Gas pressure profiles over one second interval during a typical 3HEAT experiment. The experiment was at 4 bar and 150°C with 100 ml liquid pistons. Time taken was at 1210 seconds (20 minutes 10 seconds) into the experiment.

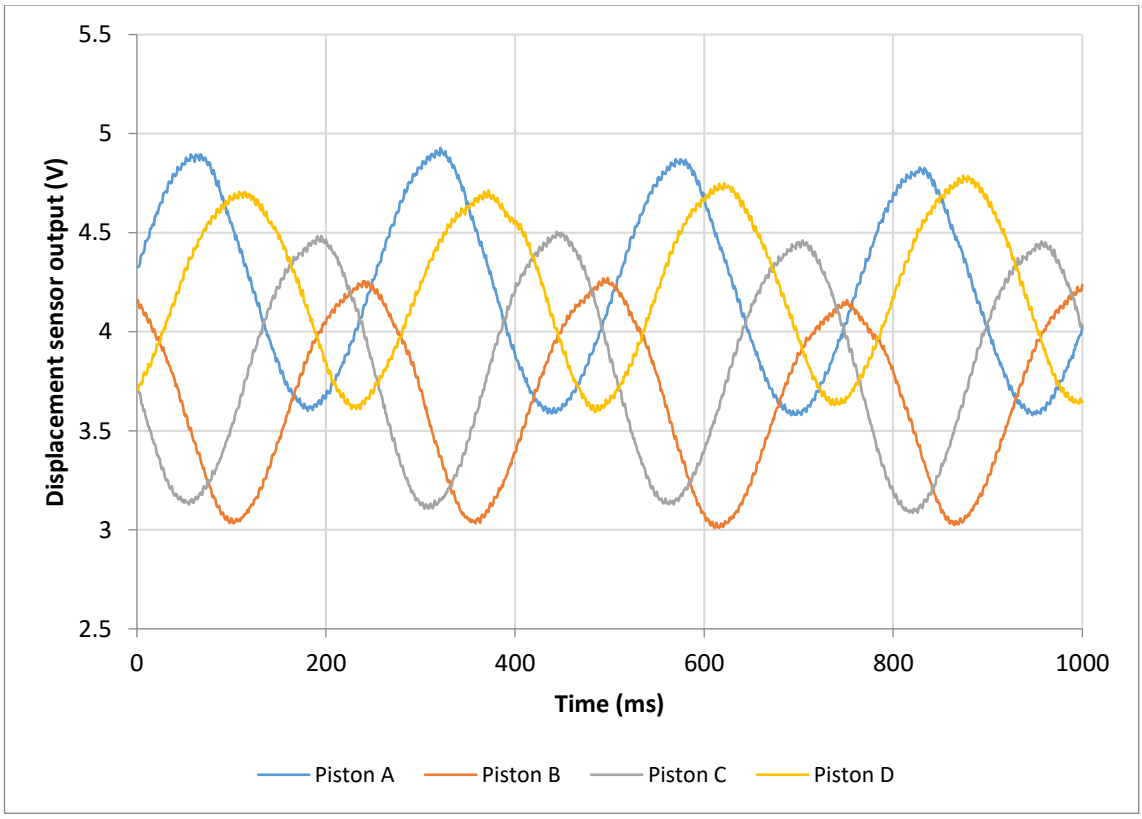

Figure 5.22 – Piston displacement profiles over one second interval during a typical 3HEAT experiment. The experiment was at 4 bar and 150°C with 100 ml liquid pistons. Time taken was at 1210 seconds (20 minutes 10 seconds) into the experiment.

As in the case of the 4HEAT experiments, the piston displacement profiles seen in Figure 5.22 appear less consistent from cycle to cycle—although they clearly have different phase angle relationships when compared with the pressure profiles. Despite pistons opposite to each other appearing to have 180° phase differences, the phase angles between adjacent pistons is not uniformly close to 90°. Applying the least mean squares approximation and calibration procedure described in Section 3.2.3, phasor expressions of the gas pressure and displacement profiles were obtained. Table 5.3 shows the values obtained for the example 3HEAT experiment. As previously carried out in the 4HEAT case, the unscaled and scaled phasor plots can then be constructed from the tabulated values (but for discussion purposes only the scaled phasor plots need to be shown). Figure 5.23 shows the scaled phasor plot for the example 3HEAT experiment.

Table 5.3 – Phasor representations of gas pressure and piston displacement amplitudes for example 3HEAT experiment.

Phasor	Amplitude (bar or cm)	Phase angle (°)
Pressure 1 (P1)	0.096	0
Pressure 2 (P2)	0.156	93.7
Pressure 3 (P3)	0.098	177.1
Pressure 4 (P4)	0.139	273.1
Displacement A (XA)	4.08	124.0
Displacement B (XB)	3.82	236.3
Displacement C (XC)	4.38	306.2
Displacement D (XD)	3.44	55.2

It is clear from Figure 5.23 that the behaviour of the 3HEAT system deviates from the symmetrical 45° phasor separations seen in the 4HEAT configuration. The two large pressure phasors P2 and P4 ‘stretch’ the system out vertically, which causes the piston phasors to gravitate towards the larger magnitude pressure amplitudes. In the case of Piston A (phasor XA), for example, the displacement of this piston is influenced by the pressures P1 and P2. P2 has the greater amplitude which forces the motion of the piston to be more similar in phase with this pressure than the lower amplitude pressure, P1. This explains why each piston displacement phasor is closer in phase to the adjacent gas space

with the highest pressure amplitude. Even with this effect, every pair of opposite phasors remains approximately 180° out of phase with each other, which is evidence of how the symmetry of the system is imposed on the dynamic response.

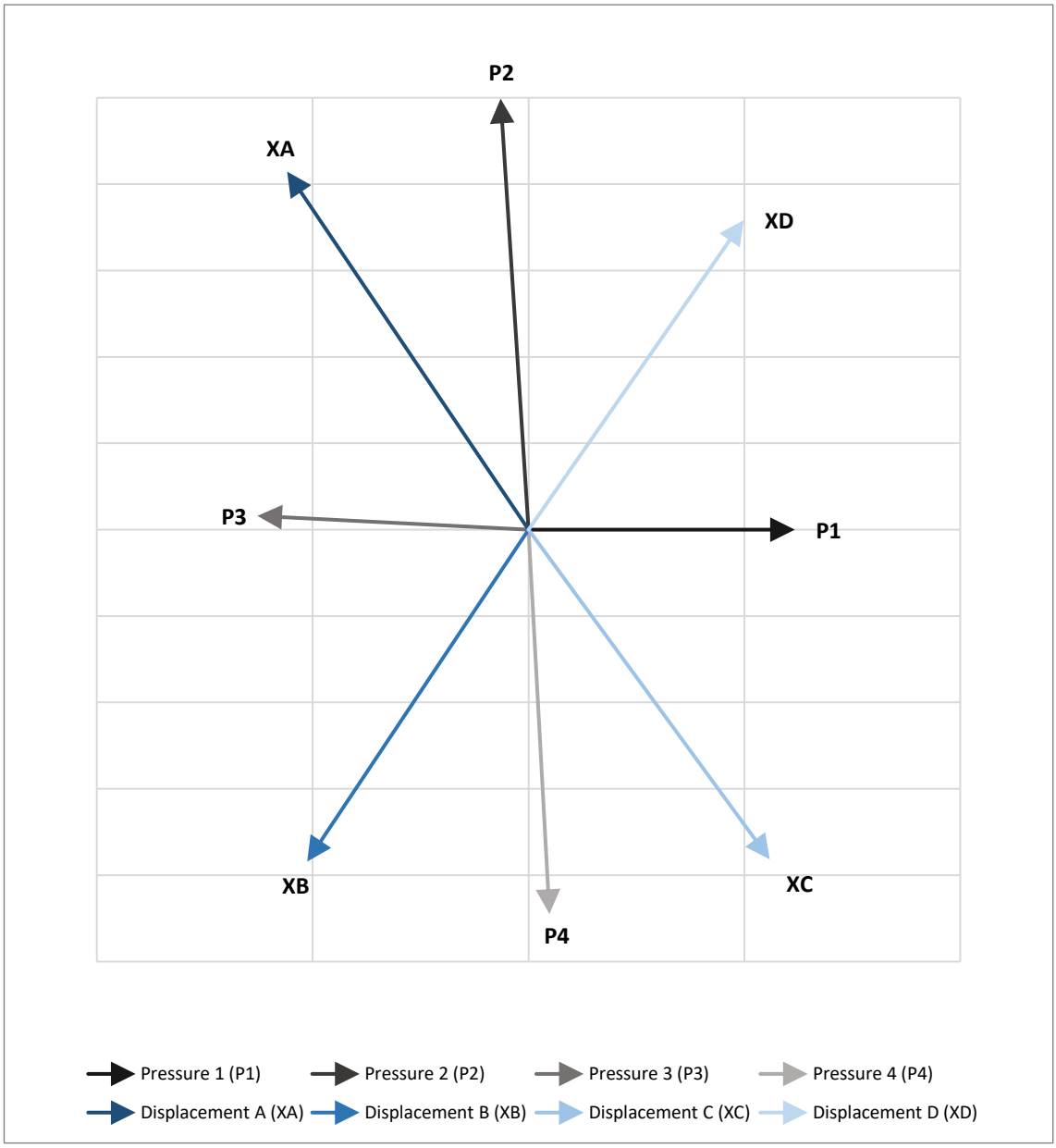

Figure 5.23 – Phasor plot of the pressure and displacement profiles for the example 3HEAT experiment. The phasor magnitudes have been scaled for more clarity. The experiment was at 4 bar and 150°C with 100 ml liquid pistons.

Figure 5.24 presents the phase angle values relating to the pressure and displacement phasors in Figure 5.23.

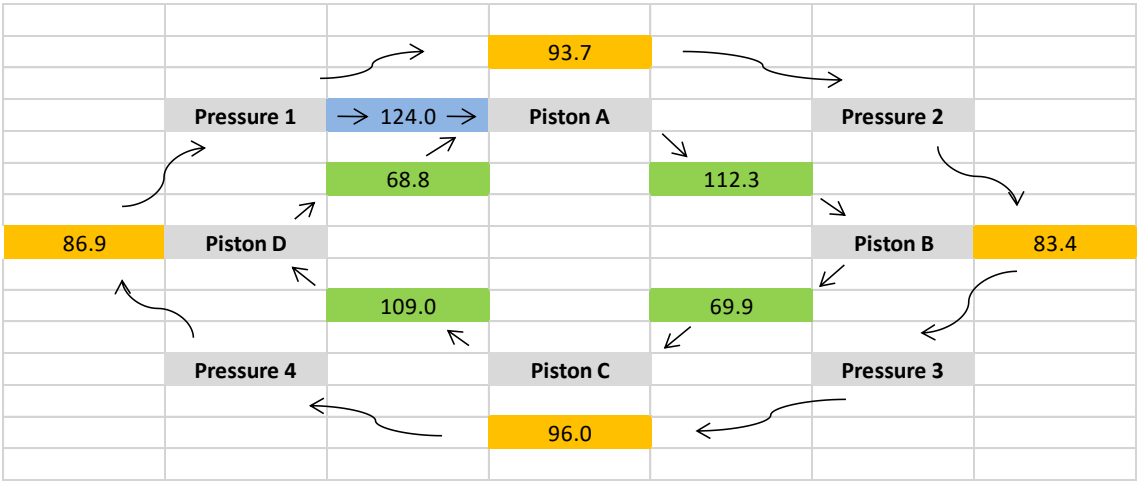

Figure 5.24 – Pressure and displacement phase angles for 3HEAT example experiment.

The relative phase angles between the pressure phasors is close to 90° as was seen in the case of the 4HEAT system. The most significant difference is seen in the relative phase angle differences between the piston displacements. The differences between neighbouring pistons alternate from approximately 110° to 70°.

5.1.2.1 100 ml Piston Results

The results presented here cover the experiments conducted with 100 ml piston volumes, using the 3HEAT configuration at three heater temperatures of 130°C, 140°C and 150°C, and across the charge pressure range of 2 bar–6 bar. A number of figures are shown to highlight how some of the key variables depend on charge pressure and heater temperature—namely pressure amplitudes, piston displacements, phase angles and gas space temperature differentials. The figures are accompanied by brief assessments and general observations about the behaviour of the 3HEAT configuration.

Figure 5.25 shows how the operational frequency of the system changes with increased charge pressure. The frequency trends of the 3HEAT experiments resemble that of the 4HEAT experiments. The frequency increases with charge pressure and, as predicted, shows a square root dependence. The experimental dependence on temperature is assessed for all 3 configurations in Section 5.1.4.

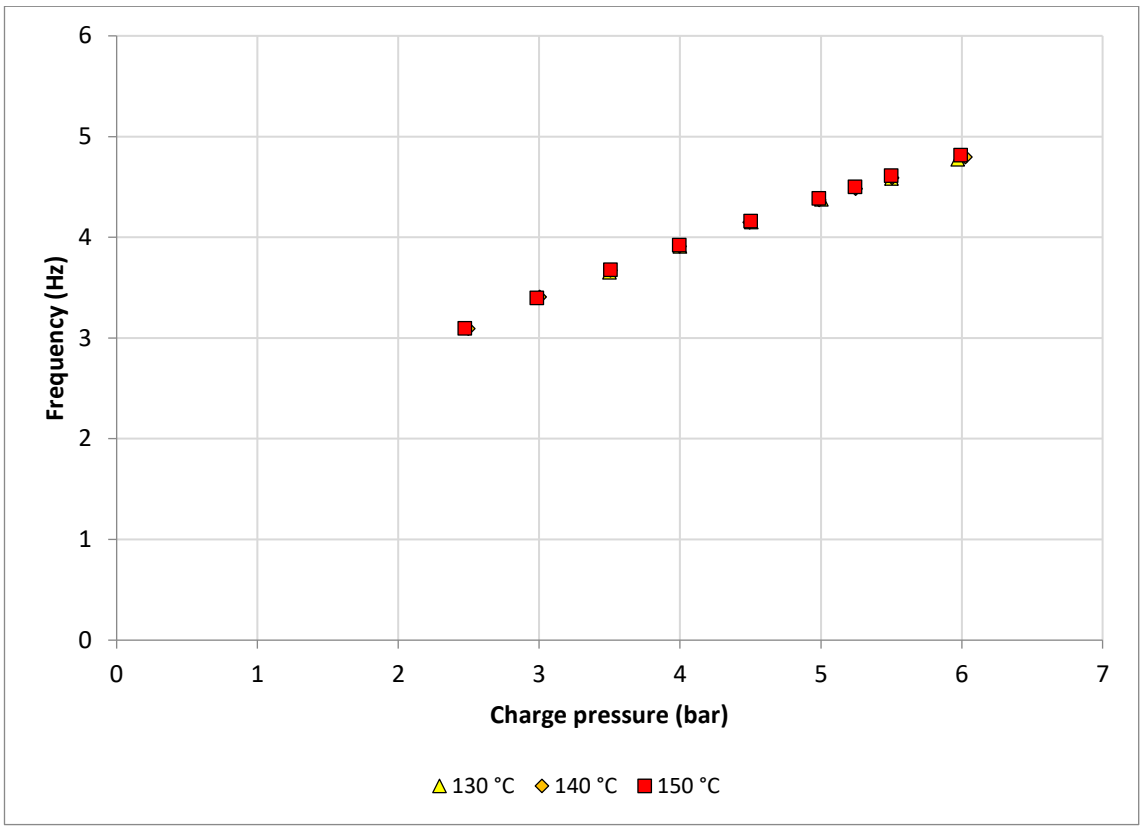

Figure 5.25 – Frequency variation with mean operating pressure for all 3HEAT configuration experiments using 100 ml liquid pistons.

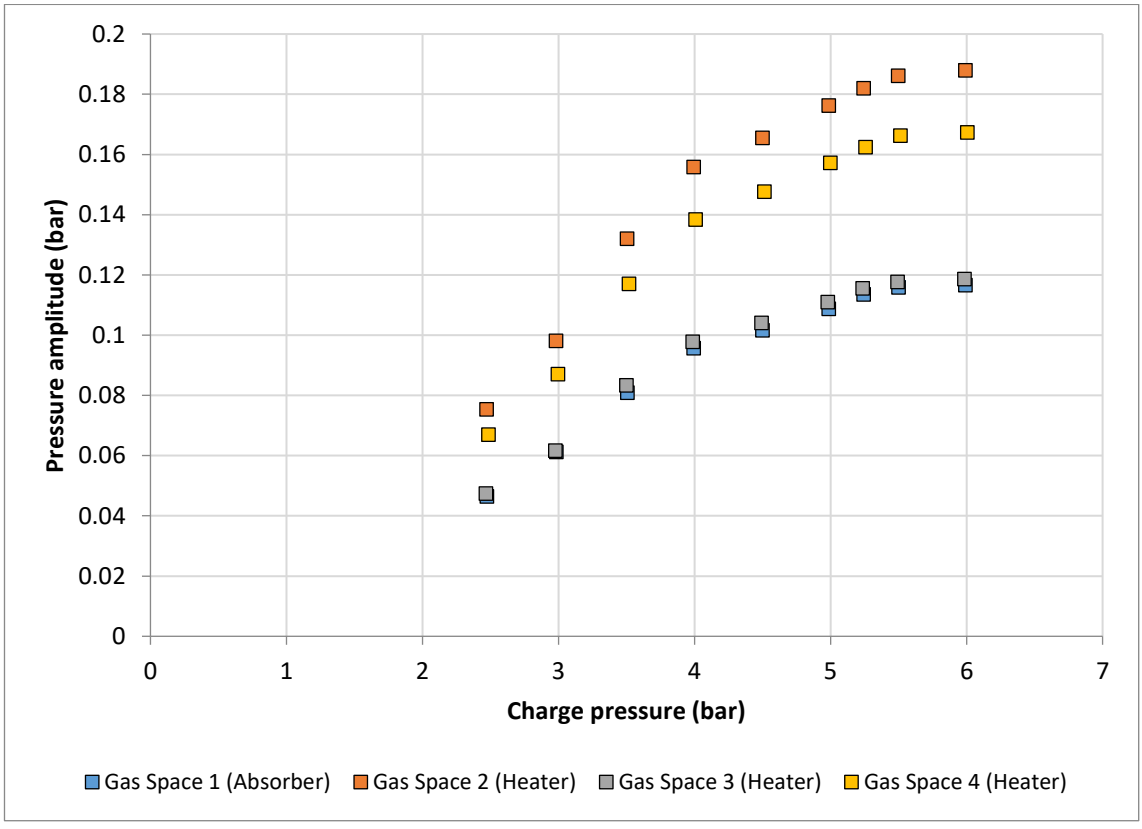

Figure 5.26 – Pressure amplitude variations of all gas spaces with increasing charge pressure for 3HEAT experiments conducted with 150°C heater temperatures and 100 ml pistons.

Figure 5.26 shows the pressure amplitudes developed for 3HEAT experiments conducted at 150°C heater temperatures. The pressure amplitude seen in each of the gas spaces retain their characteristic differences in magnitude first identified in the example 3HEAT experiment, with GS2 and GS3 achieving the highest values, and GS1 and GS3 the lowest. The pressure amplitude ratios of the three heater spaces to the absorber space remain close to constant across the charge pressure range. The mean ratios (and associated standard deviations) are 1.62 (s = 0.7%), 1.02 (s = 0.6%) and 1.44 (s = 0.7%) for GS2, GS3 and GS4, respectively. With standard deviations less than 1%, it can be inferred that the pressure amplitude ratios are an important behavioural trait, which can be used to assess the performance of each configuration. As a method for evaluating the effectiveness of the 3HEAT configuration, the conversion of pressure amplitudes developed in the heated spaces to those in the absorber space can be assessed. Summing the relative pressure ratios gives a conversion ratio of 4.08:1 (three significant figures). This ratio is used as a measure of the potential suitability of a particular configuration, and is referred to in subsequent analysis as the conversion ratio.

As the charge pressure is increased, the pressure amplitudes increase and appear to peak at the upper end of the tested range of 6 bar. This is very similar to that which occurred for the 4HEAT experiments with 100 ml pistons, except the maximum amplitudes achieved are higher in magnitude in the 3HEAT case—the largest being 0.188 bar compared with 0.156 bar from the 4HEAT experiments. The average values for the 3HEAT experiments are similar to (but slightly lower than) the 4HEAT experiments at the same charge pressure, e.g. 0.148 bar compared with 0.152 bar at 6 bar. When comparing the 4HEAT and 3HEAT experiments in this manner, it should be noted that the different heater temperatures probably imply very different heat inputs; although this comparison is still of interest considering that the heater temperatures selected are close to the minimum necessary for stable operation. Figure 5.27 shows how the other heater

temperature experiments compared in respect to the pressure amplitudes. The graph shows the data for GS1, which contained the absorption space.

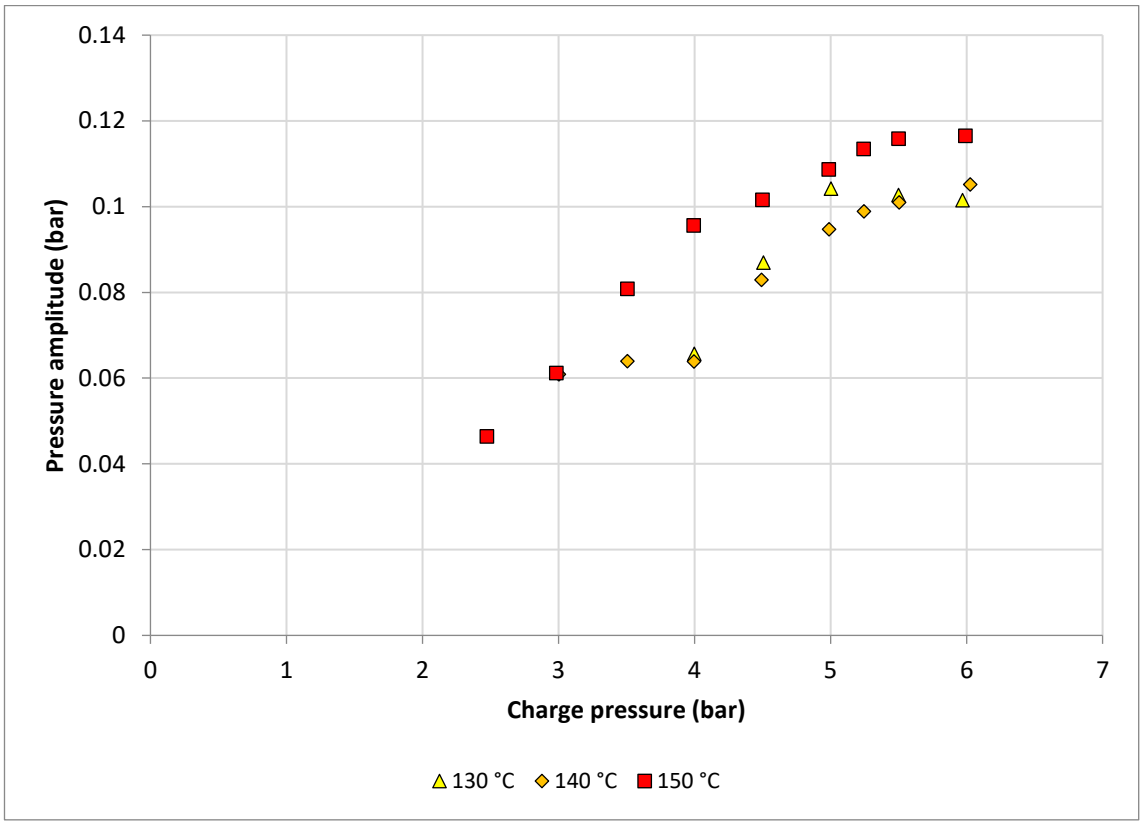

Figure 5.27 – Pressure amplitude variation of Gas Space 1 with changing charge pressure for all 3HEAT experiments using 100 ml liquid pistons.

Again evident is the possibility for different operational modes to exist; although fewer experiments exhibited bi-modal behaviour when compared with the 4HEAT case. Some of the experiments attempted at lower charge pressures and temperatures were unable to achieve steady operation. Hence, results for 130°C heaters below 4 bar and 140°C heaters below 3 bar are missing. With these pressure amplitudes being generated in the absorption space, an obvious question arises with regard to evidence of cooling. Figure 5.28 shows the temperature difference between the expansion (absorption) and compression (rejection) spaces in GS1. For the values displayed, positive values can be interpreted as the expansion space having a higher temperature than the compression space, implying that a cooling effect has not been developed. Negative values show that the absorption space has a lower temperature than the water-cooled compression space.

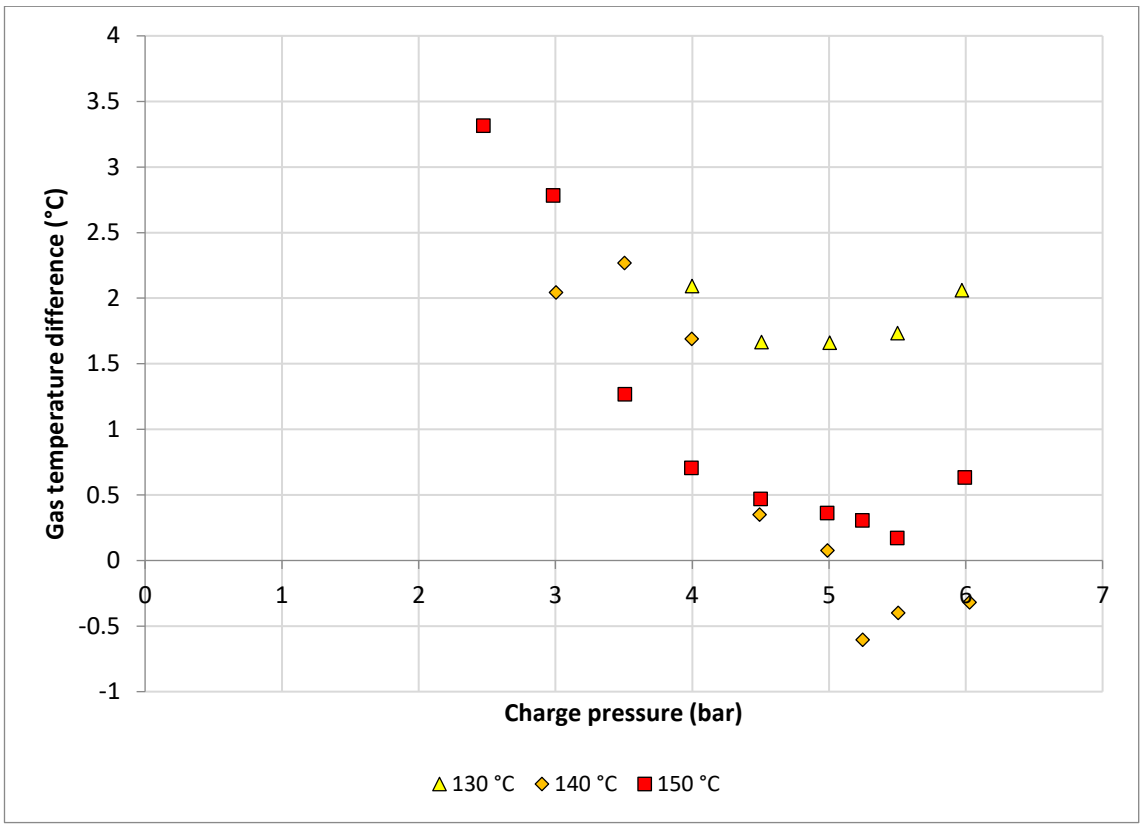

Figure 5.28 – Temperature difference between expansion and compression spaces in Gas Space 1 for the 3HEAT configuration experiments using 100 ml liquid pistons.

Although a significant cooling effect does not develop, at this stage of the research the focus is on identifying important trends and dependencies that will help in system improvements. The graph indicates that the performance of the 3HEAT system is dependent on charge pressure, with each of the three heater temperatures showing minimum turning points occurring in the region of 5 bar charge pressure. Curiously, the largest cooling effect measured occurs in an experiment with 140°C heater temperature. Considering the relatively small heater temperature differences between sets of experiments (10°C), this does not necessarily imply that better performance is possible with lower heater temperatures—since differences in cooling water or ambient temperature could have an influence. Figure 5.29 shows the gas space temperature differentials measured in the other three gas spaces, each containing a heater in the expansion space. As in the case of the example 3HEAT experiment, the largest temperature differences correspond to the gas spaces with the largest pressure amplitudes.

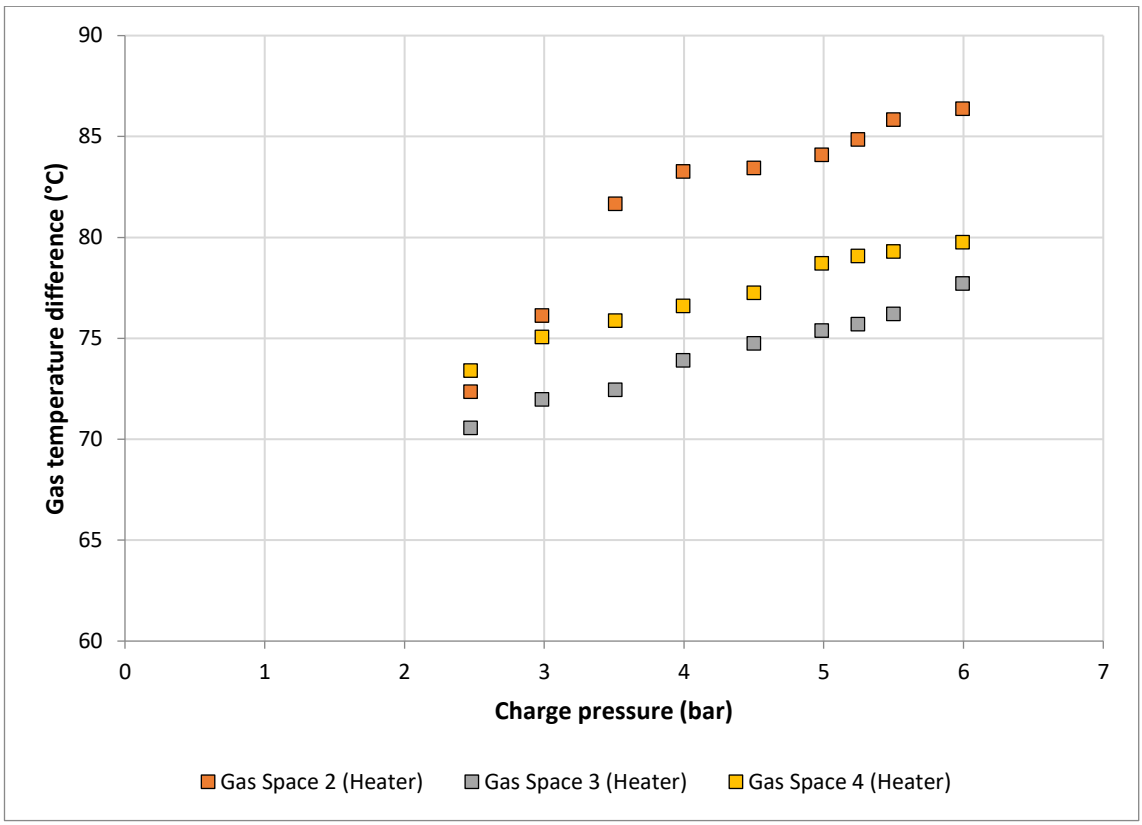

Figure 5.29 – Heater gas space temperature differentials and their variation with charge pressure for the 3HEAT experiments with 150°C heater temperatures and 100 ml liquid pistons.

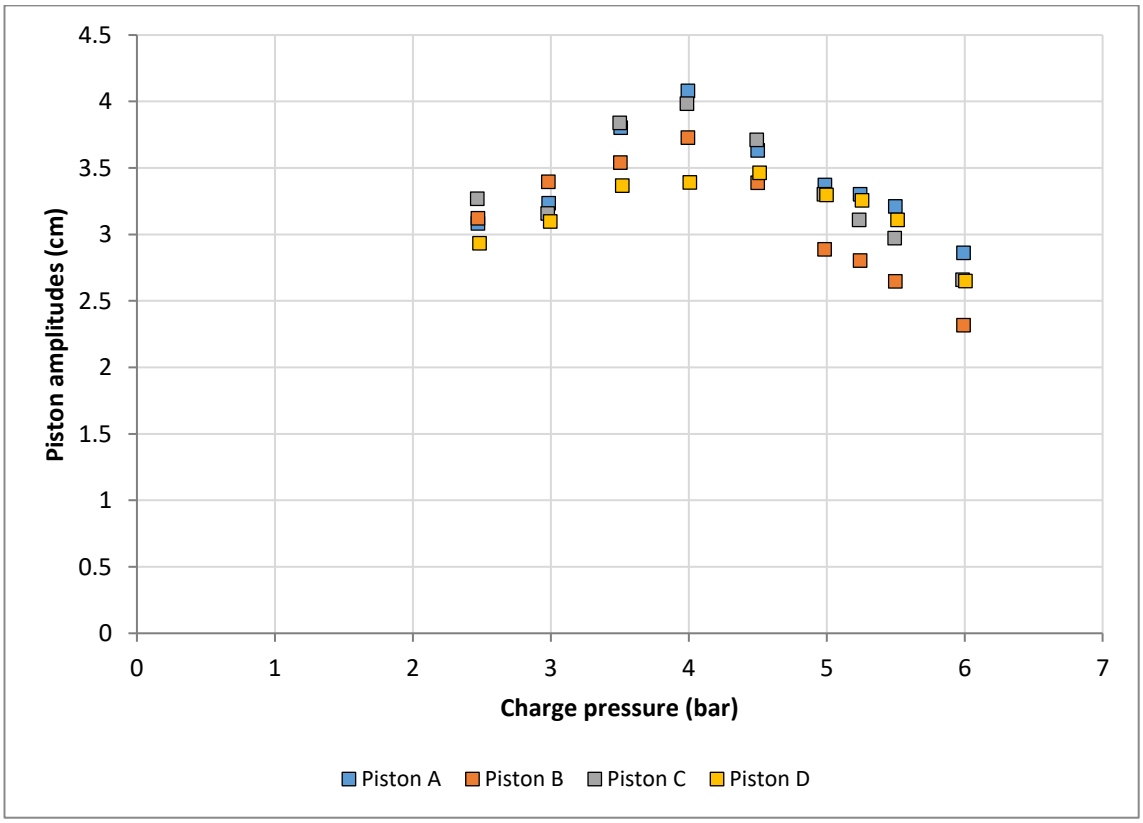

Figure 5.30 – Piston amplitude variation with charge pressure for the 150°C, 3HEAT configuration experiments using 100 ml liquid pistons.

Figure 5.30 shows the piston amplitudes for the 3HEAT experiments at 150°C heater temperature. A peak occurs at 4 bar, with amplitudes decreasing in the direction of both higher and lower charge pressure from this point. Reviewing the 4HEAT piston amplitude plots from earlier, the maximum piston amplitudes occur at roughly the same charge pressure as these tests. There does not appear to be very much difference between the amplitudes of each piston. The largest difference occurs between Piston A and Piston D and equates to 6.9 mm at 4 bar charge pressure. Apart from an increase in amplitude of Piston D relative to the other pistons at higher charge pressure, not much more can be inferred from this graph. The average piston amplitudes for each of the three heater temperatures are shown in Figure 5.31. The multi-modal characteristics are seen again, with lower energy states occurring for experiments below 5 bar, and the results for the three temperatures converging upon an apparent excitation limit above this point.

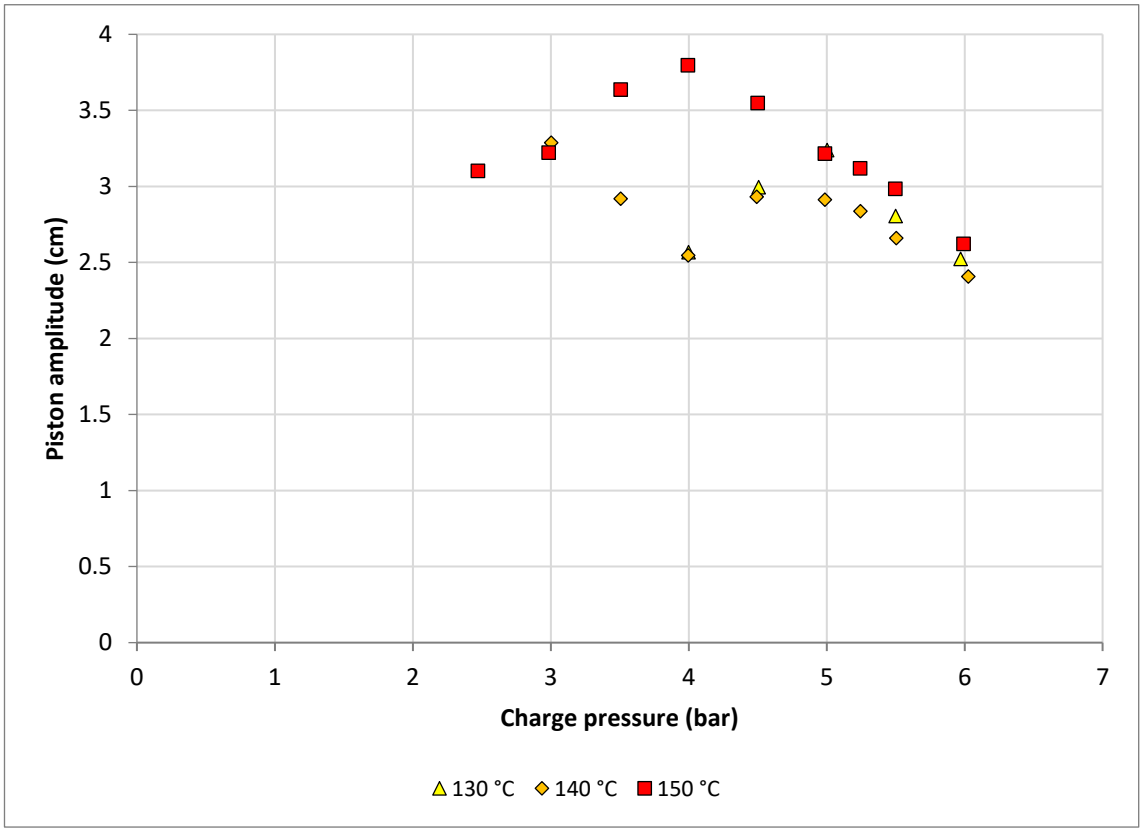

Figure 5.31 – Average piston amplitude variation with charge pressure for all of the 3HEAT experiments conducted using 100 ml liquid pistons.

The final graphs presented for the 3HEAT configuration in this general results section again concern the phase angles on the system. Figure 5.32 shows how the phase angles of the pressure amplitude phasors vary with charge pressure. Again, the only experiments plotted are those at the highest heater temperature of 150ºC. The results appear relatively consistent and within a similar range to the relative phase angles seen in the 4HEAT experiments above 3 bar. A clear separation of each relative phase angle occurs with the pairs of GS1–GS2 and GS4–GS1 having phase angles closer to 90°, while the other two pairs are ± 7° from 90°.

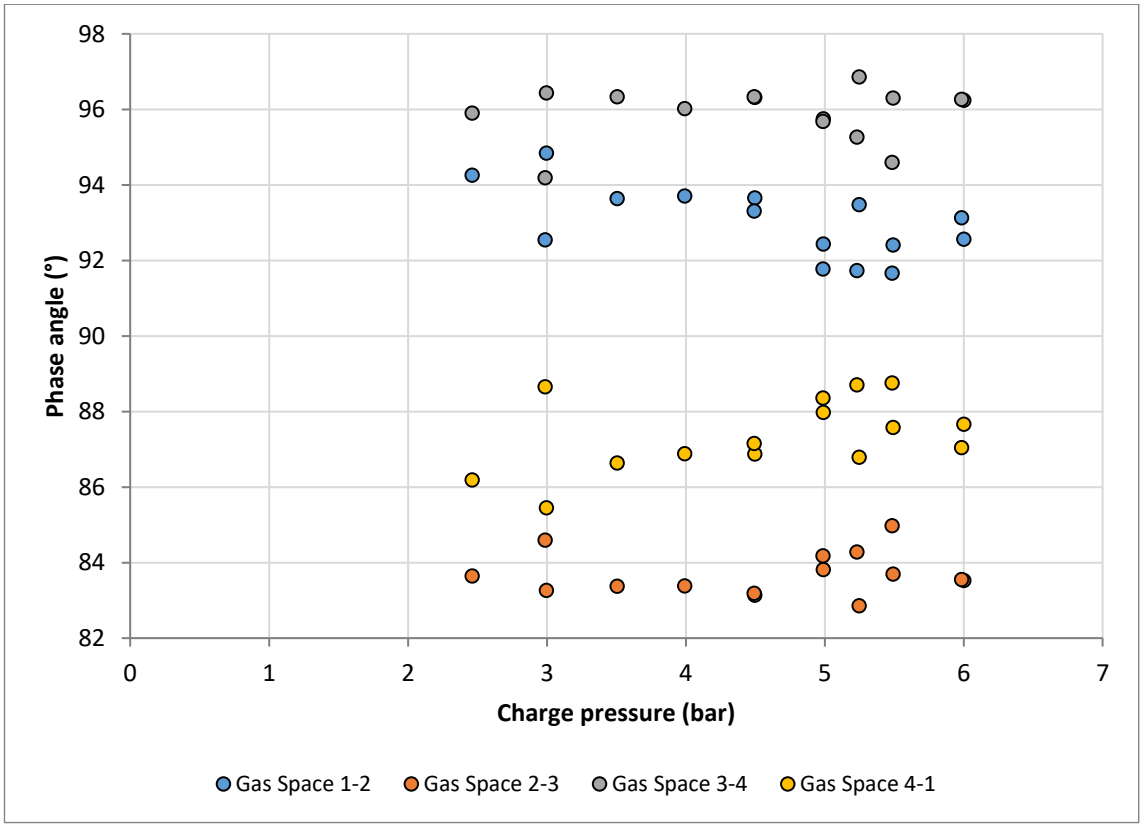

Figure 5.32 – Relative phase angle variations with gas charge pressure for the pressure phasors in the 150ºC 3HEAT experiments using 100 ml liquid pistons.

Figure 5.33 shows the relative phase angles for the piston displacements. As identified in the example 3HEAT experiment, the piston phase angles are significantly different when comparing 3HEAT to the 4HEAT operation. These differences remain across the charge pressure range tested—although towards the higher end of 5 bar–6 bar, the phase angles

appear to flare inward in contrast to the 4HEAT phase angles which flared outward. The 3HEAT system becomes more difficult to jump-start in this range as well.

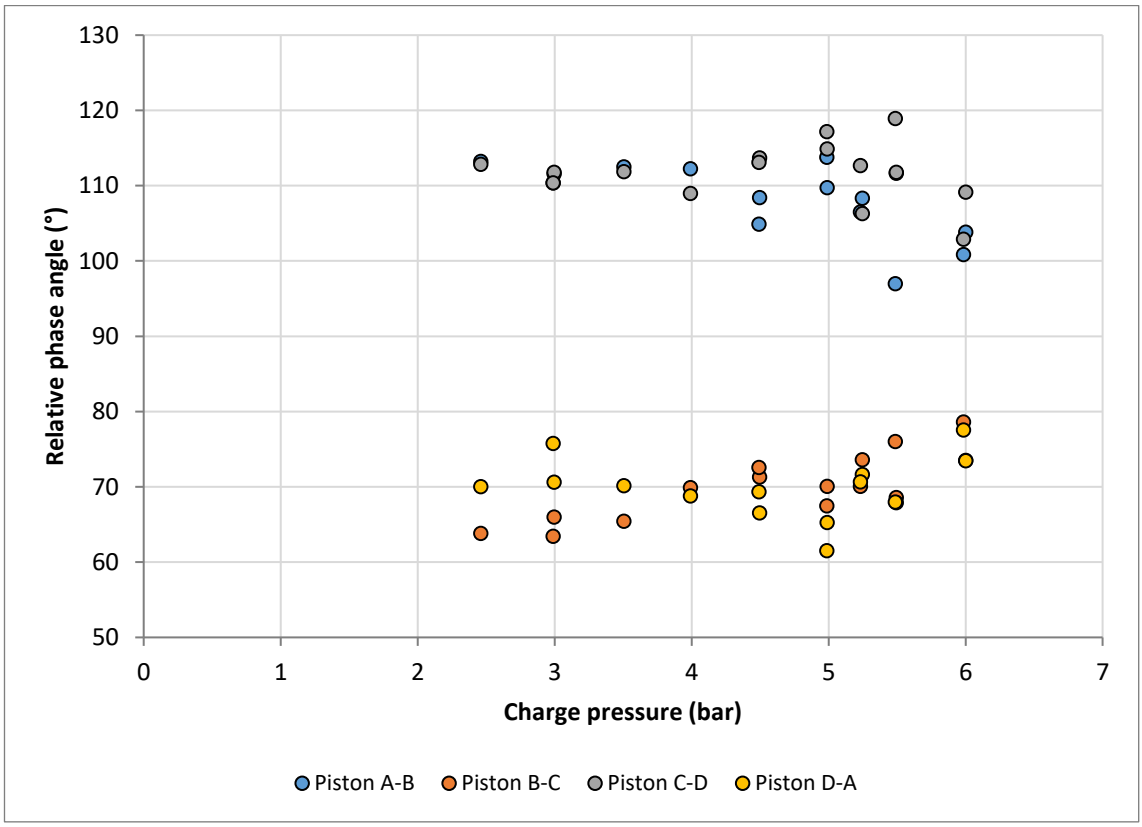

Figure 5.33 – Relative phase angle variations with gas charge pressure for the piston displacement phasors in the 150°C 3HEAT experiments using 100 ml liquid pistons.

5.1.2.2 115 ml Piston Results

As per the 4HEAT results, the 115 ml 3HEAT results are not presented with as much detail as the 100 ml piston results because of the significant similarities. Instead, instances where the results were significantly dissimilar or interesting are presented.

Figure 5.34 shows the pressure amplitude variation with charge pressure for Gas Space 1 (absorber) and all heater temperatures. The 115 ml experiments exhibited the same consistent pressure amplitude ratios seen with the 100 ml pistons, where GS2 and GS4 achieved higher values than GS1 and GS3. The range of successful experiments is larger in the 115 ml case, with stable operation starting at 2 bar for 150°C and 2.5 bar for 140°C heater temperatures. The pressure amplitudes reflect similar behaviour to that seen in both

3HEAT and 4HEAT experiments up to this point. The heater temperatures have more influence at lower pressure, with the behaviour of the system essentially identical for all three heater values above 5 bar charge pressure. The pressure amplitudes developed in the 115 ml experiments were slightly higher than their 100 ml counterparts.

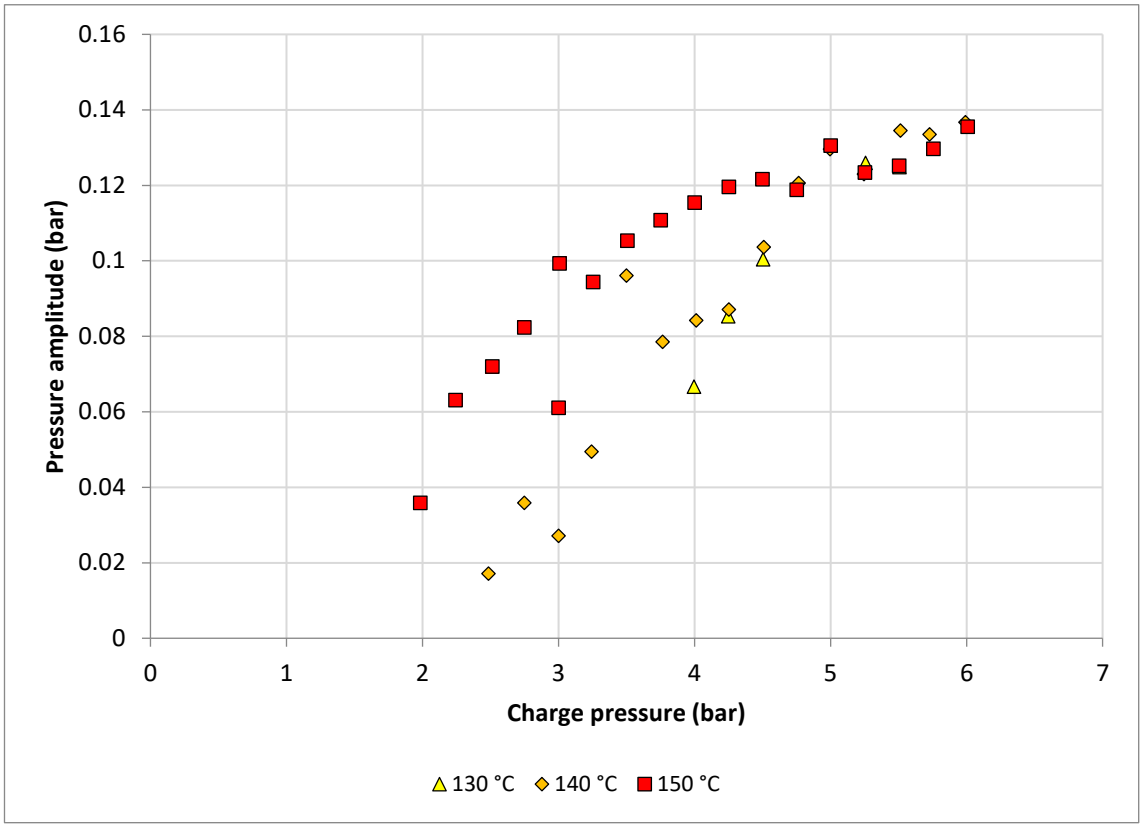

Figure 5.34 – Gas pressure amplitude variations for Gas Space 1 in the 3HEAT experiments conducted using 115 ml liquid pistons.

The gas temperature difference between the expansion and compression spaces in Gas Space 1 is shown in Figure 5.35. The trend for the temperature difference generated in Gas Space 1 suggests that the best performance occurs in the region of 4.5 bar–5 bar, although as in the 100 ml case, the level of cooling attained is not significant. Despite the higher pressure amplitudes developed in the 115 ml experiments, the temperature differences measured were not significantly larger.

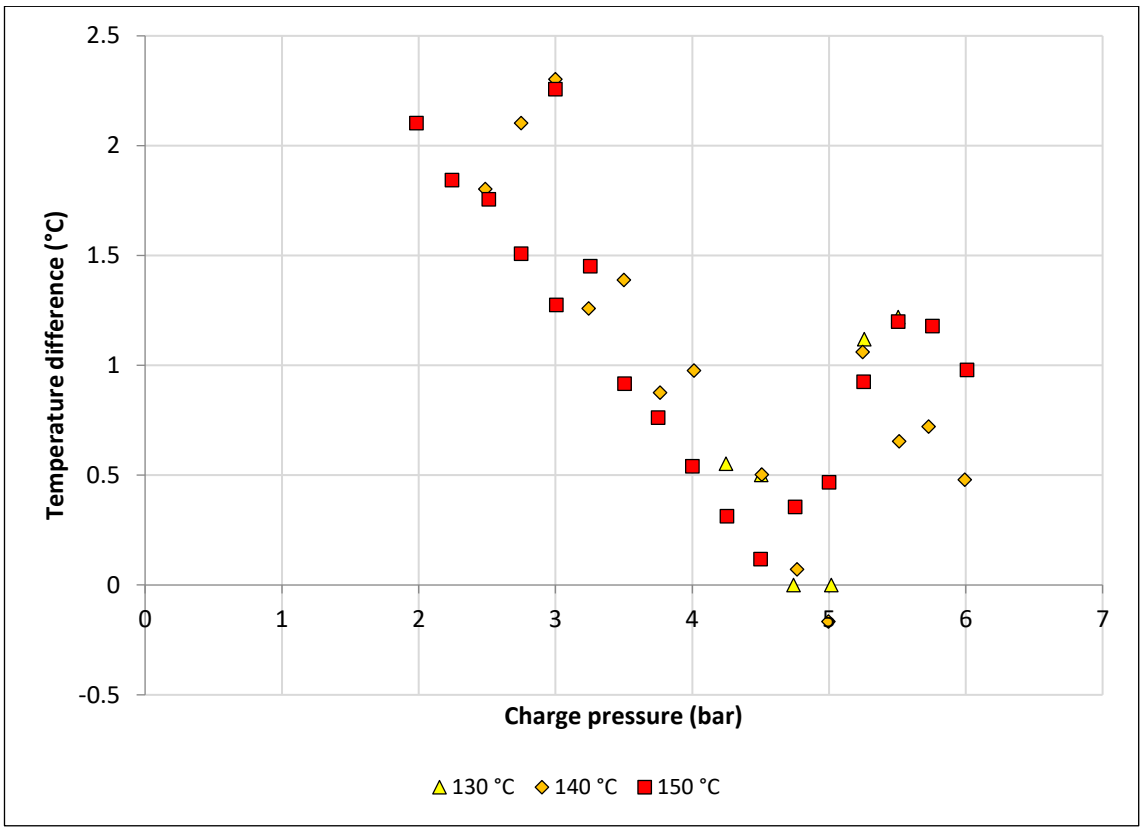

Figure 5.35 – Temperature difference between expansion and compression spaces in Gas Space 1 for the 3HEAT configuration experiments using 115 ml liquid pistons. Negative temperatures imply cooling.

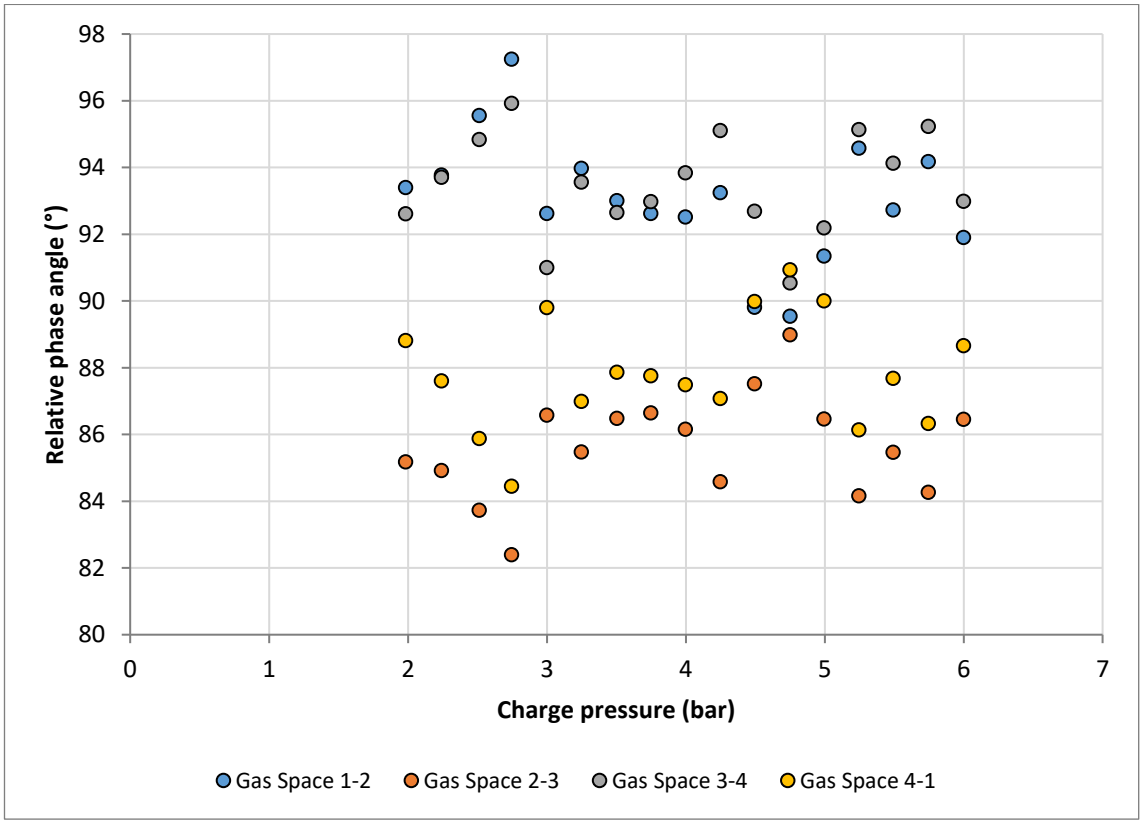

Figure 5.36 – Relative phase angle variations with gas charge pressure for the pressure phasors in the 150°C 3HEAT experiments using 115 ml liquid pistons.

Figure 5.36 shows the phase angles of the pressure phasors for 3HEAT experiments at 150°C with the 115 ml pistons. Interestingly, the graph shows the same divergence when the charge pressure approaches 3 bar, as was seen for the 4HEAT experiments with 115 ml pistons. The result at 4.75 bar is also intriguing, with all phase angles being very close to 90º, unlike the rest of the results which have similar trends to the 100 ml phase angle results. Figure 5.37 presents the relative phase angle trends for the piston displacement phasors.

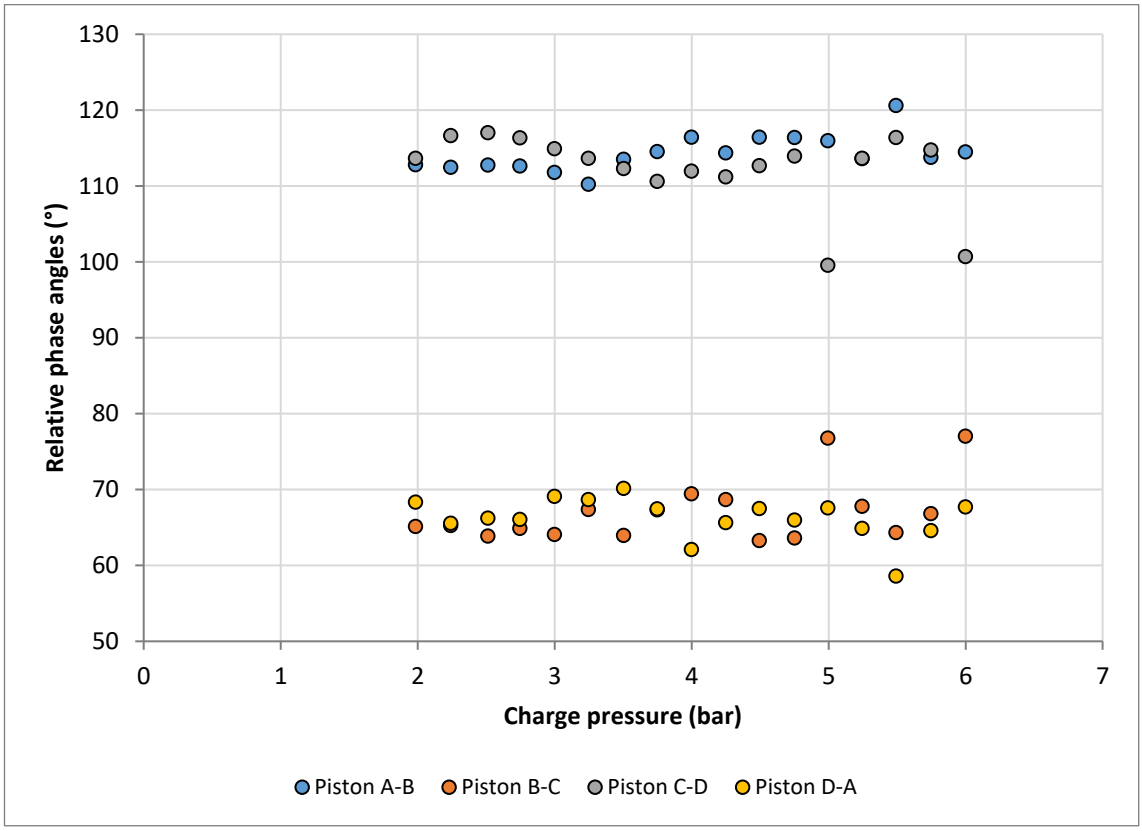

Figure 5.37 – Relative phase angle variations with gas charge pressure for the piston displacement phasors in the 150ºC 3HEAT experiments using 115 ml liquid pistons.

Apart from the two groups at 5 bar and 6 bar, the phase angles of the liquid pistons are very consistent across the pressure range. The differences between the close pairs and further away pairs are also larger in magnitude, with the relative phase angles for pistons A–B and C–D generally between 110°–120°, and for pistons B–C and D–A between 60°–70º—whereas these values were closer to 70º and 110º with the 100 ml pistons. Also of note is that the same convergence/divergence of the relative phase angles seen in the

trends for the gas pressures is not seen in the piston phase angle plots for the 115 ml pistons.

5.1.2.3 3HEAT Summary

The important findings and observations from the 3HEAT section are summarised and outlined here for clarity: (a) Similar to the 4HEAT configuration, the experimental frequency trend with charge pressure follows the analytical prediction; (b) Increased heater temperatures generally lead to higher pressure amplitudes; although increases seem to get closer to a possible maximum as the charge pressure nears 6 bar (perhaps tests at higher pressure would confirm this); (c) The pressure amplitudes developed are not equal for all gas spaces. The two opposite gas spaces containing heaters, GS2 and GS4, record the highest values—with maximum global values of 0.211 bar and 0.185 bar respectively. The other pair of opposite gas spaces, GS1 and GS3, consistently recorded equal pressure amplitudes with the global maximum being 0.136 bar. The ratios of these pressure amplitudes remained consistent across the charge pressure and temperature range investigated. This means that the lowest pressure amplitude is always developed in the absorber space, which may hinder the cooling potential of this configuration; (d) The relative phase angles between the pressure phasors at approximately 90° were very similar to the 4HEAT configuration. This was not the case for the piston displacement phase angles where the differences in magnitude of the pressure amplitudes influenced the piston phases, and aligned them closer to the higher pressure amplitude spaces. The result was phase angles between pistons of approximately 70º or 110º; (e) The temperature difference developed in the absorber gas space seemed to depend on charge pressure, indicating an optimal charge pressure existed between 4.5 bar–5.5 bar for both piston masses, although no significant cooling capability was measured for any experiment[1].

[1] It is worth reiterating that at this stage of the research, the primary objective is understanding the dynamics of the system, and not necessarily targeting the largest temperature difference.

The largest temperature difference achieved in Gas Space 1 was 0.5ºC; (f) Multi-modal behaviour was again witnessed at the lower charge pressure experiments (below 5 bar), with the developed pressure and piston amplitudes converging above this threshold, and being independent of heater temperature.

5.1.3 2HEAT Configuration

The 2HEAT configuration is the second of the two configurations which has the potential to produce a cooling effect. With two subsystems producing work and two subsystem consuming work, the 2HEAT configuration contains two heaters (GS2 and GS3), and two absorbers (GS1 and GS4). Two possible configurations exist for the 2HEAT scenario, the alternating and adjacent configurations. These were described in Section 3.3.3. After extensive efforts to operate the alternating configuration with no success, the adjacent configuration was found to function, but only with 115 ml pistons. It is probable that 100 ml pistons would have worked with higher heater temperatures, but an upper limit of 190ºC was set to protect elements of the test-rig. The results presented here aim to illustrate the behaviour of the 2HEAT configuration, and how its performance is influenced by changes in the key design parameters in Table 5.2. The results cover only one heater temperature, 190ºC, and one piston size, 115 ml. Figure 5.38 shows the pressure amplitudes trends for a typical 2HEAT. The experiment considered in this case was with a gas charge pressure of 4 bar.

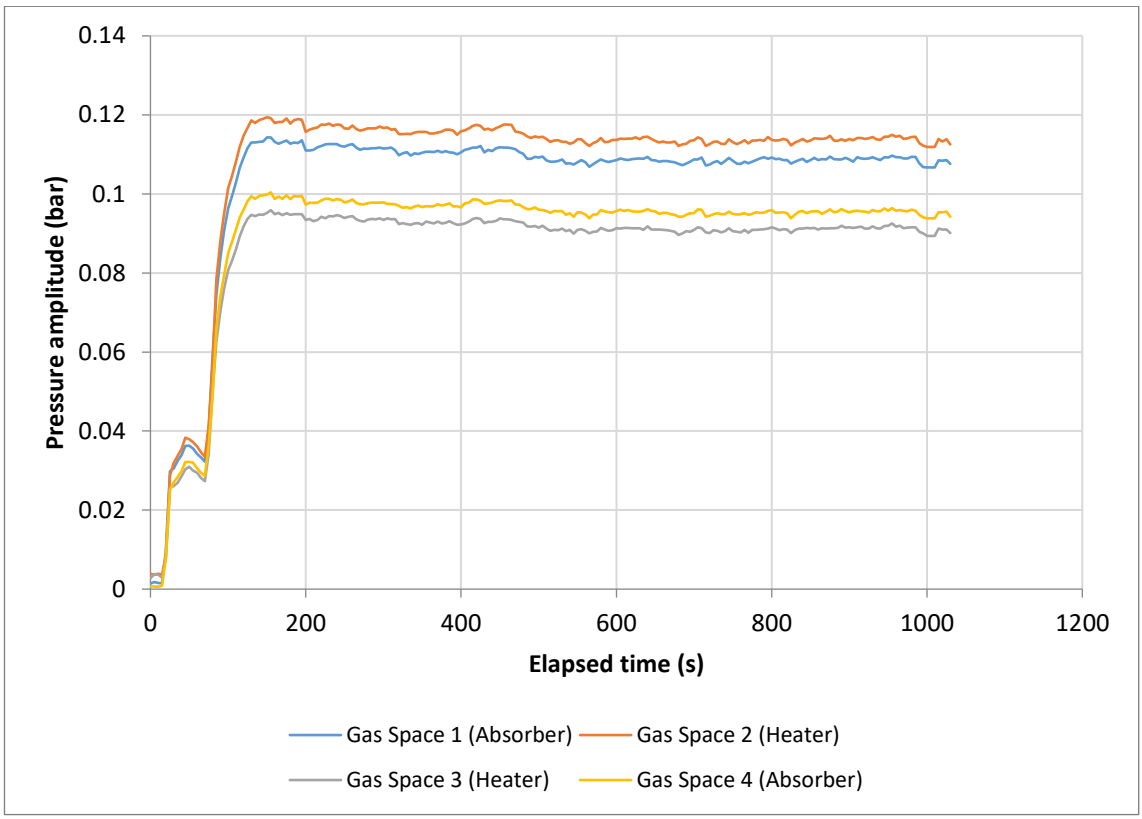

Figure 5.38 – Gas pressure amplitude variations during a typical 2HEAT experiment. Heater temperature is set at 190°C with 4 bar charge pressure and 115 ml liquid pistons.

As can be seen from Figure 5.38, the pressure amplitudes are not as similar as in the 4HEAT case, but they are closer together than the 3HEAT experiments. The largest pressure amplitude developed is roughly 0.12 bar in GS2. Somewhat surprisingly, the two gas spaces containing absorbers register the second and third largest pressure amplitudes, with the other heated space developing the lowest pressure amplitude. It can be seen at the beginning of the experiment that the jump-start was not successful at propelling the system into self-sustained operation, and the pressure amplitudes began to decrease. A second jump-start was then used. This occurred in many experiments of all configuration types. Figures 5.39 and 5.40 show the expansion space temperature trends for the heater and absorber spaces respectively in the example 2HEAT experiment.

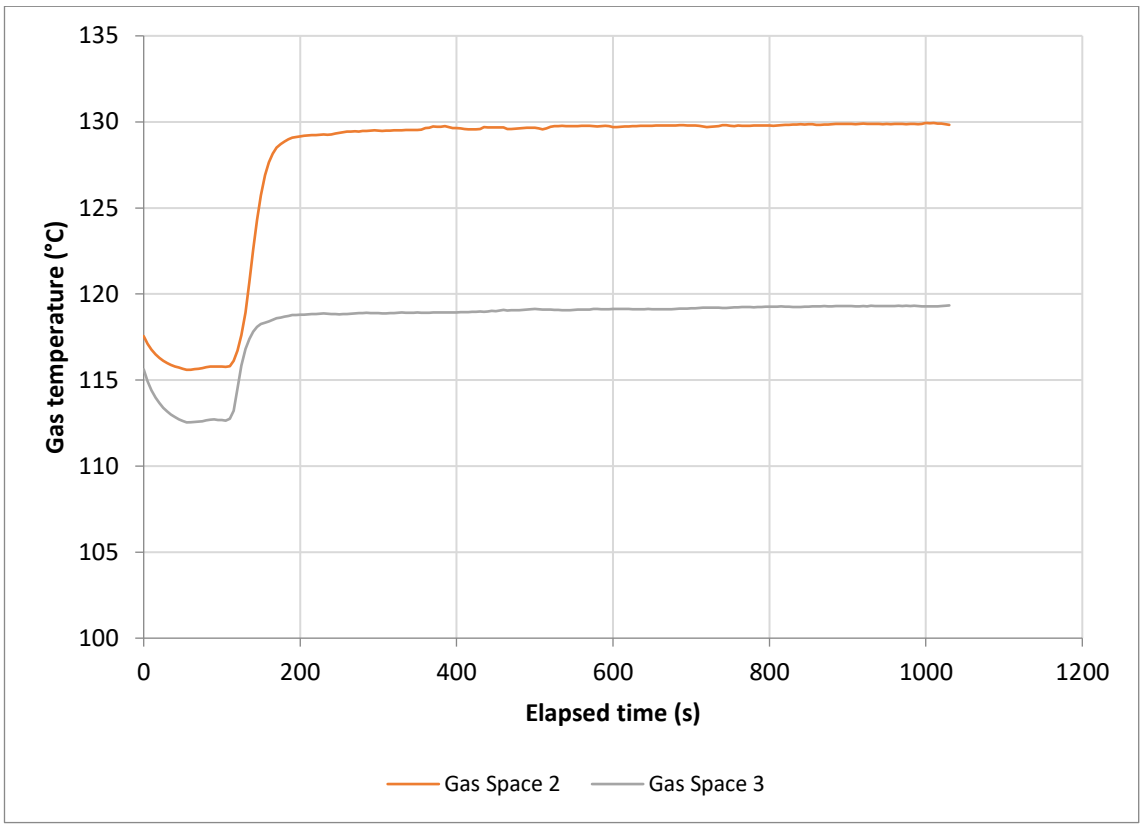

Figure 5.39 – Heater space gas temperature variations during a typical 2HEAT experiment. The experiment was at 4 bar with 190°C set heater temperature and 115 ml liquid pistons.

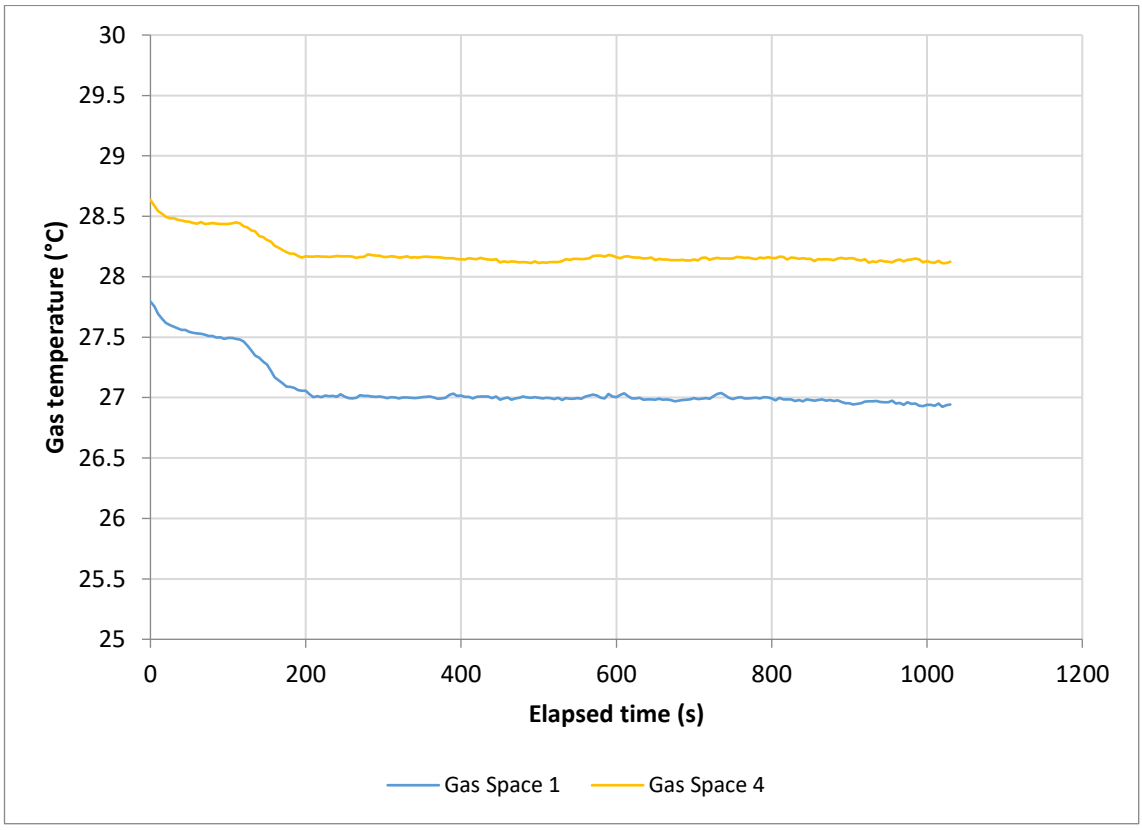

Figure 5.40 – Absorber space gas temperature variations during a typical 2HEAT experiment. The experiment was at 4 bar with 190°C set heater temperature and 115 ml liquid pistons.

As can be seen from the Figures 5.39 and 5.40, the largest pressure amplitudes correspond to the more pronounced expansion space temperatures. Gas Space 2 exhibits the largest pressure amplitude and the gas approaches 130ºC, while in Gas Space 3 the temperature approaches 120ºC. In the case of the absorbers, the lowest temperature is achieved by the space with the higher pressure amplitude, GS1. There is a noticeable drop in the absorber gas temperatures once the system achieves self-sustained operation (at approximately 150 seconds). Figures 5.41 and 5.42 show the pressure and displacement profiles during a one second snapshot taken midway through the experiment. The snapshot was taken at time, t = 450 seconds (7 minutes and 30 seconds into the experiment).

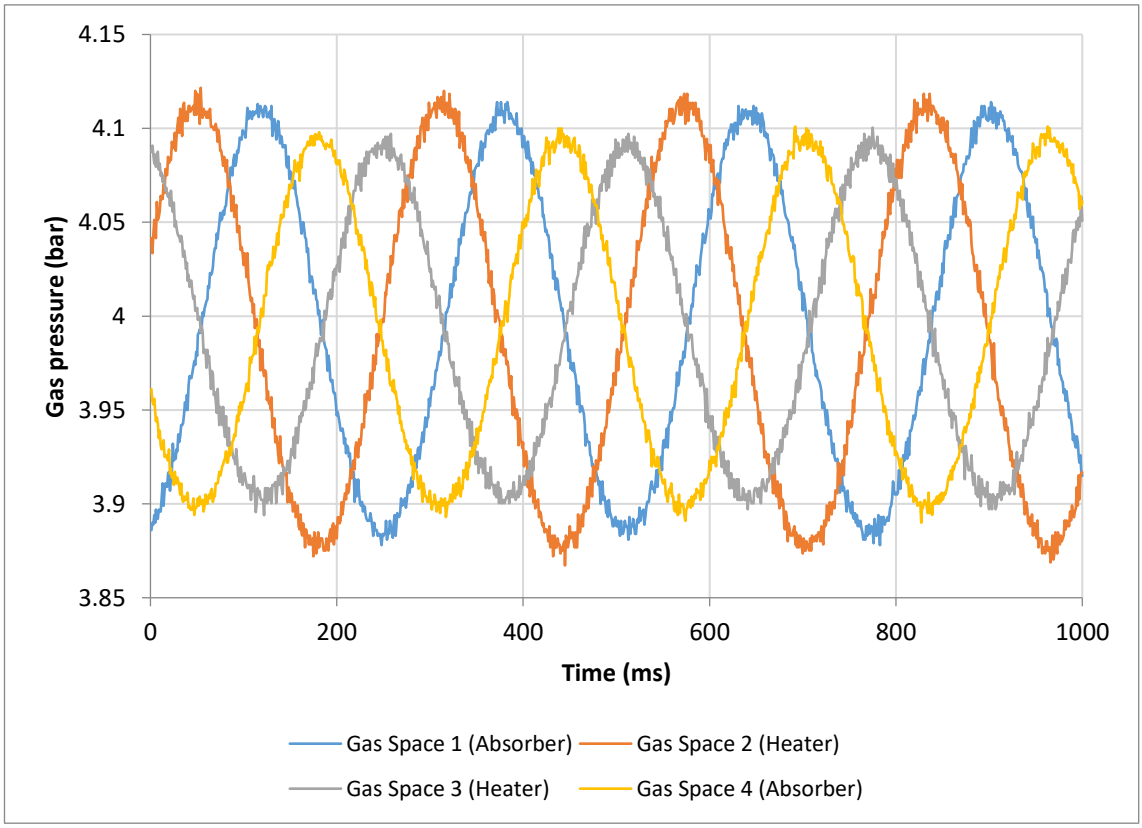

Figure 5.41 – Gas pressure profiles over a one second interval during a typical 2HEAT experiment. The experiment was at 4 bar and 190ºC with 115 ml liquid pistons. Time taken was at 450 seconds (7 minutes 30 seconds) into the experiment.

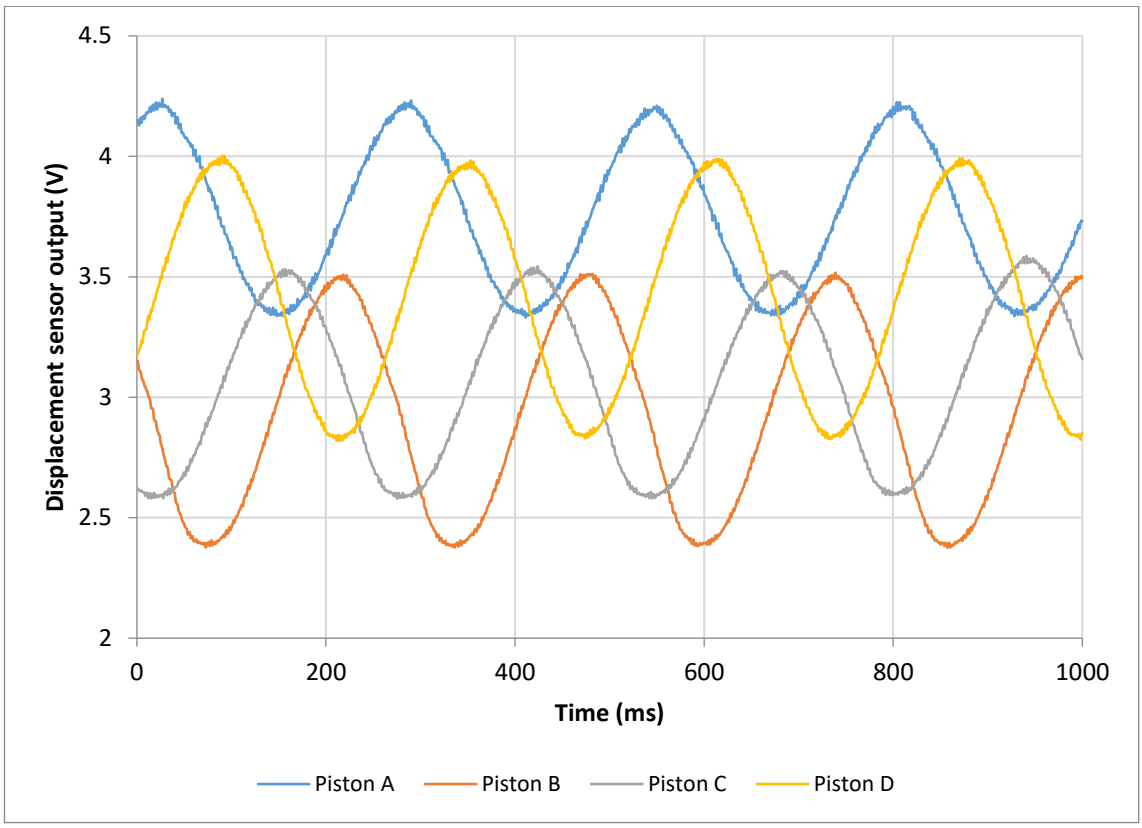

Figure 5.42 – Piston displacement profiles over a one second interval during a typical 2HEAT experiment. The experiment was at 4 bar and 190°C with 115 ml liquid pistons. Time taken was at 450 seconds (7 minutes 30 seconds) into the experiment.

The relative phase angles of the pressure profiles and displacement profiles appear to be approximately 90°; they appear much more regularly spaced than the 3HEAT configuration. Applying the same least mean squares approximation and calibration procedure from earlier will yield the phasor expressions of the gas pressure and displacement profiles. Table 5.4 shows the phasor values obtained for the example 2HEAT experiment. Figure 5.43 then shows the associated scaled phasor plot.

Table 5.4 – Phasor representations of gas pressure and piston displacement amplitudes for example 2HEAT experiment.

Phasor	Amplitude (bar or cm)	Phase angle (°)
Pressure 1 (P1)	0.112	0
Pressure 2 (P2)	0.118	90.0
Pressure 3 (P3)	0.0936	180.0
Pressure 4 (P4)	0.0982	270.0
Displacement A (XA)	3.15	139.3
Displacement B (XB)	2.63	229.4
Displacement C (XC)	2.62	319.2
Displacement D (XD)	2.65	49.3

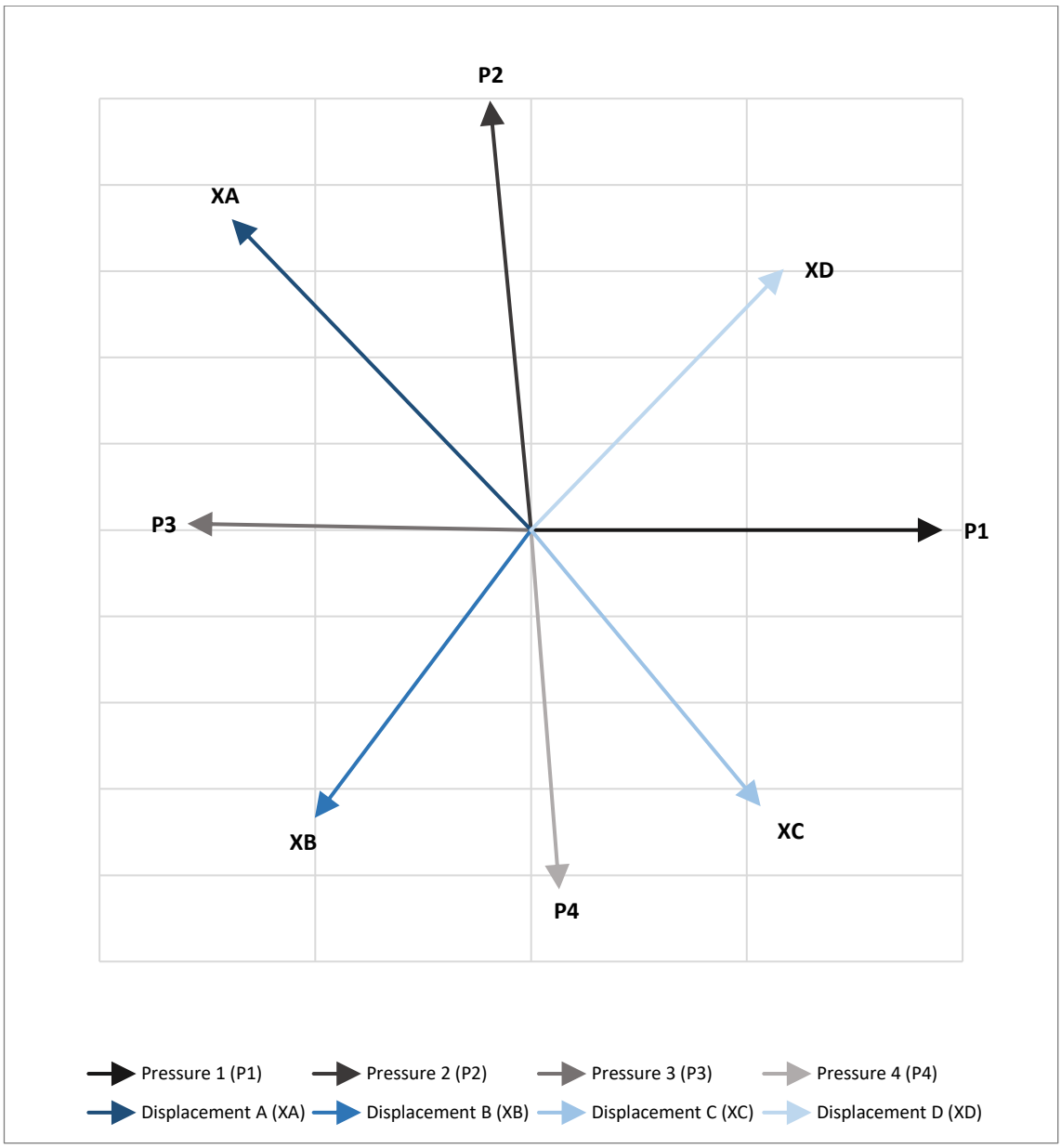

Figure 5.43 – Phasor plot of example 2HEAT experiment pressure amplitude and displacement profiles. The phasor magnitudes have been scaled for more clarity.

The pressure phasors are positioned in a very similar manner to both the 4HEAT and 3HEAT scenarios previously examined. The P2 phasor's relative phase angle to P1 is slightly greater than 90º, the P3 phasor's relative phase angle to P1 is slightly less than 180º and the P4 phasor's relative phase angle is slightly more than 270º. It seems as though the phase angles of the pressures are unaffected by the configuration of the system. The magnitudes of the phasors are different, however, and in this case the arrangement with P1 and P2 being dominant seems to have a favourable influence on the piston phases. Unlike the 3HEAT configuration, the relative phase angles between piston displacements

look much closer to the desirable 90º value for a Stirling machine. Another important feature of this plot is that it shows that opposite pistons are not constrained to having 180º phase differences, which appeared to be the case for the 3HEAT experiments. Figure 5.44 presents the phase angle values relating to the pressure and displacement phasors in Figure 5.43.

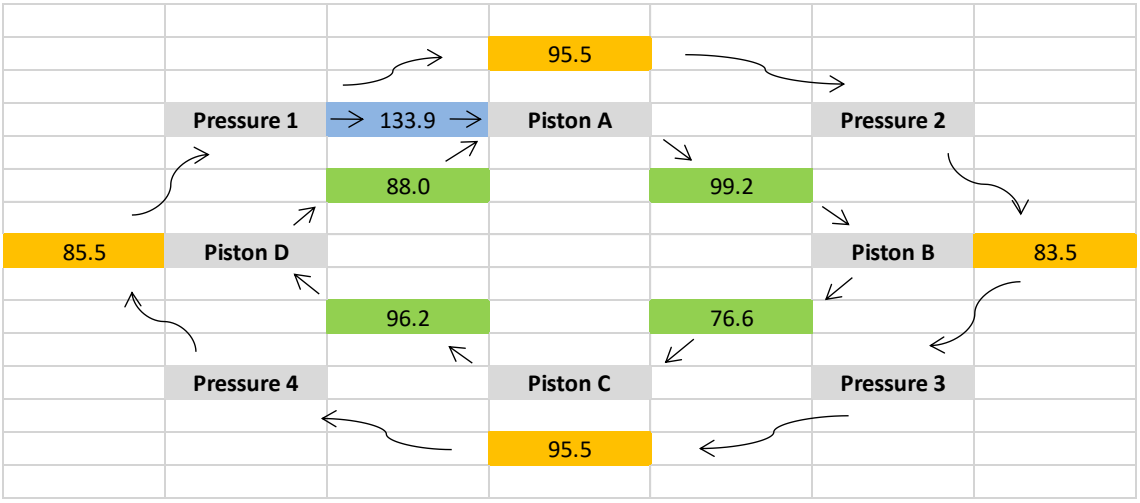

Figure 5.44 – Pressure and piston displacement phasor phase angles for 2HEAT example experiment.

As observed, the relative phase angles of the pistons are much closer to 90º than in the 3HEAT case. Understandably, they are not as close as the values seen in the symmetrical 4HEAT experiments; although for a system which has two forward and two reverse heat engines connected in series the values are encouraging. The absorber gas spaces are particularly interesting with the relative phase angles of the adjacent pistons next to gas spaces 1 and 4 at 88.0º and 96.2º respectively. This suggests that the dynamic constraints of this configuration may be more suitable for cooling than the 3HEAT configuration.

5.1.3.1 115 ml Piston Results

The results presented here cover the experiments conducted with 115 ml piston volumes, using the 2HEAT configuration at a heater temperature of 190°C, and across the charge pressure range of 2 bar–6 bar. Similar to the general overview of the previous configurations, a number of figures are shown to highlight how some of the key variables

depend on charge pressure and heater temperature. The figures are accompanied by brief assessments and general observations about the behaviour of the 2HEAT configuration. Figure 5.45 shows how the operational frequency of the system changes with increased charge pressure.

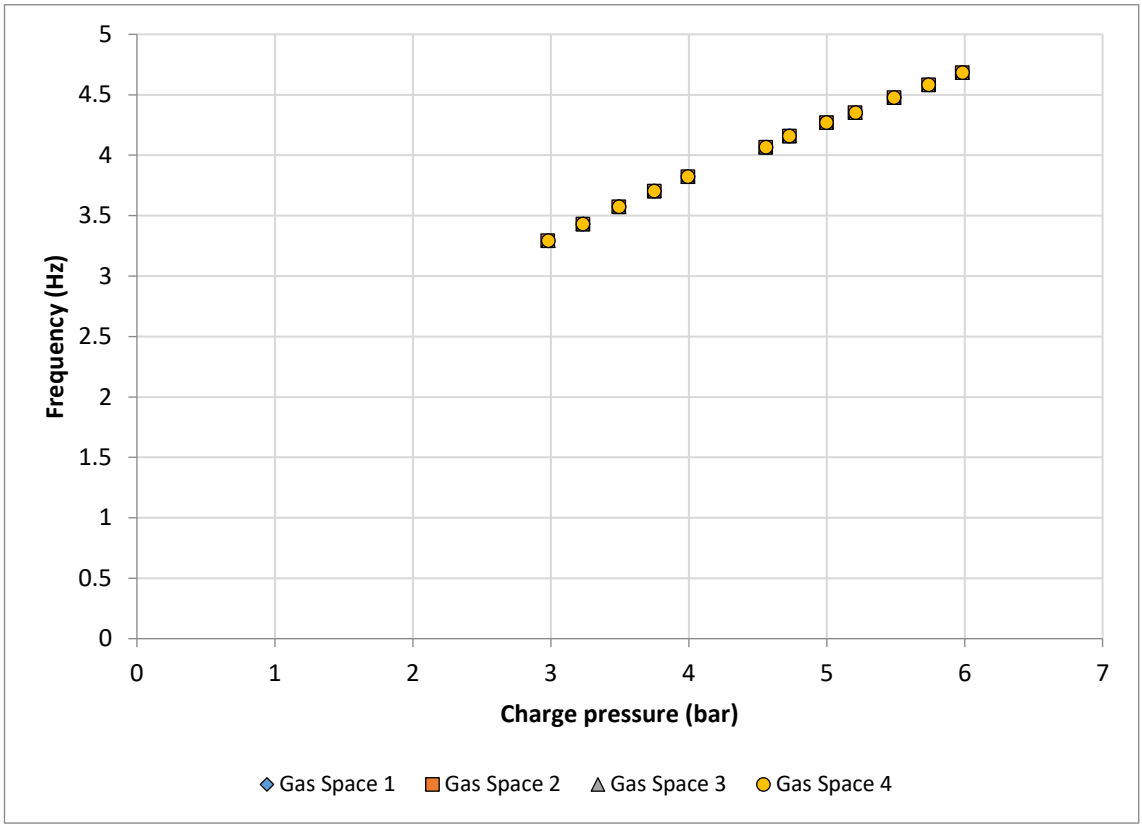

Figure 5.45 – Shows the frequency variation with mean operating pressure for all 2HEAT configuration experiments using 115 ml liquid pistons.

As expected, the results for the frequency trend are similar to the previous configurations. They appear to exhibit the same dependence on charge pressure as previously identified. The 2HEAT configuration was unable to achieve self-sustaining operation below 3 bar charge pressure; although it is likely that with increased heater temperatures, operation at lower pressures would occur (as previously explained, heater temperatures above 190ºC were not considered). The missing data point between 4 and 4.5 bar (i.e. the 4.25 bar experiment) is due to the data being accidentally corrupted and lost. Figure 5.46 presents the pressure amplitudes developed in the 2HEAT experiments.

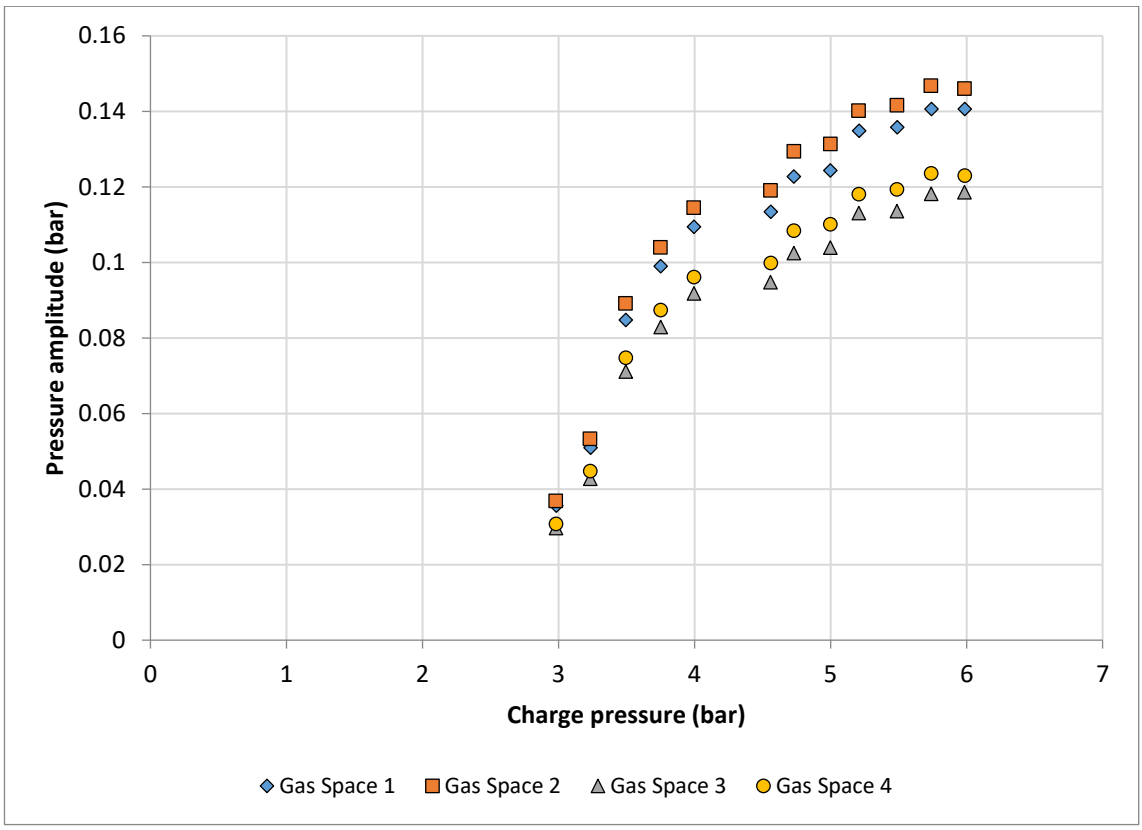

Figure 5.46 – Pressure amplitude variations of all gas spaces with increasing charge pressure for 2HEAT experiments conducted with 190°C heater temperatures and 115 ml pistons.

The pressure amplitudes increase with charge pressure, and appear to approach a local maximum in the region of 6 bar—with the largest value of 0.147 bar being recorded in Gas Space 2 at 5.75 bar. The relative magnitudes of the pressure amplitudes developed in each of the four gas spaces remains consistent across the range tested. The mean ratios with respect to GS1 are 1.05 (s = 0.6%), 0.84 (s = 0.3%) and 0.88 (s = 0.6%) for GS2, GS3 and GS4 respectively. Adding up the unrounded ratios obtained for the heater and absorber spaces gives 1.884 for the heater spaces, and 1.879 for the absorber spaces, which equates to a conversion ratio of 1.003:1 (to three significant figures).

The gas temperatures measured in the expansion spaces of each subsystem are displayed in the following graphs. Figure 5.47 shows the temperatures of the heated spaces 2 and 3, while Figure 5.48 shows the absorber temperatures in 1 and 4. The temperature differences correspond with the relative magnitudes of the pressure amplitudes in each space.

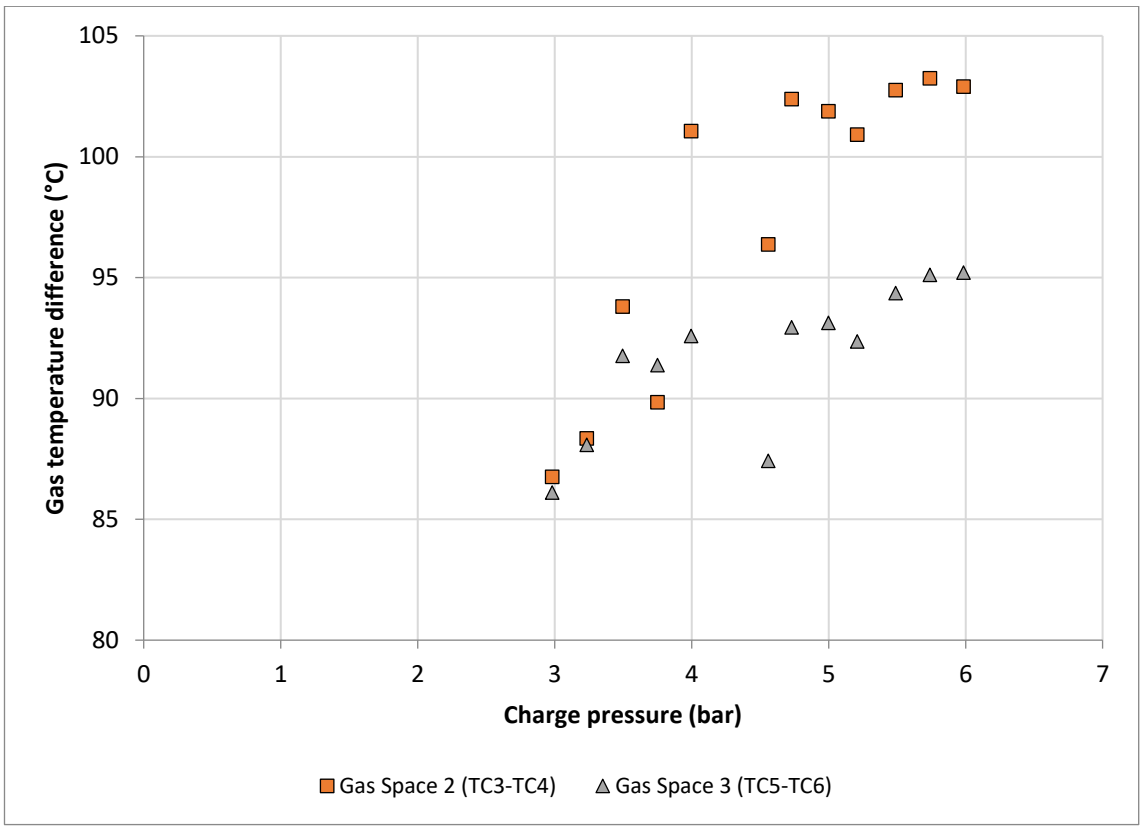

Figure 5.47 – Heater gas space temperature differentials and their variation with charge pressure for the 2HEAT experiments with 190°C heater temperatures and 115 ml liquid pistons.

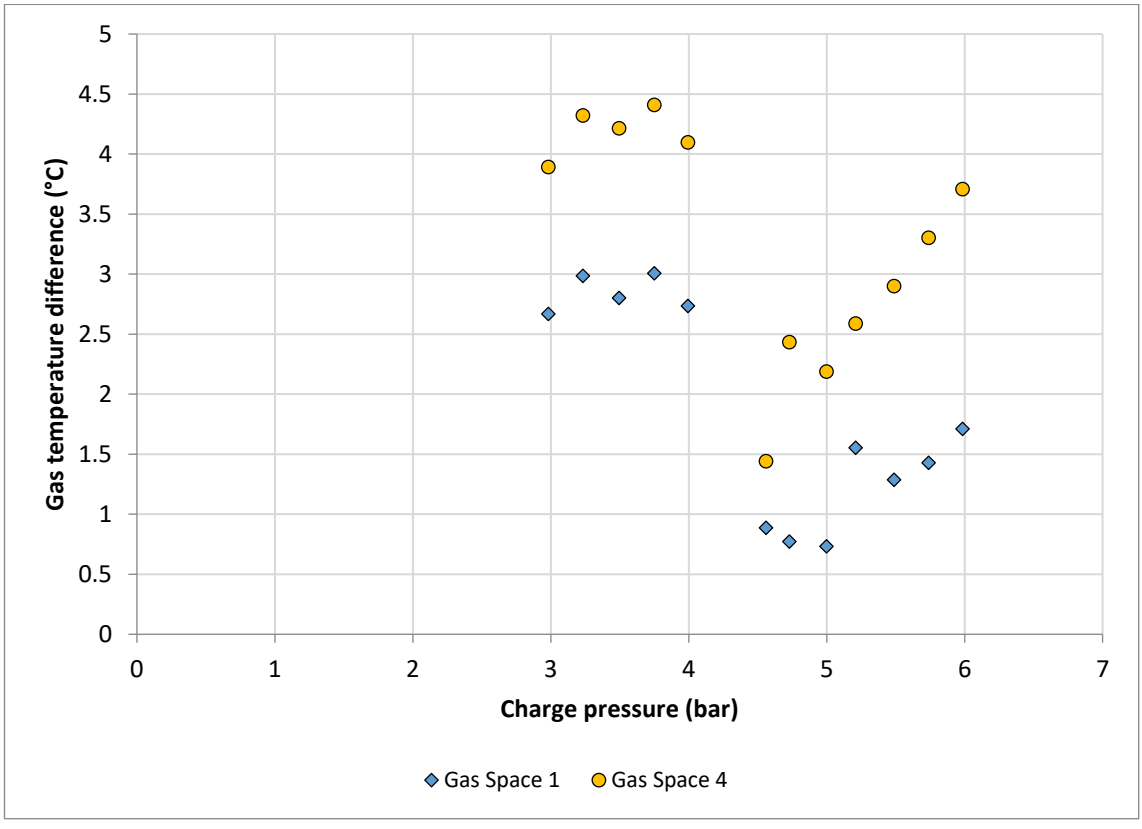

Figure 5.48 – Temperature difference between expansion and compression spaces in gas spaces 1 and 4 for the 2HEAT configuration experiments using 115 ml liquid pistons.

The behaviour of the hot spaces is similar to that expected (i.e. as charge pressure increases so does the measured gas temperature). This is a consequence of the increased frequency, density and gas velocity, which influences the heat transfer coefficients. In the absorber spaces, Gas Space 1 exhibits the lowest temperature differences. With the higher of the two pressure amplitudes, the gas is forced expand to a greater degree than in the absorber of Gas Space 4.

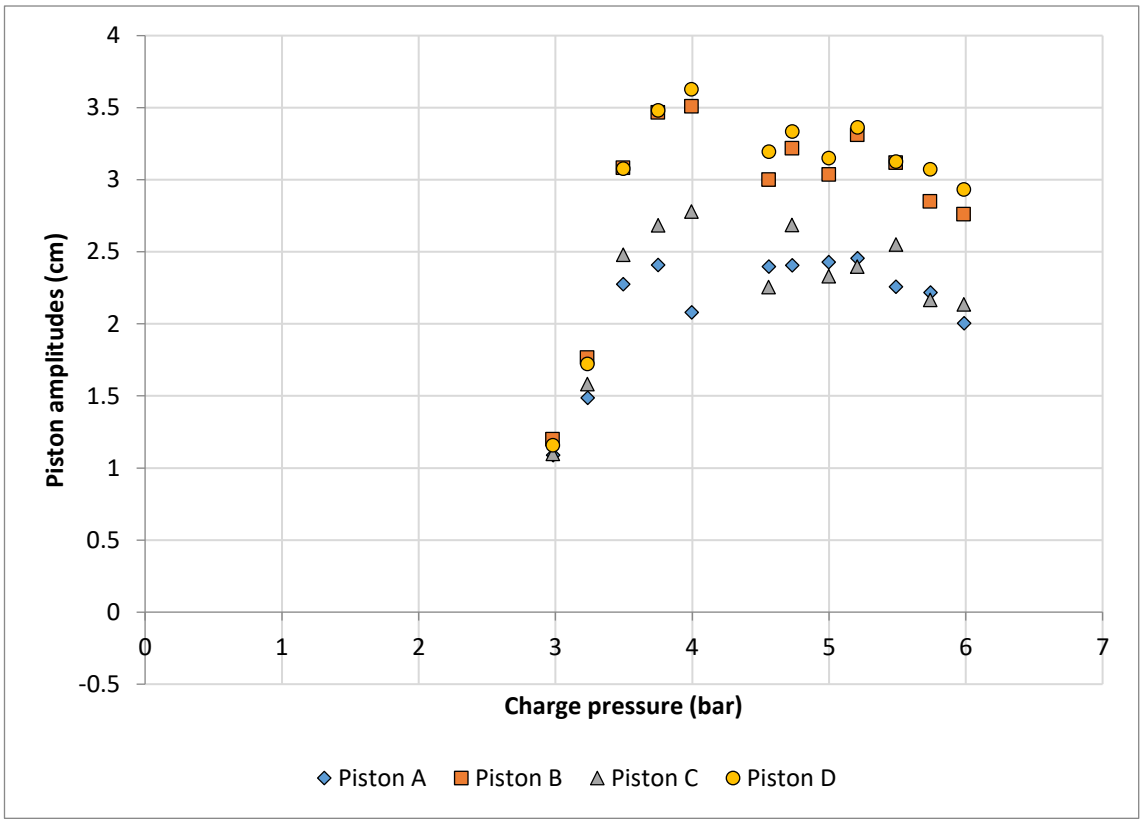

Figure 5.49 – Piston amplitude variation with charge pressure for the 190°C, 2HEAT configuration experiments using 115 ml liquid pistons.

The piston displacements for the 2HEAT experiments are shown in Figure 5.49. The amplitudes exhibit the same general trends as those seen in earlier configurations with a gradual increase towards a peak near 4.5 bar—before decreasing marginally as charge pressure is increased further. A significant difference, however, is that the piston amplitudes seem to be grouped into two pairs with pistons A and C recording similar amplitudes to each other. Pistons B and D also demonstrate similar amplitudes, but these

are consistently in the range of 10 mm larger than A and C, and often within a few millimetres of each other.

The final graphs of interest for the 2HEAT configuration are the phase angles trends of the system. Figure 5.50 shows how the phase angles of the pressure amplitude phasors vary with charge pressure, and Figure 5.51 shows the same for the phase angles of the displacement phasors.

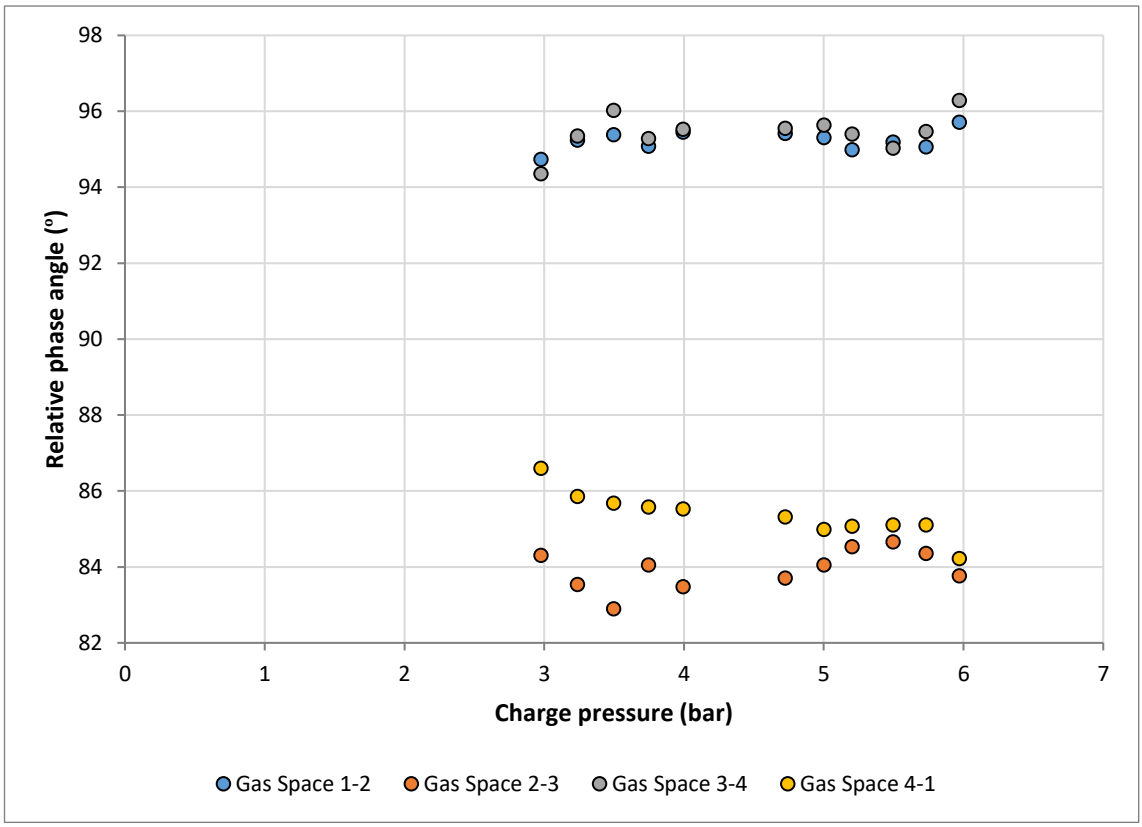

Figure 5.50 – Relative phase angle variations with gas charge pressure for the pressure phasors in the 190°C 2HEAT experiments using 115 ml liquid pistons.

As mentioned in the assessment of the example experiment phasor plot, the values of the relative phase angles between the pressure phasors are similar to the results for the other configurations. They are all close to 90º, but consistently GS1–GS2 and GS3–GS4 values are above 90º, while GS2–GS3 and GS4–GS1 values are below 90º. This differs from the other configuration plots in the uniformity of the relative phase angles across the entire charge pressure range. Each relative phase angle varies (at most) by 1º across the range

of 3 bar–6 bar, whereas the other configurations exhibit differences of up to 7º. This highlights an important characteristic of the 2HEAT adjacent configuration that was noticed during the experimental procedure. The 2HEAT experiments were always very stable; none resulted in any multi-modal behaviour, and the pressure amplitudes fluctuated to a lesser degree than the other configurations. Unfortunately, since results from other heater temperatures are absent in the 2HEAT case, it is unknown whether this trait is inherent. This is addressed in the second set of experimental parameters investigated in Section 6.2, where additional 2HEAT experiments are evaluated.

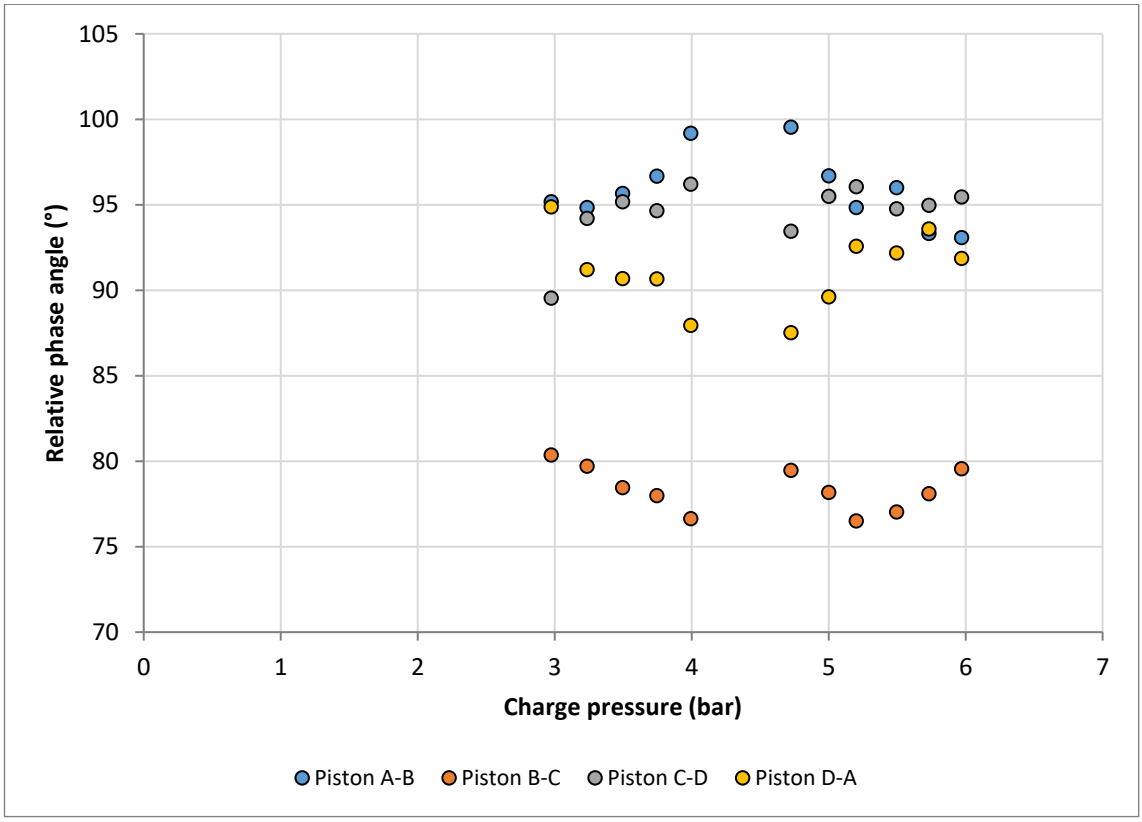

Figure 5.51 – Relative phase angle variations with gas charge pressure for the piston displacement phasors in the 190°C 2HEAT experiments using 115 ml liquid pistons.

5.1.3.2 2HEAT Summary

The important findings and observations from the 2HEAT section are summarised and outlined here for clarity: (a) In a similar manner to the 3HEAT and 4HEAT configurations, the experimental frequency follows the expected trend with charge pressure; (b) Increased heater temperatures generally lead to higher pressure amplitudes;

although the increases seem to get closer to a possible maximum as the charge pressure nears 6 bar. The pressure amplitudes developed are not equal for all gas spaces, but they are much closer in magnitude than the 3HEAT experiments. (c) Interestingly, the larger pressure amplitudes are not exclusively held by heated spaces. GS2 still registers the largest, with a global maximum of 0.147 bar at 5.75 bar charge pressure. The next largest is an absorber space, GS1, with 0.141 bar, followed by the second absorber space, GS4, with 0.124 bar. The second heated space, GS3, consistently records the lowest pressure amplitude with a maximum of 0.118 bar; (d) The relative magnitudes of these pressure amplitudes remains consistent across the charge pressure range 3 bar–6 bar, resulting in a consistent conversion ratio of 1.003:1. This distribution is potentially much more favourable for producing a cooling effect; (e) At approximately 90°, the relative phase angles between the pressure phasors were very similar to both the 3HEAT and 4HEAT configurations. Unlike the 3HEAT results, the relative phase angles of the piston phasors were much closer to the desired 90º target. The values related to the absorber spaces, C–D and D–A, were particularly promising and consistently within 85º–95º; (f) The temperature difference developed in the absorber gas spaces again showed a dependence on charge pressure, with an optimal charge pressure existing between 4.5 bar–5 bar. Despite no significant cooling effect being measured for any experiment, the dynamic behaviour of the 2HEAT system is very encouraging, with both desirable phase angle and pressure amplitude distributions; (g) Multi-modal behaviour was not witnessed for any 2HEAT experiments; (h) The experimental investigation into the 2HEAT configuration was limited because of the high heater temperatures required to achieve self-sustained operation. Sustained operation was not possible with the 100 ml pistons.

5.1.4 Configuration Comparisons

After assessing the results of each configuration's experiments, it is possible to compare their general behavioural characteristics, as well as the influence of the additional piston mass in the 115 ml experiments. Figure 5.52 shows the operational frequency measurements for all sets of experiments conducted with 100 ml, while Figure 5.53 shows the same graph for all 115 ml liquid piston experiments. As predicted, the temperature increases in the heater spaces have very little influence on the resulting frequency of the LPSC system, independent of which configuration is being considered. The primary dynamic differences between the configurations are the gas temperatures in the expansion spaces, which have a small effect on gas spring constant and therefore frequency.

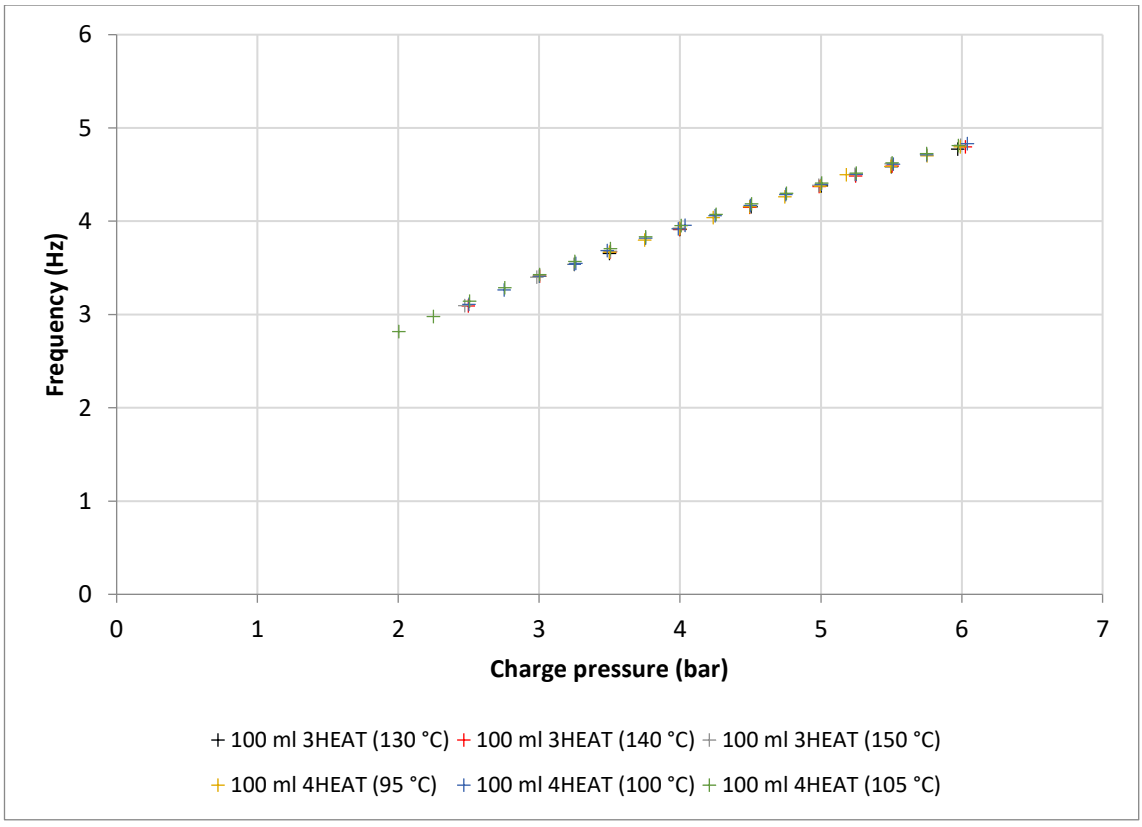

Figure 5.52 – Operational frequency variation with mean operating pressure for all experiments using 100 ml liquid pistons.

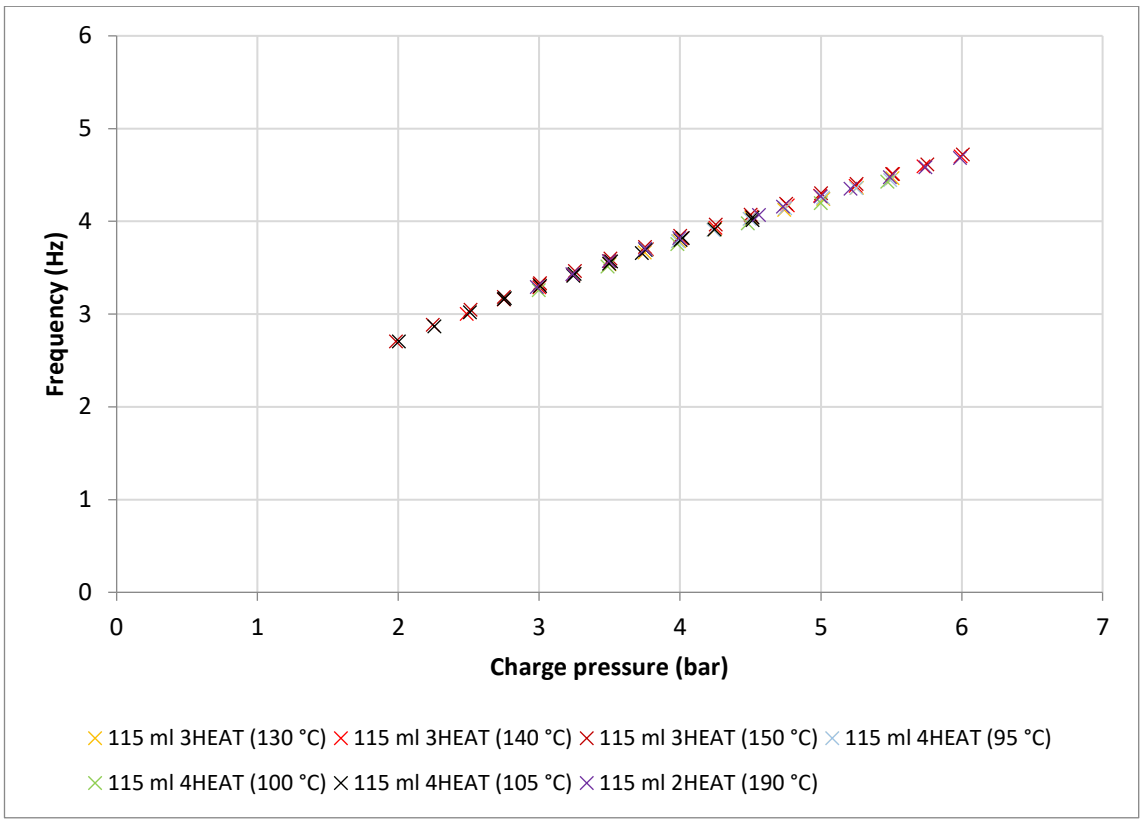

Figure 5.53 – Operational frequency variation with mean operating pressure for all experiments using 115 ml liquid pistons.

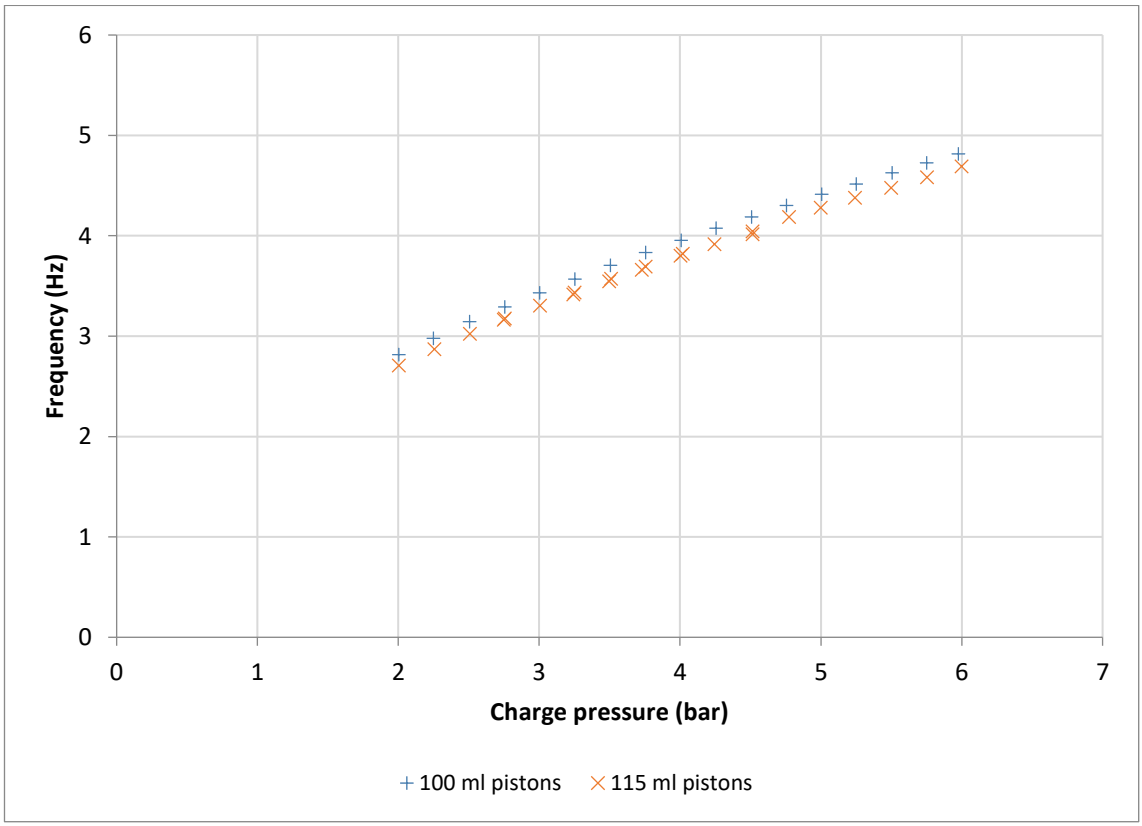

Figure 5.54 – Operational frequency differences between 100 ml and 115 ml liquid pistons.

Figure 5.54 compares the frequency trends of the 100 ml piston with the 115 ml pistons. The frequency is only slightly affected by the increase in piston mass. A 15% increase in the mass of the piston resulted in the frequency reducing by a maximum of 3.9%—with this percentage difference decreasing further with increased charge pressure. This limited influence is a consequence of the fact that—for the particular geometry of the test-rig—the natural frequency of the system is dominated by the gas spring component, which has a much larger magnitude than the piston gravitational term. Figure 5.55 shows the influence that the larger piston mass has on the pressure amplitudes developed in the 4HEAT configuration experiments. Similarly, the pressure amplitudes developed in the absorber spaces of the 3HEAT configuration experiments are compared in Figure 5.56.

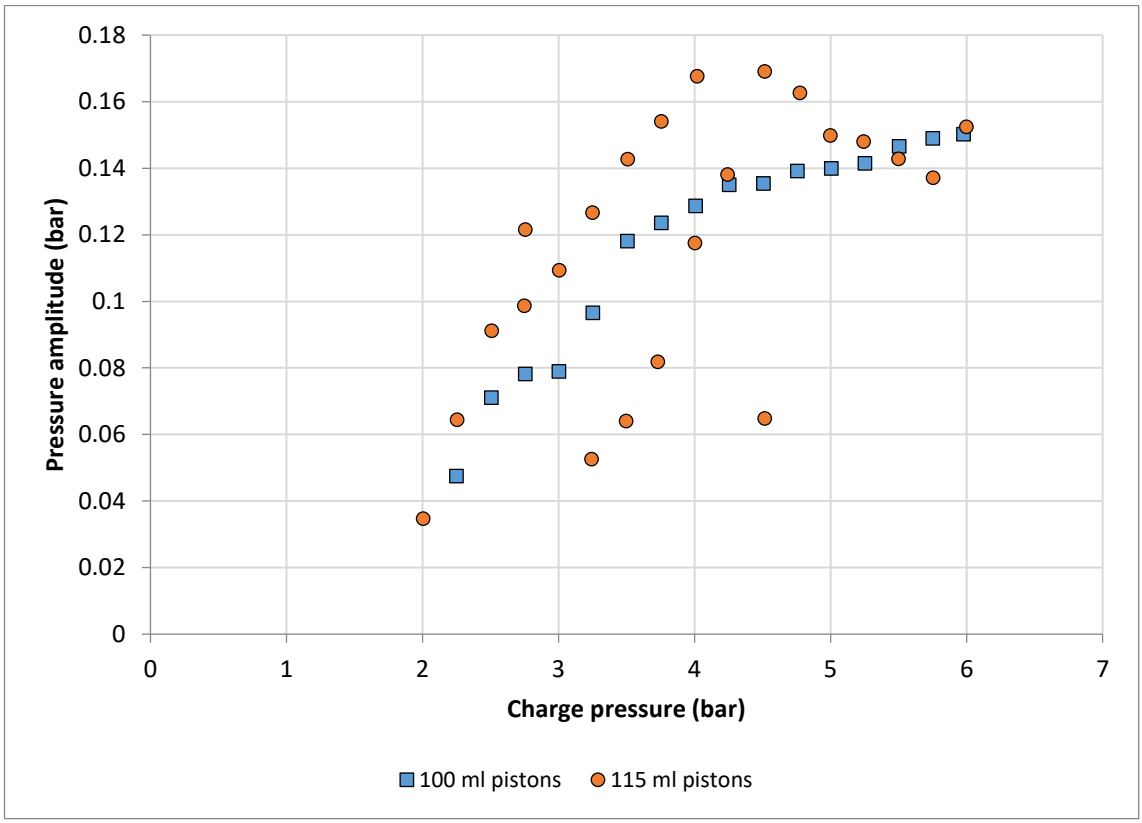

Figure 5.55 – Differences in pressure amplitudes between 100 ml and 115 ml liquid pistons for the 4HEAT, 105°C experiments.

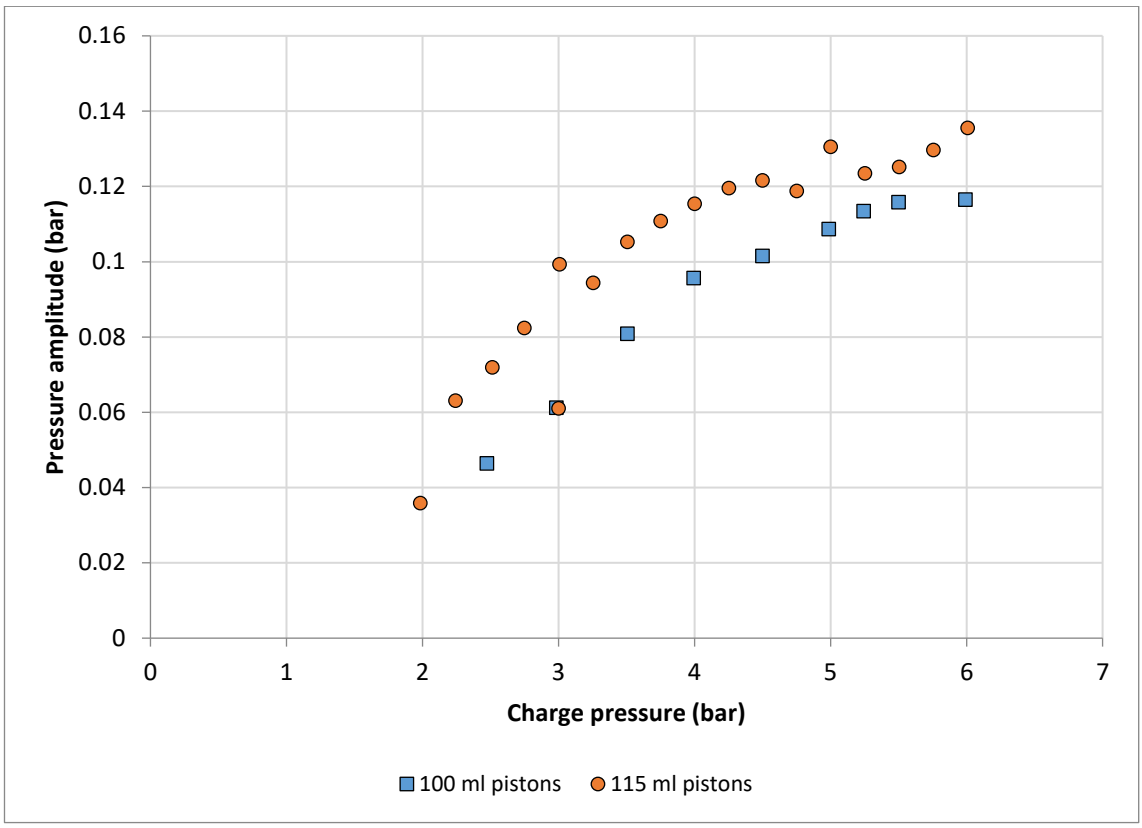

Figure 5.56 – Differences in pressure amplitudes between 100 ml and 115 ml liquid pistons for the 3HEAT 150°C experiments.

The larger piston masses produce larger pressure amplitudes at the same charge pressures in comparison to the smaller pistons. This is more obvious in the 3HEAT experiments where multi-modal behaviour at the temperatures selected is less evident. The pressure amplitude is consistently roughly 0.02 bar higher for the 115 ml piston experiments, although in both graphs the pressure amplitudes appear to converge at the higher charge pressures between 5 bar–6 bar.

Table 5.5 (shown on the following page) is a summary table listing some of the key performance data from both 100 ml and 115 ml experiments for the 15 mm piston LPSC test-rig.

Table 5.5 – Experimental results summary for 15 mm OD piston experiments.

		Configuration				
		4HEAT		3HEAT		2HEAT
Parameter		100 ml	115 ml	100 ml	115 ml	115 ml
Heater temperatures (°C)		95, 100, 105	95, 100, 105	130, 140, 150	130, 140, 150	190
Charge pressure range (bar)		2.25 – 6	2 – 6	2.5 – 6	2 – 6	3 – 6
Operational frequency range (Hz)		2.82 – 4.83	2.71 – 4.69	3.10 – 4.82	2.71 – 4.72	3.29 – 4.68
Ave. pressure amp. ratio (with respect to GS1)	GS1	1.00	1.00	1.00	1.00	1.00
	GS2	1.00	0.97	1.61	1.56	1.04
	GS3	0.99	0.97	1.02	1.00	0.83
	GS4	1.03	0.98	1.44	1.37	0.88
Relative phase angle ranges	GS1-GS2	91.0 - 94.3	88.7 – 96.6	91.7 – 94.8	89.5 – 97.2	94.7 – 95.7
	GS2-GS3	84.2 – 87.8	83.5 – 90.4	82.7 – 85.0	82.4 – 89.0	82.9 – 84.6
	GS3-GS4	90.4 – 95.4	86.7 – 95.2	94.2 – 96.9	90.5 – 95.9	94.4 – 96.3
	GS4-GS1	86.2 – 91.0	84.7 – 94.2	85.5 – 88.7	84.4 – 90.9	84.2 – 86.6
	A-B	77.1 – 92.3	84.8 – 94.3	97.0 - 113.8	110.2 – 120.6	93.1 – 99.5
	B-C	85.1 – 100.2	84.3 – 89.9	63.4 – 78.6	63.3 – 77.1	76.6 – 80.4
	C-D	85.2 – 100.5	82.1 – 95.7	102.9 – 118.9	99.6 – 117.0	89.5 – 96.2
	D-A	82.1 – 105.0	89.6 – 95.4	61.5 – 77.6	58.6 – 70.2	87.5 – 94.9
	GS1-A	128.3 – 140.5	138.1 – 143.2	118.7 – 127.8	119 – 129.5	133.9 – 139.4
Conversion ratio		N/A	N/A	4.08	3.93	1.003
Maximum cooling temp. difference (°C)		N/A	N/A	-0.6	-0.17	0.73

5.1.5 Rayleigh-Taylor Instability Assessment

One common finding was the development of pressure amplitude instability, and evidence of an associated barrier to piston motion that limited the excitation levels achievable with the system. For each configuration tested, there existed a transition charge pressure that—when exceeded for a particular heater temperature—would result in large fluctuations in the recorded pressure amplitudes of each gas space. At charge pressures below this transition value, the developed pressure amplitudes would remain relatively constant and smooth over the course of a particular experiment. An example of this is given in Figure 5.57, which shows six experiments with charge pressures close to the transition pressure. The experiments used in this example come from the 3HEAT data set with 150 ºC heater temperatures and 115 ml liquid pistons.

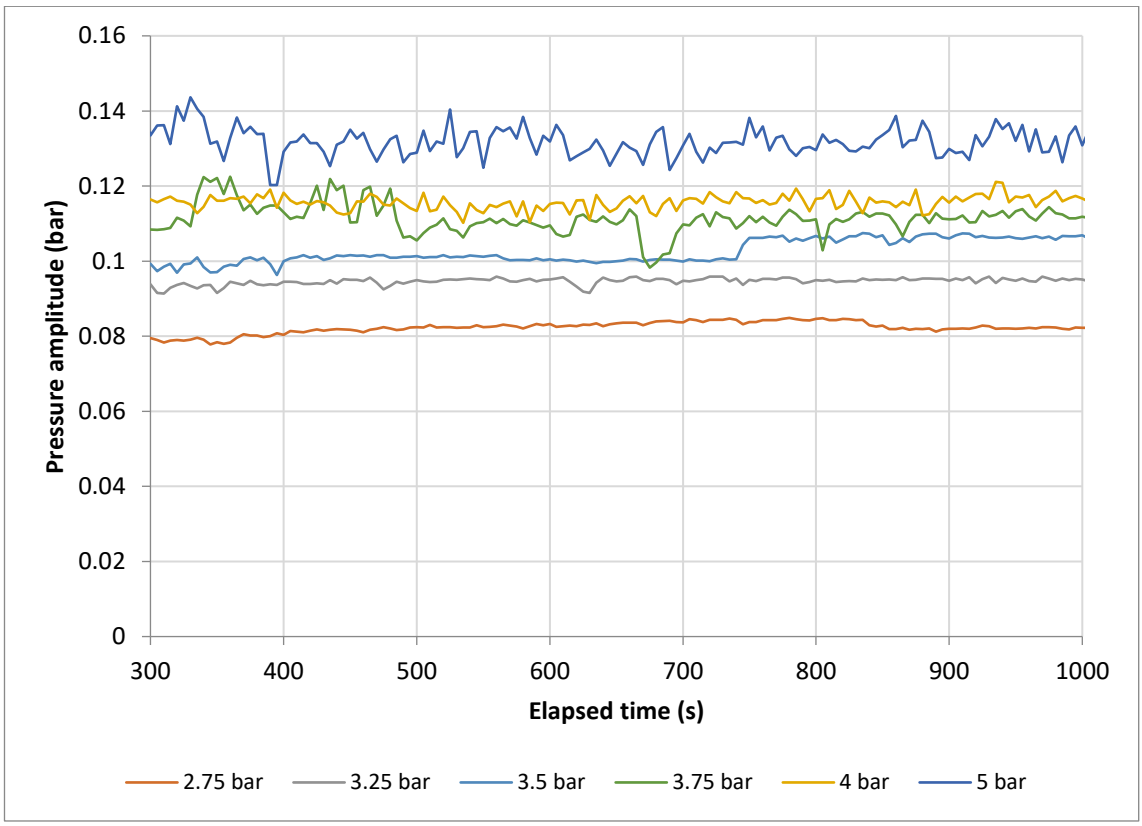

Figure 5.57 – Pressure amplitude stability for different charge pressures. Experiments are all from 3HEAT 150°C data set with 115 ml pistons.

The experiments at 3.5 bar (or below) produce pressure amplitudes that are relatively stable, while those at 3.75 bar (or above) are much more volatile, and show sudden and large fluctuations around a mean value. This same pattern is found when analysing the results of all of the data sets for the 15 mm experiments: that is, every configuration and heater temperature produced a similar occurrence of a transition from stability to instability. The charge pressures corresponding to this transition point were dependent on the heater temperature—with higher temperatures leading to lower transition pressures. In order to understand the cause of this phenomenon, the stability of the liquid pistons and their surfaces must be assessed. Figures 5.58 and 5.59 show the piston displacement profiles produced by the capacitive sensors for two of the experiments from the Figure 5.57. The first is from the 3.25 bar charge pressure experiment, and the second from the 5 bar experiment.

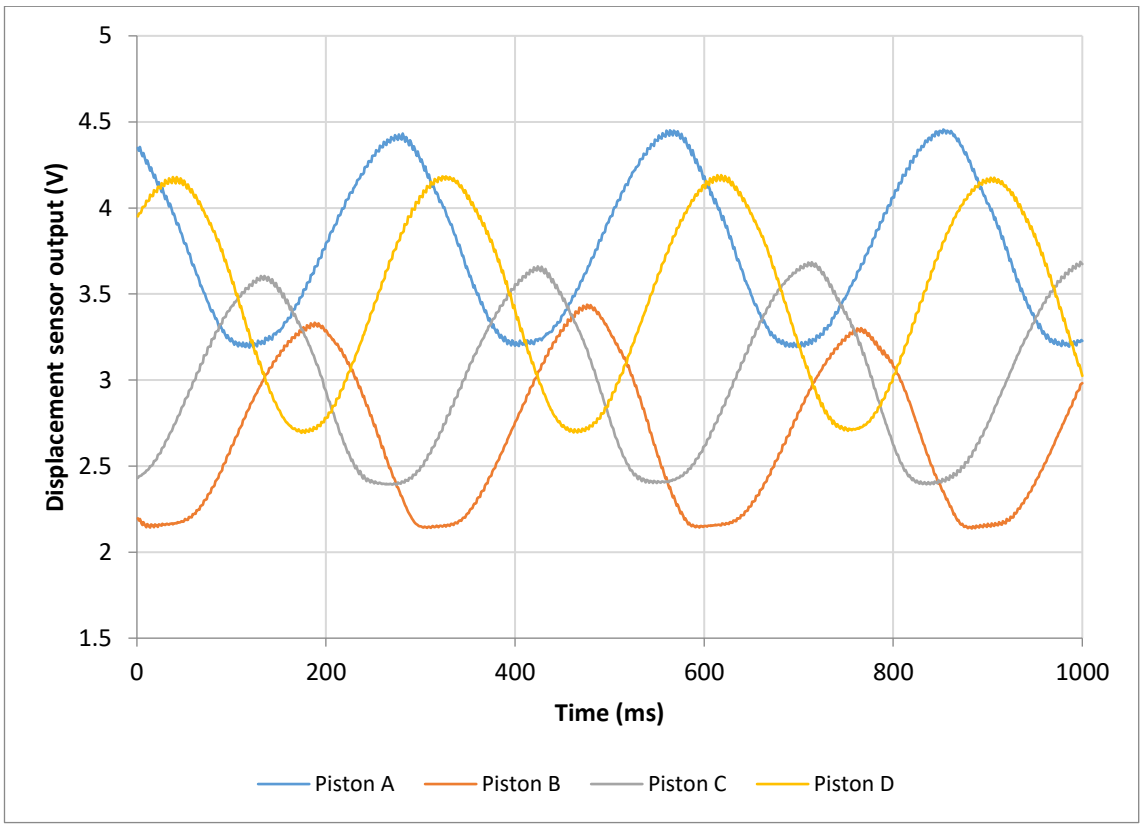

Figure 5.58 – Piston displacement profiles over a one second interval at 3.25 bar charge pressure. The experiment was with 3HEAT and 150°C heaters, using 115 ml liquid pistons.

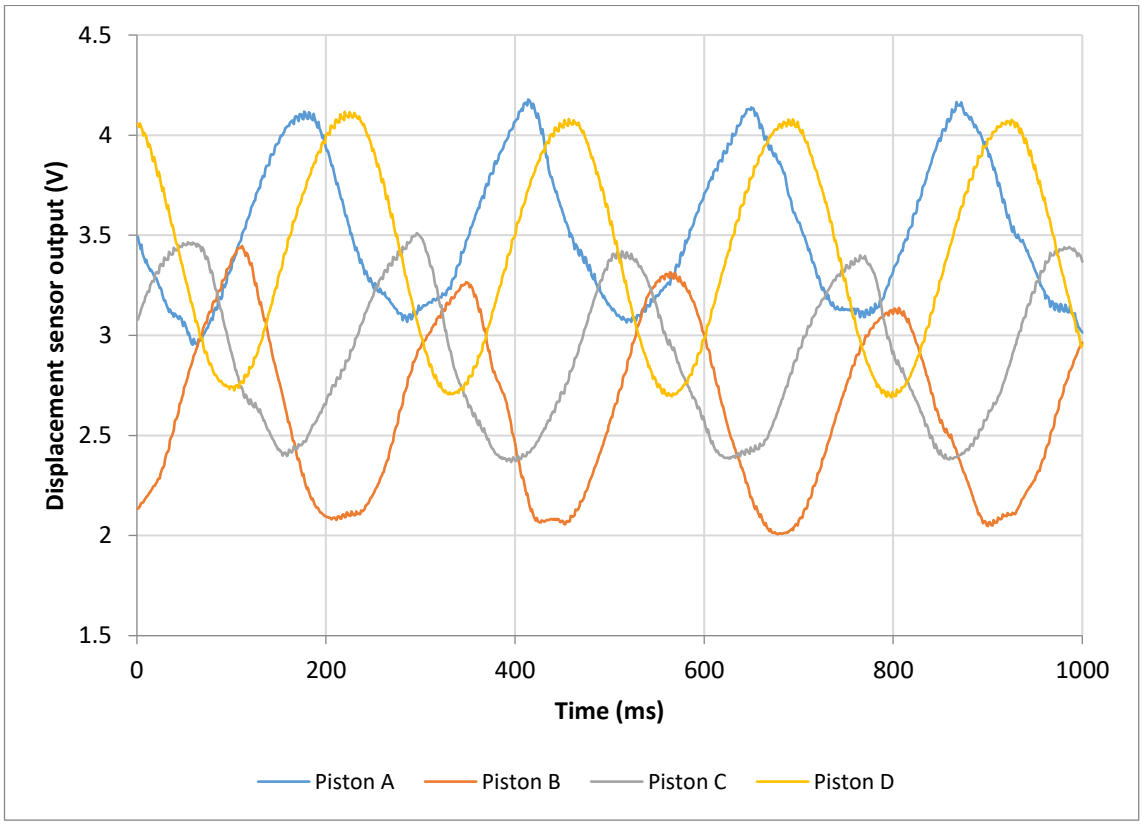

Figure 5.59 – Piston displacement profiles over a one second interval at 5 bar charge pressure. The experiment was with 3HEAT and 150°C heaters, using 115 ml liquid pistons.

Despite some slight flattening of the minimum turning points in the readings from the 3.25 bar experiment, the profiles themselves are very smooth and closely follow sinusoidal motion. This means that the liquid within the measurement volume is changing steadily (and in a repeatable way) each cycle, i.e. the piston oscillation is stable. The measurements from the 5 bar experiment are quite different. Three of the four piston profiles show irregular behaviour between cycles. The profiles retain the general sinusoidal shape, but exhibit periods of sudden accelerated or decelerated changes in capacitance. Although not noticeable from an observer's standpoint during the experiment, the liquid pistons are not perfectly stable in the 5 bar profile. It is likely that the instability is reducing the levels of excitation that would be achievable for an identical configuration with different liquid pistons—or, indeed, possibly solid pistons.

The Rayleigh-Taylor (RT) instability was considered as a potential explanation for the development of this piston instability. The RT instability, which is outlined in Appendix II, imposes an acceleration limit on the interface of two fluids having different densities, i.e. before the exponential growth of surface perturbations. It is possible to check whether the RT instability is causing the piston instability by evaluating the maximum piston accelerations that are experienced during each experiment. Figure 5.60 shows the average maximum piston accelerations sustained for the 115 ml experiments using the 15 mm piston tubes. The maximum accelerations that are sustained by the pistons begin to rise at pressures of 2 bar–4 bar—a region that normally exhibit stable pressure amplitude and piston displacement profiles. Beyond the transition pressures associated with each data set, the maximum accelerations do not show significant increases. None of the experiments were able to sustain accelerations above 30 ms^{-2}. Observing the two highest temperature data sets for each configuration, 105ºC for 4HEAT and 150ºC for 3HEAT, the maximum accelerations rose at a close to linear rate before abruptly plateauing at 4 bar, and staying within the range of 25ms^{-2}–30 ms^{-2}.

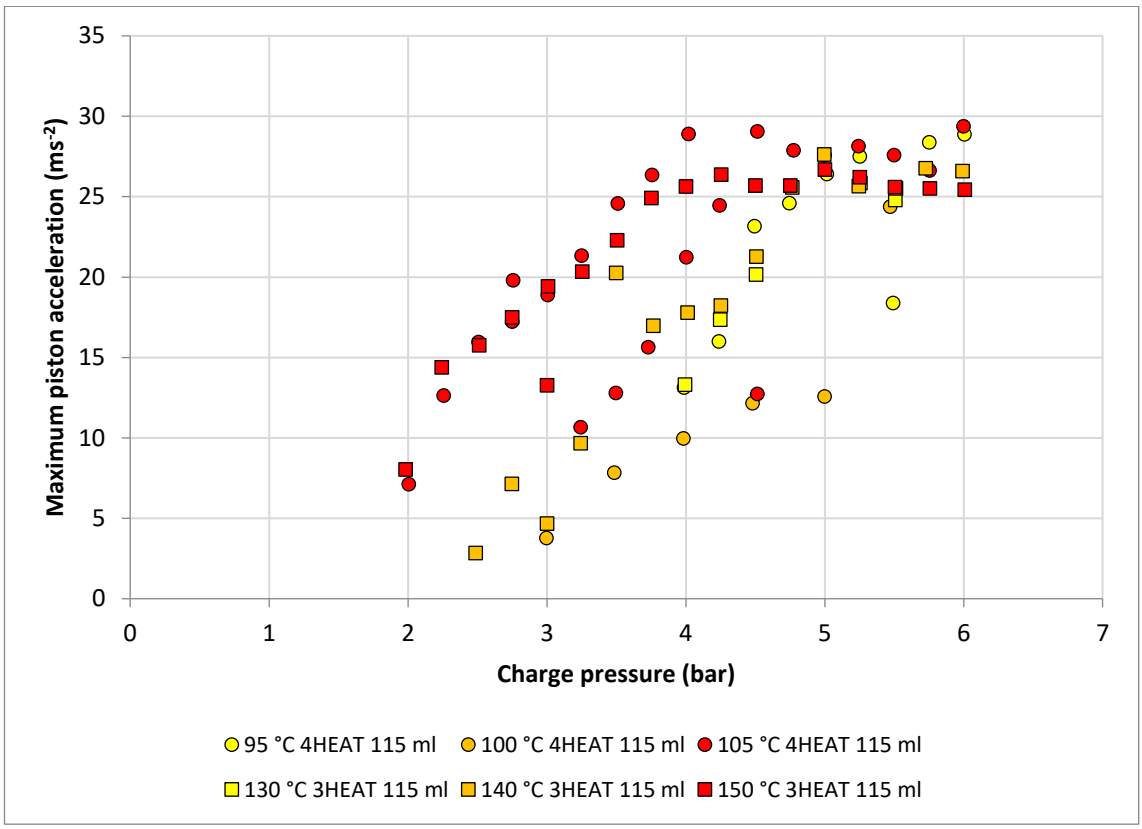

Figure 5.60 – Average maximum piston acceleration for experiments with 115 ml pistons and 15 mm piston tubes.

This would also potentially explain why the profiles of different heater temperatures seem to merge at higher operating pressure. With increased heater temperatures it is expected that the gap between excitation levels would remain across the entire spectrum of considered charge pressures; however, as seen previously, some of the pressure amplitudes developed at higher charge pressures are the same for different temperatures. If a physical limit on piston motion exists, then these results (i.e. with different data sets converging on the same values) would be an expected outcome. This is not conclusive evidence that an acceleration limit exists, but it does provide a basis for exploring this possibility when considering the Sage model predictions, and the second experimental investigation in later chapters.

5.2 Sage Modelling Results

5.2.1 Initial Validation and Sensitivity Analysis

In order to validate the model, the Sage predictions are first compared with those of the 4HEAT configuration. The solutions for the 4HEAT configuration are the easiest to obtain with Sage, due to the symmetry between gas spaces and piston motion. Figure 5.61 shows the frequency predictions produced with the Sage model compared with the experimentally obtained values. In both cases the results are for the 4HEAT configuration with 100ºC heaters and 100 ml pistons.

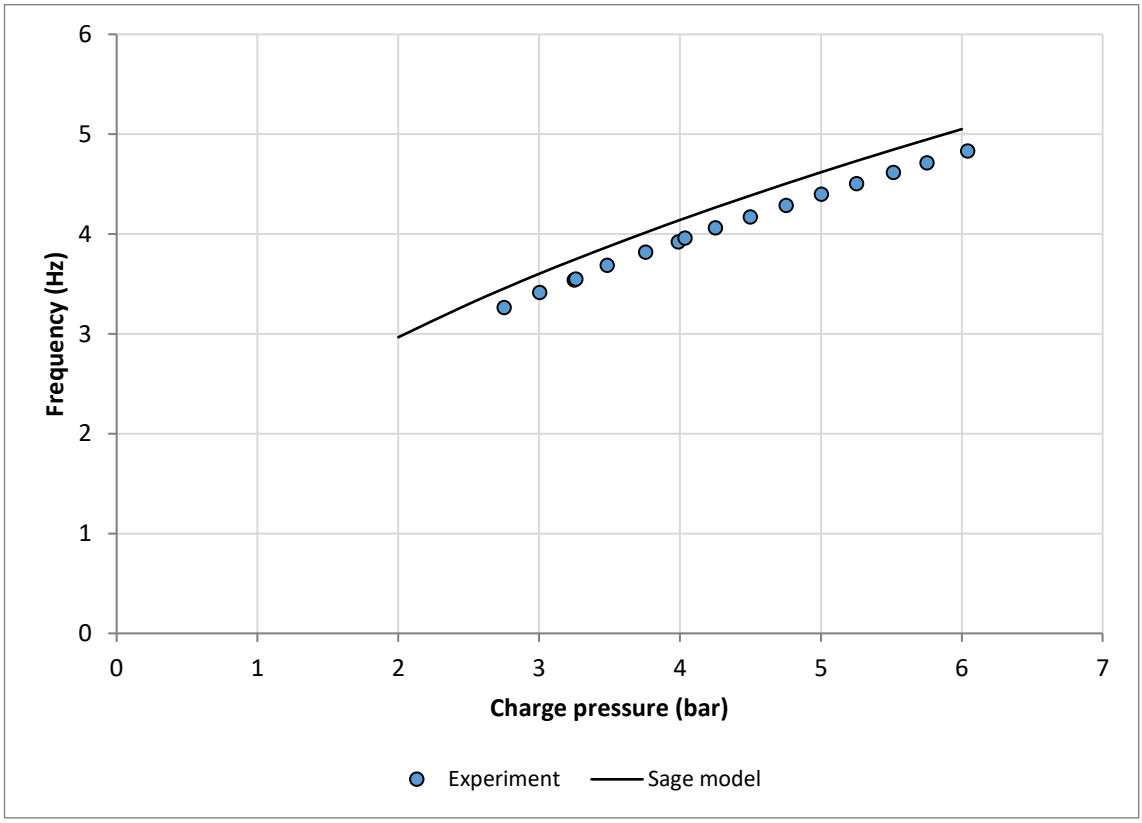

Figure 5.61 – Sage model predictions for operating frequency. 4HEAT configuration with 100°C heaters and 100 ml pistons.

It is evident that the Sage model is reasonably effective at predicting the operational frequency. The largest difference between predicted frequency and actual frequency occurs at 4 bar charge pressure and is 5.3%. This discrepancy remains relatively constant across the pressure range, remaining within 4.3%–5.3 %. Similar accuracy was achieved

when modelling the 115 ml pistons. Figure 5.62 shows the piston amplitudes predicted for the same set of simulations compared with the measured quantities from experiment.

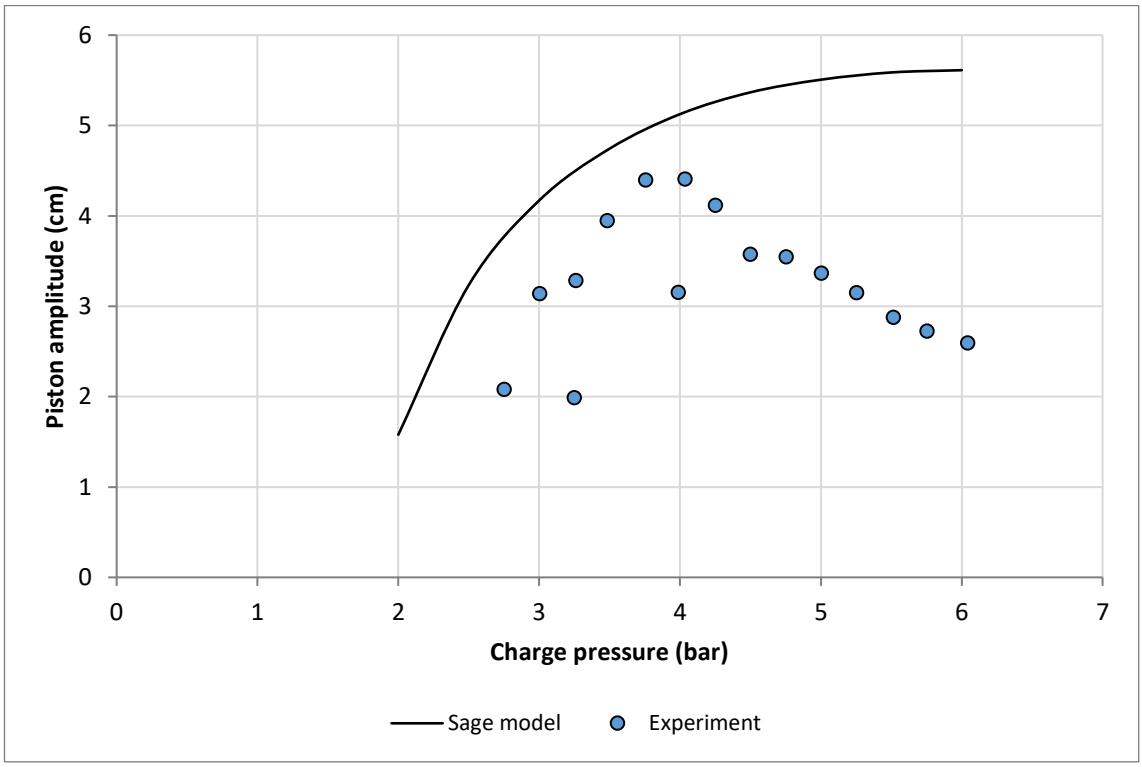

Figure 5.62 – Sage model predictions for piston amplitude. 4HEAT configuration with 100°C heaters and 100 ml pistons.

The Sage model does not predict piston amplitudes as accurately as frequency. It consistently overestimates piston amplitude, and although the model follows the same trend, and seems to agree reasonably well with the profile of the experimental results at the lower operating pressures (<4 bar), the predictions begin to diverge at higher charge pressure. This was a very interesting discovery that was not initially explainable. It seemed likely that the underlying cause is associated with the differences between liquid pistons (as used in the experiments) and solid pistons (upon which the Sage model bases its liquid piston approximation). This is further evidence of a potential physical limitation affecting the liquid pistons, which only materialises upon reaching some threshold of operation. At this stage it is inconclusive, but aside from this discrepancy, the Sage model was more accurate than expected, and capable of assessing potential performance improvements. A number of physical parameters used in the model are subject to

variation in reality. It is important to know how sensitive the model is to changes in these parameters, and therefore a sensitivity analysis (that, for the time being, ignores the discrepancies in piston amplitude) was carried out as follows:

Liquid piston viscosity – The dynamic viscosity of the water being used as liquid pistons influences the calculation of the viscous damping coefficient within the Sage model. As explained in Section 4.2.7, this value attempts to approximate the viscous energy losses associated with piston motion. The viscosity of water is not constant; it depends primarily on temperature. Since one side of the water column is in close proximity to heated gas then the water temperature can gradually change over the course of an experiment or a set of experiments. Figure 5.63 shows what happens to the Sage simulation results when the viscosity within the model is changed to reflect 20°C, 25°C and 30ºC water. The viscosity of water at these temperatures was taken to be 1.0×10^{-3} Nsm^{-2}, 8.9×10^{-4} Nsm^{-2} and 8.0×10^{-4} Nsm^{-2}, respectively.

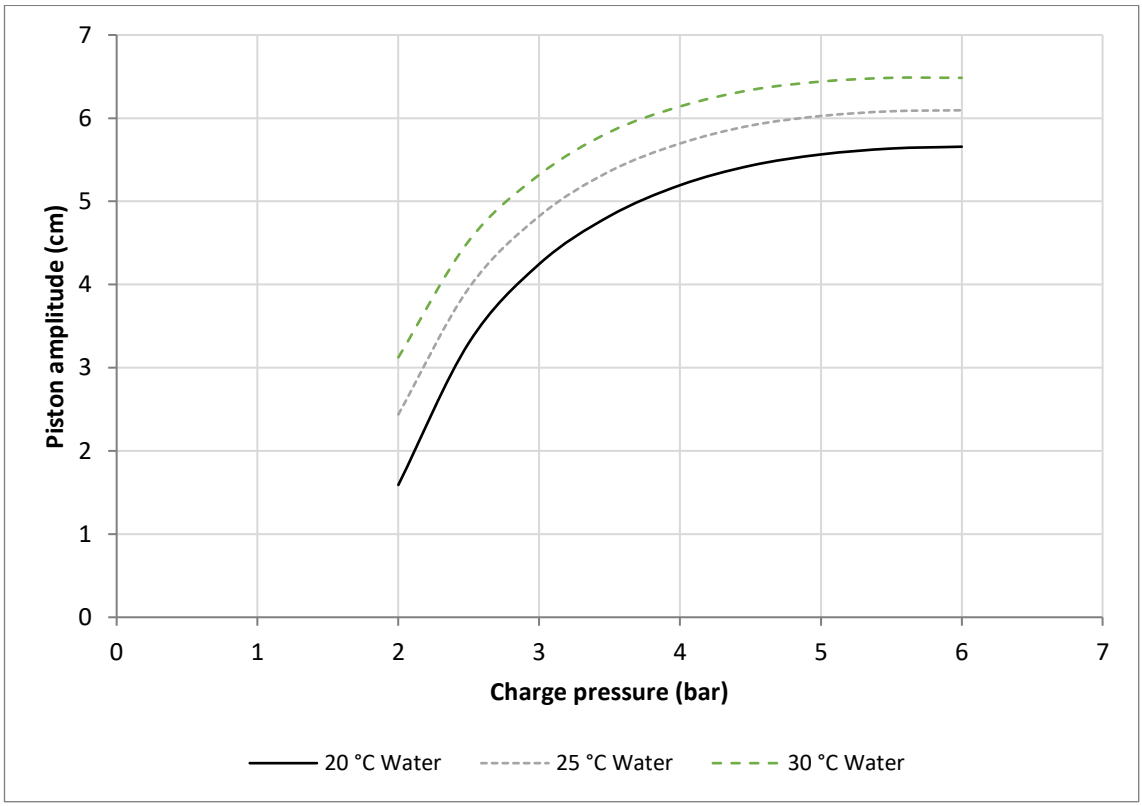

Figure 5.63 – Sage model predictions of piston amplitude for different water viscosities. 4HEAT, 100ºC and 100 ml simulation.

For an increase in water temperature of 10°C, the model predicts the piston amplitude can rise by roughly 10 mm, regardless of charge pressure. This effect is more significant at lower pressure, doubling the amplitude for simulations at 2 bar—while at 6 bar the difference is 14.6% between 20°C and 30°C water.

Sum of kinetic flow loss coefficients – The sum of the minor flow loss coefficients is used to estimate the energy dissipation caused by geometric changes in the flow path of the piston. The U-tube housing of the piston can be thought of as having two smooth 90º bends at its base (or a single 180º bend) and being otherwise straight. At the position where the steel tube transitions to PVC tube there is also a small change in cross-section; although the change in diameter produces a negligible flow loss coefficient compared to the other features. The contribution of these effects is estimated with a ΣK sum of 0.5 (see Section 4.2.7). Figure 5.64 shows the sensitivity of the model predictions with ΣK values of 0.5, 0.75 and 1.0.

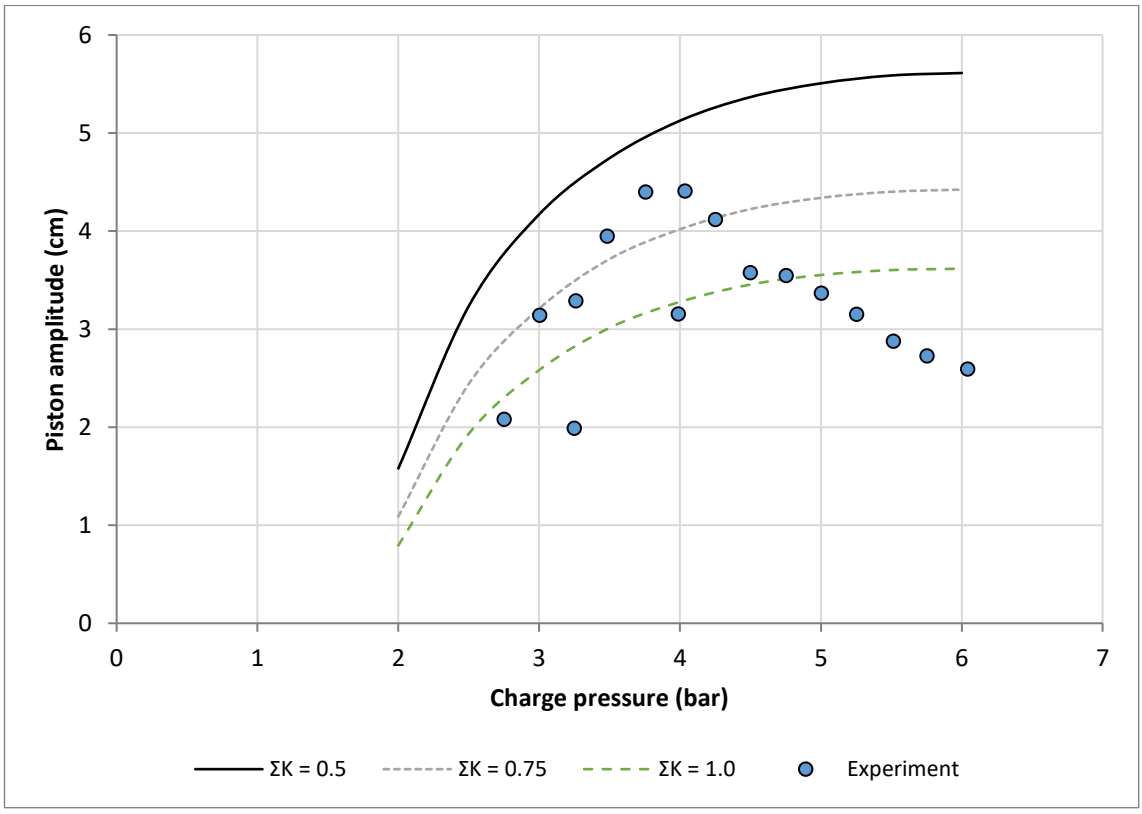

Figure 5.64 – Sage model predictions for piston amplitude with different values for the sum of the minor pipe flow loss coefficients. 4HEAT simulations with 100ºC heaters and 100 ml pistons.

The impact of the minor pipe flow loss coefficients appears roughly proportional to piston amplitude and therefore more significant as piston amplitude increases. For ΣK values of 0.5 and 1.0, differences of 1.6 cm (38.1%) and 2.0 cm (35.6%) at 3 bar and 6 bar charge pressure, respectively, are generated.

Heater temperatures – The influence of heater temperatures has already been demonstrated experimentally. It is expected that with increased heat source temperature the piston amplitudes would also increase, although in the real test-rig this was complicated by the evidence of multi-modal behaviour. It is important to consider the sensitivity of the model to heat source temperature when interpreting model predictions. Figure 5.65 shows the model's sensitivity to 5ºC changes in heater temperature.

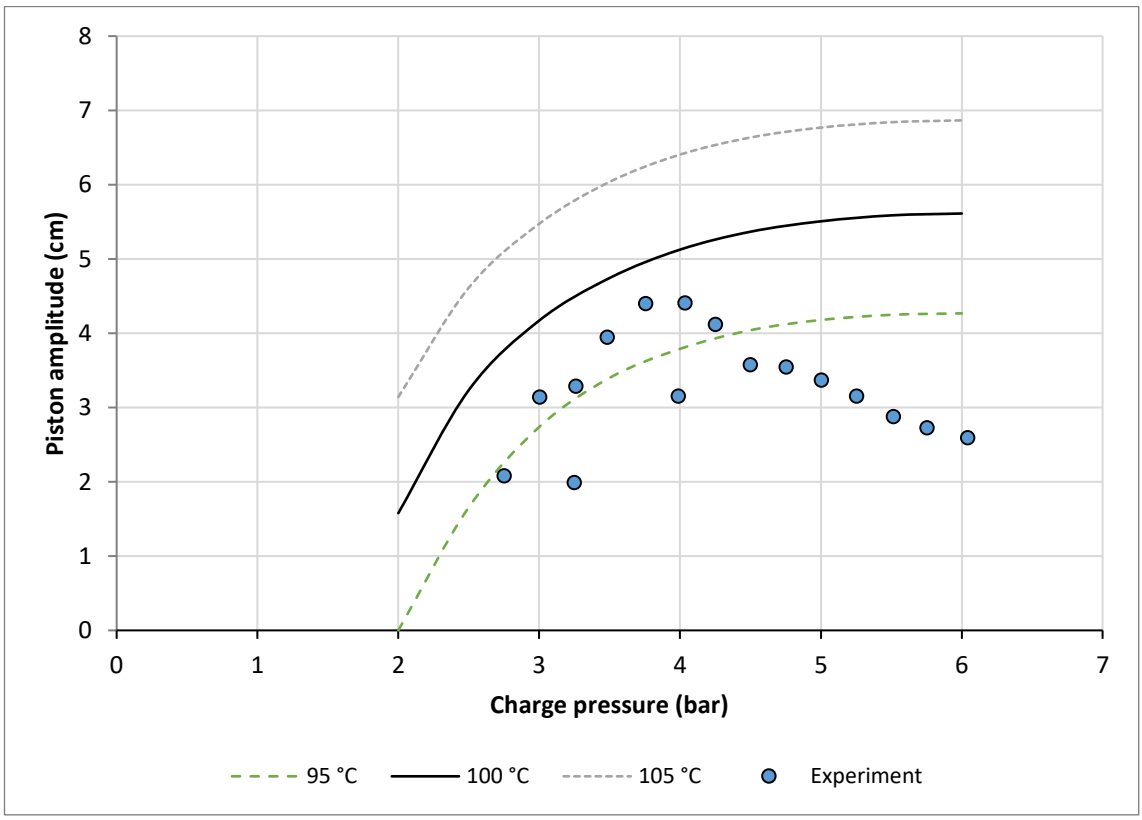

Figure 5.65 – Sage model predictions for piston amplitude with different heater temperatures. 4HEAT simulations with 100 ml pistons.

The influence of heater temperature is as expected: increased temperatures produce increased amplitudes; and, as witnessed during experimentation, the heater temperature

directly impacts the lower limits of charge pressure at which the system is capable of achieving self-sustained operation. But the magnitude of the influence of heater temperature is very surprising—a 1.5% change in heater temperature is capable of producing a 23.9% difference in piston amplitude even at the high operating pressure of 6 bar.

Heat rejection temperatures – As with heater temperature, the heat sink temperatures also play a role in influencing the performance of the LPSC machine. In the model, the heat sink (or rejector) temperature is set at 24ºC. Figure 5.66 displays the model sensitivity to changes in the ambient temperature value of ± 5ºC.

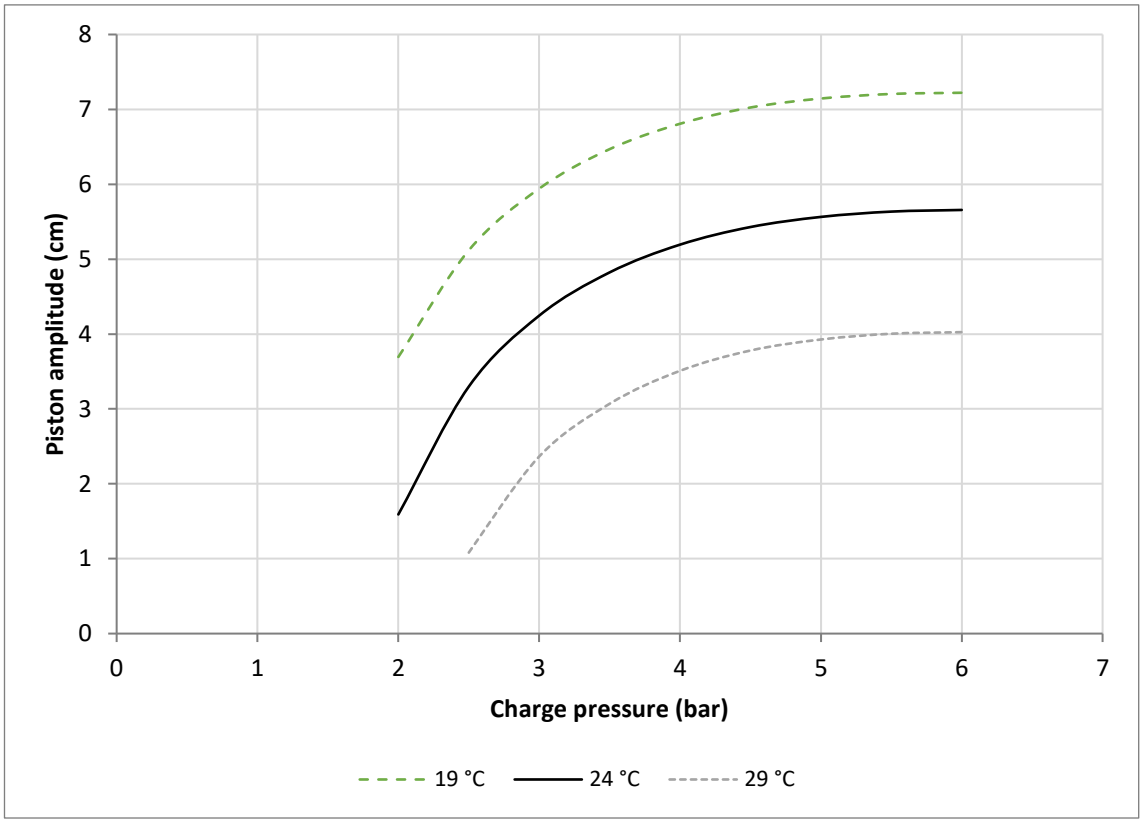

Figure 5.66 – Sage model sensitivity to heat rejection temperature. 4HEAT simulations with 100ºC heaters and 100 ml pistons.

The effect of altering the rejection temperature has the reverse impact of changing the heater temperatures—with higher temperatures decreasing piston amplitude. This is as one would expect for any thermodynamic machine: the output being dependent on the

temperature difference between the sink and source temperatures. In this case, the same change of ± 5ºC produces a more significant change in the piston amplitudes than for the heater temperature. At 6 bar the difference between 24ºC and 29ºC is 28.8%.

In summary, the model has been shown to be relatively sensitive to liquid viscosity, minor pipe flow loss coefficients, heat source and heat sink temperatures. Small changes in these parameters (1%–10%) can produce larger differences in the piston amplitude predictions (20%–40%). When considering the LPSC system dynamics, this type of outcome is what one would expect from a complicated multi-system, MDOF free-piston machine in which the dynamic and thermodynamic behaviour feeds back into itself. Small changes in important system parameters can produce larger fluctuations that compound and give rise to different levels of operation. This was shown experimentally (and previously discussed in Section 5.1) with multi-modal behaviour of the system arising in many different experiments and with no perceptual change in the governing parameters. Fortunately, these sensitivities seem limited to the outputs of the machine that are associated with the level of excitation, and not the characteristic dynamic traits such as phase angles and relative piston/pressure amplitudes that define each configuration. Obtaining an understanding of these traits will provide a direction for improving the fundamental system performance.

5.2.2 4HEAT Model

The Sage model predictions for frequency and piston amplitude for the 4HEAT system were briefly compared to experimental results in the preceding section on validation and sensitivity. The remaining variables of general significance are now compared with the results from Section 5.1.1. Table 5.6 shows the pressure and displacement amplitude phasors generated by Sage at 4 bar, 100ºC and 100 ml pistons. Figure 5.67 then displays the scaled versions of these phasors.

Table 5.6 – Sage model phasors predictions for 4HEAT experiment at 4 bar with 100°C heaters and 100 ml pistons.

Phasor	Amplitude (bar or cm)	Phase angle (°)
Pressure 1 (P1)	0.194	0
Pressure 2 (P2)	0.195	90.0
Pressure 3 (P3)	0.194	180.0
Pressure 4 (P4)	0.195	270.0
Displacement A (XA)	5.29	139.3
Displacement B (XB)	5.28	229.4
Displacement C (XC)	5.28	319.2
Displacement D (XD)	5.28	49.3

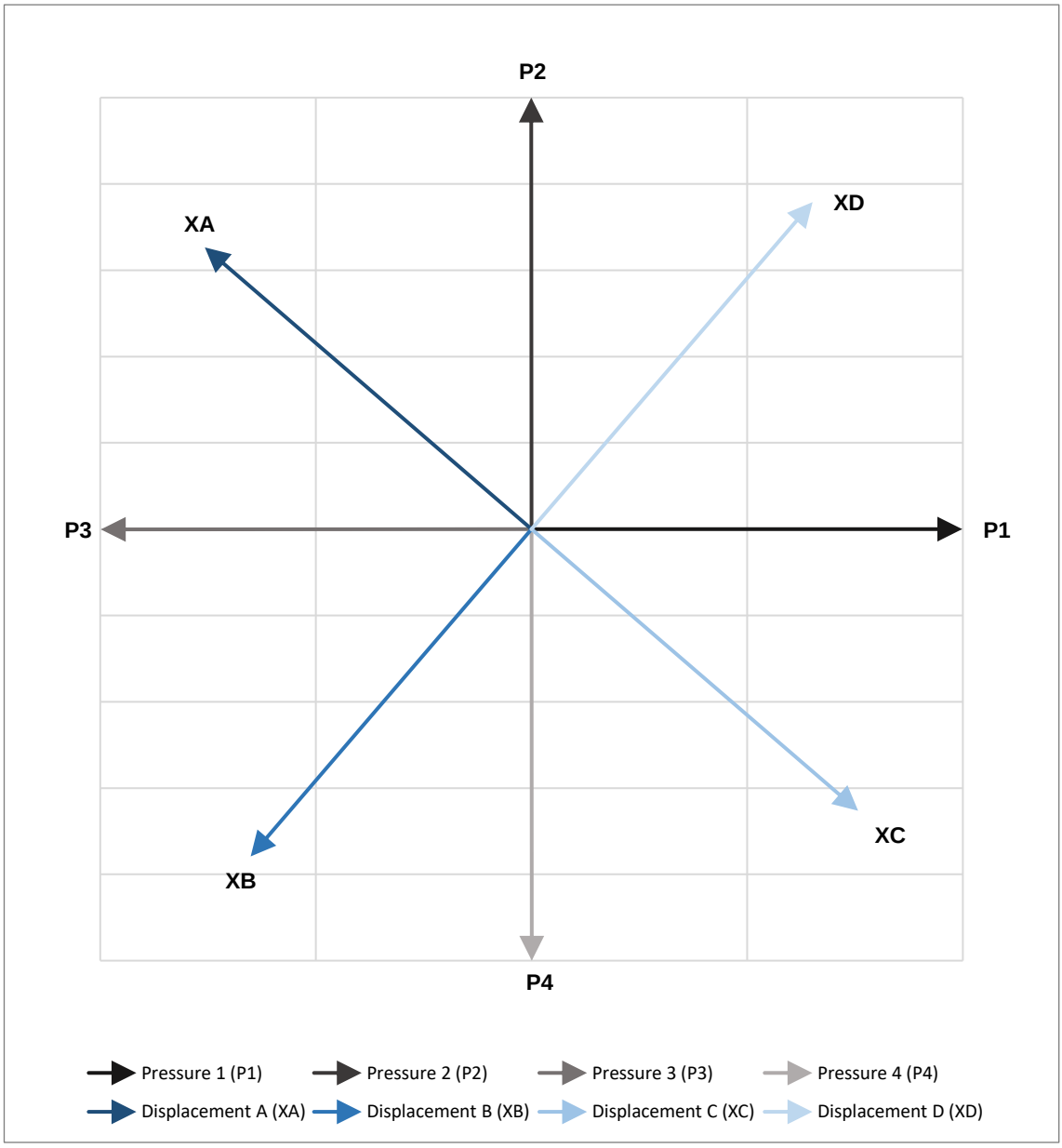

Figure 5.67 – Phasor plot of example 4HEAT Sage simulation pressure and displacement profiles. The phasor magnitudes have been scaled for more clarity. Simulation is at 4 bar charge pressure with 100°C heater temperatures and 100 ml pistons.

The phasor plot has many similarities to the example 4HEAT phasor plot from Figure 5.6. As expected in the 4HEAT configuration: (a) the pressure phasors are spaced exactly 90º apart, and (b) the displacement phasors a spaced exactly 90° apart—although the displacement phasors are not exactly spaced at 45º angles to the pressure phasors. Instead, all four appear to have a 5º anti-clockwise offset from the 45º bisector. In the case of the net pressure phasor acting on Piston A, this would have the form P1 minus P2 and would have a phase angle of -45º relative to P1. Since all four pressure phasors have the same magnitude then they should not skew the piston displacements. The 5° differences are a consequence of friction acting on the pistons from the damper within the Sage model. As discussed in Section 2.3.2, the friction phasor contributes to the phase of the net force acting on the piston, meaning it is skewed slightly from the 45° angle of the net pressure phasor. Figure 5.68 quantifies the phase angles for the phasor plot.

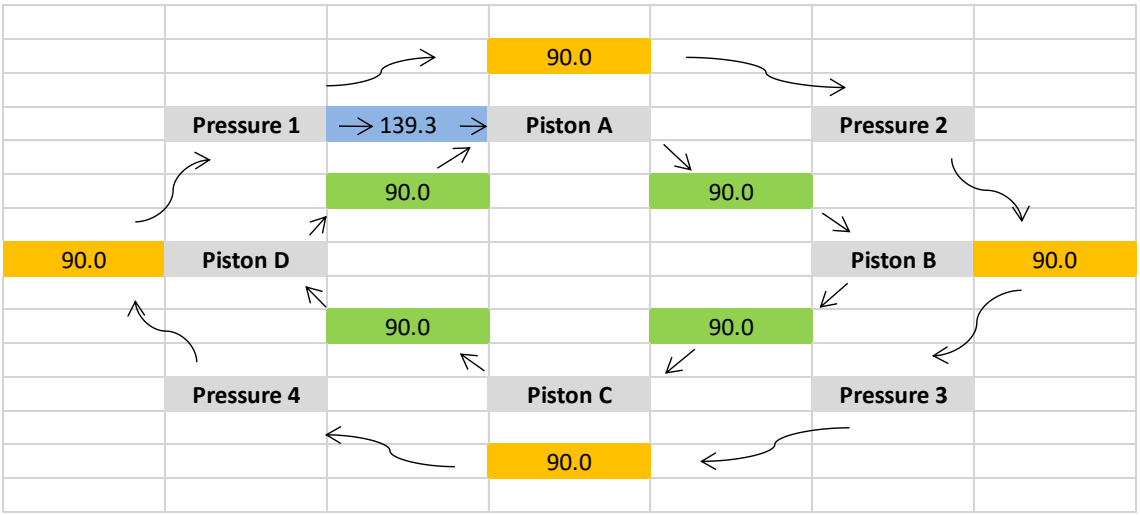

Figure 5.68 – Pressure and displacement phase angles for 4HEAT Sage simulation.

The relative phase angles of 90º are confirmed in Figure 5.68. The value highlighted in blue, 139.3º, represents the relative phase angle between the pressure in GS1 and piston A's displacement. Figure 5.69 shows the Sage model predictions for pressure amplitude compared with the experimental results over the 2 bar–6 bar range. Figures 5.70 and 5.71 show the trends for the relative phase angles between pressure and displacement phasors.

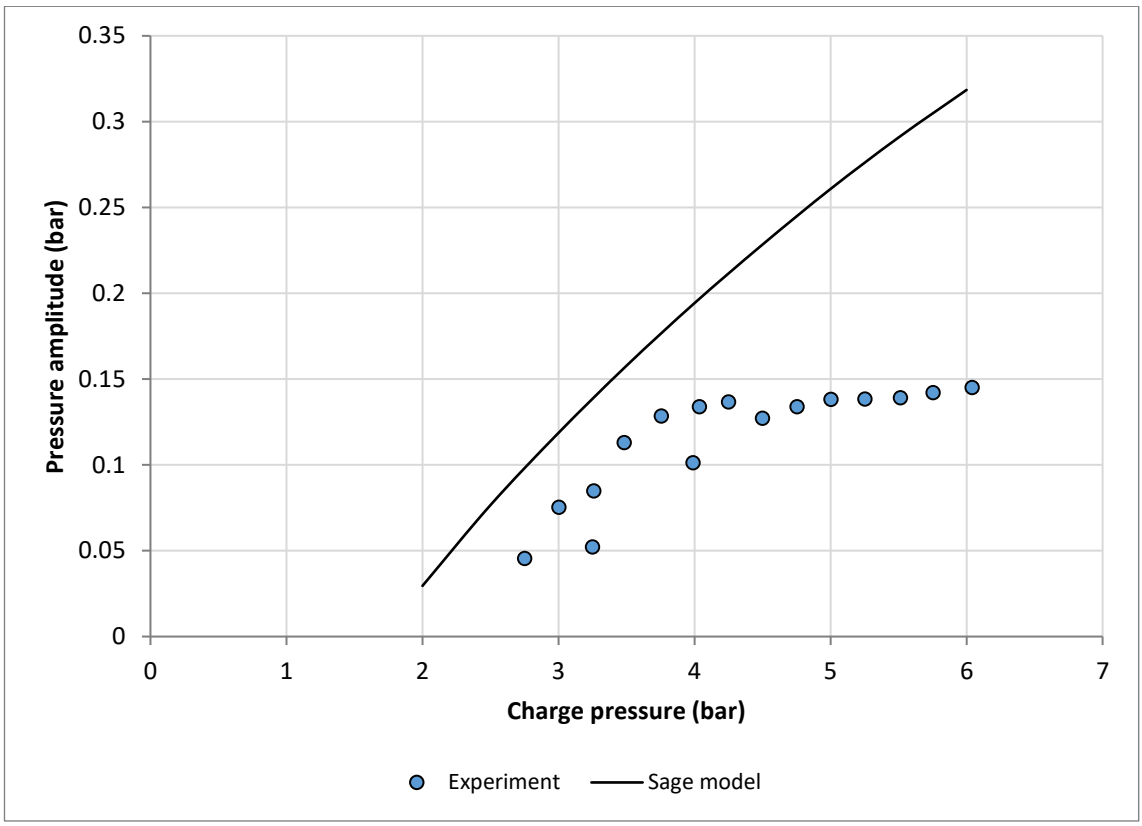

Figure 5.69 – Sage model pressure amplitude variations compared with experimental results for 4HEAT experiments conducted with 100°C heater temperatures and 100 ml pistons.

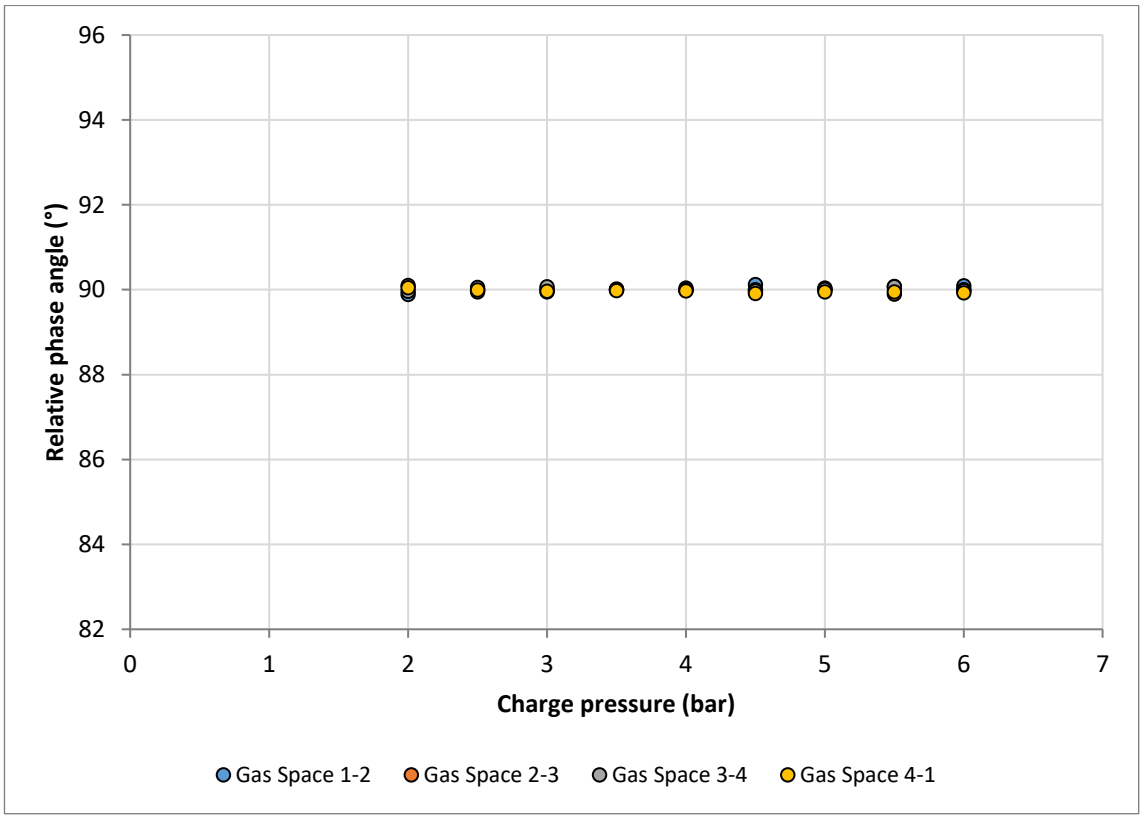

Figure 5.70 – Sage model predictions for the relative phase angles between pressure amplitude phasors. Simulations are for 4HEAT with 100°C heater temperatures and 100 ml pistons.

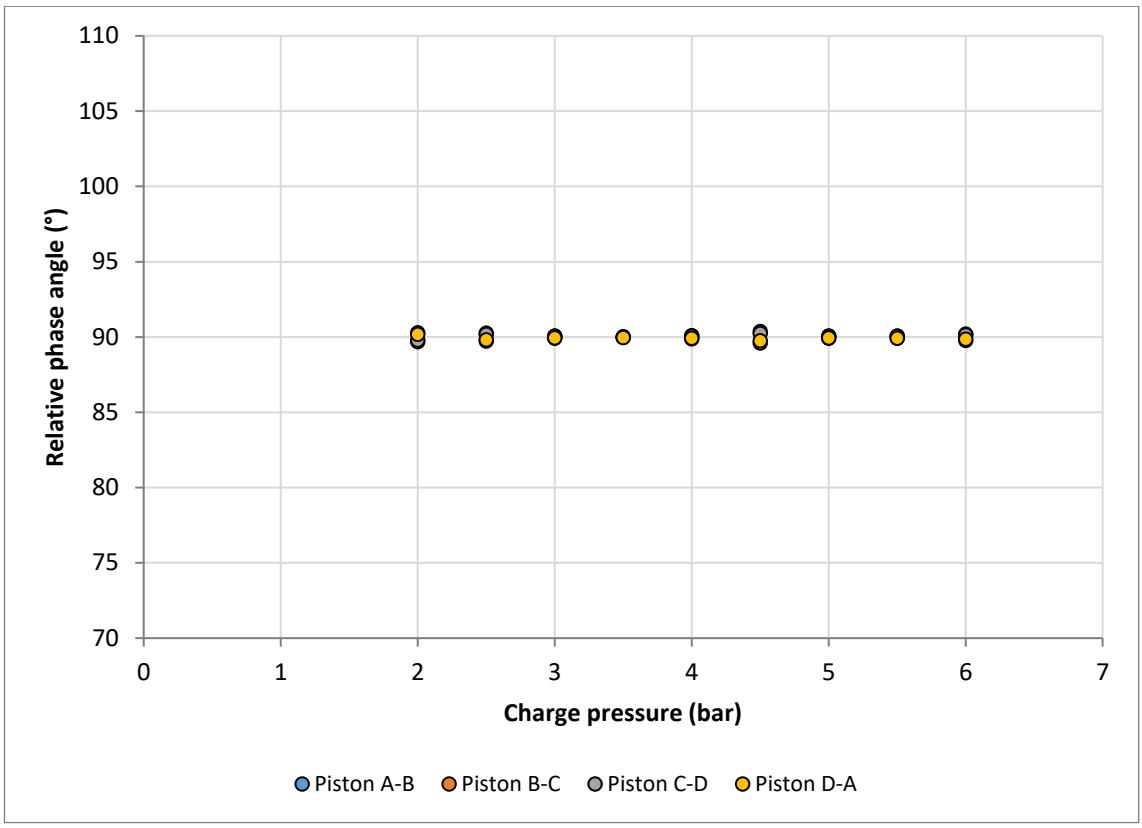

Figure 5.71 – Sage model predictions for the relative phase angles between piston amplitude phasors. Simulations are for 4HEAT with 100°C heater temperatures and 100 ml pistons.

Figure 5.69 shows a similar trend to the comparison with piston amplitudes; the behaviour of the model and the test-rig are offset but similar up until approximately 4 bar, when the experiment trend changes considerably and appears to plateau, not exceeding 0.15 bar pressure amplitude. The phase angle trends in both cases are as anticipated: they remain roughly constant and are independent of charge pressure. Results that are not shown include the temperature difference trends between expansion and compression spaces, which exhibited less than 1ºC change across the entire pressure range.

5.2.3 3HEAT Model

The true test of the Sage model is how it handles the 3HEAT and 2HEAT configurations, which are no longer constrained by symmetry. This section shows the characteristics of the 3HEAT configuration as predicted by the Sage model. Table 5.7 shows the pressure and displacement amplitude phasors generated by Sage at 4 bar, 150ºC heater temp and 100 ml pistons. Figure 5.72 then displays the scaled phasor plot for the same simulation.

Table 5.7 – Sage model phasors predictions for 3HEAT experiment at 4 bar with 150°C heaters and 100 ml pistons.

Phasor variable	Amplitude (bar or cm)	Phase angle (°)
Pressure 1 (P1)	0.195	0.0
Pressure 2 (P2)	0.322	90.4
Pressure 3 (P3)	0.199	180.3
Pressure 4 (P4)	0.268	270.4
Displacement A (XA)	5.92	125.6
Displacement B (XB)	5.92	243.7
Displacement C (XC)	5.25	311.3
Displacement D (XD)	5.17	59.2

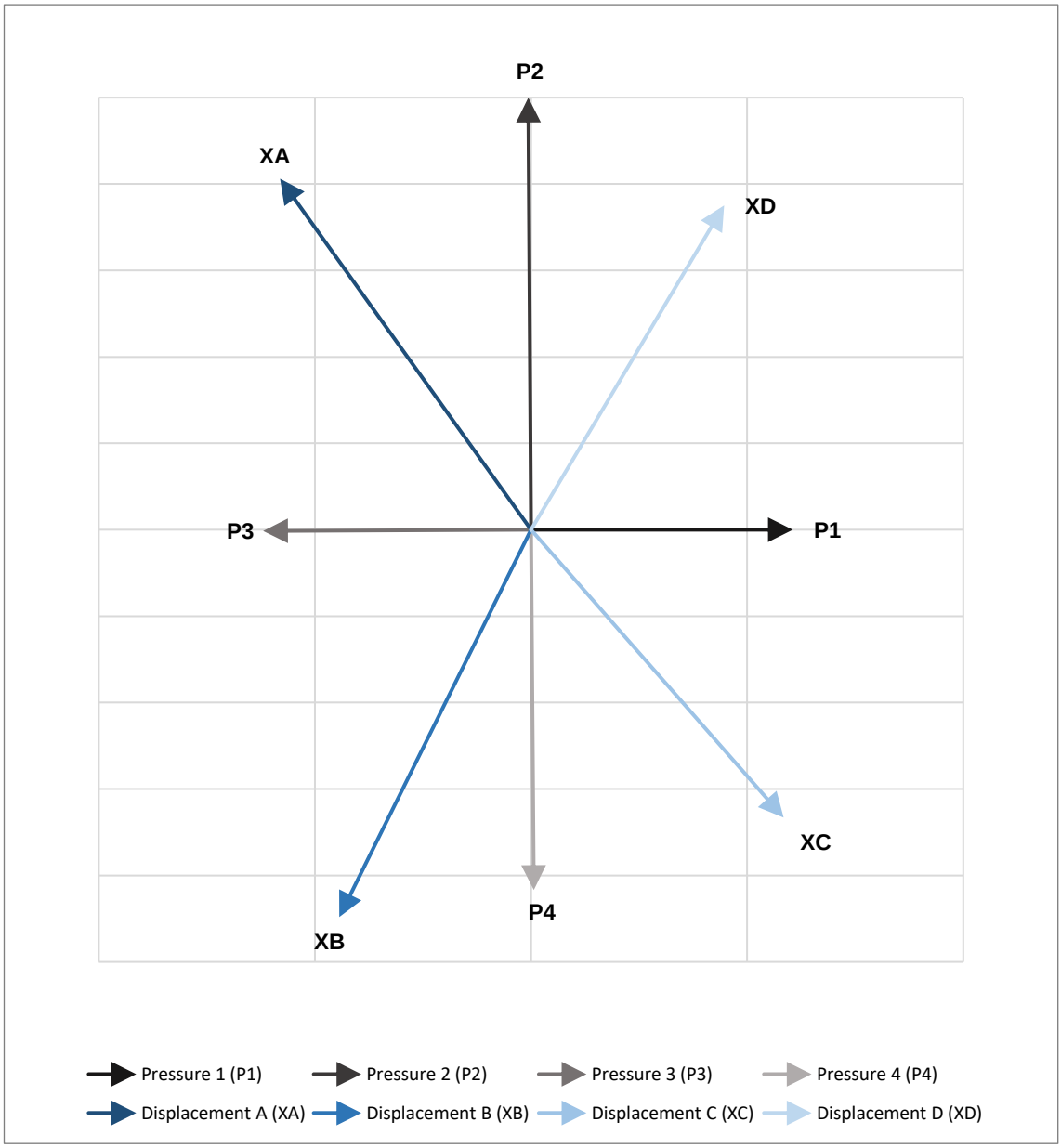

Figure 5.72 – Phasor plot of example 3HEAT Sage simulation pressure and displacement profiles. The phasor magnitudes have been scaled for more clarity. Simulation is at 4 bar charge pressure with 150°C heater temperatures and 100 ml pistons.

The first impression from this phasor plot is that phasor orientations look very similar to the experimentally obtained versions (see Figure 5.23 in Section 5.1.2). The pressure phase angles remain close to the 4HEAT predictions, which in Sage's case is almost exactly 90º. The P2 and P4 phasors have the largest magnitudes, and the displacement phasors are skewed vertically in the same manner as seen experimentally. Similarly, the magnitudes of P1 and P3 are almost identical to each other. The difference in magnitude between the largest (P2) and the smallest (P1) is 0.127 bar or 39.4%. The relative phase angles are again quantified in Figure 5.73 for better comparison with the experiment.

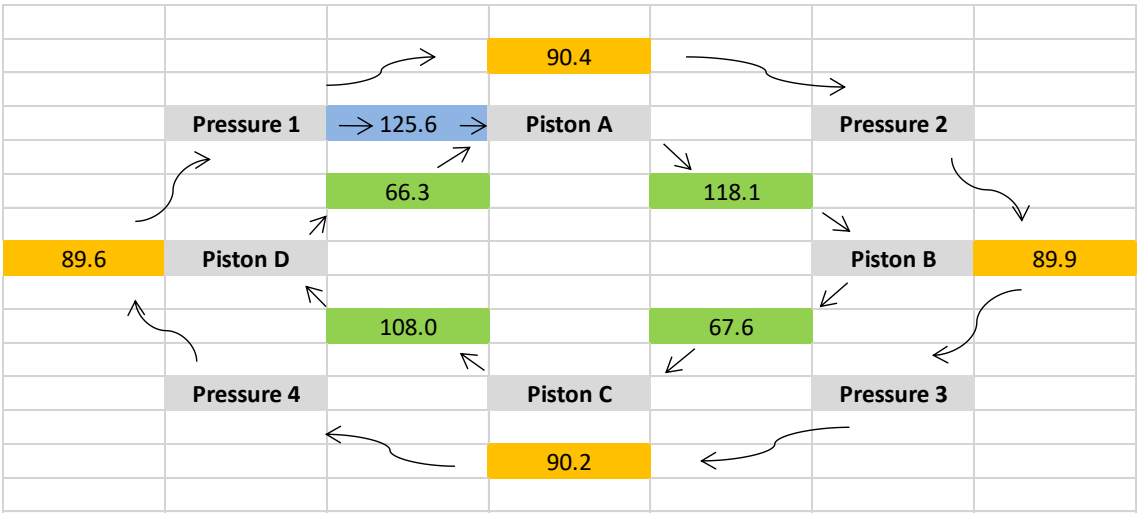

Figure 5.73 – Sage model predictions for the relative phase angles between pressure and displacement phasors in the example 3HEAT simulation. Simulation is at 4 bar charge pressure with 150ºC heater temperatures and 100 ml pistons.

The first comparison can be made for the relative phase angle between P1 and Piston A (highlighted in the blue box). The example experiment recorded a value of 124.0º, while Sage predicts 125.6º. These values are very similar, differing by only 1.3%. The values in the yellow boxes differ more significantly, with discrepancies of up to 6.2º. However, it is important to note that the pressure phase angle differences remained approximately constant across the entire experimental investigative range, and were independent of changes in configuration, temperature or pressure. This implies that their deviation from 90º resulted from physical imperfections in the symmetry between all four subsystems.

The Sage model pressure amplitude phase angles do retain their similarities to the model predictions for the 4HEAT pressure, which is of primary importance.

The final point of comparison for the phase angles is the piston displacements. The experimental results showed that relative phase angles of between 60°–80° could be expected for pistons B–C and D–A, and 100°–120° for pistons A–B and C–D. Specifically, at 4 bar the results were within 3º of the predictions, except for pistons A-B which differed by 5.8º.

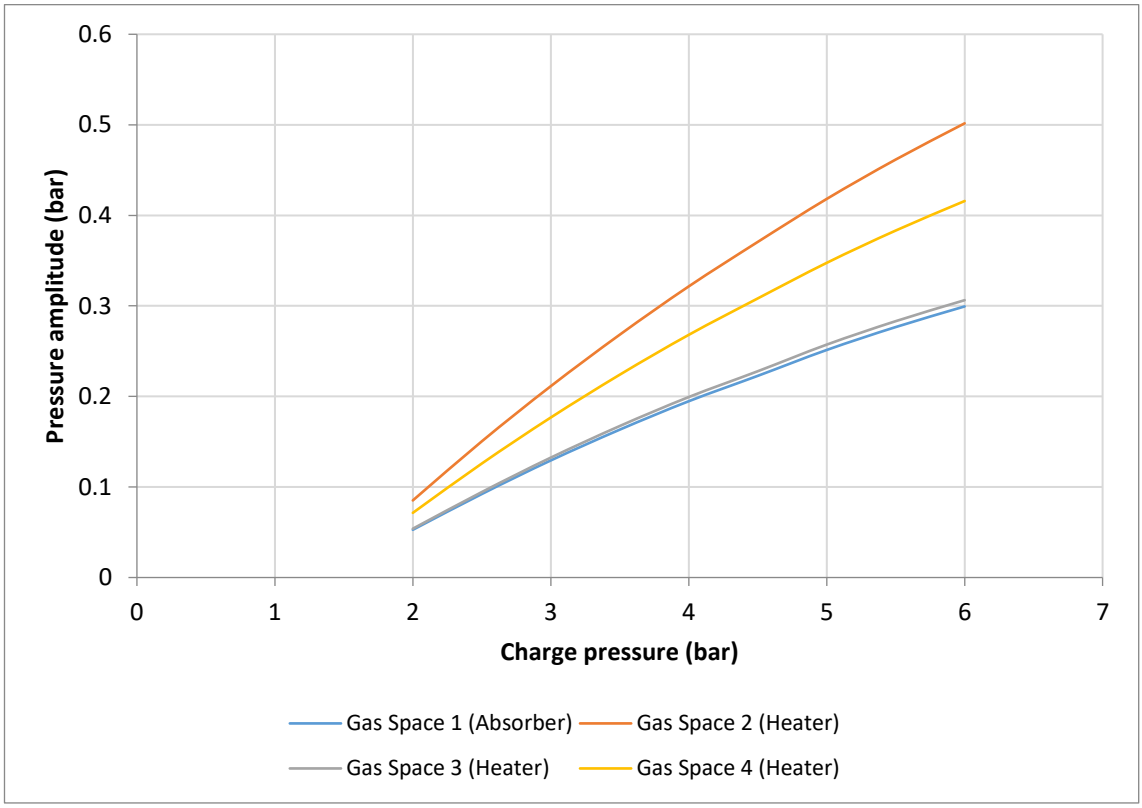

Figure 5.74 – Sage predictions for pressure amplitudes developed in all four gas spaces with increasing charge pressure for 3HEAT configuration. Simulations are with 150ºC heaters and 100 ml pistons.

The predicted pressure amplitudes for each of the gas spaces (shown in Figure 5.74) follow a similar pattern to the experimental results. The ratios between the magnitudes remain consistent from 2 bar–6 bar charge pressure. The ratios calculated and averaged over the simulation range are 1.65 (s = 1.1%), 1.02 (s = 0.04%) and 1.38 (s = 0.8%) for GS2, GS3 and GS4 respectively. The main differences compared with the experimental results from Section 5.1.2, are higher pressure amplitude magnitudes, and a less rapid

tapering off at higher charge pressure. This can be seen in Figure 5.75, which shows a direct comparison between Sage and experiment for the pressure amplitudes of GS1. The predicted amplitudes exceed the experimental values by a significant margin, even at lower pressure.

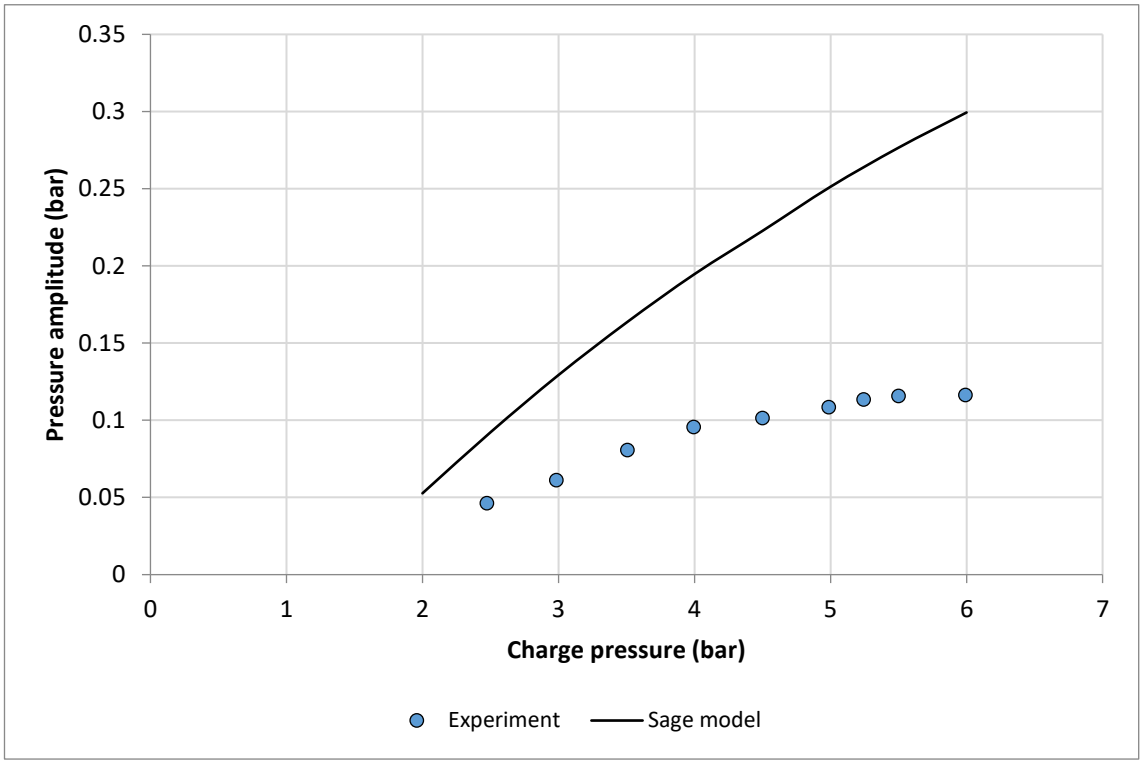

Figure 5.75 – Sage model predictions for pressure amplitude in Gas Space 1 compared with experimental results for 3HEAT configuration. 150°C heaters with 100 ml pistons.

At 4 bar, the predicted amplitude is 0.195 bar, which is 103% larger than the experiment value of 0.096 bar. This might seem like a large discrepancy (and it is) but as previously emphasised, the quantitative accuracy of the model is not of critical importance at this stage. It is much more important that the model predictions reflect the correct characteristics of each configuration and show similar trends. As demonstrated in the sensitivity analysis, small changes in the heater temperature, liquid viscosity and other variables can produce large changes in the pressure and displacement amplitudes—therefore a number of model variables could easily be altered in order to match the experimental results more precisely (but with no objective justification this might jeopardise the model validity when extrapolating the model to analyse different piston

sizes in later chapters). Once more results are obtained using different piston sizes then some of these sensitive parameters can be identified with greater certainty. Figures 5.76 and 5.77 show the piston amplitude versions of Figures 5.74 and 5.75. Unlike the piston amplitudes obtained from the experiments, the Sage model predicts distinctive differences in their magnitudes. Piston A and Piston B are predicted to have the largest amplitudes, which are very close in magnitude to each other. Piston C and D are predicted to have lower amplitudes—by almost 10 mm at 6 bar. This is explained by the magnitudes of the pressure phasors. With GS1 and GS3 having approximately the same magnitude, the significant contributions come from GS2 and GS4. The magnitude of GS2 is larger than GS4, therefore the pistons adjacent to that space (A and B) exhibit larger displacement amplitudes. The comparison between the average displacements in Figure 5.77 shows the same discrepancy seen between the pressure amplitude comparison in Figure 5.75, i.e. a significant overestimation by Sage.

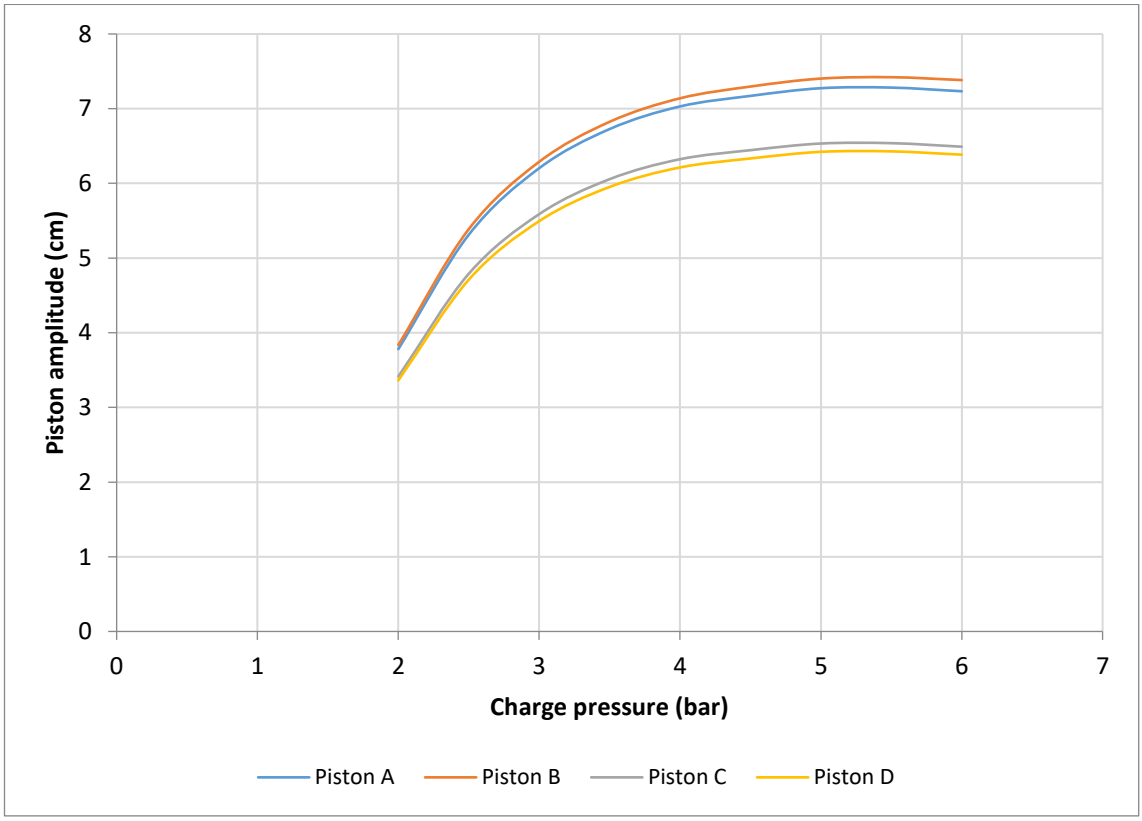

Figure 5.76 – Sage predictions for piston amplitudes with increasing charge pressure for 3HEAT configuration. Simulations are with 150°C heaters and 100 ml pistons.

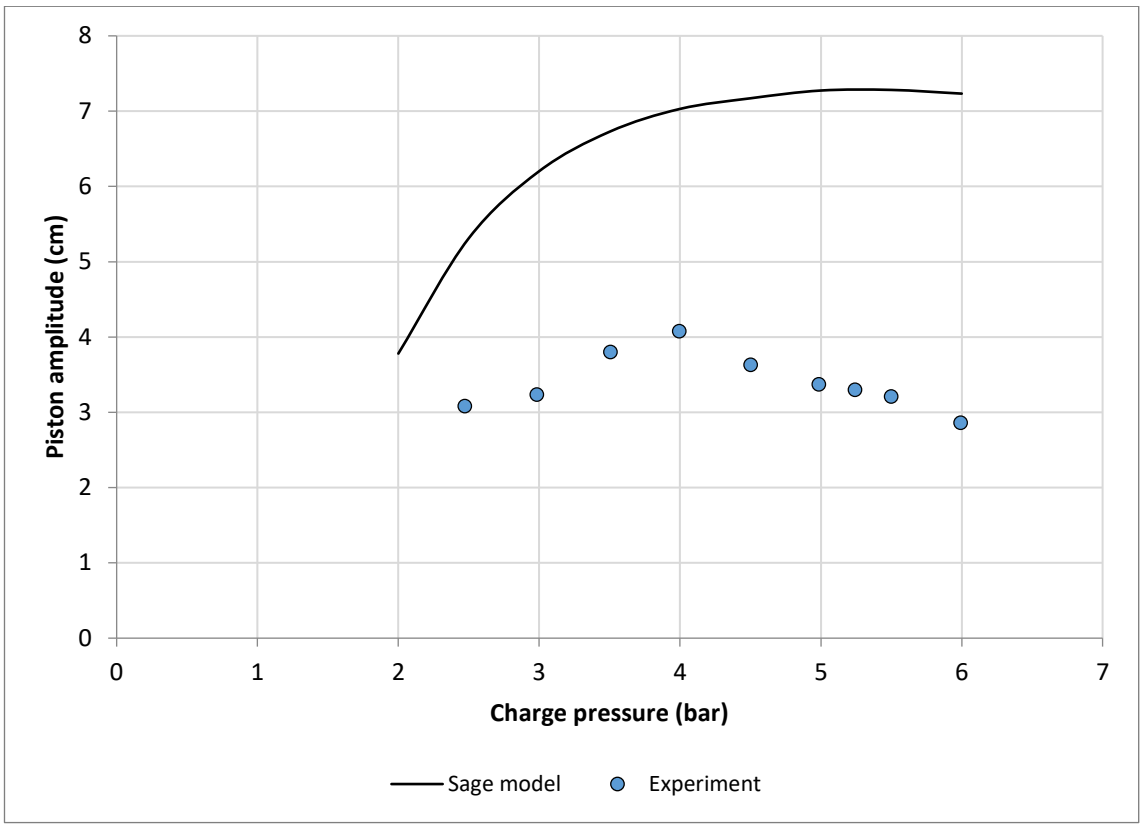

Figure 5.77 – Sage model predictions for Piston A amplitude compared with experimental results for 3HEAT configuration. 150°C heaters with 100 ml pistons.

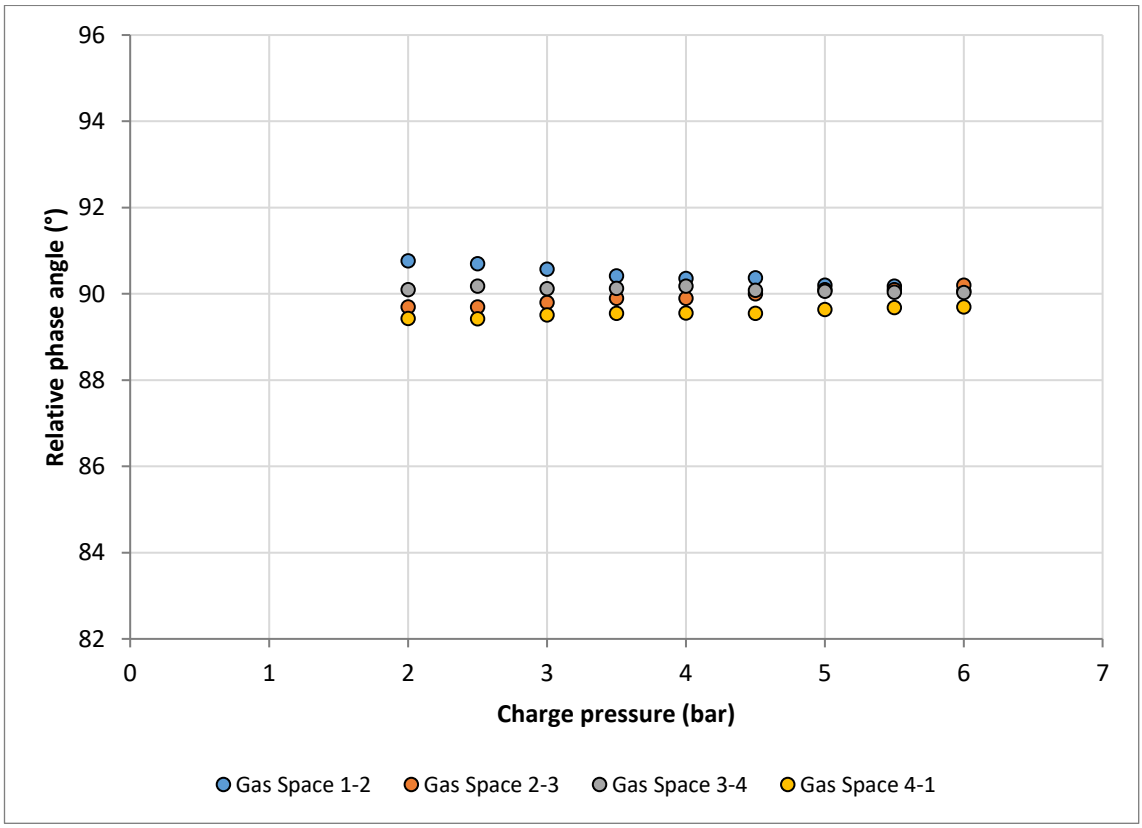

Figure 5.78 – Sage model predictions for the relative phase angles between pressure amplitude phasors. Simulations are for 3HEAT with 150°C heater temperatures and 100 ml pistons.

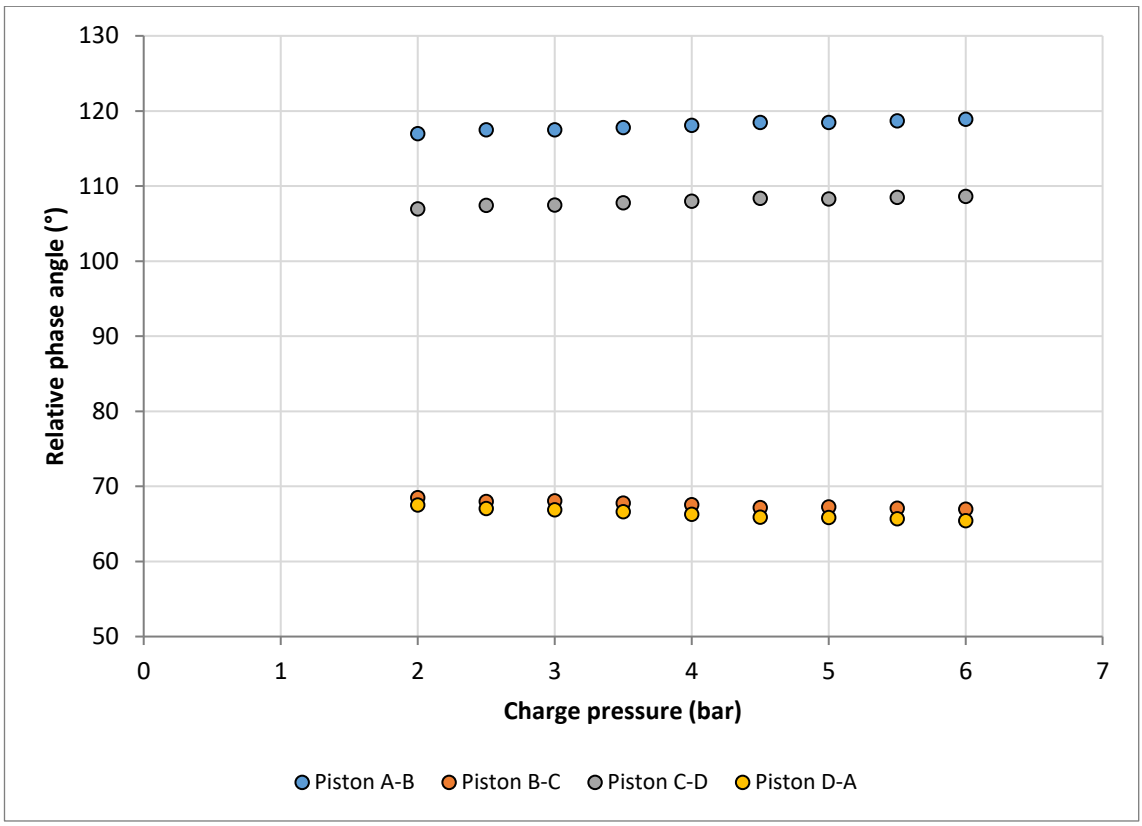

Figure 5.79 – Sage model predictions for the relative phase angles between piston amplitude phasors. Simulations are for 3HEAT with 150°C heater temperatures and 100 ml pistons.

The relative pressure and displacement phase angles are shown in Figures 5.78 and 5.79. As seen in the 4HEAT simulations, the Sage model predicts very little deviation in these values with increased charge pressure. This implies that the cause of the variation seen in the experimental values may either result from the piston instability or another physical phenomenon affecting the test-rig. This phenomenon, and why it might relate to the multi-modal behaviour, is discussed in Section 8.2.5.

There are a number of other performance indicators which can be identified with the model results that are not available from the experimental data. For now, only one will be assessed. That is the cooling efficiency or overall coefficient of performance of the machine based on heat input and heat absorbed. Figure 5.72 shows the COP predicted for the 3HEAT configuration with the same parameters outlined earlier.

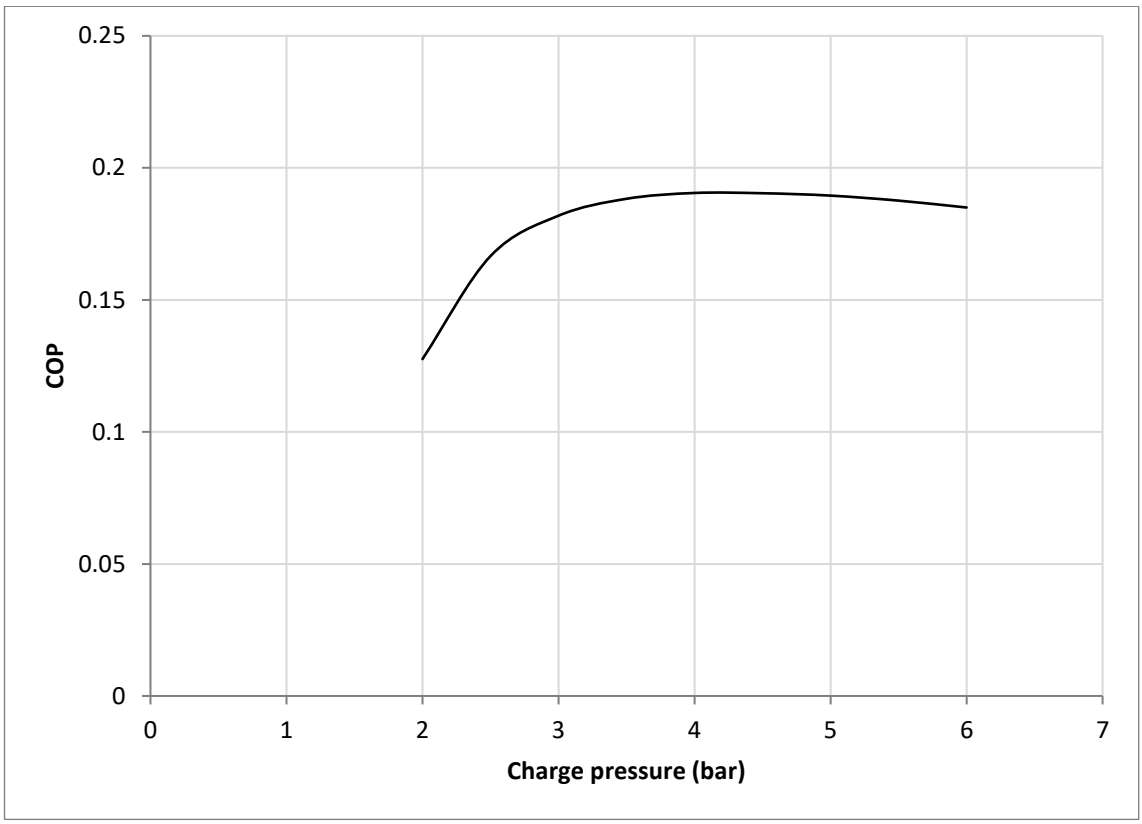

Figure 5.80 – Sage model coefficient of performance predictions for the 3HEAT configuration. Simulations are with 150 °C heaters and 100 ml pistons.

The COP values are relatively low and do not cross 0.2. The COP peaks at a charge pressure very close to what was found experimentally to be the 'sweet spot' of the system. It remains to be seen whether this is coincidental or if there is something linking these system traits.

5.2.4 2HEAT Model

This section shows the characteristics of the 2HEAT configuration as predicted by the Sage model. Unlike the experiments, the Sage model does predict functionality with 100 ml pistons at 190ºC. For consistency with the other Sage model results, these are presented instead of the simulations with 115 ml pistons. Table 5.8 shows the pressure and displacement amplitude phasors generated by Sage at 4 bar, 190ºC heater temp and 100 ml pistons. Figure 5.81 then displays the scaled phasor plot for the same simulation.

Table 5.8 – Sage model phasors predictions for 2HEAT experiment at 4 bar with 100°C heaters and 100 ml pistons.

Phasor variable	Amplitude (bar or cm)	Phase angle (°)
Pressure 1 (P1)	0.168	0.0
Pressure 2 (P2)	0.176	90.6
Pressure 3 (P3)	0.138	180.4
Pressure 4 (P4)	0.138	270.7
Displacement A (XA)	3.85	138.0
Displacement B (XB)	3.51	236.7
Displacement C (XC)	3.08	319.5
Displacement D (XD)	3.40	43.6

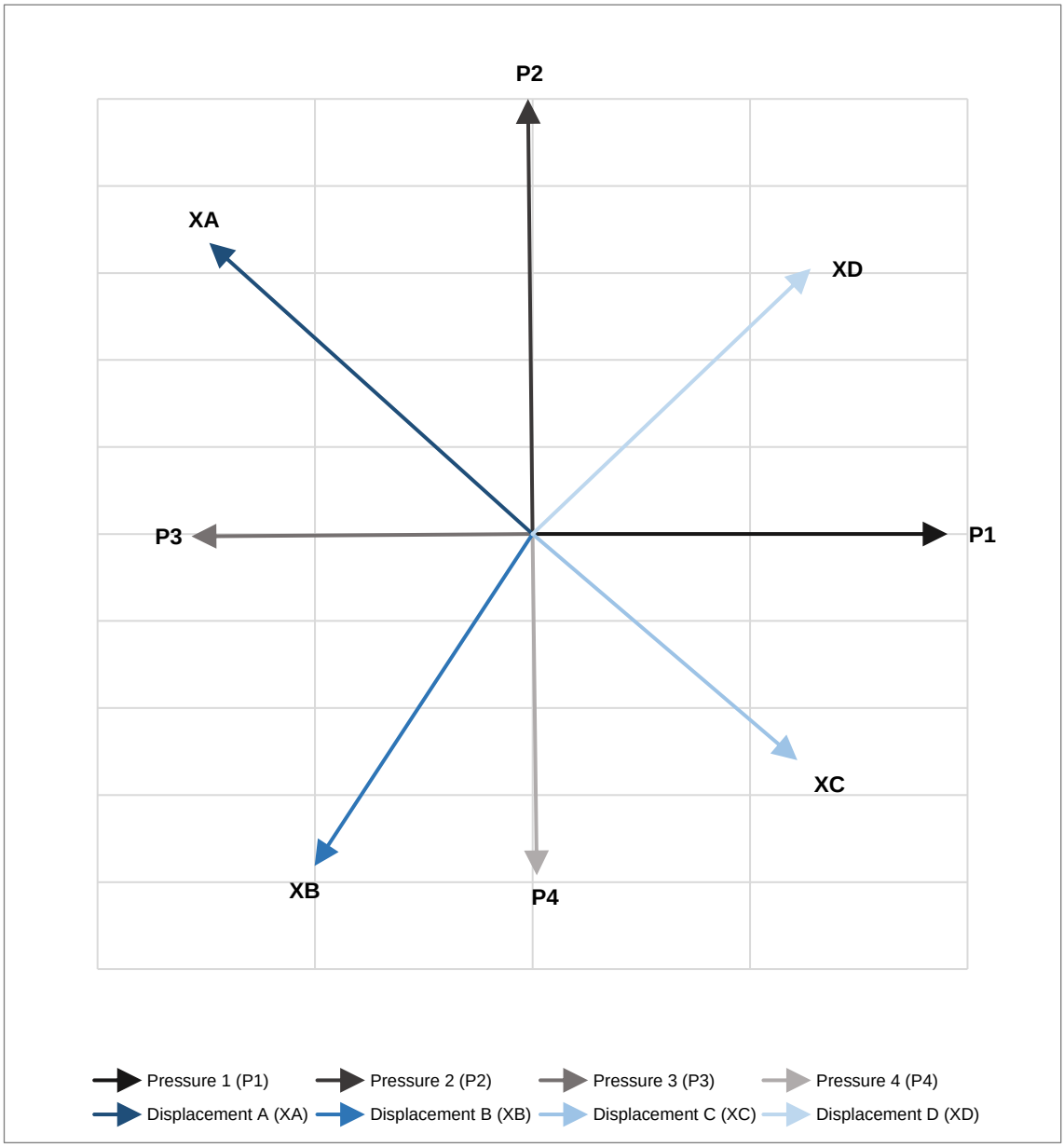

Figure 5.81 – Phasor plot of example 2HEAT Sage simulation pressure and displacement profiles. The phasor magnitudes have been scaled for more clarity. Simulation is at 4 bar charge pressure with 190°C heater temperatures and 100 ml pistons.

Again, the phasor plot produced from the Sage simulation looks very similar to the experimental phasor plot for the 2HEAT configuration with the pressure phasors retaining their similar phase angle interrelationships. The relative magnitudes of the pressure phasors are also similar to the experimental results, with P1 and P2 being the largest and closest to each other, P3 and P4 smaller but also very similar. The difference between the largest pressure amplitude, P2, and the smallest, P4, is much less than in the 3HEAT case, being only 21.6%. The relative phase angles between the phasors are given in Figure 5.82.

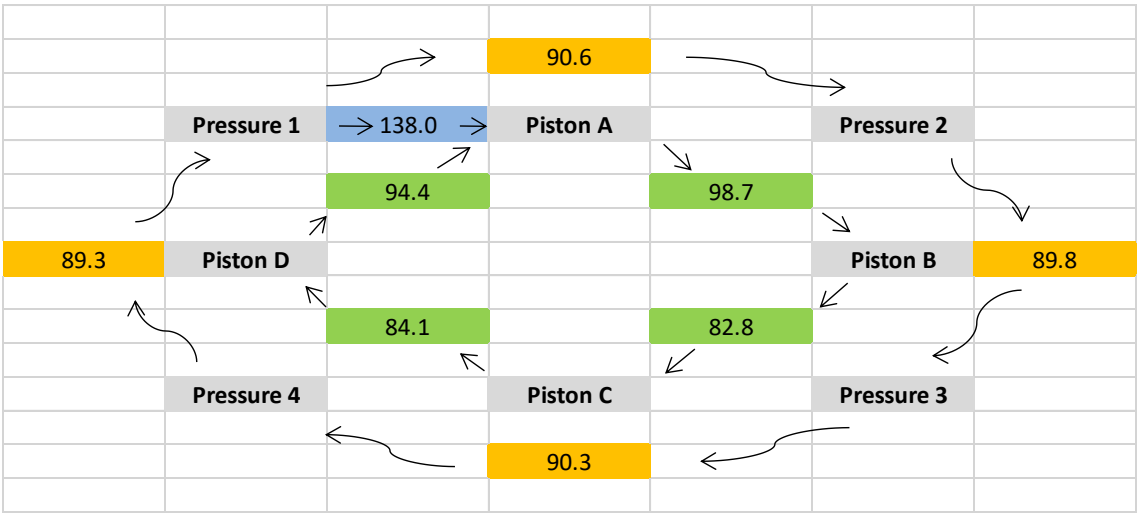

Figure 5.82 – Sage model predictions for the relative phase angles between pressure and displacement phasors in the example 2HEAT simulation. Simulation is at 4 bar charge pressure with 190°C heater temperatures and 100 ml pistons.

The angle between the pressure phasor of GS1 and the displacement phasor of Piston A is 138.0°, which is close to the experimental value of 133.9°. The angles between the pressure phasors are very close to 90° value, all are within the range 90° ± 0.7°. Comparing the angles between the pistons, the largest discrepancy from the experiment (of 12.1°) occurs for the angle between Piston C and Piston D, where 84.1° is predicted by Sage and the value from the experiment is 96.2°. It is not worth inferring too much from precise comparison with the experiments since the 100 ml piston Sage results are being compared to 115 ml piston experiment results. Figures 5.83 and 5.84 show the Sage model pressure amplitude and piston displacement predictions across the charge pressure range.

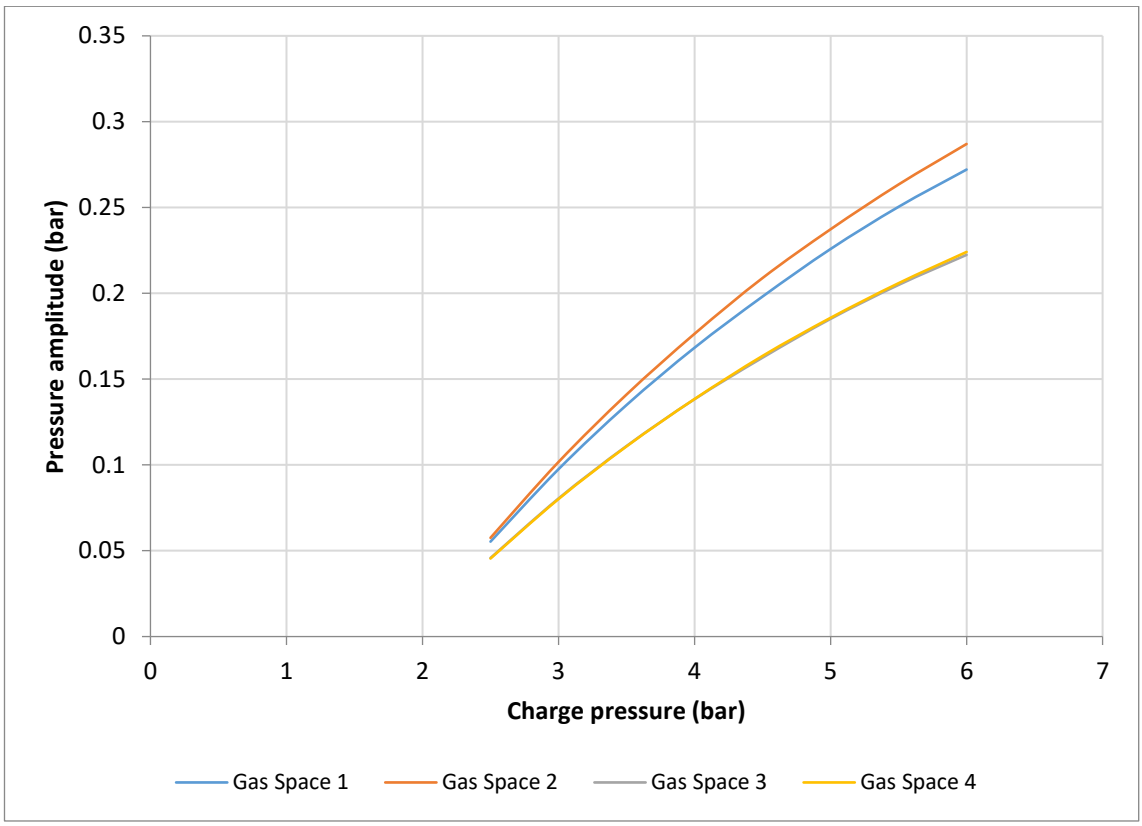

Figure 5.83 – Sage predictions for pressure amplitudes with increasing charge pressure for 2HEAT configuration. Simulations are with 190°C heaters and 100 ml pistons.

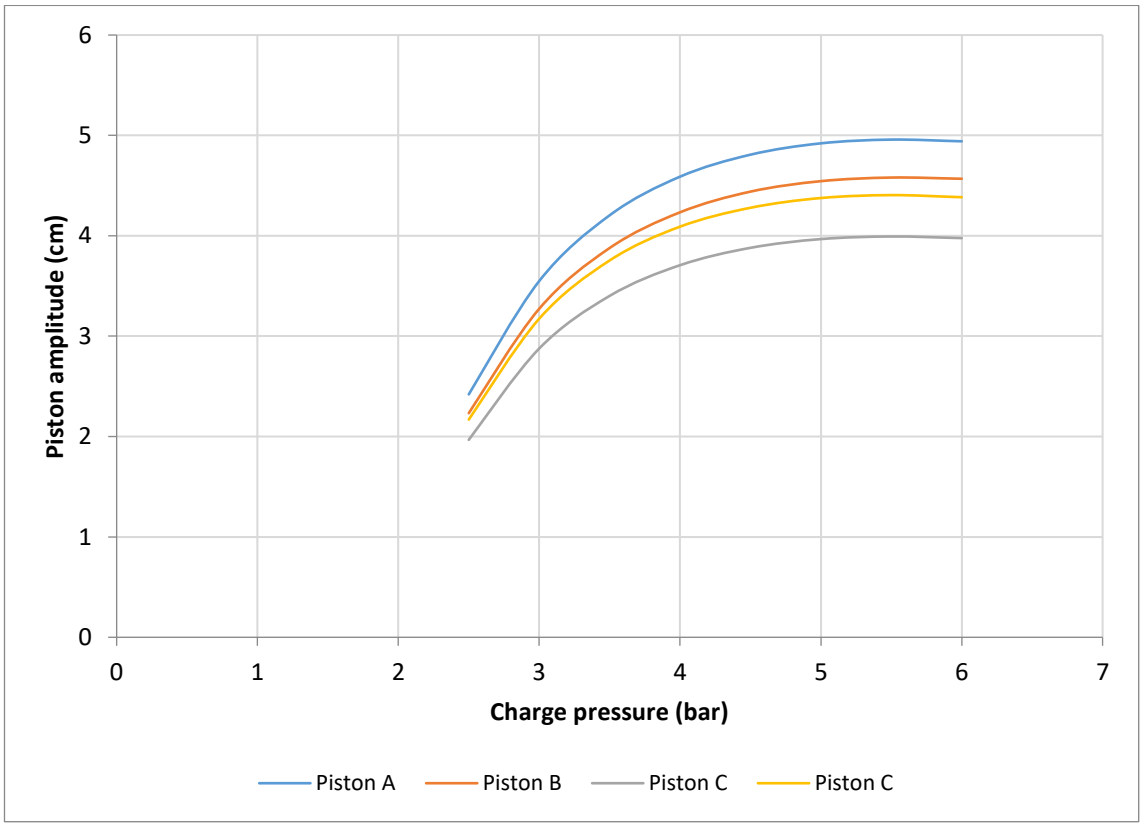

Figure 5.84 – Sage predictions for piston amplitudes with increasing charge pressure for 2HEAT configuration. Simulations are with 190°C heaters and 100 ml pistons.

The pressure amplitudes in each gas space increase with charge pressure while retaining their relative magnitude ratios. The distribution of the largest and smallest amplitudes remains consistent with the experimental results except that the difference between GS3 and GS4 is very small in the Sage predictions. The ratios calculated and averaged over the simulation range are 1.05 (s = 0.5%), 0.82 (s = 0.4%) and 0.82 (s = 0.1%) for GS2, GS3 and GS4 respectively. The ratio for GS2 is the same as seen in experiments, while those of GS3 and GS4 are 2.4% and 6.8% smaller than the experiment values. Adding up the unrounded ratios obtained for the heater and absorber spaces gives 1.870 for the heater spaces and 1.823 for the absorber spaces, which equates to a conversion rate of 1.03:1 (three significant figures). This is close to the conversion ratio of the 2HEAT experiments in Section 5.1.3 of 1.003:1. The variation in the relative phase angles of the pressure amplitudes and pistons are shown in Figures 5.85 and 5.86.

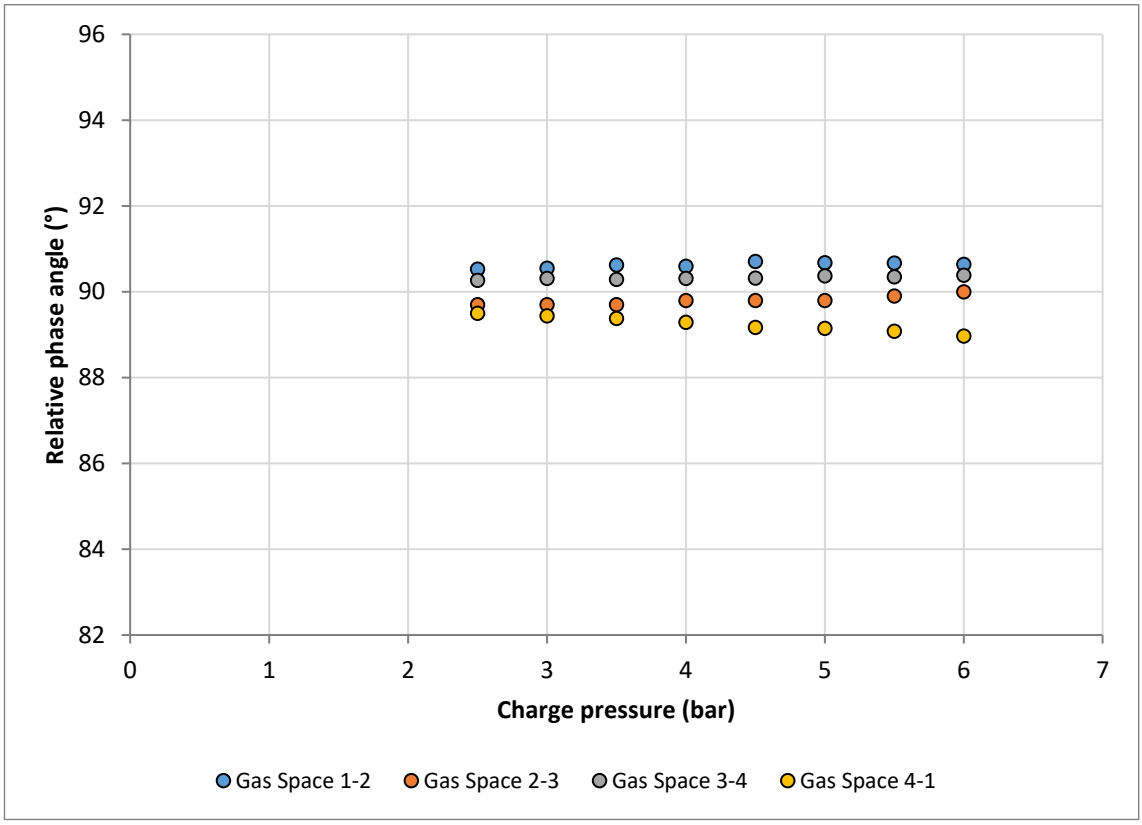

Figure 5.85 – Sage model predictions for the relative phase angles between pressure amplitude phasors for 2HEAT configuration. Simulations are with 190°C heaters and 100 ml pistons.

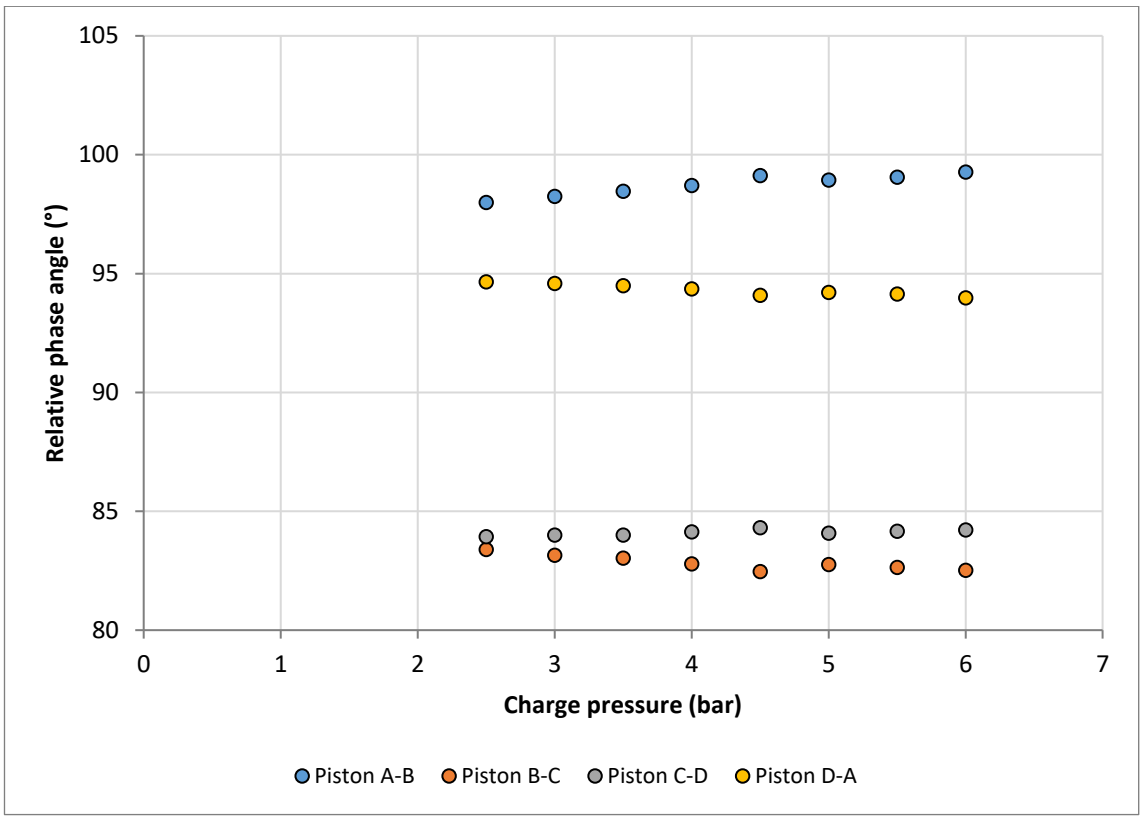

Figure 5.86 – Sage model predictions for the relative phase angles between piston phasors for 2HEAT configuration. Simulations are with 190°C heaters and 100 ml pistons.

The relative pressure phase angles are again very close to the 90° value and show little variation with increased charge pressure. The relative phase angles between piston displacements also remain close to those discussed previously for Figure 5.82, and show variations of less than 1° with charge pressures up to 6 bar.

As done for the 3HEAT simulations, Figure 5.87 shows how the COP predicted for the 2HEAT configuration varies with charge pressure. The COP values are much higher than the 3HEAT configuration. The COP peaks at 5.5 bar with a value of 0.46, which is more than twice the maximum COP achieved in the 3HEAT simulations analysed earlier. This is in line with the promising traits identified experimentally for the 2HEAT configuration. With pressure amplitudes much closer to each other in magnitude, relative piston phase angles closer to 90° and far superior conversion ratios, it would be expected that the 2HEAT configuration should outperform the 3HEAT configuration.

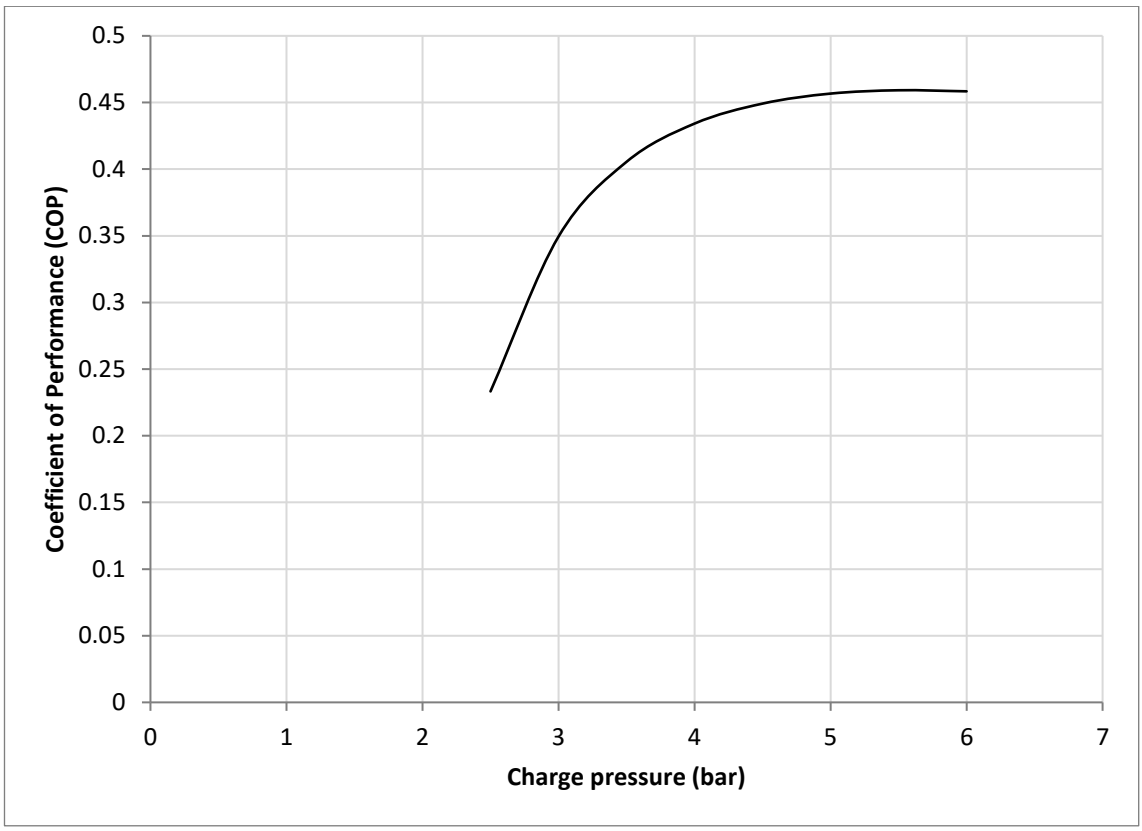

Figure 5.87 – Sage model predictions for the coefficient of performance for the 2HEAT configuration. Simulations are with 190°C heaters and 100 ml pistons.

5.2.5 Validation Summary

The development of the Sage model and the relevant procedures associated with its use not only in the 4HEAT configuration, but also in the 3HEAT and 2HEAT configurations proved very successful. Aside from lacking the inclusion of restrictions imposed by the RT instability, the model has shown the ability to independently predict the complex dynamic behaviour of the LPSC machine to a relatively high degree of similarity with experiments for all three configurations. This contributes significantly to the validity of the model's use in subsequent optimisations. The sensitivity of the model was investigated for a number of important constants including liquid viscosity, minor flow loss coefficients, as well as the heat source and sink temperatures. Model outputs related to the level of excitation, such as piston amplitudes, were found to have relatively high sensitivity to these parameters. Changes of 1%–10% in the inputs resulted in 20%–40% changes in the outputs. Whereas the model outputs which distinguish the dynamic

patterns of behaviour such as frequency, relative phase angles and relative magnitudes of excitation were found to have very little sensitivity to these changes. Also of note is that the Sage model predicts a far superior COP for the 2HEAT configuration (0.46) over the 3HEAT configuration (0.20).

Based on the model predictions for the 100 ml piston LPSC test-rig, and the sensitivity analysis conducted, it was decided that the model had been validated to a suitable level and was ready for investigating system modifications in order to achieve improved performance. One component in particular stands out as the prime candidate for adjustment—the liquid piston dimensions.

5.3 Preliminary Piston Investigation

As a consequence of the geometrical complexity of the test-rig gas spaces (in addition to containing the sensor ports, etc.) it is logical to first investigate the influence of different piston dimensions on the behaviour and performance of the LPSC machine test-rig—since the piston U-tubes are relatively easy to interchange. After validating the accuracy of the Sage model to an acceptable level, it was possible to run simulations with different piston masses and diameters (and any other related variations) without making changes to the physical test-rig. The Sage model is easy to alter for pistons of different length and cross-sectional area; and once improved piston dimensions are identified, it is much easier to implement them in the physical test-rig, thanks to the modular nature of the set-up. By testing new piston dimensions, and comparing the results with the Sage model predictions, the accuracy of the model can be improved as well. This could potentially be repeated for further improvements and lead to the design of a prototype.

There are two parameters associated with the liquid pistons which can be easily manipulated: the piston length and diameter. For the first piston redesign, it was decided that only changes in the diameter would be investigated. The diameter was chosen over

the length for a number of reasons—primarily that changes in the diameter have a much larger influence on the resulting piston mass, and do not take up as much space as equivalent changes in the piston length. This allows for a much wider scope of feasible piston masses, that can be potentially implemented. Once an optimal (or, at least, better) piston diameter was identified and tested with the test-rig, the Sage model would also now have another important reference point for comparison purposes, and this would allow for the model to be further refined (at which point it could be used to identify the optimal piston dimensions of both length and diameter).

A very simple approach was taken for this piston diameter investigation. The key performance indicator was selected as being the lowest heater temperature required for the system to achieve self-sustained operation. Although this parameter does not exhibit any specific performance data, it does highlight which systems are the easiest to start, and therefore which are the most well-balanced in terms of the vibrational dynamics and thermodynamics. This also allows the investigative process to proceed with the 4HEAT configuration model, for which identifying the frequency and solving for piston amplitudes is much simpler. The Sage model was used to assess the performance of the LPSC test-rig with six piston diameters in the range of 12.65 mm (current installation) to 25 mm. Table 5.9 outlines the specifications of each of the piston sizes investigated.

Table 5.9 – Operating frequencies and starting temperatures for 94 cm pistons of varying diameter.

Piston diameter (mm)	Piston mass (ml)	Frequency of operation (Hz)	Functional temperature ranges (°C)
12.65	100.0	4.141	87.5-100
15.00	140.6	4.890	82.0-100
17.50	191.4	5.690	79.5-100
20.00	250.0	6.487	79.0-100
22.50	316.4	7.285	79.5-100
25.00	390.6	8.083	81.0-100

A single charge pressure of 4 bar was used in the analysis, and the heater temperatures were initially set to 100ºC—before being reduced to the point at which operation ceased and no solution was found. Figure 5.88 shows the results of the simulations with the pressure amplitudes developed in the gas spaces for the operational temperature range below 100ºC.

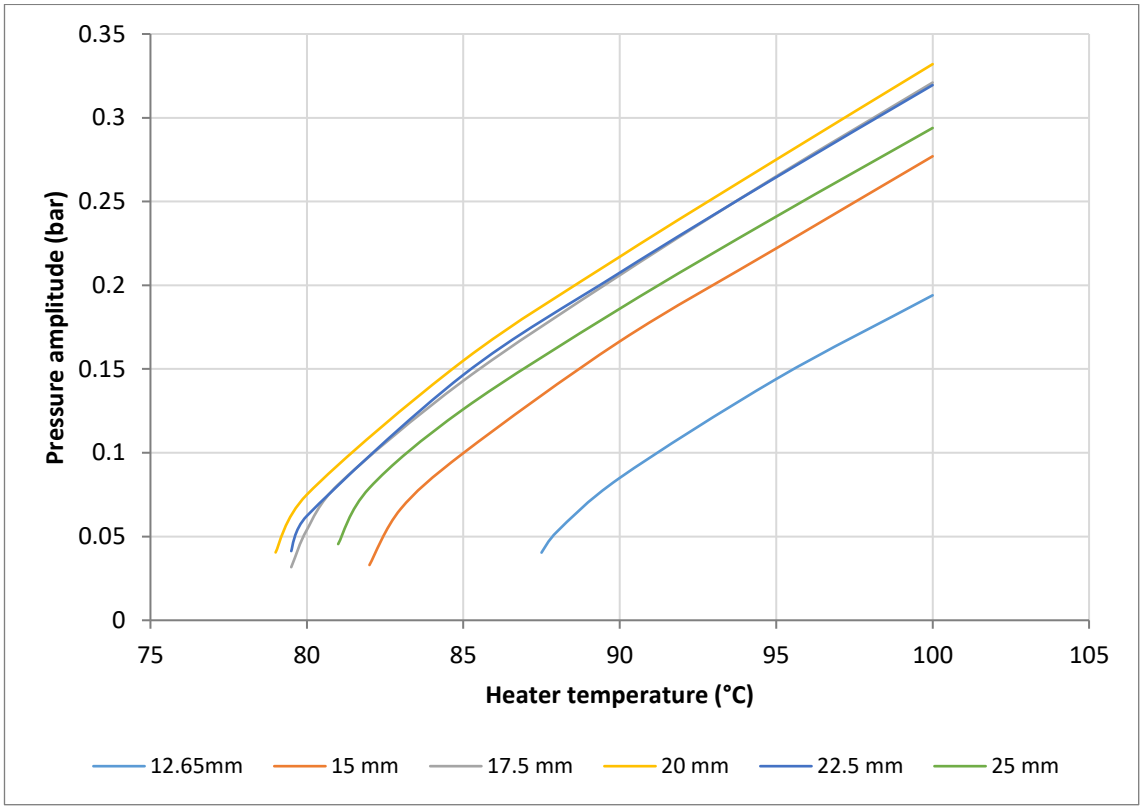

Figure 5.88 – Piston diameter influence on the heater temperatures needed for self-sustained operation. Simulations are conducted with 4HEAT configuration at 4 bar charge pressure with constant piston length.

The systems associated with the leftmost graphed functions are the easiest to start, requiring lower heater temperatures to achieve the same pressure amplitude development as those further to the right. The best predictions arise from the 20 mm diameter pistons—with piston diameters above and below leading to increased heater temperatures. The 12.65 mm pistons exhibit the worst performance, requiring heater temperatures at least 5ºC higher than the other pistons to achieve the same pressure amplitudes. Another noticeable characteristic is that as the temperature is increased, the separation between each set of predictions remains constant, which allows the relative performance of each

piston diameter to be assessed at any temperature. The pressure amplitudes developed with 100ºC heaters are plotted against the piston diameters in Figure 5.89.

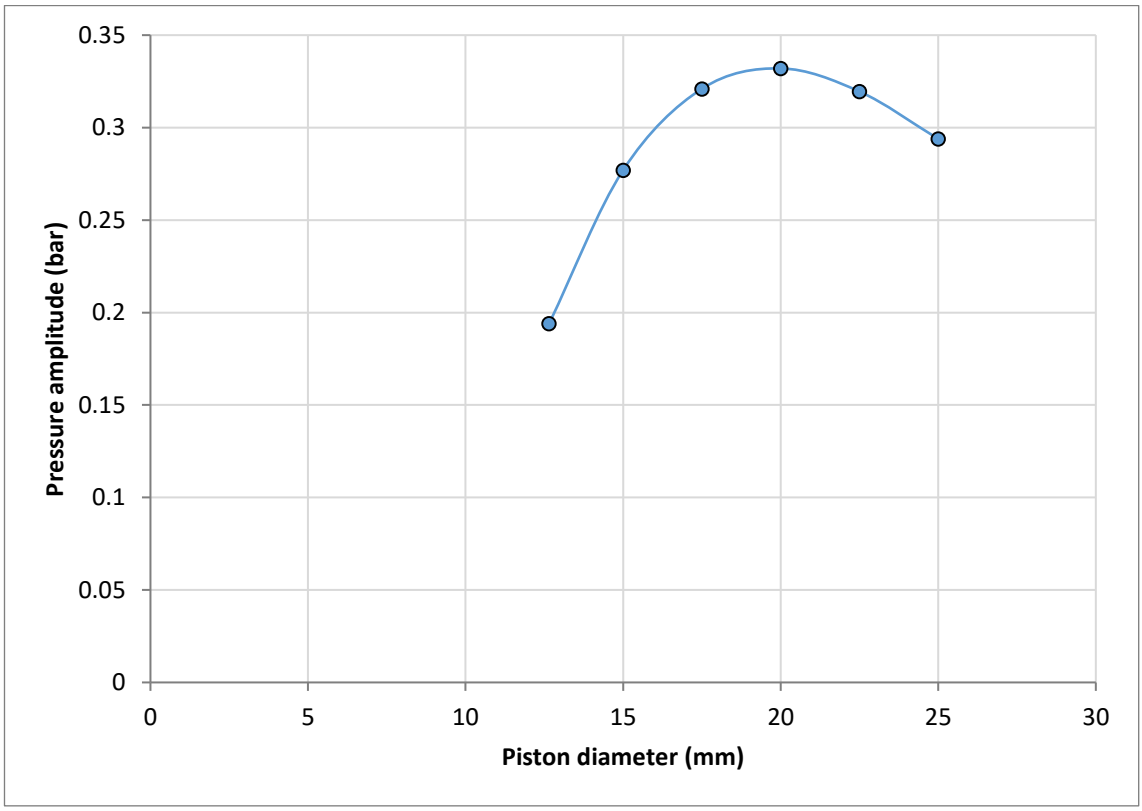

Figure 5.89 – Identification of the optimal piston diameter based on Sage model predictions with constant piston length. Simulations are with 4HEAT configuration at 4 bar charge pressure with 100°C heater temperatures.

Figure 5.89 can be used to identify the optimal piston diameter for the particular piston length of the test-rig (94 cm—which remained unchanged in the modelling process). The graph indicates that 20 mm diameter pistons should result in a system that is much easier to start at lower heater temperatures, and produces higher pressure amplitudes for the same heater temperatures when compared with other piston diameters. For example, compared to the 12.65 mm pistons (15mm OD) that were initially installed, then the same pressure amplitudes predicted at 100ºC should be reachable with heaters set at approximately 88ºC. By extension, the 3HEAT and 2HEAT minimum temperatures are also predicted to drop by significant amounts, which is particularly important for the 2HEAT configuration (considering the prohibitively high temperatures needed in this case).

6 Results for 22 mm OD Piston Tube

6.1 Test-rig Modifications and Commissioning

After identifying the optimal piston diameter, new piston U-tubes were constructed for a new set of experiments. Conveniently, the optimum diameter identified in the preceding section (20 mm) is in line with a standard steel tube size. The piston length was kept similar, but its diameter was increased from 15 mm to 22 mm, resulting in a new piston mass of 275 ml. The 22 mm OD steel tubes have a wall thickness of 1.2 mm, meaning the inner diameter is 19.6 mm on the steel side. As in the case of the first set-up, fibre reinforced PVC tube was used on the side where the displacement sensors were installed. This time ¾-inch (19.05 mm ID) tube was employed. The new pistons were implemented and after some commissioning, a secondary set of experiments was carried out. Table 6.1 shows the set of experimental parameters which were tested for the larger pistons.

Table 6.1 – Set of parameters for second experimental investigation.

Piston tube OD (mm)	Configuration	Liquid piston volume (ml)	Heater surface temperature (°C)	Gas pressure (bar)
22	4HEAT	275	75, 80	1-6
22	3HEAT	275	105, 110, 115	1-6
22	2HEAT	275	160, 165	1-6

As predicted by the Sage model, the heater temperatures required for the system to achieve stable operation were significantly reduced, and hence the tested heater temperatures are lower than in the previous experiments. Some of the experiments at lower pressure did not produce usable results because the degree of ovality of the 19 mm PVC tube was too high and the piston floats were in direct contact with parts of the tube walls, which introduced static friction. At charge pressures above 2.5 bar this was usually overcome as the PVC tube cross-section would become more circular with the increase in internal pressure. The experiments were conducted using a similar procedure to the

earlier experiments, except that a number of additional improvements were made, as follows:

New test-rig stand – Due to the increased piston diameters, a new support structure had to be built for the modified test-rig. The 22 mm diameter steel tube required a larger bending radius when forming the new U-tube components, which consequently increased the separation distances needed for the gas space housing components. The structure also needed to be able to withstand the machine's increased mass, since the piston volumes had increased almost by a factor of three. The new structure is shown in Figure 6.1.

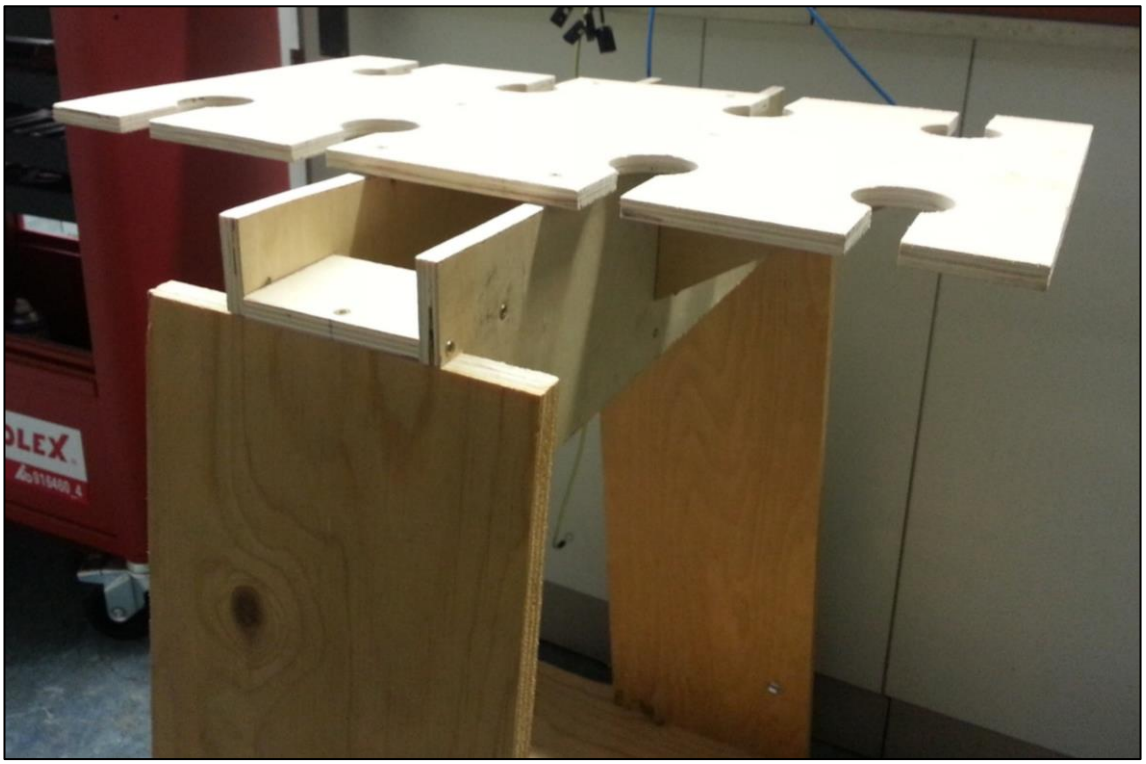

Figure 6.1 – New support structure created for larger pistons.

Video footage for piston amplitudes – After the many difficulties associated with the capacitive sensors and their calibration for piston amplitude data, it was decided that video footage would be used instead. Slow motion video was used to capture snapshots of the piston oscillations at different intervals during each experiment. The time at which the videos were taken was recorded, and the videos were later analysed to provide the relevant piston amplitude data. The uncertainty in the piston amplitude data was ± 0.25

cm. The capacitive displacement sensors were still employed for collection of the piston phase angle data. The reference capacitors were modified to account for the change in baseline piston readings.

New piston floats – With the increased piston diameter, new floats were manufactured in the workshop. They were designed with the same length-to-diameter aspect ratio and made from a similar material (Polyethylene 300) to previous experiments. The new floats were also coloured green to aid in their visual identification—as the previous white versions were sometimes obscured by the fibre reinforcing in the PVC tube walls, which made it difficult to distinguish their outline. Roughly the same clearance was kept between the piston floats and the tube walls, although the larger PVC tube had a higher ovality which meant that the floats in the PVC sections were required to be 0.5 mm smaller. The float sizes used were 18.5 mm OD in the steel side, and 18 mm OD in the PVC side. Additionally, a number of experiments were conducted without any floats at all. This was done to allow for a more objective measure of their impact on system performance, and also to test the Rayleigh-Taylor instability theory further. The no-float results are compared and evaluated in Section 6.2.1.

Piston stabilisers – An unexpected discovery was made after conducting a number of experiments with the new 22 mm set-up. As the charge pressure was increased a lull in operation was found. At pressures above and below this point, the system would achieve much higher pressure amplitudes; and, in some cases, the machine would cease to achieve self-sustained operation entirely. It was discovered that the natural frequency of vibration of the support structure itself was close to the operational frequency of the LPSC system in the vicinity of these problematic charge pressures. To combat this, the bottoms of the U-tubes were fastened to rigid stabilisers to prevent relative motion between them. This effectively increased the rigidity and natural frequency of the test-rig stand, which

prevented resonance with the LPSC machine. This resolved the issue, and the developed pressure amplitudes were restored to their expected values. It should be noted, however, that during some experiments it was necessary to disconnect a single stabiliser in order to jump-start the system; after reaching stable operation it would then be reconnected. Figure 6.2 shows the final set-up of the upgraded 22 mm piston tube test-rig.

Figure 6.2 – Fully commissioned 22 mm piston test-rig.

All other system geometry was kept the same as in the first set of experiments, although some minor inconsistencies were present in the final installation. The gas volumes of each space were increased slightly, because the length of dead gas volume above the liquid piston (and within the U-tubes) now had a much larger cross-sectional area. These values were quantified and incorporated into the updated Sage model, which is discussed in more detail in the Section 6.3.

6.2 Experiment Results

Presented here are the results from the second iteration of the LPSC experimental investigation. The piston U-tube diameter has been increased from 15 mm (13 mm ID) to 22 mm (19.6 mm ID) steel tube. Because of the large number of experiments conducted (more than 100) and their similarities with the 15 mm piston experiments, the results presented here are not as comprehensive as those in Section 5.1. Instead, it is assumed the reader is familiar with the concepts and system behaviours identified in the earlier results sections, and only the key distinguishing or critical information will be presented. Typical examples of experiments for each of the three configurations are again presented with the associated phasor analysis. The results for the 4HEAT configuration are shown first—followed by 3HEAT and 2HEAT. The first comparison includes experiments from all three configurations. Figure 6.3 shows the frequency of operation of the LPSC system and its variation with charge pressure. As with the results from the smaller 15 mm pistons, the operational frequency of the system is the same for each configuration when tested with the same charge pressure. This provides further justification for using the same frequencies for different configurations within the Sage modelling procedure. Figure 6.4 compares the frequencies obtained from the 22 mm experiments with those from the 100 ml, 15 mm experiments. Included are the predicted frequencies from Equation 4.8 (from the earlier section on theoretical analysis) assuming isothermal gas behaviour.

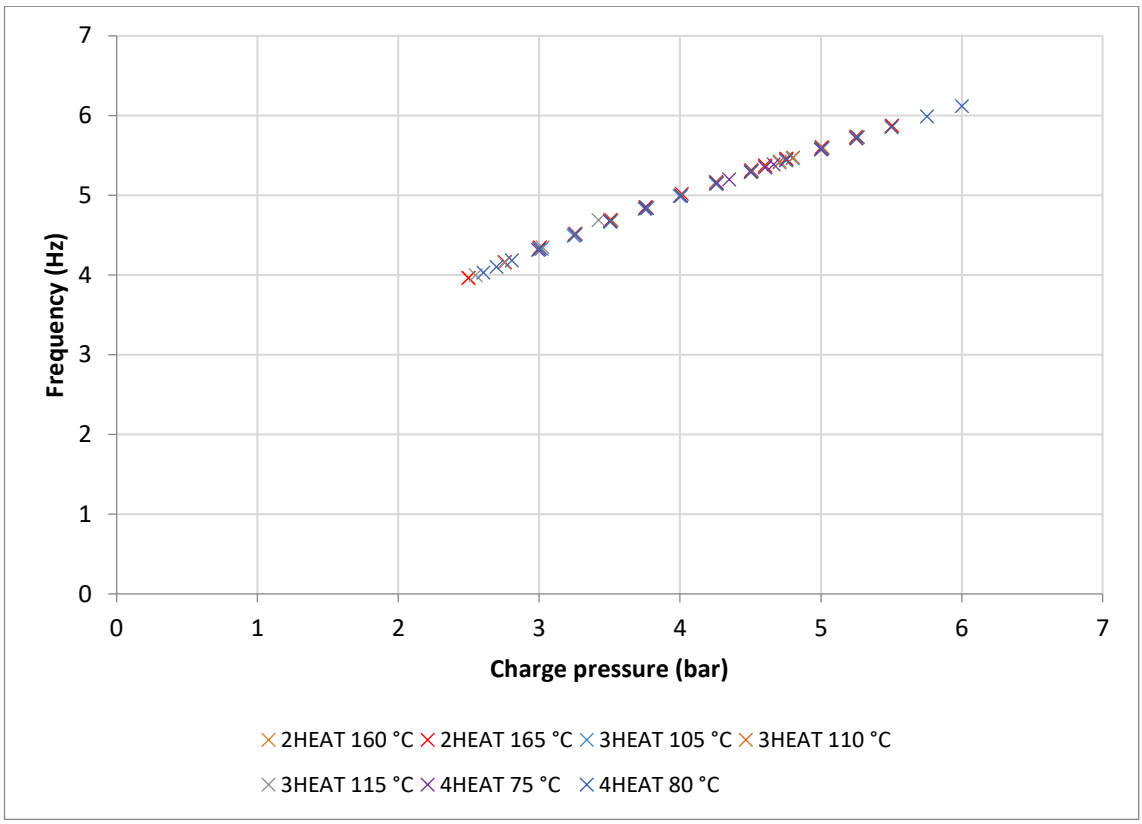

Figure 6.3 – Frequency variation of the 22 mm piston experiments with 275 ml pistons for all configurations.

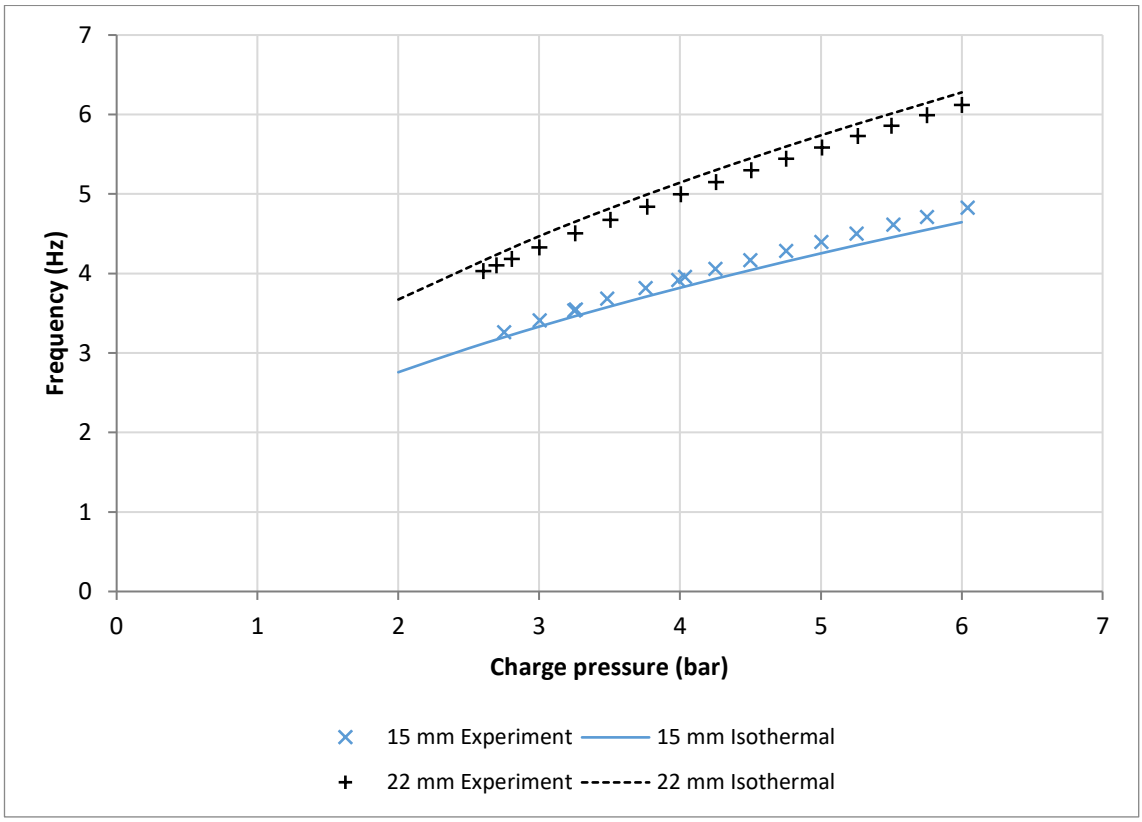

Figure 6.4 – Experimental frequencies of both piston sizes compared with predictions from natural frequency derivation.

It can be seen that the estimate of operational frequency based on isothermal gas behaviour is very similar to the values measured experimentally. Knowing the form of Equation 4.8 and its dependence on charge pressure, the close-to square root dependence observed in the experimental results is plausible. The differences remain small across the entire charge pressure range. At 5 bar for example, the predicted frequency is 3.3% lower than the value measured for the 15 mm U-tubes with 100 ml pistons. In the case of the 22 mm U-tubes with 275 ml pistons, the predicted frequency is 2.7% higher than the experiment. It is not known why the formula overestimates in one instance and underestimates in the other. It is possible that the gas is behaving less isothermally in one setup compared with the other; or there could be some small discrepancies in the quantities used for gas volume or other contributing variables.

6.2.1 4HEAT Configuration

After commissioning the new test-rig setup it was discovered that the system was capable of operating with much lower heat source temperatures than the 15 mm setup. In Section 6.3 the Sage model predicted that 250 ml pistons with 20 mm internal diameter would start at approximately 80ºC. The new setup with 275 ml, 19.3 mm diameter (average) pistons was found to operate at temperatures as low as 75ºC. The 4HEAT experiments were conducted with heater temperatures of 75ºC and 80ºC. Heater temperatures of 70ºC were attempted, although self-sustained operation was not established. Temperatures above 80ºC produced too much piston instability for useful data collection. An example experiment with 80ºC heaters at 4 bar charge pressure is considered for the phasor analysis. The phasor parameters obtained using the same procedure described earlier are listed in Table 6.2. Figure 6.5 then shows the scaled pressure and displacement phasor plot for the experiment.

Table 6.2 – Phasor representations of gas pressure and piston displacement amplitudes for example 4HEAT experiment.

Phasor	Amplitude (bar or cm)	Phase angle (°)
Pressure 1 (P1)	0.173	0.0
Pressure 2 (P2)	0.178	90.7
Pressure 3 (P3)	0.174	179.4
Pressure 4 (P4)	0.181	270.4
Displacement A (XA)	2.80	140.8
Displacement B (XB)	2.88	230.6
Displacement C (XC)	2.75	315.8
Displacement D (XD)	2.75	51.0

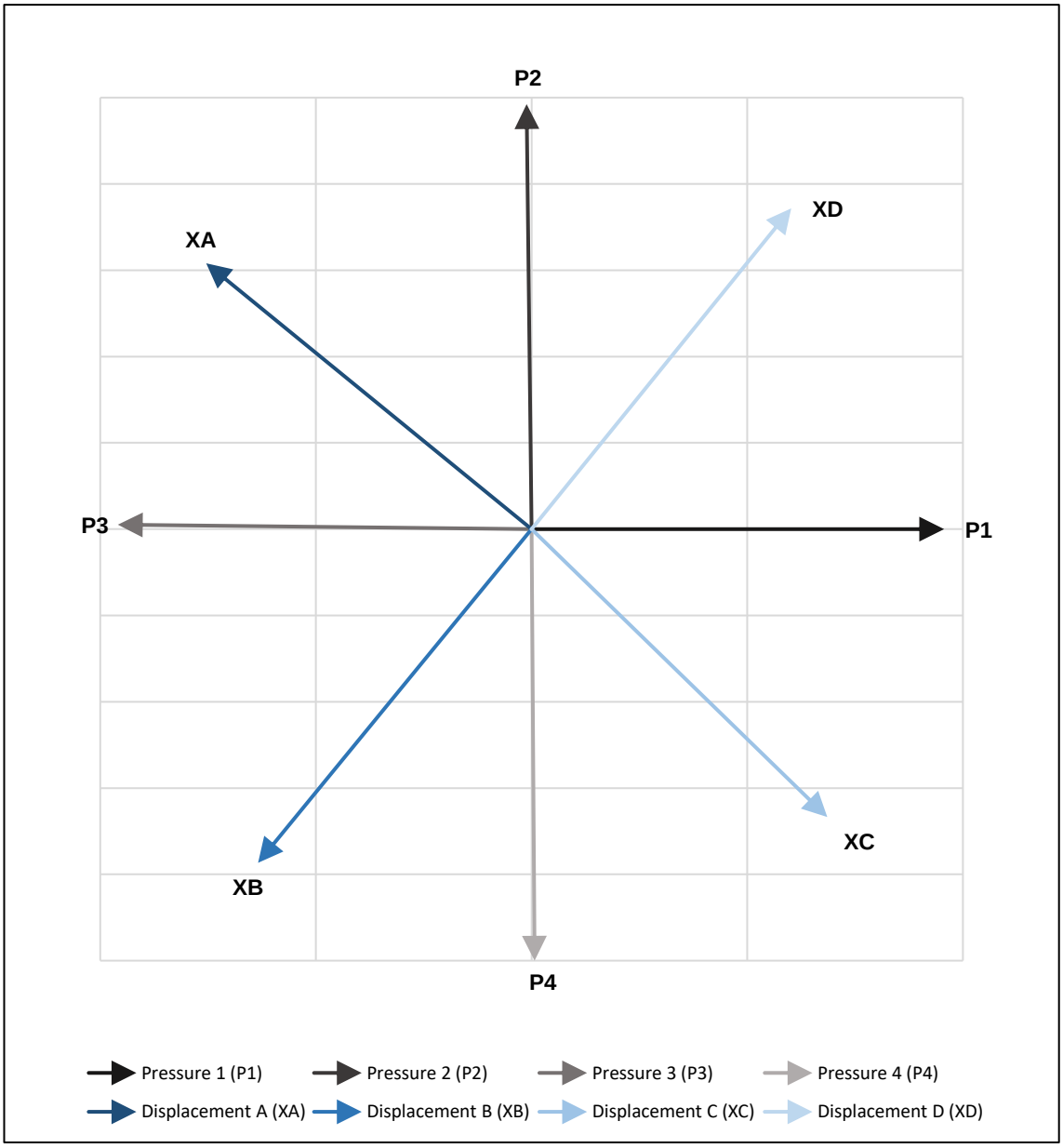

Figure 6.5 – Scaled phasor plot of pressure and displacement profiles for the example 4HEAT experiment with 22 mm piston tubes. The experiment was with 80°C heaters and 4 bar charge pressure.

The relative phase angles between the pressure phasors are much closer to 90º than any of the 15 mm piston experiments. This is in accordance with the model predictions and implies that the 22 mm test-rig has a higher aspect of symmetry. Figure 6.6 shows the corresponding chart for the relative phase angles between phasors. All four pressure phasors are within ± 1.3º of perfect symmetry. The displacement phasors show greater variation with the range being within ± 5.2º of 90º. The relative phase angle between Piston A and GS1 pressure at 140.8º is also similar to previous 4HEAT experiments and their Sage predictions.

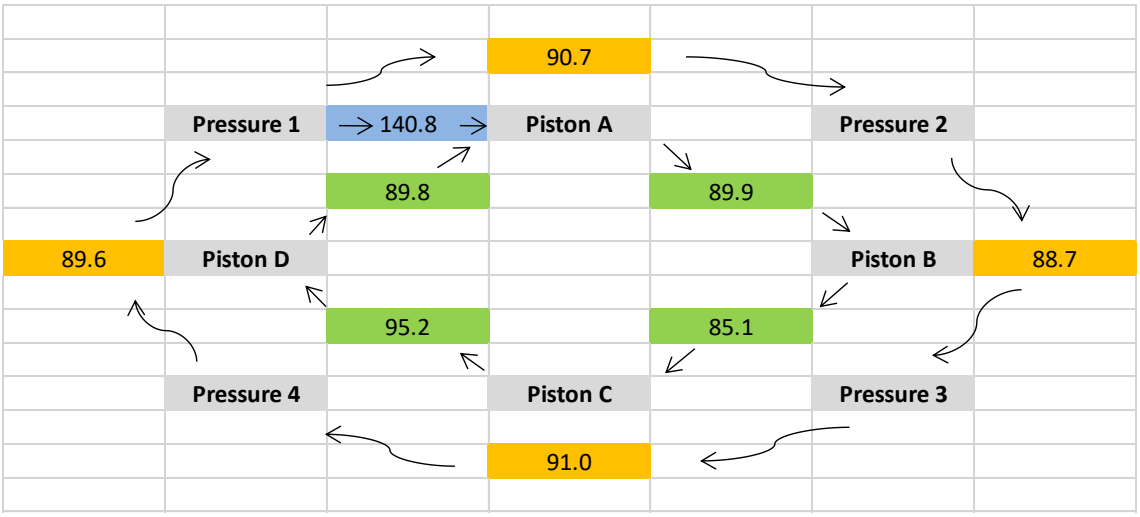

Figure 6.6 – Relative phase angles for the example 4HEAT experiment with 22 mm piston tubes. The experiment was with 80ºC heaters and 4 bar charge pressure.

Figure 6.7 shows the pressure amplitudes developed for both sets of heater temperature experiments. The pressure amplitudes developed with 80ºC heater temperature rise steeply from the first measurements at 2.5 bar until plateauing at 4 bar where they remain for all higher charge pressures. This evidence of a barrier preventing higher excitation levels is similar to that seen in the 15 mm results. Figure 6.8 presents the pressure amplitude progressions of three separate tests from the above data set: one at 3.5 bar, one at 4 bar and the other at 4.25 bar.

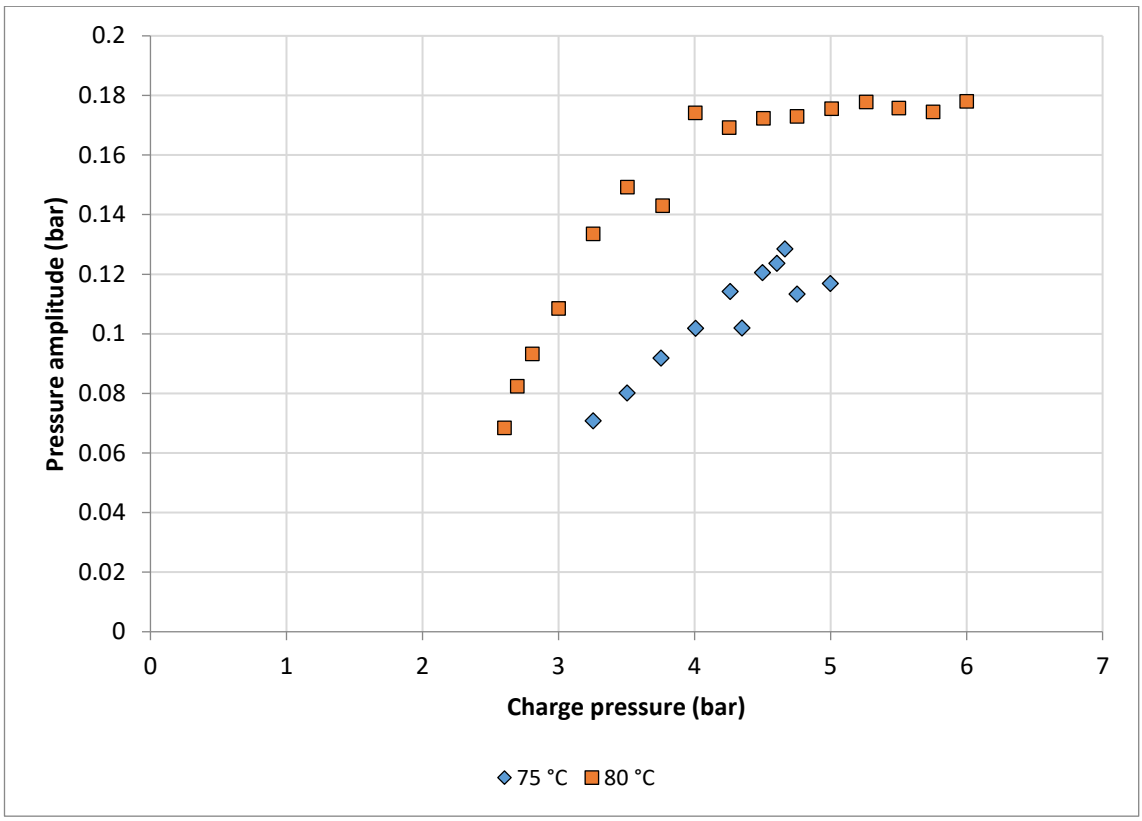

Figure 6.7 – Pressure amplitude variation of Gas Space 1 with changing charge pressure for all 4HEAT experiments using 275 ml liquid pistons.

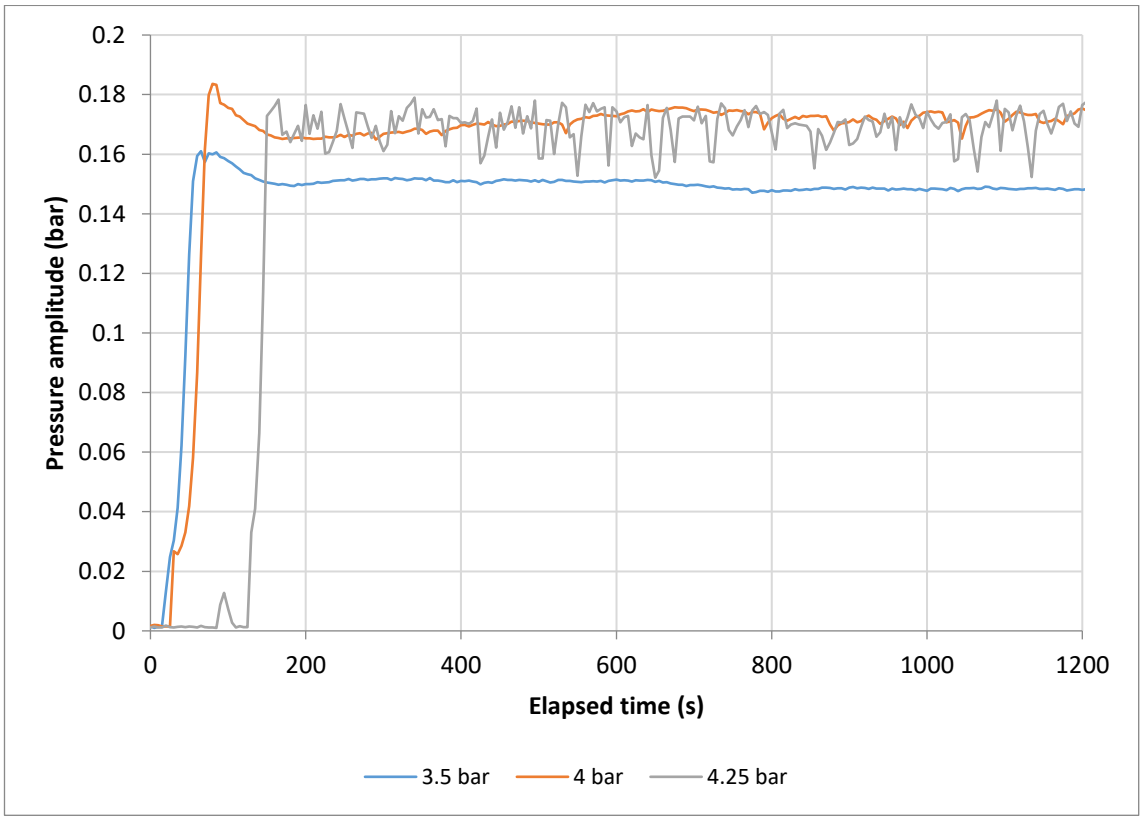

Figure 6.8 – Pressure amplitude progressions of experiments conducted at or near the transition pressure of 4 bar for the 4HEAT configuration.

Figure 6.8 shows the pressure amplitude from the 3.5 bar experiment remaining relatively constant at 0.15 bar after its initial rise, with very little fluctuation as the experiment continues. Being below the threshold pressure then the small changes in magnitude are gradual and smooth. The 4.25 bar measurements are much more erratic and show the pressure amplitude rising steeply and immediately becoming unstable. The amplitude rises and falls continuously as though constantly re-establishing itself and building up (before again becoming unstable); the average pressure amplitude recorded is below the average for the 4 bar experiment. The 4 bar experiment is very close to the transition point: the results exhibit both operation modes from the 3.5 bar and 4.25 bar experiments. It is stable and smooth for long periods while also experiencing some sudden fluctuations similar to the 4.25 bar behaviour (albeit less extreme). This behavioural pattern was identical for all of the experiments above 4 bar—with the fluctuations in pressure amplitude becoming even more significant at higher pressure.

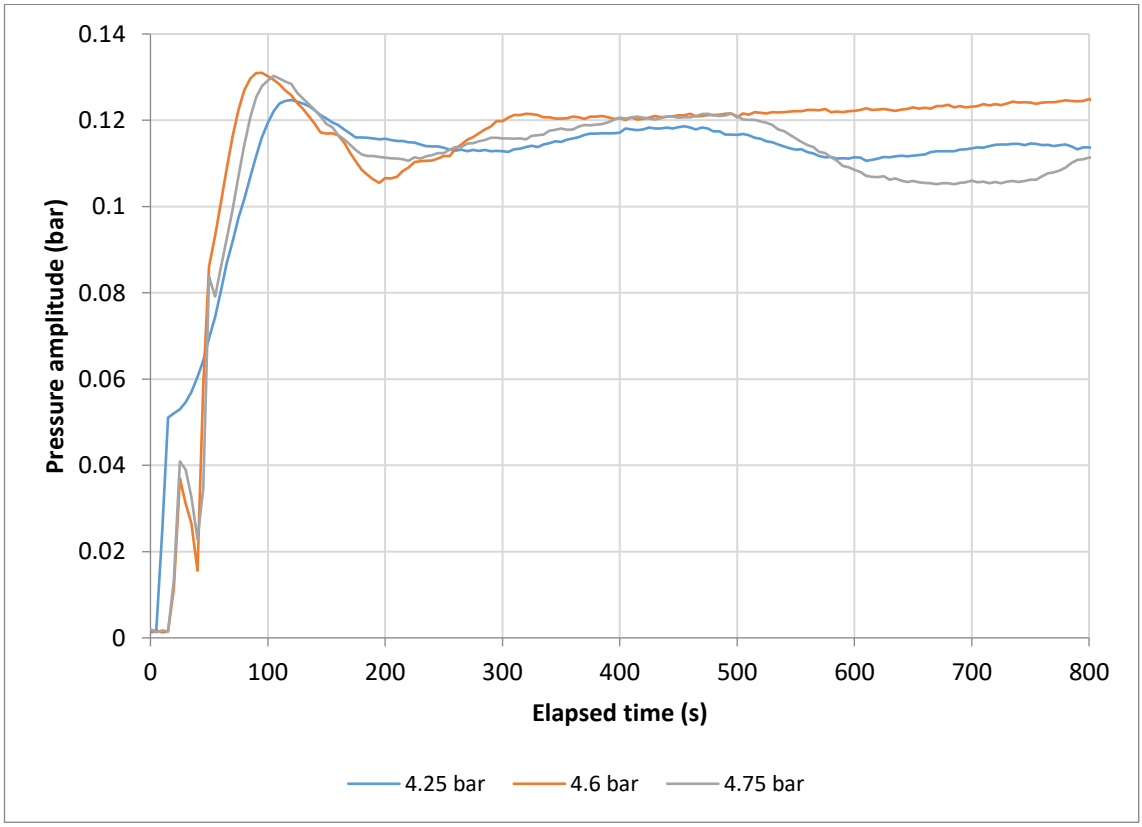

Figure 6.9 – Pressure amplitude progressions for 75°C heater experiments.

When considering the 75ºC results from Figure 6.7 it becomes evident that none of the developed pressure amplitudes are large enough to reach the threshold encountered by the 80ºC experiments. It should be expected then that the pressure amplitude progressions for these experiments should resemble the stable behaviours highlighted by the 3.5 bar experiment in Figure 6.8. Figure 6.9 shows the pressure amplitudes measured for three experiments from the 75ºC data set. Despite the pressures being above 4 bar, the same instability is not evident in these experiments; in fact, none of the 75ºC experiments exhibited unstable behaviour. This suggests that the pressure amplitudes developed are not hindered by any piston stability limitations (as those suspected for the 80ºC experiments), and were the maximum achievable for that particular pressure and temperature. This is explored further when considering the modified Sage predictions for the same set of experiments in Section 6.3. Figure 6.10 shows the piston amplitudes measured for the 75ºC and 80ºC experiments.

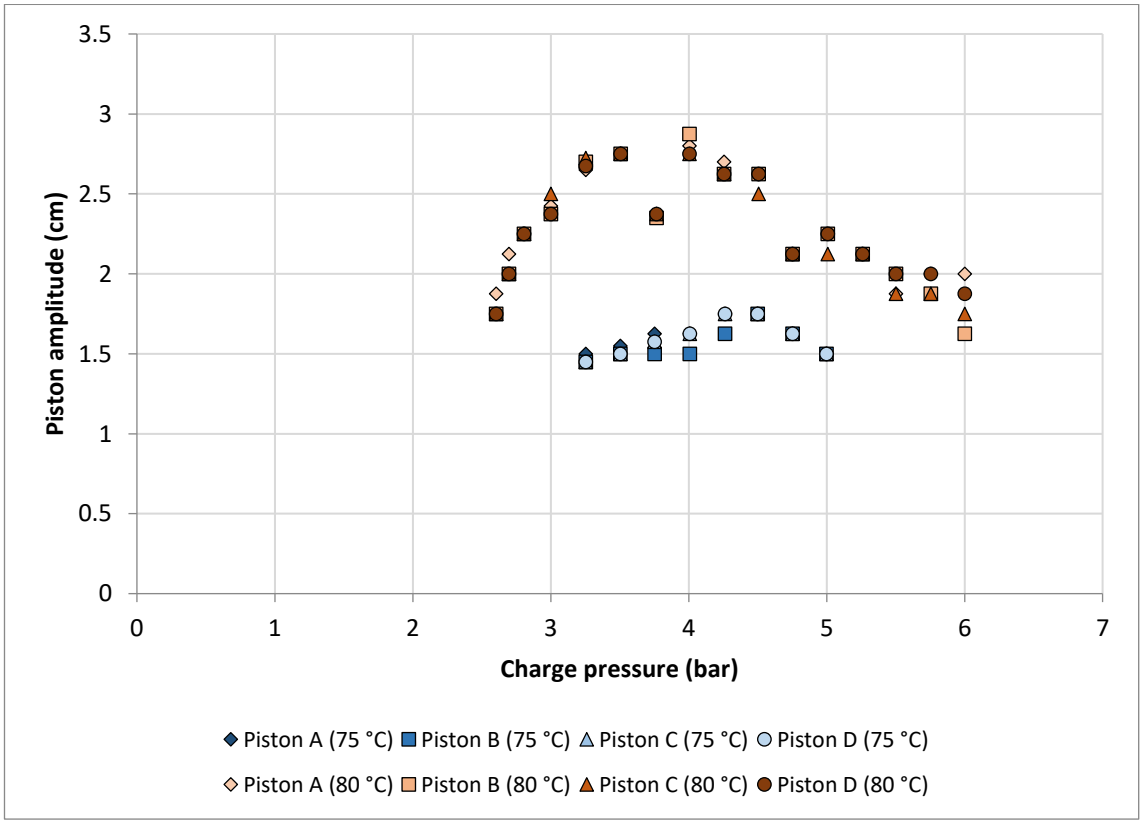

Figure 6.10 – Piston amplitude variation with charge pressure for the 4HEAT configuration experiments using 275 ml liquid pistons.

The new video-based method of obtaining the piston amplitudes is justified by these results. Unlike the 15 mm experiments, the piston amplitude measurements here reflect what is expected for the 4HEAT configuration, with very similar amplitudes for all 4 pistons at every experiment (except at 6 bar and 80ºC).

Experiments without floats were also conducted to highlight their necessity and impact. Figure 6.11 shows the pressure amplitudes developed in the no-float experiments in comparison to those already analysed with floats. Both sets of experiments were conducted with 80ºC heater temperatures.

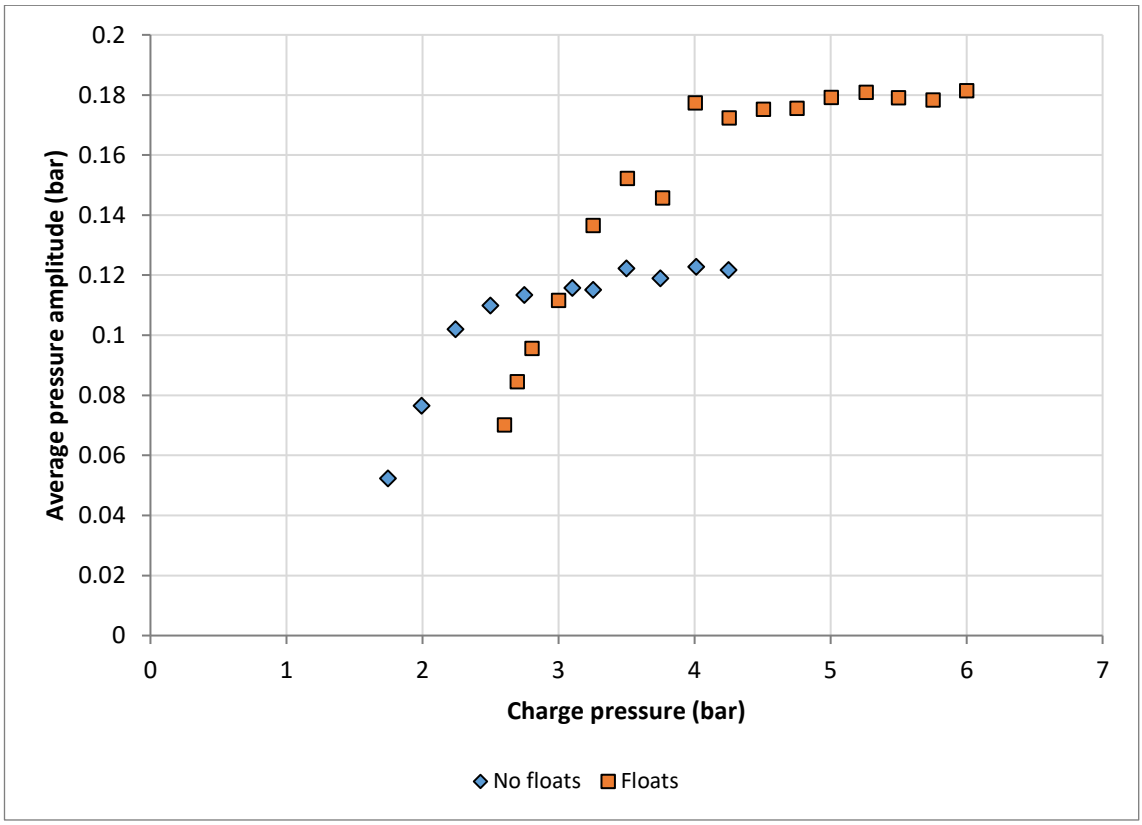

Figure 6.11 – Performance of LPSC 4HEAT system with and without piston surface floats. Experiments are with 80°C heater temperature.

The system is much easier to start without the floats, and consequently requires lower starting pressures. However, the pistons quickly become unstable when increasing the charge pressure and reach their threshold at 2.5 bar, where the developed pressure amplitudes plateau at roughly 0.12 bar. With the piston floats installed, the pistons are

able to sustain higher pressure amplitudes and accelerations, and hence retain their stability for charge pressures up to 4 bar. The pistons with floats installed perform better for all pressures above 3 bar. Unfortunately, because of the levels of instability of the piston surfaces in the no-float experiments, it was not possible to determine piston amplitudes. These results confirm that the RT instability acceleration threshold can be influenced by the use of piston floats; although at a cost in terms of increased friction and self-starting potential.

6.2.2 3HEAT Configuration

The 3HEAT experiments were conducted with heater temperatures of 105°C, 110°C and 115ºC. The experiments at 115ºC were too unstable above pressures of 4 bar, and therefore have a limited range. Temperatures below 105ºC did not produce continuous operation. Figure 6.12 shows the scaled pressure and displacement phasor plot for an example experiment with 110ºC at 4 bar charge pressure. The same relative phase angle chart is then shown in Figure 6.13. The phasor values are also listed in Table 6.3 for reference.

Table 6.3 – Phasor representations of gas pressure and piston displacement amplitudes for example 3HEAT experiment.

Phasor	Amplitude (bar or cm)	Phase angle (°)
Pressure 1 (P1)	0.121	0.0
Pressure 2 (P2)	0.202	90.7
Pressure 3 (P3)	0.124	179.4
Pressure 4 (P4)	0.182	271.0
Displacement A (XA)	2.70	124.1
Displacement B (XB)	2.63	242.8
Displacement C (XC)	2.58	307.6
Displacement D (XD)	2.43	61.7

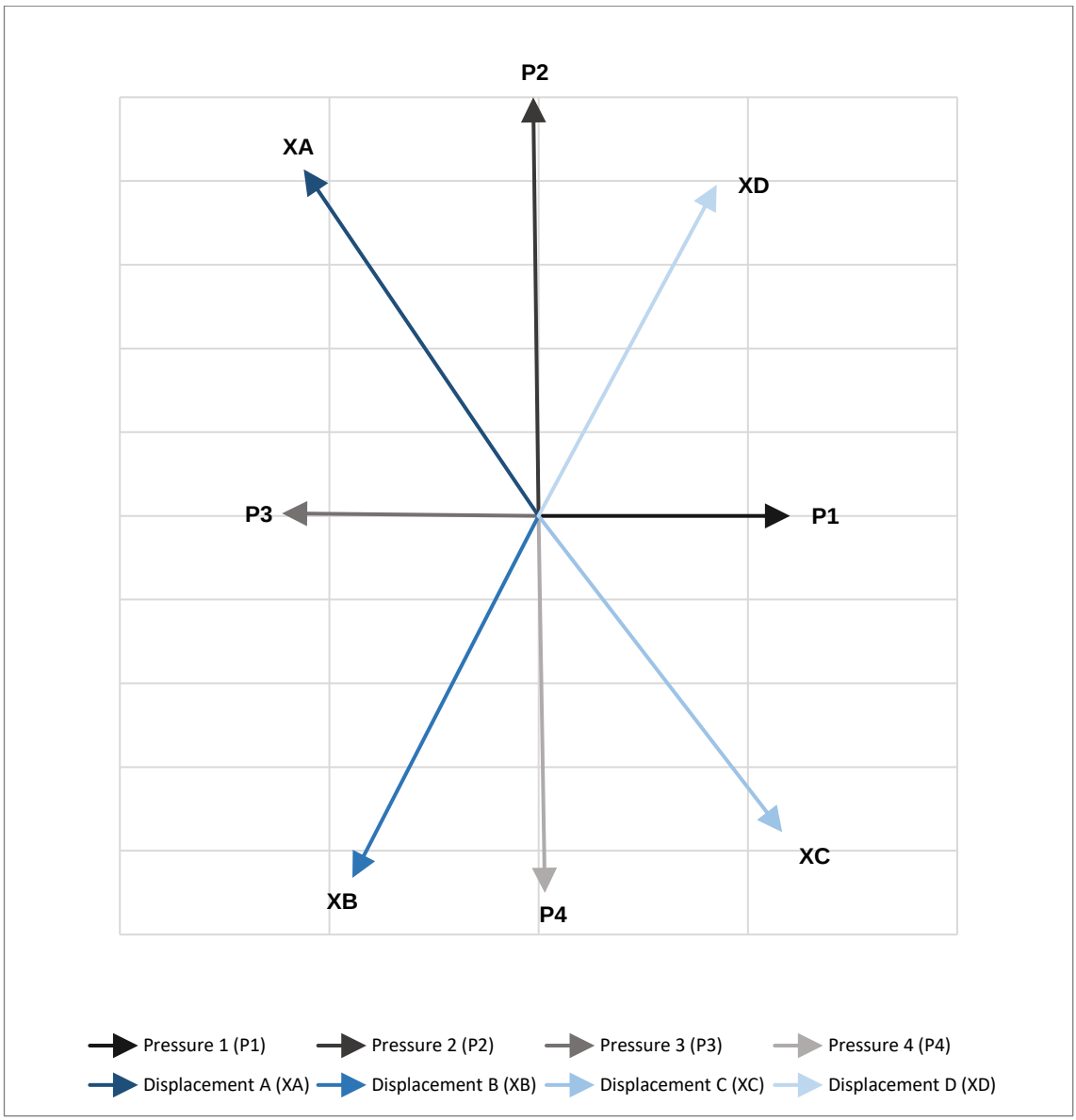

Figure 6.12 – Scaled phasor plot of pressure and displacement profiles for the example 3HEAT experiment with 22 mm piston tubes. The experiment used 110°C heaters and 4 bar charge pressure.

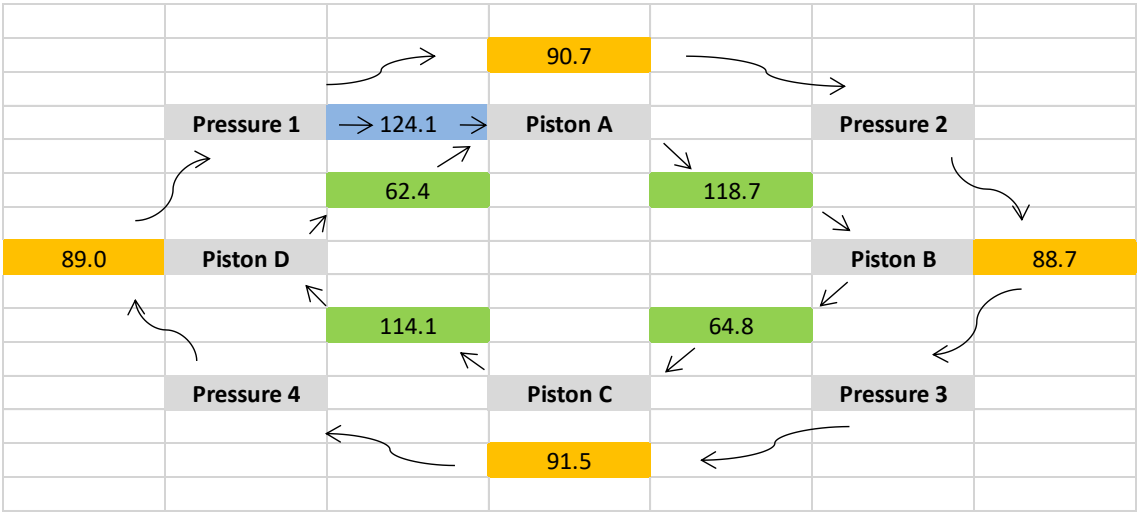

Figure 6.13 – Relative phase angles for the example 3HEAT experiment with 22 mm piston tubes. The experiment was with 110°C heaters and 4 bar charge pressure.

The shape of the phasor plot is again very similar to those of the 15 mm experiments. As in the 22 mm 4HEAT case, the pressure phasors are much closer to the 90º mark, with the largest deviation in this instance of 1.5º. The piston phasors are influenced by the two largest pressure phasors, which results in relative phase angles in the ranges of 63.6° ± 1.2° and 116.4° ± 2.3º for the displacements. The pressure amplitude trends of GS1 (the absorber space) for each of the three heater temperatures are shown in Figure 6.14. Both the 110ºC and 115ºC experiments produced results which transitioned into unstable pressure amplitude oscillations. The transition pressure for the 115ºC experiments was between 3 bar and 3.25 bar, whereas for the 110ºC experiments the transition pressure was at approximately 4.25 bar. The results at 105ºC remained below the threshold, and all experiments produced smooth pressure amplitude progression trends as those shown in Figure 6.9 (for the 75°C 4HEAT dataset).

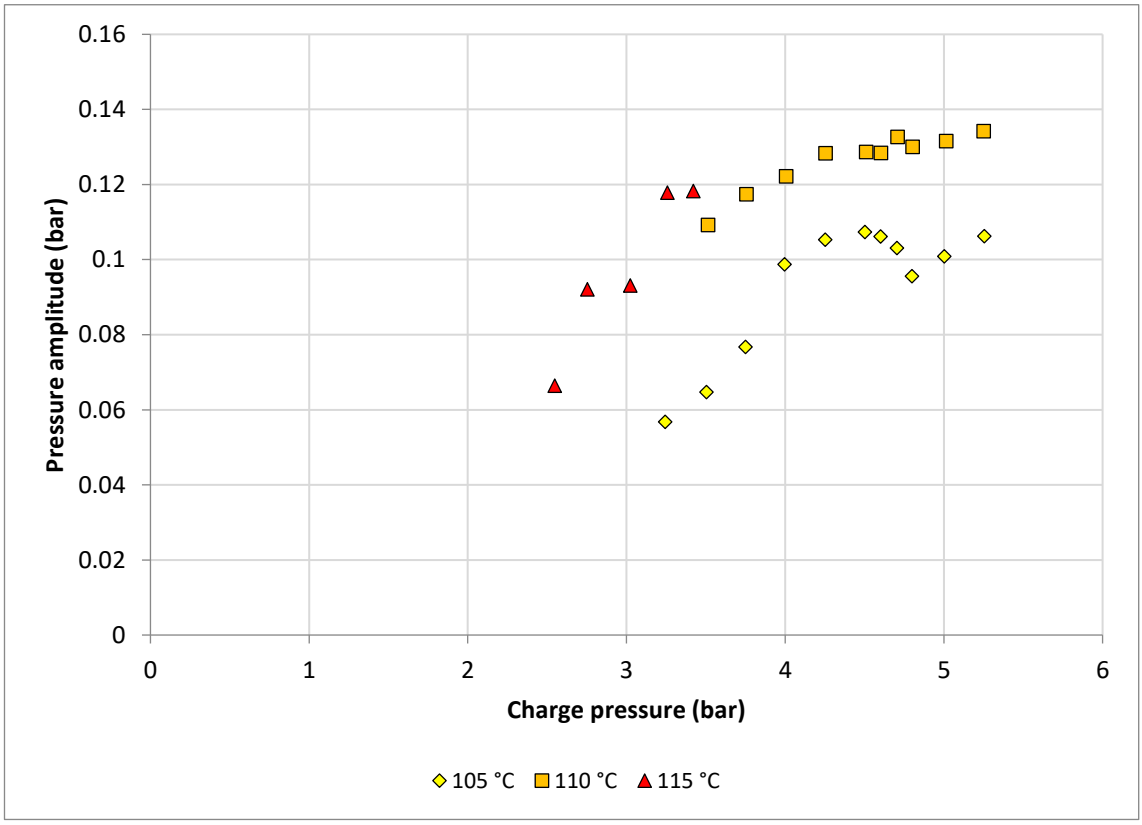

Figure 6.14 – Pressure amplitude variation of Gas Space 1 with changing charge pressure for all 3HEAT experiments using 275 ml liquid pistons.

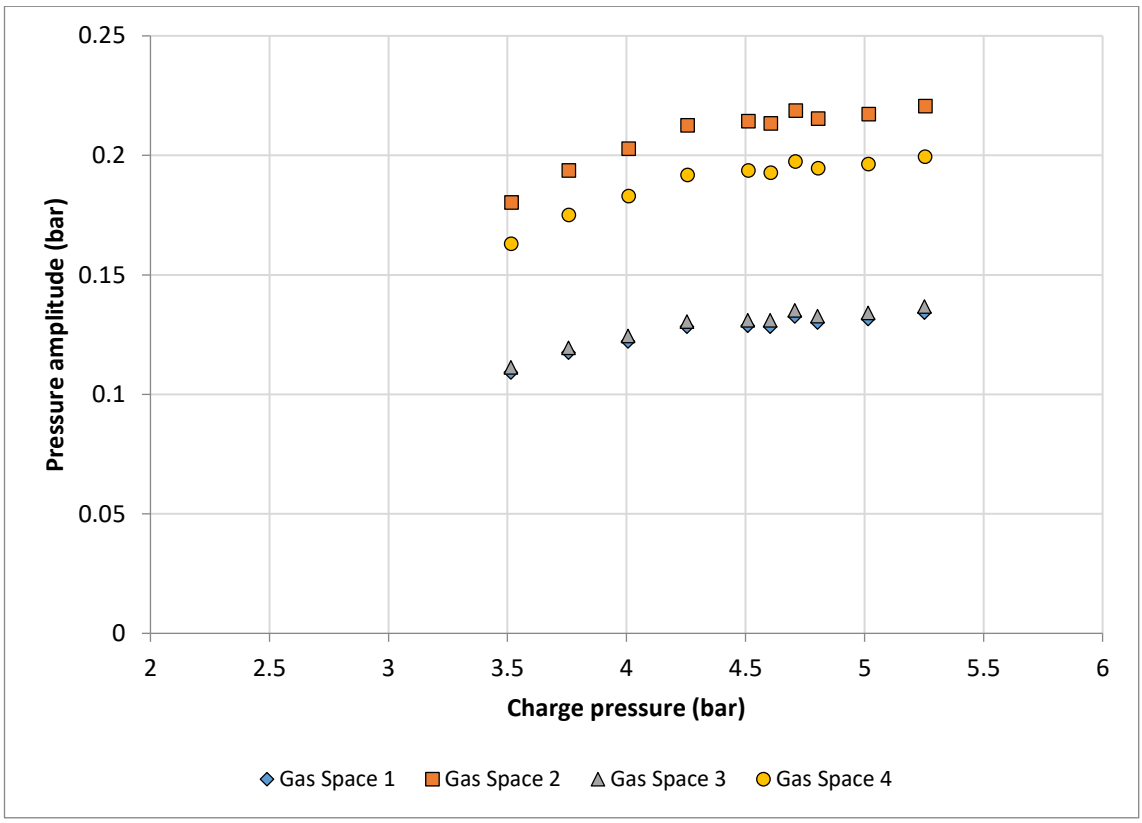

Figure 6.15 – Pressure amplitude variations of all gas spaces with increasing charge pressure for 3HEAT experiments conducted with 110°C heater temperatures and 275 ml pistons.

The pressure amplitudes of all four gas spaces are plotted in Figure 6.15 for the 110ºC heater temperature experiments. The pressure amplitudes of each space exhibit very similar ratios of magnitude to the 3HEAT experiments conducted for the 15 mm piston tubes. The relative ratios in this case are 1.66 (s = 0.4%), 1.02 (s = 0.1%) and 1.50 (s = 0.4%) for GS2, GS3 and GS4 respectively (recalling that from Section 5.1.2, the relative ratios of 1.62 (s = 0.7%), 1.02 (s = 0.6%) and 1.44 (s = 0.7%) were measured for GS2, GS3 and GS4 respectively). Calculating the percentage changes in the relative pressure ratios gives 2.3% and 3.8% increases for GS2 and GS4 respectively, with no change in the GS3 ratio. This means that despite the improvements made to the system's performance with the new pistons, the pressure amplitudes developed in the absorber space for the 3HEAT configuration are a smaller percentage of the total. Calculating the conversion ratio from the ratios above yields 4.17:1 (three significant figures). The piston displacements recorded for the experiments are shown in Figure 6.16.

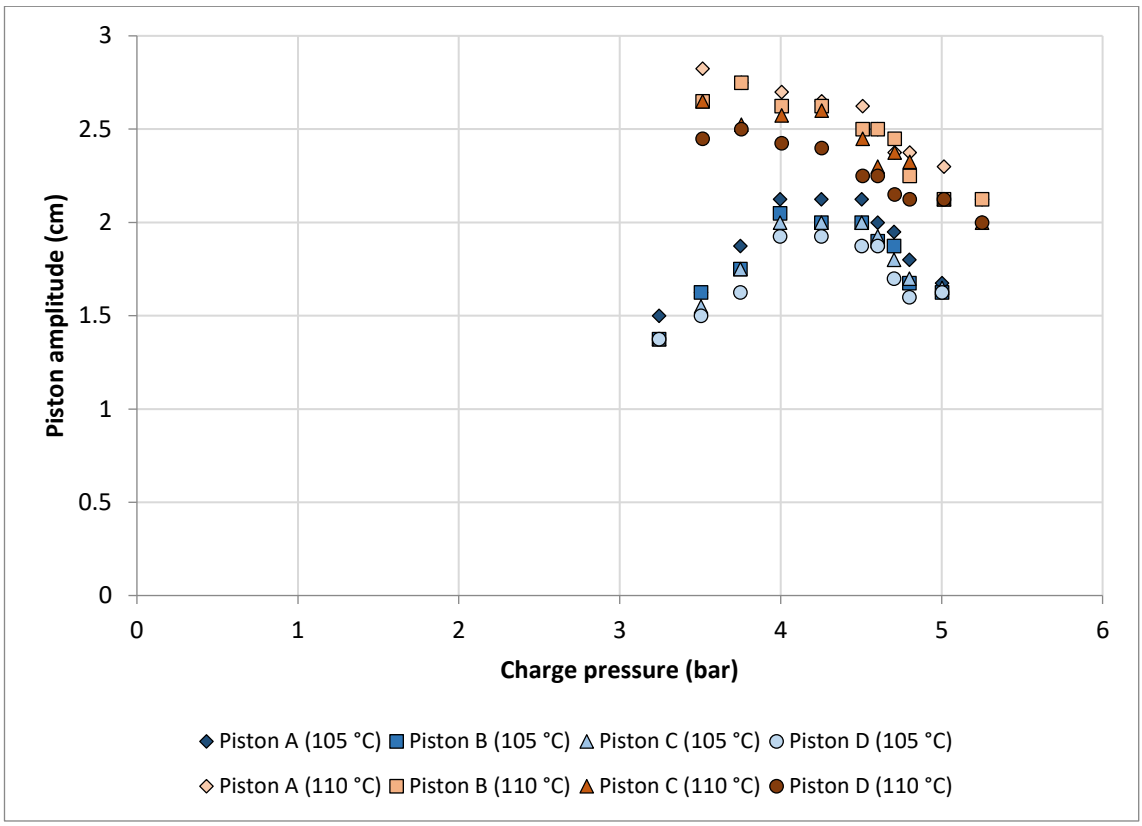

Figure 6.16 – Piston amplitude variation with charge pressure for the 3HEAT configuration experiments with 105°C and 110°C heaters and using 275 ml liquid pistons.

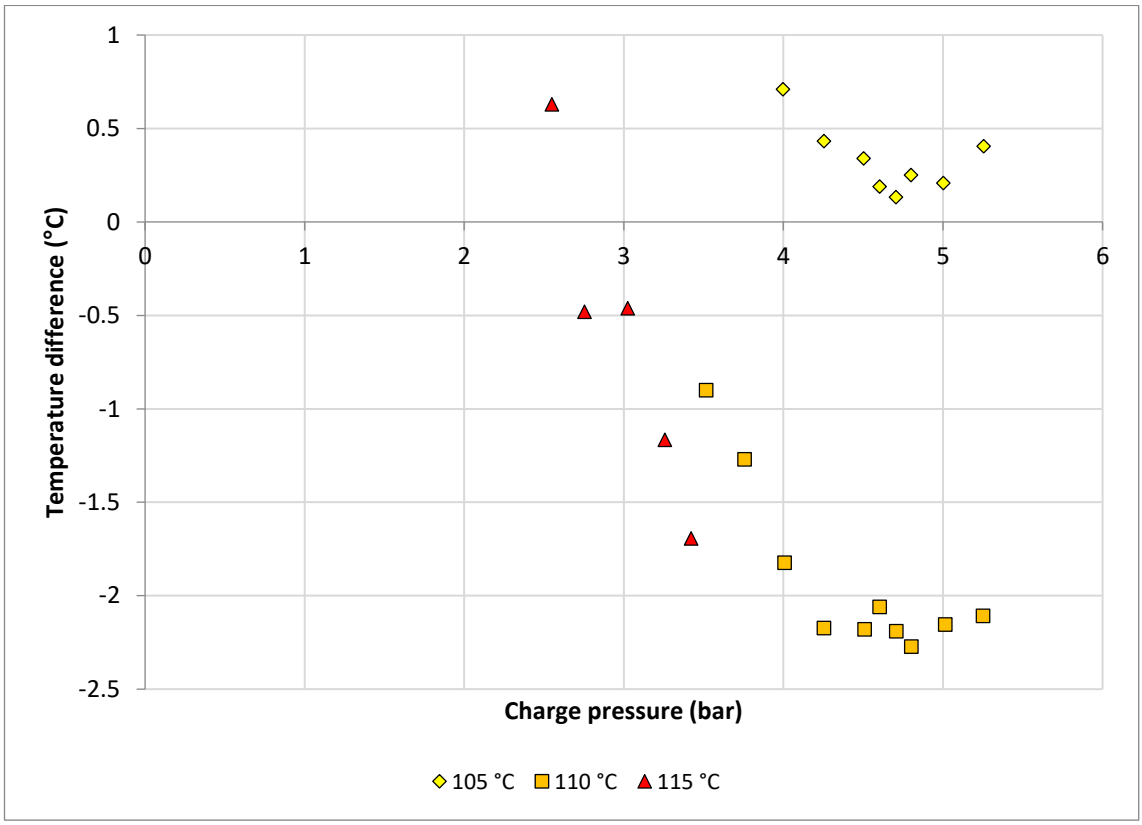

Figure 6.17 – Temperature difference between expansion and compression spaces in Gas Space 1 for the 3HEAT configuration experiments using 275 ml liquid pistons with different heater temperatures.

Figure 6.17 presents the evidence of cooling obtained for the 3HEAT configuration experiments with the new piston size. The measured difference between the expansion space temperature minus the compression space temperature of GS1 are plotted for all three data sets. The expansion space is where the temperature will drop if the system is producing a cooling effect. Examining the 110°C and 115°C measurements, the first unequivocal evidence of cooling for the project is witnessed. The 110°C values drop steadily until reaching the transition pressure of 4.25 bar, where they plateau. The largest cooling effect recorded is a temperature difference of -2.3°C. The limited data from the 115°C experiments also suggests larger temperature differences would be achievable if the pistons remained stable.

6.2.3 2HEAT Configuration

The 2HEAT experiments were conducted with heater temperatures of 160ºC and 165ºC. Temperatures below 160ºC did not produce significant results. Figure 6.18 shows the scaled pressure and displacement phasor plot for an example experiment with 165ºC at 4 bar charge pressure. The relevant relative phase angle chart is then shown in Figure 6.19. The absolute quantities of the phasors are also listed in Table 6.4 for reference.

Table 6.4 – Phasor representations of gas pressure and piston displacement amplitudes for example 2HEAT experiment.

Phasor	Amplitude (bar or cm)	Phase angle (°)
Pressure 1 (P1)	0.192	0.0
Pressure 2 (P2)	0.188	87.4
Pressure 3 (P3)	0.166	179.9
Pressure 4 (P4)	0.155	268.5
Displacement A (XA)	2.75	139.1
Displacement B (XB)	2.75	228.2
Displacement C (XC)	2.33	321.0
Displacement D (XD)	2.75	41.6

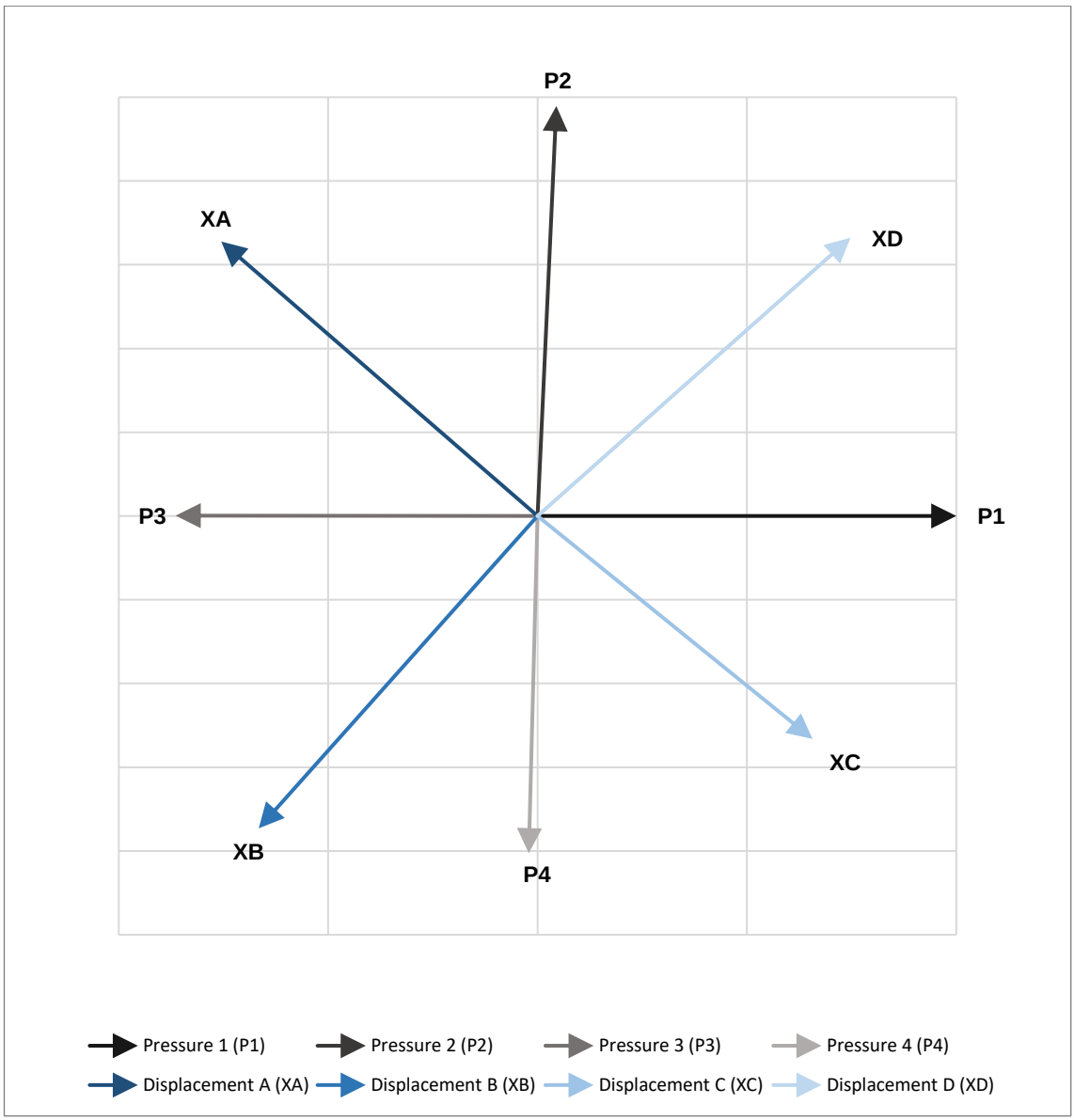

Figure 6.18 – Scaled phasor plot of pressure and displacement profiles for the example 2HEAT experiment with 22 mm piston tubes. The experiment was with 165°C heaters and 4 bar pressure.

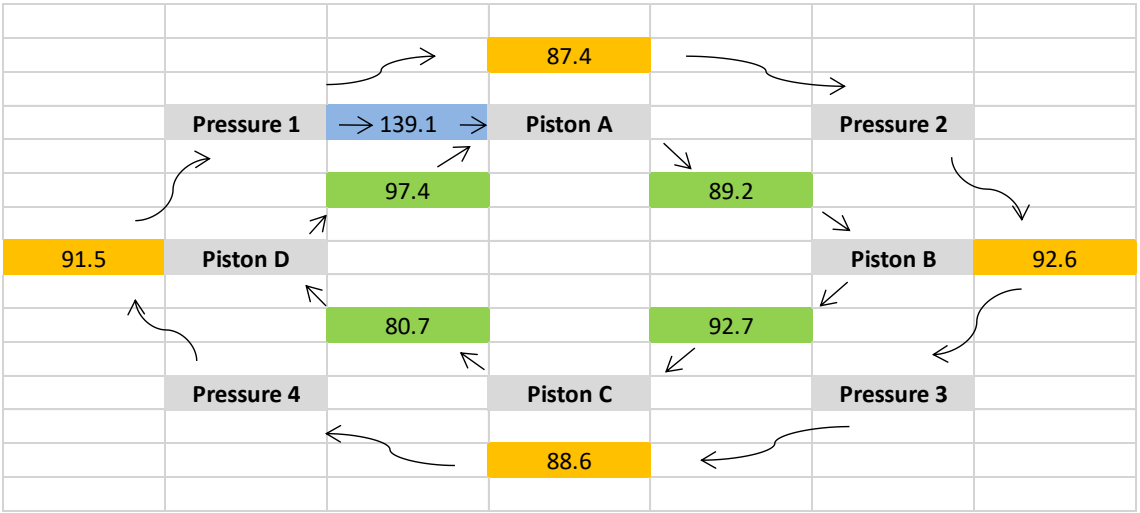

Figure 6.19 – Relative phase angles for the example 2HEAT experiment with 22 mm piston tubes. The experiment was with 165 °C heaters and 4 bar charge pressure.

Although the general shape of the phasor plot is quite similar to the previous 15 mm example, there are some notable differences. The first significant difference is that the largest pressure amplitude is now developed in one of the absorber spaces, GS1, whereas previously it was in the heated space, GS2. The lowest amplitude developed is also now the other absorber space GS4; previously it was in the heated space GS3. Because of these changes in the relative pressure amplitudes, the relative phase angles between the pistons have also been affected. The two phase angles separating the pistons on either side of the absorber spaces are not as close to the 90º as before. Even so, all relative piston phase angles are within ± 9.3º of 90º, which is an improvement over the 15 mm case where the phase angle between Piston B and C was 76.6º.

The pressure amplitude trends of GS1 for both heater temperatures are shown in Figure 6.20. Both the 160ºC and 165ºC experiments experienced transitions from stable pressure amplitude oscillations into unstable oscillations. The transition pressure for both occurred between 3.75 bar and 4.25 bar. It can be seen that the pressure amplitudes developed for both sets of experiments reach a plateau at this point, and actually decrease slightly as the charge pressure is increased up to 6 bar. Figure 6.21 shows the pressure amplitude progressions of all four gas spaces for the 165ºC experiments. The observations made about the changes in the relative pressure amplitude hierarchy for the example 2HEAT experiment, are shown to be repeated consistently across all charge pressures. Despite the GS1 and GS2 magnitudes being very similar, GS1 is always approximately 2% larger. The mean pressure amplitude ratios with respect to GS1 are 0.98 (s = 0.9%), 0.87 (s = 0.3%) and 0.81 (s = 0.7%) for GS2, GS3 and GS4, respectively. Adding up the unrounded ratios obtained for the heater and absorber spaces gives 1.851 for the heater spaces and 1.809 for the absorber spaces, which equates to a conversion ratio of 1.02:1 (three significant figures).

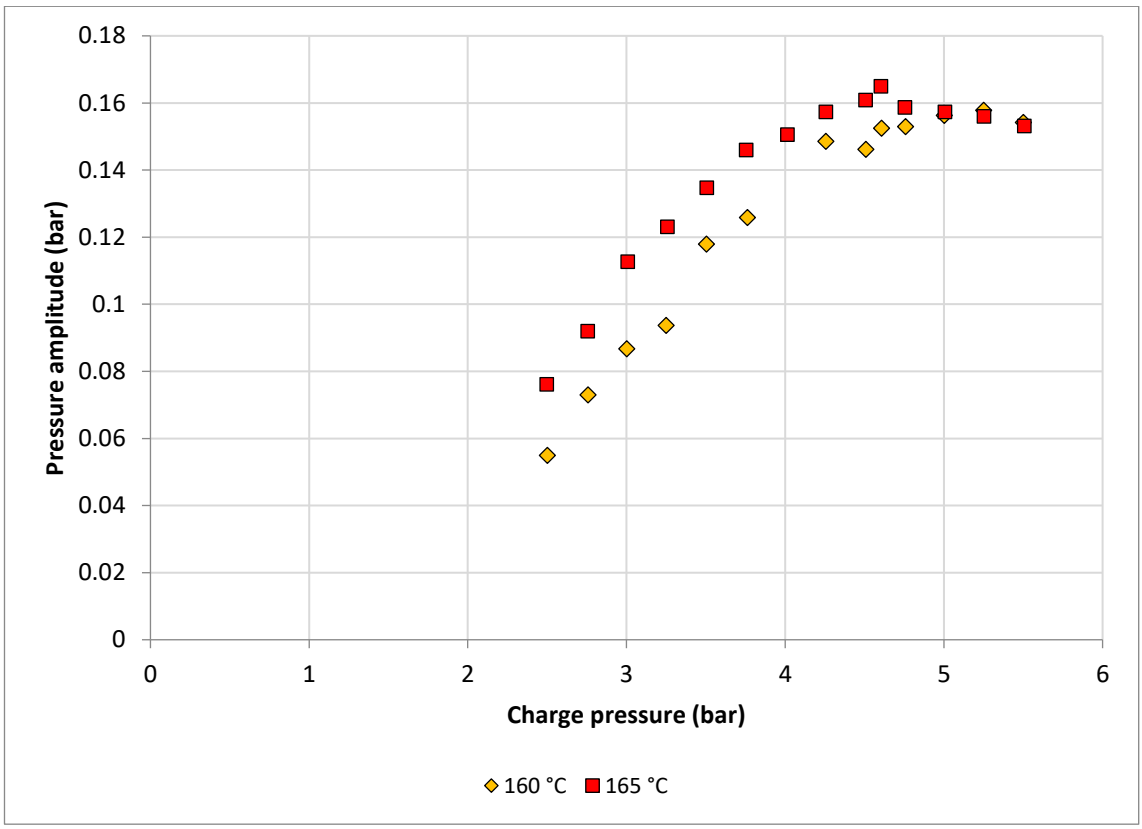

Figure 6.20 – Pressure amplitude variation of Gas Space 1 with changing charge pressure for all 2HEAT experiments using 275 ml liquid pistons.

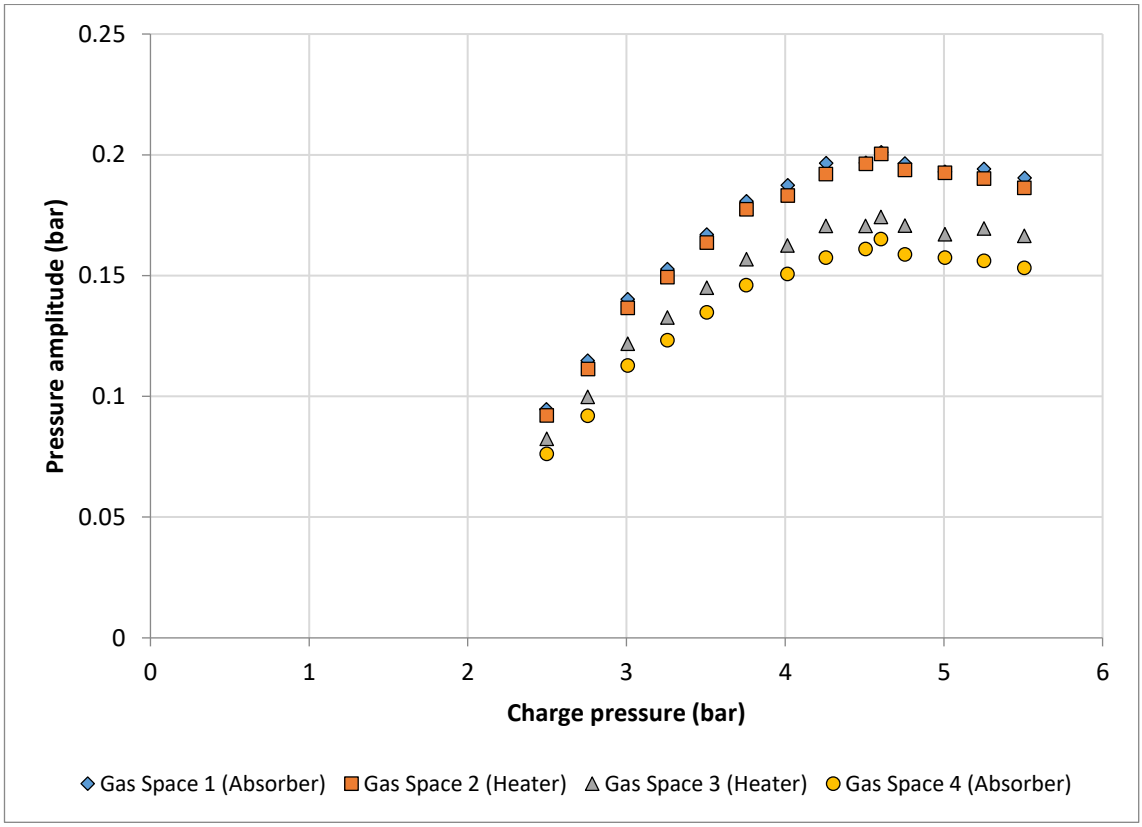

Figure 6.21 – Pressure amplitude variations of all gas spaces with increasing charge pressure for 2HEAT experiments conducted with 165°C heater temperatures and 275 ml pistons.

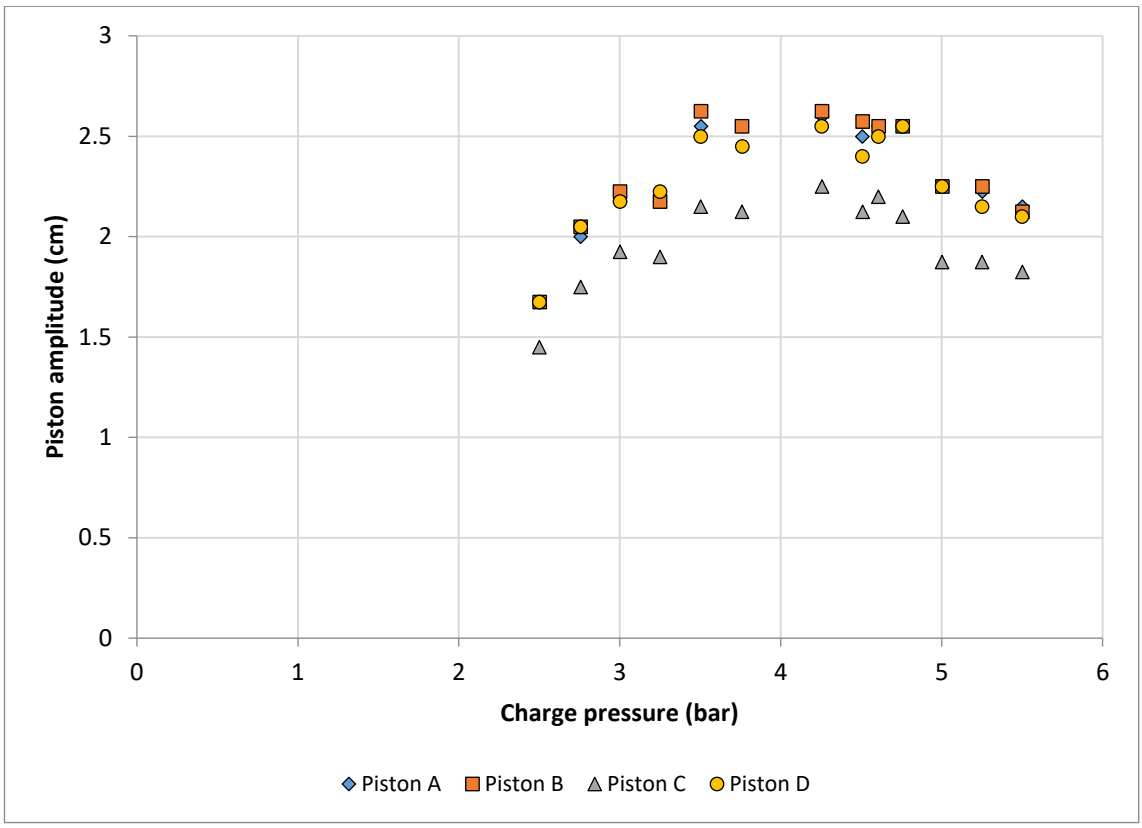

Figure 6.22 – Piston amplitude variation with charge pressure for the 2HEAT configuration experiments with 160°C heaters and using 275 ml liquid pistons.

The piston amplitudes for the 160°C experiments are presented in Figure 6.22. The amplitudes increase steadily until they reach maximums of 2.6 cm at the transition pressure of 4 bar, beyond which point they reduce with increased charge pressure. Of the piston amplitudes, pistons A, B and D are very similar in magnitude for the majority of the experiments. The amplitude of Piston C constantly measures in the range of 0.2 cm–0.5 cm below the other three pistons. The reason for this is that the two gas spaces in contact with Piston C (i.e. gas spaces 3 and 4) exhibit the two lowest pressure amplitudes; with the smallest contributing pressure amplitudes, the net pressure phasor acting on Piston C thus has the smallest magnitude of all of the four net pressure phasors. By the same measure, it could be expected that the amplitude of Piston A would be the largest, since the two gas spaces contributing to its motion are gas spaces 1 and 2, which have the two largest pressure amplitudes. However the relative phase angles also play a role in determining the magnitude of the net pressure phasor, and in this case the relative phase

angle is 87.4°, which is less than 90º. Subtracting one from the other for the net pressure phasor will therefore involve a degree of counteraction, reducing the resultant magnitude compared with the case of 90º separation. This normally would not be enough to reduce the piston amplitude to those values expected from pistons B and D, but the relative phase angles between the gas spaces contributing to the motion of pistons B and D are 91.5º and 92.6º, which are above 90º, and therefore boost their amplitudes slightly. Hence, it is easy to see how small differences in the relative phase angles between the gas space pressures can be quite influential in the resultant piston amplitudes and phase angles.

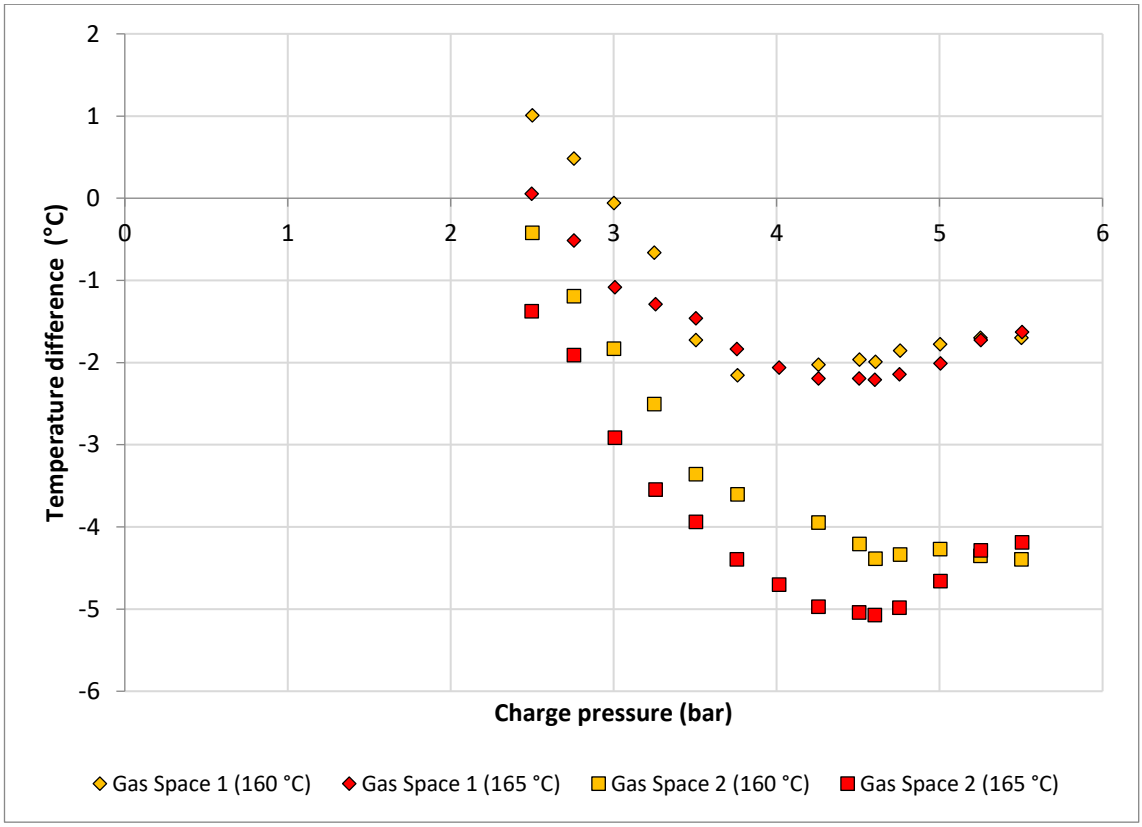

Figure 6.23 – Shows the temperature difference between expansion and compression spaces in the two absorber spaces for the 2HEAT configuration experiments using 275 ml liquid pistons with different heater temperatures.

The temperature differences between the expansion spaces and the compression spaces in the two absorber gas spaces, GS1 and GS4, are shown in Figure 6.23. The temperature differences achieved are the most significant of any experiments up until this point. The largest developed over the entire experimental range is -5ºC and occurs in the 165ºC

experiments at 4.5 bar charge pressure. The largest temperature difference developed in Gas Space 4 is -2.2ºC, which is very similar to the maximum achieved in the 3HEAT experiments in the previous section. Both sets of results show similar trends, with steadily declining values (or increased cooling potential) until reaching the transition pressures of approximately 4 bar. From 4 bar onwards, the rate of change of the temperature reduction slows down, and at 4.5 bar most of the temperature differences start to decrease in magnitude. Unlike the 15 mm experiments, the 2HEAT configuration has proven to be more effective at producing a temperature difference than the 3HEAT configuration, which is in agreement with the Sage model COP predictions from the 15 mm piston analysis.

6.2.4 Summary

Increasing the piston diameter from 15 mm to 22 mm resulted in significantly better performance of the LPSC system. Large reductions were achieved for the minimum heater temperatures required to achieve self-sustained operation. The 4HEAT configuration experiments were able to be conducted at temperatures as low as 75ºC, which equates to a 20ºC reduction compared with the 15 mm experiments. For the 3HEAT configuration a reduction of approximately 25ºC was achieved, from 130 ºC to 105 ºC, and for the 2HEAT configuration a reduction of 30ºC was realised, 190ºC to 160ºC. Reducing this minimum temperature is an important factor in determining the feasibility of such a system for use with a solar thermal energy supply due to the restrictions on the heat source temperature of many solar collectors.

The results for all three 22 mm configurations produced similar scaled phasor plots to the 15 mm experiments. The 4HEAT pressure phasors were closer to what was expected for a perfectly symmetrical system, with all of the relative phase angles between gas space pressures residing in the range of 90º ± 1.3º. When considering the 3HEAT and 2HEAT

configurations, the patterns found in the pressure amplitude ratios between the four gas spaces were found to be very similar to those identified from the earlier 15 mm experiments. The 3HEAT ratios were at most 3.8% different between the two piston sizes, while for the 2HEAT case they were up to 8.0% different. Similarly, the conversion ratios for the development of pressure amplitudes in the heated spaces to the absorber space(s) showed little change, registering 4.17:1 and 1.02:1 for the 3HEAT and 2HEAT configurations, which corresponds to changes of 2.2% and 2.1% respectively.

Although both 3HEAT and 2HEAT configurations showed improved performance compared with their 15 mm piston versions, the 2HEAT configuration was able to outperform the 3HEAT system on this occasion. The 2HEAT configuration produced the largest cooling effect measured for any experiments up to this point with temperature differences of -5ºC and -2.2ºC developed in the absorber spaces.

The 4HEAT experiments were able to show further evidence of piston instability limiting the magnitude of the pressure amplitudes developed in each gas space. There existed a threshold charge pressure for which the measured pressure amplitudes would transition from being smooth and stable into irregular and volatile. This transition pressure was different depending on the heater temperature of the experiment set; in some instances the heater temperature was low enough to avoid reaching the threshold (in a similar manner to the 75ºC experiments). The transition pressure phenomenon was encountered in the 3HEAT and 2HEAT experiments as well—with the temperature achieved in the absorber spaces plateauing in close proximity to this threshold pressure. Understanding the circumstances which induce this piston instability is critical in the successful design of an LPSC machine.

The multi-modal behaviour of the system was not witnessed with the larger diameter pistons. It is possible that the inclusion of the piston stabilisers was a factor in this regard.

The new method of using slow motion video for obtaining the piston amplitudes provided more consistent estimates than the capacitive sensors used previously, and the results were correlated more highly with the net pressure magnitudes. The capacitive sensors were still the preferred option for obtaining the piston phase angle data.

6.3 Sage Modelling Results

The Sage model required a number of small changes in order to better represent the new test-rig setup with 22 mm pistons. These changes included the piston dimensions, but also other changes to Sage model components. With the 22 mm U-tubes each filled with 275 ml of liquid water, the total volume of each gas space was increased slightly when compared with the 15 mm 100 ml piston installation. The volume of the compression and expansion spaces, as well as the hot and cold spaces, were increased within the model to account for this. A summary of the changes made to model parameters is given by Table 6.5. Note that the rejection temperature was changed from 24ºC to 21ºC to reflect the change in the prevailing average ambient temperature measured during the 22 mm experiments. The multitude of other variable changes happen automatically within the model based on the user defined and recast variables.

Table 6.5 – Sage parameter adjustments for 22 mm, 275 ml liquid piston test-rig.

Parameter Name	Description	Value	Component, level
Pmass	Piston mass (kg)	2.75×10^{-1}	System
Vvariable	Expansion and compression space volumes (m^3)	2.414×10^{-5}	System
Dpiston	Piston diameter (m)	1.93×10^{-2}	System
Tcooling	Rejection temperature (K)	294	System
Swet	Compression and expansion space wetted surface area (m^2)	5×10^{-3}	Compression and expansion Spaces, Root
Dtube	Cold and hot Space weighted average tube inner diameter (m)	2.141×10^{-2}	Cold and hot spaces, Root
Length	Cold and hot Space weighted average duct-length (m)	1.355×10^{-1}	Cold and hot Spaces, Root

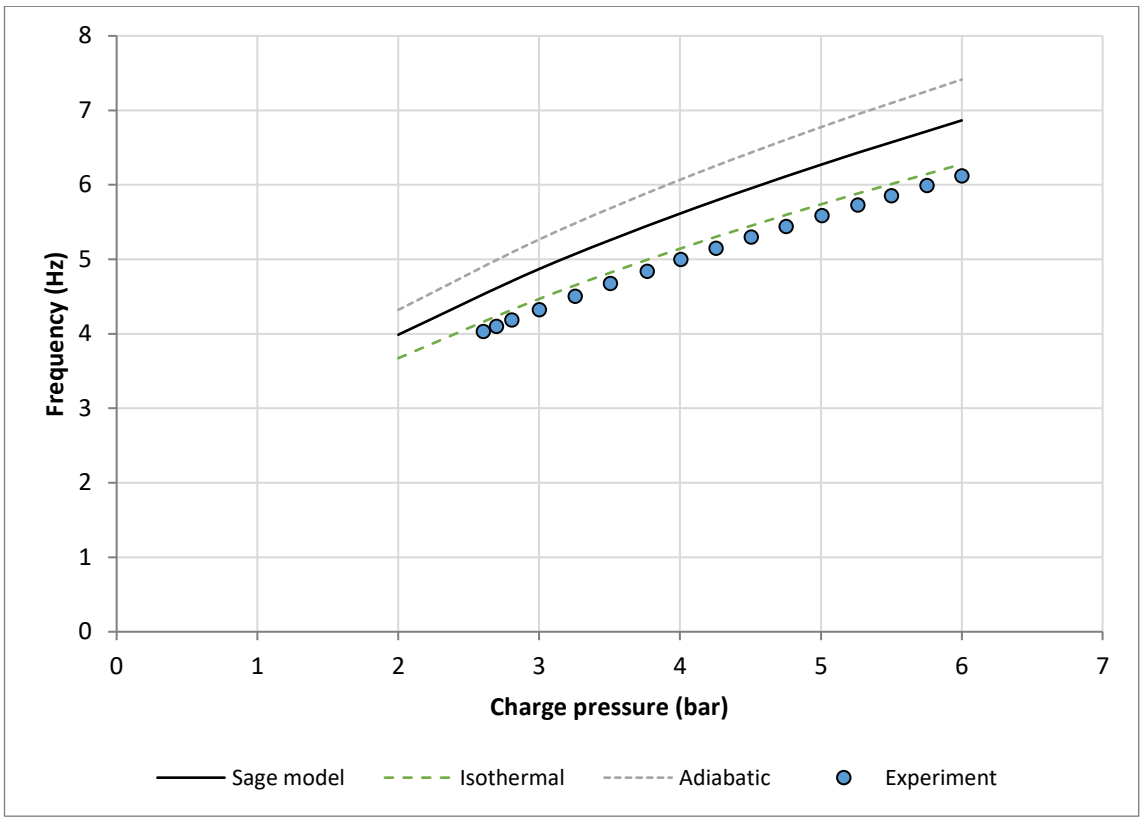

Figure 6.24 – Frequency comparison between Sage predictions, experiment and natural estimates.

Figure 6.24 shows the frequency predicted by Sage and how it compares with the experimental measurements and the analytical estimates (both isothermal and adiabatic). As with the 15 mm case, the Sage model overestimates the test-rig frequency. The trends are very similar, but the measured frequencies are much closer to isothermal gas behaviour than those predicted by the Sage model, which typically reside halfway in between isothermal and adiabatic gas behaviour. The Sage model does not account for the presence of liquid water vapour and evaporation of water from the piston surface. Both of these factors would contribute to greater isothermal heat transfer occurring in the gas spaces. The experimental measurements also register slightly below the isothermal line, which implies that there may be a small discrepancy between the model and the test-rig, most likely associated with precise gas space volumes (due to their complex geometry and the uncertainties resulting from the regenerator material), sensor ports and other fittings. The volumes used in the model were checked to ensure that the best estimates of the real system geometry were used; although without sophisticated technology capable

of measuring the gas volumes exactly, it is inevitable that there are slight differences in the model's approximation.

The Sage model results are now compared directly to the experimental results for each of the three configurations. As with the experimental results section for the 22 mm, 275 ml pistons, the scope of the analysis presented here is restricted to the most significant findings and basic understanding of the three configurations, and their traits identified in chapter 5 is assumed.

6.3.1 4HEAT Configuration

The phasor plot for the 4HEAT Sage model results is not shown because of its similarities to the previous 15 mm 4HEAT Sage model results. The pressure and piston amplitudes were predicted to be equal in each of the four subsystems. All of the relative phase angles between pressure phasors are $90^o \pm 0.1^o$, as are the relative phase angles between piston displacements. The only distinguishing parameter is the relative phase angle between pistons and pressure phasors: for the angle between P1 and XA an average value of 138.1^o was obtained. An example of the Sage solutions in phasor form is presented in Table 6.6 for the simulations at 4 bar charge pressure and 80ºC heater temperature.

Table 6.6 – Sage model phasors predictions for 4HEAT experiment at 4 bar with 80°C heaters and 275 ml pistons.

Phasor	Amplitude (bar or cm)	Phase angle (°)
Pressure 1 (P1)	0.185	0.0
Pressure 2 (P2)	0.185	89.9
Pressure 3 (P3)	0.185	179.9
Pressure 4 (P4)	0.185	270.0
Displacement A (XA)	2.22	138.1
Displacement B (XB)	2.22	228.0
Displacement C (XC)	2.22	318.1
Displacement D (XD)	2.22	48.0

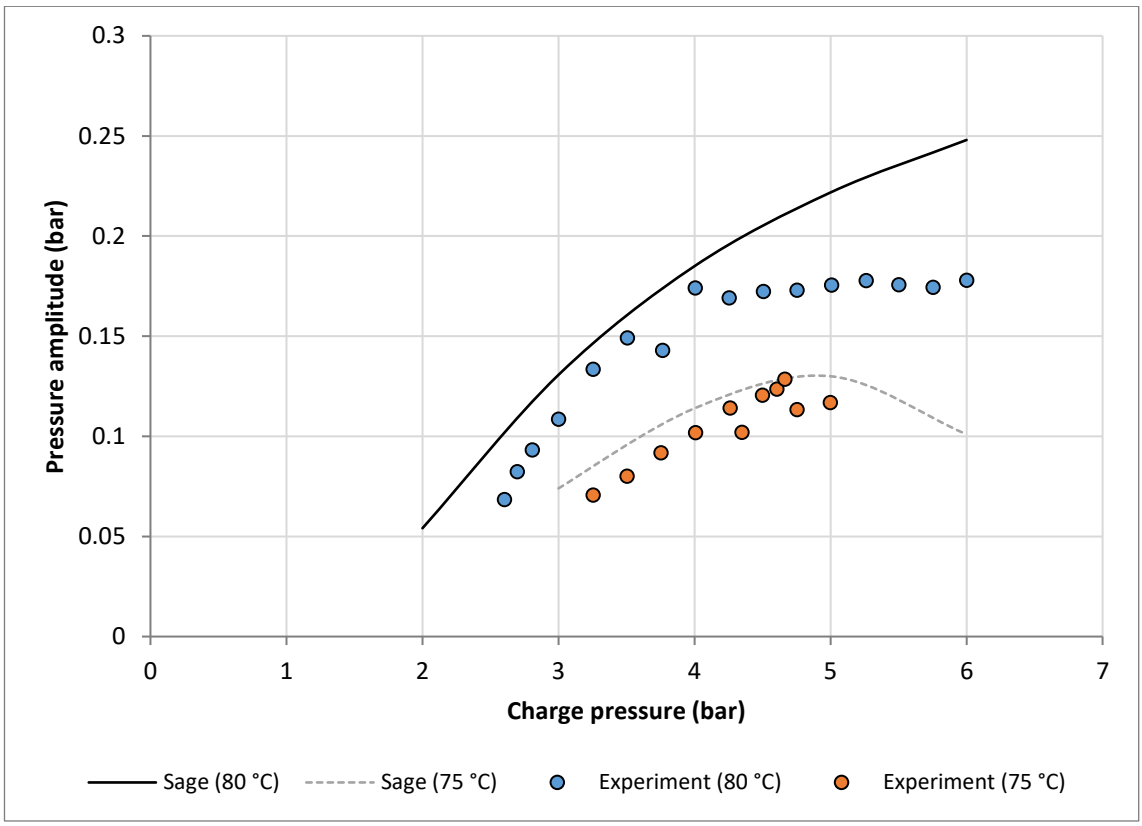

Figure 6.25 – Gas pressure amplitudes predicted by Sage compared with the experimental results for the 22 mm 275 ml pistons.

Figure 6.25 compares the pressure amplitudes predicted by the Sage model and the experimental measurements for the two heater temperatures 75ºC and 80ºC. This graph shows some very intriguing results. For the 75ºC case, the Sage predictions are quite similar to the experimentally measured values. In these experiments the heater temperature was not high enough to cause excitation levels that would approach instability (as previously explained in Section 6.2.1). The 80ºC case also shows agreement between the model and experiment, although only up until the transition pressure of 4 bar, where the model predictions continue to grow and the experimental measurements plateau. This transition pressure was shown experimentally to occur at the same point where the pistons progress from stable to unstable oscillations in Sections 5.1.5 and 6.2.1. If the cause of this transition is the onset of the RT instability, it would be expected that the same limitations would be imposed on maximum piston acceleration. Figure 6.26 presents the maximum piston accelerations predicted by Sage and compared with the

experiment data. The shaded band in green represents the potential acceleration limit identified for the 15 mm pistons (with floats installed), between 25 ms^{-2} and 30 ms^{-2}.

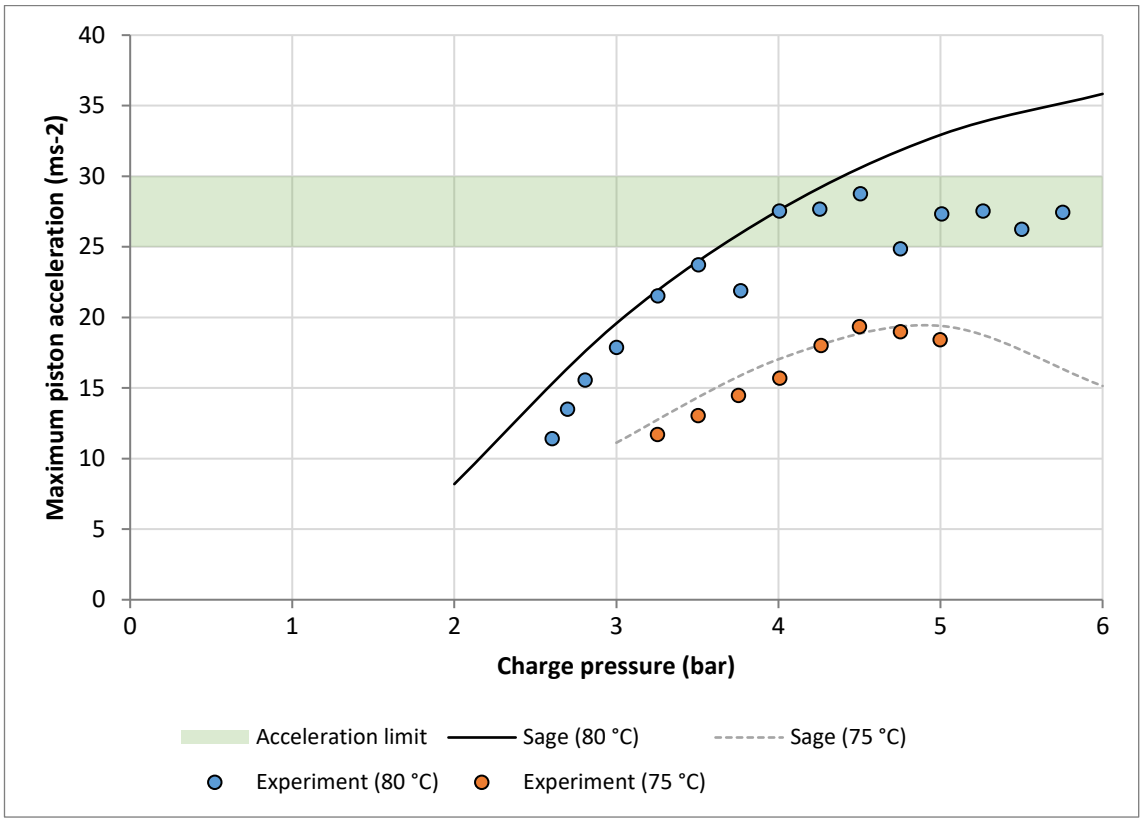

Figure 6.26 – Average maximum piston acceleration for 22 mm experiments with 275 ml pistons when compared with Sage model.

As suspected, the 75ºC results from both Sage and the experiments do not achieve high enough maximum accelerations to reach the theorised maximum piston acceleration limit. The 80ºC experiment results follow the Sage predictions until the maximum piston accelerations move into the range of 25 ms^{-2} to 30 ms^{-2}, where they remain for all higher charge pressure experiments.

6.3.2 3HEAT Configuration

An example of the Sage solutions in phasor form is presented in Table 6.7 for the 3HEAT simulations at 4 bar charge pressure and 80ºC heater temperature. Figure 6.27 then displays the scaled phasor plot for the same simulation compared with the phasor plot from the experiment with the same conditions.

Table 6.7 – Sage model phasors predictions for 3HEAT experiment at 4 bar with 110°C heaters and 275 ml pistons.

Phasor	Amplitude (bar or cm)	Phase angle (°)
Pressure 1 (P1)	0.150	0.0
Pressure 2 (P2)	0.233	89.6
Pressure 3 (P3)	0.152	180.0
Pressure 4 (P4)	0.204	269.9
Displacement A (XA)	2.34	125.0
Displacement B (XB)	2.36	240.3
Displacement C (XC)	2.15	309.3
Displacement D (XD)	2.14	57.2

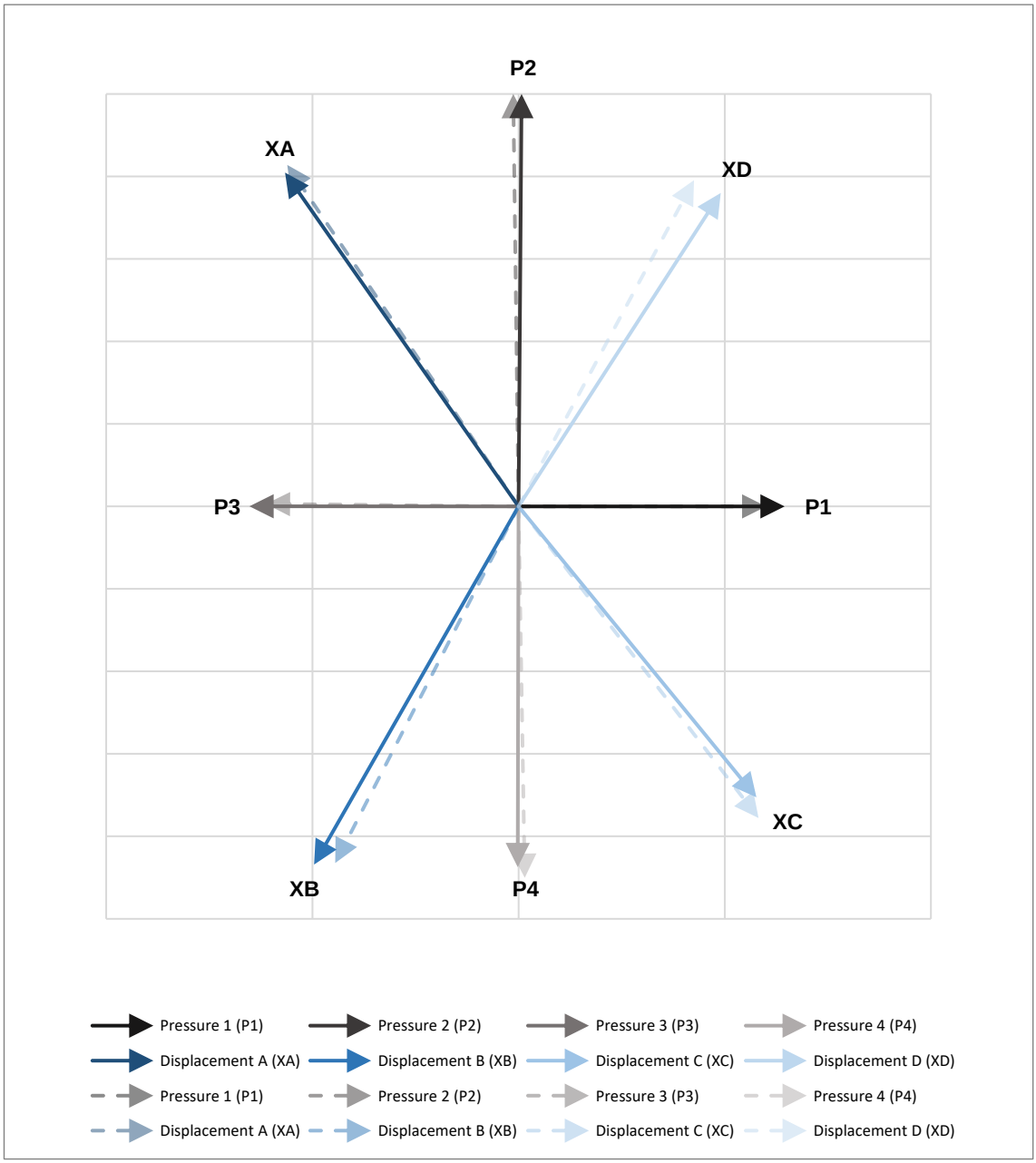

Figure 6.27 – Scaled phasor plot of example 3HEAT Sage simulation pressure and displacement profiles compared with experiment results. Simulation/experiment is at 4 bar charge pressure with 110°C heater temperatures and 275 ml pistons. Experiment phasors are dashed.

The phasors generated from the Sage model simulations are very similar to the experiment results in this scaled comparison. The primary differences result from the slightly larger relative pressure amplitudes of gas spaces 1 and 3 in the Sage phasors. They have the effect of attracting the displacement phasors, which is why all of the Sage displacement phasors are aligned slightly closer to the horizontal axis. The relative phase angles between the phasors are shown in Figure 6.28. The angle between the pressure phasor of Gas Space 1 and Piston A's displacement phasor is 125º, which is very close to the experimental value of 124.1º. The angles between the pressure phasors are very close to 90º—all are within the range 90º ± 0.4º. The angles between the pistons show greater deviation when compared to the experiment values in the same figure (the phasors with dashed arrow-lines). The largest discrepancy of 6.2° occurs for the angle between Piston C and Piston D (where 107.9º is predicted by Sage and the value from the experiment is 114.1º).

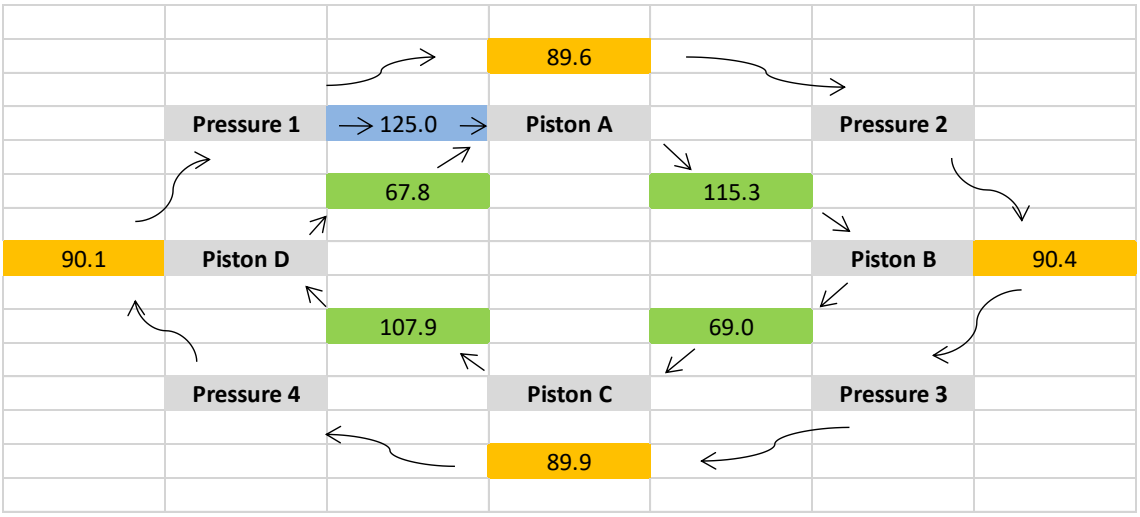

Figure 6.28 – Sage model predictions for the relative phase angles between pressure and displacement phasors in the example 3HEAT simulation. Simulation is at 4 bar charge pressure with 110ºC heater temperatures and 275 ml pistons.

Figure 6.29 shows the pressure amplitudes predicted for each gas space for Sage simulations using the 3HEAT configuration with 110ºC heater temperatures. The pressure amplitudes in each gas space increase with charge pressure while retaining their relative

magnitude ratios. The distribution of the largest and smallest amplitudes remains consistent with both the experimental results and the previous analysis for the 15 mm pistons. The ratios calculated and averaged over the simulation range are 1.54 (s = 0.5%), 1.01 (s = 0.1%) and 1.35 (s = 0.3%) for GS2, GS3 and GS4 respectively. The ratios for GS2 and GS4 are 6.7% and 9.6% smaller than the experiment values. Adding up the unrounded ratios obtained for the heater spaces gives a conversion rate of 3.91:1 (three significant figures).

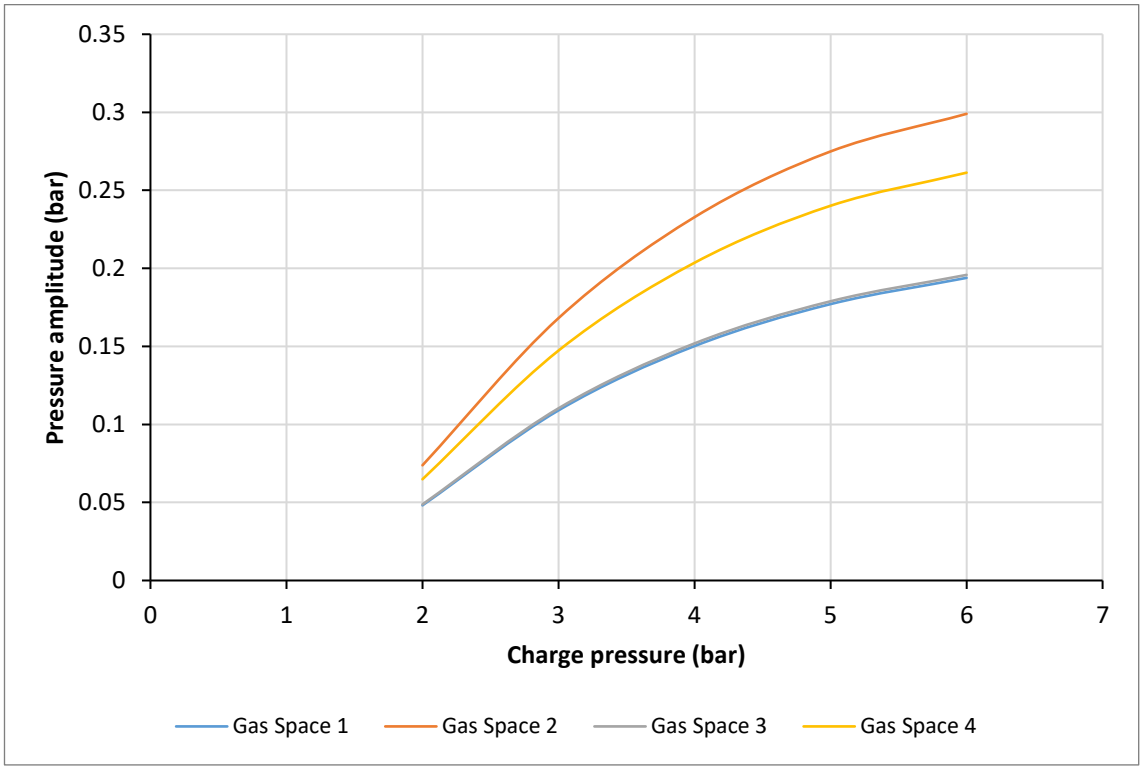

Figure 6.29 – Sage predictions for pressure amplitudes developed in all four gas spaces with increasing charge pressure for 3HEAT configuration. Simulations are with 110°C heaters and 275 ml pistons.

Figure 6.30 compares the Sage model pressure amplitudes for the absorber space (GS1) for both 105°C and 110°C heater temperature against the experiment results. For the 4HEAT simulations it was shown that the Sage model was capable of predicting not only the relative phasor magnitudes and phase angle relationships of the pistons and gas spaces, but also the absolute values for the pressure amplitudes and piston accelerations. In the 3HEAT simulations, the model overestimates the level of excitation resulting from the exact heater temperatures of 105°C and 110°C used in the experiments. The

overestimation can be accounted for by a reduction in the model temperature of 5ºC, as the graph shows good agreement between the 105ºC Sage and the 110ºC experiment values (this offset is entirely reasonable in the context of the known model sensitivity to small changes in a number of model parameters).

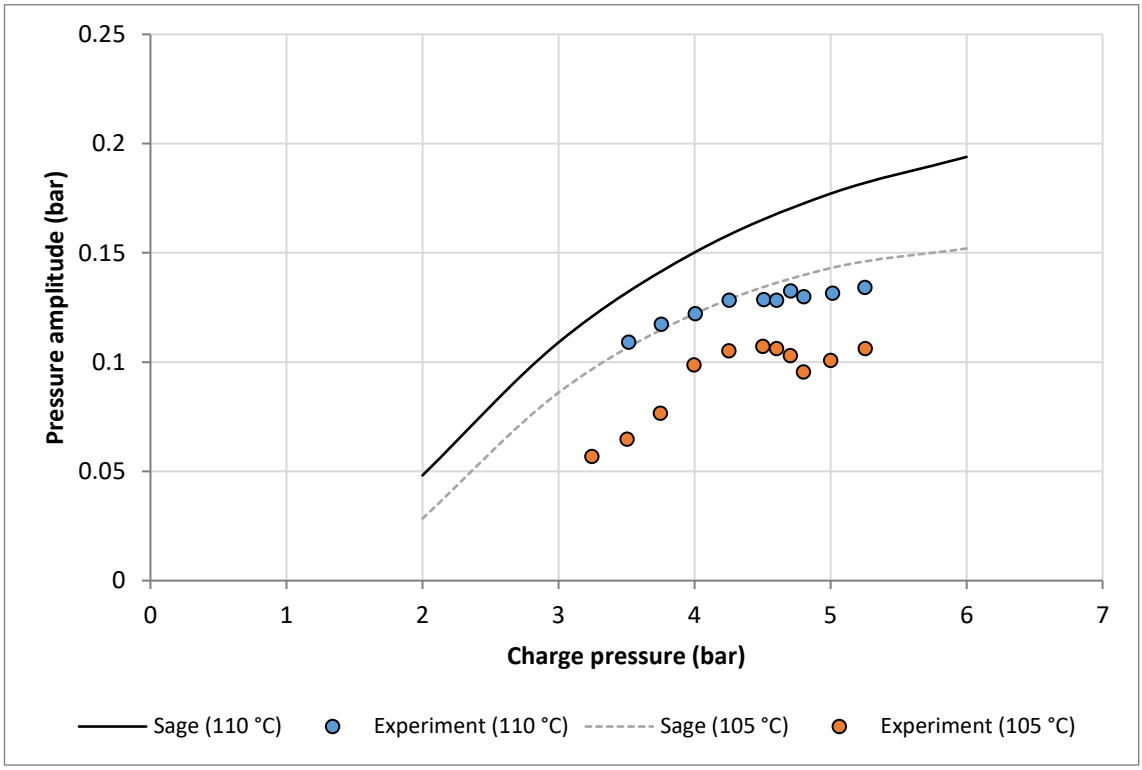

Figure 6.30 – Gas Space 1 pressure amplitudes predicted by Sage compared with the experimental results in the 22 mm 275 ml pistons for the 3HEAT configuration.

A more important model behaviour is that a change in heater temperature produces a similar change in pressure amplitude compared with the experiment results. From the above figure this can be assessed as width of the gap between both temperature trends. In this respect the Sage model produces a gap which is similar in magnitude to the experimental difference between the two temperature sets. For example, at 4 bar the difference between the Sage predictions is 0.028 bar, whereas it is 0.023 bar for the experiments. The Sage predictions for the piston amplitudes can also be compared with the experimental measurements obtained using the slow motion video recording apparatus. Figures 6.31 and 6.32 show the comparisons for the 110ºC and 105ºC heater cases respectively.

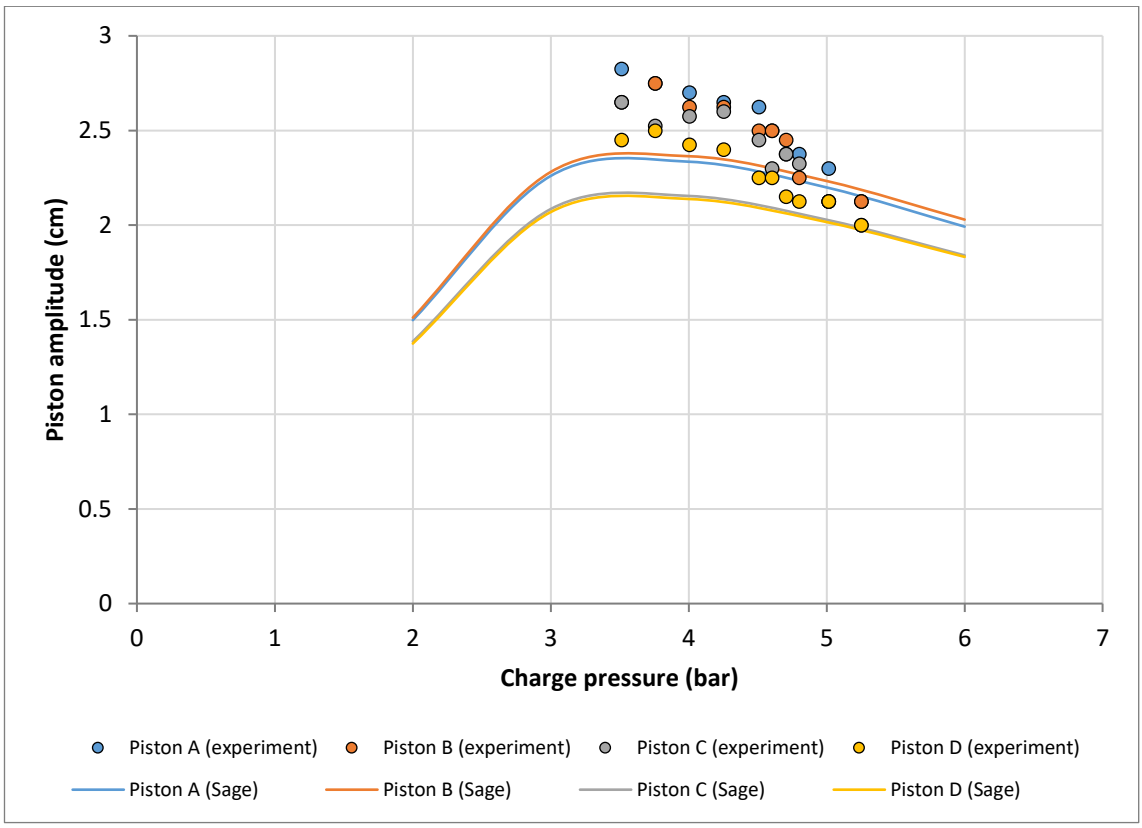

Figure 6.31 – Piston amplitudes predicted by Sage compared with the experimental results in the 22 mm 275 ml pistons for the 3HEAT configuration with 110°C heaters.

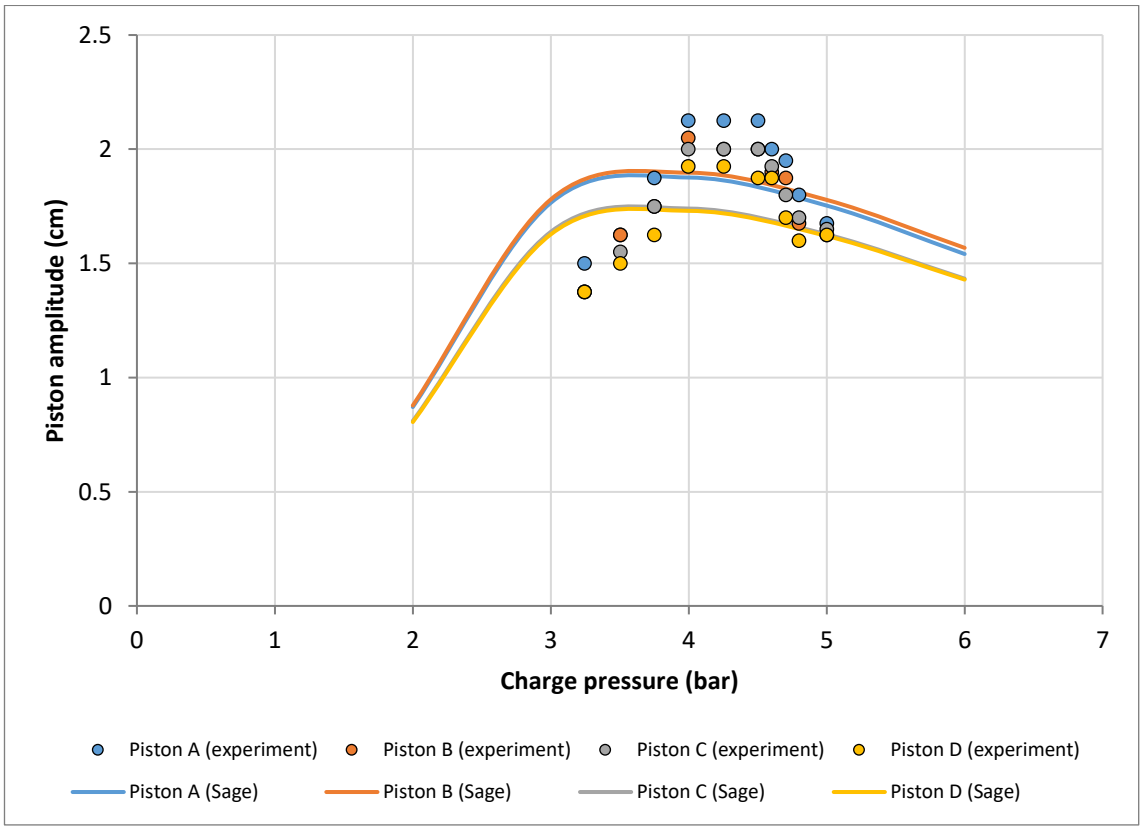

Figure 6.32 – Piston amplitudes predicted by Sage compared with the experimental results in the 22 mm 275 ml pistons for the 3HEAT configuration with 105°C heaters.

The measurements taken with the video have a potential error of ± 0.25 cm, therefore it is not necessary to infer too much from their relative magnitudes when compared with each other. The experimental values show some similarities with the Sage model predictions—pistons C and D consistently record smaller amplitudes, as the model would suggest, and the spread from largest amplitude to smallest is also approximately equal for both sets. Unlike the pressure amplitude predictions earlier, the Sage model underestimates the piston amplitude by a small margin of (at most) 0.5 cm. The reason for this apparent inconsistency comes from the differences between the model and experiment frequencies. As identified at the beginning of this section, the Sage model converges at frequencies which are typically in the region of 0.5 Hz faster than the experiments, which means the pistons have less development time per cycle to achieve maximum displacement.

A similar explanation can be used to understand why the maximum piston accelerations are higher in the case of the Sage predictions. Figure 6.33 shows the piston acceleration trend comparison for the 3HEAT configuration. Due to the higher frequencies in the Sage predictions, the piston accelerations are higher for the same amplitude. The lower amplitude predictions in combination with higher frequencies result in maximum acceleration predictions that are in close vicinity to the experimental observations. The predictions for 110ºC pass through the theorised acceleration limit at approximately 4 bar, which is where the experiments begin to produce unstable results. As with the 4HEAT results, the maximum accelerations plateau and remain at 27 ms^{-2} at charge pressures above 4 bar. The 105ºC experiments do not reach the excitation threshold where the theorised acceleration limit exists and follow the predicted behaviour of a Sage simulation between 100ºC and 105ºC Sage trends.

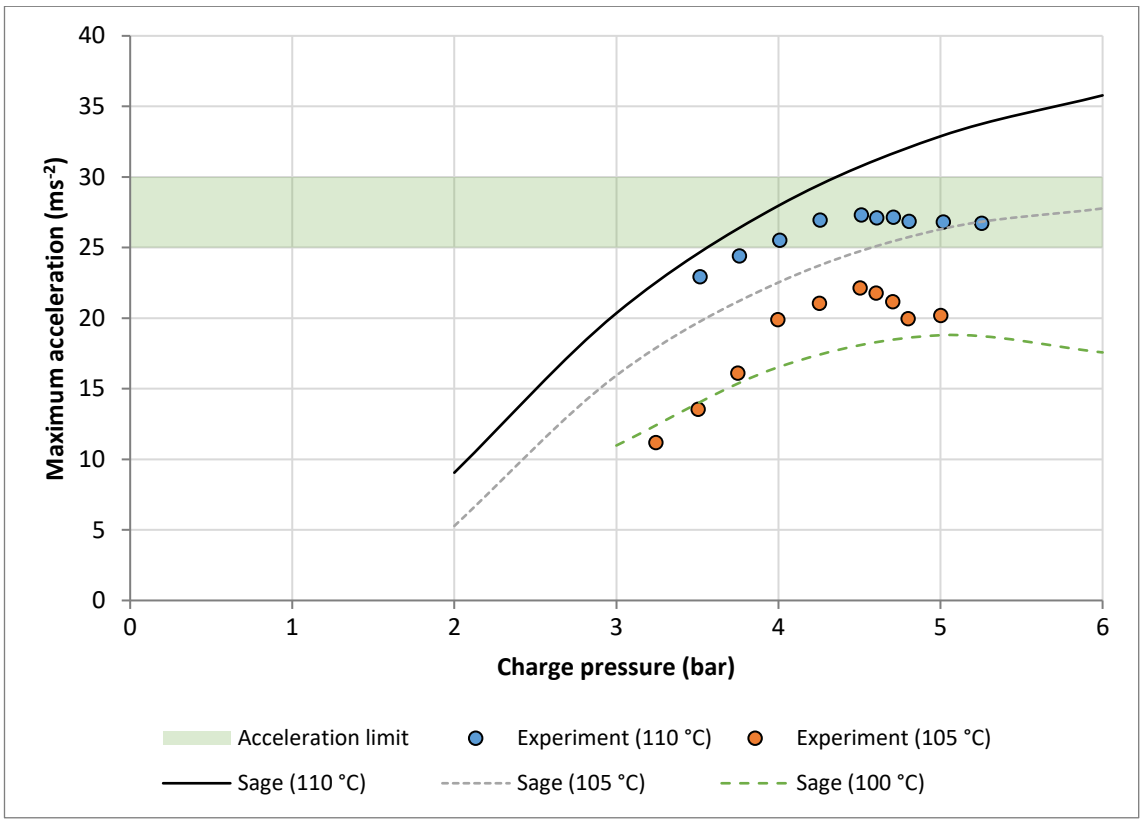

Figure 6.33 – Average maximum piston acceleration for 22 mm experiments with 275 ml pistons when compared with Sage model for 3HEAT configuration.

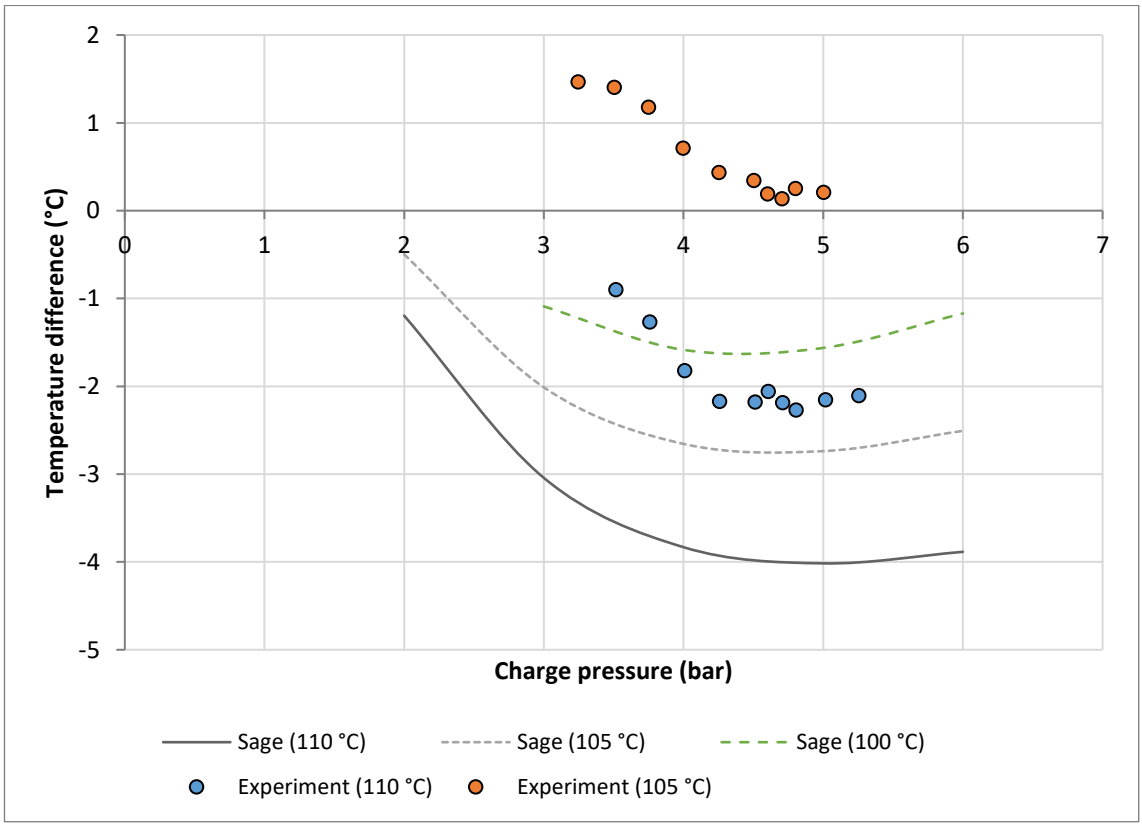

Figure 6.34 – Temperature difference between expansion and compression spaces in Gas Space 1 for the 3HEAT Sage simulations compared with experiments.

Figure 6.34 shows the temperature difference between the expansion and compression spaces in Gas Space 1 for both Sage and experiment. The Sage model predicts the largest temperature difference should occur between 4 bar–5 bar charge pressure, which is what the experimental results show. The turning points appear to depend on the heater temperature; higher temperatures lead to higher optimum charge pressures.

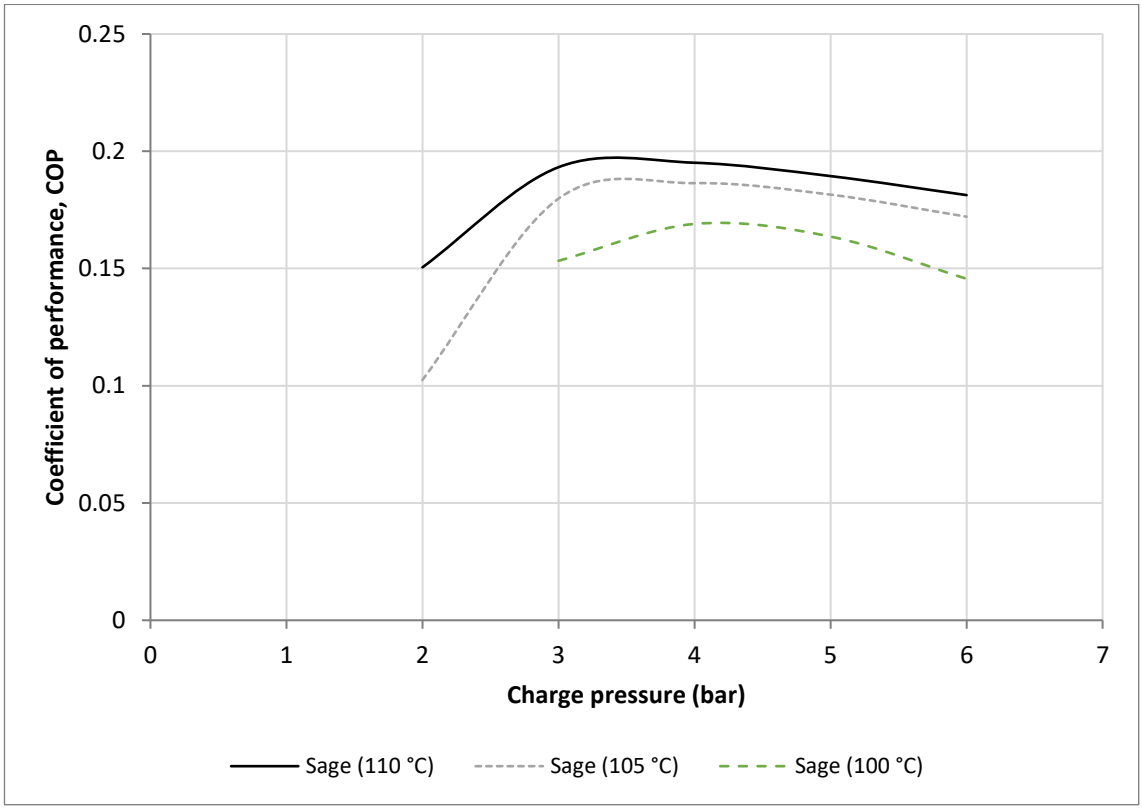

Figure 6.35 – Sage model coefficient of performance predictions for the 3HEAT configuration. Simulations are with 275 ml pistons.

Figure 6.35 shows the COP values obtained from the Sage model for the 3HEAT simulations at 110°C, 105°C and 100°C heater temperatures. The higher temperature simulations produce higher coefficients of performance. The peak coefficient of performance occurs at lower charge pressures than the maximum temperature difference in the absorber space. The COP values are relatively low, and do not suggest the 3HEAT configuration is particularly useful as a heat-powered cooling configuration. The maximum COP attained is less than 0.2, which is similar to that identified in the 15 mm investigation.

6.3.3 2HEAT Configuration

Figure 6.36 displays the scaled phasor plot for an example 2HEAT Sage simulation compared with the phasor plot from the experiment with the same parameters (4 bar charge pressure and 165ºC heater temperature). Table 6.8 then presents the absolute Sage model solutions for the pressure and displacement phasors of the same simulation.

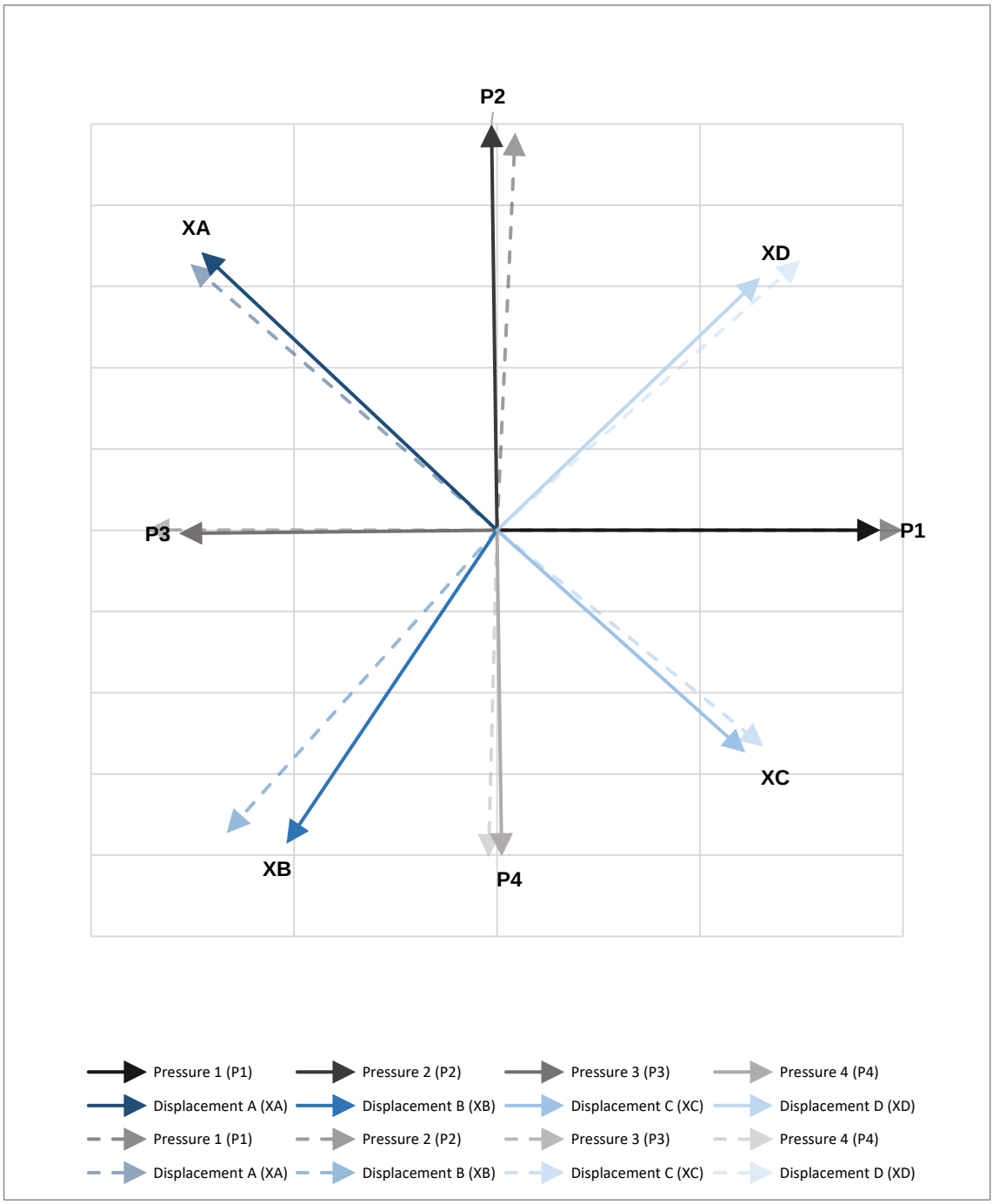

Figure 6.36 – Scaled phasor plot of example 2HEAT Sage simulation pressure and displacement profiles compared with experiment results. Simulation/experiment is at 4 bar charge pressure with 165ºC heater temperatures and 275 ml pistons. Experiment phasors are dashed.

Table 6.8 – Sage model phasors predictions for 2HEAT experiment at 4 bar with 165°C heaters and 275 ml pistons.

Phasor	Amplitude (bar or cm)	Phase angle (°)
Pressure 1 (P1)	0.241	0.0
Pressure 2 (P2)	0.255	90.8
Pressure 3 (P3)	0.200	180.6
Pressure 4 (P4)	0.205	270.8
Displacement A (XA)	2.95	136.8
Displacement B (XB)	2.74	236.1
Displacement C (XC)	2.42	318.2
Displacement D (XD)	2.65	43.8

Except for the displacement of Piston B, the phasors generated from the Sage model simulations are very similar to the experimental results in this scaled comparison. As was the case in the 3HEAT comparison, the primary differences result from the slightly larger relative pressure amplitudes of gas spaces 1 and 3, this time from the experiment side. Due to their larger relative magnitudes, they have more influence over the piston phasor orientations, which is why all of the displacement phasors from the experiment are aligned closer to the horizontal axis.

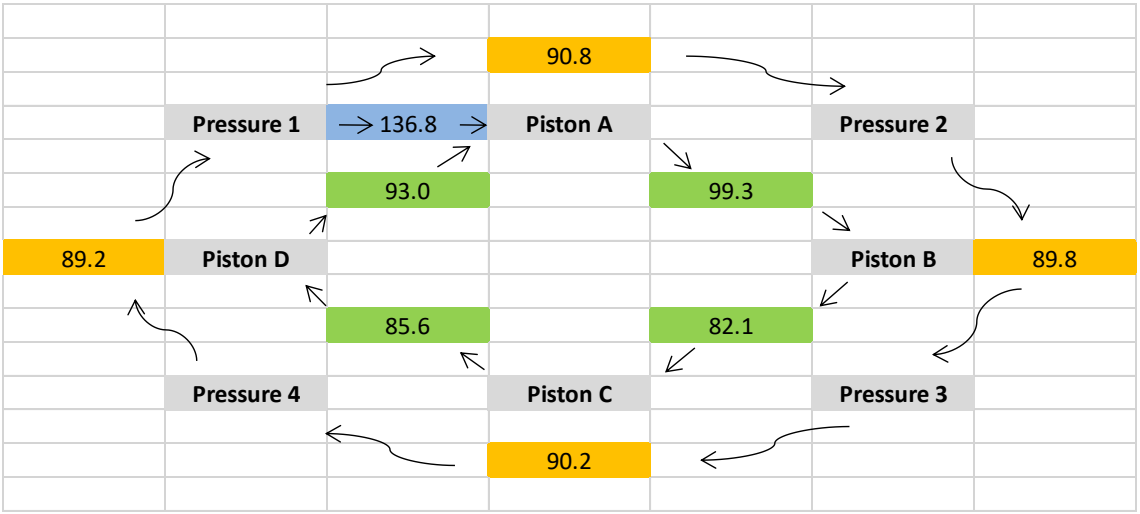

Figure 6.37 – Sage model predictions for the relative phase angles between pressure and displacement phasors in the example 2HEAT simulation. Simulation is at 4 bar charge pressure with 165°C heater temperatures and 275 ml pistons.

The relative phase angles between the phasors are shown in Figure 6.37. The angle between the pressure phasor of Gas Space 1 and the displacement phasor of Piston A is

136.8º, which is close to the experimental value of 139.1º. The angles between the pressure phasors are very close to a value of 90º; all are within the range 90º ± 0.8º. Comparing the angles between the pistons, the largest discrepancy from experiment (of 10.6°) occurs for the angle between Piston B and Piston C, 82.1º is predicted by Sage and the value from the experiment is 92.7º. Figure 6.38 shows the pressure amplitudes predicted for each gas space for Sage simulations using the 2HEAT configuration with 165ºC heater temperatures.

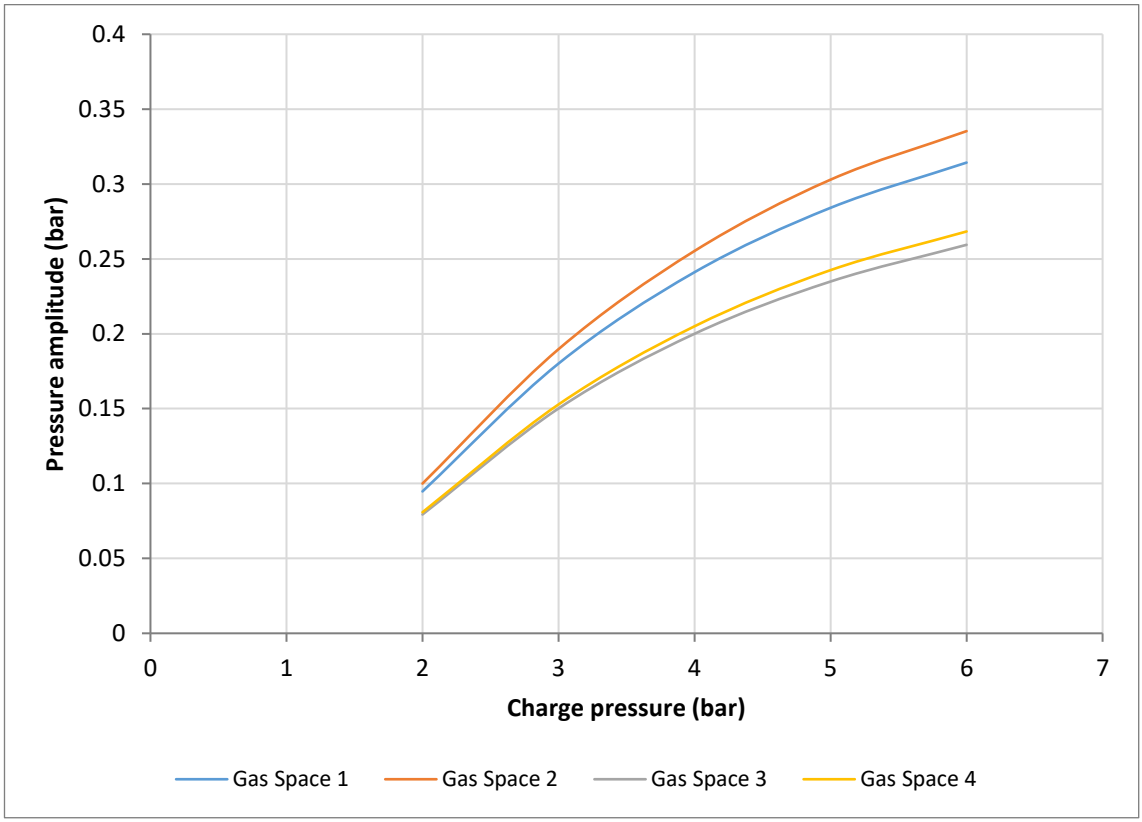

Figure 6.38 – Sage predictions for pressure amplitudes developed in all four gas spaces with increasing charge pressure for 2HEAT configuration. Simulations are with 165°C heaters and 275 ml pistons.

The pressure amplitudes in each gas space increase with charge pressure while retaining their relative magnitude ratios. The distribution of where the largest and smallest amplitudes are developed remains consistent with both the experimental results and the previous analysis for the 15 mm pistons. The ratios calculated and averaged over the simulation range are 1.06 (s = 0.6%), 0.83 (s = 0.6%) and 0.85 (s = 0.3%) for GS2, GS3 and GS4 respectively. The ratios for GS2 and GS4 are 8.2% and 4.9% larger than the

experiment values, while the GS3 ratio is 4.6% smaller. Adding up the unrounded ratios obtained for the heater and absorber spaces gives 1.891 for the heater spaces and 1.852 for the absorber spaces, which equates to a conversion rate of 1.02:1 (three significant figures). This is the same conversion ratio as the 2HEAT experiment in section 6.2.3.

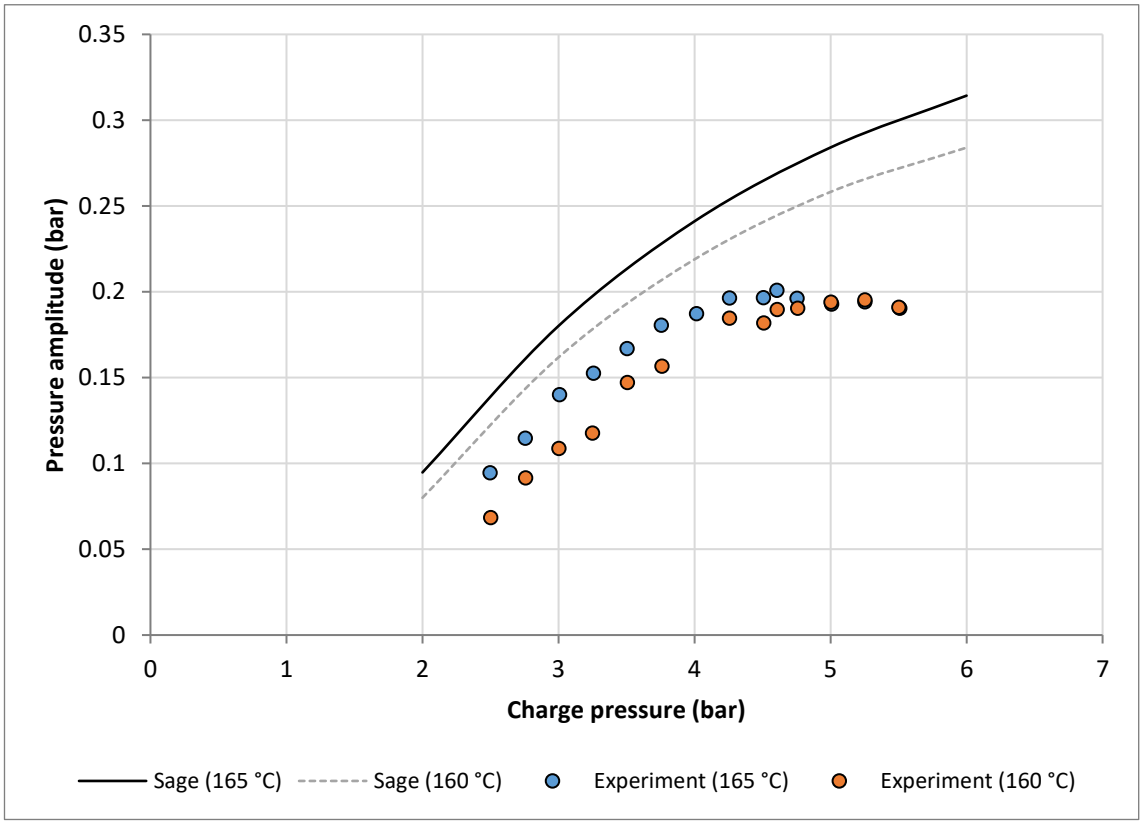

Figure 6.39 – Gas Space 1 pressure amplitudes predicted by Sage compared with the experimental results in the 22 mm 275 ml pistons for the 2HEAT configuration.

Figure 6.39 compares the Sage model pressure amplitudes for one of the absorber spaces, GS1, for both 165ºC and 160ºC heater temperatures against the experiment results. Again it is evident that the Sage model is overestimating the pressure amplitude development. In the 3HEAT cases from the previous section, the overestimation could be quantified by a heater temperature difference of approximately 5ºC, whereas here it is approximately a 10ºC difference (until both of the experiment sets reach the transition pressures and plateau from 4 bar and above). The 5ºC difference between the two heater temperatures analysed in Sage produces a similar amplitude change to that which was measured

between the experimental data sets[1]. This reinforces the model validity inferred from the same observation made for the 3HEAT comparison.

Figures 6.40 and 6.41 compare the Sage predictions for the piston amplitudes with the experimental measurements obtained from slow motion video for the 165ºC and 160ºC heater cases respectively. The trends, magnitudes and relative magnitudes predicted by Sage agree well with the experimental measurements. The displacement of Piston C is consistently evaluated at the lowest magnitude, and while the exact magnitudes of the other pistons' displacements are closer to each other in the experiments (than those predicted by Sage), they are still very close in magnitude. The amplitudes in the experiments decrease beyond the transition pressure at a faster rate than predicted, which may again be explained by the RT instability.

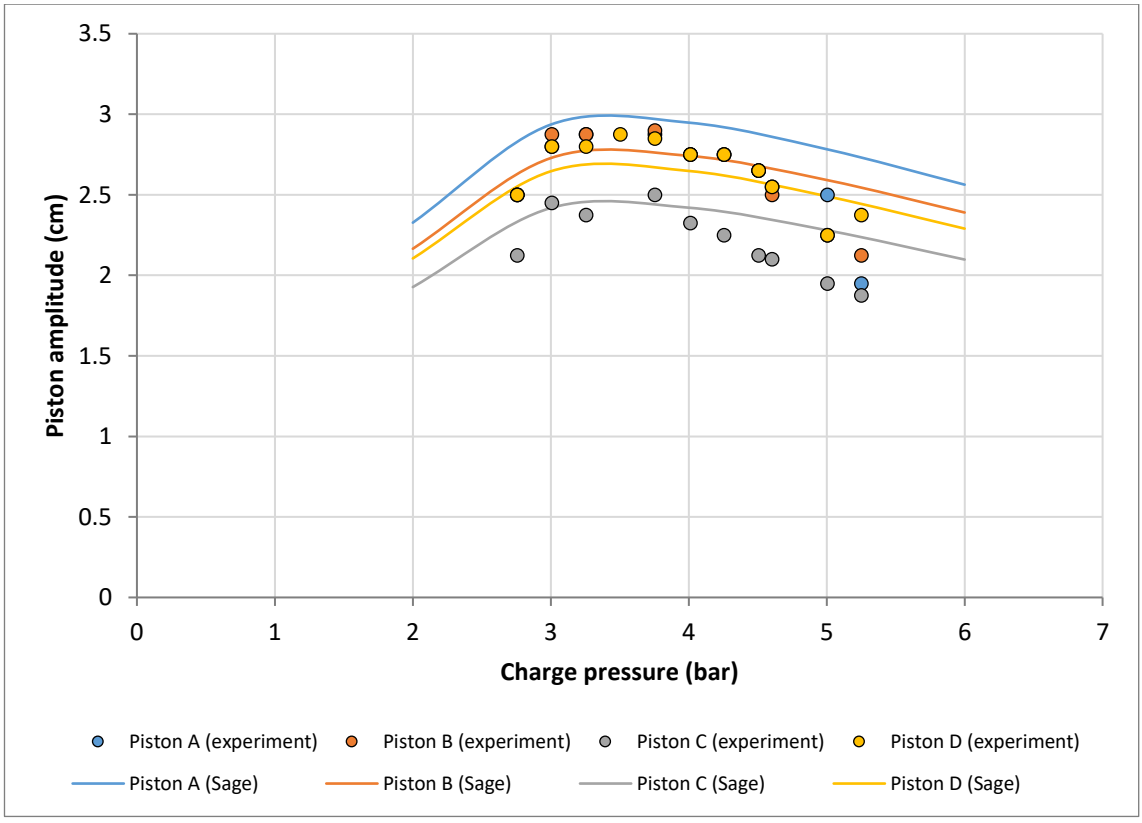

Figure 6.40 – Piston amplitudes predicted by Sage compared with the experimental results in the 22 mm 275 ml pistons for the 2HEAT configuration with 165ºC heaters.

[1] That is for charge pressures below the transition pressure, before the pistons become unstable and the resulting pressure amplitudes converge.

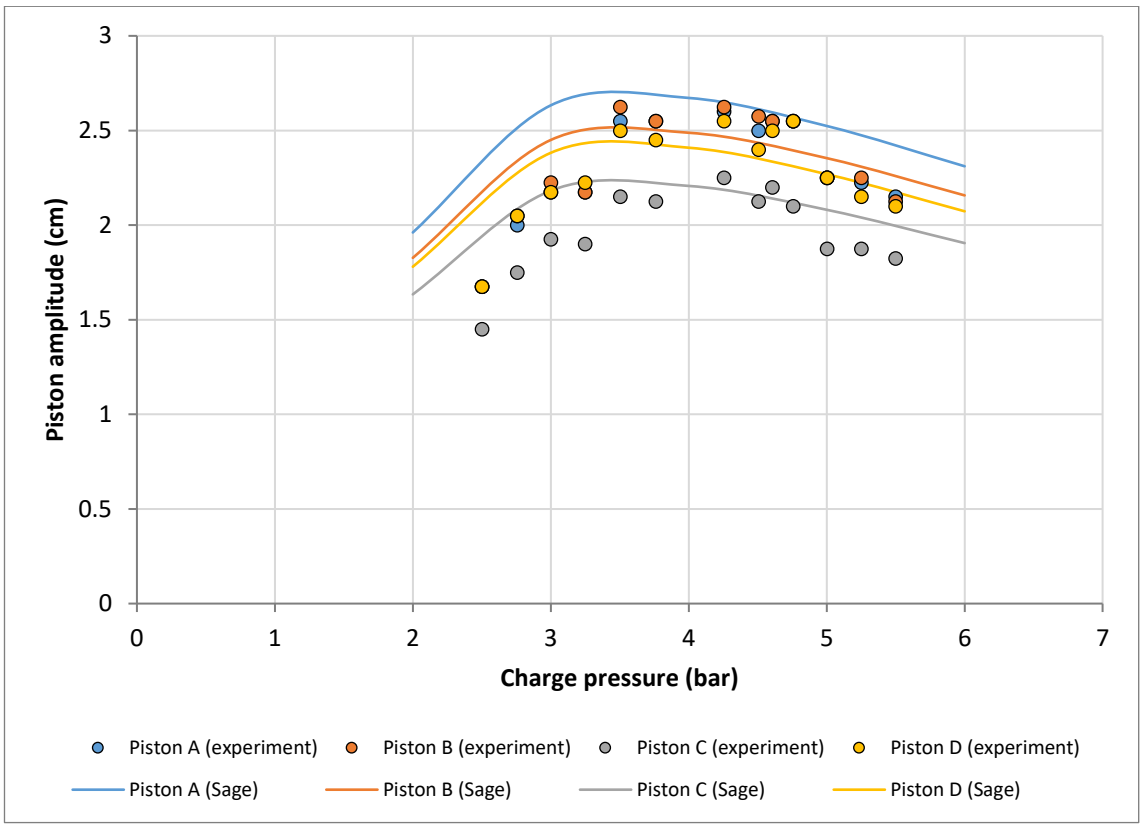

Figure 6.41 – Piston amplitudes predicted by Sage compared with the experimental results in the 22 mm 275 ml pistons for the 2HEAT configuration with 160°C heaters.

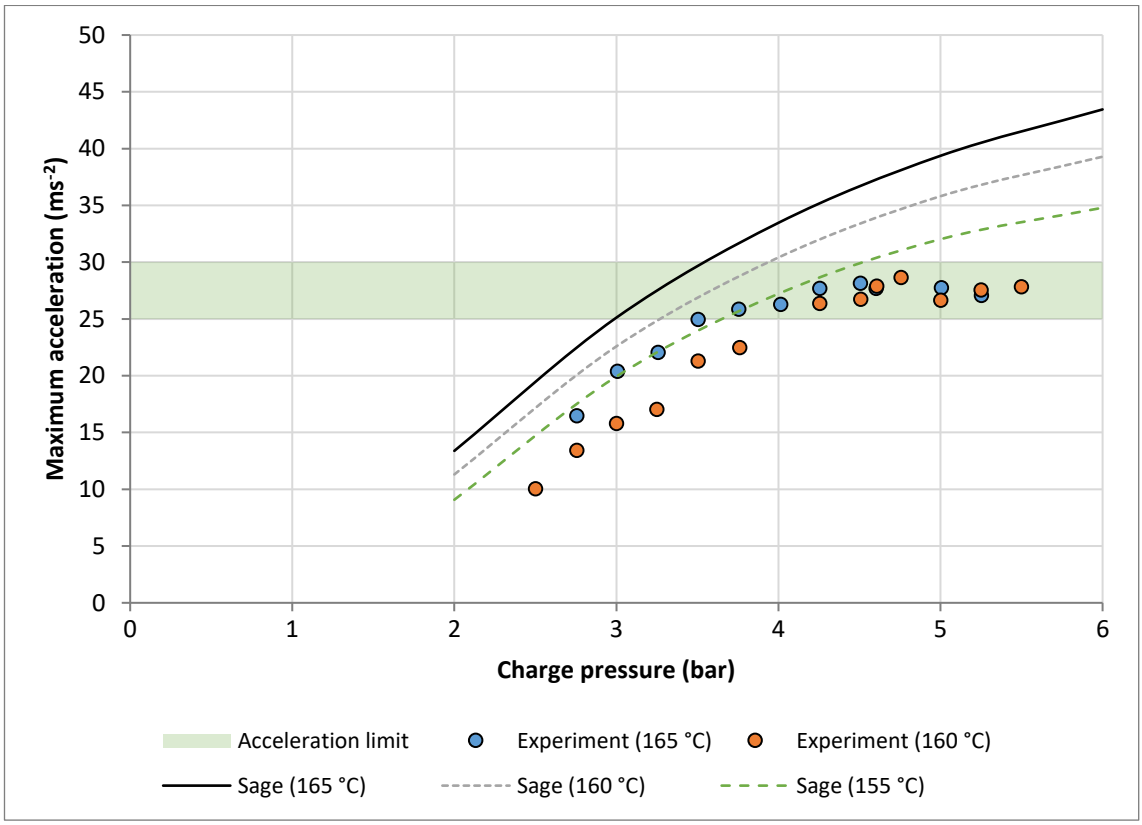

Figure 6.42 – Average maximum piston acceleration for 22 mm experiments with 275 ml pistons when compared with Sage model for 2HEAT configuration.

Figure 6.42 shows the piston acceleration trend comparison for the 2HEAT configuration. The predictions for 165ºC pass into the theorised acceleration limit at the exact charge pressure (3.5 bar) where instabilities are first detected in the experiments. In the 160ºC case, the 3.75 bar experiment produced stable pressure amplitudes, and is the last experiment below 25 ms^{-2} maximum piston acceleration. The 4.25 bar experiment exhibited unstable pressure amplitudes. Shortly after entering the acceleration limit zone, the maximum accelerations for both data sets reach a plateau and remain at between 26 ms^{-2}–28 ms^{-2}, while the Sage predictions continue their upward trends. Even when considering the temperature-adjusted Sage trend for 155ºC heater temperatures to account for the offset, the experiment exhibits the same behaviour until reaching the threshold, and is unable to replicate the predicted behaviour thereafter.

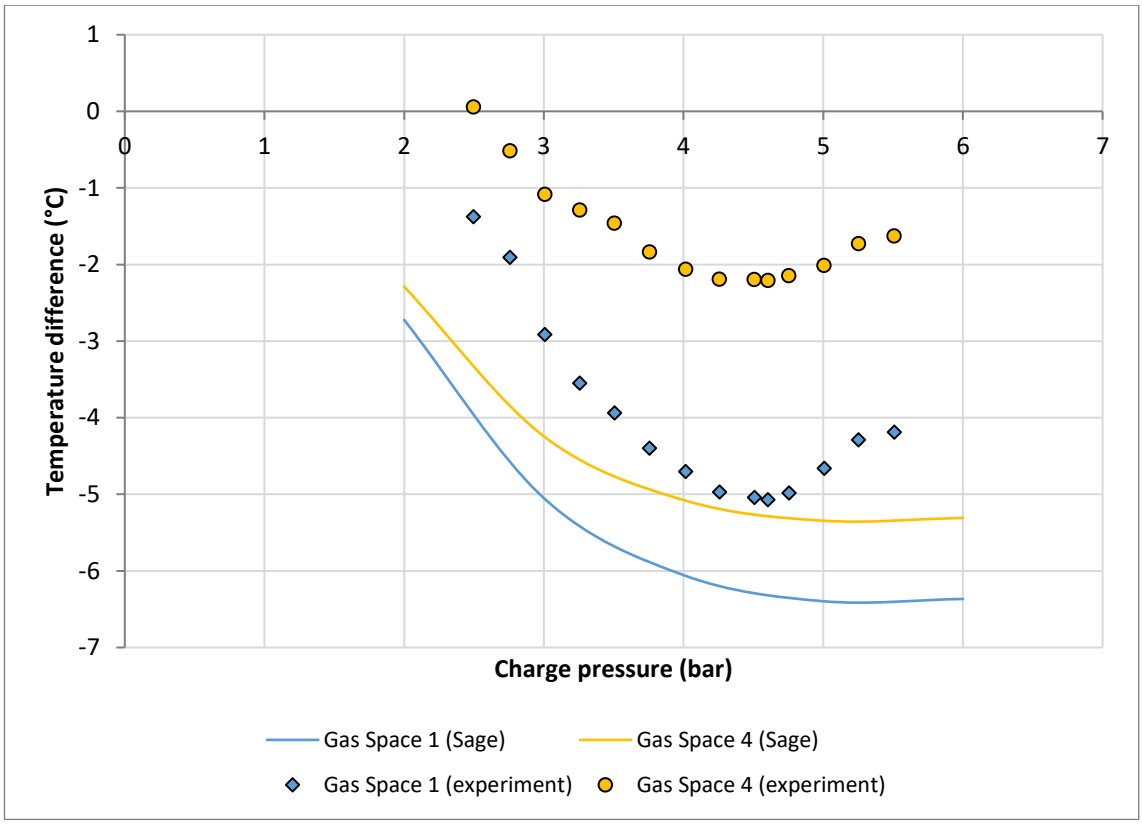

Figure 6.43 – Shows the temperature difference between expansion and compression spaces in the absorber spaces for the 165°C 2HEAT Sage simulations compared with experiments.

Figure 6.43 shows the temperature difference between the expansion and compression spaces in absorber gas spaces, GS1 and GS4, for both Sage and the experiments. The

Sage model predicts the largest temperature difference should occur between 5 bar–6 bar charge pressure. The experimental results follow a similar downward trend until the effects of the piston instability begin to influence system behaviour. The differences between the two gas spaces is larger than predicted by the Sage model. One contributing factor towards this is the different relative pressure ratios. The ratio between GS4 and GS1 is 0.85 for Sage and 0.81 for the example experiment. A larger difference in pressure ratios will result in a larger difference in the temperature differences within the associated gas space.

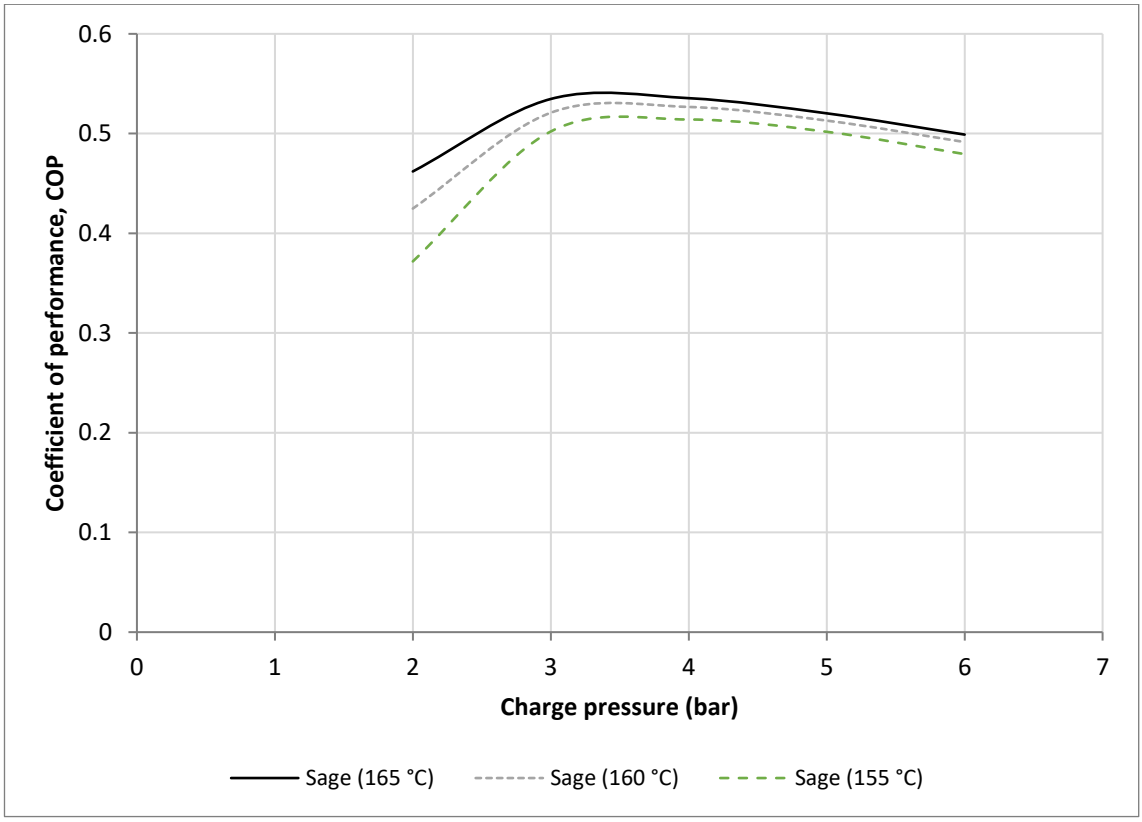

Figure 6.44 – Sage model coefficient of performance predictions for the 2HEAT configuration. Simulations are with 275 ml pistons.

Figure 6.44 shows the COP values obtained from the Sage model for the 2HEAT simulations at 165°C, 160°C and 155°C heater temperatures. The higher temperature simulations produce higher coefficients of performance. The peak coefficient of performance occurs at approximately 3.25 bar, which again is lower than where the maximum temperature differences occur. The COP values are much higher than their

3HEAT counterparts. The maximum COP predicted is 0.53, which is higher than the maximum of 0.46 identified in the 15 mm piston 2HEAT investigation.

6.3.4 Summary

The Sage model was updated to reflect the changes made to the physical test-rig when installing and commissioning the new 22 mm U-tubes with 275 ml liquid pistons. The frequency predicted by the Sage model was found to lie between the analytical estimates for adiabatic and isothermal gas behaviour. The corresponding average polytropic index was found to vary between 1.19–1.20 depending on the charge pressure. The frequency of the test-rig has consistently been much closer to what would be expected for isothermal gas behaviour. Due to the model's sensitivity to frequency as an input parameter, it is very important to identify the correct value for the model despite the fact it may differ from the experiment.

The Sage model showed high levels of accuracy in predicting system behaviours for all three configurations. In the 4HEAT case, the pressure amplitude trends were closely aligned with the measurements for all experiments conducted at both 75°C and 80°C (except for the experiments which were above the transition pressure and exhibited piston instability). For these experiments the pressure amplitude reached a plateau that was shown to correspond with the same maximum piston accelerations that were identified in the 15 mm experiments. The Sage model, unhindered by liquid piston instability and the implications of the RT instability, predicted increased pressure amplitudes and accelerations above the threshold encountered experimentally. The behaviours were observed in the 3HEAT and 2HEAT comparisons. Both sets included experiments which encountered the theorised acceleration limit, and in each case the Sage model showed similar behavioural trends within the stable operating range before diverging at the point of transition into instability.

The relative magnitudes and phase angles of the pressure and piston displacement phasors were shown to be very similar to the phasors constructed from experimental measurements. The phase angles between the pressure phasors were consistently close to 90° for all configurations. The largest differences between the relative pressure magnitudes were found to be 9.6% and 8.2% for the 3HEAT and 2HEAT configurations respectively, whereas for the relative piston phase angles they were 6.2° and 10.6° respectively. The conversion ratios for the 3HEAT and 2HEAT simulations were calculated as 3.91:1 and 1.02:1 respectively.

The highest COP values for the 3HEAT and 2HEAT configurations were estimated to be 0.2 and 0.53 respectively (for the particular heater temperatures analysed). The COP of each configuration is predicted to increase for higher heater temperatures. The COP values rise steeply from 2 bar charge pressure before peaking at 3.5 bar and gradually decreasing for higher charge pressures. The experimentally-measured temperature differences achieved in the absorber spaces were found to follow similar trends predicted by the Sage model, although they were consistently overestimated by 1°C–3°C.

After initial validation attempts with the 15 mm test-rig, the model was used to identify an improved piston diameter and accurately predicted the fall in starting temperature of the system for all three configurations. The model was used to determine pressure and displacement phasor representations that matched the experimentally measured and observed behaviour. Considering the complex nature of the physical system—and the difficulties in not only constructing a perfectly symmetrical test-rig, but also replicating it within the confines of the Sage modelling software—the ability to produce phasor approximations for the LPSC machine with the degree of accuracy demonstrated in the preceding sections is probably one of the most significant outcomes of this research project. The model's ability to accurately replicate the test-rig performance has helped to

identify a physical limitation associated with the use of liquid pistons. The deviation of the experimental results from Sage-predicted excitation levels (during and after the onset of piston instability) provides support for the theorised RT instability phenomenon and the existence of a maximum sustainable piston acceleration. Knowledge of this effect will aid in the design and optimisation processes of future work with the LPSC machine.

6.4 Results Summary Table

Table 6.9 summarises some of the key performance data from both experiments and Sage simulations for the 22 mm piston LPSC.

Table 6.9 – 22 mm piston tube results summary for 275 ml pistons.

		Configuration					
		4HEAT		3HEAT		2HEAT	
Parameter		Experiment	Sage	Experiment	Sage	Experiment	Sage
Heater temperatures (°C)		75, 80	75, 80	105, 110, 115	100, 105, 110	160, 165	155, 160, 165
Charge pressure range (bar)		2.6 – 6	2 – 6	2.5 – 5.25	2 – 6	2.5 – 5.5	2 – 6
Operational frequency range (Hz)		4.03 - 6.12	3.99 – 6.87	4.00 – 5.73	3.99 – 6.87	3.97 – 5.88	3.99 – 6.87
Ave. pressure amp ratio (with respect to GS1)	GS1	1.00	1.00	1.00	1.00	1.00	1.00
	GS2	1.03	1.00	1.66	1.54	0.98	1.06
	GS3	1.00	1.00	1.02	1.01	0.87	0.83
	GS4	1.05	1.00	1.50	1.35	0.81	0.85
Relative phase angles, (for example experiments)	GS1-GS2	90.7	89.9	90.7	89.6	87.4	90.8
	GS2-GS3	88.7	90.0	88.7	90.4	92.6	89.9
	GS3-GS4	91.0	90.1	91.5	89.9	88.6	90.2
	GS4-GS1	89.6	90.0	89.0	90.1	91.5	89.2
	A-B	89.9	89.9	118.7	115.3	89.2	99.3
	B-C	85.1	90.1	64.8	69.0	92.7	82.1
	C-D	95.2	89.9	114.1	107.9	80.7	85.6
	D-A	89.8	90.1	62.4	67.8	97.4	93.0
	GS1-A	140.8	138.1	124.1	125.0	139.1	136.8
Conversion ratio		N/A	N/A	4.17	3.91	1.02	1.02
Maximum cooling temp. difference (°C)		N/A	N/A	-2.3	-4.0	-5.0	-6.4
Maximum Coefficient of Performance		N/A	N/A	-	0.20	-	0.53

7 Liquid Piston Optimisation

On the basis of the Sage model validation conducted in Chapters 5 and 6 (for the 15 mm and 22 mm experiments) the model is considered ready for use in further test-rig optimisation. This chapter investigates the optimal piston dimensions which lead to the best test-rig performance possible. The aim is to identify the level of performance that is achievable by solely manipulating the piston dimensions, since modifications to the gas space componentry are more difficult. The resulting identification of optimised piston sizes could then lead to their implementation in a future stage of the research project.

7.1 Mapping Piston Dimensions

In Section 5.3 it was shown that there existed an optimal piston diameter for the particular piston length of 94 cm that was used in the 15 mm experiments. Figure 5.89 showed that this optimal piston diameter was approximately 20 mm. In the second set of experiments, piston tubes of 19.3 mm average ID were implemented to test the model's predictive capabilities. The results obtained from the new test-rig experiments confirmed the predicted improvements in system performance, and validated the Sage model's accuracy. The next logical step is to identify the optimal overall piston dimensions in terms of length and diameter, and what role the RT instability plays in deciding which to implement.

In this investigation lower starting temperatures are considered to be the key performance indicator; although identifying the starting temperatures of each particular piston size is a time-consuming and tedious endeavour. Recalling that in Section 5.3 it was shown that higher pressure amplitudes for simulations at the same heater temperature are predictive of lower starting temperatures, it is much more efficient to select a single heater temperature and assess the performance of each piston size based on the developed gas

pressure amplitudes. A manual optimisation process was conducted whereby the Sage model was altered to reflect different piston lengths and diameters, and simulations carried out with the results being collected and analysed. The 4HEAT configuration was used with a single heater temperature of 90ºC and charge pressure of 6 bar. A charge pressure of 6 bar was chosen to allow for the potential implementation of the optimised pistons in the current lab space where the compressed air line is limited to 6.4 bar. The design of a prototype system would likely involve significantly higher charge pressures. Table 7.1 summarises the piston dimensions used in the mapping process. All model parameters not directly affected by the pistons remained constant for all simulations.

Table 7.1 – Piston dimension variations and resulting volumes

Piston volumes (ml)		Piston Diameter (mm)						
		19.3	22.5	25.0	27.5	30.0	32.5	35.0
Piston Length (cm)	94	275	374	461	558	664	780	904
	140	410	557	687	832	990	1160	1350
	200	585	795	982	1190	1410	1660	1920
	300	878	1190	1470	1780	2120	2490	2890
	400	1170	1590	1960	2380	2830	3320	3850
	500	1460	1990	2450	2970	3530	4150	4810

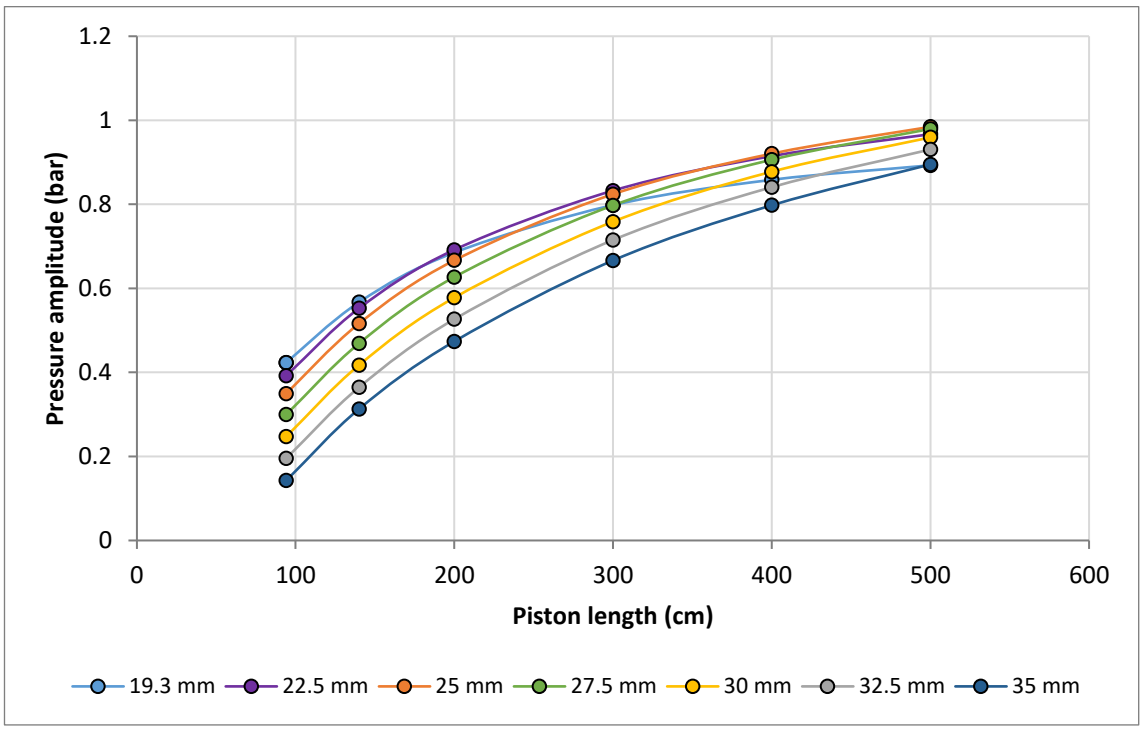

Figure 7.1 – Pressure amplitude predictions for pistons of different diameter and length. Simulations are conducted with 4HEAT configuration with 90ºC heaters and 6 bar charge pressure.

Figure 7.1 shows the pressure amplitudes predicted from the Sage simulations with piston dimensions from Table 7.1. The graph shows that increasing piston length generally has the effect of increasing the pressure amplitude developed in the gas space. Some simulations were conducted for pistons above 5 m in length, however, as can be seen, the performance improvement reduces for every meter added, and at some point it becomes unrealistic to consider extremely long pistons. For now, the practicalities associated with accommodating excessively long pistons are ignored, and a maximum of 5 m length is considered in this investigation. Five-metre-long pistons are already extremely large pistons, and solutions for using such lengths are discussed in Chapter 8.

Another result of increasing the piston length is that the frequency of operation of the system is reduced. This is good for the maximum piston acceleration, but can also reduce the power density of the machine. A crude measure of power output can be taken as the product of frequency and pressure amplitude. Figure 7.2 shows the variation of this performance indicator, termed objective function 3, for the same set of simulations.

For each diameter, there exists an optimal piston length which produces the highest power output. This length is longer for larger diameter pistons, with the peaks for 19.3 mm and 30 mm occurring at approximately 175 cm and 350 cm respectively. These lengths do not necessarily align with the optimal performance of the machine in terms of coefficient of performance and low starting temperature. In terms of the maximum power output, there is little gain available above 300 cm piston lengths. Another important consideration (in light of the RT instability effects) is the maximum piston accelerations sustained in achieving these pressure amplitudes. Figure 7.3 then shows the maximum accelerations for the set of piston parameters investigated.

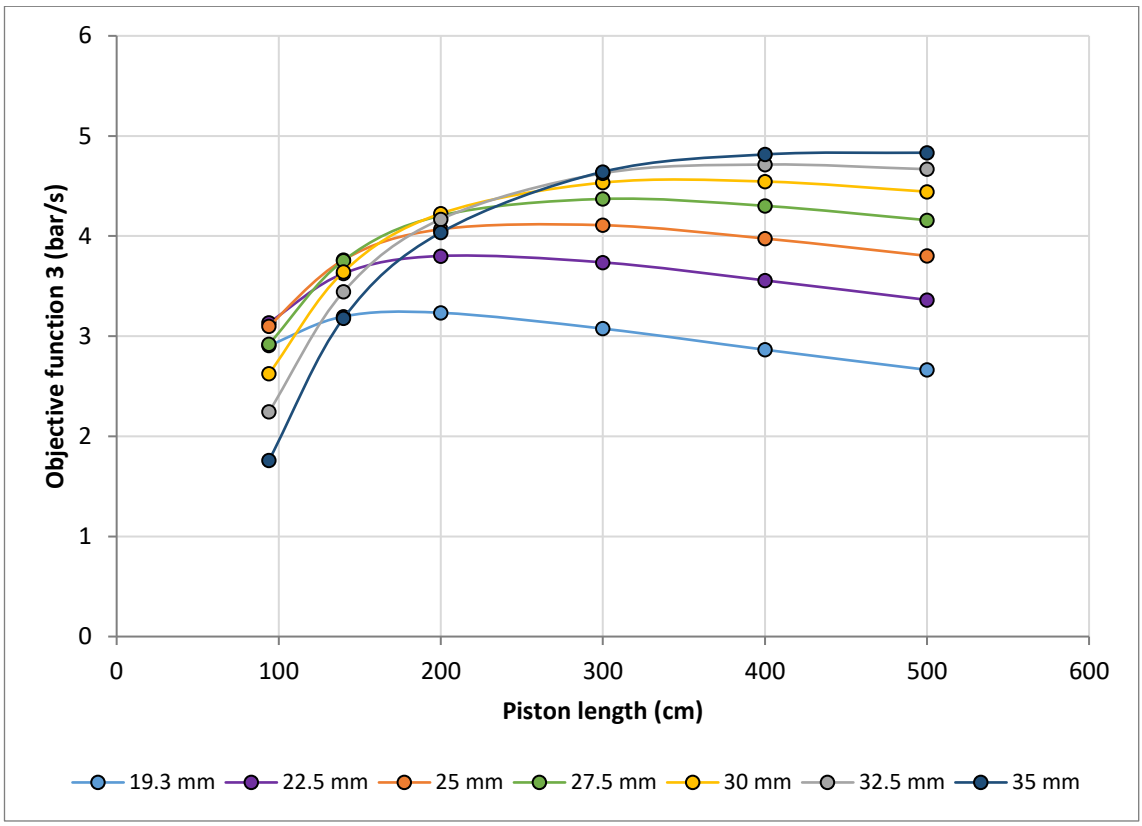

Figure 7.2 – Variation of the product of frequency and pressure amplitude (objective function 3) with increasing piston length for different piston diameters.

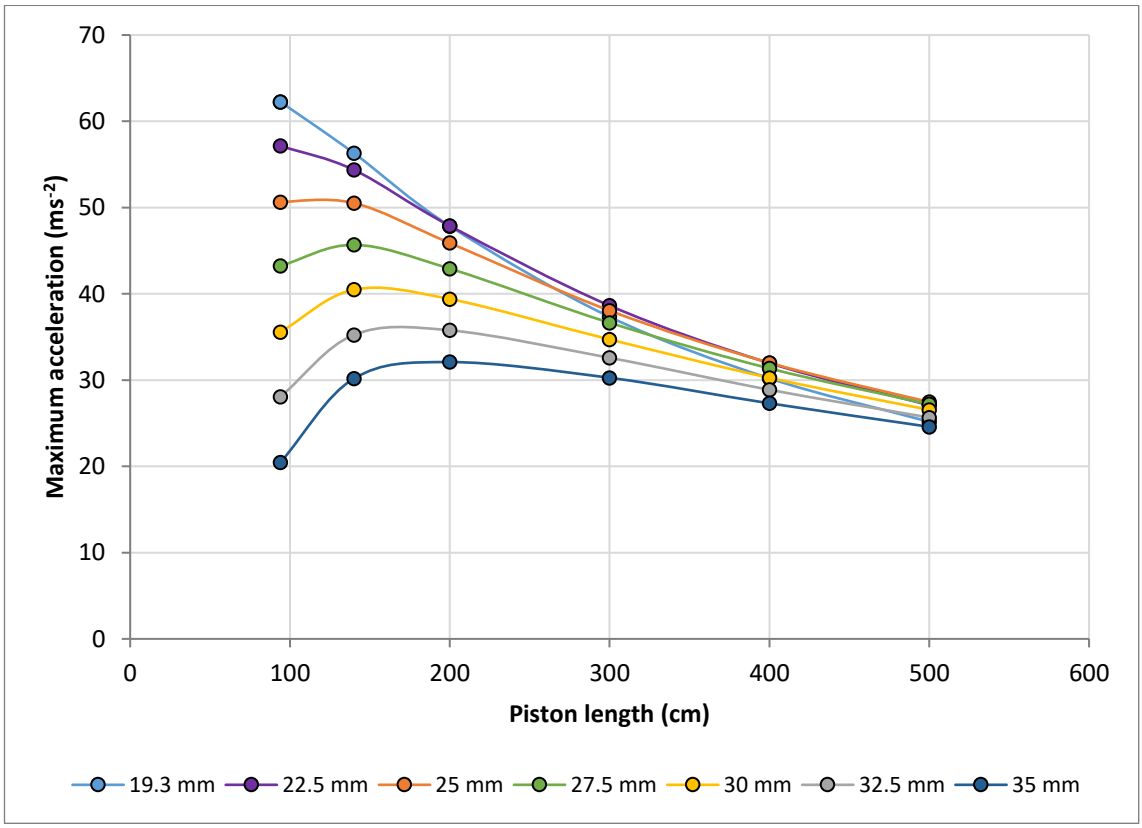

Figure 7.3 – Maximum piston accelerations sustained for variations in piston length and diameter.

For pistons within the range of 0 m–3 m the larger diameter pistons have significantly lower maximum piston accelerations, whereas for longer pistons the accelerations converge to similar values for all piston diameters. The absolute values in the above graph may seem problematic considering the theorised acceleration limit of 25 ms^{-2}–30 ms^{-2} previously identified—but the heater temperature used in these simulations is relatively high (90ºC for 4HEAT) and lower excitation levels would be targeted for the 2HEAT configuration.

7.2 Selection of Piston Length and Diameter

Considering all of the available information so far presented for the piston optimisation, the optimal piston size is not immediately apparent (or, indeed, if there even is one). It can be said, however, that the pressure amplitudes are predicted to rise steadily for increased piston length, and that piston accelerations reduce with increased length. Conversely, the estimations for relative power output appear to show little increase above piston lengths of 3 m. Since it is generally desirable to decrease both piston acceleration and length to realistic levels (while increasing gas pressure amplitude and power output) it is logical to consider pistons in the area of 3 m length. Figures 7.4 and 7.5 show the pressure amplitudes and objective function 3 variations for 3 m pistons with different piston diameters. Figure 7.4 suggests that using pistons of 23 mm diameter and 3 m in length will result in the highest pressure amplitude development, and therefore lowest starting temperature—while Figure 7.5 suggests that increasing the piston diameter to above 30 mm will result in significant power output gains. For these reasons, two separate piston diameters, 23 mm and 30 mm, are selected and compared in more detail in the subsequent section.

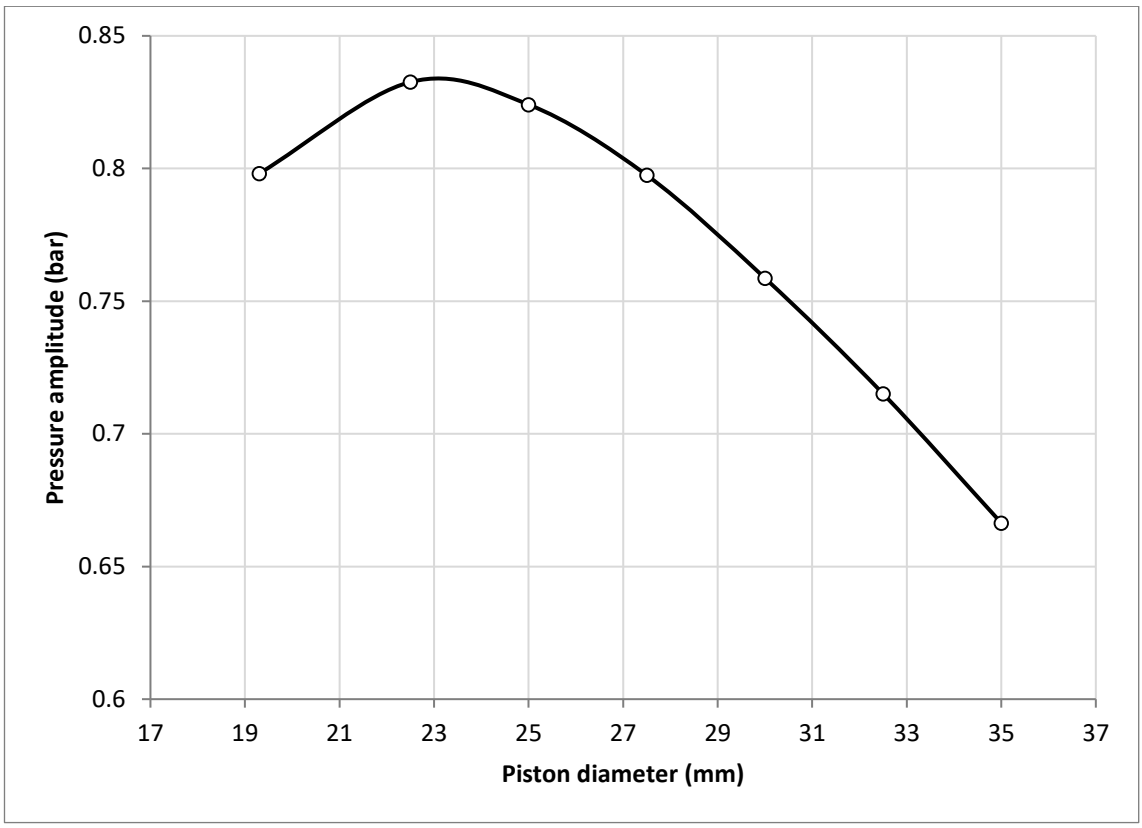

Figure 7.4 – Predicted pressure amplitudes developed for 3 m pistons with varying piston diameters.

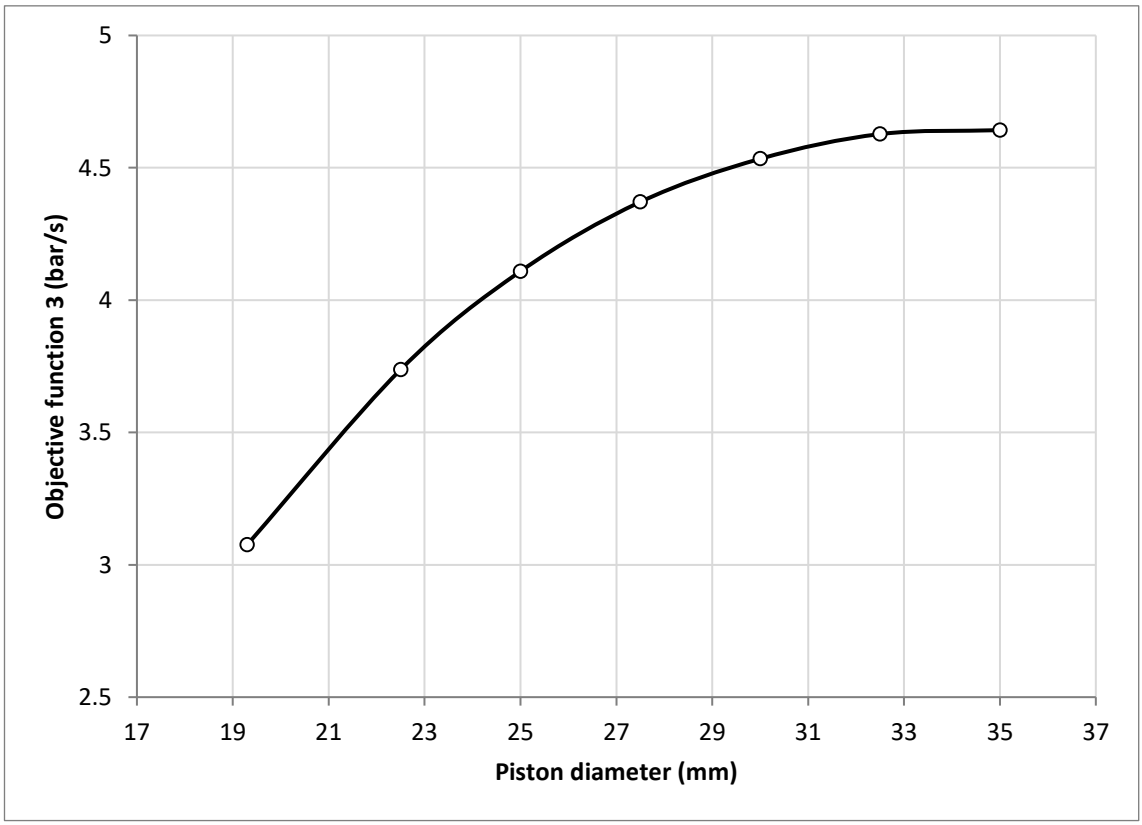

Figure 7.5 – Product of pressure amplitude and frequency (objective function 3) for 3 m pistons with varying piston diameters.

7.3 Comparison Between 23 mm and 30 mm Diameter 3 m Pistons

In the previous section, the scope of piston sizes under consideration was narrowed to pistons 3 m in length. In this section, the performance of the LPSC machine is evaluated for two potential system prototypes: one with 3 m long, 23 mm diameter pistons; and the other with 3 m long, 30 mm diameter pistons. Separate Sage models were constructed for each case and numerous simulations conducted to map the performance. The charge pressure was kept constant at 6 bar. Table 7.2 summarises the distinguishing properties between both prototypes.

Table 7.2 – Prototypes considered for performance assessment.

Properties	Prototype 1	Prototype 2
Piston length (m)	3	3
Piston diameter (mm)	23	30
Piston volume (ml)	1246	2121
Piston mass (kg)	1.246	2.121
Operational frequency range (Hz)	4.56 – 4.59	5.95 – 5.98

7.3.1 Simulation Results Overview

From the preliminary piston investigation in Section 5.3, it was concluded that the starting temperature of the machine could be reduced by varying the piston diameter. The lowest starting temperatures for the 94 cm pistons were estimated to occur at approximately 79ºC (with 20 mm diameter pistons). The lower starting temperatures predicted were verified during the experimental investigation in Section 6.2. Figure 7.6 shows a similar starting temperature analysis for the 4HEAT configuration comparison between the 23 mm and 30 mm diameter, 3 m long pistons. Interestingly, although the 23 mm pistons produce larger pressure amplitudes when assessing higher heater temperatures, both sizes exhibit similar starting temperatures, which are just slightly above 64ºC. This equates to a 15ºC improvement over the 22 mm OD, 94 cm long pistons used in the second experimental investigation.

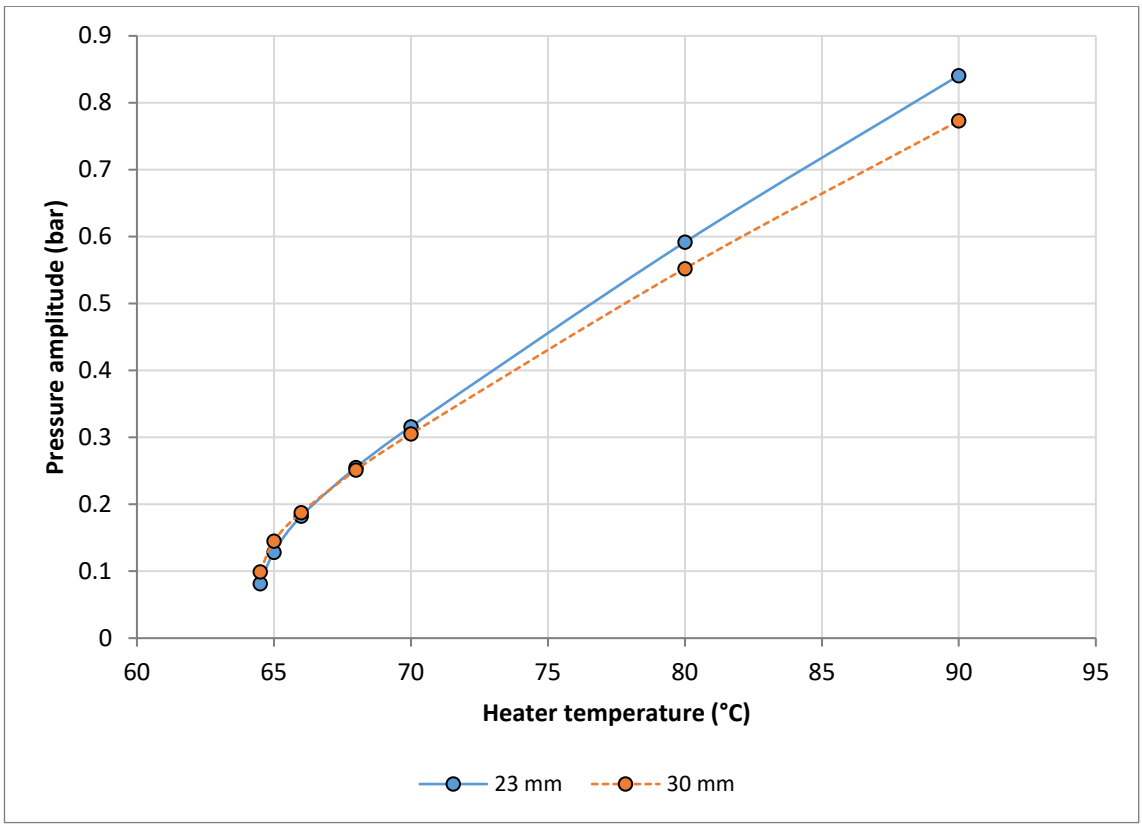

Figure 7.6 – Heater temperature influence on the pressure amplitudes developed with 3 m long pistons of diameter 23 mm and 30 mm. Simulations are conducted with 4HEAT configuration at 6 bar charge pressure.

The LPSC systems are now compared in terms of their ability to achieve the target objective, i.e. using heat input to produce a cooling effect. The configuration chosen for this objective is the 2HEAT configuration since it has consistently outperformed the 3HEAT configuration in terms of predicted COP and indicates the most promise based on the favourable phase angle relationships identified through the phasor analysis of both configurations.

Both models were found to produce 2HEAT configuration solutions with heater temperatures at 117ºC and above. Simulations were conducted for a number of different heater temperatures in the range of 117ºC to 160ºC. The charge pressure was kept constant at 6 bar (as were all other model parameters). The frequencies were identified from 4HEAT simulations in the same manner as described earlier in Section 4.2.9. The results from this analysis is summarised in Table 7.3.

Table 7.3 – LPSC performance summary for 2HEAT simulations at 6 bar and various heater temperatures.

Heater Temp. (°C)	Ave. pressure amplitude (bar)		Ave. piston amplitude (cm)		Max piston acceleration (ms^{-2})		Total heater heat input (W)		Total absorber heat input (W)		COP	
	23 mm	30 mm	23 mm	30 mm	23 mm	30 mm	23 mm	30 mm	23 mm	30 mm	23 mm	30 mm
117	0.119	0.134	0.68	0.45	5.6	6.3	1.5	2.2	0.6	1.0	0.403	0.435
120	0.177	0.178	1.01	0.59	8.3	8.3	2.6	3.4	1.3	1.7	0.491	0.492
125	0.239	0.232	1.35	0.77	11.2	10.8	4.3	5.2	2.3	2.8	0.541	0.531
130	0.290	0.277	1.64	0.91	13.6	12.8	5.9	7.0	3.4	3.9	0.565	0.550
135	0.336	0.317	1.90	1.05	15.7	14.7	7.7	8.9	4.4	5.0	0.577	0.560
140	0.378	0.355	2.13	1.17	17.7	16.4	9.5	10.9	5.5	6.2	0.583	0.564
145	0.418	0.391	2.36	1.28	19.5	18.0	11.3	12.9	6.6	7.3	0.586	0.565
150	0.456	0.424	2.56	1.39	21.3	19.6	13.3	15.0	7.8	8.4	0.585	0.564
155	0.491	0.456	2.76	1.49	22.9	21.0	15.2	17.1	8.9	9.6	0.583	0.561
160	0.525	0.486	2.95	1.59	24.5	22.4	17.2	19.2	10.0	10.7	0.580	0.557

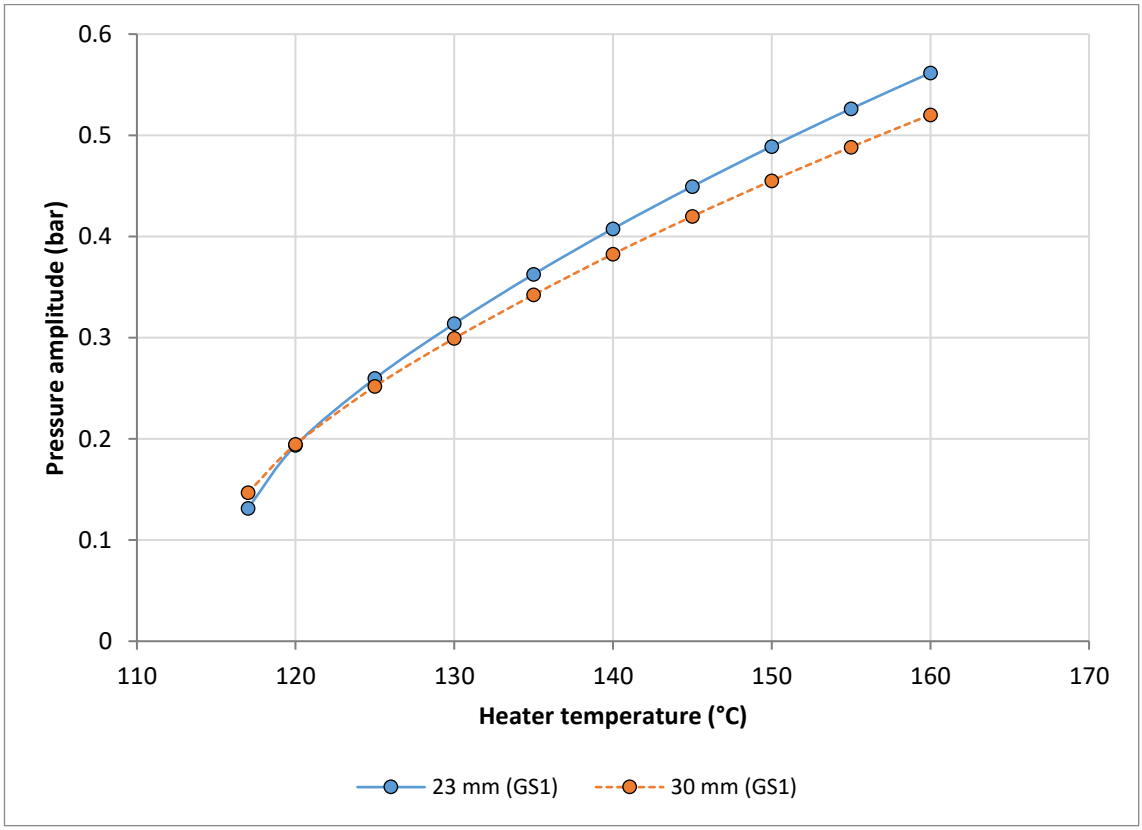

Figure 7.7 – Gas Space 1 pressure amplitude comparison for 2HEAT simulations with different heater temperatures. Charge pressure is 6 bar and piston length is 3 m.

Figure 7.7 shows the comparison for the pressure amplitude predicted in GS1 for both Sage models across the aforementioned heater temperature range. The pressure amplitudes developed in GS1 share similar trends to those observed for the 4HEAT

simulations in the previous section—they begin very close to each other near the lower starting temperature before diverging slightly as the heater temperature is increased. The total difference for a heater temperature of 150ºC is 0.034 bar or 6.9% of the 23 mm model prediction. This difference is relatively small considering the large difference in piston masses between both systems. The average piston amplitudes are now compared for both models in Figure 7.8, and Figure 7.9 shows the corresponding average maximum piston accelerations predicted. As one would expect, the piston amplitudes are larger in the case of the narrower piston tubes. For reference, the length of the expansion and compression spaces are 5.81 cm and 3.42 cm for the 23 mm and 30 mm models respectively.

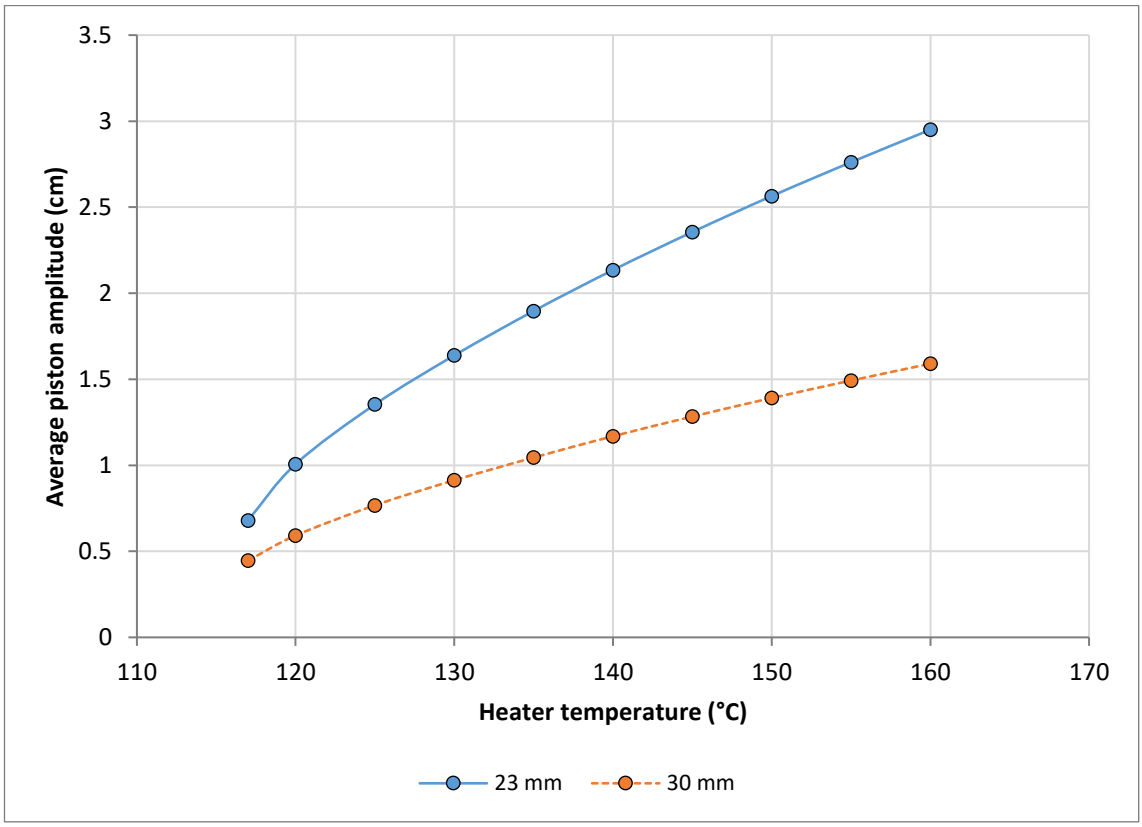

Figure 7.8 – Average piston amplitude comparison for 2HEAT simulations with different heater temperatures. Charge pressure is 6 bar and piston length is 3 m.

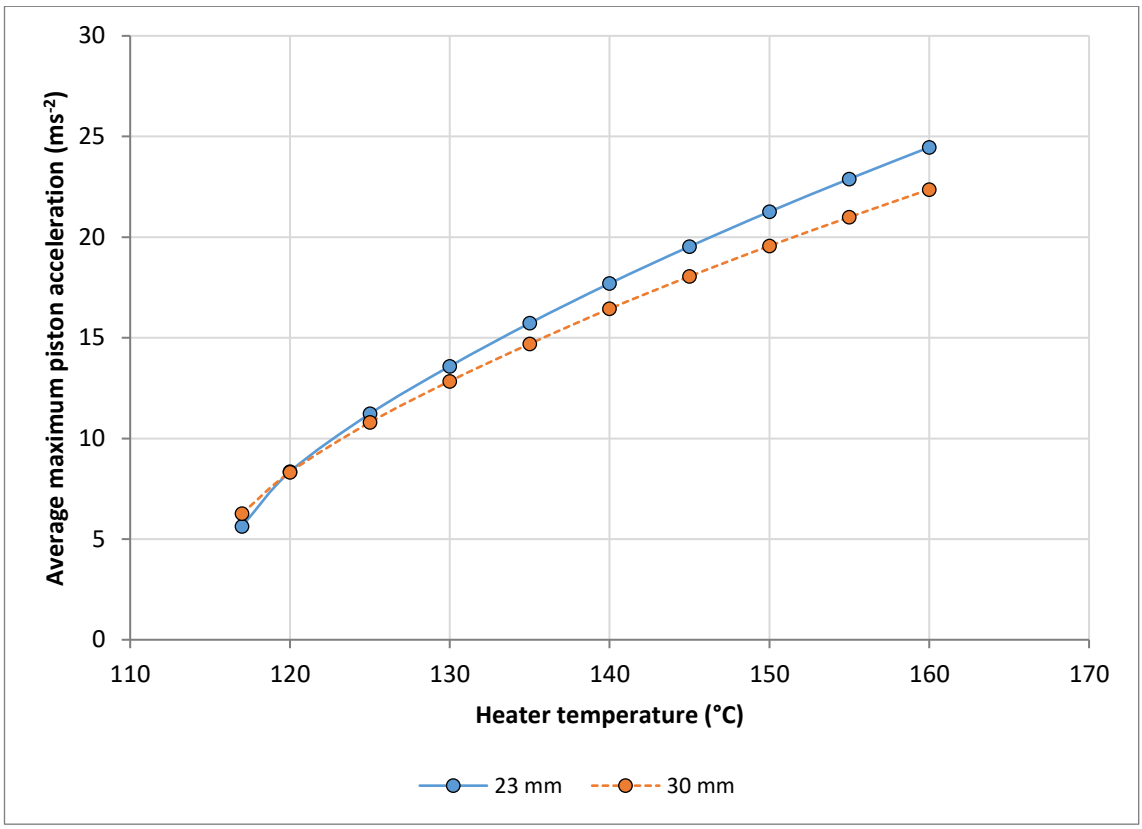

Figure 7.9 – Average maximum piston acceleration comparison for 2HEAT simulations with different heater temperatures. Charge pressure is 6 bar and piston length is 3 m.

Despite the large differences in piston amplitude, the maximum piston accelerations are comparatively similar, which is due in part to the higher frequency of operation of the 30 mm system. The 30 mm diameter pistons produce accelerations that are consistently lower than the 23 mm pistons above 120ºC heater temperature. For simulations at 150ºC the difference is 1.69 ms^{-2}—or roughly 8% of the 23 mm value. Similar acceleration predictions are expected when recalling Figure 7.3 in the mapping section (this was also the rationale used in selecting the new piston sizes). Neither system produces accelerations which exceed 25 ms^{-2} or enter into the theorised acceleration limit for the heater temperature range assessed—meaning the conditions for liquid piston surface stability should be less demanding, and therefore alternatives to the submerged polyethylene floats could be considered.

7.3.2 Cooling Potential

The performance of both systems in terms of their ability to produce the desired cooling effects are now compared. Figure 7.10 shows the COP values predicted for both systems when varying the heater temperatures (charge pressure is kept at 6 bar in this analysis).

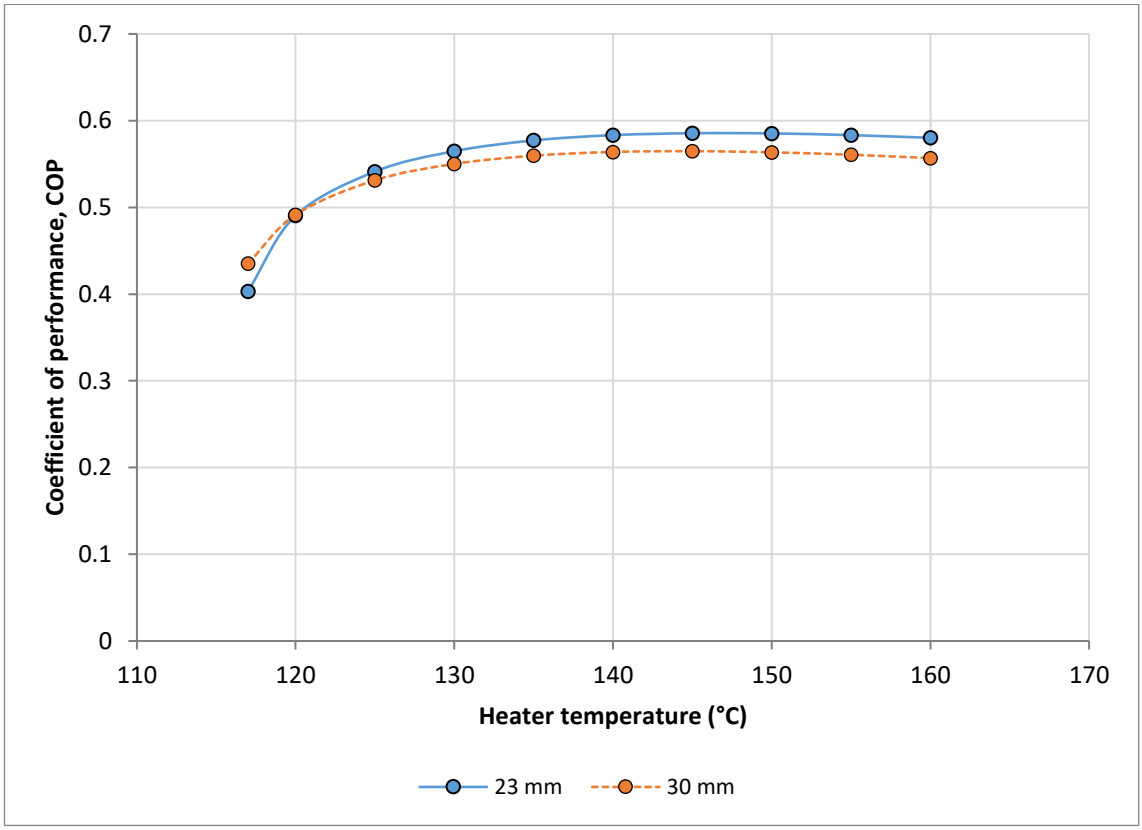

Figure 7.10 – Coefficient of performance comparison for 2HEAT simulations with different heater temperatures. Charge pressure is 6 bar and piston length is 3 m.

The 23 mm pistons outperform the 30 mm pistons in this comparison. Both experience a peak COP value at approximately 145ºC; although the rate of decrease of these COP values with respect to heater temperatures is relatively small after this point. At 150ºC, the COP values are 0.5853 and 0.5635 for the 23 mm and 30 mm diameter pistons respectively. It was expected that the 23 mm diameter pistons would show better performance in this regard considering Figure 7.4 from Section 7.2 (where the highest pressure amplitude was achieved at the 23 mm diameter for the 4HEAT simulations). Of course, coefficient of performance is not the only important performance measure. The

30 mm diameter pistons were included in this comparison to identify the differences achieved in cooling capacity.

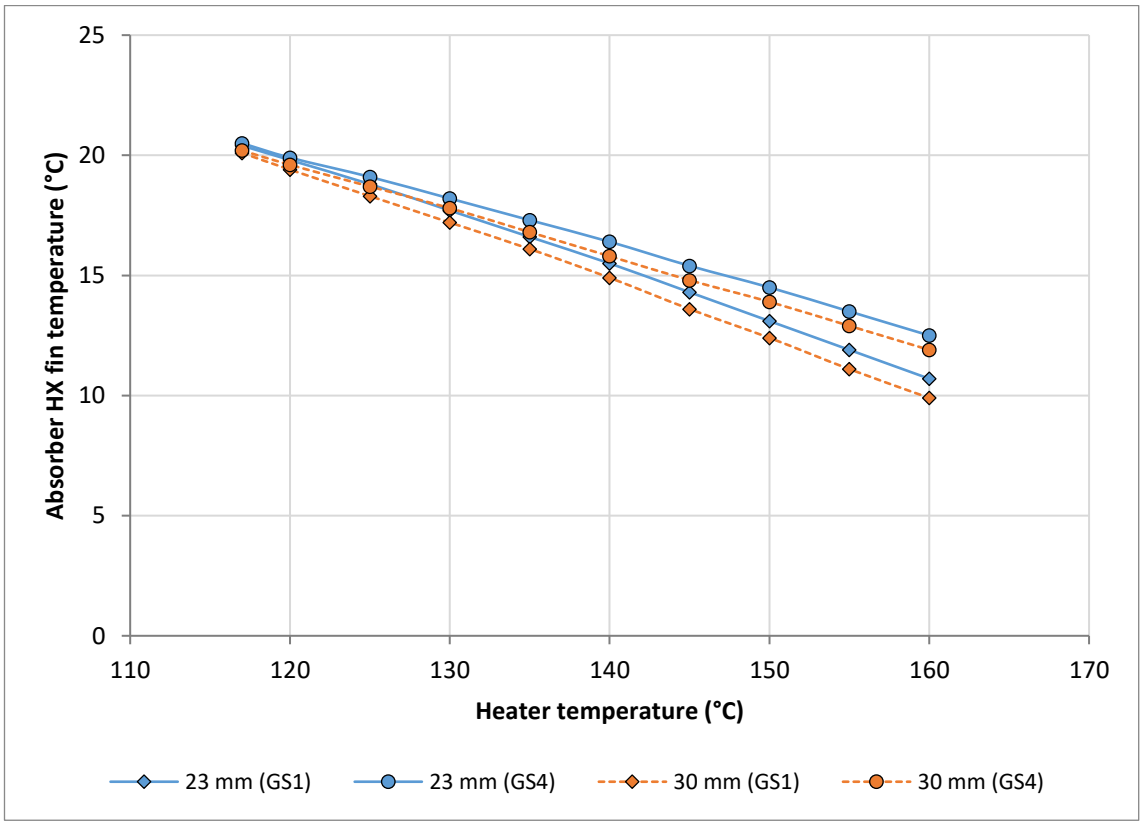

Figure 7.11 – Average absorber heat exchanger fin temperatures achieved for 23 mm and 30 mm diameter pistons in 2HEAT configuration at 6 bar charge pressure. Ambient temperature is 21°C.

Figure 7.11 shows the absorber heat exchangers' average fin temperatures achieved by both systems. The lowest temperatures are achieved by the 30 mm liquid pistons, which implies greater cooling capacity for this system despite the lower COP values. With 150°C heaters, the temperatures achieved in the GS1 absorber are 13.1°C and 12.4°C for the 23 mm and 30 mm pistons respectively. Figure 7.12 shows the corresponding heat flow through the absorber heat exchanger fins for the same set of simulations. The heat flows correlate with the absorber fin temperatures; heat transfer to the 30 mm absorbers is greater than the 23 mm system absorbers. The heat input required for the 30 mm absorbers has necessarily increased to accommodate the higher capacity cooling potential.

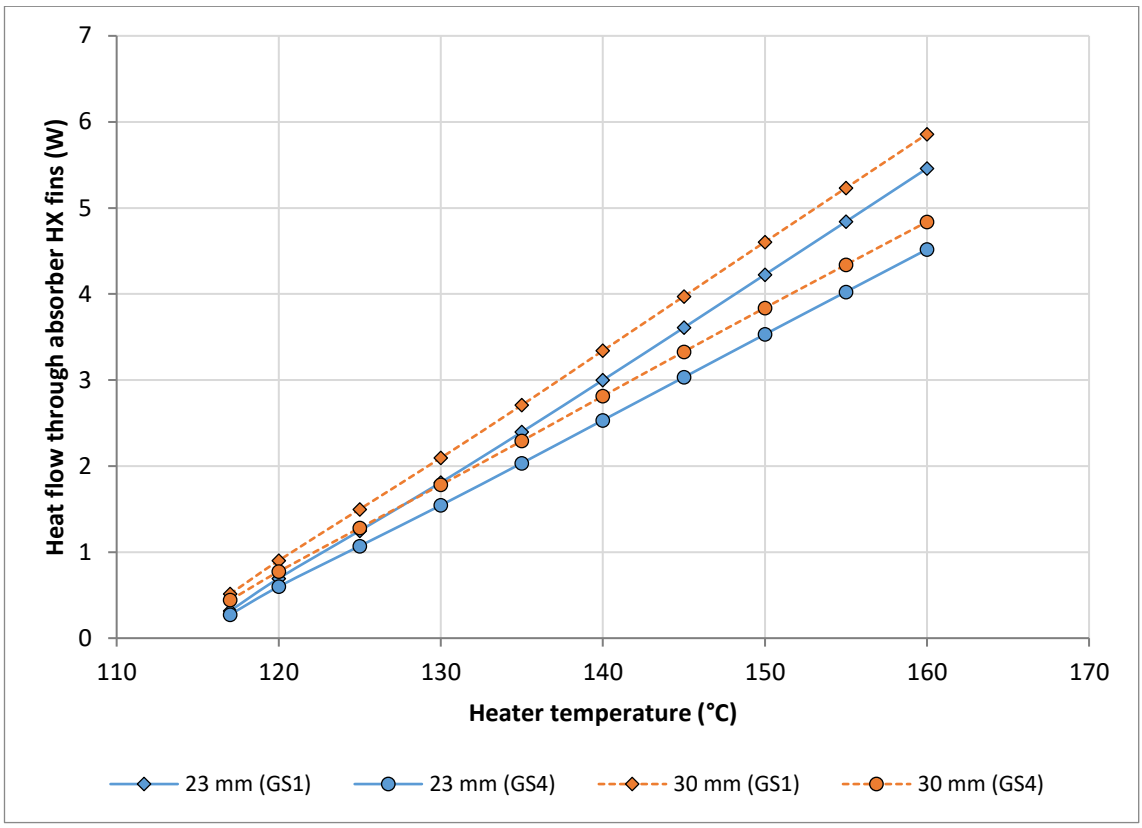

Figure 7.12 – Heat flow through absorber heat exchanger fins achieved for 23 mm and 30 mm diameter pistons in 2HEAT configuration at 6 bar charge pressure.

It must be remembered that the absorbers within Sage are modelled as if they were perfectly insulated from the internal heating cartridge (installed in each of the four expansion spaces in the physical test-rig). For a prototype system, the internal heating cartridge currently within the absorbers would be replaced with methods for utilising the cooling effect. This may involve the use of a coolant system—repositioning the absorber heat exchangers to expose the heat transfer site to an external surface. In either case, the capacity of the absorber to withdraw heat from the surroundings would be increased since there would exist a greater heat flow cross-sectional area and decreased total thermal resistance. This approach can be approximated within the Sage model by reconnecting the heat flow connections from the heat sources in the absorbers and choosing a target cooling temperature to replace the high temperature heat sources. The reduction in resistance on the absorber side could also potentially increase the overall capacity of the system since, the heaters would be able to regulate their supply to match the increased

absorber capacity. For the 23 mm and 30 mm proposed systems, a number of absorber heat source temperatures were simulated in order to estimate the significance of this effect. Table 7.4 summarises the results from the Sage simulations with these new conditions. A heater temperature of 150ºC was chosen to reflect a realistic solar thermal collector heat source. The charge pressure remained unchanged at 6 bar with ambient temperature of 21ºC.

Table 7.4 – LPSC performance summary for simulations with 150ºC heaters at 6 bar and various pre-set absorber temperatures.

Absorber Temp. (°C)	Ave. pressure amplitude (bar)		Ave. piston amplitude (cm)		Max piston acceleration (ms^{-2})		Total heater heat input (W)		Total absorber heat input (W)		COP	
	23 mm	30 mm	23 mm	30 mm	23 mm	30 mm	23 mm	30 mm	23 mm	30 mm	23 mm	30 mm
20	0.555	0.521	3.12	1.70	25.9	24.0	18.6	21.2	12.3	13.7	0.661	0.648
18	0.524	0.494	2.94	1.62	24.4	22.7	16.8	19.3	10.9	12.3	0.646	0.634
16	0.492	0.465	2.77	1.53	23.0	21.5	15.1	17.5	9.5	10.8	0.631	0.618
14	0.460	0.436	2.59	1.43	21.5	20.1	13.5	15.7	8.3	9.5	0.613	0.601
12	0.426	0.406	2.40	1.34	19.9	18.8	11.9	14.0	7.0	8.1	0.594	0.582
10	0.392	0.376	2.21	1.24	18.3	17.4	10.3	12.3	5.9	6.9	0.571	0.560
8	0.357	0.344	2.01	1.13	16.7	15.9	8.8	10.6	4.8	5.7	0.544	0.535

Comparing the results to the 150ºC simulation results from the previous analysis, it appears that the performance of the system does improve slightly when the additional absorber heat flow potential is added. For absorber temperatures at 14ºC, the total heat flows are 13.5 W and 8.3 W (COP = 0.613) for the heaters and absorbers in the 23 mm system respectively; whereas with an average absorber temperature of 13.8ºC, the 23 mm system produced heat flows totalling 13.3 W and 7.8 W (COP = 0.585). The performance of both systems increases as the absorber temperature nears the ambient temperature. Figures 7.13 and 7.14 show how the COPs and predicted heat flow quantities change depending on the absorber temperature. This type of analysis would be useful when attempting to size and select an appropriate solar collector system for integration with an optimised LPSC machine.

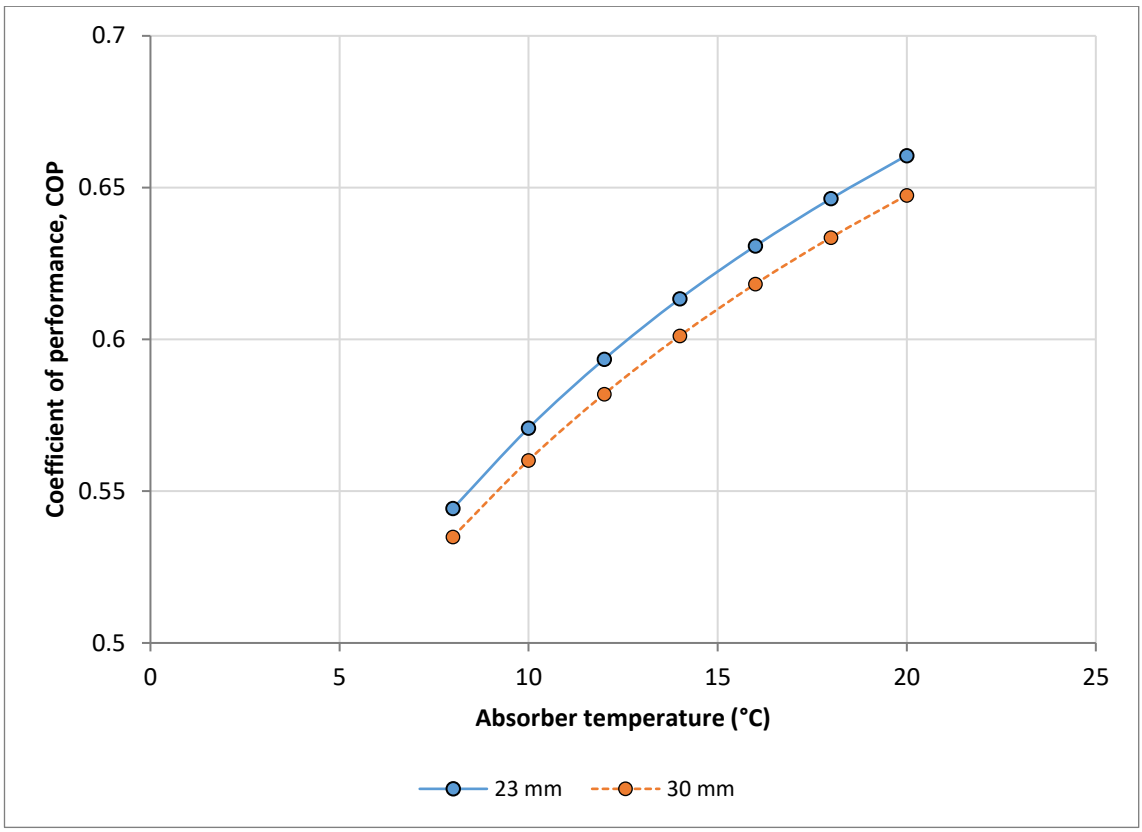

Figure 7.13 – Predicted COP values depending on the absorber temperature achieved.

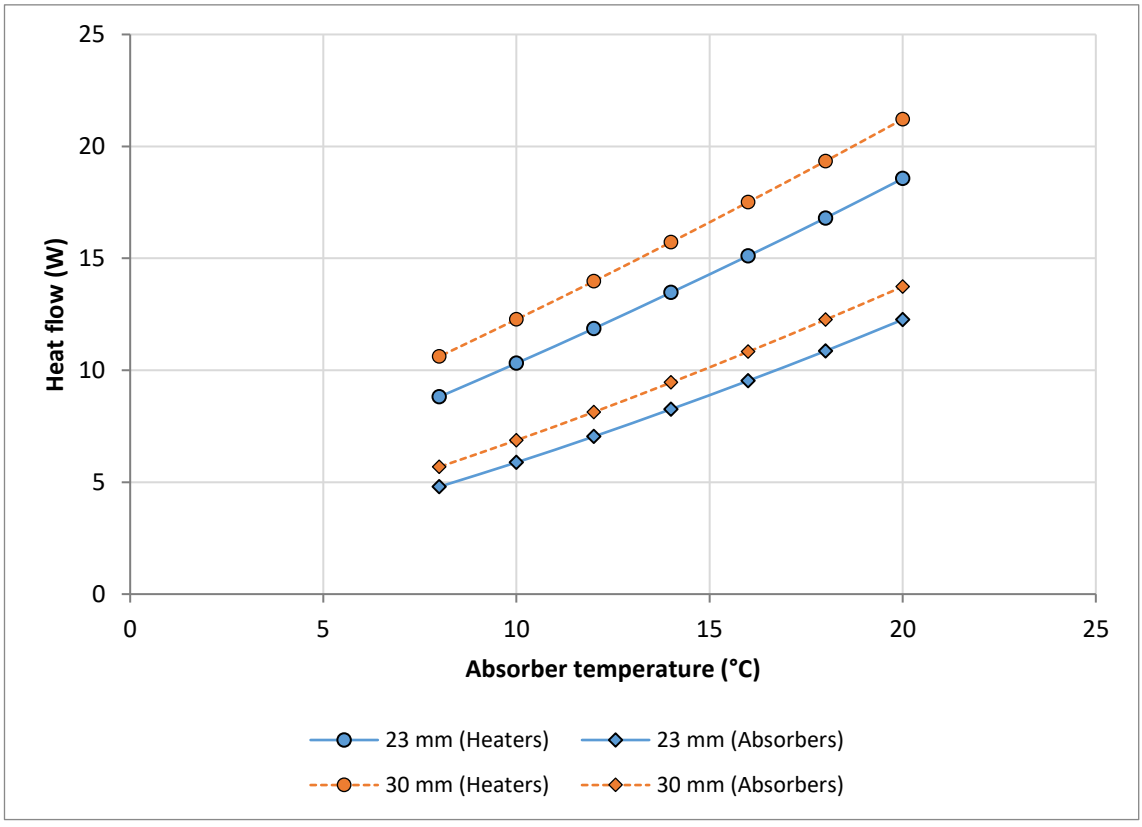

Figure 7.14 – Predicted heat flows into the system through the heaters and absorbers for different pre-set absorber temperatures.

8 Discussion

8.1 LPSC Configurations

8.1.1 4HEAT Configuration

Although obviously incapable of being used in cooling applications, the 4HEAT configuration proved extremely useful in linking the behaviours of the other configurations and providing a baseline for comparison. The procedure for using the Sage model to analyse the 3HEAT and 2HEAT configurations relies on first evaluating 4HEAT results by virtue of this configuration's symmetrical properties. The 4HEAT configuration could be considered for alternative power generation applications by utilising the developed piston motion alongside linear generators or similar external power extraction methods. With the addition of an external load, however, the dynamics of the resulting system would differ significantly from the free behaviour of the LPSC.

8.1.2 3HEAT and 2HEAT Configurations

The 2HEAT configuration is expected to produce better cooling performance based on the relative pressure amplitudes and the relative phase angles that are established from the dynamic behaviour of the system. This was verified using the Sage model, with superior COP values being predicted over the 3HEAT configuration. The highest COP value predicted for the 3HEAT configuration was 0.20, which was for the 22 mm piston tube simulations with 275 ml liquid pistons. The corresponding 2HEAT COP prediction was 0.53 for the exact same set-up.

The 2HEAT opposite configuration previously described in Section 3.3.3, was found not to function within the experimental range investigated, and the Sage model simulations showed that even with much higher heater temperatures, self-sustained operation was not possible. The suspected reason for this is a consequence of the dynamics that result from

the positioning of the two heaters—with any motion they induce causing a negating counteraction. During experimentation, this was noted in the attempts at self-starting the machine; after generating a significant piston amplitude manually and then releasing the U-tube, the piston amplitudes would decay to zero almost instantaneously, and much faster than would be expected of an individual free liquid piston with both surfaces open to the atmosphere.

One way to think of the 3HEAT system is that it is the 2HEAT opposite configuration except with an extra heater in place of one of the absorbers, this additional heater breaks the symmetrical constraints and allows the system to achieve self-sustained operation—but since the other two heaters are still attempting to cancel out the majority of each other's influence, the pressure amplitudes developed in the absorber space are significantly reduced.

8.1.3 Alternative Configurations

Aside from the configurations discussed and analysed up to this point, there are a number of other potential arrangements which could be employed for the LPSC. These arrangements are defined by the different number of subsystems they contain. In this research project only the 4-subsystems arrangements were considered, due in part to the goal of achieving phase angles of close to 90°. It is possible, however, to construct the machine with three, five, six or more subsystems, each of the double-acting alpha Stirling type connected in series. Each of these machines would have their own operating configurations, with different combinations of heaters and absorbers occupying the expansion spaces. Since this research was able to identify the 2HEAT adjacent configuration as having a conversion ratio of very close to 1:1, and relative phase angles of close to 90°, it would seem unlikely that a superior set-up could be identified from the multitude of other potential configurations; but it is not impossible and could be a future

avenue of research. With the validation of the Sage model, this process could be conducted solely through simulation.

8.2 Limitations of Research Presented

8.2.1 Frequency Considerations

The frequencies used in the Sage models are currently identified from the symmetrical properties of the 4HEAT configuration and its resulting behaviour. Using a procedure outlined in Section 4.2.9, the piston amplitude and frequency of operation of the 4HEAT system can be found through an iterative optimisation process for any particular heater temperature (as long as it is high enough to excite sustained operation, but not too high to exceed the allowable volumes of the compression and expansion spaces). The heater temperature value is usually chosen to be in the range which generates piston and pressure amplitudes close in magnitude to that expected or targeted for the 3HEAT or 2HEAT configurations. The resulting frequency is then used in the 3HEAT and 2HEAT models to determine the piston and gas pressure phasors, and generally solve for the behaviour of the LPSC machine when operating at various heater temperatures of interest for those configurations. In reality, since the frequency has some small dependence on heater temperature, it cannot be ensured that the frequency used is exactly the same as that which would naturally result in the 3HEAT or 2HEAT systems. It was shown that the potential error range for this frequency is very small across the heater temperatures being considered; although at the same time, the sensitivity of the model to changes in frequency is very high. In future work, this aspect of the modelling procedure could be improved. One possible improvement would be to create a function which attempts to relate the excitation achieved with the 4HEAT system to the 2HEAT system for different heater temperatures. Selecting a 2HEAT heater temperature would then produce the corresponding 4HEAT heater temperature which best approximates similar gas space

dynamics. This 4HEAT temperature could then be used to identify the frequency for use in the 4HEAT model.

The Sage model also predicts a different operating frequency than that of the experiments. The same difference was observed in the 15 mm and 22 mm piston tube experiments. The Sage predicted frequencies lie in between the theoretical adiabatic and isothermal gas spring limits (with an approximate average polytropic index of 1.2); whereas the experimental results are much closer to the isothermal gas behaviour limit. This difference could result from the influences of liquid water evaporation, which due to increases in heat capacity tend to produce behaviour that is closer to isothermal. However the research is at a too early stage to draw conclusions from this observation. Another potential source of this error is the average volumes of each gas space being significantly different from the model, although this was checked on multiple occasions. A method for measuring gas space volume could be used to rule out this source of error.

8.2.2 Test-rig Asymmetries

The Test-rig contains a number of physical asymmetries, which cannot be accounted for by the Sage model. Since the volume of each gas space cannot change, the gas masses of each space are always slightly different. Whether this is due to different operating configurations (some spaces being heated and others not) or from the small differences in geometry between the gas spaces, the differences in gas mass will always have an influence on the behaviour of the system—shifting relative phase angles and/or amplitudes. The different thermal conductivities resulting from the assembly of the heating cartridges within the heat exchangers potentially has a similar influence; although as described in Section 3.1.4, attempts at mitigating this by regulating power flow to each heater were implemented. To a lesser extent the heat rejection heat exchangers are subjected to small differences in the heat sink temperatures due to the single cooling line

connecting them in series. There are a number of other minor differences associated with the real test-rig set-up—many are similar to any experimental endeavour—but the final one highlighted here is the test-rig stand itself. The test-rig stand was shown to influence the behaviour of the system when the operational frequency approached the stand's own natural frequency of vibration. The movement of the stand behaved like a damper to system motion, and prevented sustained operation at some charge pressures in the 22 mm experiments (where its influence was identified). It is likely that the stand used in the 15 mm experiments also had some influence on the results attained, since stabilisers were not implemented in this first set of experiments.

The design of the stand is an interesting challenge, considering that for the interests of jump-starting the system it is necessary to be able to induce piston motion manually, but once self-sustained operation is achieved, the stand should then be transitioned into a state of high rigidity. Perhaps with the reduction in piston amplitudes associated with longer pistons, and the resulting reduced importance of piston floats, the self-starting properties of the LPSC machine will be restored and jump-starting will not be necessary. Until this is confirmed, the design of the test-rig stand should be kept in a non-rigid state to allow some form of manual excitation (if needed).

These differences between the real system and a computer model are unavoidable when using a test-rig whose purpose is to function with a number of configurations and heater temperatures (although they are worth considering in the development of a prototype).

8.2.3 Fluid Friction

The fluid friction present in the gas spaces is relatively well-known and accounted for by the correlations built into the Sage modelling software. Sage does not have the capability of selecting liquid pistons as a form of model component, however, and therefore the differences between solid pistons and liquid pistons had to be manually accounted for

within the Sage model. The fluid friction correlations used for the liquid pistons were outlined in Section 4.2.7, where formulae derived for steady flow situations were used to approximate an equivalent variable damping coefficient for use in the Sage model. This was due to the lack of experimental data in the literature on flow losses for reciprocating liquid flows. The results of the Sage simulations and their comparisons with the experimental results suggest that the approximations made were reasonably accurate; but it is not known how accurate they will remain, or how the loss relationships might differ for vastly differently-sized machines, or those with liquid pistons made up of alternative liquids. The correlations also have no dependence on the stability of the liquid surface or the RT instability, which may have an influence on the frictional losses unique to reciprocating flows. The presence of piston floats (and their influence on overall frictional flow losses) is another area which may become more relevant depending on the float requirements for an optimised prototype. It was shown in Section 6.2.1 that the presence of the polyethylene floats had a significant effect on the performance of the machine; they increased the minimum charge pressures capable of achieving self-sustained operation, which is an indication of the increased frictional losses and barrier to motion they present.

8.2.4 Liquid Evaporation

An important characteristic of this machine, which will undoubtedly have an impact on the level of performance attainable, is that of liquid evaporation at the piston surface and the resulting role the liquid vapour plays in the thermodynamic processes in the gas space. At this stage no attempts have been made to mitigate this factor, other than the inclusion of the polyethylene floats, which also function as piston stabilisers. In the present context of research into the LPSC machine (as with the piston floats) liquid evaporation and its impact on system performance does not qualify as being of primary importance. As the LPSC machine is refined and improved closer to its optimal operating parameter set, the

effects of evaporation will be able to be assessed with greater certainty. The use of liquid water as the piston fluid was made because of its abundance and simple handling requirements; however, as discussed further in Section 8.6.2, many other fluids are available for consideration and—as such—evaporation is considered outside of the present research scope. As the project progresses, a greater amount of consideration should be given to the effects of liquid evaporation and methods for mitigating it.

8.2.5 Multi-modal Behaviour

During the experimental investigation (particularly with the 15 mm piston tubes) multi-modal system behaviour was frequently observed. This behaviour was more prevalent in the 4HEAT and 3HEAT configuration experiments—possibly due to the higher degrees of dynamic instability associated with having a larger number of 'engine' subsystems. The multi-modal behaviour did not occur very frequently with the 22 mm test-rig. There are a number of physical differences between the 15 mm and 22 mm test-rigs, so it is not possible to definitively identify why multi-modal experiments were not witnessed with the 22 mm test-rig; although there is one main difference which is suspected to play the most important role—the test-rig stand. As discussed in Section 6.1, when the 22 mm test-rig experiments were first begun, the vibration of the newly created test-rig stand was found to interfere with the operation of the LPSC machine within a particular charge pressure range. It was discovered that the natural frequency of vibration of the stand coincided with the operational frequency of the LPSC machine near this point, and thus was damping the motion of the pistons. The interference was so significant that at charge pressures near 3.5 bar the machine was unable to achieve self-sustained operation entirely. In order to combat this effect, stabilisers were added to the test-rig stand. The stabilisers increased the rigidity of the stand and prevented the piston U-tubes from

entering into oscillatory motion of their own[1]. With these stabilisers installed, the experiments conducted in the affected charge pressure range now behaved consistently with the expected trends in pressure amplitude and piston displacement.

In the first experimental investigation (using 15 mm OD U-tubes) the effects of test-rig stand vibration were not as significant, and their detrimental impact on operation not yet appreciated. As a result, all of the 15 mm experiments were conducted using a test-rig stand without specialised stabilisers restricting the motion of the piston U-tubes. The 100 ml and 115 ml liquid pistons associated with the 15 mm test-rig did not produce forces as large as with the 275 ml pistons, which is one reason why the vibration of the test-rig stand was not as noticeable. It is likely that the vibration of the test-rig stand, and how this vibration changed in magnitude for different LPSC frequencies, had some influence on the development of pressure amplitudes and piston displacements during the 15 mm experiments. The multi-modal behaviour of the machine could have been caused by fluctuations in the damping from test-rig vibration—with multiple semi-stable oscillatory regimes possible since the stand can provide a variable level of energy dissipation based on its own motion. With stabilisers installed, the test-rig stand is restricted in its ability to dissipate energy, and therefore the machine behaves more like the closed dynamic system intended (and that which was modelled analytically and in Sage). The design of the test-rig stand will become more important as the liquid piston mass is increased further, since the reaction forces will increase in magnitude proportional to piston mass.

8.3 Rayleigh-Taylor Instability and Piston Floats

At the beginning of the project, it was unknown what role the behaviour unique to liquid pistons would play in the progression of the research. As the investigation progressed, it

[1] Or at least they prevented the U-tubes from entering large scale oscillations visible to an observer.

was discovered that the liquid surface would become unstable and turbulent at relatively low charge pressures in the heater temperature range being considered. In order to mitigate this instability, polyethylene floats were eventually employed, which allowed experiments to be conducted over the entire range of operating conditions targeted. When the experimental results were analysed in more detail, evidence of a transition between stable and unstable behaviour was found, and traced to the liquid pistons based on the capacitive sensor readings. The cause of the piston instability was not immediately obvious during the experimental investigation, but in a subsequent literature review the Rayleigh-Taylor instability was identified as a potential cause.

The RT instability phenomenon was not widely cited in Fluidyne research papers and texts—the reason for this is speculated to be predominantly due to the much lower frequencies (typically in the order of 1 Hz) of most Fluidyne machines. The lower frequencies correspond to lower liquid piston accelerations and therefore less instances of RT instability. It is only due to the Siemens-Stirling configuration of the LPSC, which employs the double-acting alpha configuration of the Stirling cycle, that the natural frequency of the machine is raised to levels which coincide with RT instability. This has led to some instances of the RT instability being overlooked—for example, in a paper assessing the potential of a thermoacoustic Stirling engine utilising liquid pistons (Zhang & Luo, 2015), operational frequencies of 25 Hz were being analysed, which for their 50 mm diameter, 1.5 m long liquid pistons, imposes a maximum piston amplitude of approximately 1 mm (using an acceleration limit of 25 ms^{-2}).

With the polyethylene floats employed during the experimental process of this research project, the maximum piston accelerations capable of being sustained were in the range of 25 ms^{-2}–30 ms^{-2}. The experimental measurements consistently showed that the behaviour of the system transitioned from stable to unstable liquid surfaces and pressure

amplitudes when the maximum acceleration reached this threshold level. The Sage simulations did not predict the same acceleration plateau as that observed experimentally. Without the floats, the transition occurred much earlier and at much lower maximum pressure amplitudes; therefore, much lower maximum piston accelerations were able to be sustained. Piston floats have proven useful in extending the experimental range of the test-rig and attaining more evidence of the RT instability phenomenon.

It seems that a major reason why the polyethylene floats outperformed other types was because their density is very similar to that of water. There is still a lot of room for improvement in terms of float design; although with the current research focus being on determining the key design parameters (such as piston length and diameter, etc.) the geometry of the system is subject to change, and these changes will govern the float design constraints. It was shown that the optimal performance predictions from the Sage model tended to coincide with lower piston accelerations, which suggests that as further improvements are made then the need for submerged floats may be eliminated entirely. Therefore, any attempt at optimising their presence in the test-rig may prove redundant.

The floats will and should remain an important design consideration for the test-rig in its current form and future iterations—although with a possible shift in focus from surface stability to minimising evaporation effects. With the LPSC system becoming more refined and optimised, some of the less significant considerations become more important, and float design could be used to mitigate other sources of performance degradation. As an example, shuttle heat losses between the liquid piston and the surrounding U-tube and working gas can be reduced by using an above-surface float with a length comparable to the piston stroke.

8.4 Design Considerations

8.4.1 Working Fluids

In this research project, air was used as the working gas for experimentation. Air was chosen because of its ease of use and handling when compared with the other candidates: helium and hydrogen. Both helium and hydrogen result in superior performance for Stirling engines due to their advantageous heat transfer and fluid-dynamic properties. When designing a prototype LPSC machine it is highly likely that one of these gases would be selected for use. Hydrogen does outperform helium, but its use does result in a number of other design considerations and restraints due to its flammable nature and its ability to diffuse into metal housings. Helium is disadvantaged due to its status as a finite resource.

As an indication for the increased performance possible with the use of these two working gases, the Sage model constructed for the 23 mm diameter, 3 m long liquid pistons was modified to replicate the use of hydrogen instead of air. The results are summarised below in Table 8.1. The simulations were conducted with the 2HEAT configuration, 150°C heater temperatures, 6 bar charge pressure and with all other model parameters unchanged.

Table 8.1 – Sage model predictions for air and hydrogen with the 23 mm diameter, 3 m long liquid piston test-rig.

Property	Air	Hydrogen
Frequency (Hz)	4.583	4.568
Average pressure amplitude (bar)	0.456	0.611
Heat input from heaters (W)	13.25	20.54
Heat absorbed through absorbers (W)	7.76	12.35
Absorber 1 fin temperature (°C)	13.1	7.0
Absorber 4 fin temperature (°C)	14.5	9.4
Coefficient of performance	0.5853	0.6013
Second law efficiency	5.3%	9.9%

Immediately it can be seen that the performance of the LPSC is predicted to improve significantly with the use of hydrogen. The COP has increased by 2.7% to 0.6013. The cooling capacity of the machine has increased by 59.1% from 7.76 W to 12.35 W, and the temperatures developed in the absorbers have also significantly lowered, from 13.1°C to 7.0°C and 14.5°C to 9.4°C for the fin temperatures of absorbers 1 and 4 respectively. As a result, the second law efficiency is observed to increase significantly from 5.3% to 9.9%[1]. It is also important to recognise that these improvements have resulted from the implementation of hydrogen in a prototype that was optimised for the use of air as the working fluid. It is likely that with hydrogen the optimal piston dimensions would differ from the 23 mm diameter, 3 m long ones used in the model. Identifying these would undoubtedly result in performance improvements exceeding those in the preceding table. As previously discussed, however, pursuing the optimisation of the LPSC machine with multiple geometric and physical alterations is not advised at this stage due to the uncertainty surrounding the Sage model predictions. The results for the use of hydrogen are nonetheless very encouraging, and could be considered (along with helium) during the next research phase.

8.4.2 Piston Sizing

As previously identified, the experimental results indicate that an acceleration limit is imposed on the liquid pistons. It is currently theorised that the RT instability phenomenon is responsible for this limit and that the absolute value of the limit is influenced by surface tension and the presence of surface floats (such as the polyethylene floats used in this research project). If it is assumed that the acceleration limit is independent of any other system parameters, it is possible to investigate the design implications imposed by this

[1] The second law efficiencies are calculated by comparing the Carnot efficiencies for a tri-thermal system (see Equation 2.1), with the low temperature selected as the absorber 1 fin temperature.

limitation. From Equation 4.7, the natural angular frequency of the LPSC machine can be found:

$$\omega_n = \sqrt{\frac{\frac{2nA^2p_0}{V_0}+2A\rho g}{m}}$$

In general, p_0 will be increased as much as possible, in order to obtain the 'free' performance benefits associated with doing so. When this is done, the right-hand (RH) term (within the square root function in the above equation) becomes increasingly less significant. In other words, the gas spring constant begins to dominate the piston spring constant in terms of dictating the natural frequency of operation. For example, assuming a V_0/A ratio of 1 (which is a generous effective gas space length), the RH term becomes less than 10% of the left-hand (LH) term at a charge pressure of 7 bar. As the charge pressure is increased further, this percentage continues to reduce. It is reasonable, therefore, to neglect the RH term and use:

$$\omega_n = \sqrt{\frac{2nA^2p_0}{mV_0}}$$

as an approximation for the system angular frequency. Assuming a constant cross-sectional liquid piston area, the equation simplifies to:

$$\omega_n = \sqrt{\frac{2nAp_0}{\rho LV_0}} \tag{8.1}$$

where L is the length of the liquid piston. The acceleration limit:

$$\omega^2 X \leq \alpha_{Max}$$

will provide a design constraint, where α_{Max} is the acceleration limit. Substituting in for the angular frequency from Equation 8.1 and rearranging gives:

$$\frac{XA}{V_0} \leq \frac{\alpha_{Max}\rho L}{2np_0}$$

where *XA* is equal to the half of the piston stroke volume, V_p. Multiplying the stroke volume by $\sqrt{2}$ gives the swept volume, V_S, of each gas space—assuming equal piston amplitudes and 90° phase angles. Substituting into the previous equation and simplifying gives:

$$\frac{V_S}{V_0} \leq \frac{\sqrt{2}\alpha_{Max}\rho L}{np_0} \tag{8.2}$$

The ratio of swept volume to the mean gas volume is closely related to the volume ratio of the machine and is an important design consideration. Also, as identified earlier in Section 2.3.3, the swept volume has a direct influence on the power capacity estimates for real Stirling engines. Rearranging the above equation for piston length gives:

$$L \geq \frac{V_S np_0}{\sqrt{2}V_0\rho\alpha_{Max}}$$

The above equation shows that for a particular volume ratio and operating pressure, a constraint on the minimum liquid piston length is imposed. For all shorter lengths the acceleration limit may be exceeded before the desired piston amplitude is achieved. As an indication of the significance of this constraint, it can be evaluated using some example parameters. Setting the ratio of swept volume to mean gas volume equal to 0.15, the charge pressure to 20 bar (2 MPa) and the maximum acceleration limit to 30 ms^{-2}, the minimum liquid piston length required is determined to be 2.55 m.

Accommodating the minimum required length will be an important consideration when developing a prototype machine with higher charge pressures. The shape of the current U-tubes is not optimised for space reduction and other approaches could be considered—for example, the use of a liquid piston coil, where a number of loops are added to condense

a longer liquid piston into a smaller vertical space. The use of a higher density liquid would also result in minimum length reductions. This is discussed further in Section 8.6.2.

8.5 Overall Feasibility

8.5.1 Cooling Potential

The 2HEAT configuration with adjacent heaters has been identified as the most promising configuration for heat-activated cooling. This configuration is shown again in Figure 8.1 for clarity.

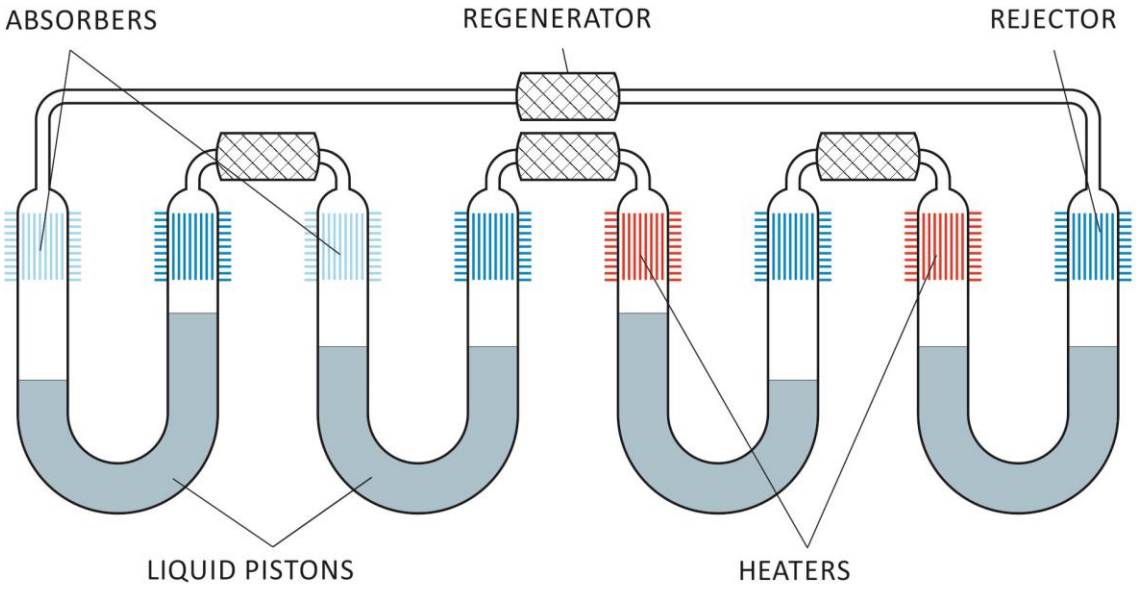

Figure 8.1 – Optimal configuration for cooling (2HEAT with adjacent heaters)

This configuration resulted in relative phase angles between adjacent pistons which were closest to the ideal region of 90°. The magnitudes of the pressure amplitudes developed in each of the four gas spaces were also relatively close, and the conversion ratios of pressure amplitudes in the heated spaces to those in the absorber spaces consistently very close to 1:1. The combination of these behavioural traits resulted in the largest temperature differences generated experimentally, and the highest predicted overall COP values of any simulations.

The COP value predicted for the test-rig in Chapter 7, with piston dimensions optimised for efficiency, was 0.585. This also included a maximum temperature difference of 7.9°C below ambient. By merely switching between air and hydrogen (as was assessed in Section 8.4.1) the COP of the same Sage model increased to 0.601, with a maximum temperature difference of 14°C below ambient, and a cooling capacity increase of 59.1%. Recalling the observations made in Section 2.1, and (in particular) Figure 2.4, it can be seen that a COP of approximately 0.6 would be very close in terms of competitiveness with the sorption technologies currently prevailing as the market-leading solar cooling options. There are a number of other important factors which affect the COP (so it is not wise to rely excessively on direct comparisons made in this manner)—although it is a clear indication that such an LPSC machine is feasible, if not commercially viable. This is reaffirmed when considering the large parasitic losses not accounted for in the sorption machine COPs in Figure 2.4, as well as the relatively un-optimised LPSC test-rig being analysed and considered here. With the entire set of heat exchangers, regenerators, and all other gas space components un-optimised, it is likely that significant performance improvements over the current LPSC machine can be obtained.

8.5.2 Capacity limitations

Traditional Stirling engines have always suffered from capacity limitations. This arises from the requirement for external heat input into the system. Unlike combustion cycles, the Stirling engines typically receive their heat input through a solid interface separating the heat source from the working gas. These interfaces impose limitations on the rates at which heat can be transferred into the working gas. The result is that Stirling engines generally have relatively low power densities. As was described in Equation 2.8 in Section 2.3.3, the power output of a real Stirling machine depends linearly on a number

of factors. If we consider unchanging temperature regimes, these factors reduce to the frequency, *f*, the charge pressure, p_0, the swept volume, V_s, and the experience factor, *F*.

The swept volume is the only extensive property out of the four, i.e. it has direct implications for the size of any machine. The experience factor is known to typically vary between 0.25–0.35 for well-designed machines. Of the remaining two, frequency and pressure, only pressure is directly controllable. As discussed already, increasing the charge pressure also increases the frequency. With the limitations imposed on frequency by the RT instability, the capacity of a particular sized machine must therefore also be limited. It is possible to analyse the design constraints associated with these limitations since approximations for the system frequency and swept volume have already been obtained. Beginning with Equation 2.8, which provides an estimate of the power output of a real Stirling engine we have:

$$P = FfV_S p_0 \frac{T_H - T_C}{T_H + T_C}.$$

Rearranging Equation 8.2 for the swept volume, V_S, and substituting into the above equation (along with Equation 8.1 for the system frequency) gives the following when simplified:

$$P \leq \frac{F\alpha_{Max}}{\pi} \sqrt{\frac{Ap_0V_0\rho L}{n}} \left(\frac{T_H - T_C}{T_H + T_C}\right)$$

This equation can be further simplified by assuming isothermal gas behaviour ($n = 1$) and replacing *AL* with the liquid piston volume, V_{lp}. This results in the following expression for the estimated power producing capacity of one of the driving subsystems:

$$P \leq \frac{F\alpha_{Max}}{\pi} \sqrt{p_0V_0\rho V_{lp}} \left(\frac{T_H - T_C}{T_H + T_C}\right) \tag{8.3}$$

If it is assumed that the heat source and sink temperatures remain unchanged, along with the acceleration limit and the density of the liquid pistons, the dependent variables reduce to the charge pressure, the mean gas volume, and the liquid piston volume. In Chapter 7, the liquid piston dimensions were optimised for the test-rig in its current form. It is possible to use the same ratio of gas space volume to liquid piston volume in order to obtain a crude approximation for the size of the machine necessary to achieve the stated goal at the beginning of this project. This goal was to develop a LPSC capable of producing a cooling effect in the vicinity of 5 kW. Using the Sage model parameters for prototype 1 (in Chapter 7) the ratio of gas space volume, V_0, to piston volume, V_{lp}, is calculated to be approximately 5:1. Therefore $V_0 \approx 0.2V_{lp}$. Substituting this into Equation 8.3 and assuming an experience factor of 0.25, an acceleration limit of 30 ms^{-2}, a charge pressure of 20 bar (2 MPa), a water density of 1000 kgm^{-3}, a heat source temperature of 150°C (423 K), and a heat sink temperature of 25°C (298 K), the expression becomes:

$$P \leq 8278\sqrt{V_{lp}}.$$

For a cooling effect of approximately 5 kW, it is reasonable to estimate that the power output of each of the two driving subsystem should be in the vicinity of 1 kW. Thus, solving the above equation for a 1 kW power output results in a minimum piston volume of 0.0146 m^3, or approximately 15 L. Four 15 L liquid pistons would result in a machine housing 60 L of liquid water, weighing approximately 60 kg, and with a rough estimate of 40 kg for other housing componentry. This results in a machine which is roughly 100 kg in total weight; a machine of this size is certainly feasible for low capacity cooling applications.

8.6 Future Research

8.6.1 Piston Floats

The piston friction and float incorporation topics were partially explored during this project, however, as discussed in Section 8.3, a considerable amount of additional work is required to establish whether they are necessary, and—if so—in what physical embodiment are they required, i.e. are they needed purely for surface stability, evaporation mitigation, heat transfer restrictions or for another purpose.

8.6.2 Liquid Pistons

In this research project only liquid water was considered (and used) in the experiments and modelling procedures. This was primarily due to its availability, stability and ease of handling. There are, however, many other potential liquids that can be considered for use in the LPSC machine. Assessing the suitability of these liquids would be another interesting avenue for further research. On the surface it appears that higher density liquids with low viscosity would be the preferred choice. By using higher density liquids, the machine's power density can be increased, since a larger amount of energy is capable of being stored in the motion of the liquid pistons. With higher density typically comes higher viscosity; although if the total volume required for the liquid piston is significantly reduced, the increase in viscosity may still result in cumulative reductions in piston friction. It seems likely that kinematic viscosity (μ/ρ) will be an important property of any potential liquid.

Related to the preceding speculation on alternative liquids is the need for experimentally verified correlations for fluid friction and kinetic flow losses in reciprocating fluid flow. The correlations currently used are for steady flow scenarios only—if the true behaviour of the liquid deviates significantly from the correlations used, then the Sage model's accuracy suffers, when extrapolating (after validation) during the design optimisation

process. Perhaps the influence of surface tension and other properties affecting flow direction change also play a role, in which case the correlations may need to be altered for different types of liquid.

8.6.3 Thermal Energy Storage

The field of Thermal Energy Storage (TES) is extensive and covers a large range of applications, including those involving solar thermal collection (Tian & Zhao, 2013). Since, the target heat source being considered is variable and inconsistent in nature, TES will need to be considered at a later stage of project development. The challenge of TES as it relates to this research project is in identifying an optimal storage method (and integrating it into the collector and LPSC design) so as to create a complete and independently operable final system prototype. This would be one of the final stages in producing a machine for commercial implementation and is not suggested for immediate consideration.

8.6.4 Solid Pistons

Although this research project has focussed solely on the implementation of liquid pistons, much of the analysis would potentially apply to solid piston machines of a similar design. Unlike liquid pistons, the solid piston machines would not be constrained by the acceleration limit imposed by the RT instability. Similarly, since the solid pistons could be fitted with custom spring supports (for example flexure bearings) their contribution to the operating frequency (see equation 4.6) would be more significant and controllable from a design perspective. This would potentially allow for machines with much higher frequencies, and therefore power densities, when compared with a similar sized LPSC. Considerable work has been conducted on solid piston heat-activated heat pumps, including machines based on the Stirling cycle (Walker & Senft, 2012). This is another research avenue that could be pursued.

9 Conclusions and Recommendations

This research presents the liquid piston Stirling cooler or LPSC—which is a 4-cylinder double-acting alpha-type Stirling test-rig capable of utilising heat input to produce a cooling effect. The objective of this research project was to establish the feasibility of such a machine. Based on the findings presented, it is clear that such a system is feasible both technically and commercially, although to what extent in either regard is still unknown. The main conclusions and recommendations are summarised as follows:

9.1 Design, Construction and Testing of the LPSC Machine

The successful development of an experimental test-rig has shown that it is possible to produce a cooling effect using the LPSC concept in conjunction with a thermal heat source. In its current un-optimised state the LPSC test-rig has proven to be functional over a wide range of relatively low mean gas pressures (1 bar–6 bar), relatively low heat source temperatures (80°C–150°C), and with air as a working gas. The (previously untested) 2HEAT adjacent configuration (with two adjacent heated spaces connected in series with two adjacent absorber spaces) proved to be the optimal configuration for cooling performance—with relative phase angles close to 90°, and a conversion ratio of heater gas pressure amplitude to absorber gas pressure amplitude of 1.02:1.

9.2 System Modelling and Performance Evaluation

A third order model of the LPSC was constructed in the computer modelling software, Sage. The model encompasses the complex system dynamics and heat transfer characteristics, and has been validated against experimental results. An approximation for the natural frequency of the system was derived analytically, and an independent procedure was developed to determine the operating frequency needed for the Sage model. These frequencies were found to have very minimal dependence on the machine's

configuration type and heat source temperatures. Some limitations of the model require further investigation, such as reciprocating flow losses in the liquid pistons and piston surface instability; although its use in predicting system performance enabled the installation of more optimised piston geometry which led to the first tangible cooling effect in the range of 5°C below ambient. When considering test-rig performance at 150°C heater temperature and 6 bar charge pressure, the Sage model predicts a thermal COP value of 0.53 for the current set-up with 19.3 mm diameter, 94 cm long liquid water pistons. This rises to 0.59 with the installation of 23 mm diameter, 3 m long liquid pistons. When the working gas in the model is replaced with hydrogen, the performance of the LPSC increases significantly: the COP increases by 2.7%, to 0.6, the cooling capacity increases by 59.1%, the cold-side temperature in the primary absorber is decreased by 77.2% (with respect to 21°C ambient) from 13.1°C to 7°C, and the second law efficiency increases from 5.3% to 9.9%.

9.3 Liquid Piston Acceleration Limit and Design Implications

Evidence of a liquid piston acceleration limit (likely resulting from the Rayleigh-Taylor instability phenomenon) was consistently observed during the experiments. The use of submerged polyethylene piston floats was found to increase surface stability and enable accelerations of 25 ms^{-2}–30 ms^{-2}. A number of design considerations for the LPSC have been explored. The existence of a potential piston acceleration limit due to the RT instability imposes a constraint on the minimum piston length, which is quantified for use as a design tool. A crude capacity evaluation was also conducted, which indicated that a LPSC capable of generating a cooling effect of approximately 5 kW was feasible with 15 L liquid water pistons and a total machine weight of roughly 100 kg.

9.4 Recommendations

The predicted COPs for the modified test-rig are close to current market-leading solar cooling options, i.e. sorption systems. With a gap in the market for low capacity machines (<5 kW) a more thorough and targeted optimisation effort is recommended. The successful validation of a third order Sage model of the LPSC provides an avenue for theoretical development and optimisation. Many aspects of the LPSC are capable of being improved, including manipulation of the gas space component dimensions such as heat exchangers and regenerators. Different working gases and piston liquids can be modelled—with higher charge pressures to advance plans for an optimised LPSC prototype. If successful, an integrated solar refrigeration system could be developed, although this particular heat-activated cooling machine would not be limited to the solar market (it could also find use in other waste heat applications).

A number of specific topics are also recommended for future research (summarised in Section 8.6). These include: (a) an assessment of the design requirements and implications of piston floats—if needed; (b) research into potential liquid piston fluid options (and their associated frictional losses, etc.) with respect to reciprocating motion specifically; (c) thermal energy storage options for integration with solar (or other) heat sources; and finally, (d) an investigation into the development of a similar machine using solid pistons instead of liquid pistons.

References

Albers, J., Kühn, A., Petersen, S., & Ziegler, F. (2011). Development and progress in solar cooling technologies with sorption systems. *Chemie-Ingenieur-Technik, 83*(11), 1853-1863. doi:10.1002/cite.201100116

Anyanwu, E. E. (2003). Review of solid adsorption solar refrigerator I: An overview of the refrigeration cycle. *Energy Conversion and Management, 44*(2), 301-312. doi:10.1016/s0196-8904(02)00038-9

Anyanwu, E. E. (2004). Review of solid adsorption solar refrigeration II: An overview of the principles and theory. *Energy Conversion and Management, 45*(7-8), 1279-1295. doi:10.1016/j.enconman.2003.08.003

Balaras, C. A., Grossman, G., Henning, H. M., Infante Ferreira, C. A., Podesser, E., Wang, L., & Wiemken, E. (2007). Solar air conditioning in Europe-an overview. *Renewable and Sustainable Energy Reviews, 11*(2), 299-314. doi:10.1016/j.rser.2005.02.003

Bocquet-Appel, J. P. (2011). When the world's population took off: The springboard of the neolithic demographic transition. *Science, 333*(6042), 560-561. doi:10.1126/science.1208880

Carlsen, H. (1994). Results from 20 kW Vuilleumier heat pump test program. *Proceedings of the 29th Intersociety Energy Conversion Engineering Conference, 2*, 927–932. doi: 10.2514/6.1994-3837

Choudhury, B., Saha, B. B., Chatterjee, P. K., & Sarkar, J. P. (2013). An overview of developments in adsorption refrigeration systems towards a sustainable way of cooling. *Applied Energy, 104*, 554-567. doi:10.1016/j.apenergy.2012.11.042

Cook-Yarborough, E. H. (1982). Multi-cylinder Stirling Engine Heat Pumps with Double-acting Free Pistons. *Proceedings of the Intersociety Energy Conversion Engineering Conference, 4*, 1790-1795.

Dyson, R. W., Wilson, S. D., & Tew, R. C. (2004). Review of computational Stirling analysis methods. *Proceedings of the 2nd International Energy Conversion Engineering Conference, 1*, 511-531.

Fan, Y., Luo, L., & Souyri, B. (2007). Review of solar sorption refrigeration technologies: Development and applications. *Renewable and Sustainable Energy Reviews, 11*(8), 1758-1775. doi:10.1016/j.rser.2006.01.007

Fauvel, O. R., Reader, G., & Walker, G. (1989). Tuning line excitation of displacer motion in a fluidyne. *Proceedings of the 24th Intersociety Energy Conversion Engineering Conference, 5*, 2271-2276.

Fauvel, O. R., & West, C. D. (1990). Excitation of displacer motion in a fluidyne: Analysis and experiment. *Proceedings of the 25th Intersociety Energy Conversion Engineering Conference, 5*, 336-341.

Gedeon, D. (2010). *Sage User's Guide*. Retrieved from www.sageofathens.com

Gerstmann, J., & Friedman, Y. (1979). *US Patent No. 4148195*. Washington, DC: U.S. Patent and Trademark Office.

Goswami, D. Y., Kreith, F., & Kreider, J. F. (1999). *Principles of Solar Engineering*. Philadelphia, USA: Taylor & Francis.

Harboe-Hansen, H. (1995). Sweden scores a first with AIP submarine. *Naval Architect*, March 1995, p E175. London, England: Royal Institution of Naval Architects.

Hargreaves, C. M. (1991). *The Philips Stirling engine*. New York, NY: Elsevier Science Publishing Compnay Inc.

Henning, H. M. (2007). Solar assisted air conditioning of buildings - an overview. *Applied Thermal Engineering, 27*(10), 1734-1749. doi:10.1016/j.applthermaleng.2006.07.021

Hong, W. J., Alhussan, K., Zhang, H., & Garris Jr, C. A. (2004). A novel thermally driven rotor-vane/pressure-exchange ejector refrigeration system with environmental benefits and energy efficiency. *Energy, 29*(12-15), 2331-2345. doi:10.1016/j.energy.2004.03.050

International Energy Agency. (2007). *Renewables for Heating and Cooling*. Retrieved from http://www.iea.org/

International Energy Agency. (2009). *Renewable Energy Essesntials - Solar Heating and Cooling*. Retrieved from http://www.iea.org/

International Energy Agency. (2011). *Solar Energy Perspectives*. Retrieved from http://www.iea.org/

International Energy Agency. (2012). *Technology Roadmap: Solar Heating and Cooling*. Retrieved from http://www.iea.org/

International Energy Agency. (2016). *Our mission*. Retrieved from http://www.iea.org/

Kim, D. S., & Infante Ferreira, C. A. (2008). Solar refrigeration options – a state-of-the-art review. *International Journal of Refrigeration, 31*(1), 3-15. doi:10.1016/j.ijrefrig.2007.07.011

Kolin, I. (1991). *Stirling motor: history, theory, practice; contributions to the 5th International Stirling Engine Conference, Inter University Center, Dubrovnik 1991*. Zagreb: University Publications.

Kongtragool, B., & Wongwises, S. (2003). A review of solar-powered Stirling engines and low temperature differential Stirling engines. *Renewable and Sustainable Energy Reviews, 7*(2), 131-154. doi:10.1016/s1364-0321(02)00053-9

Kruskal, M., & Schwarzschild, M. (1954). Some Instabilities of a Completely Ionized Plasma. *Proceedings of the Royal Society of London. Series A. Mathematical and Physical Sciences, 223*(1154), 348. doi:10.1098/rspa.1954.0120

Lamp, P., & Ziegler, F. (1998). European research on solar-assisted air conditioning. *International Journal of Refrigeration, 21*(2), 89-99. doi:10.1016/S0140-7007(98)00008-5

Martini, W. R. (1978). *Stirling Engine Design Manual*: U.S. Department of Energy, Office of Conservation and Solar Applications, Division of Transportation Energy Conservation.

Martini, W. R. (1983). Test on a 4U tube heat operated heat pump. *Proceedings from the 18th Intersociety Energy Conversion Engineering Conference, 2*, 872-874.

Mason, J. W., & Stevens, J. W. (2011). Design and construction of a solar-powered fluidyne test bed. *ASME 2011 International Mechanical Engineering Congress and Exposition, 4*(A&B), 9-20. doi:10.1115/IMECE2011-62194

Nguyen, V. M., Doherty, P. S., & Riffat, S. B. (2001). Development of a prototype low-temperature Rankine cycle electricity generation system. *Applied Thermal Engineering, 21*(2), 169-181. doi:10.1016/s1359-4311(00)00052-1

Nkwetta, D. N., & Sandercock, J. (2016). A state-of-the-art review of solar air-conditioning systems. *Renewable and Sustainable Energy Reviews, 60*, 1351-1366. doi:10.1016/j.rser.2016.03.010

Orda, E., & Mahkamov, K. (2004). Development of "low-tech" solar thermal water pumps for use in developing countries. *Journal of Solar Energy Engineering, Transactions of the ASME, 126*(2), 768-773. doi:10.1115/1.1668015

Otanicar, T., Taylor, R. A., & Phelan, P. E. (2012). Prospects for solar cooling - An economic and environmental assessment. *Solar Energy, 86*(5), 1287-1299. doi:10.1016/j.solener.2012.01.020

Özdemir, M., & Özgüç, A. F. (2003). A simple mathematical model to analyse a fluidyne heat machine. *Proceedings of the Institution of Mechanical Engineers, Part A: Journal of Power and Energy, 217*(1), 91-100. doi:10.1243/095765003321148736

Perlin, J. (1999). *From Space to Earth: The Story of Solar Electricity*. Ann Arbor, MI: Aatec Publications.

Peyret, R., & Taylor, T. D. (1983). *Computational Methods for Fluid Flow*. The University of California: Springer-Verlag.

Schmidt, G. (1871). The theory of Lehmann's calorimetric machine. *Z. Ver. Dtsch. Ing., 15*(1), 1-12.

Scott, R. (2005). Japan signs up for Stirling AIP. *Jane's Navy International* (JUL.). London, England: Jane's Information Group.

Senft, J. R. (1982). Simple Derivation of the Generalized Beale Number. *Proceedings of 17th the Intersociety Energy Conversion Engineering Conference, 4*, 1652-1655.

Slavin, V. S., Bakos, G. C., & Finnikov, K. A. (2009). Conversion of thermal energy into electricity via a water pump operating in Stirling engine cycle. *Applied Energy, 86*(7–8), 1162-1169. doi:http://dx.doi.org/10.1016/j.apenergy.2008.10.018

Smil, V. (2010). *Energy Transitions*. Santa Barbara, USA: ABC-CLIO.

Stebnovskii, S. V. (2003). Structural stability of unsteadily accelerated liquid pistons. *Fluid Dynamics, 38*(6), 832-838. doi:10.1023/B:FLUI.0000015222.32547.dd

Stephan, K. (1983). History of absorption heat pumps and working pair developments in Europe. *International Journal of Refrigeration, 6*(3), 160-166.

Stevens, J. W. (2010). Low capital cost renewable energy conversion with liquid piston stirling engines, *ASME 2010 4th International Conference on Energy Sustainability, 1*, 479-484. doi:10.1115/ES2010-90129

Sunpower. (n.d.). *Engines*. Retrieved from http://www.sunpowerinc.com/services/technology/engines.php

Tchanche, B. F., Lambrinos, G., Frangoudakis, A., & Papadakis, G. (2011). Low-grade heat conversion into power using organic Rankine cycles - A review of various applications. *Renewable and Sustainable Energy Reviews, 15*(8), 3963-3979. doi:10.1016/j.rser.2011.07.024

Tchernev, D. I. (1980). Solar Refrigeration Utilizing Zeolites. *Proceedings of the Intersociety Energy Conversion Engineering Conference, 2*, 2070-2073.

Stirling Technology (n.d.). *Total Energy Independence*. Retrieved from http://www.stirling-tech.com/energy.shtml

Thombare, D. G., & Verma, S. K. (2008). Technological development in the Stirling cycle engines. *Renewable and Sustainable Energy Reviews, 12*(1), 1-38. doi:10.1016/j.rser.2006.07.001

Tian, Y., & Zhao, C. Y. (2013). A review of solar collectors and thermal energy storage in solar thermal applications. *Applied Energy, 104*, 538-553. doi:10.1016/j.apenergy.2012.11.051

Urieli, I., & Berchowitz, D. M. (1984). Stirling cycle engine analysis. Bristol, England: A. Hilger.

Van de Ven, J. D. (2009). Mobile hydraulic power supply: Liquid piston Stirling engine pump. *Renewable Energy, 34*(11), 2317-2322. doi:10.1016/j.renene.2009.01.020

Walker, G. (1979). Elementary Design Guidelines for Stirling Engines. *Proceedings of the Intersociety Energy Conversion Engineering Conference, 1*, 1066-1068.

Walker, G., Reader, G., Fauvel, O. R., & Bingham, E. R. (1994). *The Stirling Alternative: Power Systems, Refrigerants and Heat Pumps*. Yverdon, Switzerland: Gordon and Breach Science Publishers.

Walker, G., & Senft, J. R. (2012). *Free Piston Stirling Engines*. Berlin, Germany: Springer Berlin Heidelberg.

Wang, K., Sanders, S. R., Dubey, S., Choo, F. H., & Duan, F. (2016). Stirling cycle engines for recovering low and moderate temperature heat: A review. *Renewable and Sustainable Energy Reviews, 62*, 89-108. doi:10.1016/j.rser.2016.04.031

West, C. D. (1971). The Fluidyne heat engine. *United Kingdom Atomic Energy Authority Research Group Report AERE R6775*.

West, C. D. (1981). Theoretical Basis for the Beale Number. *Proceedings of the Intersociety Energy Conversion Engineering Conference, 2*, 1886-1887.

West, C. D. (1983). *Liquid piston Stirling engines*. New York, USA: Van Nostrand Reinhold Company Inc.

West, C. D. (1984). Liquid-piston Stirling Machines. *2nd International Conference on Stirling Engines*, Shanghai, China.

West, C. D. (1986). *Principles and applications of Stirling engines*. New York, USA: Van Nostrand Reinhold Compnay Inc.

WhisperGen Ltd. (n.d.). Retrieved April 1, 2013, from http://www.whispergen.com

Wurm, J., Kinast, J.A., Roose, T.R., Staats, W.R. (1991) *Stirling and Vuilleumier heat-pumps*. New York, USA: McGrawHill, Inc.

Yu, L., & Fauvel, O. R. (1994a). Development of a composite Fluidyne regenerator. *Proceedings of Intersociety Energy Conversion Engineering Conference, 4*, 1908-1910.

Yu, L., & Fauvel, O. R. (1994b). Displacer design and testing for a barrel Fluidyne. *Proceedings of Intersociety Energy Conversion Engineering Conference, 4*, 1950-1953.

Zhai, X. Q., Qu, M., Li, Y., & Wang, R. Z. (2011). A review for research and new design options of solar absorption cooling systems. *Renewable and Sustainable Energy Reviews, 15*(9), 4416-4423. doi:10.1016/j.rser.2011.06.016

Zhang, S., & Luo, E. (2015). The thermodynamic performance of a double-acting traveling-wave thermoacoustic engine with liquid-water piston. *International Journal of Green Energy, 12*(3), 198-206. doi:10.1080/154350

Appendix I – Displacement Sensor Circuit Diagram

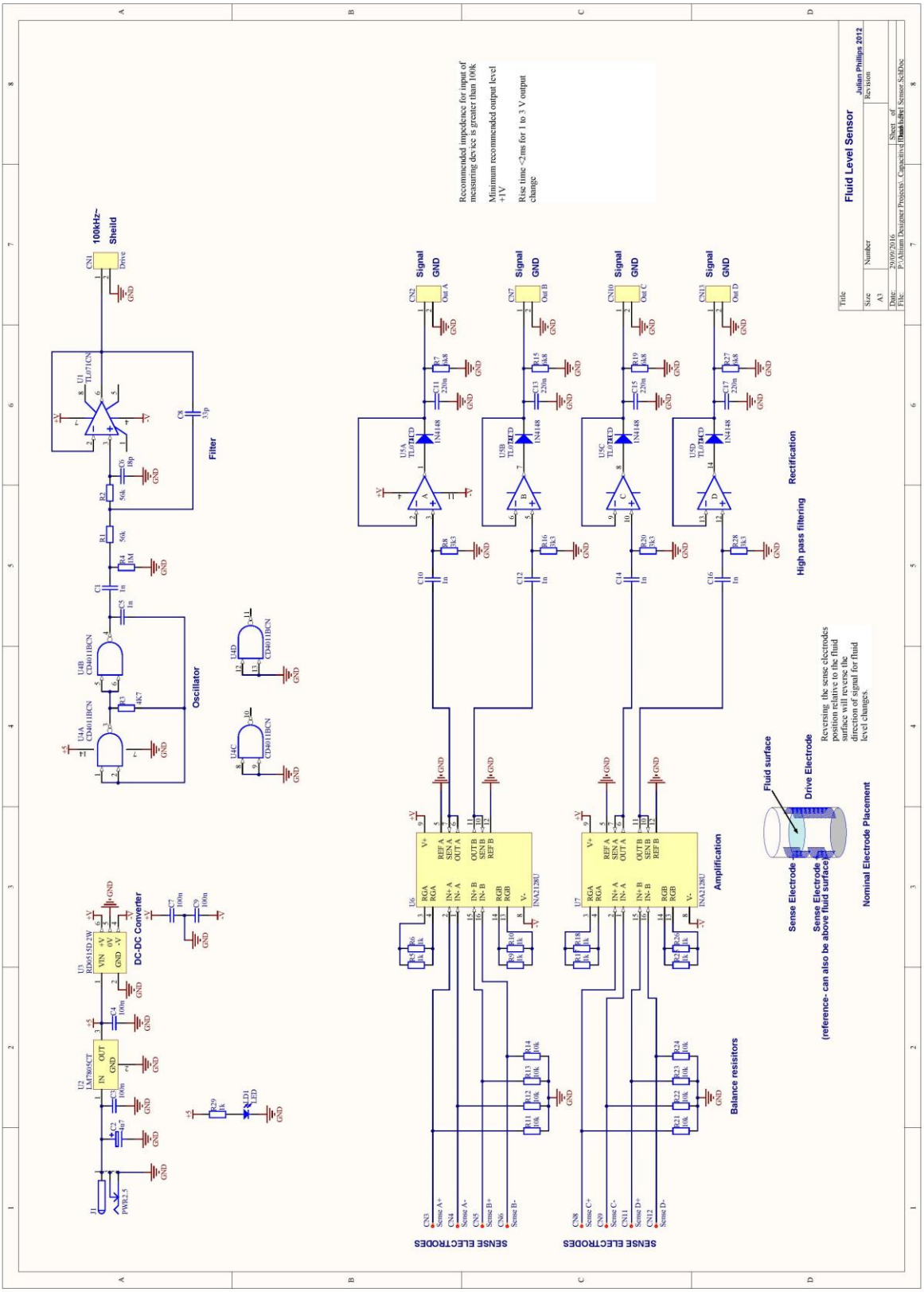

Appendix II – Rayleigh-Taylor Instability

The Rayleigh-Taylor (RT) instability describes the unstable behaviour of the surface between a dense fluid supported by another of lower density and subjected to some form of acceleration. The phenomenon was first theoretically analysed by Lord Rayleigh in 1882 (Rayleigh, 1882), who assessed the everyday scenario of water suspended above oil. Later, G. I. Taylor experimentally investigated the topic following World War II (Taylor, 1950). Taylor recognised that the phenomenon applied to liquids under any acceleration regime—not just those affected by gravity. Following Taylor's work, the RT instability received a considerable amount of research in various directions including surface tension and viscosity effects (Bellman & Pennington, 1954), as well as other areas such as magnetic fields (Kruskal & Schwarzschild, 1954), spherical geometries (Birkhoff, 1954) and bubble theories (Garabedian, 1957). More recently, the topic has expanded with developments in CFD to include numerous research focusses such as Inertial Confinement Fusion (ICF) devices. The range of applications of the RT instability is extensive—from underwater reactions to cloud stratification, and the aftermath of supernova.

The RT instability can also be applied to oscillating liquid pistons in order to access the stability of the liquid surface during operation. The derivation of the RT instability equations is relatively involved and not necessary in the context of this discussion. The reader is directed to the literature for further information. Figure A2.1 shows the case where two homogeneous incompressible fluid planes are separated by a common interface.

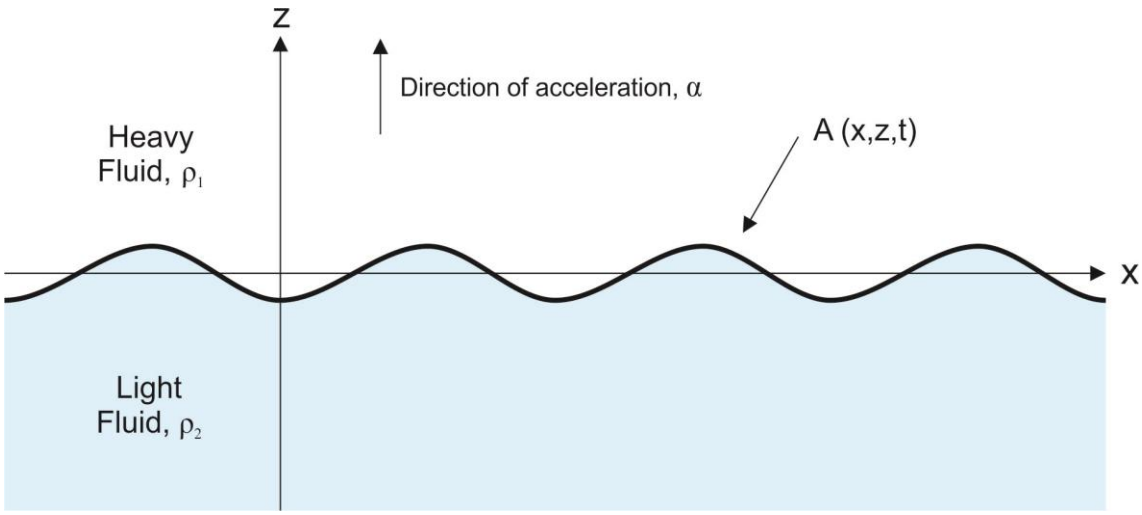

Figure A2.1 – Rayleigh-Taylor Instability interface between fluid planes of varying densities

The following equations describe the RT instability for the interface with a small sinusoidal perturbation profile imposed. Neglecting fluid friction and surface tension effects the perturbation function is given by:

$$A(x,z,t) = A(z)e^{(nt+ikx)}$$

where *k* is the wavenumber and *n* is given by:

$$n = \sqrt{k\alpha\left(\frac{\rho_1 - \rho_2}{\rho_1 + \rho_2}\right)}$$

where α is the acceleration in the positive z direction. The density fraction within the above equation is sometimes referred to as the Atwood number. So for instances where $\rho_1 > \rho_2$, i.e. positive Atwood numbers, the growth of the perturbation amplitude is exponential. Therefore, the instability only occurs in the scenario where the acceleration is in the direction of the denser fluid. In the case of the U-tube configuration of a liquid piston, this occurs when the liquid surface is above its neutral position, and the acceleration vector is pointed down—with peak acceleration occurring at top dead centre when velocity is zero.

It is important to note, however, that any experiments conducted on the surface of the earth will constantly experience the gravitational acceleration in the positive vertical direction equal to 9.81 ms^{-2}. Therefore, the RT instability will only become applicable in Fluidyne machines when the piston acceleration exceeds this quantity. Whether this occurs (or not) will depend on the frequency and amplitude of oscillation as shown in Section 2.3.2 of the main work. Since the surface motions on both sides of the U-tube are directionally opposite then the RT instability has two windows of potential influence per period of oscillation.

Although referenced as early as 1984 in relation to liquid piston Stirling engines (West, 1984), the relevance and significance of RT instability in liquid pistons has not been heavily investigated. The main reason for this appears to result from the relatively low frequencies typical of the majority of Fluidyne systems (as a consequence of their frequency having primary dependence on liquid piston dimensions). In order for the RT instability to potentially occur then the piston acceleration must exceed gravity. With typical frequencies on the order of 1 Hz (as documented by West) this corresponds to a minimum stroke of 20 cm before the onset of RT instability is possible. In the case of Fluidyne machines in the Siemens-Stirling configurations, however, the operational frequencies have a greater dependence on charge pressure—meaning RT instability can be an important consideration.

The effects of surface tension have also been investigated. Theoretically, they can lead to stabilization of perturbations with wavenumbers larger than a certain cut-off value:

$$k_c = \sqrt{\frac{\rho\alpha}{\sigma}}$$

where σ is the surface tension (N/m). In 2003, the structural stability of liquid pistons subjected to unsteady acceleration was investigated (Stebnovskii, 2003). RT instability

was observed for water liquid-pistons accelerating inside a cylindrical channel. The same experiments were also conducted with glycerine liquid-pistons, where the higher viscosity liquid counteracted the surface perturbation growth, and remained stable for the particular loading scheme investigated.

References

Bellman, R., & Pennington, R. H. (1954). Effect of surface tension and viscosity on Taylor Instability. *Quart. Appl. Math., 12* (1954), 151-162. Retrieved from http://www.rand.org/pubs/papers/P403.html.

Birkhoff, G. (1954). Note on Taylor instability. *Quart. Appl. Math.*, 12, 306-309.

Garabedian, P. R. (1957). On steady state bubbles generated by Taylor instability. *Proceedings of the Royal Society of London. Series A. Mathematical and Physical Sciences, 241*(1226), 423-431. doi:10.1098/rspa.1957.0137

Kruskal, M., & Schwarzschild, M. (1954). Some Instabilities of a Completely Ionized Plasma. *Proceedings of the Royal Society of London. Series A. Mathematical and Physical Sciences, 223*(1154), 348. doi:10.1098/rspa.1954.0120

Rayleigh. (1882). Investigation of the character of the equilibrium of an incompressible heavy fluid of variable density. *Proceedings of the London Mathematical Society, s1*-14(1), 170-177. doi:10.1112/plms/s1-14.1.170

Taylor, G. (1950). The Instability of Liquid Surfaces when Accelerated in a Direction Perpendicular to their Planes. I. *Proceedings of the Royal Society of London. Series A. Mathematical and Physical Sciences, 201*(1065), 192. doi:10.1098/rspa.1950.0052

Stebnovskii, S. V. (2003). Structural stability of unsteadily accelerated liquid pistons. *Fluid Dynamics, 38*(6), 832-838. doi:10.1023/B:FLUI.0000015222.32547.dd

West, C. D. (1984). Liquid-piston Stirling Machines. *2nd International Conference on Stirling Engines*, Shanghai, China.